広島大学学位請求論文

Stable isotopic and speciation studies on neo-rare earth element geochemistry and paleoenvironmental analysis

（安定同位体と化学種解析に基づく新しい希土類元素地球化学および古環境解明）

２０１３年

広島大学大学院理学研究科

地球惑星システム学専攻

中田　亮一

目次

1. 主論文

Stable isotopic and speciation studies on neo-rare earth element geochemistry and paleoenvironmental analysis
(安定同位体と化学種解析に基づく新しい希土類元素地球化学および古環境解明)

2. 公表論文

(1) R. Nakada, Y. Takahashi, G. Zheng, Y. Yamamoto, H. Shimizu (2010)
Abundances of rare earth elements in crude oils anf their partitions in water.
Geochemical Journal, 44 (5), 411−418.

(2) R. Nakada, Y. Takahashi, U. Tsunogai, G. Zheng, H. Shimizu, K.H. Hattori (2011)
A geochemical study on mud volcanoes in the Junggaer Basin, China.
Applied Geochemistry, 26 (7), 1065−1076.

(3) R. Nakada, Y. Takahashi (2013)
Thermogenic Methane with Secondary Alteration in Gases Released from Terrestrial Mud Volcanoes.
Hydrocarbon (Edited by V. Kutcherov and A. Kolesnikov), 29−42.

(4) R. Nakada, Y. Takahashi, M. Tanimizu (2013)
Isotopic and speciation study on cerium during its solid-water distribution with implication for Ce stable isotope as a paleo-redox proxy.
Geochimica et Cosmochimica Acta, 103, 49−62.

(5) R. Nakada, M. Tanimizu, Y. Takahashi (2013)
Difference in the stable isotopic fractionations of Ce, Nd, and Sm during adsorption on iron and manganese oxides and its interpretation based on their local structures.
Geochimica et Cosmochimica Acta, 121, 105−119.

3. 参考論文

(1) G. Etiope, R. Nakada, K. Tanaka, N. Yoshida (2011)
Gas seepage from Tokamachi mud volcanoes, onshore Niigata Basin (Japan): Origin, post-genetic alterations and CH_4-CO_2 fluxes.
Applied Geochemistry, 26 (3), 348−359.

主論文

Stable isotopic and speciation studies on neo-rare earth element geochemistry and paleoenvrionmental analysis

by

Ryoichi Nakada

Department of Earth and Planetary Systems Science,

Graduate School of Science,

Hiroshima University

Preface

In this decade, the development of analytical devices, especially inductively coupled plasma mass spectrometry (ICP-MS), makes several researchers misunderstand that “Rare earth element (REE) geochemistry is over”. It is true that the determination of the abundances of REEs in samples became much easier than in the past, which makes REE pattern as normal data in geochemistry. However, it also appears that some studies lack the knowledge on the physicochemical properties and proper analytical skills. It seems that such a bad practice has made REE geochemistry less effective. This PhD thesis attempts to correct the misunderstanding by presenting that REE geochemistry is still a useful and powerful tool to discuss the origin and reaction processes that samples had experienced. To begin with, fundamental things of REEs which are rarely mentioned in review articles, a history of their discovery, chemical properties, REE patterns, and analytical methods, are described in Chapter 1.

In Chapter 2, the cause of positive europium (Eu) anomaly is examined. The positive Eu anomaly is often observed for seafloor hydrothermal fluids in mid-ocean ridge. The preferential dissolution of plagioclase was originally suggested, whereas the formation of chloride complex which is extraordinary stable for Eu^{2+} was the alternative cause raised in this decade. Water-rock interaction experiments at three different reaction temperatures are performed in this Chapter. To clarify whether the mineralogy or stability dominates the Eu anomaly, ultra-pure water or 0.7 M NaCl solution contacted with basaltic glass or basalt that crystallized out plagioclase is used in the experiment.

Along with Eu, anomalous concentration of cerium (Ce) relative to its neighboring elements is often observed in REE pattern. In Chapter 3, three important geochemical parameters, namely, abundance, stable isotope ratio, and chemical speciation, are obtained for Ce to derive more information from the Ce anomaly. Adsorption and precipitation experiments simulating three different redox conditions are performed. This study exhibits first data on stable isotopic fractionation of REE and

discusses its possible application as a redox tracer.

The Ce isotopic fractionation data, however, were inconsistent with the previous studies reported for other cations and did not follow the most important rule governing the equilibrium isotopic fractionation. Thus, the isotopic fractionation of neighboring REEs is examined to compare the fractionation data with that of Ce in Chapter 4. Adsorption experiments with neodymium (Nd) and samarium (Sm) on hydrous ferric oxyhydroxide (ferrihydrite) and amorphous manganese oxide (δ-MnO_2) are performed since these minerals are considered as a major sink for REE in ocean. The stable isotopic fractionation data is interpreted by their chemical speciation including coordination number and bond length using X-ray absorption fine structure (XAFS) spectroscopy analysis. This study indicates that in-depth analysis of the coordination environment is important to determine the mechanisms behind equilibrium isotopic fractionation.

An interesting subject that has long been neglected in REE geochemistry, REEs in crude oil, is examined in Chapter 5. The molecular structure of sampled crude oils is determined using nuclear magnetic resonance (NMR) spectroscopy on carbon atom (^{13}C-NMR). A comparison of REE concentrations in oils with those of coexisting water and mud provides important findings on the origin and complex formation of REE.

The oils used in the study described in Chapter 5 were not completely matured. In Chapter 6, therefore, the behavior of REE during the maturation process of organic materials, which occurs after the sedimentation of mudstone or sandstone, is examined by measuring REE concentration in oil samples collected from five oil fields in Japan combined with the laboratory experiment simulating the release of REE from organic phase during the maturation. Studies in Chapters 5 and 6 can bring a new possibility on the fusion of organic and inorganic geochemistry.

As such, studies performed from Chapters 2 to 6 shows new possibilities for REE geochemistry. These studies are linked to the Chapters 8 and 9 via Chapter 7. In Chapter 7, the formation process of Mn carbonate nodules, namely whether the Mn carbonate was formed primarily or secondarily, is examined as an application of Ce

isotope ratio in geological study. This study performs geological, or sedimentrogical, methods including microscopic observation and examination of radiolarian age combined with geochemical data such as REE pattern, XAFS analysis, adsorption experiment, thermodynamic calculation, and stable isotope measurement.

The rest of the thesis, Chapters 8 and 9, showed that the XAFS analysis is a powerful geochemical tool to determine the Fe species in chert samples and brings a new perception for geological study. The first attempt to determine Fe species in chert samples using XAFS analysis was performed in Chapter 8 to reveal the pelagic environment during the Carnian. This study shows the pelagic sedimentary response to the continental climate changes. In Chapter 9, Fe and sulfur (S) species are determined to reveal the oceanic redox change during Toarcian. These studies show that the application of XAFS for chert samples to determine the chemical species is a very important and powerful tool to study the paleoenvironment.

This thesis attempts to clarify the behavior of REEs in various oceanic and sedimentary environments from ridge to subduction (Fig. 0–1). In addition, the estimation of the paleoenvironment based mainly on the chemical species of Fe and S determined using XAFS is performed for the future application of stable isotope geochemistry for REEs.

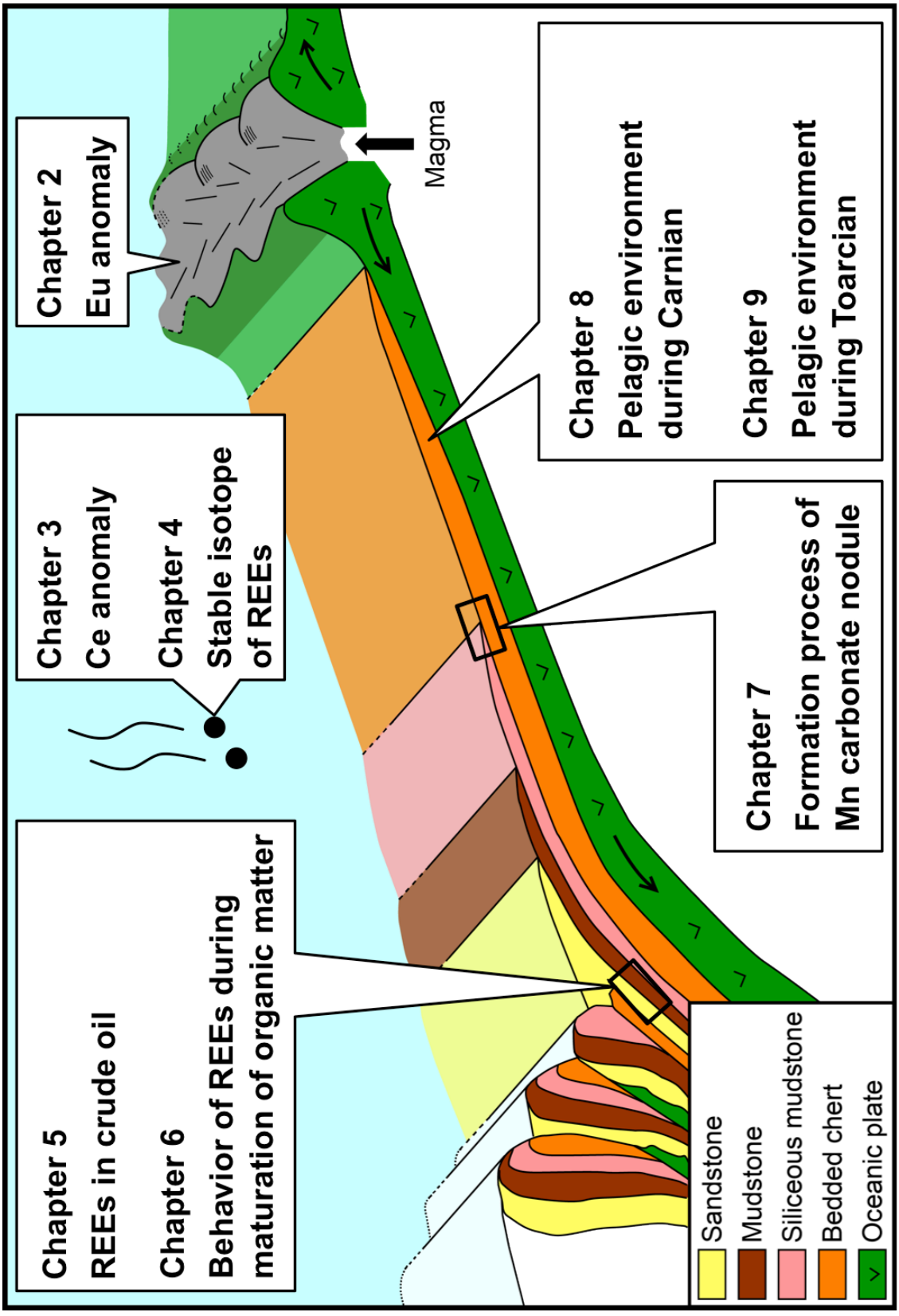

Fig. 0–1. Schematic illustration of the studies conducted in this PhD thesis.

Contents

Abstract

REE, a collection of seventeen chemical elements in the periodic table located at the group three such as scandium (Sc), yttrium (Y), and fifteen lanthanides, have been used in various geochemical studies to discuss the origin and several reaction processes that samples had experienced. After the first discovery of Y in 1794, it had taken 153 years to discover all the REEs. The similar chemical properties made the separation of REE difficult, whereas the properties make REE the most unique geochemical tool. The discovery of REE pattern has greatly contributed to the development of geochemistry.

Chapter 2 touches upon the cause of positive Eu anomaly. Water-rock reaction experiment was performed using synthesized basaltic glass and basalt that crystallized out plagioclase as the solid phase. Meanwhile, ultra-pure water or 0.7 M NaCl solution was used for the liquid phase. Comparison of each combination showed that the basalt containing plagioclase released larger abundances of REEs than the basaltic glass irrespective of any solution conditions. The degree of Eu anomaly assessed by Eu/Eu* value was smaller when 0.7 M NaCl solution was used for liquid phase for both solid phases. Therefore, it is suggested that the possible positive Eu anomaly caused by the formation of stable Cl complex was less effective in this experiment.

Similar to Eu, Ce can have anomalously high or low concentrations relative to its neighboring elements, lanthanum (La) and praseodymium (Pr), because of its chemical properties; this phenomenon is known as the Ce anomaly. This redox-sensitive property of Ce allows the estimation of the redox state of paleo-ocean environments and the evolution of the atmosphere. However, a consideration of only the relative abundance of Ce may lead to an incomplete understanding of its oxidation process. In Chapter 3, three important geochemical parameters, namely, abundance, stable isotope ratio, and chemical speciation, were obtained for Ce to derive more information from the Ce anomaly. In the adsorption experiments, the distribution pattern of REEs suggests the oxidative scavenging of Ce by δ-MnO_2. This finding is further supported by the presence of Ce(IV), as detected by the X-ray absorption near-edge structure

(XANES) spectra, which is in agreement with previous studies. However, the REE distribution pattern combined with the XANES spectra of the Ce adsorbed on ferrihydrite indicated that Ce may not have been oxidized by ferrihydrite in the Ce/ferrihydrite system during our experimental period. Assuming equilibrium fractionation, the mean isotopic fractionation factors between the liquid and solid phases (α_{Lq-So}) of (i) Ce adsorbed on ferrihydrite, (ii) spontaneous precipitation of Ce, and (iii) Ce adsorbed on δ-MnO_2 were 1.000145 (±0.000022), 1.000196 (±0.000031), and 1.000411 (±0.000079), respectively. These results indicate that the degree of isotopic fractionation of Ce between the liquid and solid phases becomes larger as the redox condition becomes more oxic in the following order: adsorption without oxidation < spontaneous precipitation < oxidative adsorption. Previously, the appearance of the Ce anomaly and/or XANES analysis constituted the tools available for exploring the redox state. This study, however, suggests that the stable isotope ratio of Ce can be used to clearly distinguish spontaneous precipitation from oxidative adsorption on δ-MnO_2, that occur under more oxic conditions than the Ce(III)/Ce(IV) boundary. The results obtained in Chapter 3 suggest that the combination of the stable isotope ratio and chemical state of Ce can be used to classify the redox condition into three stages based on Ce geochemistry, thereby offering a powerful tool for exploring redox conditions in paleo-ocean environments.

As described in Chapter 3, many elements have become targets for studies of stable isotopic fractionation with the development of various analytical techniques. Although several chemical factors that control the isotopic fractionation of heavy elements have been proposed, it remains controversial which properties are most important for the isotopic fractionation of elements. In Chapter 4, the stable isotopic fractionation of Nd and Sm during adsorption on ferrihydrite and δ-MnO_2 was examined to compare the stable isotopic fractionation data of Ce. This examination was combined with speciation analyses of these ions adsorbed on the solid phases by extended XAFS (EXAFS) spectroscopy. Neodymium isotope ratios for Nd on ferrihydrite and δ-MnO_2 systems were, on average, 0.166 and 0.410‰ heavier than those of the liquid phase, which corresponds to mean isotopic fractionation factors

between the liquid and solid phases (α_{Lq-So}) of Nd on ferrihydrite and δ-MnO_2 of 0.999834 (2σ = ± 0.000048) and 0.999590 (2σ = ± 0.000106), respectively. Similarly, averaged Sm isotope ratios on ferrihydrite and δ-MnO_2 were 0.206 and 0.424‰ heavier than those of the liquid phase and the corresponding α_{Lq-So} values were 0.999794 (± 0.000041) and 0.999576 (± 0.000134), respectively. These results indicate that the directions of isotopic fractionation in the Nd and Sm systems are the opposite to that recently found for Ce(III) systems despite the similar chemical characteristics of rare earth elements. EXAFS analyses suggest that the bond length of the first coordination sphere (REE–O bond) of Nd and Sm adsorbed on δ-MnO_2 is shorter than that of their aqua ions, although this was not clear for the ferrihydrite systems. The shorter bond length relative to the aqua ion is indicative of a stronger bond, suggesting that the equilibrium isotopic fractionation for the Nd and Sm systems can be governed by bond strength as has often been discussed for isotopic fractionation in solid−water adsorption systems. Meanwhile, EXAFS analyses of the Ce/ferrihydrite system showed a distorted structure for the first coordination sphere that was not observed for Ce^{3+} aqua ions. Such distortion was also observed for La adsorption on ferrihydrite and δ-MnO_2. In addition, previous studies have suggested a high stability of the hydrated state for La and Ce in terms of Gibbs free energy change. Thus, this study suggest that the difference in the stable isotopic fractionation for Ce (and predicted for La) vs. Nd and Sm can be explained by (i) the shorter bond lengths of adsorbed relative to dissolved species for Nd and Sm and (ii) the distorted structure of adsorbed Ce (and La) species and high stability of the aqua Ce ion.

Aside from the stable isotope study, there is another subject that has a lot of potential, REEs in crude oil. Patterns of the entire range of REE in crude oils and coexisting water, collected from mud volcanoes in Xinjiang Province of China, are reported in Chapter 5. Crude oils showed light REE enriched patterns with flat or depleted patterns in heavy REE, when normalized to chondrite. The REE concentrations in crude oils were larger than those in coexisting water by a factor of more than one hundred. Considering the hydrophobicity of oil and the high ionic characteristics of REE, it is strongly suggested that REE form complexes with ligands present in the

crude oils. Based on the ^{13}C NMR spectroscopy, small amounts of phenol and carboxyl groups were found in the crude oil samples, which could possibly provide complexing sites for REE. REE patterns of crude oils are similar to those of coexisting mud samples collected from the same mud volcanoes, which suggests that the REE in crude oils are derived from rocks and sediments where crude oils were generated.

In Chapter 6, the abundance of REEs in crude oils collected from 5 oil fields in Japan was determined to examine the behavior of REEs during the maturation of organic materials. The ^{13}C-NMR does not show peaks corresponding to the existence of carboxyl groups in crude oils used in this study. Abundances of REEs in oils without containing carboxyl groups are about three orders of magnitude lower than those having carboxyl groups (Chapter 5), suggesting that the existence of carboxyl group plays an important role for REE retention in crude oil. REE distribution experiment on a slate in a solution containing humic acid shows that REEs are released from organic phase and re-distributed to the solid phase during decomposition of carboxyl groups. The REE abundances in crude oils with or without containing carboxyl groups suggest that the production of a barrel of crude oil can be associated with release of 16 g REE from organic phase. Considering the reserve estimate of oil in the world, such amount may affect the global budget of REE. In addition, other metal elements behaving similarly to the REE may also be released from organic phase whereas those behaving differently to the REE can be retained in the organic phase.

In Chapter 7, the formation process of Mn carbonate nodules, namely whether the Mn carbonate was formed primarily or secondarily, was examined as an application of Ce isotope ratio in geological study. The optical observation of thin sections shows that Mn carbonate nodules are comprised of with abraded grains of rhodochrosite spherule with radiolarians and are sedimentarily embedded in siliceous mudstone. Microfossil radiolarians from the Mn carbonate nodules and the host red siliceous mudstone are dated as the Bajocian, but radiolarians in the nodules are somewhat older than those in the host red siliceous mudstone. XANES analysis showed dominance of trivalent Ce at present, despite of a positive Ce anomaly in the PAAS-normalized REE pattern of Mn carbonate. The REE adsorption experiment on synthesized $MnCO_3$ does

not show any distinctive positive Ce anomaly and a thermodynamic calculation suggests the possible coexistence of authigenic rhodochrosite and spontaneous oxidation of Ce. The leaching experiment that can selectively decompose carbonate phase demonstrated no Ce anomaly in the carbonate phase of Mn carbonate and poor contribution to the bulk REE concentration. In addition, Mn carbonate nodule was enriched in the heavier Ce isotopes than siliceous mudstone beyond the analytical uncertainty. The most plausible account of all the observational and experimental results is that rhodochrosite grains were primarily formed on the depositional site and subsequently transferred to the different site where siliceous mudstone was deposited.

Chapter 8 focuses on the Carnian pluvial event (CPE) which is a drastic environmental change that occurred in the shallow western Tethys during the Carnian (Late Triassic). Whether the CPE was a global event that included the pelagic environment or not is not clear. To reveal the pelagic environment during the Carnian, XAFS analysis was used to determine the Fe species in chert samples collected from the Ladinian−Carnian strata in the Tamba-Mino-Ashio Belt, Japan. The XANES analysis showed that all the red cherts contain hematite with a combination of clay minerals, such as illite, chlorite, and smectite. The existence of these minerals was identified using EXAFS. The XANES analysis of the green and the white cherts did not show any hematite signatures, while the EXAFS analysis indicated increasing amounts of chlorite. The stratigraphic change in the Fe-bearing compositions observed in this study can be divided into three stages: (i) a stage where a relatively stable mineral composition (chlorite + illite + hematite) was observed in cherts deposited during the early to middle Carnian, (ii) the abrupt change in mineral composition (lack of chlorite and appearance of smectite) observed in the middle area in the studied section and corresponding to the middle Carnian, and (iii) the recovery of the previous stable mineral composition during the late Carnian. These variations in the mineralogical composition of pelagic cherts suggest that the continental climate conditions changed during the Carnian, and different clay fractions were delivered to the pelagic region. These data, combined with the results of previous studies performed around the continental realm, can be interpreted as follows: (i) there was a relatively stable and dry climate before the CPE,

(ii) there were increasing amounts of precipitation owing to the CPE, and (iii) the climate returned to the dry conditions similar to those prior to the CPE.

Chapter 9 focuses on the Toarcian oceanic anoxic event (T-OAE), the disorder of the global ocean-atmosphere system occurred in the Early Toarcian (Early Jurassic). Several studies have focused on this topic based mainly on the carbon isotope ratio and modeling. However, discussion based on the speciation of redox-sensitive element has not sufficiently been performed. This study, therefore, aims to reveal the Fe and S species in chert samples collected from the Tamba-Mino-Ashio Belt of Japan using XAFS analysis. Iron K-edge XANES showed that pyrite dominated the Fe species in chert samples, which was further confirmed by EXAFS analysis. The EXAFS analysis of black chert suggests that the small amount of Fe exists as Fe^{3+} form, which can be due to (i) slightly oxidized during the weathering, and/or (ii) adsorption of Fe^{3+} on organic matters. Sulfur K-edge XANES also supported the dominance of pyrite. However, small amount of sulfate (S^{6+}) species were identified in both black and gray cherts. The amount of sulfate fraction increased with depositional order, namely, the lowest sulfate fraction was estimated for gray chert deposited before the deposition of black chert which suggested to be formed during T-OAE. Meanwhile, the largest contribution of sulfate species was observed from gray chert structurally above the black chert. These facts suggest that the gradual recovery, namely neutralization, from oceanic acidification occurred during the T-OAE.

Chapter 1

History and development of rare earth element geochemistry

1.1 What is rare earth element?

The International Union of Pure and Applied Chemistry (IUPAC) defines rare earth elements (REEs) as a collection of seventeen chemical elements in the periodic table located at the group three such as scandium (Sc), yttrium (Y), and fifteen lanthanides (Connelly et al., 2005). Although lanthanide means "like lanthanum (La)" and as such should not be included, it has become included by common usage. Scandium and Y are included in REEs since they tend to occur in the same ore deposits as the lanthanides and exhibit similar chemical properties. A number of review articles and books of REE geochemistry have been published in the past (e.g., Haskin and Paster, 1979; Hanson, 1980; Henderson, 1984; Taylor and McLennan, 1988; Lipin and McKay, 1989). It is unnecessary to merely duplicate these descriptions. However, these reviews did not mention more fundamental things of REEs. In this chapter, therefore, a history of their discovery, chemical properties, REE patterns, and analytical methods are described.

1.2 Discovery of rare earth element

It all began when Carl Axel Arrhenius (1757–1824), a lieutenant in the Swedish army, found an interesting and dense black mineral in a small feldspar and quartz mine in a village of Ytterby, Sweden in 1787 (Fig. 1–1). The black mineral named as ytterbite by Arrhenius was examined by the Finnish chemist Johan Gadolin (1760–1852). He found that the black mineral contained 38% of a new "earth type" element and named this new earth as ytterbia (Gadolin, 1794). His analysis was confirmed three years later by the Swedish chemist Anders Gustaf Ekeberg (1767–1813) who shortened the name to yttria (currently called as yttrium; Y). It is interesting to note that the word Ytterby means outer village and is a common name in Sweden. However, it is easy to find the

true “Ytterby Mine”, since a number of streets around the Ytterby Mine are named after elements such as yttrium, terbium, ytterbium, and tantalum (though tantalum is not REE, it was also discovered from Ytterby Mine), feldspar (fältspat), mica (glimmer), the mine itself (gruva), and gadolinite (the name of the black mineral originally called as ytterbite had finally renamed as gadolinite; see below) (Fig. 1–1C; Marshall and Marshall, 2001).

On the other hand, Vilhelm Hisinger (1766–1852), a Swedish ironmaster, together with the young chemist Jöns Jakob Berzelius (1779–1848) analyzed a sample named as the “tungsten (heavy stone in Swedish) from Bastnäs”, later called as cerite, and found another earth type element similar to yttria in 1803. They firstly named the element as ceria (= cerium; Ce) in honor of Ceres which is the first asteroid discovered in 1801 (Hisinger and Berzelius, 1804). Independently, the German chemist Martin Heinrich Klaproth (1743–1817) also analyzed the cerite and found the light brown colored element which Hisinger and Berzelius also found (Klaproth, 1803). Klaproth also renamed the black mineral found in the Ytterby into gadolinite to commemorate Johan Gadolin.

However, neither yttria nor ceria was a “pure” new element. In 1839, Carl Gusstav Mosander (1797–1858), a Berzelius’s student, extracted a new earth type element from ceria. He separated ceria into pure ceria and the new earth, lanthana (= lanthanum; La), named after the Greek word *lanthanein* (hidden), because it was hidden in ceria for 36 years (Mosander, 1839). Mosander also found that the lanthana contained another earth which he names as didymia (= didymium; Di) taken from a Greek word *didymos* meaning twins because it closely resembled lanthana (Mosander, 1842). Mosander next had interests in the yttria and separated it into three fractions: (i) a deep yellow peroxide was named as erbia (= erbium; Er), (ii) a rosy colored salt was named as terbia (= terbium; Tb), and (iii) a colorless oxide fraction was continued to be called as yttria (Mosander, 1843). Since the two new earths were separated from yttria, Mosander derived the names of them from the village Ytterby. However, the names of erbia and terbia became interchanged due to the similar properties of them. In 1862, the Swiss chemist Marc Delafontaine (1837–1911) reexamined yttria and found the yellow

peroxide. Because the name erbium had now been assigned to the rose colored oxide, he re-introduced the name terbium for the yellow peroxide. Thus, the original names given by Mosander are now switched.

A growing number of elements were discovered in the 19th century and the REEs were not exceptional. Before 1800, only 34 elements including one REE (yttria) were identified, which was increased to 84 elements at the dawn of 20th century (Krebs, 2006; Fig. 1–2). The invention of the spectroscope in 1859 by the German chemist Robert Wilhelm Bunsen (1811–1899) and the physicist Gustav Robert Kirchhoff (1824–1887) helped the discovery of the element. In particular, it was important for the identification of REEs. In 1878, the Swiss chemist Jean-Charles Galissard de Marignac (1817–1894) showed that Mosander's terbia, now erbia, could be separated into two earths: the rose-colored earth he continued to call erbia and the colorless one he named ytterbia (= ytterbium; Yb) also after the Ytterby village (Marginac, 1878). This erbia was further separated into a purified erbia and two new earths in the following year by the Swedish chemist Per Theodor Cleve (1840–1905) (Cleve, 1879a). He named a brownish precipitate as holmia (= holmium; Ho) which is the Latin name of Stockholm where he was born, and the greenish fraction as thulia (= thulium; Tm) taken after Thule, the old name for Scandinavia. In the same year, the Swedish chemist Lars Fredrik Nilson (1840–1899) found traces of an unknown earth included in ytterbia which he named scandia (= scandium; Sc) after *Scandia*, a Latin name for Scandinavia (Nilson, 1879). Cleve immediately proved that scandia was Mendeleev's hypothetical element called ekaboron (Cleve, 1879b). Also in the same year, the French chemist Paul-Émile Lecoq de Boisbaudran (1838–1912) analyzed a mineral called samarskite which was originally discovered in Southern Ural Mountains and noted that another new earth precipitated before didymia when ammonium hydroxide was added. The new earth was named as samaria (= samarium; Sm) following to the name of the mineral (de Boisbaudran, 1879). In 1880, Marignac split terbia into pure terbia and an unknown element which he provisionally named Yα (Marginac, 1880). Six years later, in 1886, Lecoq de Boisbaudran separated a pure form of the earth Yα from Mosander's didymia. Boisbaudran proposed and Marignac agreed to rename Yα to gadolinium (Gd) in honor

of Johan Gadolin (de Boisbaudran, 1886a). In the same year, Boisbaudran also found that the Clave's holmia was impure and separated a new oxide named dysprosia (= dysprosium; Dy) derived from the Greek *dysprositos* meaning difficulty to obtain (de Boisbaudran, 1886b). One year before the achievement by Lecoq de Boisbaudran, one REE was removed from the periodic table. An Austrian chemist Carl Auer von Welsbach (1858–1929) succeeded to separate didymia into two new earths. The less abundant pale green salt was named as praesodymia (= praseodymium; Pr) meaning green didymia, whereas the more abundant new earth was named as neodymia (=neodymium; Nd) meaning new didymia (von Welsbach, 1885). As seen above, 13 REEs were found within 100 years, meaning that 14 of 17 REEs were identified by the end of the 19th century. In particular, 9 REEs were discovered after the invention of the spectroscope.

In 1896, the French chemist Eugène-Anatole Demarçay (1852–1903) constructed an improved induction coil that produced extremely hot, luminous, globular sparks from electrodes of high-purity platinum and found a new element between samarium and gadolinium (Demarçay, 1896). He made a series of extensive fractionations of an impure samarium-magnesium nitrate and resulted in the discovery of a new rare earth named europium in honor of the continent of Europe where the element was discovered (Demarçay, 1901). In 1907, the French chemist Georges Urbain (1872–1938) and Auer von Welsbach independently demonstrated that ytterbia contains one more oxide. Urbain named the new element as lutecium, after the ancient name for his native city, Paris (Urbain, 1907), whereas Auer von Welsbach named as cassiopium, after the constellation Cassiopeia (von Welsbach, 1908).

It took 40 years to identify the last REE, because, as currently known, the element does not have any stable isotopes. However, an existence of the last REE on atomic number 61 was predicted in 1914 using the X-ray spectra. The English physicist Henry Gwyn Jeffreys Moseley (1887–1915) found that the square root of the multiplicative inverse of frequencies of the characteristic X-ray emitted from elements were proportional to the element's atomic number (Moseley's law; Moseley, 1913). Next year, he extended the experiment from aluminum to gold and suggested the

possible occurrence of three elements on the atomic number of 43, 61, and 75 (Moseley, 1914). The isolation and identification of element 61 was finally achieved by three American chemist at Oak Ridge National Laboratory, Jacob Akiba Marinsky (1918–2005), Lawrence Elgin Glendenin (1918–2008), and Charles DuBois Coryell (1912–1971). Although the element was separated and analyzed from the fission products of uranium fuel irradiated in a graphite reactor in 1945, they could not announce their findings until 1947 because of critical research during World War II (Marinsky et al., 1947). The name of the element, initially prometheum, was derived from Prometheus (meaning "a person of foresight" in Greek), the Titan in Greek mythology who brought fire down to humans. The IUPAC later changed the spelling to promethium to conform to the other elements.

The history of the discovery of REEs is, as described above, long and complicated (Table 1–1, Fig. 1–3). In particular, the removal of didymia from periodic table, originally found in 1842 and meant the twin of lanthana, shows how similar chemical characteristics the REEs have, because didymia was actually a mixture of Sm, Pr, Nd, Gd, and Eu. A careful look on Fig. 1–3 notifies that the lanthanide having smaller atomic number, La-Eu, were separated from cerite, while those of larger (Tb-Lu) with Sc and Y were split from gadolinite (ytterbite). Only Gd locating at the middle of lanthanide was discovered and purified from both gadolinite and cerite. This fact is not a coincidence, but closely related to the chemical characteristics of REEs. Therefore, the properties are described in the following section.

1.3 Chemical properties of REEs

Lanthanum is the first member of the third series of transition elements which are made of elements with unfilled f-orbitals. Lanthanides (Ln) can only be distinguished by their 4f-electrons (Table 1–2), hence they are often called 4f-elements, which explains their close similarity. Atoms generally have electrons in orbitals which locate closely to their nucleus. In contrast, it should be noted that, Ln have electrons in outer orbits than 4f before the complete filling of 4f orbital. This phenomenon is caused

by the higher orbital energy for 4f than the outer orbitals such as 5s and 5p. The spatial extent of 4f orbitals locates mainly inner than those of 5s, 5p, 5d, and 6s, meaning that it can be considered as isolated electron system.

The electronic configuration of Sc^{3+} ion is exactly the same with that of argon atom ($1s^2 2s^2 2p^6 3s^2 3p^6$), while that of Y^{3+} ion is the same with krypton ($1s^2 2s^2 2p^6 3s^2 3p^6 3d^{10} 4s^2 4p^6$). Lanthanum ion shows the same electronic configuration with xenon ($1s^2 2s^2 2p^6 3s^2 3p^6 3d^{10} 4s^2 4p^6 4d^{10} 5s^2 5p^6$), while Ce^{3+} fills $4f^1$ between $4d^{10}$ and $5s^2$. The electrons religiously occupy 4f orbitals from Pr^{3+} to Lu^{3+} except for Gd^{3+}. Given that 14 electrons can occupy the f-shell, the complete occupation is only achieved by Lu (Table 1–2). Thus, electrons are completely filled for Sc^{3+}, Y^{3+}, and Lu^{3+} ions, and they are considered as the typical trivalent alkali earth ions. Hence, IUPAC recommends that it is better to place Lu instead of La in the periodic table.

Two important characteristics, ionic radius and valence state, make REEs useful geochemical tool. It is generally true for most ions that with increasing atomic number, the number of electrons also increased. To contain the electrons in their orbits, the ionic radii become larger with increasing period (Fig. 1–4). The exceptions are observed for lanthanide and actinide, which have incompletely filled f orbits. Electrons in the 4f orbital cannot shield the nuclear charge by increasing atomic number, which resulted in the attraction of lanthanide's electron cloud. This characteristic, named as the lanthanide contraction, makes the REEs unique, because REEs are generally stable at trivalent state. Taking into a concept of ionic potential, charge/radius ratio, the heavier the REEs, the higher the ionic potential, which leads to the more strong bonding in a complex. Another important thing is the reduction/oxidation (redox) sensitive character. Higher ionization potentials from Ln^{2+} to Ln^{3+} are observed for Eu and Yb, meaning that these two ions can stably form divalent ions (Fig. 1–5). In contrast, lower ionization potentials for Ce, Pr, and Tb from trivalent to tetravalent state indicates that these ions can be stable in tetravalent state. Although the formation of Yb^{2+}, Pr^{4+}, and Tb^{4+} is theoretically possible, Eu^{2+} under reducing condition and Ce^{4+} under oxidizing conditions are more common in natural systems. In any case, the systematic distribution of REEs due to the lanthanide contraction and the redox sensitive characteristics make

REEs the most unique and useful geochemical (and cosmochemical) tracer in natural environment.

1.4 REE pattern

In addition to the chemical properties described above, there is a way to handle and compare the data among various types of samples, the normalized REE pattern, which makes REE unique beyond comparison. In general, even-numbered elements are more abundant than the odd-numbered elements due to the greater stability of even-numbered nuclides in the nucleosynthesis (Oddo-Harkins effect). Lanthanide also shows the Oddo-Harkins effect (Fig. 1–6A). However, a breakthrough idea was suggested by a Japanese researcher in 1962, which is now commonly used as a normalizing method of REE data (Masuda, 1962). This simple but powerful method consists of forming a ratio of one REE concentration to another (Fig. 1–6B). The procedure includes several advantages: (i) the Oddo-Harkins effect is cancelled out and a smooth curve is provided due to the similar chemical properties among REE^{3+}, (ii) if normalized by the same material, the patterns enable us to compare different samples, and (iii) relative degrees of enrichment or depletion is displayed. A comparing material is selected to reflect the fractionation on which one wants to focus. For instance, petrological (and cosmochemical) studies prefer to use CI-chondrite as the normalizing material, whereas shale is commonly used in studies on sedimentary rocks.

Several characteristics can be found in the REE pattern (Fig. 1–6B). The chondrite-normalized value of Ce in seawater is plotted out of smooth curve between La and Pr. This is caused by the chemical property of Ce. As described in the section above, Ce can be stable in tetravalent state under oxic condition with very low solubility compared to the other trivalent REEs. This fact means that, if Ce is oxidized to tetravalent state and adsorbed on particulate matters, Ce is effectively removed from seawater. As a result, Ce concentration in seawater becomes lower than the other REEs when normalized to chondrite or shale. Similarly, Eu also shows depleted values in normalized REE pattern due to its stability in divalent form. In contrast, REE patterns of

plagioclase and feldspar show enriched Eu values (Gromet and Silver, 1983). These two behaviors are called as Ce and Eu anomalies and have been quantified as Ce/Ce* and Eu/Eu*. In the case of Ce, Ce* is the theoretical value assuming no anomaly, namely a smooth pattern between La and Pr, which is calculated as:

$$Ce/Ce^* = Ce_N/\sqrt{La_N \times Pr_N}, \quad (1\text{–}1)$$

where the subscript N denotes normalized values. It is true that several methods have been established to evaluate the Ce/Ce* value;

$$Ce/Ce^* = 3Ce_N/(2La_N + Nd_N) \text{ (Elderfield and Greaves, 1982)}, \quad (1\text{–}2)$$

$$Ce/Ce^* = \log[3Ce_N/(2La_N + Nd_N) \text{ (Wright et al., 1987)}, \quad (1\text{–}3)$$

$$Ce/Ce^* = 5Ce_N/(4La_N + Sm_N) \text{ (Toyoda et al., 1990)}, \quad (1\text{–}4)$$

$$Ce/Ce^* = Ce_N/(La_N^{2/3} + Nd_N^{1/3}) - 1 \text{ (Grandjean-Lécuyer et al., 1993)}, \quad (1\text{–}5)$$

or more simply, the arithmetic mean is also widely used as follows:

$$Ce/Ce^* = Ce_N/[(La_N + Pr_N)/2]. \quad (1\text{–}6)$$

However, a geometrical mean, or Eq. 1-1, should be used because REE patterns are generally plotted on a logarithmic scale (Taylor and McLennan, 1988). If the Ce/Ce* value is larger than 1, Ce is plotted above the line connecting La and Pr, which is called as positive Ce anomaly. Meanwhile, if the Ce/Ce* value is lower than, Ce is plotted below the La-Pr line such as chondrite-normalized REE pattern of seawater (Fig. 1–6B), which is called as negative Ce anomaly. Similarly, Eu/Eu* value should also be evaluated by

$$Eu/Eu^* = Eu_N/\sqrt{Sm_N \times Gd_N}. \quad (1\text{–}7)$$

Another important character is tetrad effect, which was firstly discovered in the liquid-liquid extraction system of REE (Peppard et al., 1969). The effect causes four separate curves consisting of La-Ce-Pr-Nd, Pm-Sm-Eu-Gd, Gd-Tb-Dy-Ho, and Er-Tm-Yb-Lu in logarithmic plots of the REE patterns or distribution coefficients against the order of the atomic numbers of the lanthanides. Since the 15 lanthanides are separated into four groups, it is called as the tetrad effect. The tetrad effect shown in natural samples were firstly reported by Masuda and Ikeuchi (1979). A lot of following

theoretical and experimental studies confirmed the presence of the tetrad effect (e.g., Kawabe 1992, 1999a; Kawabe et al., 1999a; Ohta and Kawabe, 2000). Similar to the Ce and Eu anomalies, there are two kinds of tetrad effect, M-type or W-type tetrad effect. The M-type tetrad shows upward concave curve, and is generally observed for the complex forming site with ligands or solid phases which had reacted with the fluids. In contrast, the W-type tetrad, the downward concave curve, is observed for seawater (Fig. 1–6B). The direction of the tetrad effect, namely M- or W-type, is explained by the difference in Gibbs free energies of REE species in solid and liquid phases during the partitioning (Kawabe et al., 1999a).

It should also be noted that, in many cases, Y is plotted between Ho and Er in REE patterns to compare the abundance ratios of Y and Ho (Fig. 1–6). The Y and Ho are often compared as geochemical twins, since the behavior of these elements in the natural environment is similar owing to their identical ionic radii in the 6-fold coordination (Fig. 1–4; Shannon, 1976). Actually, Y/Ho weight ratios are almost 28 for chondrite, shale, and mid-ocean ridge basalt (Fig. 1–6), the much higher Y/Ho ratios are reported in seawater and marine carbonates (e.g., Alibo and Nozaki, 1999; Bau et al., 1996; Kawabe et al., 1991). In contrast, lower Y/Ho ratios are observed for deep-sea ferromanganese nodules and crusts (Bau et al., 1996). These observations are also confirmed by the laboratory experiments (Bau, 1999; Ohta and Kawabe, 2000; Tanaka et al., 2004). The Y/Ho fractionation has been attributed to the greater covalency of Ho relative to Y (Choppin, 2002) or to the difference of change in the covalency of bonding associated with ligand exchange (Tanaka et al., 2008).

As such, the REE pattern shows several characteristics which enable us to discuss the origin and several reaction processes of samples. However, it should be noted that precise analysis is necessary to elucidate some information from REE pattern. Data with analytical uncertainty of 1% and 10% differ to a large degree. Masuda (2003) indicated that the development of analytical devices enables us to determine the REE concentration easier than the past couple of decades, which resulted in a poorer quality of the REE data. The quality of the data is largely related to the analytical equipment, hence, the analytical methods of REE are reviewed in the next section.

1.5 Analytical methods

There are several methods to determine the REE abundance in unknown samples. Traditionally, spectrophotometry and X-ray fluorescence spectrometry (XRF) had been the popular devices to measure the REE content, which are currently superseded by inductively coupled plasma mass spectrometry (ICP-MS). Before the development of the ICP-MS, neutron activation analysis (NAA) (e.g., Goldberg et al., 1963; Schmitt et al., 1963; Hogdahl et al., 1968; De Baar et al., 1985) and isotope dilution mass spectrometry (ID-MS) (e.g., Masuda, 1966; Masuda and Ikeuchi, 1979; Piepgras et al., 1979; Elderfield and Greaves, 1982) were the main techniques used to determine the REE. In the NAA, the sample is bombarded with neutrons which causes the elements to form radioactive isotopes. Subsequently, radioactivities of generated radionuclides were determined to obtain abundances of the original nuclides. Sensitive determination of REE concentration is possible using NAA, because the neutron capture cross section of REE is generally large. Another merit is that NAA is non-destructive analysis. However, chemical separation for preparation is better to be done for accurate and precise analysis. The most serious disadvantage is that NAA requires large amount of samples. To give an example, NAA uses 30 L of seawater to determine all the REE concentration. On the other hand, ID-MS comprises the addition of isotopically enriched standard materials directly to the analyte. The specificity of ID-MS lies in the employment of signal ratios, though another analytical methods rely only on the signal intensity. Owing to these advantages, ID-MS is regarded as the method which enables us to determine the concentration with the highest accuracy and precision. However, this method also has two significant disadvantages: (i) accurate analysis takes long time, and (ii) the determination of monoisotopic elements is not possible. The latter is very important since Sc, Y, Pr, Tb, Ho, and Tm do not have two or more stable isotopes, which makes difficult to evaluate the third tetrad (Gd-Tb-Dy-Ho). In addition, the lack of the data on Pr disables to assess the Ce anomaly using Eq. 1–1.

The development of ICP-MS enables us to determine the REE concentration easily and quickly. The strongest point is that the simultaneous multi-element determination of trace elements can be performed with low detection limits. Because of

these advantages, application of ICP-MS to various analytical studies has been widely developed. The widespread development of ICP-MS made us to determine the REE abundance of samples as “a part of a routine work”, resulted in “the end of the studies on REE” (Masuda, 2003). In addition to the expansion of ICP-MS, Masuda (2003) suggested that the lack of knowledge on physicochemical properties of lanthanides played another role. He pointed that the Pm is occasionally removed from the horizontal axis of REE pattern because of the shallow idea that Pm does not have any stable nuclides. Masuda (2003) also wrote that the quality and value of the data differ significantly if the uncertainty is 1% or 10%. To use full advantages of brilliant and unique characteristics of lanthanides, poor quality data are not needed. It is deplorable that only a few researchers understand these important facts (Masuda, 2003).

To obtain the accurate data using ICP-MS, preparation and purification should be performed. The ionization potential of argon plasma can be decreased by the matrix elements, which can result in the underestimation of REE abundance. A comparison of analytical methods using ICP-MS clearly showed the importance of purification (Fig. 1–7; after Hirata et al., 1988). The ICP-MS itself has developed in two decades, and can provide better data without requiring a specific technique. However the knowledge on the physicochemical properties and proper analytical skills are essential to use and discuss the REE data for geochemical materials.

1.6 Concluding remarks

It had taken 113 years to discover the nature existing REEs, and more than one and a half centuries for all the REEs. The similar chemical properties made the separation of each REE difficult. On the other hand, the chemical properties make REE the most unique geochemical tool to discuss the origin and several reaction processes that samples had experienced. The discovery of the REE pattern which can cancel out the Oddo-Harkins effect has greatly contributed to the development of REE geochemistry. After the deployment of the ICP-MS, REE abundance data have been provided much more easily than before. On the other hand, abundant data quickly

obtained for REE have decreased the quality and disabled the full use of advantages. The knowledge on the physicochemical properties and proper analytical skills are necessary before the use and discussion of the REE data for geochemical materials.

Table 1–1. Discovery and isolation of REEs

Name	Symbol	Discovery	Isolation	Origin of Name
Scandium	Sc	1879	1879	Latin Scandia (Scandinavia)
Yttrium	Y	1794	1843	Ytterby village in Sweden
Lanthanum	La	1839	1842	Greek lanthanein (hidden)
Cerium	Ce	1803	1839	Ceres, an asteroid discovered in 1801
Praseodymium	Pr	1885	1885	Greek prasios didymos (green twin)
Neodymium	Nd	1885	1885	Greek neo didymos (new twin)
Promethium	Pm	1947	1947	Greek god, Prometheus
Samarium	Sm	1879	1901	the name of mineral, samarskite
Europium	Eu	1901	1901	Europe
Gadolinium	Gd	1880	1880	Finnish chemist Johan Gadolin
Terbium	Tb	1843	1880	Ytterby village in Sweden
Dysprosium	Dy	1886	1886	Greek dysprositos (difficult to obtain)
Holmium	Ho	1879	1886	Latin Holmia (Stockholm)
Erbium	Er	1843	1879	Ytterby village in Sweden
Thulium	Tm	1879	1879	the old name for Scandinavia
Ytterbium	Yb	1878	1907	Ytterby village in Sweden
Lutethium	Lu	1907	1907	Latin Lutecia (Patis)
Didymium	Di	1842		Greek didymos (twin)

Table 1–2. Electroic configurations of REEs.

	Atomic state (Ln^0)	Ionic state (Ln^{3+})
Sc	$1s^2 2s^2 2p^6 3d^1 4s^2$	$3s^2 3p^6$
Y	$1s^2 2s^2 2p^6 3s^2 3p^6 3d^{10} 4s^2 4p^6 4d^1 5s^2$	$4s^2 4p^6$
La	$1s^2 2s^2 2p^6 3s^2 3p^6 3d^{10} 4s^2 4p^6 4d^{10} 5s^2 5p^6 5d^1 6s^2$	$5s^2 5p^6$
Ce	$1s^2 2s^2 2p^6 3s^2 3p^6 3d^{10} 4s^2 4p^6 4d^{10} 4f^2 5s^2 5p^6 6s^2$	$4f^1 5s^2 5p^6$
Pr	$1s^2 2s^2 2p^6 3s^2 3p^6 3d^{10} 4s^2 4p^6 4d^{10} 4f^3 5s^2 5p^6 6s^2$	$4f^2 5s^2 5p^6$
Nd	$1s^2 2s^2 2p^6 3s^2 3p^6 3d^{10} 4s^2 4p^6 4d^{10} 4f^4 5s^2 5p^6 6s^2$	$4f^3 5s^2 5p^6$
Pm	$1s^2 2s^2 2p^6 3s^2 3p^6 3d^{10} 4s^2 4p^6 4d^{10} 4f^5 5s^2 5p^6 6s^2$	$4f^4 5s^2 5p^6$
Sm	$1s^2 2s^2 2p^6 3s^2 3p^6 3d^{10} 4s^2 4p^6 4d^{10} 4f^6 5s^2 5p^6 6s^2$	$4f^5 5s^2 5p^6$
Eu	$1s^2 2s^2 2p^6 3s^2 3p^6 3d^{10} 4s^2 4p^6 4d^{10} 4f^7 5s^2 5p^6 6s^2$	$4f^6 5s^2 5p^6$
Gd	$1s^2 2s^2 2p^6 3s^2 3p^6 3d^{10} 4s^2 4p^6 4d^{10} 4f^7 5s^2 5p^6 5d^1 6s^2$	$4f^7 5s^2 5p^6$
Tb	$1s^2 2s^2 2p^6 3s^2 3p^6 3d^{10} 4s^2 4p^6 4d^{10} 4f^9 5s^2 5p^6 6s^2$	$4f^8 5s^2 5p^6$
Dy	$1s^2 2s^2 2p^6 3s^2 3p^6 3d^{10} 4s^2 4p^6 4d^{10} 4f^{10} 5s^2 5p^6 6s^2$	$4f^9 5s^2 5p^6$
Ho	$1s^2 2s^2 2p^6 3s^2 3p^6 3d^{10} 4s^2 4p^6 4d^{10} 4f^{11} 5s^2 5p^6 6s^2$	$4f^{10} 5s^2 5p^6$
Er	$1s^2 2s^2 2p^6 3s^2 3p^6 3d^{10} 4s^2 4p^6 4d^{10} 4f^{12} 5s^2 5p^6 6s^2$	$4f^{11} 5s^2 5p^6$
Tm	$1s^2 2s^2 2p^6 3s^2 3p^6 3d^{10} 4s^2 4p^6 4d^{10} 4f^{13} 5s^2 5p^6 6s^2$	$4f^{12} 5s^2 5p^6$
Yb	$1s^2 2s^2 2p^6 3s^2 3p^6 3d^{10} 4s^2 4p^6 4d^{10} 4f^{14} 5s^2 5p^6 6s^2$	$4f^{13} 5s^2 5p^6$
Lu	$1s^2 2s^2 2p^6 3s^2 3p^6 3d^{10} 4s^2 4p^6 4d^{10} 4f^{14} 5s^2 5p^6 5d^1 6s^2$	$4f^{14} 5s^2 5p^6$

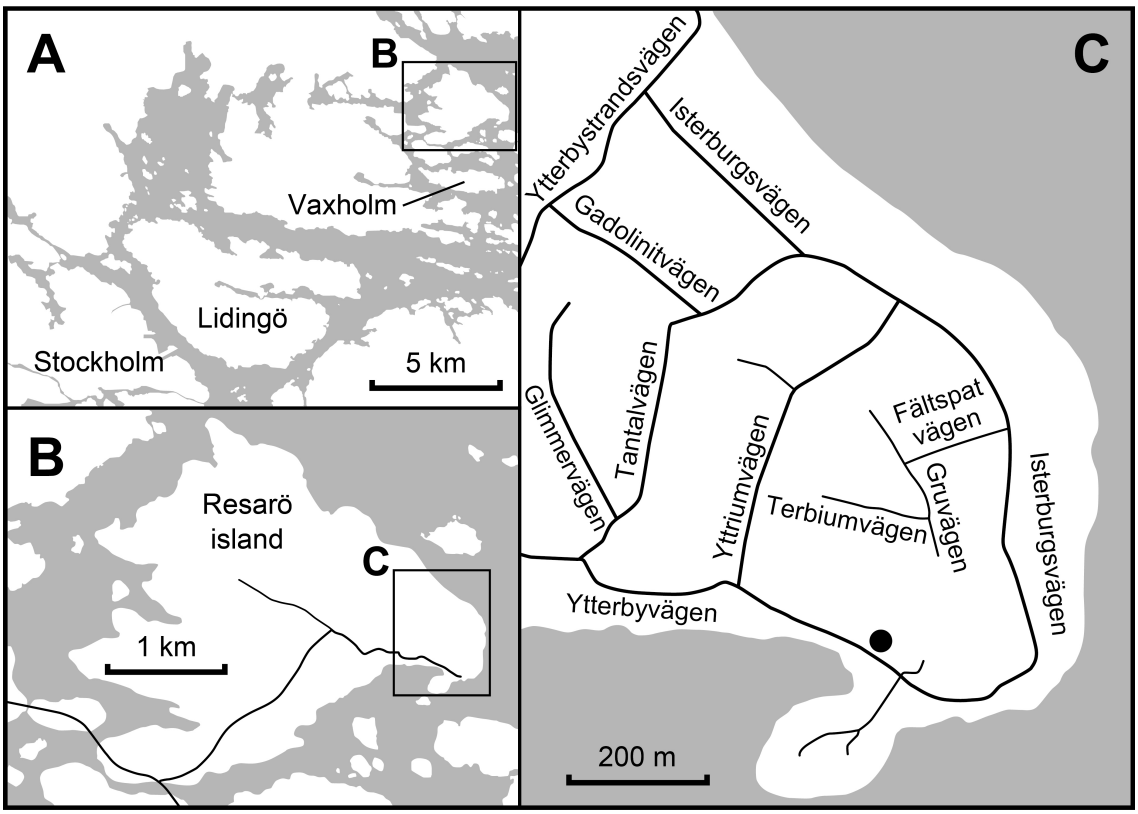

Fig. 1–1. Schematic map around (A) Stockholm, (B) Resarö island where Ytterby mine locates, and (C) Ytterby mine. Black lines in (B) and (C) denotes the road. The black circle in (C) indicates the entrance to the mine.

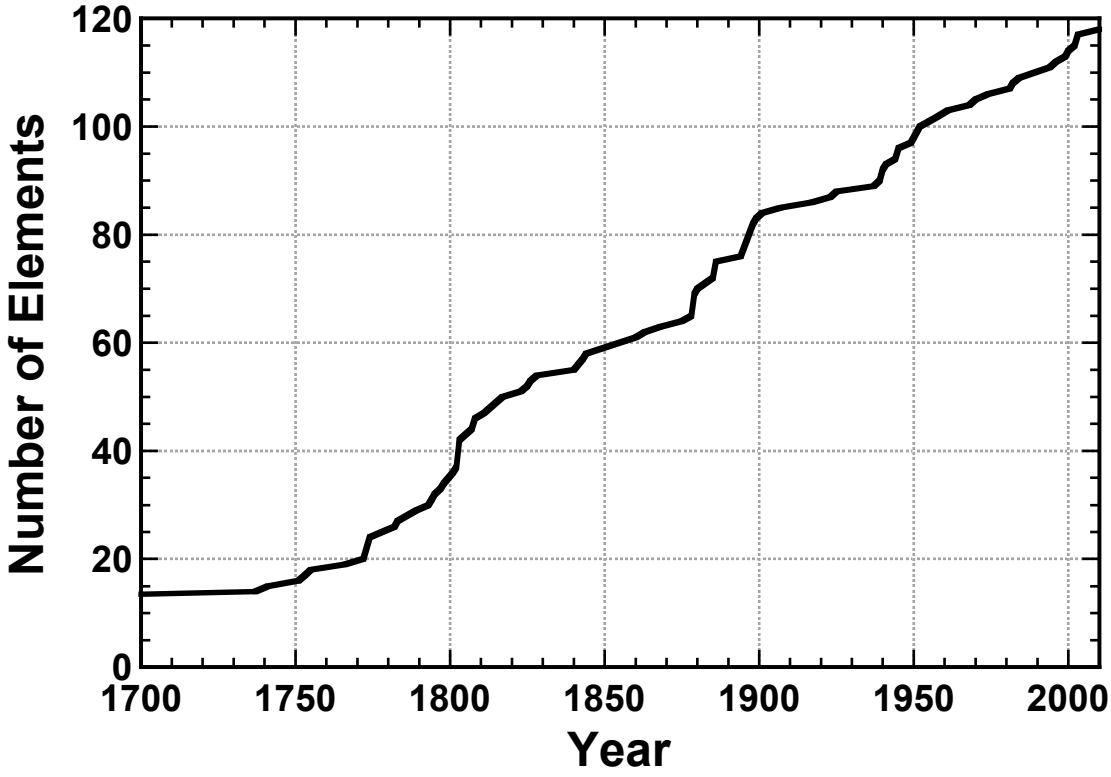

Fig. 1–2. The number of discovered elements in each year (after Krebs, 2006).

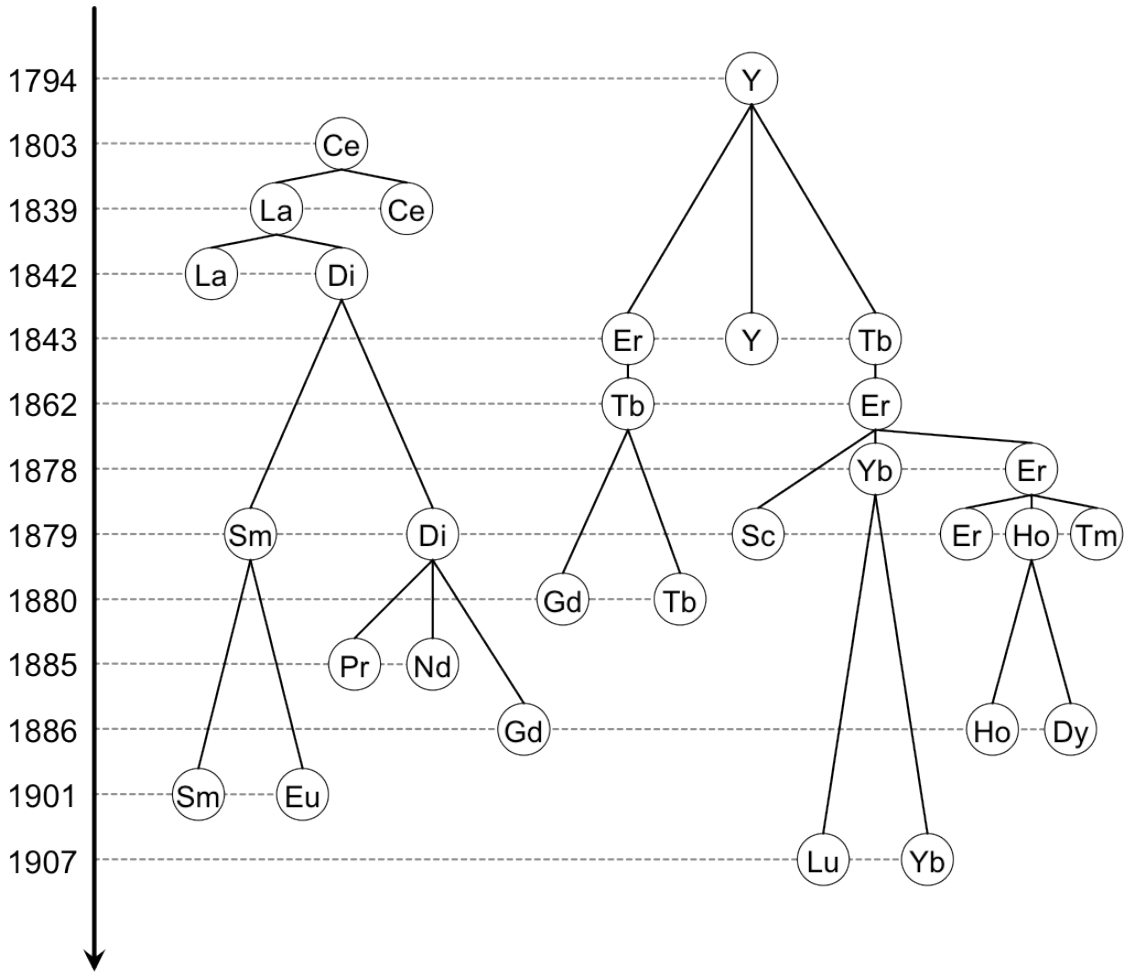

Fig. 1–3. The tree of the discovery year of REEs.

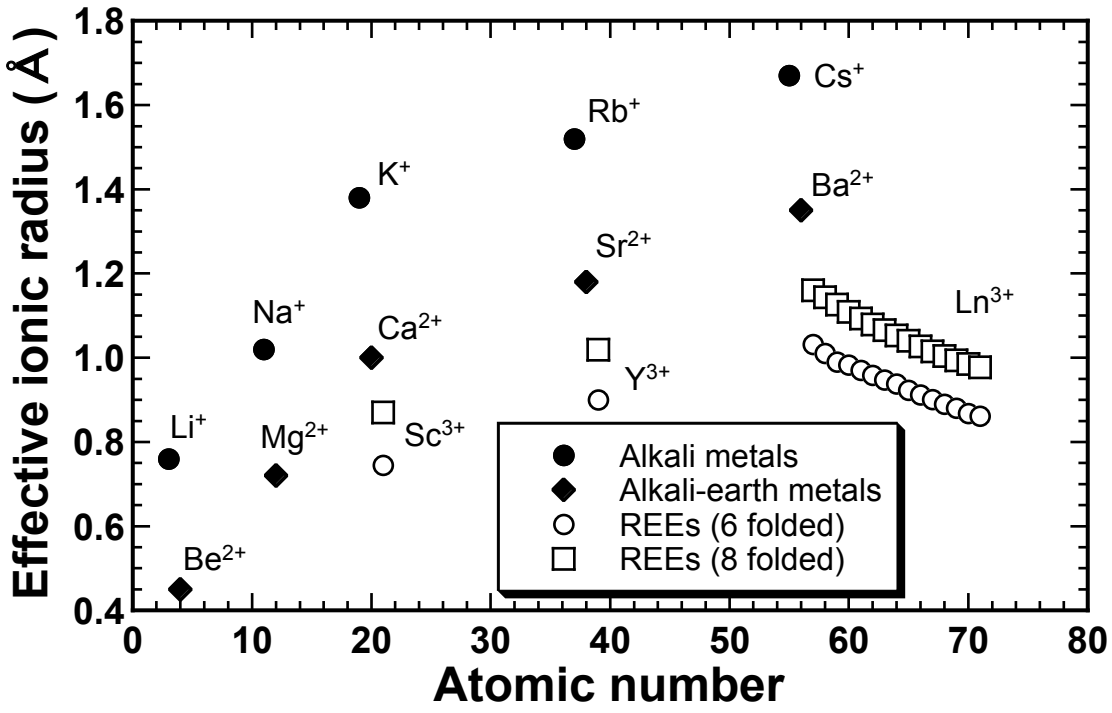

Fig. 1–4. Effective ionic radius of alkali metals, alkali-earth metals, and REEs (open symbols). Coordination numbers of alkali and alkali-earth metals are 6 folded values for comparison. Data are referenced from Shannon (1976).

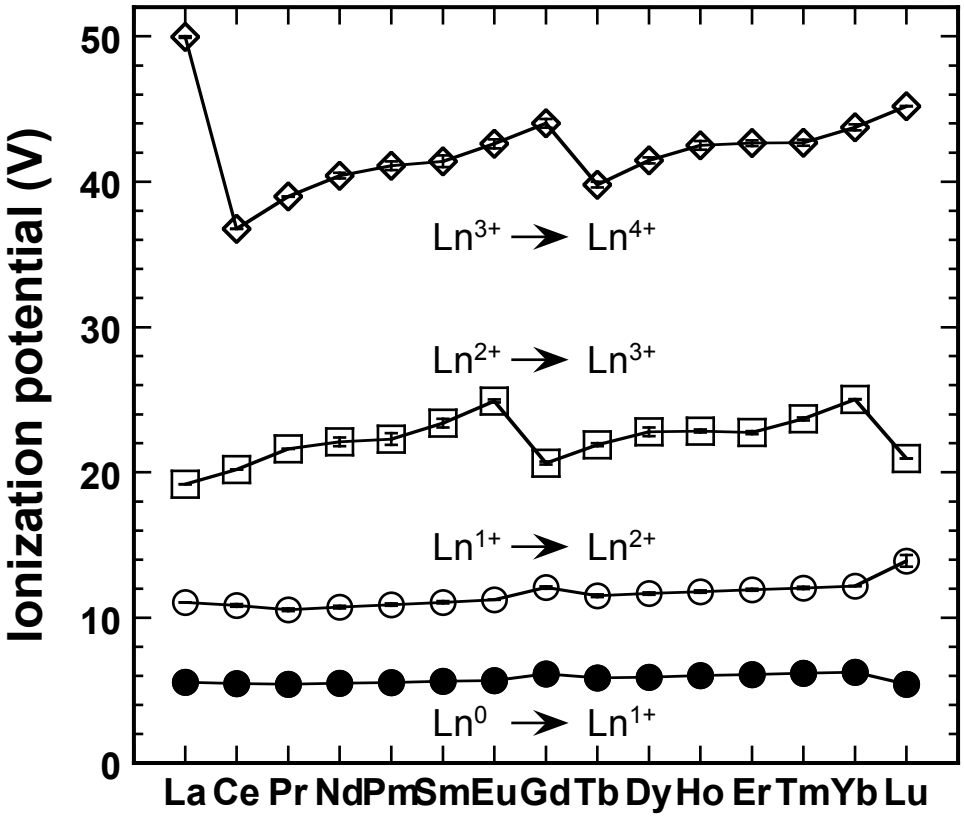

Fig. 1–5. Ionization potentials for lanthanide atomic ions summarized by Martin et al. (1974).

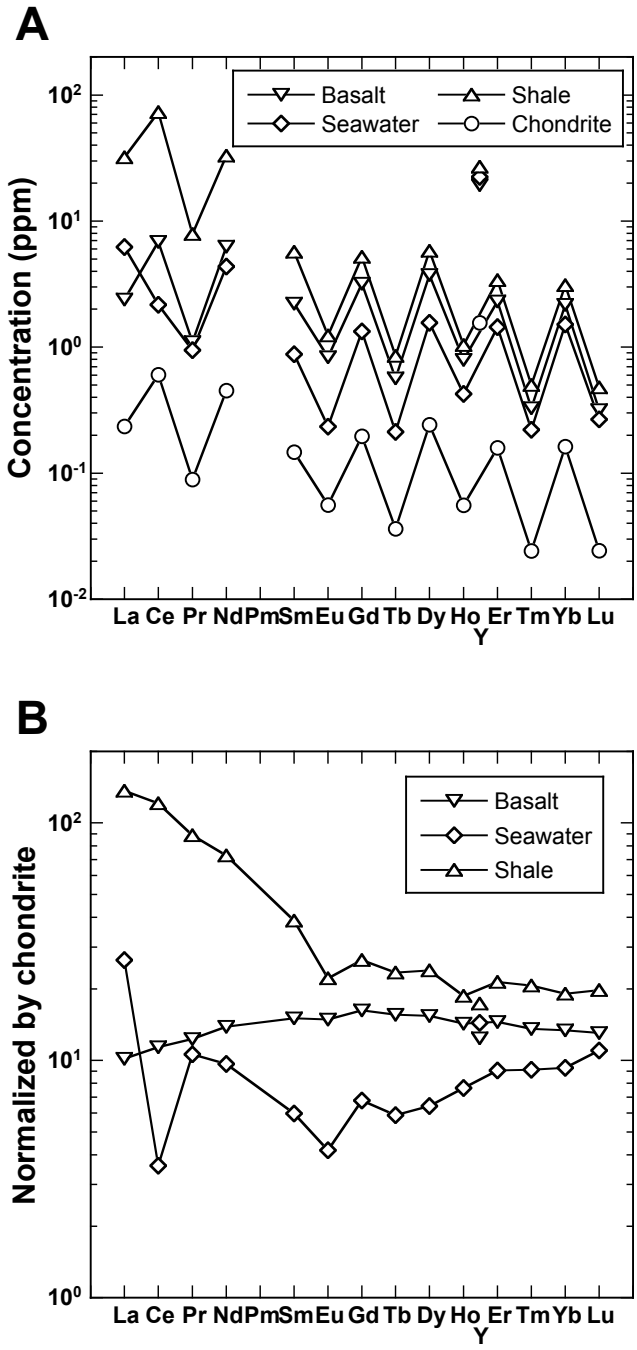

Fig. 1–6. (A) REE concentration of basalt (mid-ocean ridge basalt; Klein, 2003), shale (post Archean average shale composite; McLennan, 1989), seawater (North Pacific deep water; Alibo and Nozaki, 1999), and chondrite (CI-chondrite; Anders and Grevesse, 1989). Note that the seawater values are 10^6 times higher than the original concentration. (B) REE abundance of basalt, shale, and seawater normalized by chondrite. Oddo-Harkins effect is cancelled out and smooth curves are observed.

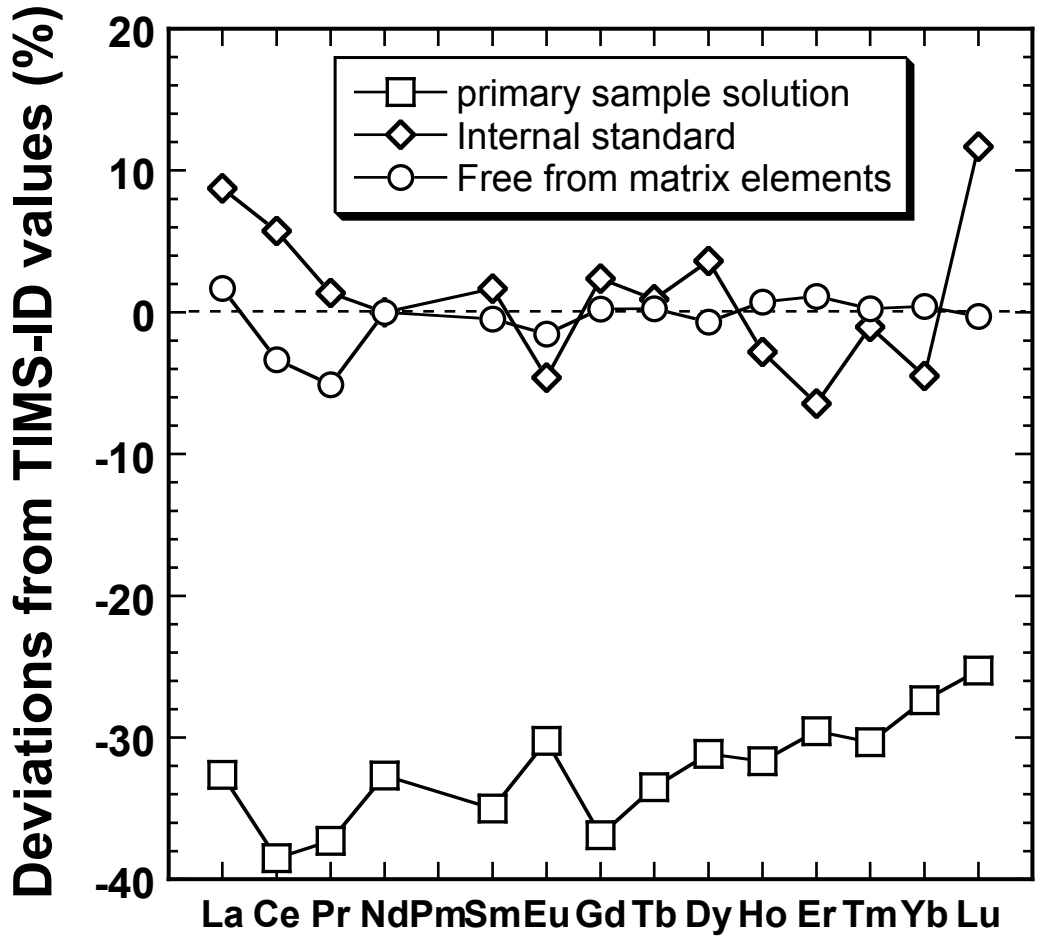

Fig. 1–7. Deviations (%) REE data of JB-3 obtained using an ICP-MS from those by thermal ionization mass spectrometry (TIMS)-ID (Hirata et al., 1988). Square: ICP-MS analysis on the primary sample solution (PRM solution) which had experienced only acid digestion; diamond: analysis using an internal standard (Sn) on the PRM solution; circle: analysis after the removal of major elements using cation exchange resin. Note that REE abundances of Pr, Tb, Ho, and Tm using TIMS-ID were calculated by interpolation of the REE pattern.

Chapter 2

The cause of Eu anomaly during the water-rock interaction

2.1 Chapter introduction

As described in Chapter 1, anomalously high abundance of europium (Eu) relative to its neighboring elements (Sm and Gd), called as positive Eu anomaly, is often observed for water which experienced high temperature water-rock interaction. A prime example of it is seafloor hydrothermal fluids (e.g., Klinkhammer et al., 1983; Michard et al., 1983). The rare earth element (REE) distributions in hydrothermal fluids are light-REE (LREE) enriched and exhibit strong positive Eu anomalies. Klinkhammer et al. (1994) have shown that when fluid/MORB end-member patterns are plotted against their ionic radii, the trends not only became linear but also showed the same fractionation trend peculiar to plagioclase during magma segregation, indicating that REE concentrations of hydrothermal vent fluids can be intrinsically linked to the high-temperature alteration of this particular mineral. If the REE patterns of hydrothermal fluids are dominated by the alteration of plagioclase, however, it is questionable why the REE patterns of fluids from different vents of the same site showed different patterns. To give an example, the hydrothermal fluids corrected from several vents in Lucky Strike site showed variations in their REE patterns (Douville et al., 1999), though these vents are located closely with each other and the compositions of minerals can be almost same.

On the other hand, it is suggested that positive Eu anomaly shown in hydrothermal fluids can be due to the formation of chloride complex (Bach et al., 2003; Allen and Seyfried, 2005). The species distribution calculation suggests that chloride complex dominates the Eu^{2+} species to a large degree than the other REEs under high temperature condition (Bach et al., 2003). A hydrothermal experiment under 400 °C at 500 bar using harzburgite which does not contain plagioclase supported the formation of chloride complex at high temperature (Allen and Seyfried, 2005). The negative Eu anomaly was observed within 816 hours, but after injection of NaCl and $MgCl_2$

solutions, Eu anomaly turned to be positive side. Thus, they suggested that Eu^{2+} formed strong aqueous complexes with dissolved Cl^{-}, while other trivalent REEs were not greatly affected by fluid speciation. The existence of Eu^{2+} at high temperature condition is supported by thermodynamic calculations (Sverjensky, 1984; Bau, 1991). As such, the hydrothermal experimental study raises a question about the cause of positive Eu anomaly.

Although it is well known that hydrothermal fluids show positive Eu anomaly, the relationship between the degree of Eu anomaly and the temperature of water-rock interaction is poorly understood. Minami et al. (1995) showed that slightly positive Eu anomaly (Eu/Eu* = 1.1) is observed when basalt collected from Fuji (can be considered as JB-3, one of the geochemical reference sample of basalt) interacted with water at 70 °C. In contrast, Shibata et al. (2006) showed that negative Eu anomaly is observed when basalt (JB-2, another geochemical reference sample of basalt) was interacted with water at 46 °C. Here, Eu/Eu* is the index of degree of Eu anomaly, defined by the Eq. 1−7. Though Minami et al. (1995) and Shibata et al. (2006) used different kind of basalt in a narrow sense, it is expected from their results that the degree of Eu anomaly may be used as a thermometer.

This Chapter, therefore, aims to reveal the cause of positive Eu anomaly, namely whether it is governed by mineralogy or solution chemistry, and to evaluate the degree of the Eu anomaly as a potential water-rock interaction thermometer. Water-rock interaction experiments were performed under 40, 60, and 80 ºC using synthesized basaltic glass or plagioclase-bearing basalt with or without 0.70 M NaCl solution.

2.2 Experimental

2.2.1 Blank hydrothermal experiment

The steel-alloy autoclave was used for the hydrothermal experiment in this study (Fig. 2−1). The autoclave is made of Inconel-alloy, which is corrosion-resistant and possesses adequate strength at elevated temperatures and pressures (up to 600 °C and 60 MPa). The reaction cell is made of a gold tube with a titanium head because these

materials are inert to high-temperature water. In addition, gold is flexible, allowing that fluid sample inside the reaction cell is pressurized by water around it. The surface of the Ti head was oxidized prior to use. The flexible gold reaction cell allows on-line sampling of the aqueous fluid at almost constant temperature and pressure simply by adding a small amount of water under high pressure to the autoclave surrounding the cell. Thus, internally filtered fluid samples can be obtained from the reaction cell through a gold-lined sampling tube at any time during an ongoing experiment. All materials that had contact with the reaction fluid in the experiment were baked in a muffle furnace at 500 °C for 3 hours before the use to eliminate organic matter.

The standard REE solution (XSTC-1; Spex Certiprep., USA) diluted by ultra pure water into about 50 ng/L, which is highest among reported concentrations of water at seafloor hydrothermal vent for light-REE, was put into the gold tube. The temperature and pressure was adjusted and kept at 350 °C and 50 MPa, respectively. The hydrothermal experiment was continued for 168 hours with the collection of sample through the sampling tube after 72 and 120 hours. After cooling, the autoclave used in this experiment was disassembled and residual sample fluid was collected. The pH values of collected small amount of fluid (less than 5 drops) were determined using a pH meter (HORIBA) with uncertainty ±0.1 pH unit. The concentration of REE was determined using ICP-MS (Agilent 7500).

2.2.2 Basalt synthesis

In this study, basalts which have similar major element composition with higher REE concentration was synthesized by melting several reagents. The used reagents are listed in Table 2−1. Chloride reagents such as NaCl and KCl were not used, because chloride cannot be excluded from the basalt. Therefore, oxides and carbonates were used in the synthesis. Not only the major element, but also the REE oxide reagents were used. Approximately 30 g of well homogenized reagents was placed in a platinum crucible and heated at 1000 ºC for 1 hour using a Siliconit furnace. Subsequently, the sample's temperature was raised to 1350 ºC in 2 hours and kept at the temperature for 1

hour. The sample was finally quenched to room temperature, and the synthesized basaltic glass (hereafter named as Gl-bas) was obtained (Fig. 2−2A). Basalt containing plagioclase (hereafter Pl-bas) was obtained by re-heated the Gl-bas at 1190 ºC for 67 hours (Pupier et al., 2008), and then quenched (Fig. 2−2B). During the use of the furnace, oxygen fugacity was adjusted at QFM (quartz-fayalite-magnetite) buffer by mixing the H_2 and CO_2 gas pressure. Both Gl-bas and Pl-bas were powered using an agate mortar and sieved to obtain the <45 μm fraction.

2.2.3 Low-temperature water-rock interaction experiment

Four grams of Gl-bas or Pl-bas fractions were placed in Teflon bottles with 8 mL of ultra-pure water or 0.7 M NaCl solution and heated at 40, 60, and 80 ºC for 3 and 6 months using an incubator. After the reaction, basalts were separated from solutions and air-dried to determine the X-ray diffraction (XRD) pattern and observe particles using a field emission scanning electron microscope (FE-SEM; Hitachi High-Tech S-5200) equipped with an energy dispersive X-ray spectrometry (EDX; EDAX Genesis XM2). In addition, Fe K-edge (7111 eV) X-ray absorption near edge structure (XANES) spectra were measured at BL-12C of KEK-PF (Tsukuba, Japan). Prior to the measurements, the X-ray energy was calibrated with the pre-edge peak maximum of hematite at 7114 eV. The XANES spectra of the reference materials, wüstite, fayalite, augite, and magnetite, and two samples were measured in transmission mode. The XANES spectra were analyzed using REX2000 software (Rigaku Co. Ltd.). The contributions of the various Fe species in each sample were estimated by linear combination fitting (LCF) of each XANES spectrum with the spectra of the reference materials. The LCF was conducted using no more than three minerals in the energy range of 7100–7180 eV. The quality of the fit was given by the residual value, the goodness-of-fit parameter *R*, defined by

$$R = \frac{\sum[x_{obs}(\mathrm{E}) - x_{\mathrm{cal}}(\mathrm{E})]^2}{\sum[x_{obs}(\mathrm{E})]^2} \qquad (2\text{–}1)$$

where $\chi_{\mathrm{obs}}(E)$ and $\chi_{\mathrm{cal}}(E)$ are the experimental and calculated absorption coefficients at

a given energy (E), respectively. A smaller R value means a better fit in the LCF procedure.

Meanwhile, Na concentrations in the liquid phase originally ultra-pure water were measured using an ion chromatography (Thermo Dionex ICS-1100) immediately after the separation. The rest of the liquid phase for ultra-pure water and NaCl solution was acidified to 0.5 M HCl and the REEs were separated from major cations via column chemistry. The 15 g of 2.0 M HCl solution was passed through a column (5 cm long; 1.0 cm diameter) loaded with an AG 50W-8X cation exchange resin (Bio-Rad). Almost 100% (more than 99%) of the REEs were recovered by elution using a 6.0 M HCl solution (Fig. 2−3). The major cation concentrations (K, Mg, and Ca) were determined using an ICP atomic emission spectrometer (AES; SII NanoTachnology, Inc.), whereas the REE concentrations were determined using an ICP-MS (Agilent 7700).

2.3 Results and Discussion

2.3.1 Blank hydrothermal experiment

The REE concentrations and pH values of fluid sample collected during and after the hydrothermal experiment are listed in Table 2−2 along with the calculated initial concentrations and measured initial pH value. As shown in the table, the pH values are almost constant during the experiment. However, the concentrations of REE in fluid are drastically decreased within 72 hours, making the concentrations of 6 elements below the detection limit of ICP-MS (1 ng/kg). The concentrations of REE are further decreased in the next 48 hours, where only 5 elements can be determined among 15 REEs. On the other hand, except for Sm, REE concentrations of fluid sample collected after cooling increased from those collected during the experiment (120 hours).

The depletion of REE concentration with increasing experimental time can be due to the adsorption onto Ti head. The increase of REE concentrations after cooling may be re-dissolution of elements which was adsorbed onto Ti head during the experiment. Whatever the case, it is proved that REE was lost from fluid during the

hydrothermal experiment, meaning that this kind of experimental apparatus using Au/Ti reaction cell cannot be used to discuss the behavior of REE during water-rock interaction. Therefore, the REE data of hydrothermal study by Allen and Seyfried (2005) can be skeptical because they use similar experimental system, namely Au/Ti reaction cell. This fact is very important, since Allen and Seyfried (2005) suggested that positive Eu anomaly shown in hydrothermal fluids could be due to the formation of Cl complex, which is clearly different from the observation by Klinkhammer et al. (1994).

2.3.2 Low-temperature water-rock experiment (solid phase)

The XRD patterns of Gl-bas did not show any sharp peaks corresponding to minerals, whereas a broad peak around 26.5º (2θ) was observed for starting material, Gl-bas reacted with ultra-pure water for half a year at 80 ºC, and Gl-bas with 0.7 M NaCl solution at the same period and temperature (Fig. 2−4A). It is not surprising that the starting material did not show any peaks, since amorphous materials generally do not present sharp peaks in the XRD pattern. Meanwhile, it is surprising that no peaks were observed for Gl-bas experienced water-rock interaction at 80 ºC for 6 months, since the formation of secondary minerals, mainly clay minerals, was expected to be observed. The lack of the presence of any sharp peaks suggests that secondary minerals were not formed in this experimental condition using Gl-bas.

Several peaks were identified for XRD patterns of Pl-bas before and after the experiment with the largest intensity at around 27.8º, which corresponds to the anorthite or albite (Fig. 2−4B). The second largest peak at around 29.8º corresponds to the strongest peak of augite, though we followed the method only to crystallize out plagioclase (Pupier et al., 2008). Other peaks than plagioclase and augite, such as clay minerals, were not obtained for Pl-bas after the water-rock interaction experiment. The crystallization of augite makes it difficult to assess the Eu anomaly caused by the preferential dissolution of anorthite, because augite also contains Ca^{2+}. However, the relative intensity of these two minerals enables us to discuss the possible contribution to the Eu anomaly. The peak corresponding to the plagioclase was approximately 1.5

times larger than that of augite for starting material, which decreased to 1.2−1.3 times (Fig. 2−5). The decrease of the peak intensity of plagioclase after the experiment suggests the preferential dissolution of plagioclase. In addition, Pl-bas reacted with water at 40 ºC showed the lowest relative peak intensity. This fact may indicate that the dissolution of plagioclase occurs more preferentially at lower temperature condition.

The presence of augite in Pl-bas was also confirmed using the Fe K-edge XANES spectra (Fig. 2−6). The smallest *R* value, 0.013, was achieved when assuming a mixture of augite and wüstite with 68% and 32%, respectively. The second smallest *R* value was achieved by combination of 59% of fayalite and 41% of magnetite (R = 0.026). It is interesting that the XANES spectrum of Pl-bas was largely different from that of Gl-bas showing broader absorption spectrum, though major element compositions of these two samples were the same. This fact means that the chemical form of Fe in these two materials is completely different. In addition to the XANES spectra, pre-edge peak of these two materials also showed a different shape (Fig. 2−7). However, valence state analysis on Fe based on the pre-edge peak analysis (Wilke et al., 2001; Giuli et al., 2002; and the detail is described in the Chapter X) showed averaged valence state of Fe within the analytical uncertainty, which were 2.24 ± 0.09 and 2.38 ± 0.09 for Pl-bas and Gl-bas, respectively. Since the oxygen fugacity was adjusted to the QFM buffer during the basalt synthesis, this result is consistent.

The particle observation using a FE-SEM showed a flat surface for the starting material of Gl-bas (Fig. 2−8A), while the surface locked lumpy for the Pl-bas (Fig. 2−8B). The line analysis using SEM-EDX showed uniformity for Gl-bas (Fig. 2−8C), whereas the major element abundance varied to a large degree even within a particle of Pl-bas (Fig. 2−8D), probably due to the elemental partition during the crystallization. Although two materials showed different surface area for starting materials, the surface of both particles after the experiment seems to be similar with a vermiculate-like surface (Fig. 2−8E, F).

2.3.3 Low-temperature water-rock experiment (liquid phase)

The highest concentration in the liquid phase among major elements was Na and the second highest was Ca (Table 2−3). Although Mg abundance in the solid phase was the second highest among Na, K, Mg, and Ca (Table 2−1), Mg released to the liquid phase was the lowest. As expected, the higher the reaction temperature, the larger the dissolution rate for all the major cations. The concentration in the liquid phase along with the period showed that the reaction had still proceeded in this experimental period (Fig. 2−9). The general trend observed for the cations is that liquid phase reacted with Pl-bas contained higher concentration of major cations, and 0.7 M NaCl solution showed higher dissolution rate than ultra-pure water (Table 2−3, Fig. 2−9).

The REE fractions after the experiment were listed in the Table 2−4. Although it is not clear for Gl-bas systems, Pl-bas contacted with fluids under higher temperature released larger abundances of REEs (Fig. 2−10). The depletion at Pr and Tb observed in the liquid phases can be due to the enrichment in the starting materials, while the enrichment of Ce in the liquid phases was observed owing to the depleted Ce abundance in the starting materials. In contrast to the major cations, REE released from basalts was smaller using the 0.7 M NaCl solution for the liquid phase of Gl-bas and Pl-bas systems. REE fraction of fluids using 0.7 M NaCl solution can be more affected by the heterogeneous compositions of starting materials for both systems. In regard to the heterogeneous composition, the large variation of the REE fraction observed for the Pl-bas system can be due to the preferential dissolution of weaker part in the particles. Most surprisingly, positive Eu anomaly was not observed in this experiment, though basalt contacted with water at 70 ºC showed positive Eu anomaly due to the presence of the plagioclase (Minami et al., 1995). However, Eu/Eu* values clearly becomes larger with increasing reaction temperature using ultra-pure water (Fig. 2−11). In Fig. 2−11, Y/Ho ratio which shows variation during the water-rock interaction (Takahashi et al., 2002a) is also plotted. The Y/Ho ratios of 0.7 M NaCl solution contacted with basalts were totally larger than those of ultra-pure water system. Meanwhile, Eu/Eu* values of 0.7 M NaCl solution were clearly smaller than those of ultra-pure water. This fact raises a question about the cause of positive Eu anomaly governed by the formation of Cl

complex (Bach et al., 2003; Allen and Seyfried, 2005).

2.4 Conclusions and Implications

In this Chapter, the cause of positive Eu anomaly during the water-rock interaction was investigated. Although the high temperature experiment could not be performed properly due to the problem in the experimental apparatus, the behavior of REEs was determined in detail during the low temperature water-rock interaction. Larger abundance of REEs was released from Pl-bas to low salinity water compared to the 0.7 M NaCl solution. The REE fraction became larger with increasing water-rock interaction temperature. The Pl-bas released larger abundances of REEs than Gl-bas irrespective of any solution conditions, which can be due to the heterogeneous compositions of elements in the Pl-bas particles. Since Eu/Eu* values were smaller when basalts contacted with 0.7 M NaCl solution, it is suggested that the possible positive Eu anomaly caused by the formation of stable Cl complex was less effective in this experiment. The Eu/Eu* values became larger with increasing reaction temperature when ultra-pure water was used, which can be applied to the water-rock reaction thermometer under low salinity condition.

In the case that the concentration of REE in hydrothermal vent fluid is controlled by the alteration of minerals especially plagioclase, it is expected that the combination of isotope ratio and chemical state shows a difference. The end-member of plagioclase is anorthite and albite containing Ca^{2+} and Na^{+}, respectively. Since ionic radius of Eu^{2+} is similar to that of Ca^{2+}, these two elements can be substituted with each other, meaning that (divalent) Eu is richer in plagioclase than other REE. In this case, stable isotope ratio of Eu would be different whether Eu is incorporated into a mineral as divalent or trivalent. That is, during the hydrothermal water-rock interaction, the residual rock should be rich in trivalent Eu and stable isotope ratio of Eu in reacted fluid should reflect that of plagioclase. On the other hand, if the Eu anomaly is controlled by composition of the solution, stable isotope ratio of Eu would not be affected only by that of rock-forming minerals.

Table 2−1. Reagents used to synthesize basalts.

Reagents	Amount (g)
SiO_2	50.16
TiO_2	1.47
Al_2O_3	15.79
FeO	9.51
MnO_2	0.20
MgO	7.58
$CaCO_3$	21.76
Na_2CO_3	4.72
K_2CO_3	0.20
P_2O_5	0.13

Table 2−2. The REE concentrations (ng/L) and pH values of fluid sample collected before, during (72 and 120 hours) and after the experiment.

	Before	72 hours	120 hours	After cooling
Y	46.6	0.267	0.222	3.96
La	46.6	0.363	< DL	16.8
Ce	46.5	0.289	< DL	< DL
Pr	46.4	0.521	0.389	1.93
Nd	46.6	3.13	2.80	5.68
Sm	46.5	14.3	9.45	7.32
Eu	46.6	< DL	< DL	0.170
Gd	46.4	< DL	< DL	1.63
Tb	46.0	< DL	< DL	0.728
Dy	47.1	< DL	< DL	1.03
Ho	47.1	0.067	< DL	0.749
Er	46.3	0.116	0.085	0.947
Tm	46.6	< DL	< DL	0.469
Yb	46.5	< DL	< DL	0.565
Lu	45.7	0.059	< DL	0.963
pH	4.7	4.9	4.8	4.7

Note that DL denotes detection limit of the measurement using ICP-MS.

Table 2−3. The major element concentrations of liquid phase after the experiment.

		Ultra-pure water						0.7 M NaCl					
		Pl-bas			Gl-bas			Pl-bas			Gl-bas		
	Period	40	60	80	40	60	80	40	60	80	40	60	80
Na	3	4.98	5.76	8.61	3.82	4.62	4.80						
	6	5.44	6.79	9.93	4.37	4.71	5.06						
K	3	9.83	12.8	13.2	10.7	10.7	13.7	20.4	31.2	37.6	32.5	25.4	29.8
	6	13.9	14.6	15.0	12.9	15.8	17.2	29.7	46.1	50.2	41.9	42.6	48.5
Mg	3	1.79	5.64	7.56	3.36	3.88	5.89	9.40	15.3	22.4	6.78	14.0	15.1
	6	2.87	7.89	9.93	3.64	6.03	7.17	13.8	25.2	30.7	9.11	18.5	20.8
Ca	3	49.7	60.6	69.5	23.4	31.0	50.4	125	175	258	26.8	47.2	75.3
	6	60.7	66.2	80.1	35.3	53.1	68.4	202	231	287	37.6	51.8	98.0

Note that the unit of Na is mM, while that of others are μM.

Table 2−4. The major element concentrations of liquid phase after the experiment.

		Ultra-pure water						0.7 M NaCl					
		Pl-bas			Gl-bas			Pl-bas			Gl-bas		
	Basalt	40	60	80	40	60	80	40	60	80	40	60	80
Y	143	834	1393	5310	1183	696	762	114	376	571	200	566	140
La	38.8	261	390	1670	408	168	195	39.0	126	185	71.9	2.6	68.3
Ce	67.2	615	1024	4164	905	343	375	89.9	294	445	155	473	123
Pr	63.4	183	317	1252	180	212	242	12.9	37.1	56.5	25.6	61.1	26.4
Nd	112	432	736	2235	550	455	513	45.7	147	220	85.4	234	69.5
Sm	34.8	127	224	661	163	141	157	35.8	44.5	65.3	28.1	70.1	19.8
Eu	13.7	37.1	80.9	242	52.9	60.3	68.5	2.81	4.67	6.11	6.69	9.47	4.97
Gd	46.6	158	298	748	192	196	223	15.3	49.5	75.5	30.7	76.9	24.8
Tb	16.9	43.1	93.6	266	45.6	65.7	75.1	3.22	9.27	14.5	6.61	15.0	5.17
Dy	60.1	190	385	908	235	241	169	19.1	60.7	94.0	34.3	95.5	26.0
Ho	12.3	40.5	82.8	194	49.2	50.7	57.8	4.39	13.3	19.7	7.81	19.5	5.92
Er	33.2	189	237	575	144	139	156	12.5	40.8	61.2	22.2	59.5	16.6
Tm	4.26	17.2	33.7	85.6	20.9	18.8	20.7	2.11	6.12	9.28	3.69	9.29	2.42
Yb	32.3	121	231	609	149	134	151	14.0	42.6	65.5	23.0	62.6	16.1
Lu	4.67	18.4	34.7	88.3	21.9	19.8	22.6	2.04	6.28	9.47	3.66	9.42	2.64

Note that the Basalt is starting materials with mg/Kg, concentrations of liquid phases after 6 months are given in ng/L.

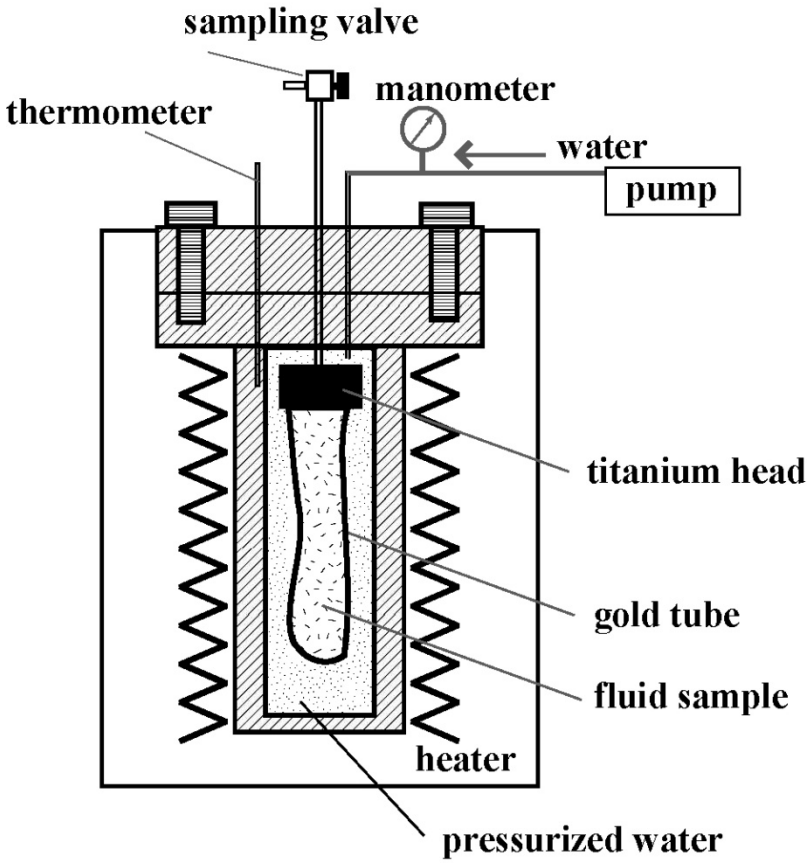

Fig. 2−1. Schematic illustration of the Inconel-alloy autoclave and flexible-cell hydrothermal apparatus used in this laboratory experiment (after Yoshizaki et al., 2009).

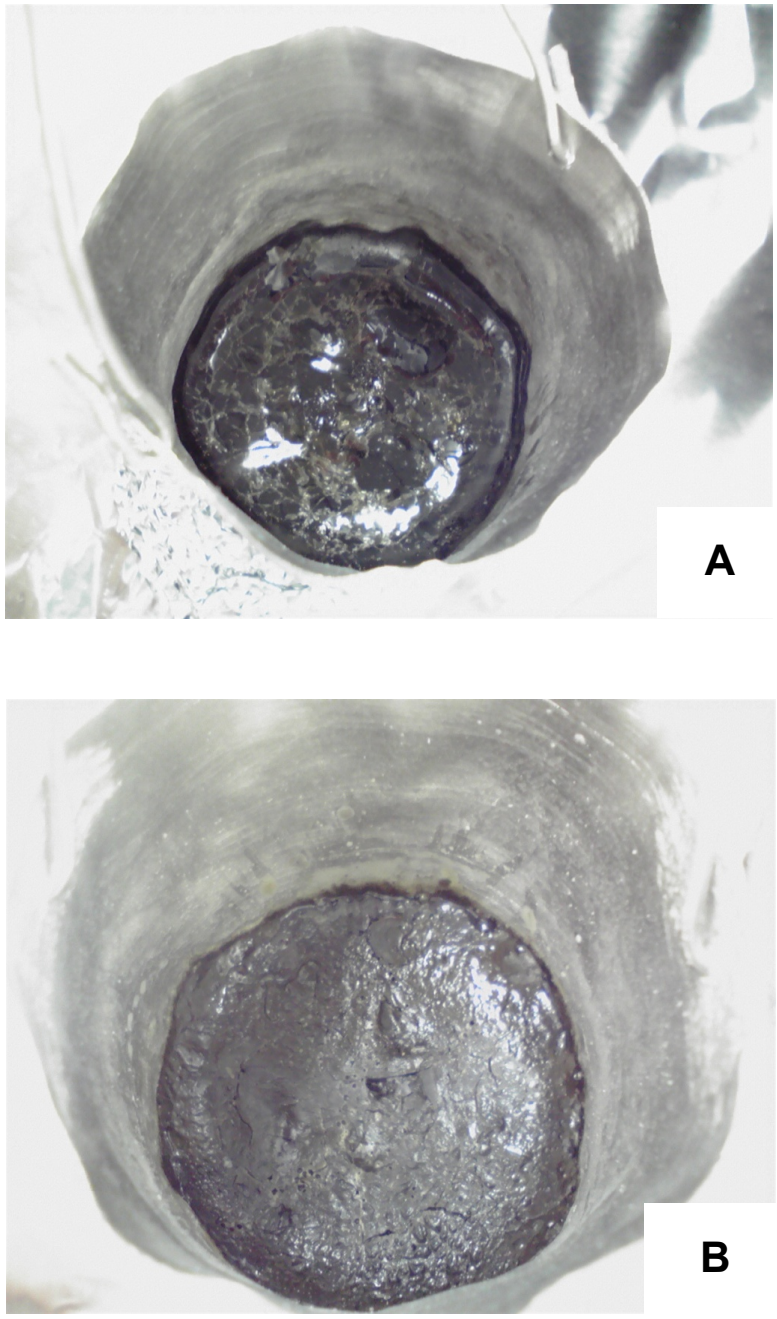

Fig. 2−2. Photographs of (A) Gl-bas and (B) Pl-bas after quench.

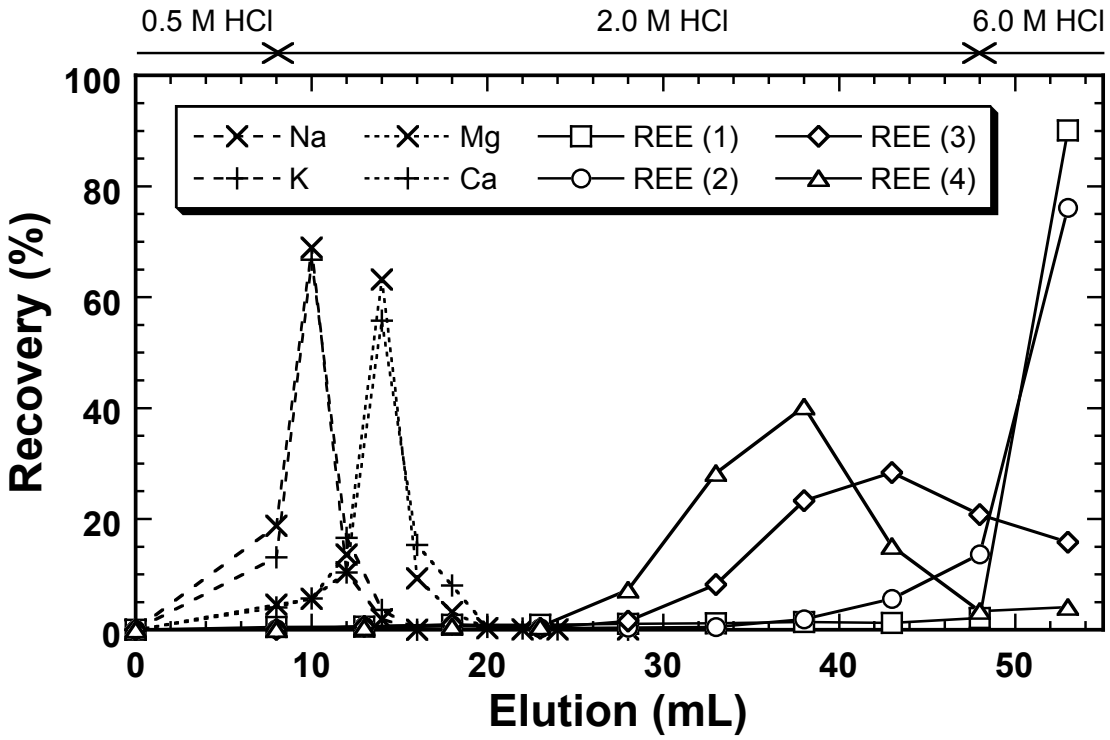

Fig. 2−3. Elution curve for major elements (Na, K, Mg, and Ca) and REEs. Note that REE (1) shows averaged value of La−Nd, REE (2) for Sm−Gd, REE (3) for Tb−Er, REE (4) for Ho−Lu.

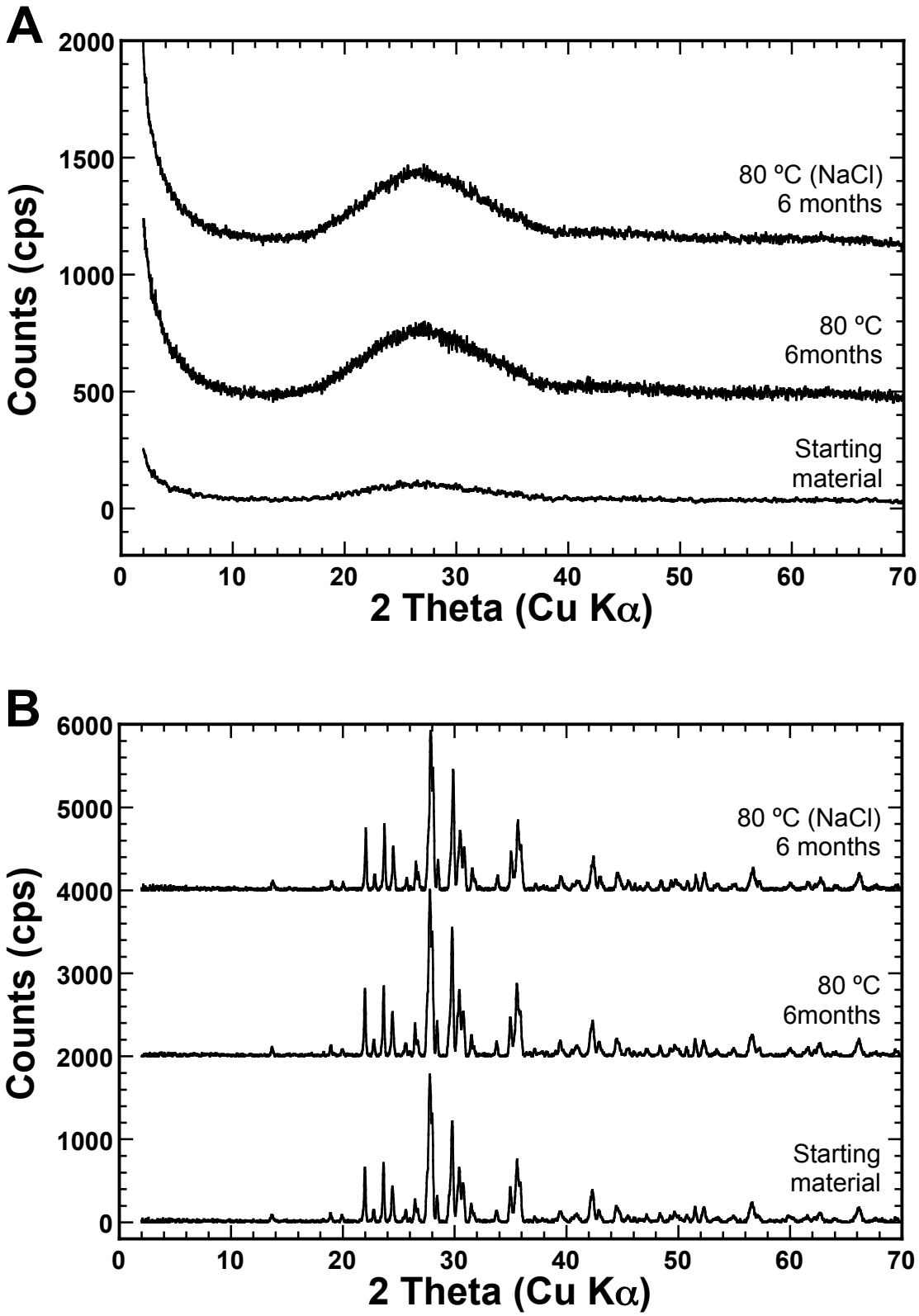

Fig. 2−4. XRD patterns of (A) Gl-bas and (B) Pl-bas.

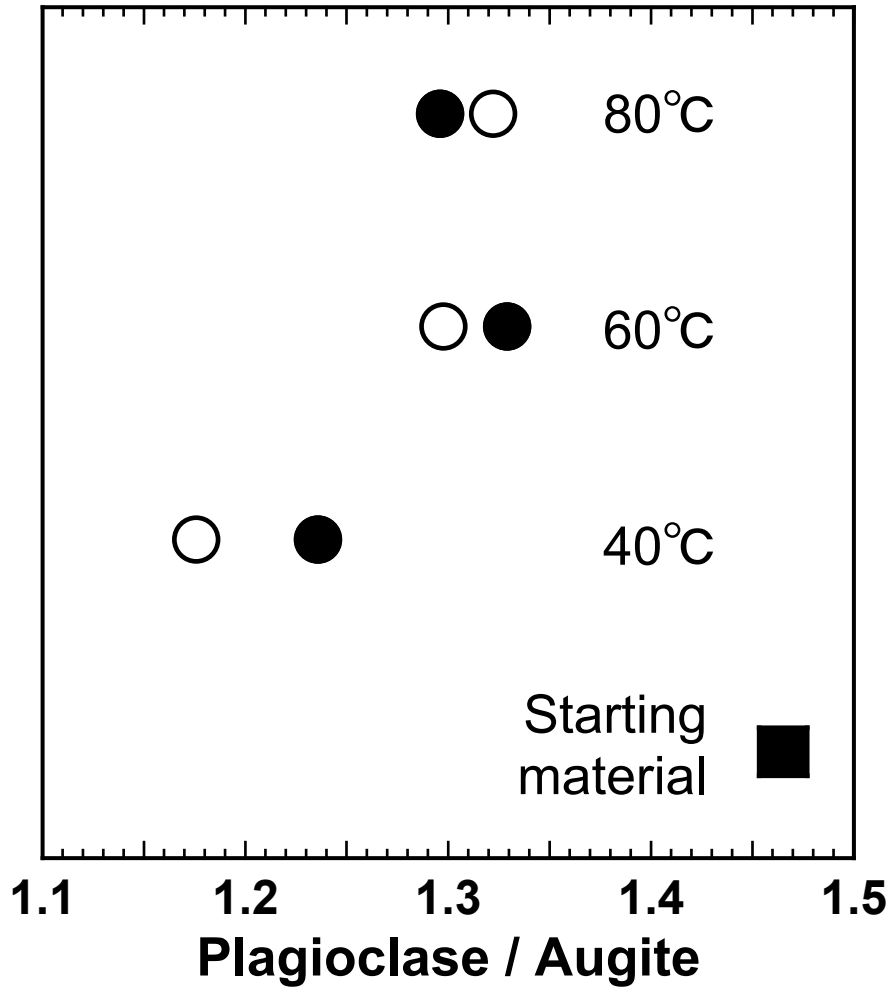

Fig. 2−5. The relative intensity ratio of plagioclase and augite. Open circle denotes the ratio for Pl-bas reacted with ultra-pure water, while the filled circle for 0.7 M NaCl solution.

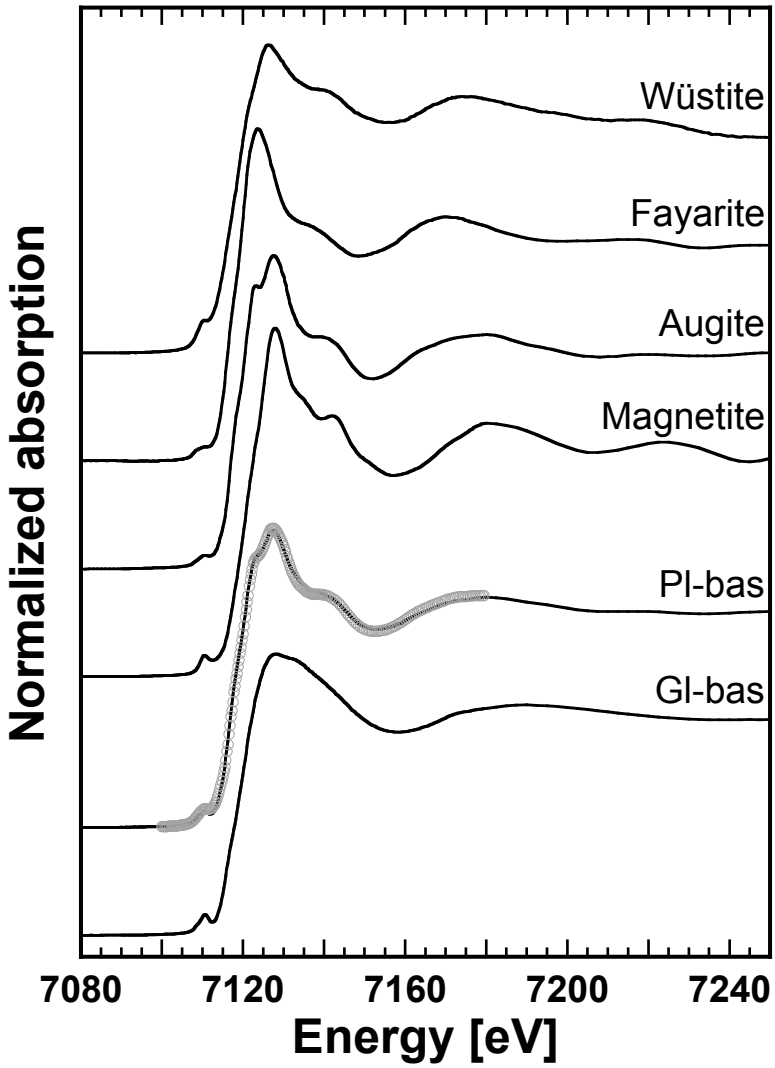

Fig. 2−6. Iron K-edge XANES spectra of reference materials (wüstite, fayalite, augite, and magnetite) and two samples. Gray circles denotes fitting curve assuming 68% of augite and 32% of wüstite.

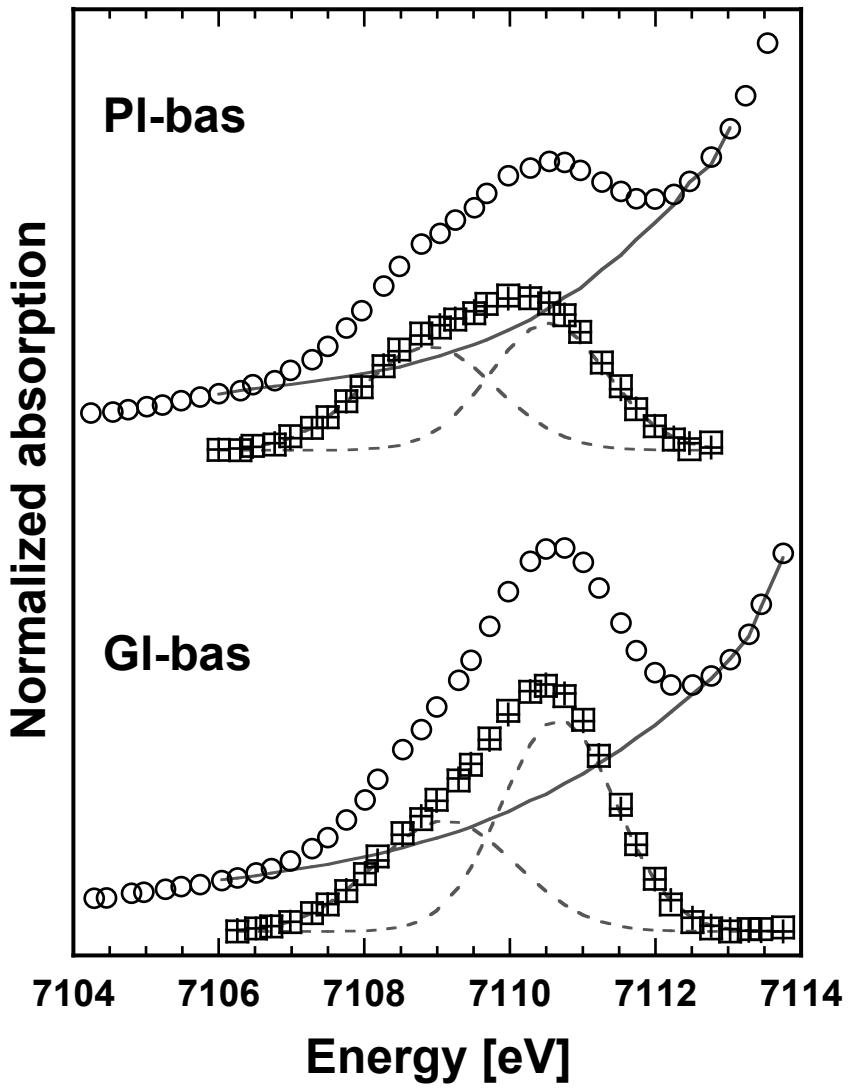

Fig. 2−7. Iron K-edge pre-edge spectra. Circle: measured absorbance; solid line: background spectrum calculated using a spline function; square: normalized absorbance; dashed line: Gaussian functions; cross: the sum of the Gaussian functions.

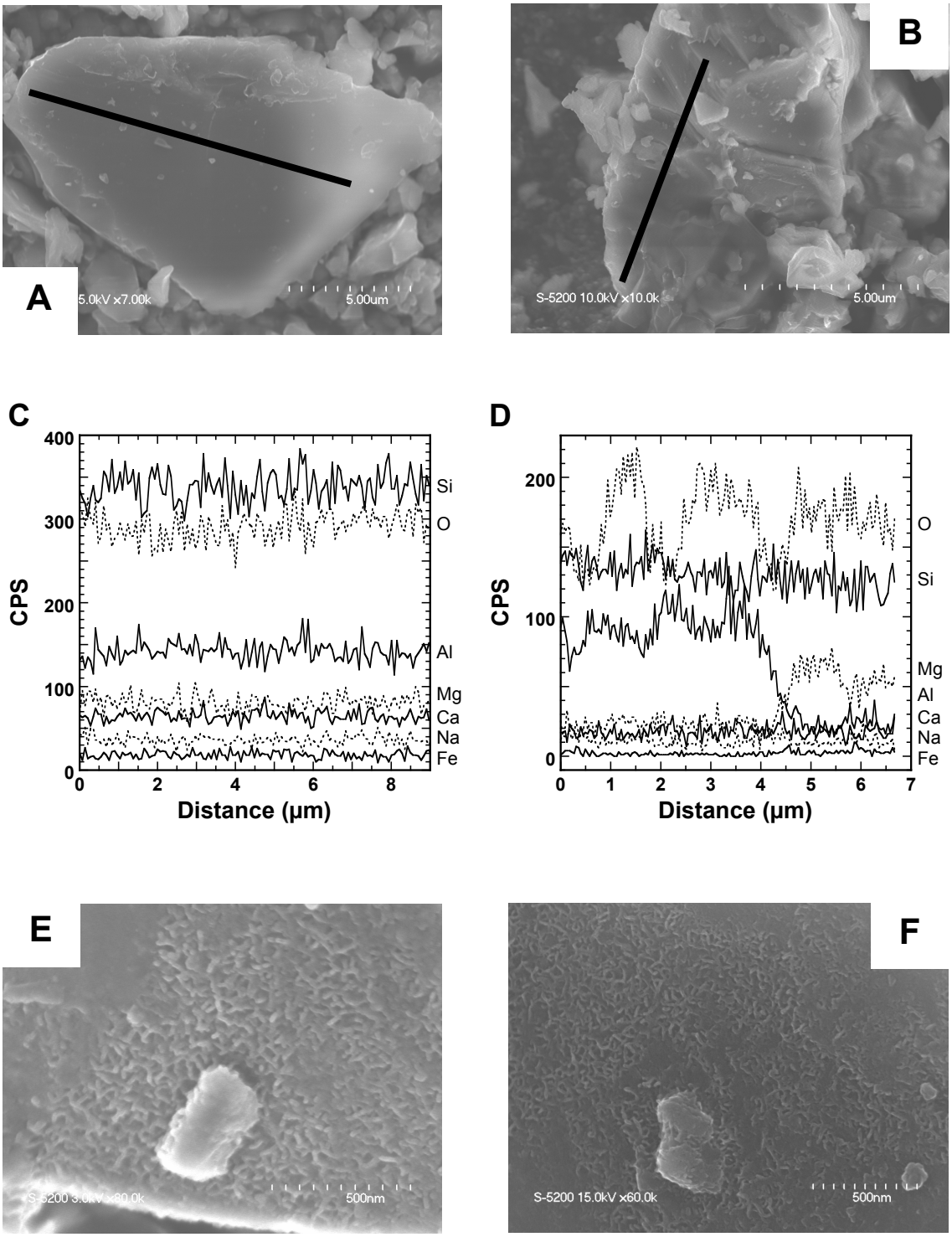

Fig. 2−8. SEM images of starting materials (A) Gl-bas and (B) Pl-bas. Major element abundance determined using SEM-EDX of (C) solid line shown in (A) from left to right and (D) solid line shown in (B) from above to below. SEM images after the experiment of (E) Gl-bas and (F) Pl-bas.

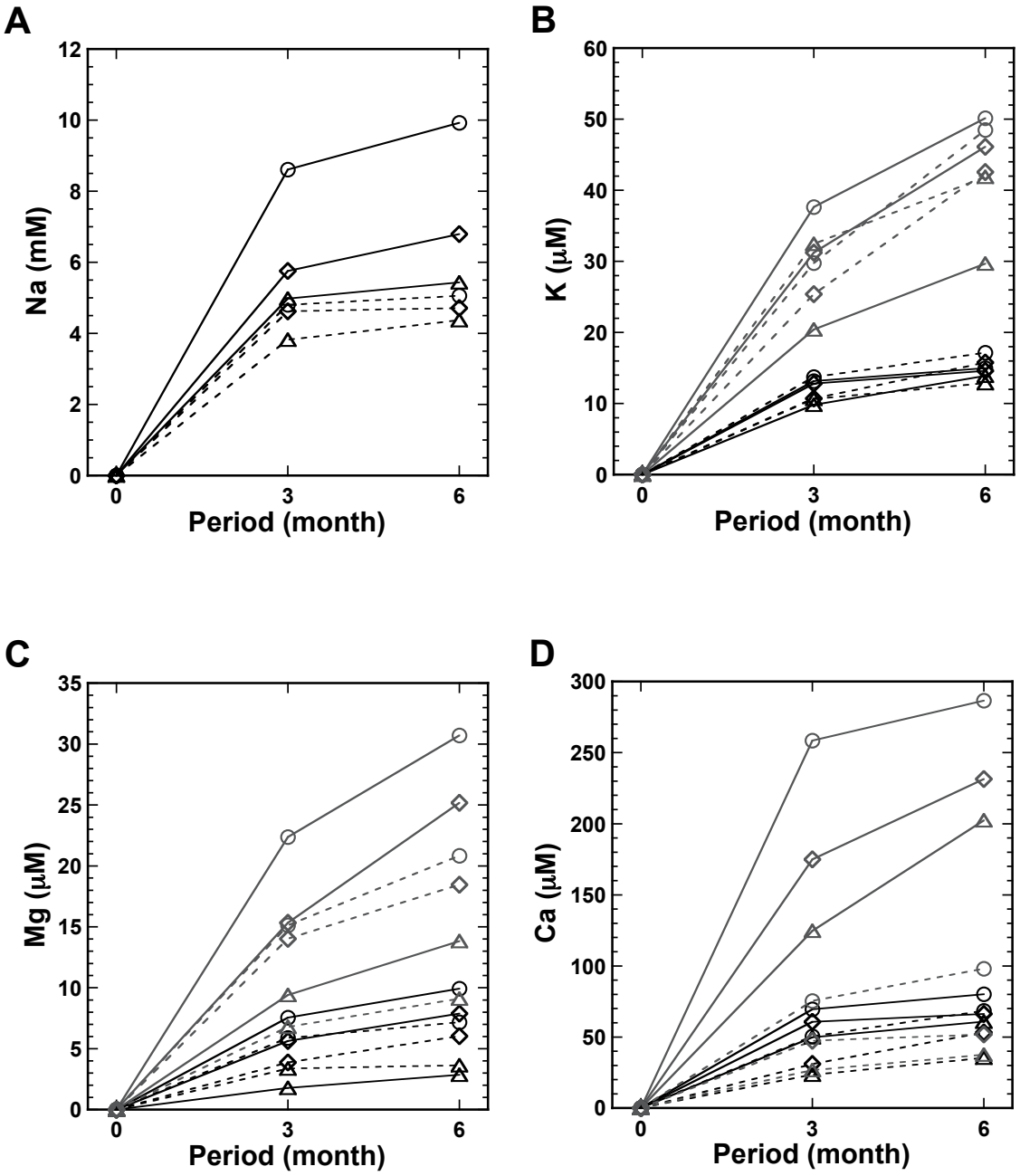

Fig. 2−9. Major cations released from Pl-bas (solid line) and Gl-bas (dashed line). Black color shows experiment using ultra-pure water, while gray color illustrates 0.7 M NaCl solution. Trigonal symbol: 40 ºC, quarry: 60 ºC, and cirlcle: 80 ºC.

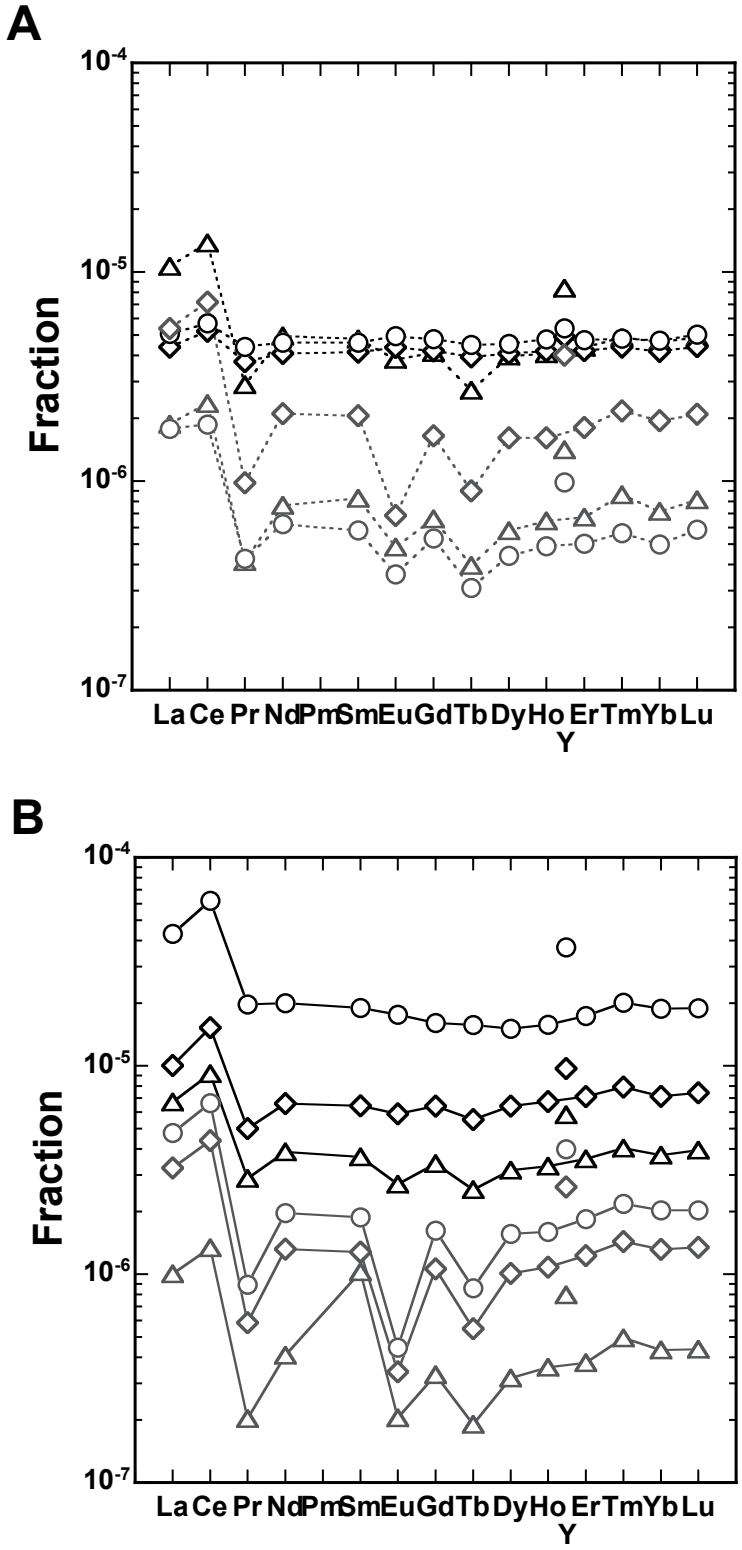

Fig. 2−10. REE fractions released from Gl-bas (A) and Pl-bas (B). Note that the legends are the same with those of Fig. 2−9.

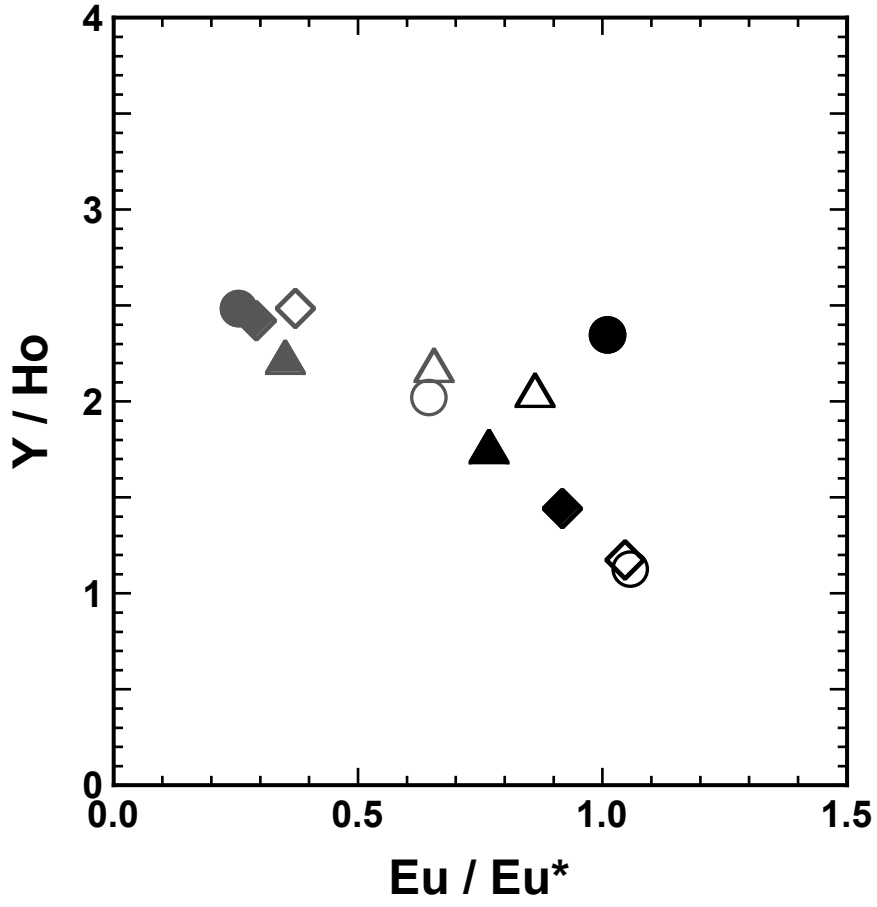

Fig. 2−11. Eu/Eu* values and Y/Ho ratios of liquid phase contacted with Pl-bas (filled symbols) and Gl-bas (open symbols). Black color shows experiment using ultra-pure water, while gray color illustrates 0.7 M NaCl solution. Trigonal symbol: 40 ºC, quarry: 60 ºC, and cirlcle: 80 ºC.

Chapter 3

Isotopic and speciation study on Ce during its solid-water distribution with implication for Ce stable isotope as a paleo-redox proxy

3.1 Chapter introduction

Cerium (Ce), one of the rare earth elements (REEs), has the unique characteristic of being able to form tetravalent cations under oxic conditions, whereas the other REEs are stable in a trivalent state. Although Ce(IV) carbonate species are soluble (Möller and Bau, 1993), Ce is relatively insoluble in seawater compared with other REEs following the oxidation from Ce(III) to Ce(IV), due to the low solubility of Ce(IV). Two formation processes for the oxidation of Ce(IV) are possible. The first is oxidation after adsorption onto a solid phase, namely, oxidative adsorption, which may occur on manganese oxide (e.g., Taylor and McLennan, 1988; Takahashi et al., 2000a, 2007). The other process is oxidation in the liquid phase followed by precipitation as $Ce(OH)_4$ or CeO_2 (De Baar et al., 1988; German and Elderfield, 1989; Braun et al., 1990). Given these chemical properties, an anomalously high or low concentration of Ce relative to its neighboring elements, lanthanum (La) and praseodymium (Pr), known as a positive or negative Ce anomaly, respectively, is often observed in REE abundance patterns following the generation of Ce(IV) (Henderson, 1984). This redox-sensitive property allows the estimation of the redox state of a paleo-ocean environment (e.g., Shimizu and Masuda, 1977; Wang et al., 1986; Wright et al., 1987; Murray et al., 1991) and the study of the redox evolution of the atmosphere (e.g., Fryer, 1977; Murakami et al., 2001; Kato et al., 2006).

In seawater, REEs are adsorbed on various types of suspended matter and solid phases. In particular, marine ferromanganese deposits show large positive Ce anomalies in their REE patterns (e.g., Piper, 1974; Elderfield et al., 1981; Bau et al., 1996). Large negative Ce anomalies in REE patterns are observed in seawater as a counterpart to these positive anomalies (e.g., Elderfield and Greaves, 1982; Piepgras and Jacobsen, 1992; Möller et al., 1994). The positive Ce anomalies in marine ferromanganese oxides

are possibly caused by the oxidative adsorption of Ce (Takahashi et al., 2000a, 2007). Takahashi et al. (2007) showed that the chemical state of Ce in marine ferromanganese deposits is tetravalent, regardless of the formation environment, namely, hydrogenetic, diagenetic, and hydrothermal. In addition, adsorption experiments have suggested the oxidation of Ce by δ-MnO_2 (Takahashi et al., 2000a; Ohta and Kawabe, 2001). The Eh–pH diagram indicates that the Mn^{2+}/MnO_2 boundary is located at a higher Eh level than that of Ce^{3+}/CeO_2 (Brookins, 1988; Fig. 3−1A). These facts support the suggestion that Mn oxides can act as an oxidant for Ce(III), indicating that the oxidative adsorption of Ce on Mn oxides can generate a positive Ce anomaly. Meanwhile, the $Fe^{2+}/Fe(OH)_3$ boundary is located at an Eh level lower than the Ce^{3+}/CeO_2 boundary (Brookins, 1988; Fig. 3−1A), indicating that $Fe(OH)_3$ may be less powerful in oxidizing Ce into CeO_2, as suggested by previous studies (De Carlo and McMurtry, 1992; Kawabe et al., 1999b; Takahashi et al., 2007). However, Kato et al. (2006) summarized the REE pattern of Precambrian banded iron formations (BIFs) and showed that both positive and negative Ce anomalies were observed regardless of their formation age. Surprisingly, although some Precambrian BIFs may have undergone recent weathering or post-depositional alteration (e.g., Bau, 1993), some Archean BIFs show positive Ce anomalies. If Mn oxides are necessary to generate positive Ce anomalies, it is questionable whether Mn oxides existed in ancient periods when the atmospheric oxygen level was estimated to be less than 10^{-5} atm (e.g., Pavlov and Kasting, 2002; Catling and Claire, 2005).

Recently, Bau and Koschinsky (2009) suggested the oxidative scavenging of Ce by Fe hydroxides, following leaching experiments with a hydrogenetic ferromanganese crust. Furthermore, Bau (1999) performed scavenging experiments and demonstrated oxidative scavenging of Ce by Fe hydroxide, especially at lower pH ($pH \leq 4.6$). Their result suggested that discussions relying only on the Eh–pH diagram would be risky if applied to the natural environment. All these findings imply that the geochemical processes responsible for the occurrence of Ce anomalies are not fully understood, and that any discussion based only upon the intensity of the Ce anomaly will have limitations. Therefore, alternative and quantitative evidence is needed to fully determine the cause of Ce anomalies.

In this study, the Ce stable isotope ratio is examined as an alternative geochemical tool that may have better resolution in discerning redox conditions. This study aims to provide information on the relationship between redox conditions and the mass-dependent isotope fractionation of the Ce stable isotope ratio. More information on redox conditions in the paleo environment may be obtained if fractionations of the Ce stable isotope respond differently to different geochemical processes as follows: (i) adsorption of Ce^{3+} without oxidation; (ii) precipitation as CeO_2 or $Ce(OH)_4$; and (iii) oxidative scavenging on Mn oxide (corresponding to fields (i), (ii), and (iii), respectively, in Fig. 3−1A). To date, several geochemical (isotopic) tracers have been introduced to clarify paleo-redox conditions, such as $\Delta^{33}S$, $\delta^{56}Fe$, $\delta^{53}Cr$, and Mo isotopes (e.g., Farquhar et al., 2000; Johnson et al., 2008; Frei et al., 2009; Anbar et al., 2007). However, most of these indicators are sensitive only under low atmospheric oxygen conditions, indicating that geochemical tracers that are useful after the great oxidation event (c.a. 2.2 Ga) are lacking. Therefore, the stable isotopic fractionation of Ce may be used as an alternative tool sensitive to suboxic conditions. Speciation analysis of Ce in the solid phase has also been examined by X-ray absorption near-edge structure (XANES) and extended X-ray absorption fine structure (EXAFS) analyses to support the determination of redox conditions, thereby providing data on the oxidation state of Ce in the solid phase and quantitative information about the distance to neighboring atoms and the coordination number (CN), respectively. This study includes three parameters for Ce that are important in inorganic geochemistry: abundance (degree of the Ce anomaly); the Ce stable isotope ratio; and the chemical speciation of Ce. This study was confined to a lower pH region (pH = 5) where the aqua complex is stable, to focus on the Ce isotopic fractionation from an aqua complex of Ce^{3+} as the first step (Fig. 3−1B).

3.2 Experimental

3.2.1 REE adsorption experiment

Synthetic ferrihydrite was prepared by dissolving 40 g $Fe(NO_3)_3$ in 500 mL ultrapure water. KOH solution was then added to the $Fe(NO_3)_3$ solution and pH was adjusted to between 7 and 8 (Schwertmann and Cornell, 2000). δ-MnO_2 was prepared by mixing equal volumes of a 30 mM $MnCl_2$ solution with a 20 mM $KMnO_4$ solution at pH 10 (Foster et al., 2003). Both precipitates were washed several times in ultrapure water, and then freeze-dried. The precipitates were freeze-dried to allow use of the same materials for various experiments in this study (adsorption experiments, isotopic study, and XAFS measurements), and to avoid the change of their crystal structure before and/or during the measurement of EXAFS spectra. Identification of both minerals was conducted with an X-ray diffractometer (Multi Flex, Rigaku Co. Ltd.) and Fe and Mn K-edge EXAFS at BL-12C at the Photon Factory (Tsukuba, Japan).

A standard REE solution (Spex Certiprep., USA) containing all REEs, except promethium (Pm), at a concentration of 10.0 mg/L each was placed in plastic bottles with 100 mg ferrihydrite or 30 mg δ-MnO_2 for the solid phase. In the REE/ferrihydrite system, 1 mL REE solution and 10 mL ultrapure water served as a liquid phase, whereas 6 mL REE solution with 1 mL ultrapure water was mixed in the REE/δ-MnO_2 system. Diluted NaOH and HCl solutions were used to adjust the pH to 5.00 ± 0.05, where REE is dissolved as hydrated free ion in water without the formation of a REE carbonate and/or a hydroxide complex. Ionic strength was not considered in this study because our primary aim was to understand Ce isotopic fractionation under the simplest conditions. Notably, in our experiment, the Ce^{3+} aqua complex dominated the Ce species in the liquid phase (Fig. 3−1B). The suspension was stirred for 6 h at 25 °C using a shaking apparatus, based on findings that the apparent distribution coefficients of La, Ce, gadolinium (Gd), and lutetium (Lu) are almost constant from 3 h to 130 h (Ohta and Kawabe, 2001). This finding indicated that 6 h is a sufficient time to reach equilibrium. At the end of the experimental period, the liquid phase was separated from the solid phase by filtration using a hydrophilic PTFE filter (0.2 μm; ADVANTEC).

The filtrate was acidified with HNO_3 to obtain a final concentration of 2 wt% for the determination of the REE concentration using an inductively coupled plasma mass spectrometer (ICP-MS; Agilent 7700). Indium (In) and bismuth (Bi) were also added at

a concentration of 1 μg/L as internal standards. The precision of the ICP-MS measurement was better than 1% for all the REEs, except for erbium (Er) (1.7%), as calculated from repeated measurements. The distribution coefficient (K_d) of a REE between the liquid and solid phases is defined as

$$K_d(\mathrm{L/g}) = \frac{[\mathrm{REE}]_{init} - [\mathrm{REE}]_{fil}}{c \times [\mathrm{REE}]_{fil}} \quad (3-1)$$

where $[REE]_{fil}$ is the REE concentration in the filtrate and $[REE]_{init}$ is the initial concentration of dissolved REE. c (g/L) denotes the ratio of the solid phase (ferrihydrite or δ-MnO_2, dry weight) to water, which was 0.0097 and 0.0040 g/L for adsorption on ferrihydrite and δ-MnO_2, respectively. The adoption of different solid–water ratios between ferrihydrite and δ-MnO_2 systems was necessary to obtain appropriate K_d values for the determination of isotopic fractionation factors. δ-MnO_2 exhibited much higher affinity for REE than ferrihydrite, so that, the REE concentrations remaining in the solution were lower than the detection limit of our measurement in the δ-MnO_2 system.

3.2.2 Adsorption and precipitation of Ce

A Ce(III)Cl_3 reagent (Wako, Japan) dissolved in ultrapure water was used to adsorb Ce on both ferrihydrite and δ-MnO_2. Various amounts of $CeCl_3$ solution were placed in plastic bottles with 100 mg ferrihydrite or 30 mg δ-MnO_2 for the solid phase. In this experiment, the amounts of the solid phase were fixed, whereas the Ce concentration was systematically changed to prepare samples with different adsorbed or precipitated fractions (the ratio of the adsorbed or precipitated Ce to the total Ce added into the system). The adsorbed fraction was 1 if all the Ce added into the system were adsorbed on the solid phase. For the REE adsorption experiment, the pH was adjusted to 5.00 ± 0.05 and the suspension was stirred for 6 h at 25 °C. At the end of the experimental period, the liquid phase was separated from the solid phase, as described in Section 3.2.1.

The liquid samples were acidified with 2 wt% HNO_3 to prevent Ce precipitation. Ferrihydrite was dissolved with 6 M HCl, and δ-MnO_2 was dissolved with 6 M HCl and H_2O_2. Both minerals were then finally dissolved in 0.5 M HCl solution, followed by the separation of Ce from Fe or Mn by cation exchange column chemistry. For the elution of Fe, 2.0 M HCl solution was passed through a column (length: 10 cm, diameter: 1.0 cm) loaded with cation exchange resin (Bio-Rad, AG50W-X8), whereas 2.0 M HNO_3 solution was used to elute Mn. Almost 100% (better than 99%) Ce was recovered by the elution using 6.0 M HCl solution, indicating that no isotopic fractionation occurred during the column chemistry. The Ce concentrations in both solid and liquid samples were determined using an ICP-MS (Agilent 7700). Procedural blanks in the experiments for Ce were checked using ultrapure water, which was below the detection limit (0.5 ng/kg).

Adsorption experiments under various elapsed times were also performed to examine whether isotopic equilibrium was attained. In this experiment, the adsorbed fraction was adjusted between 0.25 and 0.35 for the ferrihydrite system, and adjusted to 0.90 to 0.99 for the δ-MnO_2 system. In both systems, ionic strength was adjusted to 0.10 and 0.70 M by NaCl solution and pH was adjusted to 5.00 ± 0.05. The suspension was stirred for 24, 120, 168, and 240 h. The procedure after the experiment was similar to those previously described. In this experiment, Ce in the liquid phase was separated from Na using the cation exchange column before the measurement. After the elution of Na using 1.5 M HCl, more than 99% Ce was recovered by 6.0 M HCl.

Spontaneous precipitation of Ce(IV) from the $CeCl_3$ solution was induced at pH 5.00 ± 0.05 in an O_2 gas bubbling environment. The solutions were left for 1 week to obtain Ce(IV) precipitates. The precipitate obtained was recovered using a 0.2 μm hydrophilic PTFE filter (ADVANTEC). Various Ce concentrations in the initial solution (from 0.5% to 2%) were tested to prepare the Ce precipitates. The oxidation state of Ce in the precipitates was determined by Ce L_{III}-edge XANES (Section 3.2.4).

3.2.3 Isotopic analysis

Isotope ratios of Ce were determined at the Kochi Institute for Core Sample Research, Japan Agency for Marine-Earth Science and Technology (JAMSTEC) using a double-focusing multiple collector (MC) ICP-MS (Neptune, Thermo Fisher). The details of this instrument were previously described (Weyer and Schwieters, 2003; Wieser and Schwieters, 2005).

Ce has four stable isotope masses, namely, 136, 138, 140, and 142, with isotopic abundances of 0.19%, 0.25%, 88.45%, and 11.11%, respectively. Among these isotope masses, ^{140}Ce and ^{142}Ce abundances were determined using an MC-ICP-MS. ^{136}Ce and ^{138}Ce were not measured because their relative isotopic abundances are two orders of magnitude lower than those of ^{140}Ce and ^{142}Ce. The analyzed Ce solutions were diluted to concentrations of about 200 μg/L. During the measurements, the neodymium (Nd) on mass 146 was also monitored to estimate the influence of ^{142}Nd, which can interfere with ^{142}Ce. The signal of ^{146}Nd was negligible (<0.01% of the ^{142}Ce signal) for all samples and standard solutions, indicating that the isobaric interference by ^{142}Nd was negligible in this study. Furthermore, the ion signal of Ce as ^{140}Ce^{16}O was checked before the isotopic analysis. The CeO/Ce ratio was adjusted in the range of 5% to 8% (average: 6%) by decreasing the carrier gas flow rate.

The measured isotope ratio of ^{142}Ce/^{140}Ce was corrected using the samarium (Sm) doping technique in wet plasma mode. Among the Sm stable isotopes (144, 147, 148, 149, 150, 152, and 154), the relative abundances of ^{147}Sm and ^{149}Sm are similar at 14.99% and 13.82%, and do not interfere with Ce isotopes. Therefore, these two Sm isotopes were measured by adding a Sm standard solution (Wako, Japan) diluted to about 200 μg/L to the Ce solutions just before the Ce isotope analysis. No Sm signals were observed for all the samples before the doping with the Sm solution.

In the Sm doping technique, the observed ^{142}Ce/^{140}Ce isotope ratios were corrected based on an exponential law using the ^{147}Sm/^{149}Sm ratio of a reference Sm solution. The relationship between the observed and normalized isotope ratios of Ce and Sm is described by the following equations:

$$(^{142}\mathrm{Ce}/^{140}\mathrm{Ce})_{\mathrm{norm}} = (^{142}\mathrm{Ce}/^{140}\mathrm{Ce})_{\mathrm{obs}} \times (^{142}\mathrm{A}/^{140}\mathrm{A})^{f\mathrm{Ce}} \qquad (3-2)$$

$$(^{147}Sm/^{149}Sm)_{norm} = (^{147}Sm/^{149}Sm)_{obs} \times (^{147}A/^{149}A)^{f_{Sm}} \quad (3-3)$$

$$f_{Ce} = f_{Sm} \quad (3-4)$$

where f and A are the mass discrimination correction factor and the atomic masses of the Ce and Sm isotopes, respectively.

The isotopes measured using MC-ICP-MS were ^{140}Ce, ^{142}Ce, ^{146}Nd, ^{147}Sm, and ^{149}Sm. The $CeCl_3$ solution used in the adsorption experiment was employed as a standard solution that was analyzed every three or four samples. The isotope ratios are expressed in standard delta notation relative to the average standards, as shown in the following equation:

$$\delta^{142}Ce = \left[\frac{\left({}^{142}Ce/{}^{140}Ce \right)_{sample}}{\left({}^{142}Ce/{}^{140}Ce \right)_{CeCl3}} - 1 \right] \times 10^3. \quad (3-5)$$

The analytical uncertainty for the measurement was 0.064‰ (2σ), which was calculated from repeated analysis of the standard $CeCl_3$ solution (n = 26).

3.2.4 XAFS analysis

The Ce adsorption experiment was conducted again for both δ-MnO_2 and ferrihydrite under the same conditions, and the solid phases were filtrated using a 0.2 μm mixed cellulose filter (ADVANTEC). Immediately after filtration, the solid samples were packed into individual polyethylene bags, and then frozen. The Ce L_{III}-edge (5.723 keV) XANES was measured at BL-12C at the Photon Factory (Tsukuba, Japan). The Ce L_{III}-edge XANES spectra, which are sensitive to the covalent/ionic bond character and the oxidation state, were measured for the adsorbed samples in fluorescence mode using a 19-element germanium (Ge) semiconductor detector. The spontaneous precipitation of Ce and the three reference materials diluted by boron nitride powder, namely, $CeCl_3$, CeO_2, and $Ce(SO_4)_2$ were measured in transmission mode. The measurements were conducted under ambient pressure and temperature. The X-ray energy was calibrated with the first peak of CeO_2 at 5.723 keV. The Ce K-edge (40.453 keV) EXAFS spectra of the adsorbed samples and the standard materials, namely, $CeCl_3$ and CeO_2, were

measured at BL-01B1 at SPring-8 (Hyogo, Japan). The K-edge EXAFS spectra, which provide quantitative information about the distance to the neighboring atoms and the CN, were also measured in fluorescence mode using a 19-element Ge semiconductor detector. The energy was calibrated with the first peak of CeO_2 at 40.453 keV. The repeated scans of XANES and EXAFS yielded identical spectra to one another, indicating that X-ray-induced redox change of Ce did not occur in our experiments.

Both XANES and EXAFS spectra were analyzed using the REX2000 software (Rigaku Co. Ltd.). The parameters generated by the FEFF 7.0 code (Zabinsky et al., 1995) were used for the EXAFS analysis. After extracting the EXAFS oscillation and its Fourier transform, the inversely Fourier-filtered data were analyzed using a standard curve-fitting method. The theoretical phase shifts and amplitude functions for the Ce–O, Ce–Ce, Ce–Fe, and Ce–Mn pairs employed in this fitting procedure were extracted from FEFF 7.0 (Zabinsky et al., 1995). Finally, the EXAFS spectrum in the whole k- and R-space ranges employed in the procedure was compared with the measured EXAFS spectrum in k- and R- spaces to confirm the good fitting of the measured to the simulated spectrum. Multiple scattering was initially included in this study, but was found to be a very weak contribution to the EXAFS spectra. The error estimates of the interatomic distance and CN obtained by the fitting were ±0.02 Å and ±20%, respectively (O'Day et al., 1994). The quality of the fit was given by the goodness-of-fit parameter *R*, defined by

$$R = \frac{\sum[x_{obs}(\mathrm{E}) - x_{\mathrm{cal}}(\mathrm{E})]^2}{\sum[x_{obs}(\mathrm{E})]^2} \qquad (3\text{–}6)$$

where $\chi_{\mathrm{obs}}(E)$ and $\chi_{\mathrm{cal}}(E)$ are the experimental and calculated absorption coefficients at a given energy (E), respectively.

3.3 Results

3.3.1 REE distribution patterns

The REE distribution patterns for the adsorption of REEs on ferrihydrite and δ-MnO_2 are shown in Fig. 3–2A. Both distribution patterns exhibited a convex M-type tetrad effect and smaller log K_d(Y) than the log K_d(Ho) values. These findings are consistent with a previous report by Ohta and Kawabe (2001). In addition, both patterns showed "apparent" positive Ce anomalies (Ce/Ce* > 1). In this study, Ce/Ce* is defined as

$$\mathrm{Ce/Ce^*} = \frac{\mathrm{Ce}}{\sqrt{\mathrm{La} \times \mathrm{Pr}}} \tag{3–7}$$

where the chemical symbol represents the log K_d value of the element. However, according to the "true" Ce anomaly defined by Bau and Dulski (1996), the distribution pattern of REEs adsorbed on δ-MnO_2 shows a positive Ce anomaly, whereas that of REEs on ferrihydrite shows a negative La anomaly (Fig. 3–2B). This result indicates that "apparent" positive Ce anomaly was caused by the presence of the M-type tetrad effect, and that Ce is not oxidized by Fe minerals, but is scavenged by Mn oxide through oxidation to Ce(IV) from the liquid phase. The formation of Ce(IV) was further supported by the XANES analysis, as will be discussed later.

3.3.2 Isotopic fractionation of Ce between the solid and liquid phases

First, the time dependence of the Ce isotopic data in the liquid phase was examined for the Ce/ferrihydrite and Ce/δ-MnO_2 systems (Fig. 3–3). Although the δ^{142}Ce values for the ferrihydrite system presented only a small fractionation, the values for the δ-MnO_2 system were fractionated to positive values, indicating that the lighter ^{140}Ce isotope was partitioned into the solid phase to a greater degree than the heavier ^{142}Ce. The variation of δ^{142}Ce values in the liquid phase was within the analytical uncertainty in this experimental period, both for the ferrihydrite and δ-MnO_2 systems, suggesting that isotopic equilibrium was attained within 6 h. The degree of isotopic fractionation did not vary with ionic strength.

The results of the isotopic fractionation of Ce during adsorption and spontaneous precipitation are presented in Table 3–1 and Figs. 3–4A (adsorption on ferrihydrite), 3–4B (spontaneous precipitation), and 3–4C (adsorption on δ-MnO_2), versus the fraction of total Ce adsorbed or precipitated. In Fig. 3–4, model lines for the equilibrium isotopic fractionation and the Rayleigh fractionation are shown as solid and dashed lines, respectively. As a constraint on the model lines, the δ^{142}Ce value for the solid phase should be 0‰ when the adsorbed or precipitated fraction is 1. By contrast, if all the Ce remains in the liquid phase, the δ^{142}Ce value for the liquid phase should not vary from that of the original $CeCl_3$ solution. The mean α_{Lq-So} value listed in Table 3–1 was used in calculating these model lines. In the table, the isotopic fractionation factor α between the liquid and solid phases was calculated as

$$\alpha_{Lq-So} = \frac{10^3 + \delta^{142}Ce_{Lq}}{10^3 + \delta^{142}Ce_{So}}. \qquad (3–9)$$

In relation to the degree of isotopic fractionation between the liquid and solid phases in the three systems, the mean α_{Lq-So} value is largest when Ce is adsorbed on δ-MnO_2. For the spontaneous precipitation of Ce, although we could achieve only a low precipitation fraction, the mean α_{Lq-So} value was slightly higher than that of the Ce/ferrihydrite system.

3.3.3 XAFS spectra

The Ce L_{III}-edge (5.723 keV) XANES spectra of both Ce adsorbed on ferrihydrite and δ-MnO_2 measured at BL-12C at the Photon Factory (Tsukuba, Japan), along with results for certain reference materials, are shown in Fig. 3–5. The L_{III}-edge XANES spectrum of Ce precipitated from the same $CeCl_3$ solution is also shown. The shapes of the spectra revealed a clear distinction between trivalent and tetravalent Ce, that is, Ce(III) presents one sharp peak and Ce(IV) shows a two-humped peak. In addition, the indicated energy of the peak tops for Ce(III) and Ce(IV) differs. The results illustrate that Ce adsorbed on ferrihydrite was trivalent in our samples. By

contrast, the two-humped peak of the Ce L_{III}-XANES spectrum of Ce(III) adsorbed on δ-MnO_2 suggests that Ce was oxidized to the tetravalent state. This result is consistent with expectations based on the Eh–pH diagram (Fig. 3–1A).

Similar to the XANES spectra, the Ce K-edge EXAFS spectra can be classified into two groups based on their frequency patterns. The phase of EXAFS oscillation in the k-space for the $CeCl_3$ solution and the Ce adsorbed on ferrihydrite was shifted from the other three spectra, that is, spontaneous precipitation of Ce, Ce adsorbed on δ-MnO_2, and tetravalent CeO_2 reagent (Fig. 3–6A). The amplitude of the oscillation for the CeO_2 spectrum increased with the increase in *k* range. Difference among the spectra was also observed in the R-space after Fourier transformation (FT). The FT magnitude of the $CeCl_3$ solution and Ce on ferrihydrite showed one peak, whereas those of the spontaneous precipitation of Ce, Ce on δ-MnO_2, and CeO_2 showed two peaks (Fig. 3–6B). The first ($R + \Delta R = 1.75$) and second ($R + \Delta R = 3.5$) peaks correspond to the first and second coordination spheres, respectively. Oxygen is an element in the first coordination for all spectra. The second coordination can reflect the shell of Ce–Ce or Ce–Mn, indicating spontaneous precipitation and CeO_2 or Ce adsorbed on δ-MnO_2, respectively. The fitting results for the Fourier transform spectra are listed in Table 3–2. The bond length of Ce–O is approximately 2.52 Å to 2.53 Å for the $CeCl_3$ solution and the Ce/ferrihydrite system, whereas it is approximately 2.30 Å for the Ce precipitation, Ce/δ-MnO_2 system, and CeO_2 reagent. In the Ce/δ-MnO_2 system, a better-fitting result was obtained by assuming a Ce–Ce shell instead of a Ce–Mn shell. This process is discussed in Section 3.4.2.2.

3.4 Discussion

3.4.1 Change in oxidation state during adsorption and precipitation

Given that a "true" positive Ce anomaly was not observed for the sample of Ce(III) adsorbed on ferrihydrite (Fig. 3–2), it is suggested that Ce was not oxidized by Fe minerals. By contrast, a large positive Ce anomaly was observed from the sample of Ce adsorbed on δ-MnO_2, suggesting that Ce was scavenged oxidatively for the liquid

phase by Mn oxide (Fig. 3–2). Previously, this kind of REE pattern was used as the basis of discussions on the valence of Ce. Although the REE pattern can provide some indication as to whether Ce is trivalent or tetravalent, XANES spectra can provide the direct evidence on Ce oxidation state.

The Ce L_{III}-XANES spectrum clearly showed that the Ce adsorbed on ferrihydrite is trivalent, at least on the timescale considered in this study (Fig. 3–5). An important point from this result is that ferrihydrite does not oxidize Ce on the timescale of this study, as expected based on the Eh–pH diagram (Fig. 3–1A). This result is consistent with previous studies (De Carlo and McMurtry, 1992; Kawabe et al., 1999a; Takahashi et al., 2007). Compared with leaching experiments (Bau and Koschinsky, 2009), the XANES data can provide more direct evidence and from these data it was clarified that oxidative scavenging of Ce does not occur by means of interaction with Fe minerals within the time range employed in this study. By contrast, Ce adsorbed on δ-MnO_2 was oxidized to a tetravalent state, which is consistent with the expectations based on the Eh–pH diagram (Fig. 3–1A) and as suggested in other studies (Takahashi et al., 2000a, 2007; Ohta and Kawabe, 2001). This outcome is also consistent with the results of the REE adsorption experiment, which showed the positive Ce anomaly (Fig. 3–2). In addition, the XANES spectrum of the spontaneous precipitation of Ce also showed a two-humped peak, suggesting that Ce was oxidized by the bubbling of O_2 gas to a highly insoluble tetravalent state.

Although REE patterns and XANES spectra suggest whether Ce is trivalent or tetravalent, as shown in Fig. 3–2 and 3–5, the timing of oxidation, that is, whether Ce is oxidized during adsorption or in the water column before adsorption, cannot be clearly determined, which may be related to the isotopic fractionation found in our system. This issue is explored in the discussion in Section 3.4.2.

3.4.2 Stable isotopic fractionation of Ce between the solid and liquid phases

In this section, the isotopic fractionation based on the local structural data of Ce by XAFS is discussed in the framework of equilibrium isotopic fractionation. The

attainment of the isotopic equilibrium is suggested because (i) the δ^{142}Ce values of the liquid phase with similar adsorbed fraction did not show isotopic variation against elapsed time (Fig. 3–3) and (ii) the isotopic fractionation of Ce during the adsorption experiment and the formation of spontaneous precipitate obeyed the model line of the equilibrium isotopic fractionation (Fig. 3–4). Although a study of natural ferromanganese nodules and crusts showed that the magnitude of Ce anomaly was kinetically controlled (Takahashi et al., 2007), the growth rate of natural ferromanganese crust is very slow, irrespective of the formation environments, compared with our experimental study. Thus, the reaction in the natural sample can be regarded as a pseudoequilibrium adsorption reaction over a short period, which can be treated by adsorption experiments in the laboratory, as conducted in this study.

The main factors controlling the degree of equilibrium isotopic fractionation are temperature, relative mass difference between isotopes (Bigeleisen and Mayer, 1947; O'Neil, 1986; Schauble, 2004). In addition, the heavier isotope preferentially partitions into stronger bonding sites relative to the weaker bonding site, including a higher oxidation state, highly covalent bonds, shorter bond lengths, low-spin electronic configurations, and a lower CN (Bigeleisen and Mayer, 1947; O'Neil, 1986; Schauble, 2004). Data for the chemical state of Ce before and after the adsorption experiment are necessary to clarify the reason for the Ce isotopic fractionation. This issue is discussed, along the Ce K-edge EXAFS spectra, below.

3.4.2.1 Coordination environment and isotopic fractionation: Ce/ferrihydrite and Ce precipitation systems

There are two main types of adsorbed species, namely, outer-sphere and inner-sphere surface complexes. The former species is adsorbed as hydrated species without direct bonding to the solid surface, whereas the latter shares oxygen between the adsorbed species and adsorbent surface. The absence of the second shell for the Ce/ferrihydrite system (Fig. 3–6B) suggests that Ce mainly forms an outer-sphere complex on the surface of ferrihydrite, which is in contrast to the clear second shell

peak found in the Ce/δ-MnO_2 system (Fig. 3–6B). Moreover, the interatomic distance between Ce and first neighbor O, and the CN of the first shell, for the Ce^{3+} adsorbed on ferrihydrite are similar to those for the Ce^{3+} aqua complex (Table 3–2). These results show that the local coordination environment of Ce^{3+} adsorbed on ferrihydrite is similar to that of the Ce^{3+} aqua complex. By contrast, the local structure of Ce was changed from the aqua complex in the Ce-precipitation and Ce/δ-MnO_2 systems. For the isotopes, the degree of isotopic fractionation of Ce was the smallest for the ferrihydrite system among the three systems, which can be attributed to the similarity in local structure between the Ce adsorbed on ferrihydrite and the Ce aqua complex. Similar phenomena have been found in other adsorption systems. For example, molybdate forms an outer-sphere complex on ferrihydrite, indicating that the local structure of Mo does not vary in the system, and consistent with the small Mo isotopic fractionation in the ferrihydrite system (Goldberg et al., 2009). Therefore, the smallest isotopic fractionation for Ce in the Ce/ferrihydrite system, among the three systems, can be explained within the framework of equilibrium isotopic fractionation, that isotopic fractionation must be accompanied with changes in the local structure of the ion during the reaction (Bigeleisen and Mayer, 1947; O'Neil, 1986; Schauble, 2004).

In the Ce-precipitation system, $\delta^{142}Ce$ becomes larger for the Ce remaining in solution. The XANES spectra showed that Ce in the spontaneous precipitation was oxidized to Ce(IV), a higher oxidation state than Ce in Ce^{3+} solution (Fig. 3–3). Therefore, the bond length of Ce–O is shorter because of the increase in the charge, which is reflected in the EXAFS results for the Ce(IV) species (Table 3–2). Furthermore, in general, it is strongly expected that CN decreases as the ionic radius decreases, although the decrease is not clear from our results due to the large analytical uncertainty in CN. These results indicate that the factors controlling the isotopic fractionation of Ce cannot be attributed to the stronger bonding of Ce–O in the Ce(IV) precipitates or Ce(IV) (hydr)oxides relative to the aqua complex. Therefore, the preferential retention of the heavier isotope in the aqueous phase cannot be explained reasonably based on the structural data or on the rule of equilibrium isotopic fractionation, as discussed by Bigeleisen and Mayer (1947). However, in a manner

analogous to the case for Ce, stable isotopic fractionation between aqueous Fe(III) and precipitated Fe(III) showed that Fe precipitation had a smaller δ^{56}Fe value than that of coexisting $Fe(III)_{aq}$ (Skulan et al., 2002; Balci et al., 2006), indicating that lighter isotopes can be partitioned into the solid phase when the precipitation occurs from aqueous solution. This fractionation is qualitatively consistent with the isotopic fractionation of Ce in the Ce-precipitation system.

3.4.2.2 Ce species incorporated into δ-MnO_2

The notable result obtained from the EXAFS spectra signatures was that the spectrum of the Ce adsorbed on δ-MnO_2 was similar to that of spontaneous precipitation of Ce (Fig. 3–6A). A study of natural ferromanganese crusts showed that the XANES spectra of the samples do not resemble $Ce(OH)_4$ (Takahashi et al., 2007), which was also observed in our XANES spectra. However, the EXAFS spectrum of Ce/δ-MnO_2 showed its similarity to that of $Ce(OH)_4$. This difference could be caused by the high concentration of Ce in our experiment compared with that of the real deep ocean, where the Ce concentration is several pmol/kg. In addition, the Fourier transform magnitude of the Ce adsorbed on δ-MnO_2 suggests that the interatomic distance of the second shell is similar to that for spontaneous precipitation of Ce, namely $Ce(OH)_4$ and CeO_2 (Fig. 3–6B). These findings suggest that the atom indicated in the second shell in the Ce/δ-MnO_2 system is not Mn but Ce. Assuming that the second neighboring atom is Mn, the interatomic distance between the center Ce and Mn is estimated as 4.113 ± 0.013 Å based on the EXAFS fitting; this value is even longer than the estimated values for the Ce–Ce shell (Table 3–2). The ionic radius at CN = 6 for Mn^{4+} (= 0.530 Å; Shannon, 1976) is much smaller than that for Ce^{4+} (= 0.870 Å), also suggesting that the assignment of Mn to the second shell is incorrect. Therefore, it is reasonable to expect that the atom at the second neighbor site in the Ce/δ-MnO_2 system is also Ce, indicating that Ce(IV) (hydr)oxide was formed at the surface of δ-MnO_2.

Although the EXAFS spectra in k-space showed similarities between the Ce/δ-MnO_2 system, Ce precipitation, and CeO_2, the relative intensity of the Ce–Ce peak

at R + ΔR = 3.8 Å in the R space decreased in the order of CeO_2 > Ce precipitation > Ce on δ-MnO_2 (Fig. 3–6B). In particular, the peak for Ce on δ-MnO_2 was much smaller than those for CeO_2 and Ce precipitation, as reflected in the CN of the Ce–Ce shell: 2.4 for Ce on δ-MnO_2 compared with 6.6 and 4.7, respectively, for CeO_2 and Ce precipitation (Table 3–2; note that the difference of the CN becomes larger if we assume the Debye-Waller factor for Ce-Ce is constant for the three species). In this case, the lower CN of Ce in the Ce/δ-MnO_2 system might be explained by the formation of nanoparticles of Ce(IV) (hydr)oxide, which has a lower CN value for the second neighboring Ce compared with the Ce bulk in CeO_2, as similarly observed in the K-edge EXAFS results for the Cu nanoparticles (Manceau et al., 2008). The smaller contributions of Ce-Ce shell in the Ce/δ-MnO_2 system compared to that of nanoparticles of $Ce(OH)_4$ in the k-space spectrum was also observed (Fig. 3–6C). Thus, the present results show that nanoparticles of Ce(IV) (hydr)oxide were formed in the Ce/δ-MnO_2 system. The Debye–Waller factor indicates that the degree of disorder of the coordination environment of Ce increases in the order of CeO_2 < Ce precipitation < Ce on δ-MnO_2 (Table 3–2), which is also compatible with the suggestion that Ce is present as nanoparticles of Ce(IV) (hydr)oxide on δ-MnO_2.

In addition to the EXAFS results, the formation of $Ce(OH)_4$ nanoparticles is also reflected in the XANES spectra of Ce in the Ce/δ-MnO_2 and Ce precipitation systems. The absorbance of Ce(IV) (hydr)oxide and CeO_2 is higher at first maxima and the two spectra have a shoulder (Fig. 3–5). These two features are attributed to many-body effects and to the covalent nature of the Ce–O–Ce bond (Kaindl et al., 1988; Hu et al., 1994; Soldatov et al., 1994; Takahashi et al., 2002b, 2007). However, such shoulders were not observed in the spectra of the Ce adsorbed on the δ-MnO_2 and $Ce(SO_4)_2$ reagents because of the more ionic character of the Ce(IV)–O bond in these compounds (Takahashi et al., 2002b). Alternatively, the absorbance of these two XANES spectra is higher at the second maxima (Fig. 3–5). The smaller the particle becomes, the greater the number of Ce–$(OH)_x$ bond becomes, leading to a decrease in the number of Ce–O–Ce bonds that represents more covalent bonding. An electronic polarization occurs when Ce forms a Ce–O–H bond, leading to a more ionic character. Therefore, the

formation of Ce(IV) (hydr)oxide nanoparticles is responsible for both the EXAFS and XANES spectra.

The formation of nanoparticles probably occured after the adsorption on δ-MnO_2 for the following reasons: (i) in the Co/δ-MnO_2 system, which behaves similarly to Ce in terms of the oxidative adsorption on δ-MnO_2, the oxidation of Co^{2+} to Co^{3+} occurred after the adsorption of Co^{2+} on δ-MnO_2 (Manceau et al., 1997); and (ii) the EXAFS spectrum of Ce on δ-MnO_2 differs from that of Ce in the spontaneous precipitation system. Based on these facts, it is suggested that Ce(III) is initially adsorbed on the δ-MnO_2 surface and Ce(III) is oxidized to Ce(IV) by δ-MnO_2 after the initial adsorption of Ce(III). The subsequent oxidation after the adsorption results in the formation of nanoparticles of Ce(IV) (hydr)oxide associated with δ-MnO_2.

3.4.2.3 Coordination environment and isotopic fractionation: Ce/δ-MnO_2 system

The relationship between Ce isotopic fractionation and Ce species in the Ce/δ-MnO_2 system is based on the Ce species on δ-MnO_2. The linear isotopic fractionation line in Fig. 3–4C shows that the system consisting of dissolved Ce(III), dissolved Ce(IV), Ce(III) adsorbed on δ-MnO_2, and Ce(IV) nanoparticles on δ-MnO_2 is at equilibrium. This observation indicates that Ce(IV) in the aqueous phase is also present and equilibrated with Ce(IV) nanoparticles in the solid phase, although the main pathway for the formation of Ce(IV) nanoparticles is the oxidation of Ce(III) after the adsorption of Ce(III) on δ-MnO_2, as suggested in the Section 3.4.2.2.

Here, the isotopic fractionation between aqueous Ce and $Ce(OH)_4$ nanoparticles on δ-MnO_2 is focused. Considering the very low solubility of Ce(IV), it is most likely that Ce(III) is the main species dissolved in the aqueous phase, whereas $Ce(OH)_4$ nanoparticles are the main Ce species in the solid phase. Thus, two fractionation pathways have to be considered if we assume equilibrium isotopic fractionation; that is, dissolved Ce(III) and $Ce(OH)_4$ nanoparticles are in equilibrium with both Ce(IV) in the aqueous phase and Ce(III) adsorbed on δ-MnO_2, respectively. The difference in the two

pathways is the timing of the oxidation, specifically, whether Ce is oxidized in the aqueous phase or after the adsorption.

In the first pathway, the equilibrium isotopic fractionation between dissolved Ce(III) to the Ce(IV) nanoparticles on δ-MnO_2 through Ce(IV) in the aqueous phase (Dissolved Ce(III) ↔ Ce(OH)x in the solution ↔ $Ce(OH)_4$ nanoparticles on δ-MnO_2) is considered. Although it is difficult to predict the direction and degree of the equilibrium fractionation between aqueous Ce(III) and Ce(IV) precipitates theoretically, as suggested in Section 3.4.2.2, the results obtained for the Ce-precipitation system showed that the heavier isotope remains in the aqueous phase during the precipitation (Fig. 3–4B). However, our results show a much greater isotopic fractionation factor in the Ce/δ-MnO_2 system than in the Ce-precipitation system. Considering the large difference in the isotopic fractionation between the two systems, it is speculated that the formation of $Ce(OH)_4$ nanoparticles on δ-MnO_2 is the main reason for the larger isotopic fractionation in this system compared with the Ce-precipitation system. In considering the nanoparticles, the following points arise: (i) the coordination environment of Ce at the surface of the $Ce(OH)_4$ nanoparticles is different from that of the larger $Ce(OH)_4$ particles; and (ii) the $Ce(OH)_4$ nanoparticles have a much greater population of Ce at the surface compared with larger particles. These distorted structures of Ce in the nanoparticles might cause greater isotopic fractionation, as suggested by previous studies (Kashiwabara et al., 2011; Wasylenki et al., 2011).

In the second pathway, assuming the adsorbed Ce(III) as the intermediate species, possible isotopic fractionation between dissolved Ce(III) and Ce(III) adsorbed on δ-MnO_2 (Dissolved Ce(III) ↔ Ce(III) on δ-MnO_2 ↔ $Ce(OH)_4$ nanoparticles on δ-MnO_2) can be suggested based on equilibrium isotopic fractionation during the adsorption reaction. Ohta et al. (2009) reported local structures of La(III) and Pr(III) adsorbed on a δ-MnO_2 surface, where the bond lengths of La–O (= 2.608 Å) and Pr–O (= 2.558 Å) were larger than the respective corresponding La–O (= 2.551 Å) and Pr–O (= 2.489 Å) distances in their aqua complexes. It is highly likely, therefore, that the Ce(III)–O bond length adsorbed on δ-MnO_2 may be much greater than that of the Ce(III) aqua complex. These suggestions appear reasonable in the framework of

equilibrium isotopic fractionation, as the results suggest that heavier Ce remains in the aqueous phase. In addition, Ohta et al. (2009) reported the bond length of REE–O in the REE/ferrihydrite system, stating that the REE–O distance increased in the order of REE^{3+} aqua complex < REE/ferrihydrite system < REE/δ-MnO_2 system. The larger difference in distance can explain the greater isotopic fractionation in the REE/δ-MnO_2 system compared with the REE/ferrihydrite system. The isotopic fractionation in the subsequent processes of Ce(III) oxidation on the δ-MnO_2 surface and the formation of Ce(IV) nanoparticles may be similar to that in the first case.

Therefore, it is reasonable to conclude that there is preferential adsorption of lighter Ce onto the solid phase, if we accept that (i) a heavier isotope remains in the aqueous phase in the Ce-precipitation system and (ii) equilibrium is attained in the Ce/δ-MnO_2 system, as suggested by Fig. 3–4C.

3.4.3 Application of XAFS and the Ce isotope ratio to geochemical samples

Given that the Ce/δ-MnO_2 system attains, at least apparently, equilibrium isotopic fractionation, the two reactions described in the Section 3.4.2.3 occur in the Ce/δ-MnO_2 system. It is strongly suggested that the initial reaction proceeds via the adsorption of Ce(III) on the δ-MnO_2 surface, followed by surface oxidation to Ce(IV). Final equilibrium was achieved in the Ce/δ-MnO_2 system. Oxidation at the δ-MnO_2 surface leads to the formation of $Ce(OH)_4$ nanoparticles on the surface. It was speculated that the formation of nanoparticles is related to the degree of isotopic fractionation in the Ce/δ-MnO_2 system, which is significantly greater than that in the Ce-precipitation system. Although the reason for the large isotopic fractionation in the Ce/δ-MnO_2 system is not yet clear, the difference in the isotopic fractionation in the three systems (Ce spontaneous precipitation, Ce/ferrihydrite, and Ce/δ-MnO_2) suggests that the Ce stable isotope may be used as a new redox indicator.

Even with the recent development of XANES analysis, the previous discussion on redox conditions has only referred to the Ce(III)/Ce(IV) boundary. Although the Ce L_{III}-XANES spectra can show the mixing ratio of trivalency and tetravalency, which

would be difficult to determine using only the size of the Ce anomaly, the situation has not changed significantly. Identifying the formation process of Ce(IV), that is, oxidative adsorption or oxidation in the liquid phase followed by precipitation, would enable more detailed discussion of the redox state. In this respect, the stable isotope ratio of Ce can give definitive data.

The isotopic fractionation of $\delta^{142}Ce$ between the liquid and solid phases is the lowest in the case of adsorption on ferrihydrite, which is not accompanied by the oxidation of Ce and occurs above the $Fe^{2+}/Fe(OH)_3$ boundary, below the Ce^{3+}/CeO_2 boundary in the Eh–pH diagrams (field (i) in Fig. 3–1A). For spontaneous precipitation of Ce, the $\delta^{142}Ce$ fractionation is greater than for Ce adsorbed on ferrihydrite, whereas it is less than that for Ce incorporated into δ-MnO_2. This situation occurs above the Ce^{3+}/CeO_2 boundary and below the Mn^{2+}/MnO_2 boundary, that is, in the relatively oxidative condition (field (ii) in Fig. 3–1A). Although the extent of $\delta^{142}Ce$ fractionation in these two cases is within analytical uncertainty, the size of the Ce anomaly and the XANES spectra data provide a clear distinction between adsorption without oxidation and spontaneous precipitation. The largest isotopic fractionation between the liquid and solid phases is observed when Ce is removed by δ-MnO_2 (field (iii) in Fig. 3–1A) via oxidative adsorption, which cannot be distinguished clearly from the spontaneous precipitation by the Ce anomaly and XANES data alone.

Thus, the combination of the Ce anomaly (and Ce oxidation state) and the stable isotope ratio of Ce may offer a powerful tool in detecting a consecutive variation from a reductive to an oxidative condition. This variation can be seen in geochemical samples such as Precambrian BIFs and carbonates, which may preserve redox information on paleo seawater when the Earth was under (i) a reductive condition, (ii) a moderately oxidative condition, or (iii) an oxidative condition. In addition, this method can be used to clarify the cause of the positive Ce anomaly seen in Archean BIFs (Kato et al., 2006), i.e. whether it is generated under moderately oxidative conditions (field (ii) in Fig. 3–1A) or oxidative conditions with the existence of Mn oxides (field (iii) in Fig. 3–1A). This combination could be especially useful for samples formed between 2.3 Ga and 2.1 Ga. To date, the atmospheric O_2 level is believed to be below 10^{-5} PAL (present

atmospheric level) until 2.3 Ga because of the appearance of sulfur mass-independent fractionation (Farquhar et al., 2000; Pavlov and Kasting, 2002). The presence of a eukaryote recently discovered in a 2.1 Ga black shale in Gabon (Albani et al., 2010) shows that an O_2 level greater than 1% PAL existed at that time. However, the lack of other evidence makes it difficult to discuss in detail the increase of atmospheric O_2 between these two time points. The combination of the stable isotope ratio and the Ce anomaly may enable a more precise estimation of the redox state of the paleo-ocean environment and the evolution of the atmosphere.

For example, if there is no Ce anomaly in Precambrian BIFs, it is expected that isotopic fractionation of Ce between a BIF and carbonate is small, as seen in the Ce/ferrihydrite system. Furthermore, as described above, such a condition is attained when the Eh–pH state is between the $Fe^{2+}/Fe(OH)_3$ and the Ce^{3+}/CeO_2 boundaries (field (i) in Fig. 3–1A), which generally corresponds to euxinic marine water. If a Ce anomaly is observed in a Precambrian BIF, analysis of the stable isotope ratio of Ce allows further investigation of whether the Ce(IV) is generated by spontaneous precipitation or by oxidative adsorption in the presence of a small amount of Mn oxide, which cannot be distinguished using other methods. If the Ce isotopic fractionation suggests that Mn oxide was present (but easily disappears due to the subsequent diagenetic process), the ocean at that time could be as oxic as it is today. It is therefore likely that the Ce isotope ratio will enable the determination of redox conditions more precisely than with a Ce anomaly alone. Although our study ultimately aims to use the Ce isotopic fractionation to understand the paleo-redox condition, the experiments were performed under low pH and high Ce concentration—conditions which are different from natural seawater. Thus, further studies are necessary more analogous to natural seawater conditions as follows: (i) Ce species in the aqueous phase must include dissolved complexes such as carbonate; (ii) experiments in the Ce/δ-MnO_2 system must be conducted at lower Ce concentration where the formation of $Ce(OH)_4$ nanoparticles is suppressed. However, the current study represents the first step in elucidating more quantitative redox information from Ce chemistry during adsorption reactions.

3.5 Conclusions

In this study, three data consisting of Ce—abundance, stable isotope ratio, and chemical state—were provided for the first time. The REE distribution coefficient pattern combined with Ce L_{III}-edge XANES spectra suggested that Ce is not oxidized by ferrihydrite, but is oxidatively scavenged by δ-MnO_2, as expected from the Eh–pH diagrams. The degree of isotopic fractionation of Ce between the liquid and solid phases increases as the redox condition becomes more oxic in the following order: adsorption without oxidation, Ce(IV) precipitation, and oxidative adsorption (incorporation). In particular, the latter two processes were distinguished by the Ce stable isotope ratio, and cannot be discerned using the Ce anomaly alone. The difference between the two systems originated from the different Ce isotopes in the solid phase of a $Ce(OH)_4$ precipitate in the spontaneous Ce precipitation and $Ce(OH)_4$ nanoparticles in the Ce/δ-MnO_2 system. Although we have to continue similar studies in systems more similar to the natural marine environment (e.g., carbonate complex in the aqueous phase, lower Ce concentration, etc.), it is expected that applying Ce geochemistry to Precambrian BIFs and carbonates in future research will lead to a better understanding of the paleo-redox state of the ancient oceans.

Table 3–1. Isotope ratio and fractionation factor for Ce during adsorption and precipitation.

System	Fraction	δ^{142}Ce (Lq)	δ^{142}Ce (So)	$\alpha_{Lq\text{-}So}$	Average
Ce/ferrihydrite	0.85	0.085	−0.073	1.000158	
	0.73	0.051	−0.089	1.000140	
	0.60	0.045	−0.089	1.000134	
	0.44	0.035	−0.106	1.000141	
	0.29	0.021	−0.139	1.000159	
	0.18	−0.001	−0.138	1.000137	1.000145
					±0.000022
Ce precipitation	0.12	0.045	−0.127	1.000173	
	0.09	0.033	−0.169	1.000202	
	0.06	0.020	−0.183	1.000203	
	0.03	0.000	−0.207	1.000207	1.000196
					±0.000031
Ce/δ-MnO_2	1.00	0.417	−0.004	1.000421	
	0.86	0.350	−0.065	1.000416	
	0.74	0.264	−0.163	1.000427	
	0.63	0.248	−0.219	1.000467	
	0.46	0.116	−0.238	1.000355	
	0.32	0.106	−0.272	1.000378	1.000411
					±0.000079

Note that deviations are expressed in 2σ values calculated from the respective $\alpha_{Lq\text{-}So}$ values.

Table 3–2. Fitting results of Fourier transform spectra.

System	Shell	CN	R (Å)	σ^2 (Å^2)	R factor (%)
Ce^{3+} solution	Ce–O	8.6 ±1.3	2.521 ±0.013	0.012	0.086
Ce/ferrihydrite (Ce/Fe = 0.0177)	Ce–O	7.5 ±1.3	2.526 ±0.014	0.013	0.056
Precipitation	Ce–O	8.4 ±1.2	2.303 ±0.014	0.015	6.3
	Ce–Ce	4.7 ±1.1	3.846 ±0.010	0.0058	
Ce/d-MnO_2 (Ce/Mn = 0.0199)	Ce–O	6.5 ±1.1	2.296 ±0.019	0.019	9.5
	Ce–Ce	2.4 ±1.3	3.850 ±0.024	0.0085	
CeO_2	Ce–O	8.5 ±1.2	2.335 ±0.011	0.0094	4.7
	Ce–Ce	6.6 ±2.0	3.855 ±0.012	0.0022	

Note: CN denotes the coordination number, R (Å) denotes the distance from the center atom, σ: Debye-Waller factor, and the R factor (%) is the quality of fit (see Eqn. 3–6).

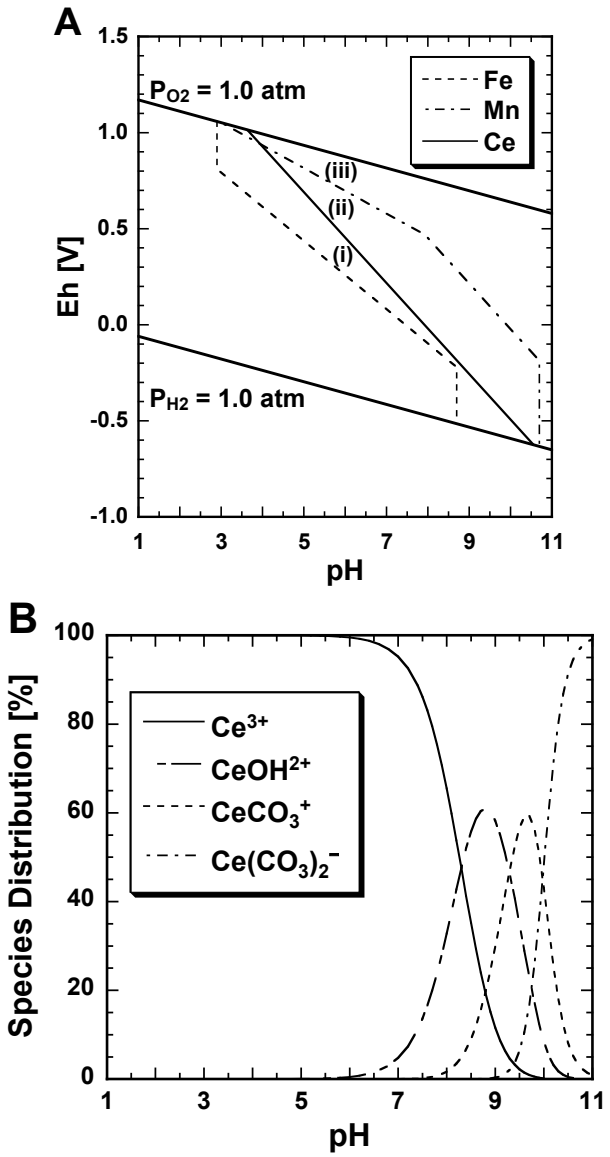

Fig. 3–1. (A) Eh–pH diagram for Fe, Mn, and Ce in the system metal–H–O at 25 °C. The dashed lines represents the soluble–insoluble boundary for Fe (soluble species: Fe^{2+} and Fe^{3+}; insoluble species: $Fe(OH)_3$ and $Fe(OH)_2$) and Mn (soluble species: Mn^{2+}; insoluble species: MnO_2, MnO, Mn_3O_4, and $Mn(OH)_2$). The solid line represents the boundary between Ce^{3+} (soluble) and CeO_2 (insoluble). In this calculation, the concentrations of both Fe and Mn are 10^{-6} M, and that of Ce is 10^{-10} M. (B) Calculated species distribution of Ce under the experimental conditions. The data for REE–carbonate complexation constants were obtained from Luo and Byrne (2004), and the equilibrium constants of the carbonate species were obtained from Nordstrom et al. (1990).

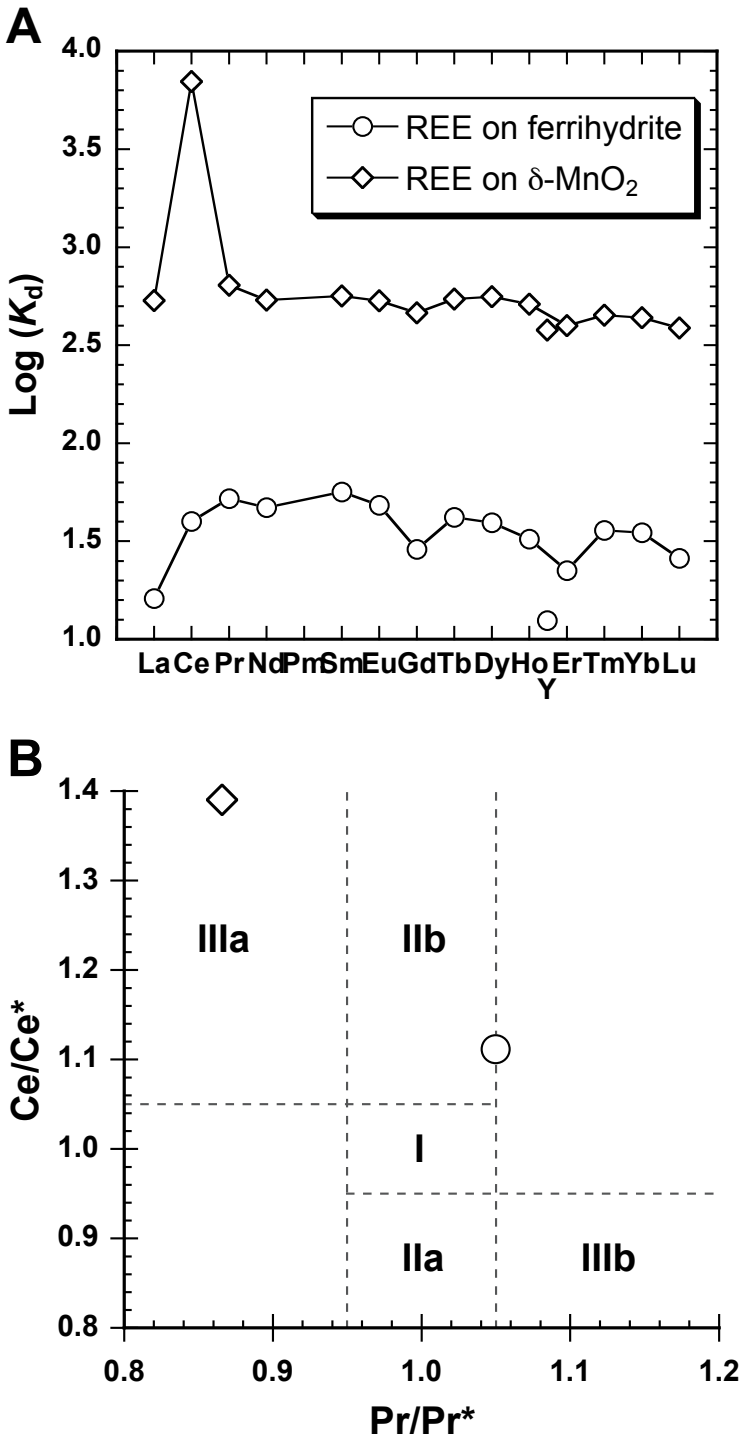

Fig. 3–2. (A) Distribution coefficient pattern of REEs between the liquid and solid phases. K_d is defined in the text (Eqn. 3−1). (B) Diagram to define "true Ce anomaly". Field I: neither Ce nor La anomaly; field IIa: positive La anomaly, no Ce anomaly; field IIb: negative La anomaly, no Ce anomaly; field IIIa: positive Ce anomaly; field IIIb: negative Ce anomaly. The legend is the same as that of 3−2A.

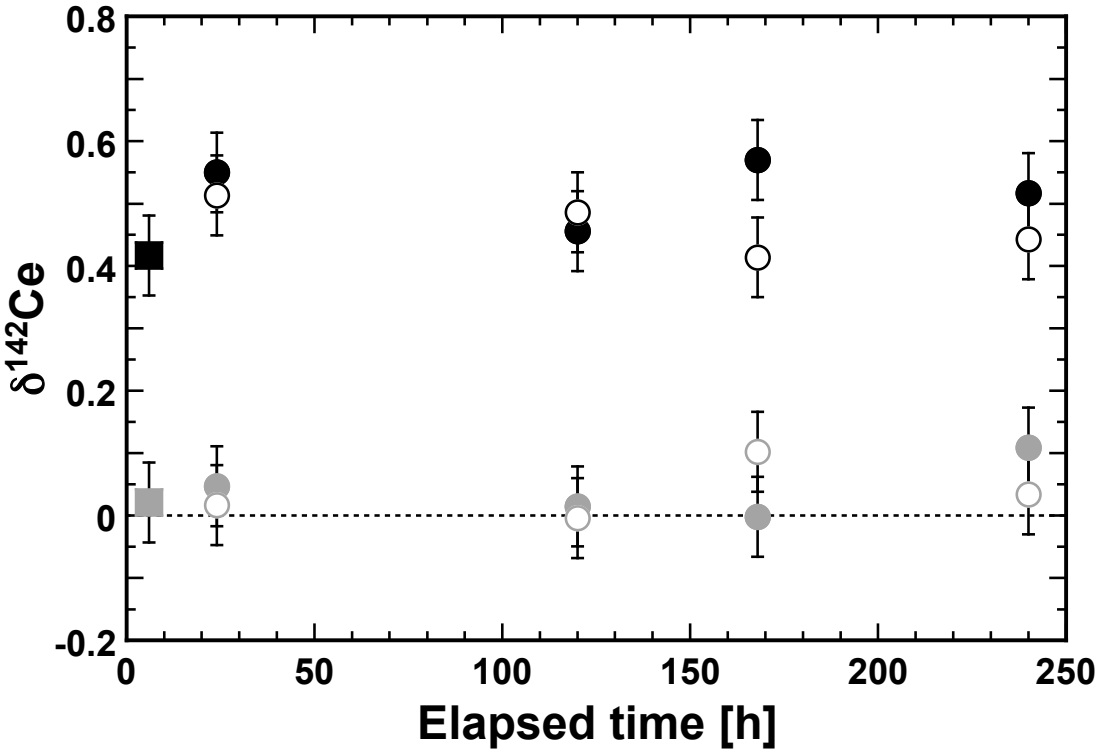

Fig. 3–3. Variation of δ^{142}Ce values in the liquid phase during the adsorption experiment at various elapsed times. Black symbols: Ce/δ-MnO_2 system with adsorbed fraction of 0.90−0.99; gray symbols: Ce/ferrihydrite system with adsorbed fraction of 0.25−0.35 (only a datum in 120 h, 0.70 M system was taken from the adsorbed fraction of 0.40); square symbols: data from Table 3−1; closed circles: ionic strength of 0.10 M; open circles: ionic strength of 0.70 M.

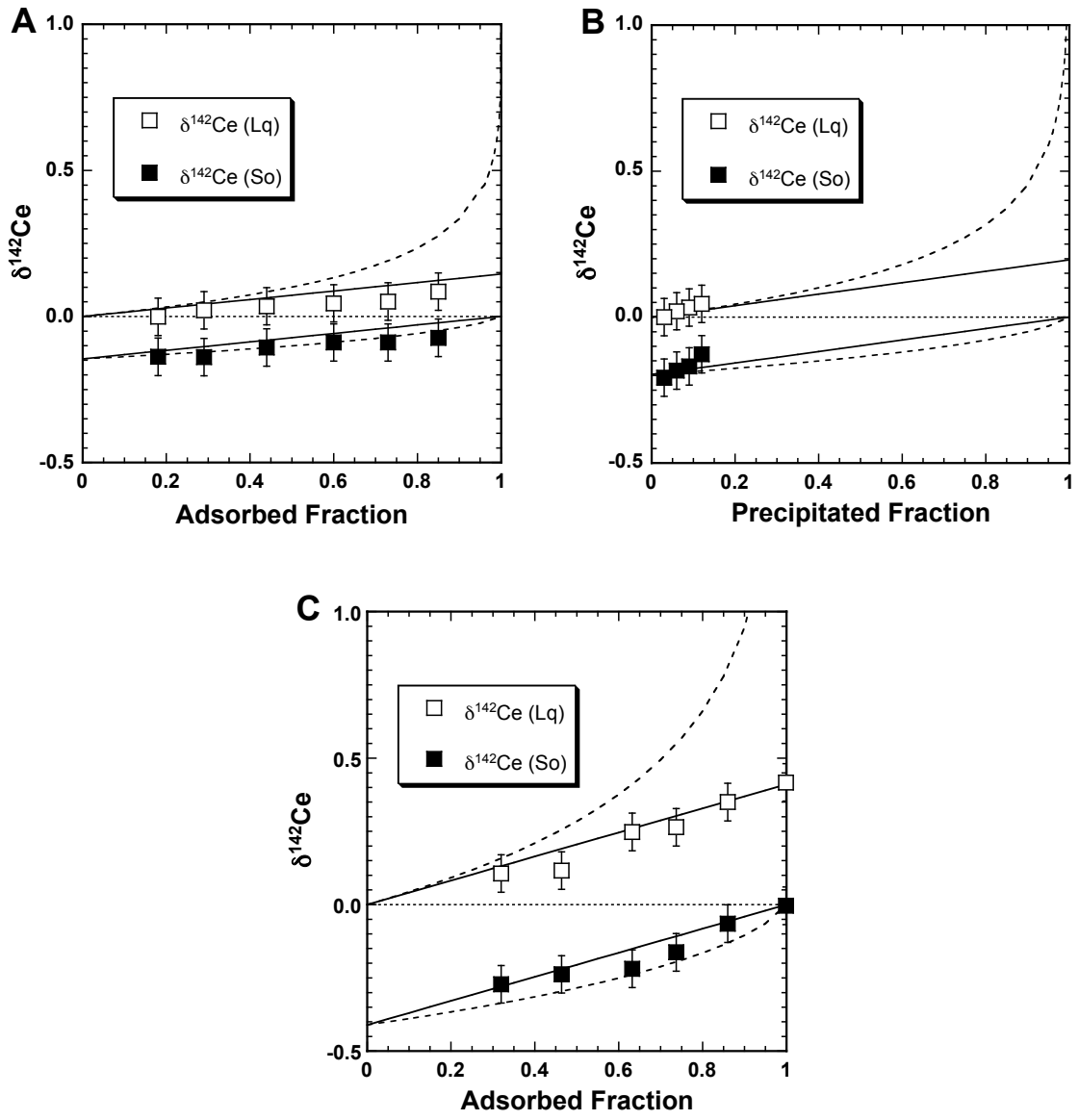

Fig. 3–4. Isotopic fractionation of Ce during (A) adsorption on ferrihydrite, (B) spontaneous precipitation, and (C) adsorption on δ-MnO_2, along with the adsorbed fraction in the system. Open squares represent the δ^{142}Ce values of the liquid phase, and closed squares represent the solid phase. The error bar indicates the analytical error calculated from repeated measurements of a standard solution. The solid lines correspond to a model of equilibrium fractionation and the dashed lines to a Rayleigh fractionation.

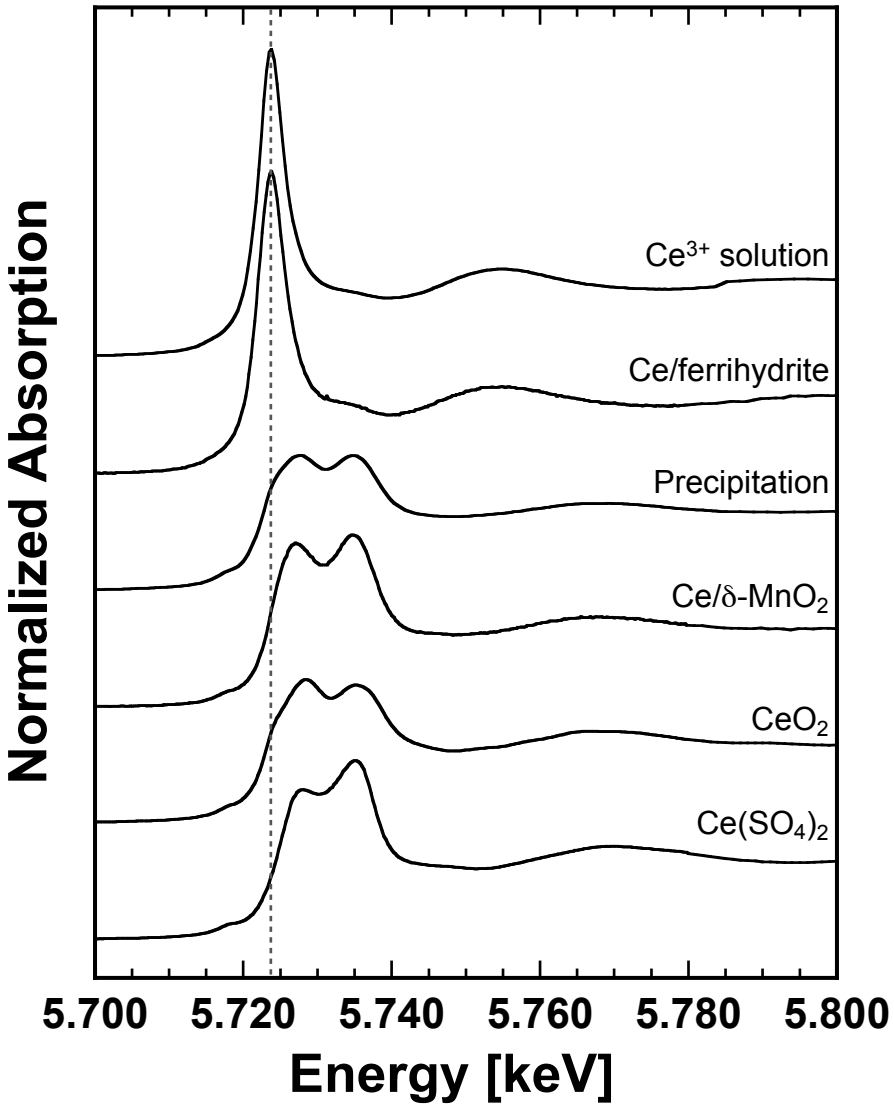

Fig. 3–5. Cerium L_{III}-edge XANES spectra of adsorption and reference materials (Ce^{3+} solution, CeO_2, and $Ce(SO_4)_2$). The dashed line runs through the peak top of Ce(III).

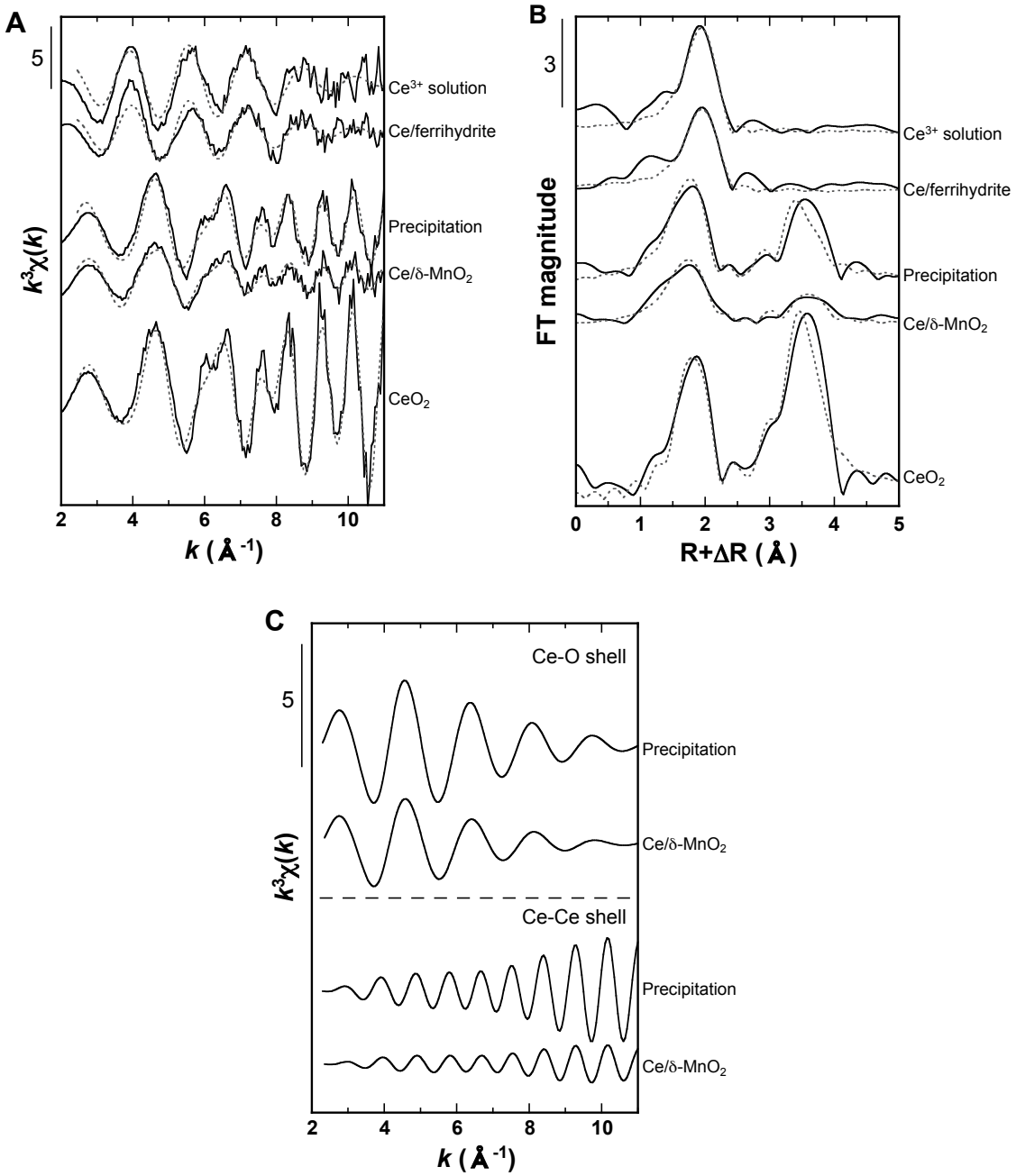

Fig. 3–6. (A) The k^3-weighted Ce K-edge EXAFS spectra of samples and reference materials (Ce^{3+} solution and CeO_2). (B) The radial structure functions of the samples and reference materials ($CeCl_3$ solution and CeO_2). In both figures, the solid lines represent measured data, and the dashed lines represent fitting results. (C) Contributions of Ce-O and Ce-Ce shells in the k-space spectrum of the spontaneous precipitation of Ce and Ce adsorbed on δ-MnO_2.

Chapter 4

Difference in the stable isotopic fractionations of Ce, Nd, and Sm during adsorption on iron and manganese oxides and its interpretation based on their local structures

4.1 Chapter introduction

The advent of multicollector-inductively coupled plasma-mass spectrometry (MC-ICP-MS), has enabled the study of the isotopic fractionation of heavy non-traditional elements (i.e., those heavier than sulfur), leading to a robust assessment of the behavior of elements such as silicon (Si) (De La Rocha et al., 2000), calcium (Ca) (Gussone et al., 2005), chromium (Cr) (Ellis et al., 2002; Frei et al., 2009), iron (Fe) (Beard and Johnson, 2004; Icopini et al., 2004; Johnson et al., 2004a), copper (Cu) (Maréchal et al., 1999; Mason et al., 2005), zinc (Zn) (Maréchal et al., 1999; Juillot et al., 2008; Moynier et al., 2009), selenium (Se) (Johnson et al., 1999; Johnson and Bullen, 2004), molybdenum (Mo) (Barling et al., 2001; Anbar, 2004: Barling and Anbar, 2004), antimony (Sb) (Rouxel et al., 2003), and thallium (Tl) (Rehkämper et al., 2002; 2004; Nielsen et al., 2009). Such work on the isotopic fractionation of heavy elements has provided a better understanding of ancient Earth and biogeochemical cycles (e.g., Halliday et al., 1998; Johnson et al., 2004b; Anbar and Rouxel, 2007), but despite the increasing attention given to the isotopic fractionation of heavy elements, the mechanisms controlling isotopic fractionation for some elements have yet to be clearly explained.

Elements that are present as cations in a solution, such as Fe, Cu, and Zn, have been shown to exhibit enrichment of the heavier isotopes on solid phases in adsorption experiments (Cacaly et al., 2004; Icopini et al., 2004; Clayton et al., 2005; Crosby et al., 2005; Pokrovsky et al., 2005; which are summarized in Balistrieri et al., 2008), whereas elements that form soluble oxyanions, such as germanium (Ge), Se, Sb, and Mo are subject to adsorption of lighter isotopes on Fe and/or Mn oxides (Johnson et al., 1999; Galy et al., 2002; Barling and Anbar, 2004; Ellis et al., 2004; Balistrieri et al., 2008;

Tanimizu et al., 2011). Isotopic fractionation is not observed during adsorption of hexavalent Cr on goethite and γ-Al_2O_3 although Cr(VI) is dissolved as an oxyanion (Ellis et al., 2004). Major factors that control equilibrium isotopic fractionation include temperature, the relative mass difference between isotopes, and the nature and strength of the bonding environment (Bigeleisen and Mayer, 1947; O'Neil, 1986; Schauble, 2004). The degree of equilibrium isotopic fractionation usually decreases as the temperature increases, the factor of which is roughly equal to $1/T^2$ for most elements, whereas isotopic fractionation is greater for lighter elements owing to the larger relative mass differences among their isotopes. At equilibrium, the heavy isotope of an element is preferentially concentrated in the component where the element forms a stronger bond. The bond strength is greater for the species that have (i) shorter bond lengths; (ii) higher oxidation states; (iii) highly covalent bonds between atoms with similar electronegativities; and (iv) lower coordination numbers (CNs) (Criss, 1999; Schauble, 2004). These rules suggest that large equilibrium isotopic fractionations occur at low temperatures between substances with highly varying oxidation states, bond lengths, or CNs. Knowledge on whether the adsorption occurs via inner-sphere complexation (ions have direct bond with the surface of a solid phase) or outer-sphere complexation (ions do not have direct bond but are attracted by electrostatic force to a solid phase) can also be important for isotopic fractionation in elements such as Fe and Mo (e.g., Barling and Anbar, 2004; Butler et al., 2005). Although several possible causes of isotopic fractionation have been presented, the chemical property that has the greatest influence on bond strength remains unknown.

The results in the Chapter 3 showed that the stable isotopic fractionation of cerium (Ce) observed during adsorption on ferrihydrite and δ-MnO_2 cannot be explained by the isotopic fractionation mechanisms described above. Under their experimental conditions, Ce should be dissolved as a free cation, specifically, the Ce^{3+} aqua ion, which suggests that the heavier isotope of Ce should be concentrated in the solid phase according to the general observation of cation adsorption. In particular, Ce adsorption on δ-MnO_2 was accompanied by the oxidation of Ce(III) to Ce(IV) on the surface of the substrate, suggesting that the heavier Ce isotope should be concentrated

in δ-MnO_2 because both the higher oxidation state and the resulting shorter bond length indicate a stronger chemical bond compared with the aqua Ce(III) ion in the liquid phase. However, it was found that the lighter Ce isotope was preferentially distributed to both ferrihydrite and δ-MnO_2, which is inconsistent with the studies reported for cations (Balistrieri et al., 2008). In the former Chapter, this inconsistency is explained by postulating that (i) Ce adsorbed on ferrihydrite possibly formed an outer-sphere complex and (ii) Ce adsorbed on δ-MnO_2 showed a distortion by the formation of $Ce(OH)_4$ nanoparticles. Whether these interpretations are adequate or not can be assessed by a comparison with the other REEs.

The current study aims to compare the isotopic fractionation data of Ce with neighboring rare earth elements (REEs) and presents results for stable isotopic fractionation of neodymium (Nd) and samarium (Sm) during adsorption on ferrihydrite and δ-MnO_2. Unfortunately, since praseodymium (Pr) is a monoisotopic element and promethium (Pm) only has radionuclides, stable isotope ratios of these elements cannot be measured. Although we also tried to measure the isotope ratio of lanthanum (La), we do not include La isotopic data, because repeated measurements (32 times) of the $LaCl_3$ solution used in the adsorption experiment showed an uncertainty of approximately 0.5‰ (2σ), which is better than that reported in the literature (Shen et al., 1994) but larger than the Ce isotopic fractionation observed during adsorption (Chapter 3). The relative mass difference of La isotopes ($^{139}La/^{138}La$) is about a half to that of Ce ($^{142}Ce/^{140}Ce$). As such, the isotopic fractionation of La during the adsorption is expected to be smaller than that of Ce, suggesting that the isotopic fractionation of La during adsorption cannot be precisely measured.

In spite of these difficulties, a systematic analysis of REE isotopic fractionation caused by adsorption on common mineral phases can offer insights into the geochemical behavior of REEs. For example, in seawater, REEs are adsorbed on various types of suspended matter and solid phases. It is noteworthy that Ce can behave differently than other trivalent REEs owing to its oxidation to Ce(IV). Cerium is present in seawater at anomalously low concentrations relative to those of neighboring REEs, La and Pr (e.g., Elderfield and Greaves, 1982; Piepgras and Jacobsen, 1992; Möller et

al., 1994), whereas Ce enrichment is observed in ferromanganese nodules (e.g., Piper, 1974; Elderfield et al., 1981; Bau et al., 1996). Although trivalent REEs have similar chemical properties, they can show systematic variations in their distributions to various natural samples as a function of the atomic number due to the lanthanide contraction (e.g., Henderson, 1984; Taylor and McLennan, 1988; Byrne and Sholkovitz, 1996). For instance, seawater is characterized by relative enrichment of heavy REE (HREE) compared with those in suspended particles due to their larger stability of carbonate complexes caused by the smaller ionic radii of HREE. Meanwhile, the high reactivity of REEs results in the short residence times of REEs in the ocean and low REE concentration in seawater (e.g., Elderfield and Greaves, 1982; Piepgras and Jacobsen, 1992; Möller et al., 1994). These observations suggest that the isotopic fractionation mechanisms may show a systematic variation among REEs due to the change in stabilities of adsorbed species over the REE series.

In this study, Fe and Mn oxides were used as an adsorptive medium, since marine ferromanganese deposits play a role as a major sink for REEs (e.g., Piper, 1974; Elderfield et al., 1981; Bau et al., 1996). K-edge extended X-ray absorption fine structure (EXAFS) spectroscopy analyses of these elements were conducted to determine their chemical speciation including coordination number (CN) and bond length for their adsorbed species, which were used to interpret the isotopic fractionation data. EXAFS analyses for La, Ce, and Pr were also included, though isotopic data are not available for La and Pr. The pH condition in this study was confined to the lower pH region (pH = 5), where the aqua ion is stable for REEs, to focus on the mass-dependent isotopic fractionation between the aqua ion and the adsorbed species and to compare the data with those reported for Ce in the Chapter 3.

4.2 Experimental

4.2.1 Adsorption experiment

Synthetic ferrihydrite and δ-MnO_2 were used as adsorptive media. The procedure for the preparation of the synthetic ferrihydrite and δ-MnO_2 is detailed in the

Chapter 3 and follows the scheme of Schwertmann and Cornell (2000) for ferrihydrite and that of Foster et al. (2003) for δ-MnO_2. All experiments were performed in a manner similar to that described in the Chapter 3. A $LaCl_3$, $NdCl_3$, or $SmCl_3$ reagent (purity of 99.9%; Wako, Japan) dissolved in ultrapure water was used for the adsorption experiments on ferrihydrite and δ-MnO_2. Similarly, an adsorption experiment for Pr on these minerals was performed using a 99.5% $PrCl_3$ reagent (Wako, Japan). For the adsorption experiments of Nd and Sm, 10 g of varying concentration of their solutions were poured into plastic bottles with 100 mg of ferrihydrite or 30 mg of δ-MnO_2 as the solid phase. In this experiment, both the amounts of the solid phase and the volume of the liquid phase were fixed, whereas the REE concentration in the solutions were systematically varied to prepare samples with different adsorbed fractions (the ratio of adsorbed REEs to total REEs added into the system: F_{ad}). In the case of the adsorption experiment for EXAFS measurement, about 10 g of solution containing 10 mg REE (Nd or Sm) were poured into plastic bottles with 250 mg of ferrihydrite or 100 mg of δ-MnO_2 as the solid phase.

The other experimental parameters, such as the pH and the experimental period, were identical to those reported in the Chapter 3. The pH was adjusted to 5.00 ± 0.05 with dilute NaOH and HCl solutions because the REE^{3+} aqua ion dominates the REE species in the liquid phase at pH = 5. Speciation calculations under the experimental condition showed that more than 99.5% of La, Ce(III), Pr, Nd, and Sm were dissolved as REE^{3+} aqua ions under our experimental condition. In the calculation, the data for REE–carbonate complexation constants were obtained from Luo and Byrne (2004), and the equilibrium constants of the carbonate species were obtained from Nordstrom et al. (1990). The suspension was stirred for 6 h at 25ºC at 130 rpm. At the end of the experiment, the liquid phase was separated from the solid phase by filtration using a 0.2 μm hydrophilic polytetrafluoroethylen filter (ADVANTEC).

4.2.2 Isotopic analysis

After the solid−water separation in the adsorption experiments, the liquid

samples were acidified to 0.3 M HNO_3 to prevent the precipitation of REEs. The ferrihydrite was dissolved in 6 M HCl (ultrapure grade), while the δ-MnO_2 was dissolved in 6 M HCl and H_2O_2 (ultrapure grade). Both mineral digests were finally diluted to 0.5 M HCl, and the REEs were separated from Fe or Mn via column chemistry. For Fe elution, 15 g of 2.0 M HCl solution was passed through a column (4 cm long; 1.0 cm diameter) loaded with an AG 50W-X8 cation exchange resin (Bio-Rad); for Mn elution, 20 g of 2.0 M HNO_3 solution was used. The column chemistry had been checked prior to the sample introduction using an ICP-MS (Agilent 7700) with precision better than 1%. Almost 100% (more than 99%) of the REEs were recovered by elution using a 6.0 M HCl solution, ensuring the absence of isotopic fractionation during the column chemistry. REE concentrations in both solid and liquid samples were determined with precision of 2% using an SPS3500 Series ICP-atomic emission spectrometer (SII NanoTechnology, Inc.) to determine F_{ad} and for the subsequent dilution prior to MC-ICP-MS analyses. Procedural blanks in the adsorption experiments (REE-free experiments), measured using ICP-MS, indicated that the ferrihydrite and δ-MnO_2 contained less than 10 pg of the REE, which corresponds to less than 0.01% of REE added in our experiments.

The isotope ratios of Nd and Sm were determined at the Kochi Institute for Core Sample Research, Japan Agency for Marine-Earth Science and Technology using a double-focusing MC-ICP-MS (NEPTUNE, Thermo Fisher Scientific) previously described by Weyer and Schwieters (2003) and Wieser and Schwieters (2005). Sample solutions were introduced at 100 μL/min using a GE Micromist nebulizer (Glass Expansion, Australia) in free aspiration mode attached to a dual cyclonic/double Scott quartz glass spray chamber. The measurements were performed in low-resolution mode using an X-type skimmer cone. The typical operating conditions of the instrument are given in Table 4−1. The measured isotope ratios were corrected by an element doping technique. The doped element (Sm and Eu for Nd and Sm isotope measurements, respectively) used has a similar mass to the analyte and more than one stable isotope, and was added to the sample solutions immediately before MC-ICP-MS analysis. Through the element doping technique, the observed isotope ratios were corrected

according to an exponential law using the isotope ratio of the doped solutions. The relationship between the observed and normalized isotope ratios is described by

$$R_{a\text{-}norm} = R_{a\text{-}obs} \times A_a^{f_{analyte}}, \quad (4-1)$$

$$R_{d\text{-}norm} = R_{d\text{-}obs} \times A_d^{f_{dope}}, \quad (4-2)$$

$$f_{analyte} = f_{dope}, \quad (4-3)$$

where R_a and R_d are the measured isotope ratios of the analyte and doping element, and f and A are the mass discrimination correction factor and the ratio of exact atomic masses of the analyte or doping isotope, respectively. The exact atomic masses were obtained from the ICPAC Technical Report by de Laeter et al. (2003). The REE chloride solutions used in the adsorption experiment were employed as the standard solution. The isotope ratios are expressed in a standard delta notation relative to the average standards, as described by

$$\delta(^iE)_S = [(R_S / R_{RM}) - 1] \times 10^3, \quad (4-4)$$

where R_S and R_{RM} are the isotope abundance ratios $n(^iE)/n(^jE)$ in a sample (S: also corresponds to $R_{a\text{-}norm}$) and a standard solution used in the adsorption experiment, respectively. The E represents the elements (Nd or Sm) and superscripts *i* and *j* denote heavy and light isotopes of the element, respectively.

A possible mass spectrometric interference in wet plasma mode is the REE-hydride, which can affect isotope ratio of another element, for example, ^{144}SmH on ^{145}Nd, ^{146}NdH on ^{147}Sm, and ^{148}NdH on ^{149}Sm. To reduce the variation in the hydride formation, the ratio between measuring and doping elements was fixed through the measurement. The contribution of hydride was estimated using 1000 μg/L Nd and Sm solutions. The NdH/Nd ratio estimated from the ion signal intensity at the mass number 151 as ^{150}NdH/^{150}Nd, was about 3×10^{-6}. Similarly, ^{154}SmH/^{154}Sm was measured as approximately 3×10^{-6}. Although the ^{150}NdH/^{150}Nd and ^{154}SmH/^{154}Sm ratios can be affected by contamination from ^{151}Eu and ^{155}Gd, respectively, measured the 151/150 and 155/154 ratios of 3×10^{-6}, were small enough to ignore. The ion signals of Nd as ^{145}Nd^{16}O and Sm as ^{147}Sm^{16}O were also checked before each isotopic analysis. The

NdO/Nd and SmO/Sm ratios were adjusted to 1% on average by tuning the carrier gas flow rate.

The interferences generated by Sm impurities in Nd and Eu impurities in Sm (on Nd and Sm isotopic measurements, respectively) were also estimated before the addition of doping elements. We examined the contribution of ^{146}NdH and ^{147}Sm by measuring the ion signal intensity at the mass number 147 when introducing a 1000 μg/L Nd solution. The measured (^{146}NdH+^{147}Sm)/^{146}Nd ratio was slightly higher than the ^{150}NdH/^{150}Nd ratio owing to the contribution of ^{147}Sm. Similarly, the intensity at the mass number 151 was measured when a 1000 μg/L Sm solution was introduced and the contribution of ^{151}Eu was estimated from the (^{150}SmH+^{151}Eu)/^{150}Sm ratio by comparison with the ^{154}SmH/^{154}Sm ratio. The estimated amounts of Sm and Eu were less than 0.01% of Nd and Sm in each solution. Thus, the interferences from neighboring REE were negligible. In the following, the isotope measurement of each element is described in detail.

For the Nd isotopic analyses, ^{143}Nd, ^{145}Nd, and ^{146}Nd were measured simultaneously with the doping element isotopes ^{147}Sm and ^{149}Sm using the MC-ICP-MS. Samples and Nd standard solutions were diluted to about 200 μg/L, which corresponds to a ^{145}Nd signal of about 1.3 V. In contrast, the standard Sm solution (Wako, Japan) serving as a doping element was diluted to 100 μg/L, which provided a ^{147}Sm signal of about 2V. The Nd isotope ratios are expressed as δ^{145}Nd and δ^{146}Nd when the isotope ratios of ^{145}Nd/^{143}Nd and ^{146}Nd/^{143}Nd correspond to R in Eq. 4−4. The determination of both δ^{145}Nd and δ^{146}Nd allows us to assess the accuracy of the measurement. In the natural environment, both mass-dependent and mass-independent (including nuclear-volume) isotopic fractionations occur. The mass-dependent isotope effect is due to differences in atomic weight, which implies that relative isotopic fractionations can be calculated for elements that have more than three stable isotopes. The relative isotopic fractionation assuming an equilibrium is calculated as

$$\delta^{145}\mathrm{Nd}/\delta^{146}\mathrm{Nd} = \frac{[1/(143+143)]-[1/(143+145)]}{[1/(143+143)]-[1/(143+146)]}, \qquad (4-5)$$

where 143, 145, and 146 correspond to exact atomic masses of each Nd isotope. Therefore, mass-dependent fractionation of the two Nd isotope ratios is expected to follow

$$\delta^{145}Nd = 0.669 \times \delta^{146}Nd. \quad (4-6)$$

The analytical uncertainties in the measurement of the $\delta^{145}Nd$ and $\delta^{146}Nd$ value were 0.048 and 0.069‰ (2σ), respectively, as calculated from repeated analyses of the standard $NdCl_3$ solution (n = 14). In addition, Nd isotope measurements were performed twice by preparing one sample with a similar F_{ad} to confirm the quality of the experiment, and the results were the same within the analytical uncertainty.

For the Sm isotope measurements, ^{147}Sm, ^{149}Sm, and ^{152}Sm were measured simultaneously alongside the doping element isotopes ^{151}Eu and ^{153}Eu. The ion signals of ^{147}Sm and ^{151}Eu were about 1.4 and 3 V, respectively, using Sm and Eu standard (Wako, Japan) solutions that were respectively diluted to about 100 and 50 μg/L. During the measurement, ^{156}Gd was also monitored to estimate the influence of ^{152}Gd, which can interfere with ^{152}Sm. The ^{156}Gd signal was negligible (< 0.001% of the ^{147}Sm signal) for all samples and standard solutions, which indicates that isobaric interferences by ^{152}Gd were negligible in this study. Similar to the case for Nd isotope ratios, two independent Sm isotope ratio can be determined, $\delta^{149}Sm$ and $\delta^{152}Sm$, when R in Eq. 4−4 is $^{149}Sm/^{147}Sm$ and $^{152}Sm/^{147}Sm$, respectively. Here, it is expected that

$$\delta^{149}Sm = 0.404 \times \delta^{152}Sm. \quad (4-7)$$

The analytical reproducibility for the measurements of the $\delta^{149}Sm$ and $\delta^{152}Sm$ value were 0.038 and 0.069‰ (2σ), respectively, as calculated from repeated analyses of the $SmCl_3$ standard solution (n = 8).

4.2.3 EXAFS analysis

Immediately after filtration, solid samples were packed into individual polyethylene bags and frozen. Lanthanum, Pr, Nd, and Sm K-edge EXAFS spectra, which provide quantitative information on neighboring atom distances and the CN,

were measured at BL-01B1 of SPring-8 (Hyogo, Japan). For light REEs, such as La, Pr, Nd, and Sm, analysis of the K-edge EXAFS is more suitable than that of the L-edge EXAFS because (i) the L-edge for a lighter REE is subject to interferences by multi-electron excitation and (ii) the energy range applicable to EXAFS analysis is short because of the close energy gap between the L_{III} and L_{II} edges. Furthermore, measurement of the L_{III}-edge EXAFS spectra of Sm in fluorescence mode is severely affected by the Mn K-line in the Sm/δ-MnO_2 system.Thus, we employed K-edge EXAFS analysis to obtain information on the local coordination environment of La, Pr, Nd, and Sm adsorbed on ferrihydrite and δ-MnO_2. Prior to the measurement of samples, the monochromator was calibrated to the first inflection point for each element using the following standard compounds (diluted with boron nitride): $LaCl_3$ (38.938 keV), $PrCl_3$ (41.999 keV), Nd_2O_3 (43.578 keV), and $SmCl_3$ (46.856 keV). The K-edge EXAFS spectra of standard materials and chloride solutions used in the adsorption experiments were measured in transmission mode, whereas adsorbed samples were measured in fluorescence mode using a 19-element Ge semiconductor detector. Each sample was scanned several times to obtain the spectra with better statistics. Repeated EXAFS scans were identical, showing that any X-ray-induced alteration of the samples was unlikely in our experiments.

The EXAFS spectra were analyzed using REX2000 software (Rigaku Co. Ltd.) with parameters generated by the FEFF 7.0 code (Zabinsky et al., 1995). In addition to La, Pr, Nd, and Sm measured in this study, the EXAFS of the Ce^{3+} and Ce/ferrihydrite system measured in the Chapter 3 was reanalyzed here. After extracting the EXAFS oscillations and its Fourier transform, the inversely Fourier-filtered data were analyzed using a standard curve-fitting method. The theoretical phase shifts and amplitude functions for the REE–O, REE–REE, REE–Fe, and REE–Mn shells employed in this fitting procedure were extracted from FEFF 7.0 (Zabinsky et al., 1995). In the fitting process, the threshold energy shifts of the first and second shells were constrained to be the same. Finally, the processed EXAFS spectra in the whole k- and R-space ranges employed in the fitting procedure were compared with the measured EXAFS spectra in k- and R-space to confirm that the fits developed for the processed spectra also provided

good matches to the measured spectra. The uncertainty estimates for the interatomic distance and CN obtained from the fitting were ± 0.02 Å and ± 20%, respectively (O'Day et al., 1994). The quality of the fit was given by the goodness-of-fit parameter *R* (R-factor), defined as

$$R = \frac{\sum[x_{obs}(k) - x_{\mathrm{cal}}(k)]^2}{\sum[x_{obs}(k)]^2} \qquad (4-8)$$

where $\chi_{\mathrm{obs}}(k)$ and $\chi_{\mathrm{cal}}(k)$ are the experimental and calculated absorption coefficients at a given *k*, respectively. The multiple-scattering effect was initially included in the EXAFS analyses in this study, but was found to make a very weak contribution to the EXAFS spectra.

4.3 Results

4.3.1 Isotopic fractionation

Table 4−2 lists the Nd isotope ratios expressed as delta notation of both solid and liquid samples after the adsorption experiments. The table gives both δ^{145}Nd and δ^{146}Nd, along with the initial weight in the adsorption experiment and adsorbed fraction (F_{ad}). The δ^{145}Nd and δ^{146}Nd values of the solid phase have positive values except for a datum with the highest F_{ad}, whereas all the values of the liquid phase are negative. This means that the heavier Nd isotopes were enriched in the solid phase, resulting in the liquid phase becoming enriched in lighter Nd isotopes. All the data fall on a straight line in a plot of δ^{145}Nd vs. δ^{146}Nd as expected from the theoretical calculation of Eq. 4−6 (solid line; Fig. 4−1A), indicating that the measurements were performed well and no mass-independent fractionation was observed. Given that the δ^{145}Nd and δ^{146}Nd values have a clear correlation, only the δ^{145}Nd data are discussed further. Figure 4−2 shows the isotopic fractionation of Nd during the adsorption experiment, along with F_{ad} (Fig. 4−2A: adsorption on ferrihydrite; Fig. 4−2B: adsorption on δ-MnO_2). In the figure, the model lines for the equilibrium and Rayleigh fractionations are shown as solid and dashed lines, respectively (Fig. 4−1). In calculating these model lines, the mean $\alpha_{\mathrm{Lq-So}}$,

which is the isotopic fractionation factor between the liquid and solid phases (Table 4−2), was calculated as

$$\alpha_{Lq-So} = \frac{10^3 + \delta^{145}Nd_{Lq}}{10^3 + \delta^{145}Nd_{So}}. \quad (4-9)$$

The uncertainty in the mean α_{Lq-So} (Table 4−2) is the deviation (2σ) of five α_{Lq-So} values measured at various F_{ad}. The figure shows that both experimental systems are in accord with the line of equilibrium isotopic fractionation.

Table 4−2 also lists $\delta^{149}Sm$ and $\delta^{152}Sm$ of solid and liquid samples along with the initial concentration and F_{ad}. Similar to the case for Nd, heavier and lighter Sm isotopes were enriched in the solid and liquid phases, respectively. The clear correlation observed between $\delta^{149}Sm$ and $\delta^{152}Sm$ (Fig. 4−1B) indicates that mass-independent fractionation was not observed, and as such only $\delta^{149}Sm$ is discussed further. Figures 4−2C and 4−2D show the isotopic fractionation of Sm during the adsorption experiment along with F_{ad} (Fig. 4−2C: adsorption on ferrihydrite; Fig. 4−2D: adsorption on δ-MnO_2) and the model lines for the equilibrium and Rayleigh fractionations. As in the case of the Nd system, the mean α_{Lq-So} is calculated as

$$\alpha_{Lq-So} = \frac{10^3 + \delta^{149}Sm_{Lq}}{10^3 + \delta^{149}Sm_{So}}. \quad (4-10)$$

Similar to the case for the Nd system, the uncertainty in the mean α_{Lq-So} (Table 4−2) is the deviation (2σ) of five α_{Lq-So} values measured at various F_{ad}. The figure shows that the Sm system also follows the line of equilibrium isotopic fractionation.

4.3.2 EXAFS

In presenting EXAFS results, we include the results for La and Pr adsorbed on ferrihydrite and δ-MnO_2 and Ce on ferrihydrite for comparison. The La K-edge EXAFS spectra and radial structural function (RSF) obtained from the Fourier transform of the spectra are shown in Fig. 4−3. The dashed lines show the fitting result, from which we obtained the EXAFS parameters listed in Table 4−3. Assuming an oxygen atom in the

first shell, the La−O bond lengths are approximately 2.56, 2.55, and 2.53 Å for the La^{3+} solution, La on ferrihydrite, and La on δ-MnO_2 systems, respectively (Table 4−3). However, as observed in the broader RSF of the La–O shell for La on ferrihydrite and δ-MnO_2 compared with La^{3+} solution, the La–O shell actually consists of two La–O shells. The pronounced dip at k = 6.5 ($Å^{-1}$) not only requires a La−Fe/Mn shell but also the negative amplitude of the La–O_1 and La–O_2 shell to obtain a better fit (Fig. 4−3A). The existence of two inner O shells for La was also suggested by Ohta et al. (2009). The La–O bond length is 2.56 Å for the La^{3+} solution, which is longer than the La–O_1 bonds of the La/ferrihydrite (2.45 Å) and the δ-MnO_2 systems (2.46 Å). The presence of shorter bonds between La and the O atoms of the mineral surfaces is reasonable considering that the total CN (= CN_1 + CN_2) of the adsorbed species is smaller than the CN for hydrated La^{3+}.

The results of the re-examination of Ce K-edge EXAFS spectra and the RSF of the Ce^{3+} solution and Ce/ferrihydrite system are presented in Table 4−3 and Fig. 4−4. For comparison, the previous analysis assuming only one oxygen shell is also presented. The k-space EXAFS spectra show that a better fit was obtained when assuming two oxygen shells located at different distances (Fig. 4−4A), similar to that found for La. In the previous examination of the Ce/ferrihydrite system, the *R* factor (Eq. 4−8) was 0.056% determined from the fitting in the range of R+ΔR = 1.47–2.42 Å which covered the first shell only (Chapter 3). Although the *R* factor itself was worse in the current analysis, the factor was determined in the range of R+ΔR = 1.00–4.00 Å. The comparison in the k-space spectra clearly showed the improvement in the new fitting (Fig. 4−4A).

The Pr K-edge EXAFS spectra and their Fourier transform magnitudes also suggest two shells of oxygen atoms located at different distances; that is, distortion in the first coordination sphere (Table 4−3; Fig. 4−5). Similar to the case for the La and Ce/ferrihydrite systems, the Pr–O_1 bond of the adsorbed species was shorter than for Pr^{3+} in solution. The CN value of REE–O is correlated with the bond length (Shannon, 1976), which is consistent with the low CN value for the Pr/δ-MnO_2 system (CN_1 + CN_2 = 7.6±1.3) compared with that of the aqua complex (CN = 10.4±1.6).

In contrast with the La, Ce(III), and Pr systems, distortions were not observed in the first coordination sphere of Nd adsorbed on ferrihydrite or δ-MnO_2 (Table 4−3; Fig. 4−6). In the δ-MnO_2 system, the CN of the first coordination sphere is smaller than that of Nd^{3+} solution beyond analytical uncertainty, whereas the CN is identical within the analytical uncertainty for the ferrihydrite system. The Nd–O bond length is about 2.49, 2.48, and 2.46 Å for the Nd^{3+} solution, Nd adsorbed on ferrihydrite, and Nd adsorbed on δ-MnO_2 systems, respectively.

Distorted coordination spheres were also not observed for the Sm systems (Table 4−3; Fig. 4−7). The Sm–O bond lengths in the ferrihydrite system and the Sm^{3+} solution are essentially identical (2.45 Å), whereas the Sm–O bond length in the δ-MnO_2 system is 2.41 Å, which is smaller than that of the aqua complex beyond the range of analytical uncertainty.

A possible formation of a distorted first coordination sphere for Nd and Sm is also examined (Table 4−3). Smaller R values were obtained by assuming two oxygen shells at different distances, however, in contrast with the La and Pr systems, the CN values for these systems differed by more than a factor of four ($CN(REE–O_2)$ / $CN(REE–O_1) > 4.5$). The large differences between the two CNs suggest that the assumption of a distorted structure with two REE−O shells was not required to accurately fit the Nd and Sm EXAFS.

4.4 Discussion

4.4.1 Isotopic fractionation between the liquid and solid phases

Similar to the case of Ce in the Chapter 3, the isotopic fractionation for the Nd and Sm systems obeyed equilibrium fractionation. As for the degree of isotopic fractionation, adsorption in the ferrihydrite system showed less fractionation than that in the δ-MnO_2 system for Ce, Nd, and Sm. The most important result obtained in the Nd and Sm measurements was the preferential partitioning of heavier isotopes into the solid phases (Table 4−2, Fig. 4−2). This isotopic fractionation trend was different from that of Ce where it was reported that (i) Ce was not oxidized during adsorption on

ferrihydrite, whereas Ce adsorbed on δ-MnO_2 was oxidized to the tetravalent state, and (ii) lighter isotope enrichment of the solid phase for Ce(III)/ferrihydrite may be accompanied with formation of an outer-sphere complex. Although Schauble (2007) suggested the possible enrichment of lighter Ce isotopes in reduced species during the $Ce^{3+} \rightarrow Ce^{4+}$ reaction may be due to nuclear-volume isotope fractionation, the Ce/ferrihydrite system was unaffected here by the oxidation reaction. A nuclear-volume driven effect was also reported for Nd and Sm (Fujii et al., 1998; 2000), but the current study shows that the δ^{145}Nd vs. δ^{146}Nd and δ^{149}Sm vs. δ^{152}Sm correlations are in accord with a purely mass-dependent isotope effect (Figs. 4−1), meaning that nuclear-volume driven fractionation was negligible in the experiments.

Figure 4−8 summarizes α_{Lq-So} for the ferrihydrite and δ-MnO_2 systems with Ce, Nd, and Sm. The general trend previously observed for cations in the literature, such as Fe^{2+}, Cu^{2+}, and Zn^{2+}, suggests that heavier isotopes should be distributed in the solid phase during adsorption of REE^{3+} on metal oxides (e.g., Cacaly et al., 2004; Icopini et al., 2004; Clayton et al., 2005; Crosby et al., 2005; Pokrovsky et al., 2005; Balistrieri et al., 2008). Thus, it was found that Nd and Sm systems follow the expected trend but Ce does not. This isotopic fractionation contrasted with the Nd and Sm systems, indicating that a systematic change in a physicochemical factor among REEs (especially between Ce and Nd) is responsible for the different fractionations observed during the adsorption reactions. Even though REEs have similar chemical properties in a trivalent state, the direction of the isotopic fractionation can differ among light REEs (LREEs).

4.4.2 Coordination environment and isotopic fractionation

The most important rule governing stable isotopic fractionation is that the heavy isotopes of an element are concentrated in species with stronger bonds when two species with different bond lengths are in equilibrium (Bigeleisen and Mayer, 1947; O'Neil, 1986; Criss, 1999; Schauble, 2004). Considering that the REEs have similar chemical characteristics, the factors that control equilibrium isotopic fractionation may be considered similar among all trivalent REEs. The REEs examined in this study are in

a trivalent state (except for Ce on δ-MnO_2), which indicates that isotopic fractionation is not caused by a redox change. In our results (Table 4−3), the CNs of REEs adsorbed on δ-MnO_2 were smaller than the CNs of the REE aqua ions, which is consistent with a shorter REE−O bond length in the REE/δ-MnO_2 system. The EXAFS spectra obtained for the Sm systems did not show large oscillations, which makes it difficult to discuss whether Sm forms an inner-sphere or outer-sphere complex. In the case of the Nd systems, inner-sphere complexes formed for both Nd adsorbed on ferrihydrite and δ-MnO_2 (Fig. 4−6), though the Nd/δ-MnO_2 system showed larger isotopic fractionation than the Nd/ferrihydrite system. Although it was not clear for the ferrihydrite systems, the smaller CN observed for the δ-MnO_2 systems and related shorter bond length was reflected in an increase in the ratio of inner-sphere to outer-sphere complexes. The increase of this ratio is consistent with the larger isotopic fractionation observed in the δ-MnO_2 systems. However, the precise determination of the CN, which is highly correlated with the Debye–Waller factor, was difficult in the EXAFS analyses, thus impeding discussion of the equilibrium isotopic fractionation of REEs based on the CN alone.

Hereafter, we focus on the interatomic distances of the REE–O bonds summarized in Fig. 4−9A. It should be noted that the interatomic distances for adsorbed La, Ce, and Pr are shown as weighted mean values based on CN_1 and CN_2 values. For the REE^{3+} aqua ions and ferrihydrite systems, the interatomic distance decreased as the atomic number increased, due to the lanthanide contraction. The lanthanide contraction was also observed for the δ-MnO_2 system except for Ce, which was oxidized to Ce(IV) during adsorption on δ-MnO_2. In Fig. 4−9B, the REE–O interatomic distances for the ferrihydrite and δ-MnO_2 systems are normalized to those of the REE^{3+} aqua ions. If this ratio is less than 1, the REE–O bond length has shortened due to adsorption of the REE on the Fe or Mn oxide surface. In the ferrihydrite system, the REE–O interatomic distances were almost identical (within analytical uncertainty) to those of the REE^{3+} aqua ions for Nd and Sm. In the δ-MnO_2 system, however, the REE–O distances were shorter than for the REE^{3+} solutions beyond analytical uncertainty. The shorter bond length indicates that REEs have stronger REE–O bonds during adsorption onto δ-MnO_2,

thereby favoring the preferential enrichment of heavy isotopes in the solid phase for these elements, as was observed for Nd and Sm in our isotopic measurements (Table 4−2, Figs. 4−2 and 4−8). Therefore, we propose that the interatomic distance between the REEs and the first coordinated atom (oxygen) is the main factor that affects the equilibrium isotopic fractionation of Nd and Sm. The larger isotopic fractionation observed for the δ-MnO_2 system compared with the ferrihydrite system is likely due to the shorter REE–O bond lengths of REE adsorbed on δ-MnO_2.

In the case of La, EXAFS analysis showed two oxygen shells in the first coordination sphere for both the ferrihydrite and δ-MnO_2 systems (Table 4−3, Fig. 4−3). A better fit was obtained by assuming two oxygen atoms at different distances in the first coordination sphere, suggesting that the coordination structure is more distorted than that of the La^{3+} aqua ion. The distorted structures of adsorbed La and Pr species found in this study and by Ohta et al. (2009) imply that the distortion is also expected to be observed in the first coordination sphere of the Ce/ferrihydrite system, as identified in this study. The enrichment of lighter isotopes (by ca. 0.15‰) in adsorbed Ce species can be related to the distorted structure of Ce on ferrihydrite. Although we were unable to resolve La isotope compositions at the required level of precision, the distortion seen in the first coordination sphere of the La/ferrihydrite and La/δ-MnO_2 systems suggests that a light isotope enrichment is to be expected for La in the solid phase.

Isotopic fractionation caused by a distorted adsorbed structure has also been reported for other elements. The formation of highly distorted bidendate complexes is thought to explain the light isotopic composition of adsorbed trigonal boron (Lemarchand et al., 2007). Juillot et al. (2008) found a smaller fractionation for octahedral Zn adsorbed to goethite relative to the free Zn^{2+} ion hydrated by six water molecules. They suggested that the distortion of the octahedral environment of Zn when sharing oxygens with Fe atoms may account for the small fractionation on goethite. A similar case was also reported for Mo systems (Kashiwabara et al., 2011; Wasylenki et al., 2011). These results are consistent with our observations for the isotopic fractionation of Ce.

Not only the species adsorbed on the solid phase but also the stability in the liquid phase can cause the contrasting stable isotopic fractionation. Kawabe (1999b) compared the standard Gibbs free energy changes of the nonahydrated REE relative to isostructural $REE(H_2O)_8^{3+}$ species of REE^{3+} from La^{3+} to Gd^{3+}. The Gibbs free energy changes were reported to be −7.16, −5.27, −4.09, −3.02, −0.67, −0.17, and −0.06 kJ/mol for La^{3+}, Ce^{3+}, Pr^{3+}, Nd^{3+}, Sm^{3+}, Eu^{3+}, and Gd^{3+}, respectively. These results indicate that the hydrated state is extraordinarily stable in terms of both Gibbs free energy and enthalpy for La^{3+} and Ce^{3+} compared to Nd^{3+} and Sm^{3+}, which reflects stabilization by the formation of stronger chemical bonds in the compounds. This effect is suggested to be responsible for the much lower K_d, partition coefficient of REE between solid and liquid phases, of La^{3+} and Ce^{3+} adsorption on ferrihydrite and δ-MnO_2 compared with heavier REE^{3+} (Kawabe et al., 1999a; Ohta and Kawabe, 2000). In other words, the lower stability of the adsorbed species is due to the higher stability of the hydrated species in the aqueous phase. The new results, which include a comparison among REEs, suggest that the factors governing the lighter isotope enrichment of Ce (and possibly La) on the solid phase are (i) the distorted structure of La^{3+}, Ce^{3+}, and Pr^{3+} adsorbed on the solid phases; and (ii) the higher stability of the hydrated species. We suggest that these anomalies for La and Ce in terms of thermodynamic and structural characteristics affect not only K_d but also the isotopic fractionation incurred during adsorption.

4.4.3 Geochemical implications

The results of this study suggest that REE partitioning between solid and aqueous phases can cause contrasting stable isotopic fractionation for Ce(III) vs. Nd and Sm. The contrasting fractionation of Ce vs. Nd and Sm may not be seen in other reactions such as magmatic processes without solid−water interactions, because the fractionation should occur with the change of coordination environment of the REE such as in an adsorption reaction. Adsorption reactions are important in the geochemical behavior of REEs at the Earth's surface, since REEs are readily adsorbed on various

types of suspended matter and solid phases in rivers and seawater. In particular, our findings on the contrasting fractionation between Ce vs. Nd and Sm isotopes during adsorption on ferrihydrite and δ-MnO_2 can improve our understanding of REE behavior when considering that ferromanganese deposits are the major sink for REEs in the marine environment (e.g., Piper, 1974; Elderfield et al., 1981; Bau et al., 1996). In addition, the stable hydrated states of Ce^{3+} (and La^{3+}) can explain the preferential adsorption of lighter isotopes on the solid phase. Hence, the difference in the direction of the isotopic fractionations among LREEs is a new indicator of water−rock interactions inherent in the formation of natural REE-bearing samples.

However, the isotopic fractionation factor obtained in this study may be subject to change when a similar experiment is performed at higher pH depending on the dominance of different soluble species such as REE carbonate complexes. In addition, the possible occurrence of nuclear-volume isotope fractionation cannot be ignored in the natural environment. For example, according to Bigeleisen and Mayer (1947), mass dependent isotopic fractionation of Tl should be about 1/15th to that of Fe. In contrast, Rehkämper et al. (2002) showed approximately 2‰ fractionation for Tl isotopes between seawater and hydrogenetic Fe−Mn crusts. Thus, while the work presented here improves our knowledge of the processes behind systematic isotopic fractionation of selected REEs during adsorption on two common mineral phases, further work is required to elucidate the dominant mechanisms governing isotopic fraction of heavy elements in the natural environment.

4.5 Conclusions

Adsorption experiments with Nd and Sm on ferrihydrite and δ-MnO_2 were performed in this study to determine the factors governing equilibrium isotopic fractionation among REEs. Heavier isotopes of Nd and Sm were found to be enriched in the solid phase. EXAFS analyses showed that shortening of REE–O bonds during adsorption was the governing factor responsible for equilibrium isotopic fractionation of Nd and Sm. In contrast, the coordination structures of adsorbed La, Ce, and Pr were

more distorted than those of their aqua ions. This comparison among the REEs enables us to improve our understanding of the cause of such stable isotopic fractionation. The distorted adsorbed structure and the stability of hydrated species leads to lighter-isotope enrichment in the solid phase for Ce (and is also expected for La) adsorbed on ferrihydrite. In-depth analysis of the coordination environment, revealed by EXAFS analyses, was important to determining the mechanisms behind equilibrium isotopic fractionation. It is possible that the systematic isotopic fractionation over the REE series could be a new geochemical tool which can be used to study REE behavior during water−rock interaction in natural systems.

Table 4−1. Typical instrumental operation conditions.

RF frequencies	27.12 MHz
RF power	1.2 kW forward, <1 W reflection
Fassel-type torch Ar gas flow rates:	
Nebulizer	1.14 L/min
Auxiliary	0.70 L/min
Cool	15.7 L/min
Nebulizer	Glass Expansion Micromist
Spray chamber	Dual synchronic/double Scott glass chamber (ambient temperature)
Sample uptake	100 μL/min (free aspiration)
Cones	X-type skimmer cone
Ion energy	10000 V
Extraction	2000 V
Pressures during operation:	
ESA	$1.0–1.5 \times 10^{-5}$ Pa (9×10^{-6} Pa during standby)
Analyzer	$4–9 \times 10^{-7}$ Pa (4×10^{-7} Pa during standby)

Table 4−2. Isotope ratio and fractionation factor for Nd and Sm during adsorption.

System	Initial (mg) [1]	F_{ad} [2]	δ1 (Lq) [3]	δ1 (So) [3]	δ2 (Lq) [3]	δ2 (So) [3]	$\alpha_{Lq\text{-}So}$ [4]	Average
Nd/ferrihydrite	0.05	0.86	−0.113	0.088	−0.156	0.147	0.999799	
	0.30	0.68	−0.079	0.102	−0.107	0.179	0.999819	
	1.00	0.32	−0.037	0.112	−0.030	0.181	0.999851	
	2.01	0.16	−0.029	0.126	−0.032	0.197	0.999845	
	3.21	0.08	−0.012	0.132	−0.028	0.207	0.999855	0.999834 ± 0.000048
Nd/δ-MnO_2	5.22	1.00	−0.466	0.001	−0.690	−0.001	0.999533	
	6.27	0.91	−0.395	0.064	−0.588	0.105	0.999541	
	7.51	0.77	−0.320	0.089	−0.477	0.140	0.999590	
	8.69	0.69	−0.250	0.112	−0.367	0.190	0.999638	
	10.2	0.57	−0.207	0.145	−0.298	0.231	0.999647	0.999590 ± 0.000106
Sm/ferrihydrite	0.32	0.62	−0.103	0.123	−0.227	0.326	0.999774	
	0.64	0.49	−0.092	0.135	−0.233	0.324	0.999773	
	1.07	0.34	−0.061	0.143	−0.165	0.327	0.999796	
	1.89	0.22	−0.036	0.157	−0.088	0.391	0.999806	
	3.04	0.10	−0.018	0.162	−0.044	0.393	0.999820	0.999794 ± 0.000041
Sm/δ-MnO_2	5.44	1.00	−0.479	0.005	−1.195	0.005	0.999516	
	6.74	0.89	−0.407	0.083	−0.999	0.155	0.999510	
	8.12	0.76	−0.305	0.115	−0.740	0.275	0.999580	
	9.34	0.66	−0.244	0.151	−0.615	0.345	0.999606	
	10.9	0.57	−0.186	0.143	−0.471	0.363	0.999671	0.999576 ± 0.000134

1) Initial (mg) denotes initial amount of Nd and Sm in the adsorption experiments added into a 10 g of ultra-pure water.

2) F_{ad} means the ratio of adsorbed fraction of REE to initial REE.

3) δ1 and δ2 correspond to (i) $\delta^{145}Nd$ or $\delta^{149}Sm$ and (ii) $\delta^{146}Nd$ or $\delta^{152}Sm$ values, respectively.

4) The definition of α is given by Eqs. 9 and 10 for Nd and Sm systems, respectively.

Table 4−3. Fitting results of EXAFS spectra for La, Ce, Pr, Nd, and Sm.

System	Shell	CN	R (Å)	σ^2 (Å^2)	*R* (%)
La^{3+} solution	La−O	12.5 ± 1.9	2.555 ± 0.012	0.011	0.57 [3]
La/ferrihydrite [1]	La−O	8.3 ± 0.8	2.551 ± 0.019	0.010†	8.93 [3]
	La−Fe	3.9 ± 0.5	3.513 ± 0.027	0.010†	10.1 [4]
La/ferrihydrite [2]	La−O_1	3.5 ± 0.7	2.453 ± 0.020	0.010†	
	La−O_2	4.3 ± 0.8	2.548 ± 0.026	0.010†	0.68 [3]
	La−Fe	3.5 ± 1.1	3.524 ± 0.030	0.010†	2.26 [4]
La/δ-MnO_2 [1]	La−O	5.9 ± 0.5	2.527 ± 0.016	0.009†	12.0 [3]
	La−Mn	3.0 ± 0.8	3.506 ± 0.019	0.010†	15.7 [4]
La/δ-MnO_2 [2]	La−O_1	4.1 ± 0.7	2.459 ± 0.023	0.009†	
	La−O_2	2.7 ± 0.8	2.568 ± 0.021	0.009†	1.01 [3]
	La−Mn	3.0 ± 1.0	3.528 ± 0.019	0.010†	4.25 [4]
Ce^{3+} solution [a]	Ce−O	8.6 ± 1.3	2.521 ± 0.013	0.012	0.09 [5]
Ce^{3+} solution	Ce−O	11.5 ± 0.9	2.535 ± 0.017	0.010	0.10 [3]
Ce/ferrihydrite [a]	Ce−O	7.5 ± 1.3	2.526 ± 0.014	0.013	0.06 [5]
Ce/ferrihydrite	Ce−O_1	4.7 ± 0.6	2.418 ± 0.022	0.011	
	Ce−O_2	5.3 ± 0.7	2.535 ± 0.025	0.010†	1.57 [3]
	Ce−Fe	0.8 ± 0.3	3.531 ± 0.062	0.013	3.96 [4]
Pr^{3+} solution	Pr−O	10.4 ± 1.6	2.500 ± 0.013	0.009	0.55 [3]
Pr/ferrihydrite [1]	Pr−O	8.4 ± 1.5	2.472 ± 0.013	0.010†	10.4 [3]
	Pr−Fe	1.1 ± 0.5	3.497 ± 0.028	0.010	13.3 [4]
Pr/ferrihydrite [2]	Pr−O_1	4.4 ± 0.5	2.353 ± 0.027	0.010†	
	Pr−O_2	5.5 ± 0.5	2.499 ± 0.024	0.010†	2.23 [3]
	Pr−Fe	0.9 ± 1.0	3.479 ± 0.047	0.009	6.16 [4]
Pr/δ-MnO_2 [1]	Pr−O	6.8 ± 0.5	2.431 ± 0.012	0.010†	2.61 [3]
	Pr−Mn	2.0 ± 0.6	3.404 ± 0.059	0.010†	6.42 [4]
Pr/δ-MnO_2 [2]	Pr−O_1	3.7 ± 0.6	2.381 ± 0.018	0.010†	
	Pr−O_2	3.9 ± 0.8	2.481 ± 0.049	0.010†	1.71 [3]
	Pr−Mn	0.7 ± 0.5	3.407 ± 0.053	0.010†	4.40 [4]
Nd^{3+} solution	Nd−O	10.0 ± 1.5	2.487 ± 0.012	0.010	0.36 [3]
Nd/ferrihydrite [1]	Nd−O	6.5 ± 1.1	2.484 ± 0.013	0.011	1.75 [3]
	Nd−Fe	1.3 ± 0.4	3.342 ± 0.064	0.010†	2.96 [4]

Table 4−3. (continued)

System	Shell	CN	R (Å)	σ^2 (Å^2)	R (%)
Nd/ferrihydrite [2)]	Nd−O_1	0.8 ± 0.4	2.279 ± 0.043	0.010†	
	Nd−O_2	7.1 ± 0.6	2.494 ± 0.007	0.010†	1.00 [3)]
	Nd−Fe	1.4 ± 0.6	3.356 ± 0.024	0.010†	4.06 [4)]
Nd/δ-MnO_2 [1)]	Nd−O	5.7 ± 0.9	2.458 ± 0.012	0.010	7.99 [3)]
	Nd−Mn	1.0 ± 0.4	3.359 ± 0.068	0.010†	11.8 [4)]
Nd/δ-MnO_2 [2)]	Nd−O_1	1.1 ± 0.3	2.211 ± 0.022	0.010†	
	Nd−O_2	5.0 ± 0.5	2.490 ± 0.007	0.010†	1.16 [3)]
	Nd−Mn	0.9 ± 0.6	3.420 ± 0.041	0.010†	6.18 [4)]
Sm^{3+} solution	Sm−O	10.6 ± 1.5	2.445 ± 0.011	0.009	0.79 [3)]
Sm/ferrihydrite [1)]	Sm−O	5.1 ± 0.8	2.447 ± 0.014	0.011	1.81 [3)]
	Sm−Fe	0.3 ± 0.4	3.337 ± 0.049	0.010	3.11 [4)]
Sm/ferrihydrite [2)]	Sm−O_1	0.1 ± 1.2	2.264 ± 0.043	0.010†	
	Sm−O_2	5.4 ± 1.1	2.456 ± 0.024	0.010†	0.80 [3)]
	Sm−Fe	0.1 ± 0.9	3.352 ± 0.067	0.010†	2.26 [4)]
Sm/δ-MnO_2 [1)]	Sm−O	6.9 ± 1.0	2.413 ± 0.014	0.014	6.64 [3)]
	Sm−Mn	1.0 ± 1.4	3.349 ± 0.036	0.010†	8.80 [4)]
Sm/δ-MnO_2 [2)]	Sm−O_1	0.1 ± 0.2	2.143 ± 0.074	0.010†	
	Sm−O_2	4.7 ± 0.4	2.418 ± 0.007	0.010†	3.92 [3)]
	Sm−Mn	2.6 ± 0.6	3.373 ± 0.015	0.010†	5.55 [4)]

Note: CN denotes the coordination number; R (Å) denotes the distance from the center atom; σ is the Debye−Waller factor; R (%) is quality of fit (see Eq. 8).

[1)] Fitting results assuming one oxygen shell

[2)] Fitting results assuming two oxygen shells

[3)] Fitting from 1.00 to 2.50 Å in R+ΔR space

[4)] Fitting from 1.00 to 4.00 Å in R+ΔR space

[5)] Fitting from 1.42 to 2.43 Å in R+ΔR space

[a)] Fitting results reported in Chapter 3

† The parameter was fixed in the EXAFS fitting.

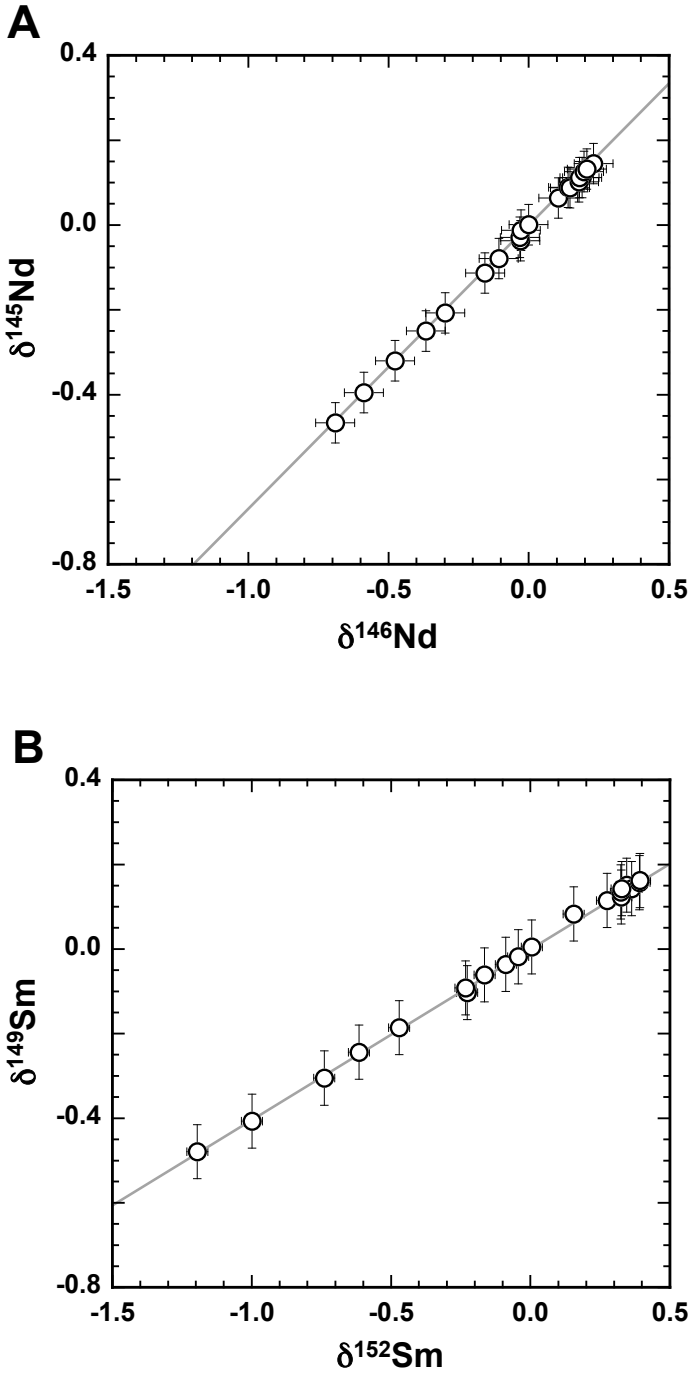

Fig. 4−1. Relationship between (A) δ^{145}Nd and δ^{146}Nd and (B) δ^{149}Sm and δ^{152}Sm. Solid line suggests calculated relative isotopic fractionation line shown in the Eq. 4−6 and Eq. 4−7 in the sentence, respectively.

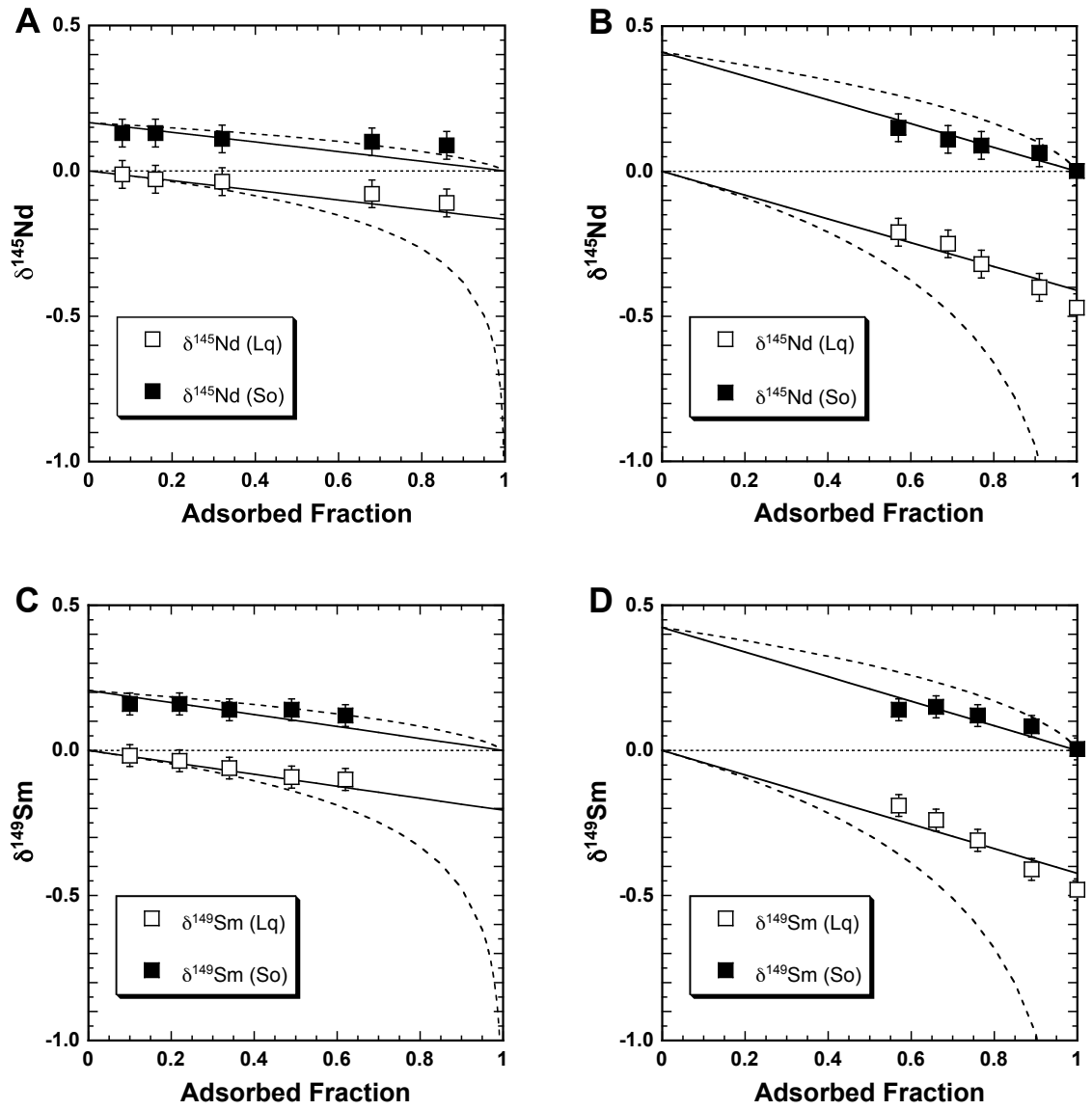

Fig. 4−2. Isotope ratios of the liquid and solid phases and adsorbed fractions (F_{ad}) obtained during adsorption experiments in the following systems: (A) Nd on ferrihydrite, (B) Nd on δ-MnO_2, (C) Sm on ferrihydrite, (D) Sm on δ-MnO_2. Open squares represent the δ^{145}Nd and δ^{149}Sm values of the liquid phase, and closed squares represent the solid phase. The error bar indicates the analytical uncertainty calculated from repeated measurements of a standard solution. Solid lines correspond to a model of equilibrium fractionation, while dashed lines correspond to Rayleigh fractionation.

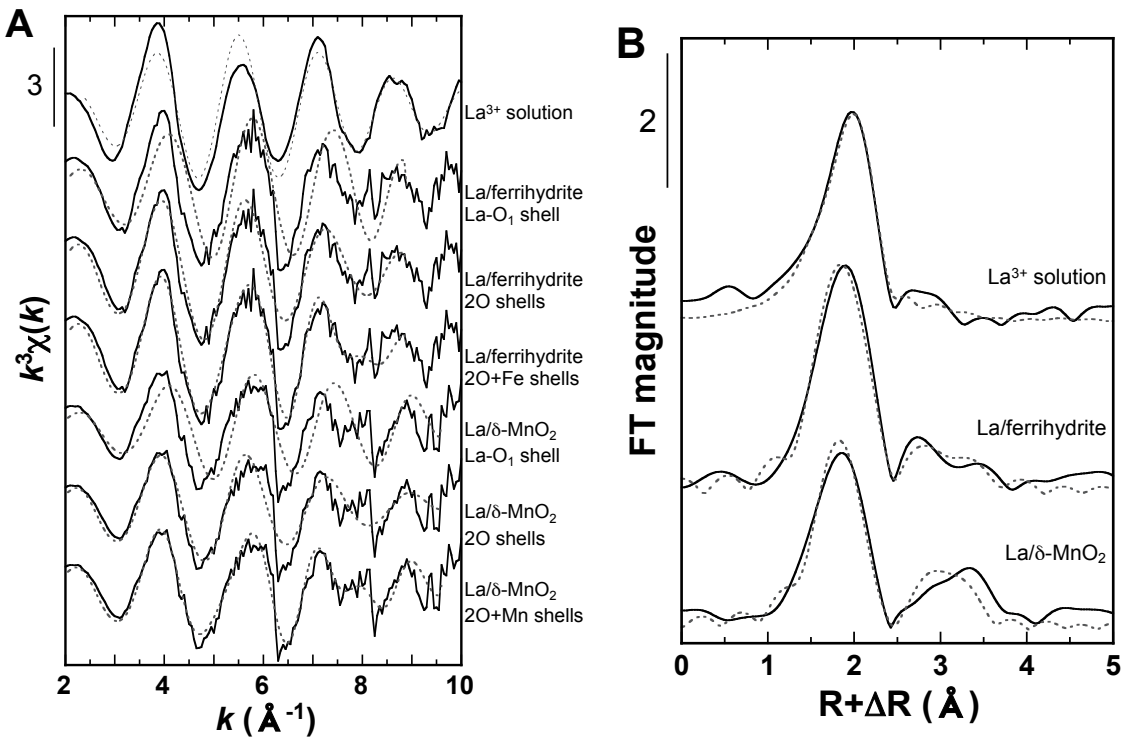

Fig. 4−3. (A) K^3-weighted La K-edge EXAFS spectra of samples and reference material (La^{3+} solution). The contributions of each shell are shown for La/ferrihydrite and δ-MnO_2 systems. (B) Radial structure functions (RSFs) of the samples and reference material (La^{3+} solution). In both figures, the solid lines represent the measurement data, and the dashed lines represent the fitting results.

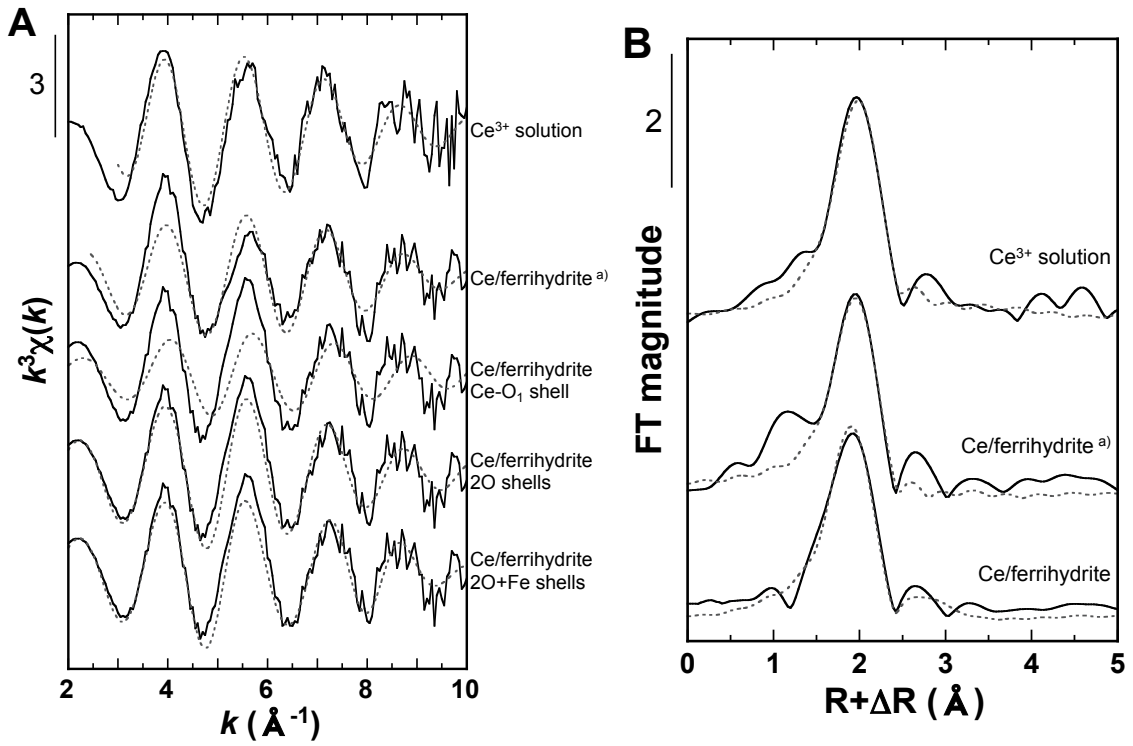

Fig. 4−4. (A) K^3-weighted Ce K-edge EXAFS spectra with the contributions of each shell and (B) RSF of the samples and reference material (Ce^{3+} solution). In both figures, the superscript a) denotes the analysis performed in the Chapter 3. The solid and dashed lines represent the measurement data and fitting results, respectively.

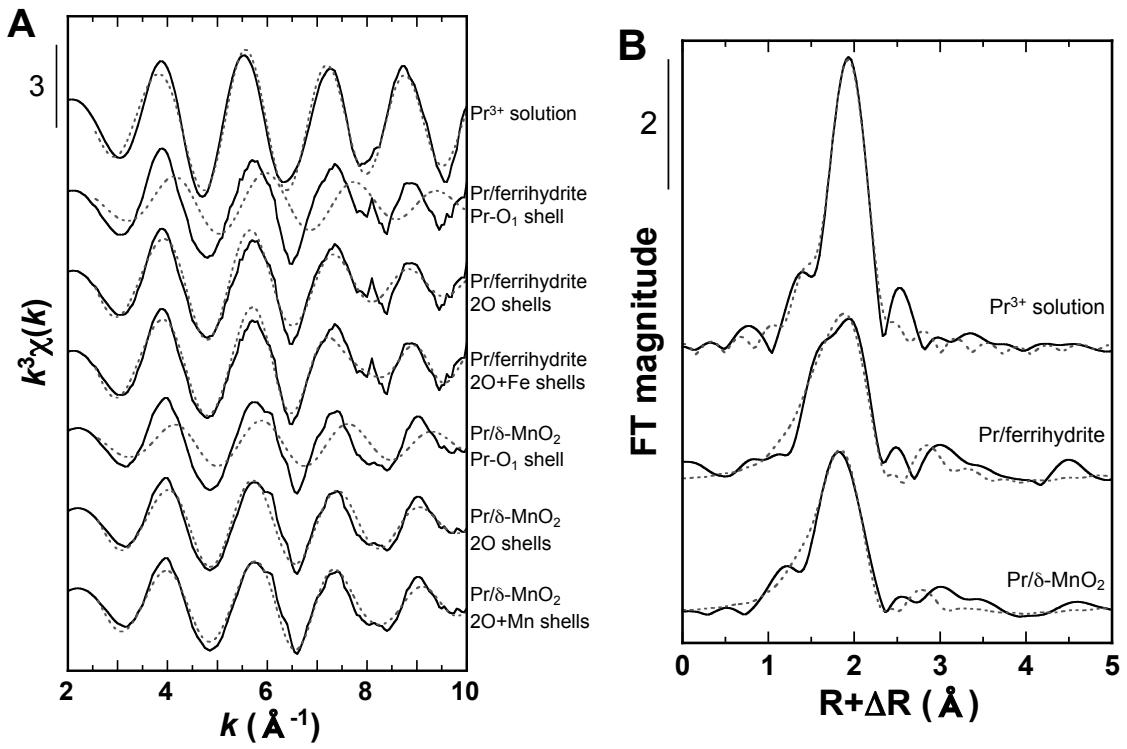

Fig. 4−5. (A) K^3-weighted Pr K-edge EXAFS spectra with the contributions of each shell and (B) RSF of the samples and reference material (Pr^{3+} solution). The solid and dashed lines represent the measurement data and fitting results, respectively.

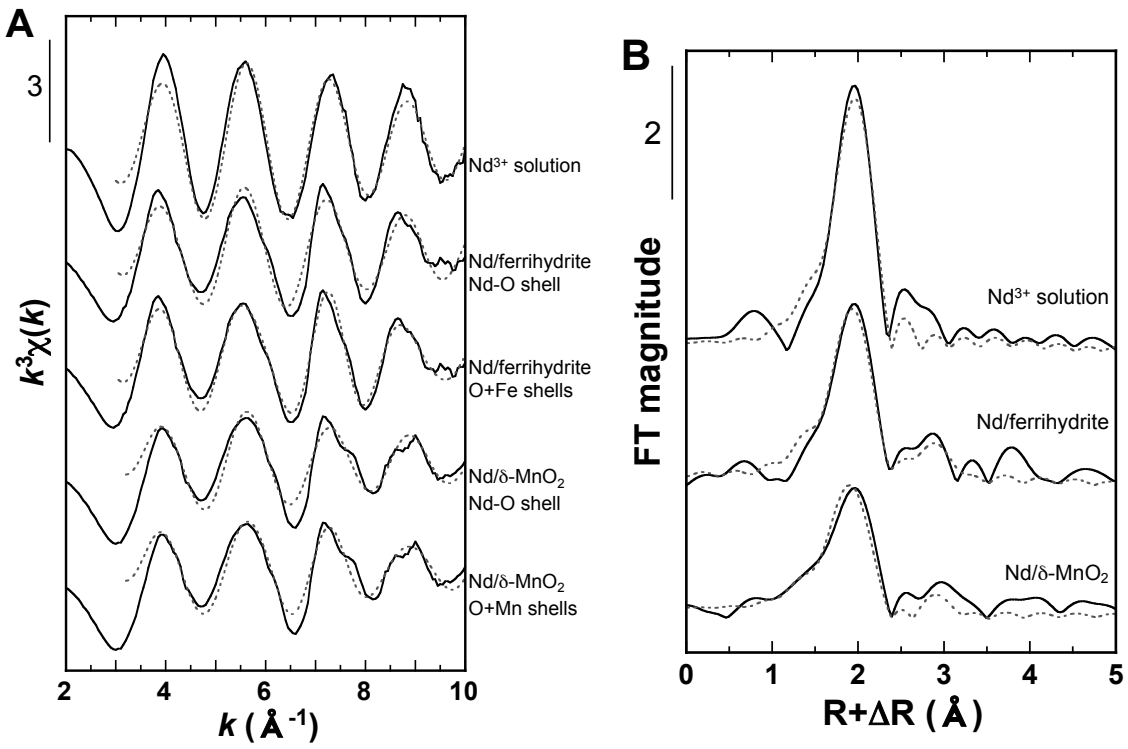

Fig. 4−6. (A) K^3-weighted Nd K-edge EXAFS spectra with the contributions of each shell and (B) RSF of the samples and reference material (Nd^{3+} solution). The solid and dashed lines represent the measurement data and fitting results, respectively.

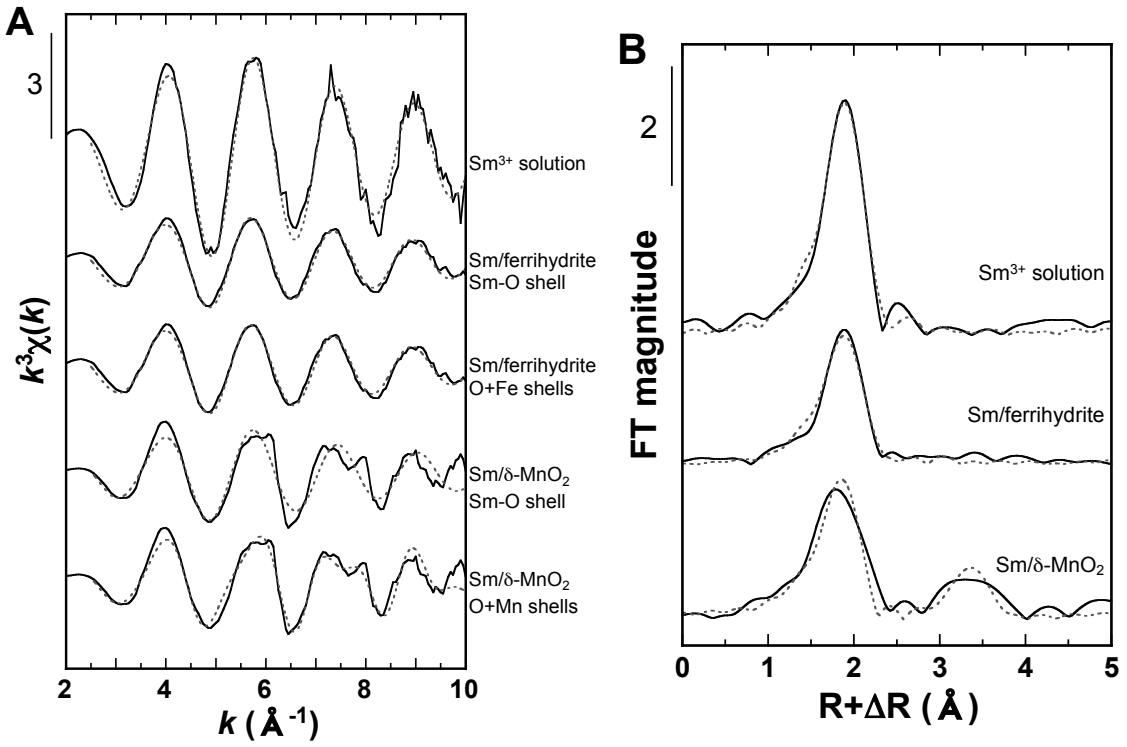

Fig. 4−7. (A) K^3-weighted Sm K-edge EXAFS spectra and (B) RSF of the samples and reference material (Sm^{3+} solution). The solid and dashed lines represent the measurement data and fitting results, respectively.

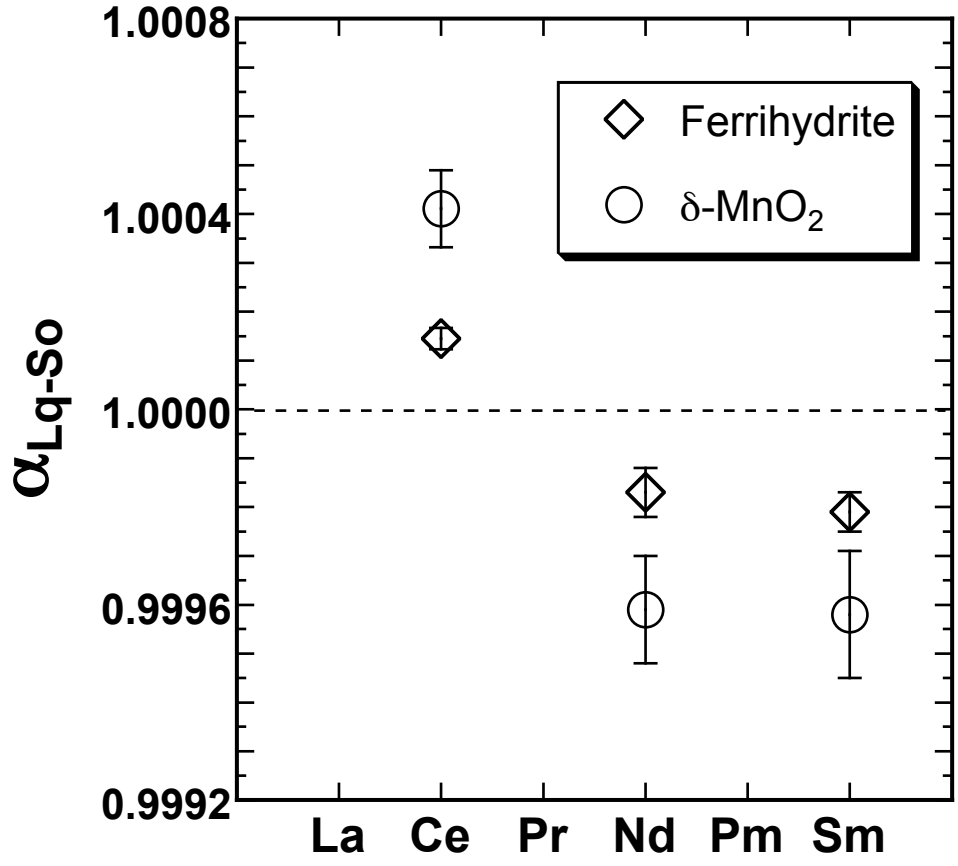

Fig. 4−8. Summary of factors of isotopic fractionation between liquid and solid phases (α_{Lq-So}) defined by Eqs 4−9 and 10. α_{Lq-So} values of the Ce system are cited from the value shown in the Chapter 3. By definition, $\alpha_{Lq-So} > 1$ indicates lighter-isotope enrichment in the solid phase. The error bar denotes the deviation (2σ) of five α_{Lq-So} values measured at various F_{ad}.

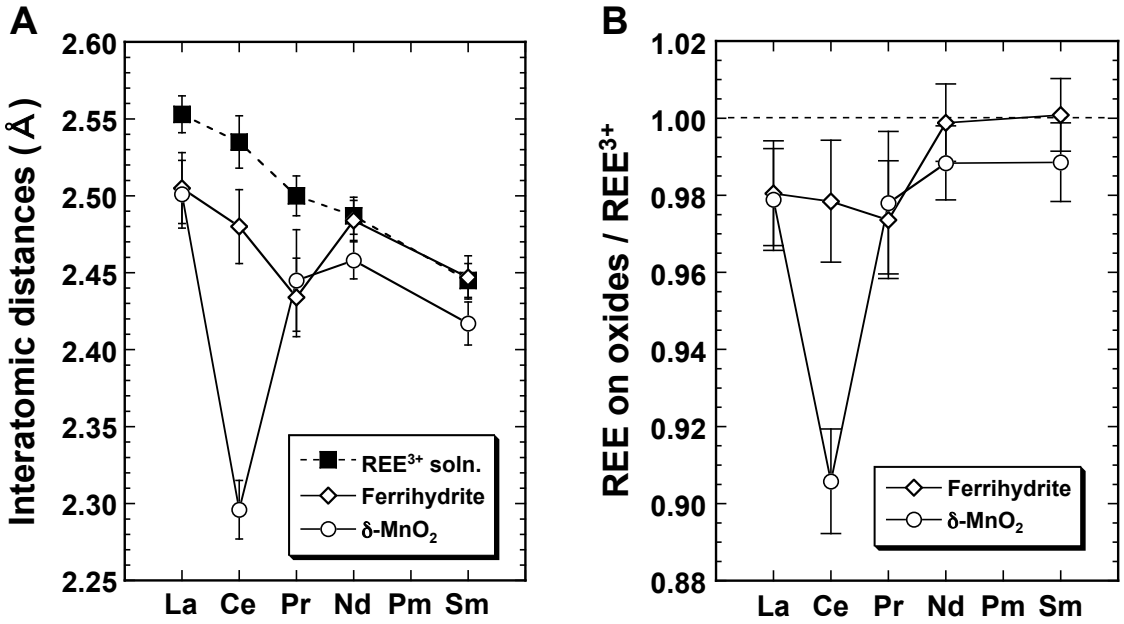

Fig. 4−9. (A) Summary of interatomic distances between REE–O bonds. Data for the Ce/δ-MnO_2 system are shown in the Chapter 3. The interatomic distances of La/ferrihydrite, La/δ-MnO_2, Ce/ferrihydrite, Pr/ferrihydrite, and Pr/δ-MnO_2 are shown as weighted mean values. (B) REE–O bond lengths of adsorption systems (ferrihydrite and mδ-MnO_2) normalized to the bond length of the REE^{3+} aqua ion using the data shown in Fig. 4−9A. A ratio smaller than 1 indicates shortening of the bond length relative to the aqua ion.

Chapter 5

Abundances of rare earth elements in crude oils and their partitions in warer

5.1 Chapter introduction

Rare earth element (REE) which is consisting of lanthanoid and yttrium show similar chemical properties with each other, because the outermost electron orbits are same. Ionic radius of lanthanoid gradually decreases from La^{3+} to Lu^{3+}, which causes the slight increase of the ionic potential with increasing atomic number. Their chemical similarities with slight difference induce systematic partition in various natural systems. Consequently, relative abundances of REE, namely REE pattern, reflect chemical processes occurring in various systems on the earth. These properties enables REE pattern to be a useful effective geochemical tracer (Henderson, 1984).

Recently, Zhang et al. (2009) suggested that REE patterns of crude oils could provide genetic information on the oils, while Akinlua et al. (2008) noted that REE contents of oils are useful in the classification of oils. However, the existing quantum of REE data of crude oil samples is still insufficient. Complete REE patterns are neither reported by Akinlua et al. (2008) nor by Takeda and Arikawa (2005). Here REE abundances measured in crude oils from the Xingiang Province, China are reported to provide more data towards the building of a database on REE abundances of crude oils.

A correct interpretation of the chemical state of REE in crude oils is necessary to ascertain genetic processes and provenances of the oils. Further it controls the shape of REE patterns which depends on the REE partition of species between the aqueous and the solid phases (Byrne and Kim, 1990; Takahashi et al., 2005; Yamamoto et al., 2010). For example, complexation with carbonate ions induces a preferential distribution of heavy-REE (HREE) into the aqueous phase (e.g., Byrne and Sholkovitz, 1996; Johannesson et al., 1996). Thus, it is expected that REE distribution between crude oil and water phase involves the information of REE species incorporated into the crude oil. Consequently, REE abundances were measured in both crude oils and coexisting water.

5.2 Samples and methods

5.2.1 Samples

Samples of crude oils along with their coexisting muddy water were collected from the mud volcanoes along the southern margin of the Junggar Basin in Xinjiang Uyghur Autonomous Region of China. The Xinjiang Province can be divided into two sedimentary basins, the Junggar Basin in the north and the Tarim Basin, south of the Tianshan Mountains. The Xinjiang Province is well known for its large oil deposits (e.g., Lee, 1985; Desheng, 1996), and several oil fields occur along the margin of these basins. There are several active mud volcanoes along the south margin of the Junggar Basin (Fu et al., 2007), erupting gas, oil, water and mud. Samples were collected from four sites along the southern margin of the Junggar Basin (Fig. 5−1). Site 1 is located in an area where many mud pies, flat mud extrusive feature, discharge mud and gas. Sites 2 and 3 are "twin" mud volcanoes which are located in a mountainous region, while site 4 is situated near the Dushanzi refineries. Oil slick and crude oil were seen in all sites studied here. Samples of muddy water were collected directly from the crater of mud volcanoes, and were filtrated on site by 0.45 μm membrane filters. After filtration, samples were acidified to 2 wt.% nitric acid solution to prevent the precipitation of Fe and REE. Samples of crude oils were centrifuged for 20 minutes at 2,000 rpm to separate oil from water and mud.

Previous studies (e.g., Clayton et al., 1997) indicate that crude oil samples that we collected in the Dushanzi area have relatively lower maturity with predominance of saturated hydrocarbons relative to aromatics and non-hydrocarbons.

5.2.2 Analytical methods

To determine the molecular structure of sampled crude oils, nuclear magnetic resonance (NMR) spectroscopy was conducted on carbon atom (^{13}C NMR) for samples from sites 2 and 4 using a JEOL ECA600 at the Natural Science Center for Basic Research and Development (N-BAND), Hiroshima University. The NMR spectra for other crude oils could not be obtained due to the low amount of collected samples.

CHNS analysis was not possible because the weight of the oil could not be correctly measured due to the volatilization of volatile components.

The difficulty in measuring the concentrations of REE in crude oils lies in the separation of REE from crude oils (Takeda and Arikawa, 2005; Akinlua et al., 2008). If organic matter is not perfectly decomposed, the residual organic matter can have harmful effects on the measurement of REE by inductively coupled plasma mass spectrometry (ICP-MS); (i) introduction of organic matter into the ICP-MS leads to the formation of carbon-containing ions such as C^{2+}, CO^{2+} and ArC^{+} (Lord, 1991); (ii) some carbon-bearing materials can be deposited at the interface into the mass spectrometer of the ICP-MS; (iii) high viscosity and boiling point of crude oils lower their atomization efficiency. Thus, a complete decomposition of organic matter is necessary to determine the concentration of REE in crude oils. In this study, about 0.1 g of weighed crude oil was decomposed by heating (at ca. 180 °C) for a week in 68 wt.% HNO_3 solution in a Teflon vessel with a screw cap. After evaporation, the organic matter was thoroughly digested using H_2SO_4 (at ca. 230 °C). The samples were evaporated again at 230 °C and finally dissolved in 2 wt.% HNO_3 and analyzed using an Agilent 7500 ICP-MS. In this study, Y was also determined as well as the lanthanoids. The loss of REE during decomposition, evaporation and redissolution processes is negligible as suggested by results from rock samples treated in the same way (Takahashi et al., 2002a).

The REE concentrations in water samples were also determined by ICP-MS. Since concentrations of some REE in groundwater are generally lower than ppt level, REE were pre-concentrated using a column (diameter 1.0 cm, length: 10 cm) loaded with a cation exchange resin AG50W-X8 (Takahashi et al., 2002a). About 250 mL of weighed sample was introduced into the column. Major cations were eluted by 2 M HCl solutions and REE were eluted by 40 mL of 6 M HCl solution. The eluted solution containing REE was evaporated and redissolved by 2 wt.% HNO_3 solution, which was used for the REE determination by ICP-MS. In addition, total organic carbon (TOC) in water samples was determined using a TOC analyzer (TOC-V_{CSH}; Shimazu). Abundance of iron (Fe) in water samples was determined using an ICP-atomic emission spectrometry (ICP-AES; SII Nano Technology).

5.3 Results

The ^{13}C NMR spectra of two samples (sites 2 and 4) show several peaks from 10 to 60 ppm, around 77 ppm and from 120 to 150 ppm. These peaks, often observed in crude oils (Hasan et al., 1983; Sharma et al., 2008) can be ascribed to the presence of functional groups of aliphatic carbons (0–70 ppm), formyl groups (77 ppm) and aromatic carbons (110–160 ppm), respectively (Fig. 5−2). In addition, we observed peaks at 145 ppm for crude oil samples collected at sites 2 and 4, which suggest the presence of phenol groups (Thorn et al., 1989). A peak at 191 ppm observed in a crude oil sample from site 2 is due to the presence of a carboxyl group.

The REE concentrations in crude oil samples have been normalized to a CI chondrite (Anders and Grevess, 1989; Table 5−1, Fig. 5−3A). Light-REE (LREE) enrichment is observed in all the REE patterns of crude oils. Flat heavy-REE (HREE) patterns are observed for oil samples collected from sites 1, 2 and 3, while HREE-depleted pattern is observed for that collected from site 4. The former three samples from sites 1 to 3 have convex patterns in the Gd-Tb-Dy-Ho span, i.e., M-type effect shown in the third tetrad (Masuda et al., 1987). The concentrations of REE collected from site 3 are the highest among all collected crude oils, while site 1 has the lowest REE concentrations. Although the concentrations of REE have wide variations among each site, such a variation can be caused by different abundances of functional groups in crude oils (Zhang et al., 2009). All the crude oil samples showed negative Eu anomalies, whereas no distinct Ce anomalies were found.

The concentrations of REE in coexisting water were also determined and have been normalized to the CI chondrite (Anders and Grevess, 1989; Table 5−2, Fig. 5−3B). The chondrite-normalized REE pattern for water sample of site 1 is enriched in LREE, while that for water collected at site 2 shows a V-shaped pattern (Fig. 5−3B). Both REE patterns have distinct positive Eu and small positive Ce anomalies, respectively. The results of XRD analysis of mud samples showed that the mud contained feldspars. Thus, the positive Eu anomalies shown in the REE patterns can be induced by the dissolution of anorthite (Byrne and Sholkovitz, 1996), while the positive Ce anomalies can be

related to the formation of Ce(IV)-carbonate species in alkaline water with a high carbonate content (Möller and Bau, 1993). Actually, according to the classification of the "true Ce anomaly" suggested by Bau and Dulski (1996), water sample collected at site 1 exhibits positive Ce anomaly. On the other hand, water sample collected at site 2 shows negative La anomaly, suggesting the presence of M-type tetrad effect as seen in the upward concave curve in the La-Ce-Pr-Nd span in the REE patterns (e.g., Bau, 1996; Takahashi et al., 2002a). The REE concentrations in mud and surface soil samples have been normalized to the CI chondrite (Anders and Grevess, 1989; Table 5−3, Fig. 5−3C). All samples are rich in LREE, typical for sedimentary rocks, with negative Eu anomalies with Eu/Eu* varying from 0.47 to 0.68.

5.4 Discussion

5.4.1 Comparison of REE abundances in crude oils with previous reports

Previous reports on REE abundances in crude oils (Takeda and Arikawa, 2005; Akinlua et al., 2008) mostly provided patterns of LREE, but not the complete REE patterns. Total REE abundances reported by Akinlua et al. (2008) and Takeda and Arikawa (2005) are less than 3 ng/g. Recently, Zhang et al. (2009) reported REE patterns for crude oils, which show a zigzag structure with enrichments of Nd, Eu, Tb, Ho, Tm and Lu in all their crude oil samples except one. They suggested that the enrichment of MREE with an even number of "f" electrons and the enrichment of HREE in crude oils result from higher stability constants of organic complexes with these elements. However, such zigzag REE patterns can be an analytical artifact, because the odd numbered REE generally occur in lower concentrations, often well below the detection limit of available instruments. Our report of complete REE patterns of crude oils is thus important, since resolution of the fine structure of REE patterns allows us to estimate the REE species in the samples. Total REE abundances of the crude oil samples showing zigzag patterns in Zhang et al. (2009) are less than 30 mg/g, while the sample with smooth pattern contains more than 140 mg/g (Zhang et al., 2009). Compared with the Zhang (2009) data, our crude oil samples have higher REE

abundances (except for Y), ca. 160, 1500, 5360, 2050 mg/g for sites 1, 2, 3 and 4, respectively (Table 5−1).

5.4.2 REE complexes in crude oils

It must be noted that concentrations of REE in crude oils are much larger than those in water. The preferential REE partitioning into the crude oil rather than water suggests that REE form neutral species and complexes with organic matter in the oil phase, because crude oil is hydrophobic and REE have high ionic properties. ^{13}C NMR spectra of crude oils collected from the sites 2 and 4 demonstrate the presence of aliphatic carbons, formyl group, aromatic carbons and phenol groups. Furthermore, the crude oil collected from site 2 shows a peak at 191 ppm, which indicates the presence of carboxyl group (Fig. 5−2). The phenol and carboxyl groups can act as binding sites for metal cations, similarly to metal complexation in humic substances (Tipping, 2002). Thus, it is suggested that the large partition of REE into crude oil relative to water can be caused by the formation of complexes with these ligands occurring in crude oils.

The evidence that REE form complexes with ligands in the oils is supported by the M-type tetrad in the Gd-Tb-Dy-Ho span observed for some of our oil samples. It has been often reported that M-type tetrad is observed in complex formation of REE with ligands such as found in the complexation with extractant in organic phases in liquid-liquid extraction system (Peppard et al., 1969; Yaita and Tachimori, 1996; Yamamoto et al., 2010). In addition, the differences observed in the REE patterns between crude oils collected from sites 2 and 4 could be due to the presence of different REE complexes they are bound to.

5.4.3 Partition coefficients of REE between crude oil and water

REE partition coefficients between crude oil and water were calculated for samples from sites 1 and 2, where both phases were collected. Partition coefficient patterns show that the coefficients for the samples collected from site 2 are higher than

those of the samples collected from site 1 by more than an order of magnitude, with negative Eu anomalies presented in both patterns (Fig. 5−4). If REE in both phases were in equilibrium, the degree of Eu anomalies would be expected to be similar between oil and water phases, which obviously is not the case. Our results suggest that although the two phases are in contact, the REE partition between oil and water is not at equilibrium. The strong binding of REE in the oil phase perhaps inhibits the redistribution of REE into the water phase. This might also explain the large discrepancy of the partition coefficients calculated in samples collected from sites 1 and 2.

To evaluate the complexation of REE in the oil phase, it is better to obtain partition of REE in the oil phase relative to free REE ions in water. The partition coefficient of REE in the oils phase to free ions in the aqueous phase can be directly compared with the stability constants (β) of REE with known ligands (= L^{z-}) formulated for free REE ions (= Ln^{3+}) as $\beta_{REE\text{-}L} = [Ln\text{-}L^{(3-z)+}]/([Ln^{3+}][L^{z-}])$. A speciation calculation using the Windermere Humic Aqueous Model (WHAM; Tipping, 1994) was conducted to determine the free REE ions in our water samples. Intrinsic stability constant ($\log K_{MA}$) values of REE and humic complexes were obtained from Yamamoto et al. (2010). We assumed that humic acid constitutes 50% of the total organic carbon and that all iron dissolved in the water is bound to humic acid as Fe(III) (Herbert and Bertsch, 1995; Yamamoto et al., 2009). Based on the concentrations of free REE ions, we reevaluated the partition coefficient of REE into oil phase normalized by free REE ions in the water. A relatively high pH and a large content of carbonate ions in the water samples (Table 5−2) can lead to lower fractions of free REE ions for the heavier REE. Although a complete equilibrium of REE between oil and water phases may not be attained, the REE partition coefficients to free REE ions in water phase clearly show enrichments for Sm and Lu (Fig. 5−5). Such a trend is known for the stability constants of REE with carboxylic acids (Smith and Martell, 1987), which were detected in our crude oil samples by ^{13}C NMR spectra. It is most likely that the complexation of REE with these ligands induces larger partitions of REE into crude oils relative to the water phase.

5.4.4 Origin of REE in crude oil

The REE patterns of the crude oils were compared with those of coexisting mud (Table 5−3; Fig. 5−6). Samples of crude oils collected from sites 1, 2 and 3 show flat mud-normalized REE patterns, while the crude oil collected from site 4 shows an HREE-depleted pattern. The flat patterns suggest that REE in crude oils principally inherit those in coexisting mud which originates from surrounding sedimentary rocks. The HREE depletion observed at sample collected from site 4 in Fig. 5−6 can be due to the lower abundances of HREE in crude oil itself shown in Fig. 5−3A, since REE patterns of mud samples erupted from mud volcanoes were very similar among all sites (Table 5−3). The absence of carboxyl groups, as discussed above, can cause the depletion of HREE in the oil samples. Thus, we speculate that REE in crude oil sample collected from site 4 is also derived originally from sediments.

Difference of Y/Ho ratio shown in Fig. 5−6 can be caused by the difference of their source reservoirs, in particular REE abundances in water contacted with oil in each reservoir. Although the Y/Ho ratios of mud samples are almost the same in a range from 20.1 to 25.4 (Fig. 5−3C), the ratio varies greatly among water samples with the ratio of 25.6 for site 1 while 40.5 for site 2 (Fig. 5−3B). Water-rock interactions can induce the increase of Y/Ho ratio in water relative to the original rock source to various extents depending on the degree of water-rock interaction (Bau, 1996; Takahashi et al., 2002a). Since REE abundances in water primarily affect REE abundances in oils, the Y/Ho ratio in oil can be variable depending on the ratio in water in each system. In addition, water-rock interaction causes positive Eu anomalies in water samples, which in turn induces positive Eu anomaly in the oil normalized to mud as shown in Fig. 5−6. The degree of Eu anomaly is also dependent on the water-rock interaction in each system. Thus, both Y/Ho ratio and degree of Eu anomaly are variable among different samples (Fig. 5−6).

The cerium anomaly, which is often observed in plants (Fu et al., 1998) or in marine organic matters (e.g., Fleet, 1984), is absent in our crude oil samples. If REE in crude oils are originated from the precursors of oils such as the plants and the marine

organic matters, it is most likely that REE patterns of the crude oils have Ce anomalies, which is obviously not the case in our samples. This implies that REE in our crude oil samples are originated from those in surrounding rocks during diagenetic processes associated to the maturation of the crude oils.

5.5 Conclusions

The study of REE abundance patterns in crude oils and coexisting water and mud samples from the Xingiang Province, China, brought to the following conclusions:

(1) REE in crude oils derived from thier source rocks and sediments;

(2) REE in crude oils mainly form carboxylate and phenolate complexes, which induce a larger partition of REE into the crude oil relative to the coexisting water phase.

Due to a lack of reported data of REE in crude oils, the present study can constitute a preliminary database which may contribute to understand the genetic processes of maturation of hydrocarbons.

Table 5−1. REE concentrations (μg/g) in crude oil samples.

Element	Site 1	Site 2	Site 3	Site 4
Y	22.8	337	1350	242
La	33.6	288	861	386
Ce	66.6	662	2150	843
Pr	7.91	59	278	102
Nd	30.1	233	1140	397
Sm	6.52	47.2	182	84.4
Eu	1.55	11.2	38.2	16.7
Gd	5.70	44.4	166	74.6
Tb	1.01	8.1	32.4	12.0
Dy	5.31	48.0	187	62.2
Ho	1.08	10.1	39.2	11.0
Er	3.23	32.8	125	29.3
Tm	0.446	4.74	17.9	3.45
Yb	2.98	32.4	124	21.0
Lu	0.437	4.93	18.4	2.77
ΣREE	189	1820	6710	2290

Table 5−2. REE concentrations (ng/L), pH, alkalinity (mM), calculated CO_3^{2-} concentrations (mM), TOC (mg/L) and concentration of iron (mg/L) in water samples.

Element	Site 1	Site 2
Y	90.7	44.5
La	126	5.61
Ce	299	14.1
Pr	27.2	1.53
Nd	110	6.17
Sm	25.3	1.47
Eu	17.9	1.52
Gd	23.2	2.26
Tb	3.73	0.511
Dy	18.6	4.03
Ho	3.54	1.10
Er	10.2	3.74
Tm	1.35	0.630
Yb	9.31	4.39
Lu	1.35	0.790
ΣREE	767	92.3
pH	8.40	7.35
Alkalinity	71	53
CO_3^{2-}	70	48
TOC	7.20	6.54
Fe	4.52	3.85

Table 5−3. REE abundances (mg/kg) of mud and rocks determined using ICP-MS.

Element	Rock (i)	Mud Site 1	Rock (ii)	Mud Site 2	Mud Site 3	Rock (iii)	Mud Site 4
Y	23.6	19.0	28.7	29.2	30.1	21.2	19.4
La	30.5	22.6	29.5	31.0	31.3	26.7	21.4
Ce	75.7	53.1	75.4	82.5	78.2	57.8	43.3
Pr	8.00	5.80	7.91	8.50	8.07	6.11	5.15
Nd	34.1	24.4	34.3	37.2	35.2	25.9	19.5
Sm	7.03	5.07	7.41	7.98	7.52	5.48	4.03
Eu	1.36	1.00	1.62	1.66	1.55	1.10	0.583
Gd	6.55	4.91	7.17	7.67	7.40	5.33	3.60
Tb	1.03	0.769	1.15	1.22	1.16	0.847	0.646
Dy	5.93	4.35	6.84	7.10	6.76	4.98	3.63
Ho	1.18	0.869	1.40	1.45	1.36	1.00	0.764
Er	3.50	2.60	4.22	4.35	4.10	3.02	2.21
Tm	0.508	0.373	0.606	0.628	0.576	0.421	0.331
Yb	3.34	2.51	4.09	4.20	3.93	2.87	2.11
Lu	0.503	0.378	0.618	0.634	0.604	0.429	0.326
Ce/Ce*	1.16	1.11	1.18	1.22	1.18	1.09	0.99
Eu/Eu*	0.61	0.61	0.68	0.64	0.63	0.62	0.47
ΣREE	203	148	211	225	218	163	127

$Ce/Ce^* = Ce_{CN} / \sqrt{La_{CN} \times Pr_{CN}}$, $Eu/Eu^* = Eu_{CN} / \sqrt{Sm_{CN} \times Gd_{CN}}$ where CN means chondrite normalized values.

Note that rock (i) is a sedimentary rock sample collected around mud volcanoes locate site 1, rock (ii) is collected around sites 2 and 3, and rock (iii) is collected around site 4.

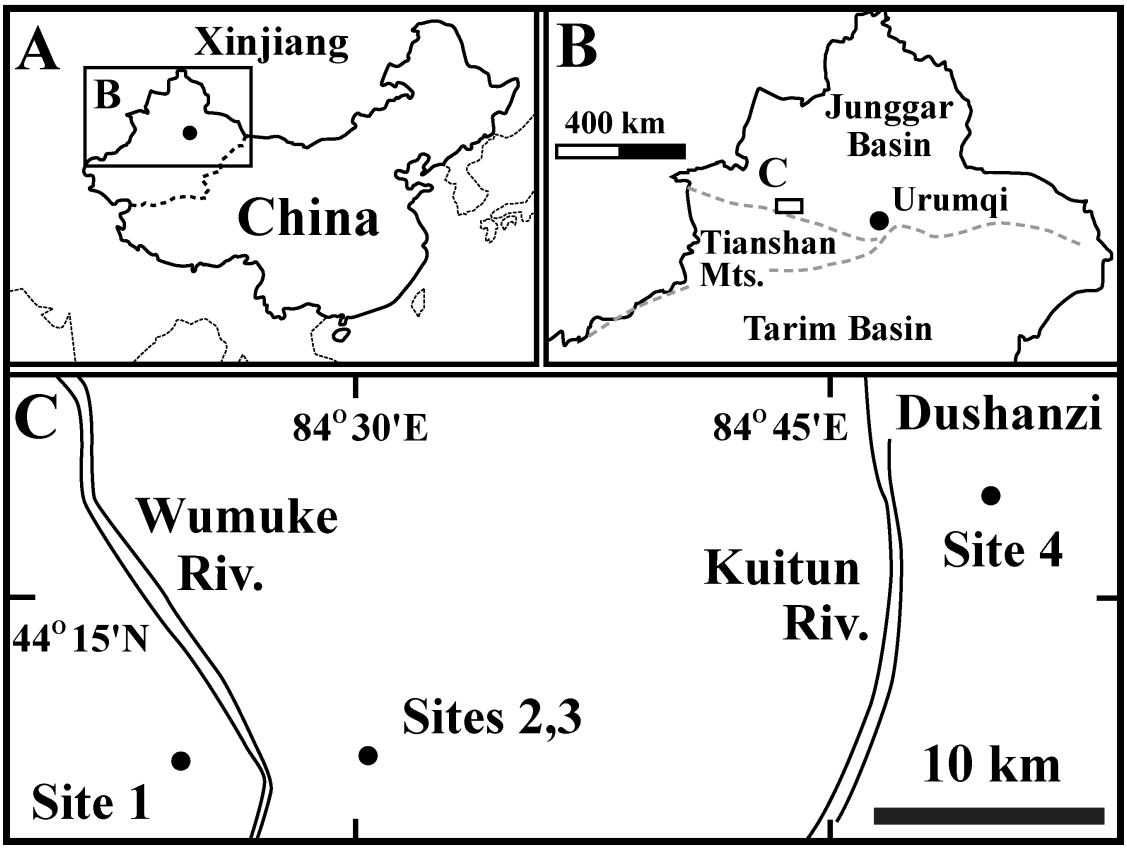

Fig. 5−1. Schematic map of sampling locations. Map A depicts entire China and the dashed line represents the border of Xinjiang Uyghur Autonomous Region. Map B depicts three quarters of Xinjiang and the dashed lines represent Tianshan Mountains. Location of a star marked on map B is enlarged to map C. Site 4 is situated near Dushanzi District.

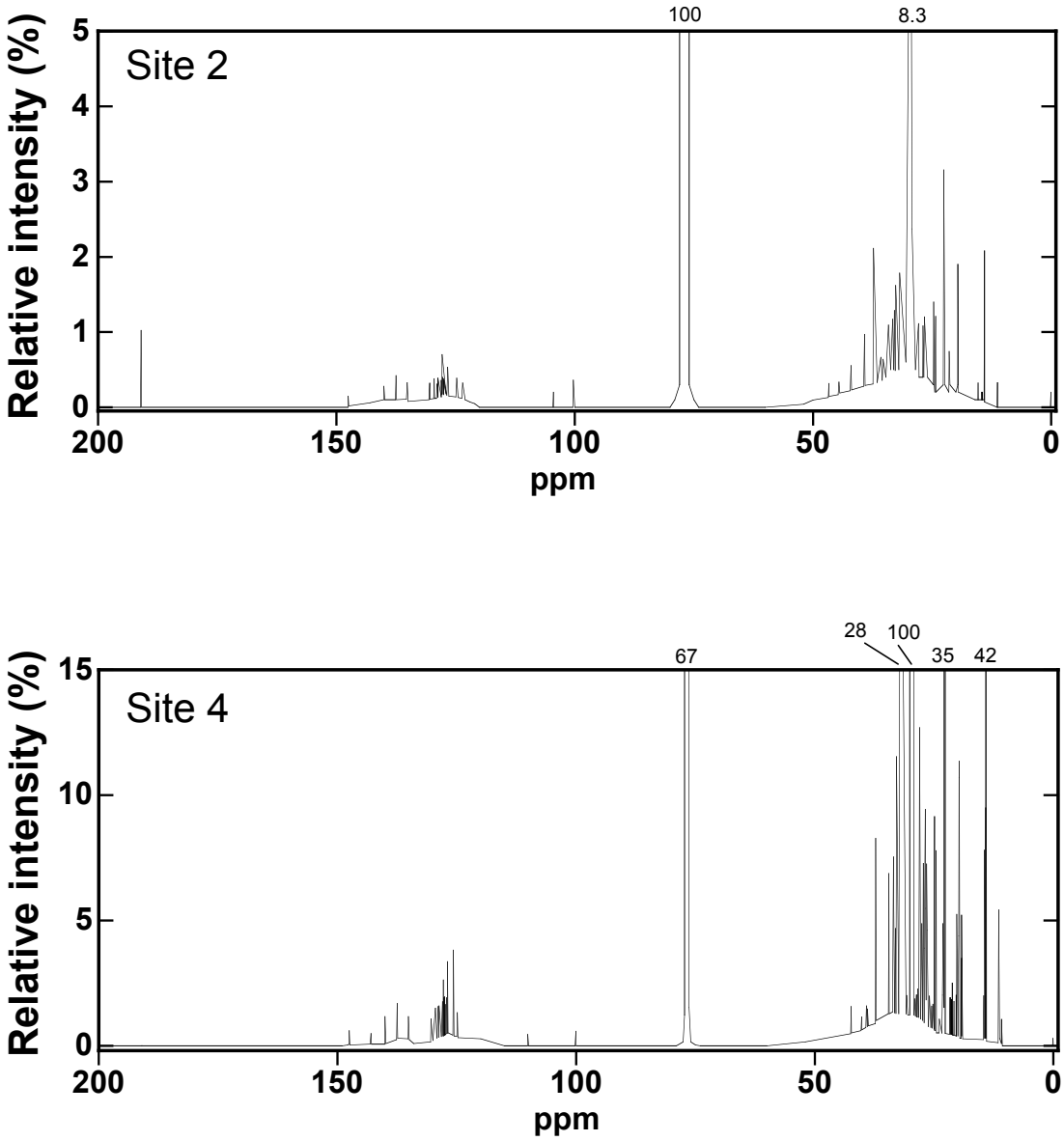

Fig. 5−2. ^{13}C NMR spectra of crude oil samples at sites 2 and 4. The numbers at the top of the figures indicate the relative intensities of the peaks presently out of range of the figures.

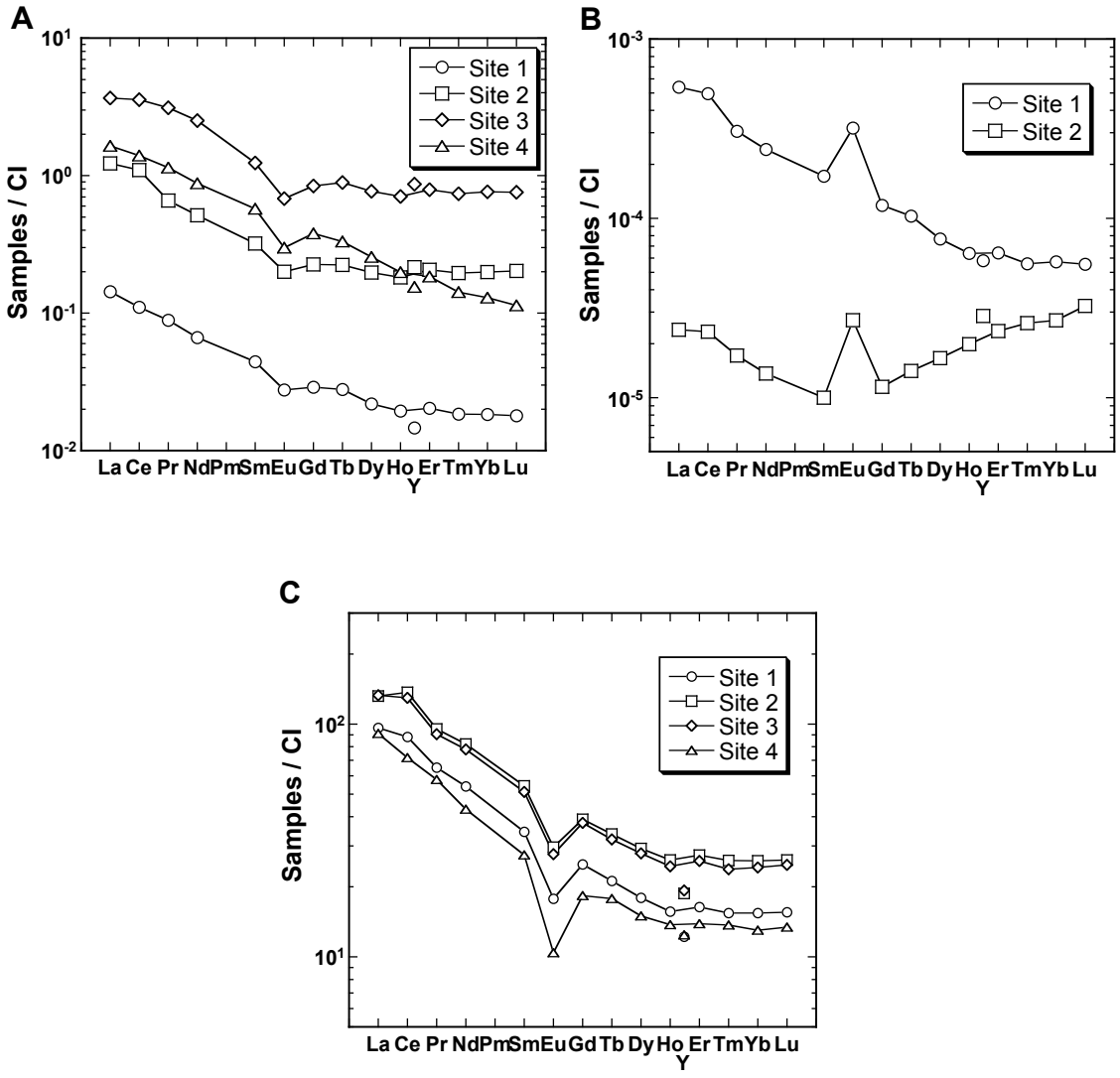

Fig. 5−3. Chondrite-normalized REE patterns of (a) crude oil, (b) water and (c) mud samples collected at mud volcanoes in Xinjiang Province, China. REE concentrations of CI chondrite are taken from Anders and Grevesse (1989).

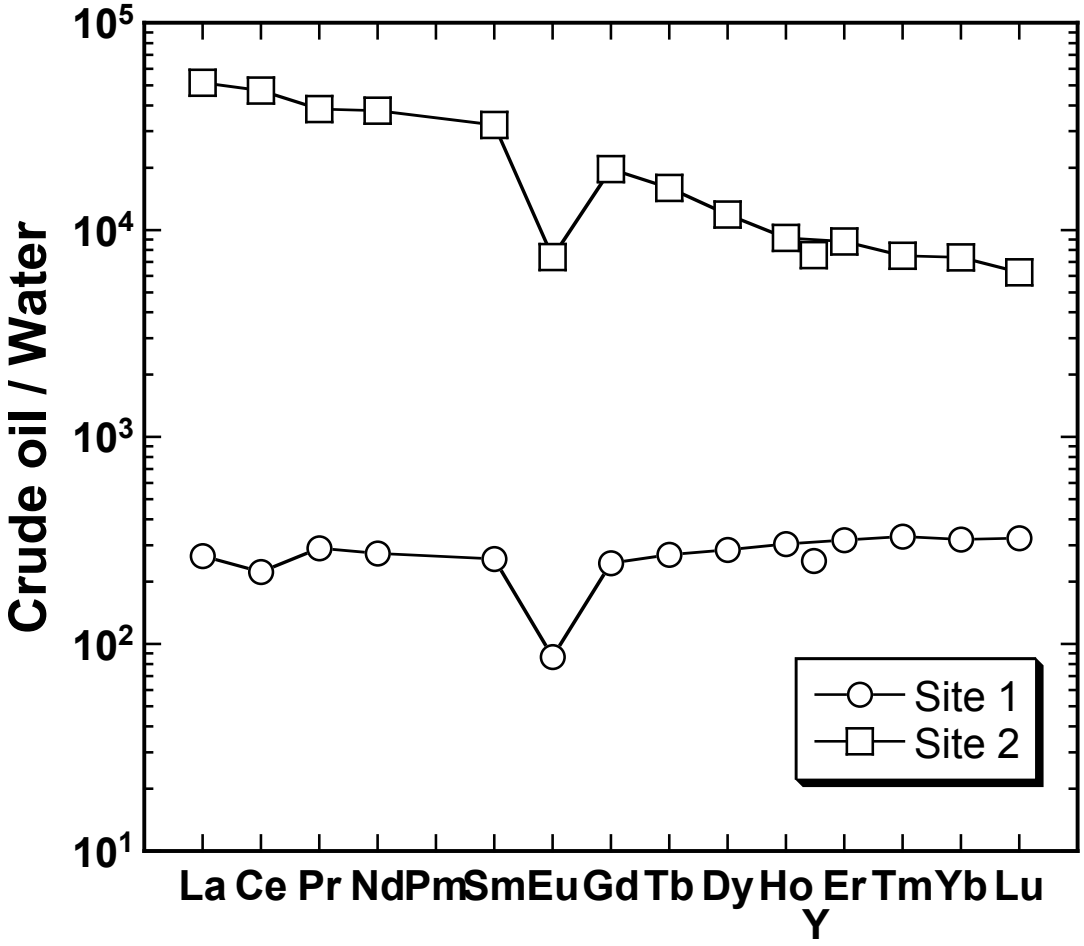

Fig. 5−4. Partition coefficients between crude oil and water.

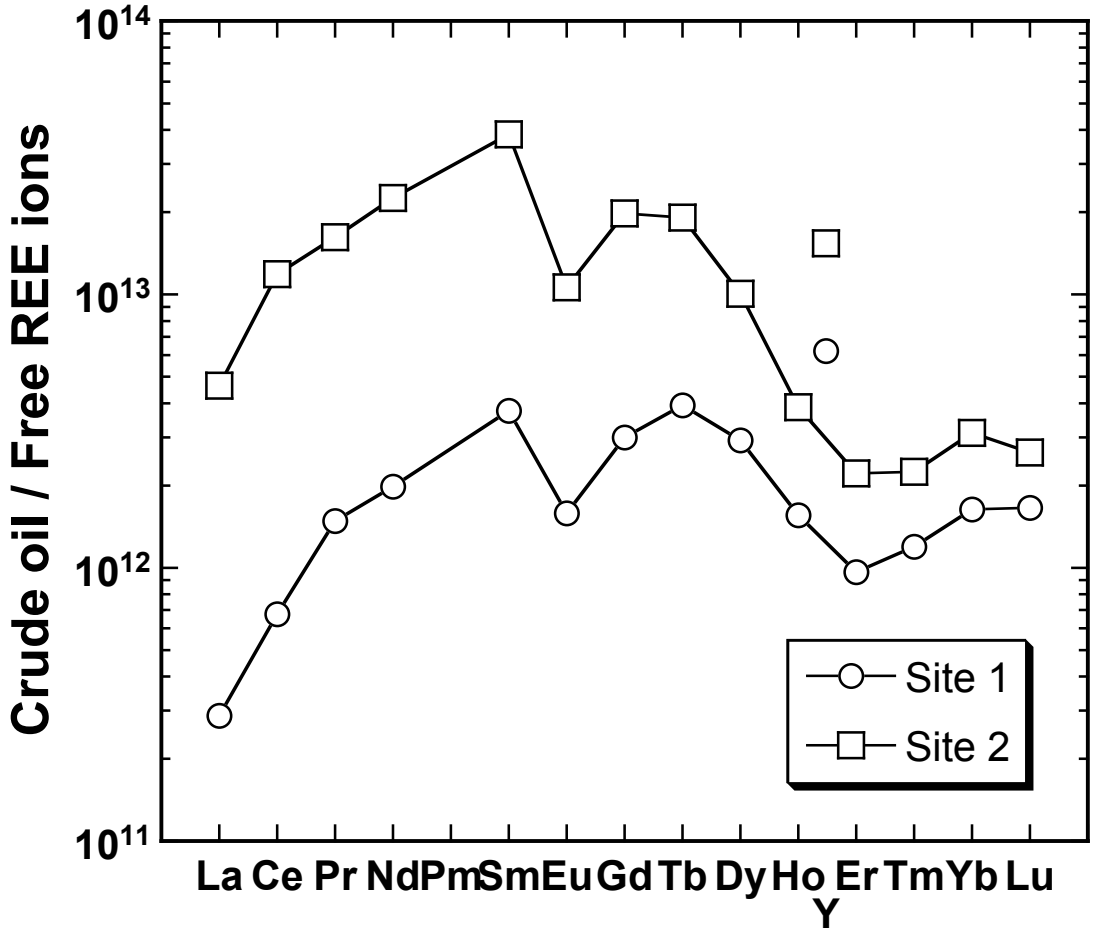

Fig. 5−5. Partition coefficients between crude oil and free REE ions in water.

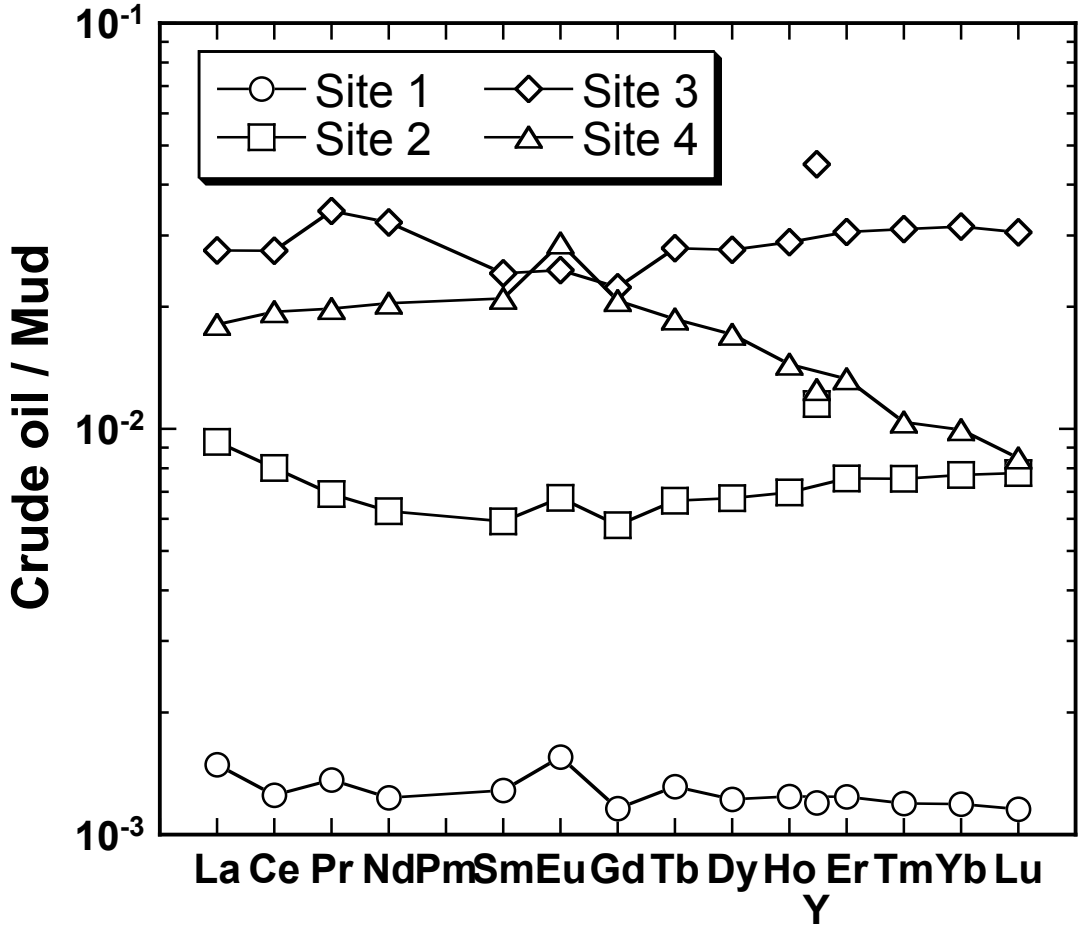

Fig. 5−6. Coexisting mud-normalized REE patterns of crude oils.

Chapter 6

The behavior of REE during the maturation process of organic matter

6.1 Chapter introduction

Retention of the same outer electron orbits, 6s, makes rare earth elements (REEs) similar chemical properties one another. Together with the lanthanoid contraction, their chemical similarities induce systematic partition in various natural systems, which have led to the that the relative abundances of REE, namely REE pattern, reflect chemical processes occurring in various systems on the earth (e.g., Henderson, 1984; Taylor and McLennan, 1988). These characteristics enables REE pattern to be an effective geochemical tracer in several systems. In particular, unique characteristics shown in REE pattern, namely Ce and Eu anomalies, Y/Ho ratios, and M- and W-type tetrad effect, enable to discuss REE behavior in two systems contacting one another such as low and high temperature water-rock interactions (e.g., Bau et al., 1998; Klinkhammer et al., 1983; Michard et al., 1983; Takahashi et al., 2002a). Despite its great applicability in the field of inorganic geochemistry, REE studies in organic geochemistry have been poor.

It has been suggested that the REE contents of oils are useful in the oil classification and the REE patterns of crude oils can provide genetic information on the oils (Akinlua et al., 2008; Zhang et al., 2009). Although these studies suggested the possible application of REE in organic geochemistry, the accurate determination of REE including yttrium (Y) has not been achieved in these studies. The first report on the entire range of REE concentration with smooth CI-normalized pattern showed that the REE concentrations in crude oils are larger than those in coexisting water by a factor of more than one hundred (Chapter 5). The result showing high affinity between REE and crude oils appears to be unusual if the ionic characteristics of REE and the hydrophobicity of oil are taken into account. However, it was found that phenol and carboxyl groups forming complexes with REE presented in the oils, which induces a larger partition of REE into the crude oil relative to the coexisting water phase.

Considering the genetic process of oils, the finding of carboxylate complex in oil could be rare because the kerogen decarboxylation reaction should occur during the maturation process. In this Chapter, therefore, the REE behavior during the maturation process is examined by measuring REE concentration in various oil samples and performing a laboratory experiment simulating the release of REE from organic phase during the oil maturation.

6.2 Samples and methods

6.2.1 Crude oil samples

Crude oil samples were collected from Sagara, Nagaoka-Higashiyama, Biratori, Yurihara, and Sarukawa oil fields in Japan (Fig. 6–1). The Sagara oil field located in the southern part of Shizuoka Prefecture is the only oil field on the Pacific Ocean side of Japan. This region is composed of conglomerate, sandstone, mudstone, and limestone, which are considered to be fore-arc basin sediments on the Nankai accretionary prism (Tsuchi, 1961; Ujiie, 1962). The oil collected from Sagara is unique in terms of its lighter specific gravity compared to the ordinary oils (Kato, 1992).

Nagaoka-Higashiyama oil field is located in the Niigata Prefecture. In Niigata Basin, commercial oil and gas accumulations are hosted in clastic and volcanic reservoirs such as, tuffaceous mudstones and rhyolite, while Miocene siliceous mudstones seem to be the main source rocks with predominant Type II kerogen (Waseda and Iwano, 2008; Kato et al., 2009; Tomaru et al., 2009). Na-Cl-type geopressured fossil formation waters, related to the hydrocarbon reservoirs, are source of numerous hot springs in the basin (Xu et al., 2006). The geology of the area is mainly composed of sandstone, mudstone, and siltstone (Kobayashi et al., 1991).

Biratori oil field locates about 30 km east from Tomakomai city, Hokkaido. Crude oil is produced from Furuoi layer and is originated from terrigenous organic matters (Fujioka and Saga, 1980; Masatani, 1980). Oils collected from three different wells (SK-1, SK-2, and SK-5) were used in this study.

Yurihara and Sarukawa oil fields are located in the Akita Prefecture. The Cenozoic sediments in Akita are one of the major oil-producing basins in Japan. The basin is composed of Monzen (Oligocene), Daijima (Oligocene–Miocene), Nishikurosawa (Oligocene–Miocene), Onnagawa (Miocene), Funakawa (Miocene–Pliocene), Tentokuji (Pliocene–Pleistocene), Sasaoka (Pleistocene), and Karanishi (Pleistocene) Formations (Ozawa and Suda, 1980). Oil samples collected from five different wells (SK-9S, SK-12, SK-15, SK-17HD, and SK-18) in Yurihara oil field hosted by Nishikurosawa Formation mainly composed by basaltic lava were used. In addition, oils from five different wells (SK-67, SK-68, SK-75, SK-80, and SK-81) were collected in Sarukawa oil field mainly composed of Onnagawa Formation.

6.2.2 Analytical method

Functional groups contained in oil samples were determined by a nuclear magnetic resonance (NMR) spectroscopy on carbon atom (^{13}C-NMR) using a JEOL ECA600 at the Natural Science Center for Basic Research and Development (N-BARD), Hiroshima University. 0.2 ml of oil sample and 0.4 ml of deuterated chloroform solvent (D, 99.8%) containing 0.05% tetramethylsilane (Cambridge Isotope Laboratories, Inc.) which serves as an internal standard were placed in a NMR tube (ϕ 4.950×178 mm) with 2 mg $Fe(acac)_3$ as a relaxation agent (after Hasan et al., 1983). Operating frequency was 150.913 MHz. Each scan required 2.7 s and repeated 12,000 times.

The difficulty in measuring the concentrations of metal elements including REE in crude oils lies in the separation of REE from crude oils. Complete decomposition of organic compounds is required in the measurements of REE using an inductively coupled plasma mass spectrometry (ICP-MS), because the organic matter can induce a harmful effect on the measurement (Lord, 1991; Akinlua et al., 2008); (i) introduction of organic matter into the ICP-MS leads to the formation of carbon-containing ions such as C^{2+}, CO^{2+}, and ArC^{+}; (ii) some carbon-bearing materials can be deposited at the interface into the mass spectrometer of the ICP-MS; (iii) high viscosity and boiling point of crude oils lower their atomization efficiency. These problems prevent the

accurate and precise determination of REE concentration using ICP-MS, meaning that the complete decomposition of organic matter is necessary to determine the concentration of REE in crude oils. In this study, about 0.5 g of crude oil was placed into a Teflon vessel and decomposed by heating at 180 ºC in a 68 wt.% HNO_3 solution. After evaporation, the residue was thoroughly digested using a 1:1 mixture of 35 wt.% H_2O_2 and the HNO_3 solution. Further digestion was performed using a 1:2 mixture of 70 wt.% $HClO_4$ and the HNO_3 solution. All the solutions used to decompose the samples were ultra-pure grade (TAMAPURE-AA-100; Tama Chemicals Co., Ltd.). The samples were evaporated again and finally dissolved in 2 wt.% HNO_3 and analyzed using an Agilent 7700 ICP-MS. Indium (In) and Bismuth (Bi) were added to the sample solution before the measurements at a concentration of 1 μg/L as internal standards. The precision of the ICP-MS measurement was better than 1.1% for all the REEs as calculated from repeated measurements. Repeated decomposition of oil samples showed identical REE concentrations within the analytical uncertainty, suggesting loss of REE during decomposition, evaporation, and re-dissolution processes is negligible.

6.2.3 REE distribution experiment

About 0.1 g humic acid (Aldrich) was dissolved with 100 g ultrapure water (hereafter, humic solution). Seven grams humic solution was placed into a Teflon vessel with 1 g REE solution (Spex Certiprep., USA) containing all REEs except for Pm at a concentration of 10.0 mg/L of each. The pH of the REE-doped humic solution was adjusted to 6.0 using a diluted solution of NaOH or HCl to prevent precipitation of humic acid and shaken for 24 hours. Then, 0.1 g of powdered slate (JSl-1) was placed into the bottle. Because slate, originally derived from fine grained mudstone or shale, contains clays after low-grade regional metamorphism, it is suitable to simulate the reactions occurring in the oil reservoir. One fraction was shaken at 25 ºC for 72 h and the other fraction was heated at 40, 60, 80, 100, 120, 140, and160 ºC for 72 h. At the end of the experimental period, the slate was separated using a mixed cellulose filter (0.45 μm; ADVANTEC). The filtrated slate was finally dissolved in 0.5 M HCl solution

following a digestion in a mixture of HF, $HClO_4$, and HNO_3 solutions. Then purification of REE was performed by cation column chemistry. Major cations such as Fe were eluted by 2.0 M HCl solution, while 2.0 M HNO_3 solution was used to elute Mn and Ba. Almost 100% of REE was recovered by passing the 6.0 M HCl solution. The eluted REE solution was dried and finally dissolved by 2 wt.% HNO_3 solution for the determination of the concentrations of REEs using the ICP-MS (Agilent 7700). Similar to the REE measurement for oil samples, In and Bi were added at a concentration of 1 μg/L to serve as internal standards. The accuracy and precision of the measurement were better than 1% for all the REEs. The amount of REE distributed from the REE doped humic solution was then calculated. The experiment was repeated three times. In addition, blank experiment, namely REE adsorption on slate (without containing humic solution), was also performed. The REE distribution ratio is given by the following equation:

$$\text{Distribution ratio (\%)} = (REE_{meas.} - REE_{blk.})/REE_{ini.}\ , \qquad (6\text{–}1)$$

where subscripts meas., blk., and ini. respectively denote measured REE concentration, blank REE concentration (REE adsorbed on slate without humic solution), and initial REE concentration in the humic solution.

In this experiment, the amount of carboxyl groups in humic acid was determined by titration following a methodology described by Schnitzer (1972) and Tsutsuki and Kuwatsuka (1978). The humic solutions before and after heating were respectively placed into a conical flask with 50 mL ultrapure water and 10 mL of 1 M calcium acetate solution and shaken for 16 h at 25 ºC. After the experimental period, the reaction solution was filtrated by a paper filter (ADVANTEC No.6) and precipitates on the filter were washed by ultrapure water. The filtrate was titrated until the solution became slightly red-colored using a 0.1 M NaOH solution with a phenolphthalein as an indicator. A blank experiment without containing humic solution was also performed. The amount of carboxyl groups (mol/kg) was calculated as follows;

$$0.1 \times (T_{fs} - T_{blank}) \times f / A_{fa} \qquad (6\text{–}2)$$

where T_{fs} and T_{blank} denotes titration amounts (mL) of humic solution and blank,

respectively. The correction factor of the NaOH solution is described as f, whereas A_{fa} means the amount of humic acid used to prepare humic solution (mg).

6.3 Results

The ^{13}C-NMR spectra of oil samples show several peaks from 10 to 60 ppm and around 77 ppm (Fig. 6–2). These peaks, often observed in crude oils can be ascribed to the presence of functional groups of aliphatic carbons (0–70 ppm) and formyl groups (77 ppm) (Hasan et al., 1983; Sharma et al., 2008). The spectra from 110-160 ppm show several peaks, suggesting the existence of aromatic series and phenolic groups (Hasan et al., 1983; Thorn et al., 1989), which can be act as a complex forming site for REE. However, any peaks were not observed from 160-200 ppm, suggesting that oils examined here do not contain the carboxyl groups (Fig. 6–3).

The total REE concentration of crude oils collected from Sagara, Nagaoka-Higashiyama, Biratori, Yurihara, and Sarukawa oil fields in Japan are less than 10 μg/g. In particular, for most of the samples, the total REE concentration are less than 2 μg/g, which are more than three orders of magnitude lower than those collected from Xinjiang province (Chapter 5) (Table 6–1). The oils present similar REE patterns with each other when normalized to CI chondrite (Anders and Grevesse, 1989) (Fig. 6–4). The oil samples are enriched in light-REE (LREE) and flat or slightly enriched in heavy-REE (HREE). Especially in the HREE region, patterns show W-type tetrad effect, a downward concave curve in Gd-Tb-Dy-Ho and Er-Tm-Yb-Lu spans, which is often observed in water phase during the water-rock interaction (Masuda and Ikeuchi, 1979). The Ce anomaly, which is often observed in plants or in marine organic matters (Fleet, 1984; Fu et al., 1998), is observed in most of the oils, suggesting that REE in oils can be originated from the precursors of oils.

Table 6–2 lists the distribution ratios of REE from humic solution to solid phase. The amount of REE released to the solid phase became larger with increasing experimental temperature. For all the experimental conditions, the light-REEs (LREE) distributed to the solid phase were smaller than the heavy-REEs (HREE). In addition, Y

released to the slate was smaller than Ho (Fig. 6–5).

6.4 Discussion

6.4.1 Behavior of REE during maturation

Considering the maturation process to form crude oil, the precursor of oil is a kerogen which is produced from humic substances such as humic and fulvic acids. The humic substances have a lot of capacities to adsorb REE because they have the carboxyl and phenol groups (Yamamoto et al., 2010). However, the kerogen decarboxylation reaction occurs during the oil-generating process, leading to the decomposition of carboxyl groups to CO_2 gas. It is highly possible that most of the REE can be excluded from the organic phase during the reaction because REE cannot form complex in the gas phase. Thus, it should be expected that the more the maturity increases, the lesser amount of REE remains in the organic phase. Indeed, the total concentration of REE in oils without having carboxyl groups is more than two orders magnitude lower than that includes carboxyl groups (Table 6−1). Therefore, it is possible that the REE abundance in oils reflects the maturity.

Next, it is highly possible that the oil reservoir contains not only organic matters but also oil-field brine. Considering that the REE has ionic characteristics, preferential distribution of REE from organic phase to water phase can be expected in the reservoir during the decarboxylation. The high temperature in the reservoir is also expected to promote maturation of the organic matter, leading to the formation of clay minerals. Furthermore, the existence of clay minerals can induce the re-distribution of REE from water phase, which is also suggested by the REE patterns. The REE patterns examined in this study show W-type tetrad effect (Fig. 6–4), indicating the presence of the M-type tetrad effect, which is an upward concave curve, should be shown in the counterpart phase (Kawabe et al., 1999b). The appearance of the W-type tetrad effect in the oil samples, thus, indicates the re-distribution of REE to material(s) presenting an M-type tetrad effect through water phase. The possible material in the reservoir presenting the M-type tetrad effect is clay minerals (Takahashi et al., 2004). Hence, we suggest that the

REE originally derived from humic substances are excluded from organic phase during the decarboxylation and re-distributed to clay minerals through brine water in the reservoir. Therefore, it is possible that REE is enriched in the oil-hosting rocks.

6.4.2 Can oil-hosted rocks be enriched in REE?

The REE distribution experiment supports the hypothesis above. About 35% of REE is distributed to the solid phase only by shaking, which can be due to the adsorption of humic acid on the solid phase. The REE distributed to the solid phase did not significantly increase by heating below 60 ºC. Although the mean REE distribution exceeded 40% by heating at 80 ºC, the concentration of carboxyl group in humic acid was within the analytical uncertainty with that of 25 ºC (Fig. 6–6). On the other hand, the distribution experiment performed above 80 ºC showed clear decrease in the carboxyl group with increasing REE distribution to the solid phase. Approximately 75% of REE was distributed to the solid phase after heating at 160 ºC. Hence, the experiment shows that the REEs originally adsorbed on carboxyl group in humic acid were released and re-adsorbed onto the solid phase owing to the decarboxylation reaction. The relationship shown in Fig. 6–6 suggests that the complete removal of REEs from humic acid is possible by the decomposition of carboxyl group.

The amount of REE in partially maturated crude oil containing the carboxyl group (Chapter 5) was more than 10^3 times larger than those in fully maturated oils (this study), suggesting the loss of 1 mg REE from a gram of oil. Then, the generation of a barrel of crude oil accompanies with the release of 140 g of REE, when assuming that the specific gravity of crude oil is 0.9. Taking into account the fact that some of the supergiant oil fields can produce more than 10 billion barrels of crude oil, oil fields can be considered as potential deposits for REE. Furthermore, other elements which have high affinity to carboxyl groups may also be enriched in the oil-hosting rocks. If REE and other metal elements are largely excluded during the maturation of organic matters, it is possible that the process can affect the global budget of metal elements. Given the present circumstances, there are still large unknown things in organic geochemistry

including maturation process and oil generating process. This study presents a possible application of metal elements to reveal these uncertain things, thus can bring new possibilities on the fusion of organic and inorganic geochemistry.

6.5 Conclusions

In this Chapter, the behavior of REE during the maturation of organic matter, which has long been neglected in REE geochemistry, was examined. The REE concentrations of completely maturated crude oils collected from 5 oil fields in Japan were determined. ^{13}C-NMR spectra did not show peaks corresponding to the carboxyl group for all the oils studied here. The REE abundance of oils without containing carboxyl group was more than three orders of magnitude lower than those showing existence of the carboxyl group. REE distribution experiment showed that REEs adsorbed on humic acid were released to the solid phase in association with the decrease of the concentration of carboxyl group. A comparison between oils with or without containing carboxyl group suggests that approximately 16 g of total REEs are released during the production of a barrel of crude oil. This study brings a new possibility on the fusion of organic and inorganic geochemistry.

Table 6–1. REE concentrations (ng/g) in crude oil samples and the total REE abundance (μg/g).

	Y	La	Ce	Pr	Nd	Sm	Eu	Gd	Tb	Dy	Ho	Er	Tm	Yb	Lu	ΣREE
Sagara	104	237	314	23.3	80.8	20.0	4.87	19.5	2.85	19.6	5.76	18.6	2.27	15.1	3.17	0.871
Nagaoka	409	398	635	51.9	163.4	29.1	9.40	48.7	8.51	63.7	16.1	60.5	8.01	57.3	12.6	1.97
Biratori																
SK-1	169	74	298	27.6	97.0	25.0	6.63	32.3	5.35	33.5	8.02	24.4	3.13	23.2	4.97	0.832
SK-2	227	139	416	34.7	121	37.3	7.99	45.7	7.71	45.0	11.5	33.8	4.53	34.2	7.01	1.17
SK-5	204	186	359	29.6	104	26.7	6.92	36.7	6.34	36.3	9.04	25.8	3.75	27.8	6.03	1.07
Yurihara																
SK-9S	472	514	1266	100	380	68.3	14.0	65.5	8.67	43.1	9.02	29.7	3.86	26.0	5.06	3.01
SK-12	268	366	1266	71.5	286	55.7	5.50	47.3	6.85	33.8	6.54	19.2	2.78	17.5	3.44	2.46
SK-15	196	322	607	56.8	229	37.3	10.3	35.1	4.93	24.6	5.08	13.9	2.08	13.9	2.60	1.56
SK-17HD	249	371	783	71.7	284	51.7	13.1	43.0	6.79	35.9	7.88	24.2	3.21	23.6	4.35	1.97
SK-18D	1422	1343	2809	288	1198	229	34.5	240	34.7	168	36.0	104	15.3	107	20.3	8.05
Sarukawa																
SK-67	110	157	326	27.7	133	24.0	6.73	23.7	3.46	17.9	3.84	11.4	1.68	11.9	2.52	0.860
SK-68	166	235	559	40.4	186	32.8	6.81	32.9	5.97	31.5	5.86	18.5	2.62	19.5	3.38	1.35
SK-75	319	419	971	54.2	247	48.4	9.43	41.0	7.25	51.9	11.4	36.5	5.57	37.3	7.48	2.27
SK-80	113	731	420	26.3	117	22.4	3.51	23.2	3.68	21.1	4.96	12.9	2.32	18.0	4.20	1.52
SK-81	192	322	598	65.7	285	45.3	8.76	37.3	5.40	32.1	6.57	21.1	3.39	22.7	4.43	1.65

Table 6–2. REE distribution ratio (%) defined by Eq. 6–1.

	Y	La	Ce	Pr	Nd	Sm	Eu	Gd	Tb	Dy	Ho	Er	Tm	Yb	Lu
25 ºC	27.6	32.5	30.4	35.7	31.6	34.2	34.4	34.2	34.1	33.8	34.1	35.0	34.2	33.9	33.8
	±2.79	±4.30	±5.44	±3.25	±3.59	±2.89	±2.67	±3.10	±2.70	±2.52	±2.58	±2.40	±2.40	±2.53	±2.70
40 ºC	26.7	30.4	30.3	32.2	32.3	35.4	35.8	35.8	35.3	35.4	36.1	36.4	35.6	35.4	35.5
	±2.57	±1.67	±1.75	±2.90	±2.00	±1.67	±1.40	±1.70	±1.99	±1.63	±1.59	±1.97	±1.72	±1.57	±1.92
60 ºC	33.1	34.6	34.5	35.9	35.8	37.2	37.4	37.9	37.6	38.4	38.8	39.1	38.8	38.7	39.2
	±2.36	±2.14	±1.93	±2.16	±2.14	±2.41	±2.19	±2.21	±2.15	±2.28	±2.21	±2.19	±2.19	±2.25	±2.20
80 ºC	38.2	40.4	40.8	41.5	41.4	41.9	42.7	42.8	43.2	42.9	43.4	43.6	43.7	43.9	44.1
	±2.51	±2.67	±2.66	±2.79	±2.87	±2.87	±3.00	±3.04	±2.98	±3.07	±3.17	±3.08	±3.01	±3.06	±2.96
100 ºC	44.7	45.6	46.7	47.5	47.7	48.0	48.9	48.7	49.5	49.4	49.6	49.7	49.7	49.6	50.0
	±5.15	±5.49	±3.95	±5.68	±5.45	±4.77	±4.94	±6.06	±4.05	±4.32	±4.18	±4.67	±3.85	±4.73	±5.04
120 ºC	54.5	57.1	58.9	59.3	58.3	58.6	59.2	59.5	59.1	59.6	59.0	59.9	59.0	59.5	59.8
	±7.72	±7.95	±7.12	±7.05	±7.42	±7.00	±7.18	±7.21	±7.34	±7.46	±7.66	±8.08	±7.83	±6.85	±6.49
140 ºC	64.5	67.2	68.4	69.1	68.0	69.3	69.4	70.2	69.5	70.3	69.6	70.1	70.0	69.7	70.3
	±9.10	±6.29	±5.97	±7.89	±7.78	±8.22	±8.83	±8.76	±8.98	±8.46	±8.23	±9.23	±8.92	±8.35	±8.71
160 ºC	71.7	73.3	75.0	77.3	72.7	76.9	77.2	77.0	77.0	78.1	78.6	79.8	79.0	78.7	78.5
	±9.90	±7.62	±0.54	±9.22	±9.02	±10.1	±9.27	±10.0	±9.77	±9.92	±10.1	±9.80	±9.89	±9.74	±10.2

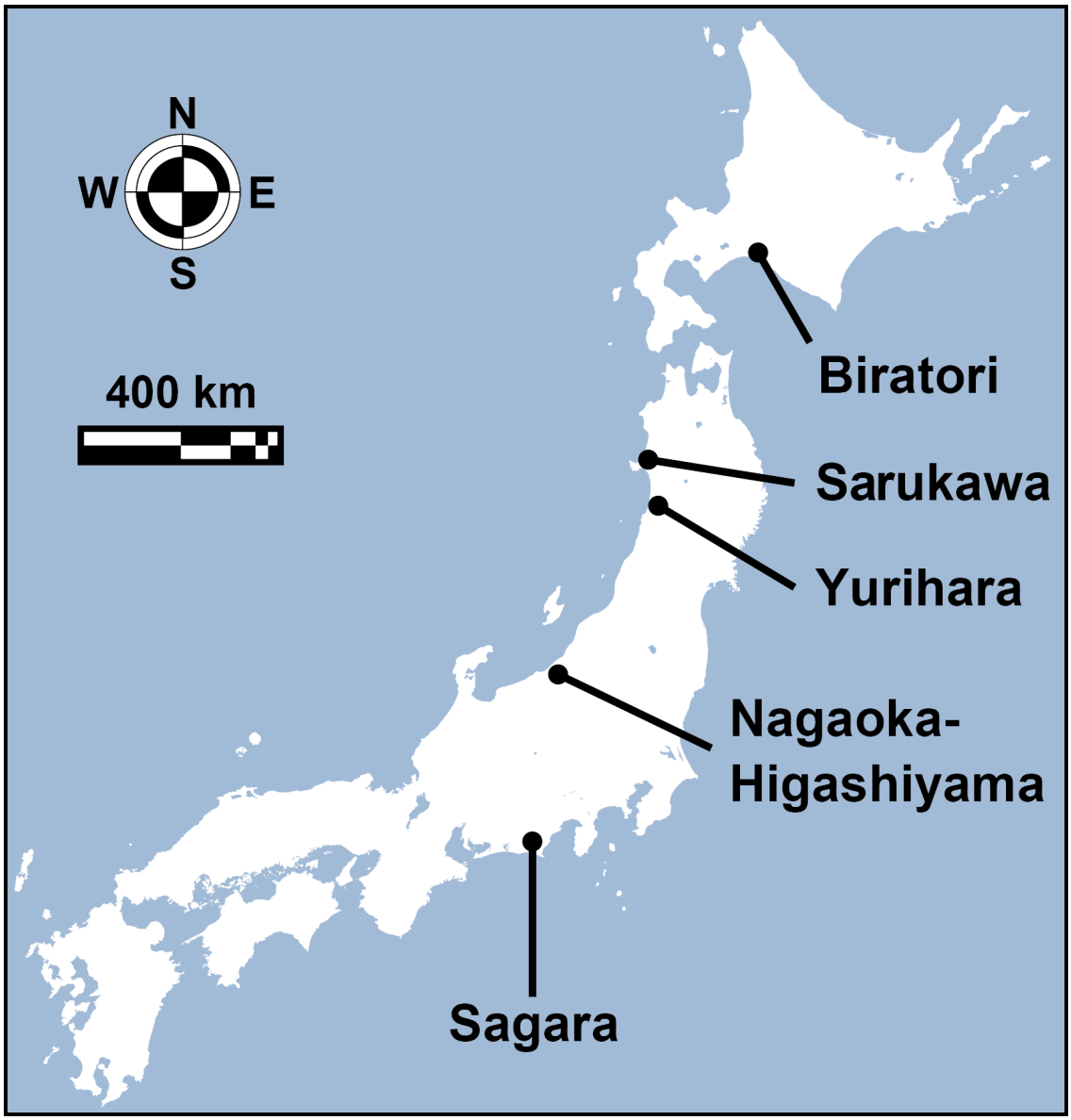

Fig. 6–1. Locations of oil fields studied here.

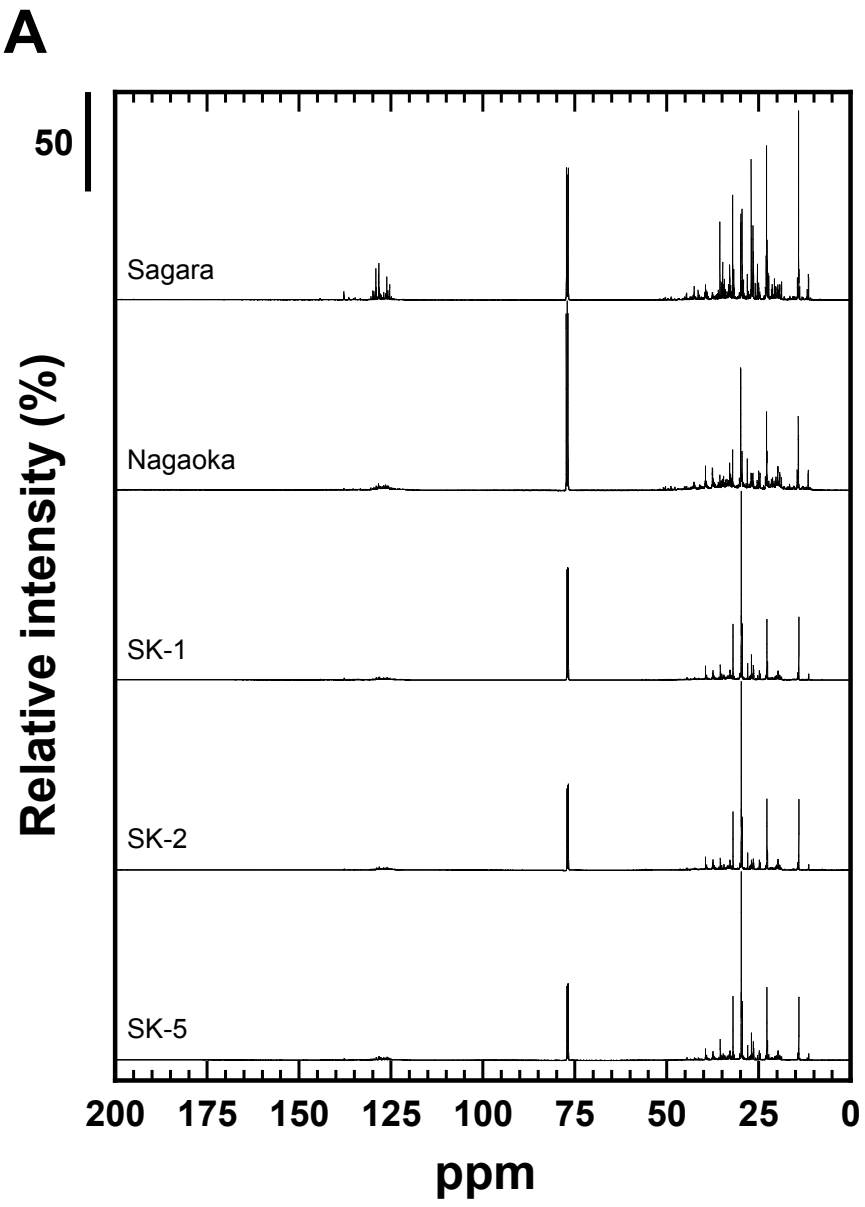

Fig. 6–2A. ^{13}C-NMR spectra of oils collected from Sagara, Nagaoka-Higashiyama, and Biratori oil fields.

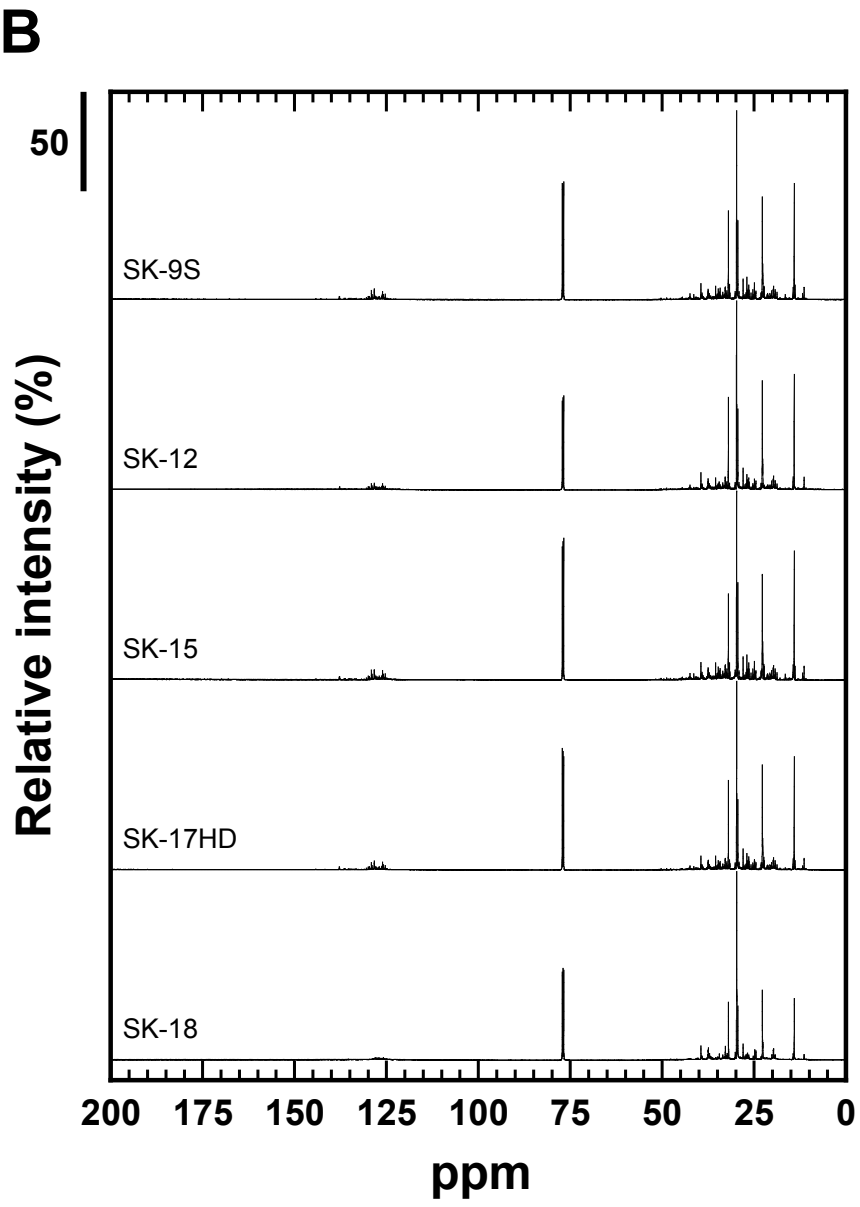

Fig. 6–2B. ^{13}C-NMR spectra of oils collected from Yurihara oil field.

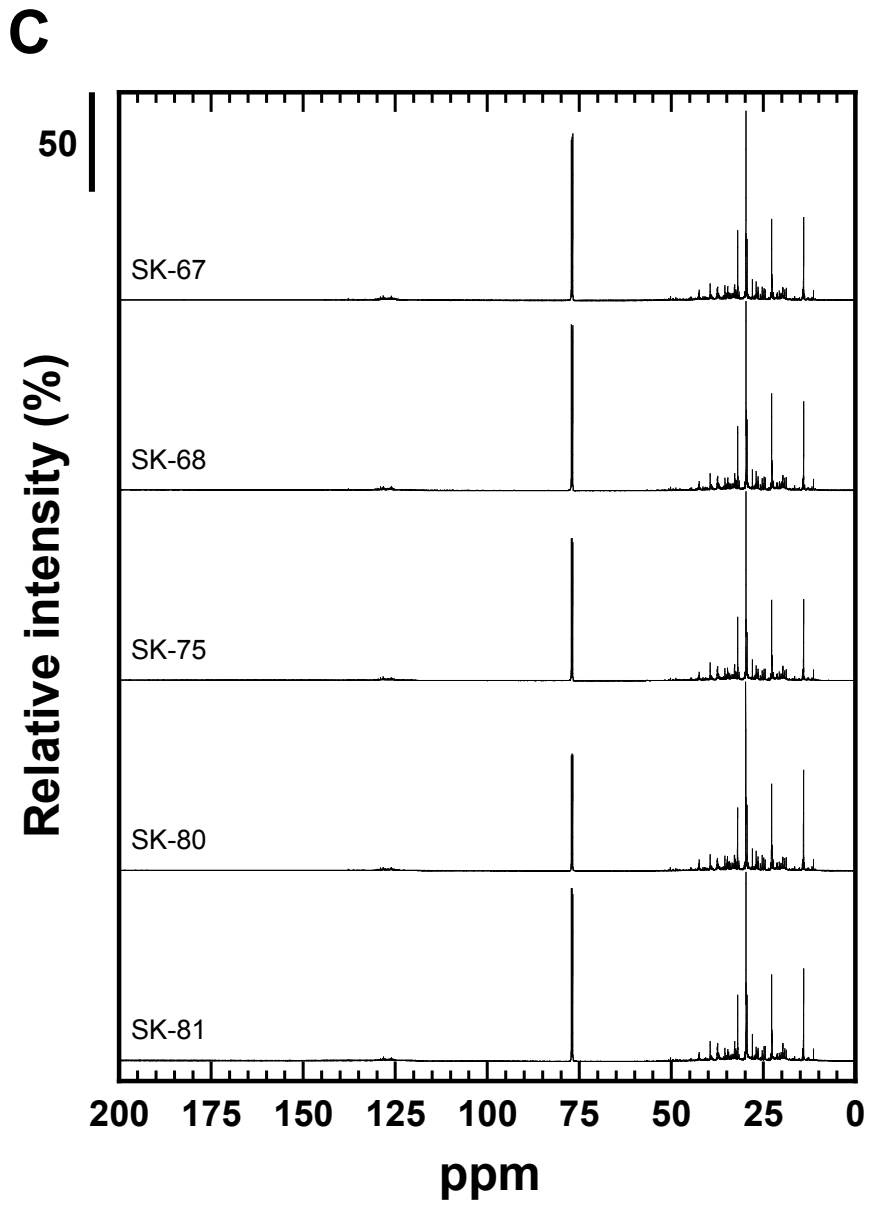

Fig. 6–2C. ^{13}C-NMR spectra of oils collected from Sarukawa oil field.

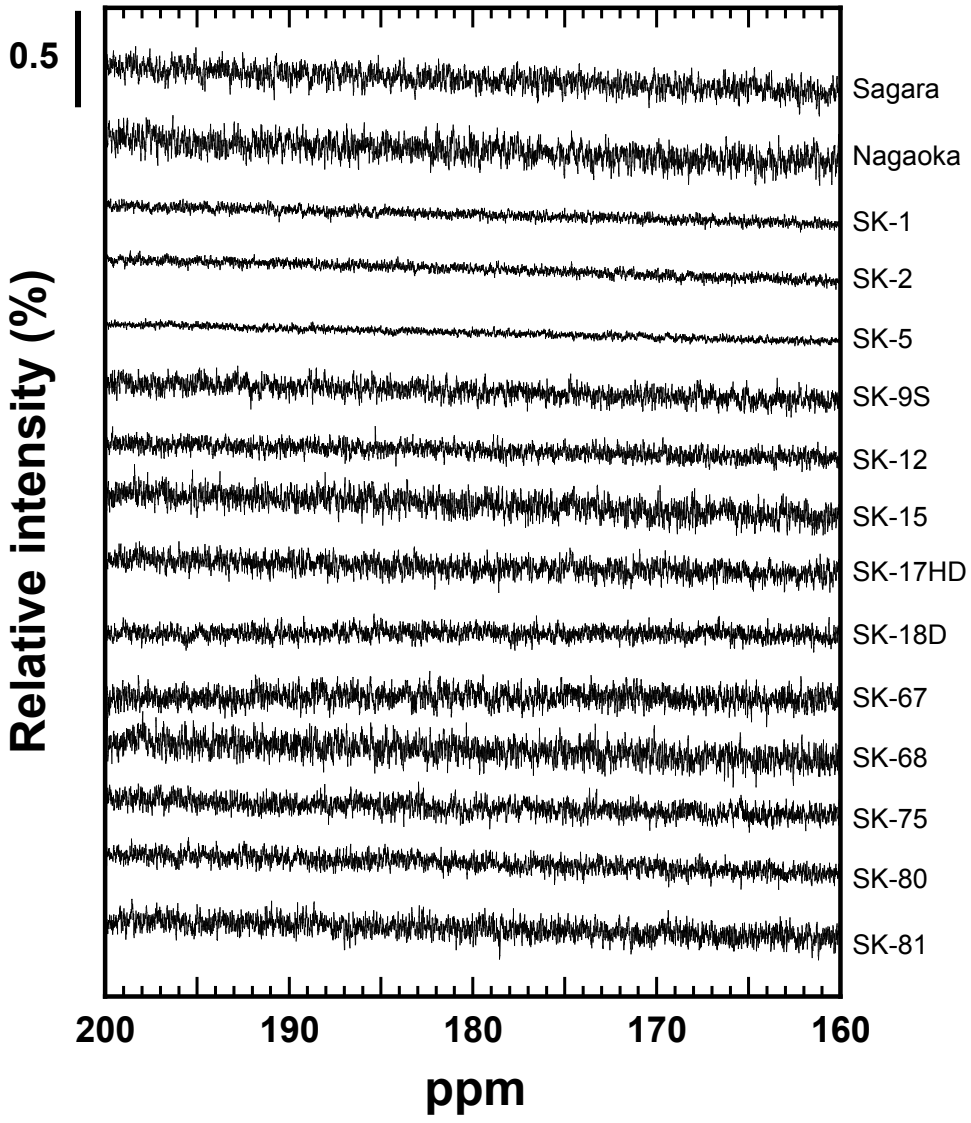

Fig. 6–3. ^{13}C-NMR spectra from 160 to 200 ppm region of oils studied here.

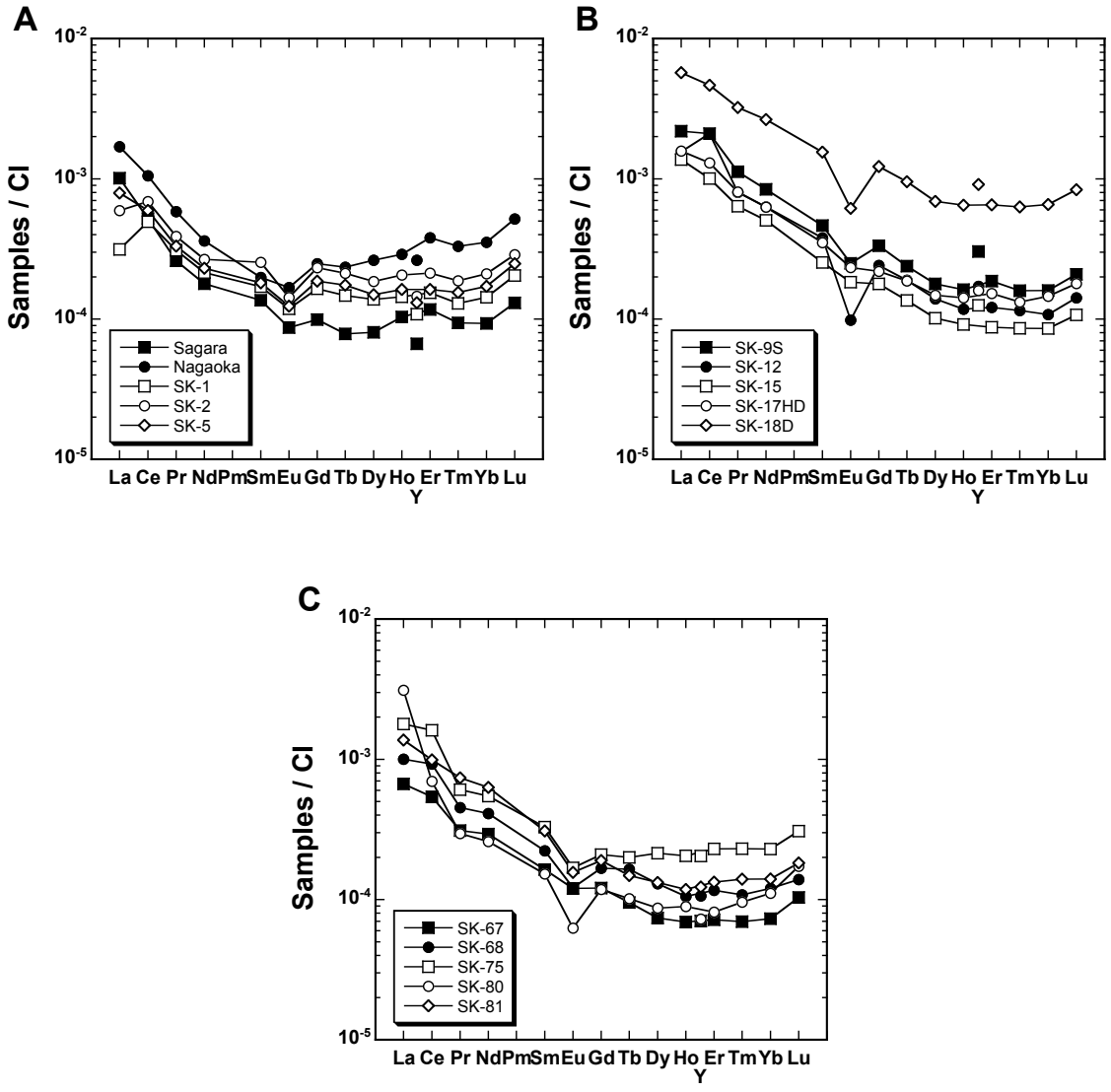

Fig. 6–4. Chondrite normalized REE patterns of oils collected from (A) Sagara, Nagaoka-Higashiyama, and Biratori, (B) Yurihara, and (C) Sarukawa oil fields.

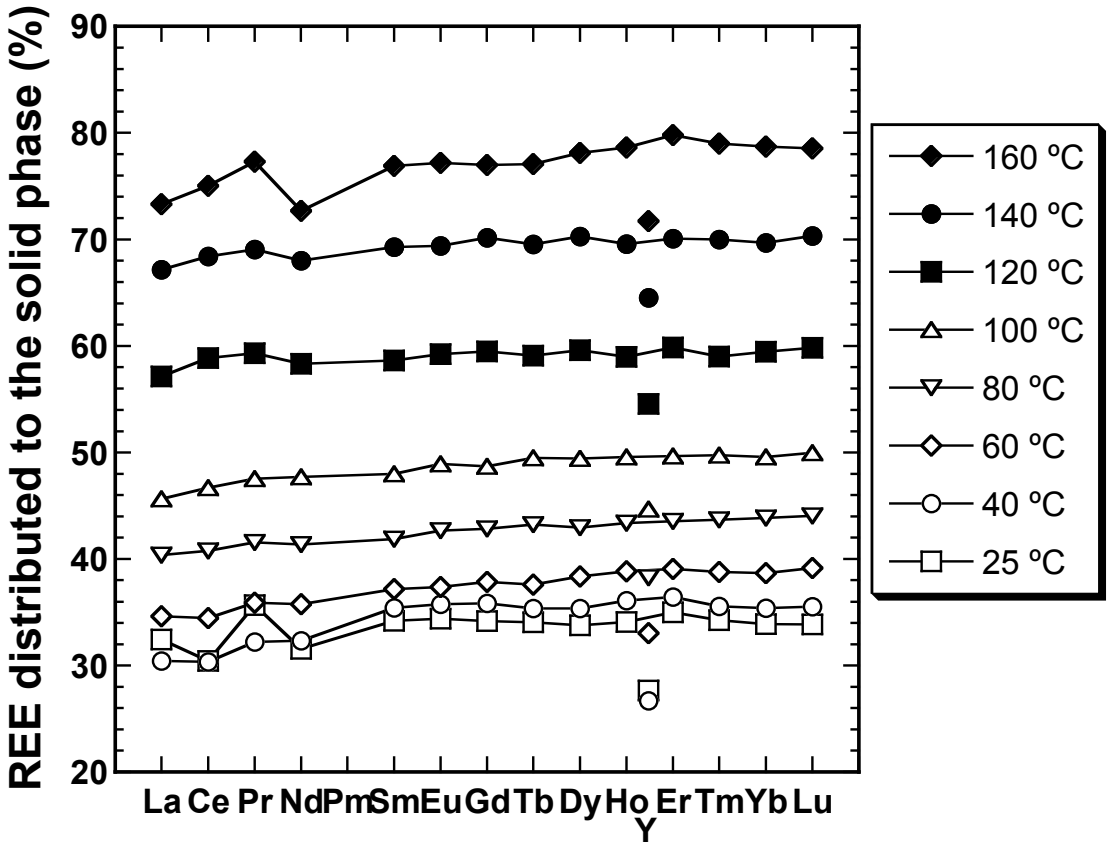

Fig. 6–5. REE distribution ratio given by Eq. 6–1.

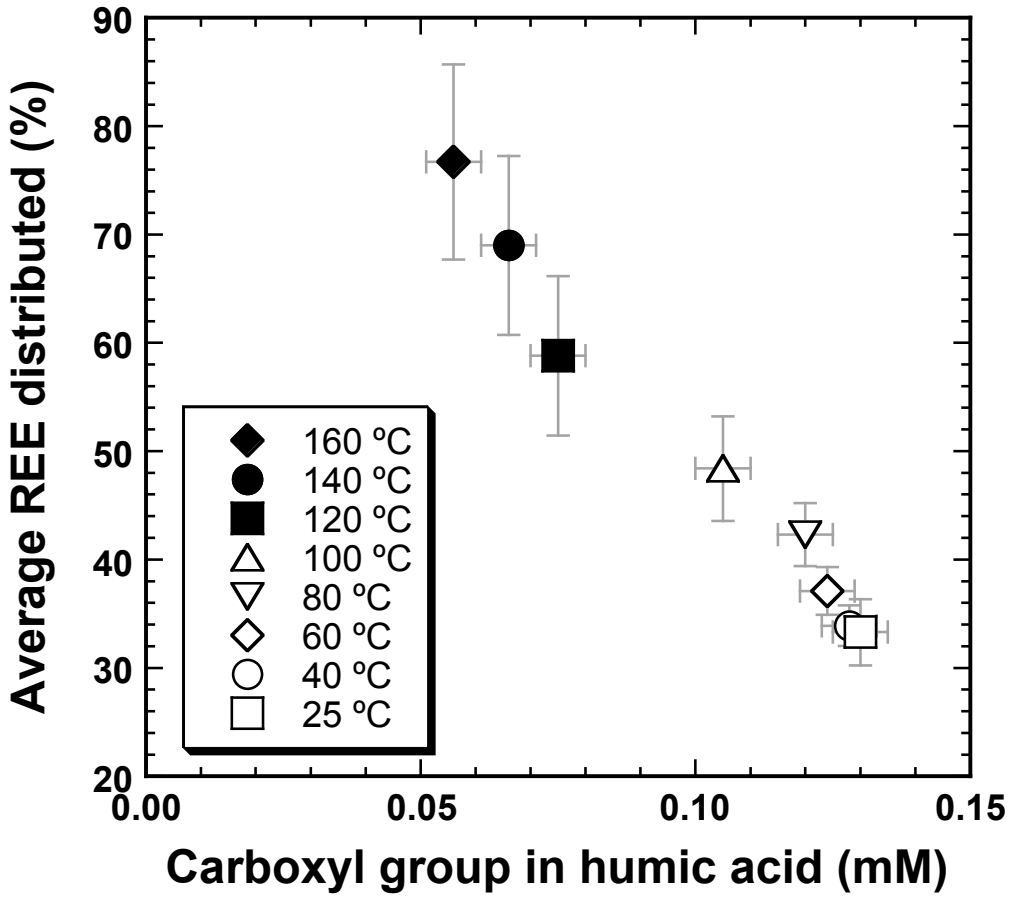

Fig. 6–6. REE distribution ratio and concentration of carboxyl group in humic acid after the experiment.

Chapter 7

A geochemical constraint on the formation process of a manganese carbonate nodule in the siliceous mud stone of the Jurassic accretionary complex

7.1 Chapter introduction

Manganese (Mn) carbonate composed of rhodochrosite is often observed as lenses in the Jurassic accretionary complexes in Japan such as the Northern Chichibu, Tamba-Mino-Ashio, and Northern Kitakami belts (Arakawa, 1998; Hattori, 1988; Hori and Wakita, 2006; Suzuki and Ogane, 2004; Yamakita and Hori, 2009). The sedimentary rocks of the Jurassic accretionary complexes are composed of the accreted plate-oceanic stratigraphy from the greenstones as a basement through pelagic chert and hemipelagic siliceous mudstone to clastic rocks of mudstone and sandstone (Matsuda and Isozaki, 1991). Manganese deposits of the Jurassic accretionary complexes are identified as ferromanganese deposit in chert (e.g., Fujinaka and Kato, 2005) and Mn carbonates in siliceous mudstone (e.g., Minoura et al., 1991). The occurrence condition of Mn in the Jurassic accretionary complexes are variable of the stratiform Mn deposit between chert beds (Komuro et al., 2005), stratiform ferromanganese deposit associated with N-MORB type greenstone (Nozaki et al., 2005), and distinctive nodules associated laminae composed of spherules of rhodochrosite aggregations in siliceous mudstone and mudstone (Fujihara, 2009; Suzuki and Ogane, 2004; Minoura et al., 1991). This variable occurrence condition of Mn deposits is presumably interpreted by different origin and different formation process (Nakagawa et al., 2011).

The scientific interest of the origin and formation process of Mn deposits in the Jurassic accretionary complexes was used to be mainly based on the interest of resource geology prior to 1970's. Since the discovery of Jurassic radiolarians inside the Mn carbonate nodules in siliceous mudstone of the Tamba-Mino-Ashio Belt (Yao, 1972), the interest of this topic has been widely extended to the geologic history of the Jurassic accretionary complexes along the East Asian margin. As Mn carbonate nodules in the

siliceous mudstone of the Tamba-Mino-Ashio Belt normally include well-preserved siliceous microfossils, radiolarians, inside the spherules of rhodochrosite, these and then Mn deposits are presumed to be formed in the depositional site *in situ*. It is interesting that radiolarian-bearing Mn deposits in siliceous mudstone is limitedly found from in the Northern Chichibu, North Kitakami, Tamba-Mino-Ashio belts of Japan (Yamakita and Hori, 2009), and the Taukha Terrane of Far East Russia which is a tectonic northern extension of the North Kitakami Belt (e.g., Suzuki et al., 2005, 2007). By contrast, such Mn deposits have never been reported form the other Jurassic accretionary complexes of the circum-Pacific region including the South Chichibu Belt of Japan (Matsuoka et al., 1998), the North Palawan Block of Philippines (Marquez et al., 2006), and the Coast and Intermontane Belt of southern British Colombia, North America (Cordey, 1998). This fact implies that the radiolarian-bearing Mn deposit in siliceous mudstone of the Jurassic accretionary complexes is a unique characteristic in the sequence in the East Asia.

The interpretation of the origin and formation process of Mn in the Jurassic accretionary complexes is proposed by many studies. Several studies suggested the hydrothermal alteration as the formation process of most of the Mn ores (Yoshimura, 1969), whereas other studies suggested the sedimentary origin (Watanabe et al., 1970). Minoura et al. (1991) studied Mn carbonate nodules in Tamba-Mino-Ashio Belt and suggested that agglutinated foraminiferal tests were replaced by Mn carbonate. Recently, Nakagawa et al. (2009) proposed Mn deposits in the Sambagawa, Mikabu, Chichibu, and Shimanto belts in Shikoku were formed by metamorphism of Mn nodules in siliceous sediments on the ocean floor. However, the occurrence condition of Mn deposits is so different that the examination of the origin and formation process of them using geochemical analysis should be carefully performed in consideration with the geologic age and the sedimentary structures. Minoura et al. (1991) examined a geochemical analysis on Mn carbonate deposits hosted by siliceous mudstone. They showed carbon and oxygen isotopic ratios of Mn carbonate and suggested the depositional environment of Mn carbonate in Tamba-Mino-Ashio Belt is a transitional zone between aerobic oxidation and sulfate reduction. However, other geochemical data,

such as rare earth elements (REEs) which have been widely used in several geochemical and geological systems (e.g., Henderson, 1984; Taylor and McLennan, 1988), were not reported so far.

In this study we performed a geochemical study combining with stratigraphic information to understand the origin of Mn carbonate nodules using the samples collected from the Tamba-Mino-Ashio Belt, along the Kiso River in central Japan. Rare earth element geochemistry which is well established in geochemical study combined with X-ray absorption near-edge structure (XANES) analysis is performed. In addition, REE adsorption experiment combined with thermodynamic calculation has been done to give a constraint on the formation process of Mn carbonate nodules.

7.2 Geological setting and samples

The Mn carbonate nodules examined in this study were collected from the outcrop southwest of the Furou-fall Park along the Kiso River, Inuyama City, Aichi, central Japan (35°23’53.46”N, 136°57’37.38”E; Fig. 7−1). In this area, the four sets of the Triassic-Jurassic bedded chert (CH-1, CH-2, CH-3 and CH-4) and clastic rocks sequence are widely distributed (Yao et al., 1980). The Furou-fall Park section is placed between CH-2 in the north and CH-1 in the south, where red siliceous mudstone with Mn carbonate nodules is exposed. This outcrop is just the opposite bank in the stratigraphic strike direction of the Inuyama section where the sedimentological and geochemical studies of Mn nodules were performed in previous studies (Fujihara, 2009; Minoura et al., 1991). In the Furou-fall section, siliceous microfossil radiolarians were extracted from Mn carbonate nodules by diluted HCl (Nagai, 1986, 1989; Nagai and Mizutani, 1990), dating the depositional age as Bajocian (170.3–168.3 Ma) of Jurassic.

There are many Mn carbonate nodules on the Furou-fall Park section, but the easily recognized nodules were unexceptionally weathered. Weathered Mn nodules with many yellowish-white small spherules are black in color, brittle, and softer than surrounding red siliceous mudstone. Such weathered nodules are easily destroyed. On the other hand, fresh Mn nodules are very hard as same as surrounding red siliceous

mudstone, and the surface of these nodules tends to be colored in black-silver on the outcrop. The cross-section of fresh nodules is colored rose-red to pink. Differing from weathered Mn nodules, fresh nodules are comprised with many white small spherules in the host red siliceous mudstone. Although the contact between these nodules and the surrounding siliceous mudstone looks sharp, a few white small spherules (approximately 0.5 mm in diameter; probably particles of rhodochrosite) lined as like laminae are recognized in red siliceous mudstone, suggesting that these carbonate nodules were derived from another place and incorporated into the siliceous mudstone. After careful observation, we selected one lump of Mn carbonate nodule with the best preservation for the geochemical study from the study section (Fig. 7−2). This Mn nodule is ellipsoid in shape (approximately 60 cm in maximum length and 30 cm in thickness), is interbedded in red siliceous mudstone (Fig. 7−2). The boundary between the Mn nodule and the host red siliceous mudstone is sharp, but no evidence was found to be sheared by deformation. The presence of homogenously scattered microspherules of Mn carbonate within the red siliceous mudstone of the same horizon where the ellipsoid Mn nodule is present, and this apparently indicates its sedimentary origin but not tectonic inclusion.

From this nodule, we collected samples carefully so as not to be contaminated weathered portion by deeply digging the outcrop. The host red siliceous mudstone both above and below the Mn nodule (named as SMa and SMb, respectively) were also collected for the examination of radiolarian ages whether the age-gap is present between the nodule and the host siliceous mudstone or not. For each sample, microscopic observation, radiolarian analysis, and geochemical measurements were performed using the fragment of the same samples specimens.

7.3 Analytical method

This study focuses on the geochemical analysis of the Mn carbonate nodule. Prior to the geochemical analysis, the sedimentary structure was observed under a polarizing microscope and radiolarian ages were estimated for both the Mn carbonate

nodule and the host red siliceous mudstone samples. Radiolarians were extracted from Mn carbonate nodule using diluted HCl solution and from siliceous mudstone by 5 wt% HF solution, respectively, and were identified at the species level under Scanning Electron Microscope (SEM) or transmitted light microscope (LM).

Manganese carbonate sample and the host red siliceous mudstones, SMa and SMb, were powdered using agate motor. Mineralogy of the samples was determined using a Rigaku MultiFlex X-ray diffractometer (XRD). Scans were carried from 2º to 90º (2θ) using Cu K_α source. To determine the REE concentrations, the powdered materials were digested using a mixture of HF, HNO_3, and $HClO_4$. After the dissolution with 0.5 M HCl solution, the REEs in samples were separated using cation column chemistry. The separated REE was finally dissolved with 2% HNO_3 solution and introduced into an ICP-MS (Agilent 7700). Indium (In) and bismuth (Bi) were also added at a concentration of 1 μg/L as internal standards. The accuracy and the precision of the measurement were better than 1.5% estimated from the measurement of standard geological material of chert (JCh-1) and repeated measurements of our samples.

The contribution of pure Mn carbonate to REE concentration was determined by sequential leaching following a procedure described by Koschinsky and Halbach (1995). A 1 g powdered sample was placed in a Teflon bottle with 30 ml of 1 M acetate buffer at pH 5. The bottle was shaken for 5 hours at 25 ºC using shaking apparatus. The leaching solution, which corresponds to carbonate phase, was separated from residual solid phase by filtration using a hydrophilic PTFE filter (0.2 μm; ADVANTEC). The solid remaining on the filter was rinsed three times with ultra-pure water, then digested using a mixture of HF, HNO_3, and $HClO_4$. REEs in two fractions, namely carbonate phase and residue, were separated using the column chemistry described above and REE concentrations were measured using the ICP-MS.

The Ce L_{III}-edge (5723 eV) XANES was measured at BL-12C at Photon Factory (Tsukuba, Japan). The Ce L_{III}-edge XANES spectra, which are sensitive to the covalent/ionic bond character and the oxidation state, were measured for the samples in fluorescence mode using a 19-element germanium semiconductor detector. The two

reference materials diluted by boron nitride powder, namely, $CeCl_3$ and CeO_2, were measured in transmission mode. The measurements were conducted under ambient pressure and temperature. The X-ray energy was calibrated with the first peak of CeO_2 at 5723 eV. The repeated scans of XANES yielded identical spectra to one another, indicating that X-ray-induced redox change of Ce did not occur during our experiments. The XANES spectra were analyzed using the REX2000 software (Rigaku Co. Ltd.).

REE adsorption experiment was also performed in this study. A standard REE solution (Spex Certiprep., USA) containing all REEs, except promethium (Pm), at a concentration of 10.0 mg/L each was in plastic bottles with 100 mg synthesized $MnCO_3$ (Wako, Japan) for the solid phase. A diluted NaOH or HCl solution was used to adjust the pH to 8.00 ± 0.05 and ionic strength was adjusted to be 0.70 M using a NaCl solution. The suspension was stirred for 24 h at 25 °C using a shaking apparatus. At the end of the experimental period, the liquid phase was separated from the solid phase by filtration using a hydrophilic PTFE filter (0.2 μm; ADVANTEC). The REEs in filtrate were separated using the column chemistry and finally acidified with HNO_3 to determine the REE concentration using ICP-MS. The distribution coefficient (K_d) of a REE between the liquid and solid phases is defined as

$$K_d(\mathrm{L/g}) = \frac{[\mathrm{REE}]_{init} - [\mathrm{REE}]_{fil}}{c \times [\mathrm{REE}]_{fil}} \quad (7\text{–}1)$$

where $[REE]_{fil}$ is the REE concentration in the filtrate and $[REE]_{init}$ is the initial concentration of dissolved REE. The c (g/L) denotes the ratio of the solid phase to water.

Thermodynamic calculation was conducted using the Geochemist's Workbench (GWB, Volume 6; Bethke, 2006) to estimate the Eh-pH condition where rhodochrosite ($MnCO_3$) precipitates. In our calculation, concentration of bicarbonate (HCO_3^-) was fixed at 10^{-3} M which is slightly lower than the HCO_3^- concentration in seawater (2.25 mM; Bruland and Lohan, 2003). Meanwhile, concentration of dissolved Mn^{2+} was cited from reference values where deposition of rhodochrosite was observed in modern sea sediments as 20 μM (Thomson et al., 1986), 60 μM (Pedersen and Price, 1982), 160 μM

(Pedersen and Price, 1982), and 250 μM (Calvert and Price, 1970). A boundary between soluble and insoluble species of Ce was also calculated using the GWB. Soluble Ce species considered in the calculation were Ce^{3+}, $CeCO_3^+$, and $Ce(CO_3)_2^-$. In the calculation, the HCO_3^- concentration was also fixed at 10^{-3} M, while two dissolved concentrations, 1 and 100 pM, were examined for Ce, because Ce^{3+} in the ocean column are generally several pM order (e.g., Alibo and Nozaki, 1999). The occurrence of the positive Ce anomaly is expected above this boundary.

Stable isotope ratios of Ce were also determined at the Kochi Institute for Core Sample Research, Japan Agency for Marine-Earth Science and Technology (JAMSTEC) using a double-focusing multiple collector (MC) ICP-MS (Neptune, Thermo Fisher). The details of the measurement was described in Chapter 3. The $CeCl_3$ solution used in the adsorption experiment in Chapter 3 was employed as a standard solution that was analyzed every three or four samples. The isotope ratios are expressed in standard delta notation relative to the average standards, as shown in the following equation:

$$\delta^{142}Ce = \left[\frac{\left({}^{142}Ce/{}^{140}Ce \right)_{sample}}{\left({}^{142}Ce/{}^{140}Ce \right)_{CeCl3}} - 1 \right] \times 10^3. \quad (7-2)$$

The analytical uncertainty for the measurement was 0.189, 0.078, and 0.058‰ (2σ) for Mn carbonate nodule, SMa, and SMb, respectively, which was calculated from triplicate analyses.

7.4 Results

7.4.1 Microscopic observation

Manganese carbonate nodule is comprised with spherical or distorted spherical grains of 0.5–1.0 mm in diameter and its fillings similar to the surrounding red siliceous mudstone (Fig. 7−3A). Each grain is composed of radial accumulation of acicular crystal which is characterized by cross shaped extinction under closed polarized (Fig. 7−3A, B). These characteristics are consistent with those of rhodochrosite and previous

reports on Mn carbonate nodules collected from this area (Fujihara, 2009; Minoura et al., 1991). It is noted that these grains contain almost unbroken radiolarian shells. The number of radiolarian shells incorporated in one grain varies to a large degree. Manganese carbonate grains and radiolarian shells in the grain were found to contain no clay minerals inside of their grain and shell. The radiolarian test on the periphery of each grain is always rounded or broken so as to form a smooth surface of each grain, and no radiolarians are exposed outside of each grain nor are bridged between different grains. It is important that no radiolarian shells were preserved at the boundary between different Mn carbonate grains. There are few ill-preserved radiolarians, if present, in the fillings of Mn carbonate grains in the nodule.

The SMa and SMb contain many radiolarians but are not associated with any remains of Mn carbonate grains. As like the field observations, no tectonic disturbances like S-C fabric, R1 shear, asymmetric cataclastic tails were recognized in thin sections. Differing from radiolarians inside of Mn carbonate grains in the nodule, radiolarian shells in siliceous mudstones are slightly broken (Fig. 7−3C−F). The exactly same observation results to Mn carbonate nodules and their host rocks are reported by Fujihara (2009).

7.4.2 Radiolarian ages

Radiolarians extracted both from the manganese carbonate nodules and the surrounding siliceous mudstone are generally well preserved, and consist of more than 50 species at minimum. The manganese carbonate nodule yields *Eucyrtidiellum unumaense* (Yao), *Japonocapsa fusiformis* (Yao), *Striatojaponocapsa plicarum plicarum* (Yao) *sensu emend.* Hatakeda et al. (2007), *Unuma echinatus* Ichikawa et Yao, and *U.* aff. *echinatus* Ichikawa et Yao (Fig. 7−4). Despite of well-preserved and high diversify radiolarian faunas in the manganese carbonate nodule, *Unuma latusicostatus* (Aita), *Eucyrtidiellum semifactum* (Nagai et Mizutani) and *Striatojaponocapsa synconexa* O'Dogerty et al. have never been encountered in this sample. This faunal composition is correlative to the *Striatojaponocapsa plicarum plicarum* Zone in

Hatakeda et al. (2007) and Nishizono et al. (1997). This zone in Nishizono et al. (1997) is defined by the interval between the first occurrence of *S. plicarum plicarum* and that of *U. latusicostatus,* whereas that in Hatakeda et al. (2007) by the interval between the first occurrence of *S. plicarum plicarum* and that of *S. synconexa*. Although the first occurrence horizons of *U. latusicostatus* and *S. synconexa* have not been discerned in the same stratigraphic section hitherto, these two studies are presumed to be nearly the same age interval. This fossil zone is assigned to be Bajocian of Middle Jurassic in several papers (Matsuoka, 1995; Hatakeda et al., 2007; Nishizono et al., 1997).

The SMa and SMb also contained relatively well-preserved and high diversity radiolarians. The radiolarian faunas from both horizons of the siliceous mudstone are characterized by *E. unumaense*, *J. fusiformis*, *S. plicarum plicarum,* and *U.* aff. *echinatus* (Fig. 7−4). These fauna are absent as for not only *S. synconexa* and *U. latusicostatus* but also a typical *U. echinatus*. Although these faunas are correlated to the *S. plicarum plicarum* Zone of Hatakeda et al. (2007) and Nishizono et al. (1997) as like for the Mn carbonate nodule, the species *S. plicarum plicarum* in the siliceous mudstone is assigned as an evolutionary-advanced form by having smaller a dish-like final segment beneath the inflated globular segment (34.8 μm in width, n=10 for SMb and 31.5 μm in width, n=10 for SMa) than that in the manganese nodule (44.3 μm in width, n=10). The one-direction reducing phenomenon to the width of the dish-like final segment is well known between the early evolutionary form and evolutionary-advanced form of *S. plicarum plicarum* (e.g., Hatakeda et al., 2007). The evolutionary-advanced form of *S. plicarum plicarum* from siliceous mudstone is interpreted that the radiolarians in the Mn carbonate nodule is somewhat older than radiolarians in both overlain and underlain siliceous mudstone. Fujihara (2009) also recognized older fauna in the Mn carbonate nodules than those in the host rock in their samples as well.

7.4.3 Geochemical analysis

Figure 7−5 shows XRD pattern of Mn carbonate and the host red siliceous mudstone. As expected, all the peaks observed for siliceous mudstone corresponds to

quartz. Meanwhile, peaks found for Mn carbonate are equivalent to those of rhodochrosite and quartz. Peaks of rhodochrosite were predictable, since it was found by microscopic observation. The peaks of quartz found in Mn carbonate are due to the large abundance of radiolarian shells in the rhodochrosite grain and small amount of clay minerals in the matrix.

REE concentrations in Mn carbonate and siliceous mudstones are listed in Table 7−1. Figure 7−6 shows REE patterns of Mn carbonate and siliceous mudstones normalized by PAAS (McLennan, 1989). Both SMa and SMb show a similar flat REE pattern with positive Ce anomalies and M-type tetrad effect. The Mn carbonate shows a positive Ce anomaly and enrichment toward heavy-REE (HREE; Ho, Er, Tm, Yb, and Lu). The REE patterns of sequential leaching are shown in Fig. 7−7. This result implies that carbonate phase is free from the positive Ce anomaly. The absolute concentration of REE in carbonate phase is about one tenth of the residual phase which is mainly dominated by clay minerals and radiolarian shells.

The Ce L_{III}-edge (5723 eV) XANES spectra of samples along with results for certain reference materials are shown in Fig. 7−8. The shapes of the spectra revealed a clear distinction between trivalent and tetravalent Ce, that is, Ce(III) presents one sharp peak and Ce(IV) shows a two-humped peak. In addition, energy of the absorption maximum for Ce(III) and Ce(IV) differs. The results illustrated that Ce in both host red siliceous mudstone and Mn carbonate is a trivalent form, despite of their positive Ce anomalies.

Adsorption experiment of REE on synthesized $MnCO_3$ does not show any positive Ce anomaly (Fig. 7−9). The distribution coefficient show K_d of Y is smaller than that of Ho which is an opposite result of a natural Mn carbonate nodule (Figs. 7−6 and 7−7). Thermodynamic calculation shows that the precipitation of rhodochrosite can be observed in a large region of the Eh-pH diagram under our calculation condition (Fig. 7−10). The calculation also shows whether the rhodochrosite precipitates or not largely relies on the dissolved Mn^{2+} concentration. If the Mn^{2+} concentration is lower than 0.16 μM, rhodochrosite is not formed at any HCO_3^- concentration. Although the required

Mn^{2+} concentration to precipitate rhodochrosite is about three orders of magnitude higher than the dissolved Mn^{2+} concentration in oceans (varies from 0.08 to 5 nM, with an average of 0.3 nM; Bruland and Lohan, 2003), the threshold concentration is low enough to form the rhodochrosite in oceanic sedimentary column (Calvert and Price, 1970; Pedersen and Price, 1982; Thomson et al., 1986). In Fig. 7−10, sulfate/sulfide boundary (Brookins, 1988) is also presented, because Minoura et al. (1991) suggested that the depositional environment of Mn carbonate in Tamba-Mino-Ashio Belt is a transitional zone between aerobic oxidation and sulfate reduction.

Stable isotope ratios for Mn carbonate nodule and two siliceous mudstones are shown in Table 7–2 and Fig. 7–10. The $\delta^{142}Ce$ values of siliceous mudstones are within the analytical uncertainty, while that of Mn carbonate nodule is enriched in the heavier Ce beyond the uncertainty.

7.5 Discussion

This study performed geochemical analysis of samples from a fresh Mn carbonate nodules and the surrounding host red siliceous mudstone after the careful examination of field observation, microscopic observation, and the depositional age determination by radiolarian fossils. Such field and microscopic observations as well as radiolarian age determination have already been done in the outcrop of Mn carbonate nodules locating at the other side of the Kiso River by previous studies (Fujihara, 2009; Yao, 1997; Minoura et al., 1991). Although we examined different outcrops, our age determination is confirmed to be identical to their results, namely, Bajocian of Middle Jurassic. Fujihara (2009) and Minoura et al. (1991) estimated that Mn carbonate microspherules were precipitated in pelagic condition, and then transported and reworked on a hemipelagic oceanic floor. The interpretation of the re-depositional process differs between the two studies: Minoura et al. (1991) considered upward movement by agguligated benthic foraminifers, while Fujihara (2009) presumed a transportation on the sea floor by bottom water currents.

In our measurements, a positive Ce anomaly is observed in Mn carbonate (Fig.

7−6), and thermodynamic calculation suggests a possible occurrence of the positive Ce anomaly in rhodochrosite precipitation (Fig. 7−10). However, the direct analysis using XANES and the adsorption experiment indicates that Ce in Mn carbonate is in trivalent state and positive Ce anomaly is not expected (Figs. 7−8 and 7−9). In the case of ferromanganese deposits, they showed positive Ce anomalies (e.g., Aplin, 1984; Elderfield et al., 1981), which was supported by adsorption experiments (e.g., Ohta and Kawabe, 2001; Takahashi et al., 2000a) and thermodynamic calculations (Brookins, 1988; Chapter 3). In addition, XANES analysis also suggested that the Ce existed as tetravalent state irrespective of their formation environment (Takahashi et al., 2007). The oxidative adsorption of Ce on MnO_2 is caused by the release of an electron from Ce^{3+} to Mn^{4+}, which cannot be the case of $MnCO_3$, because Mn in $MnCO_3$ is divalent state. The $MnCO_3$ cannot oxidize Ce into tetravalent state, which is certified by the REE adsorption experiment (Fig. 7−9). The thermodynamic calculation shows that the boundary between soluble Ce species and CeO_2 is included in the stability region of rhodochrosite, suggesting that the Ce oxidation can occur possibly by dissolved oxygen without the formation of MnO_2. In other words, Ce(IV) species can coexist with Mn carbonate. In addition, if the depositional environment of Mn carbonate suggested by Minoura et al. (1991) is taken into account, our calculations suggest that the coexistence of rhodochrosite precipitation in association with the positive Ce anomaly is not achieved around the sulfate/sulfide boundary (Fig. 7−10). Therefore, the most probable interpretation from this calculation is spontaneous oxidation of Ce(III) possible by dissolved oxygen in the aqueous phase in seawater, but not by the oxidative adsorption of Ce by $MnCO_3$.

Another possibility is reduction during diagenesis. In regardless of positive Ce anomalies in Mn carbonate and the host red siliceous mudstone in the PAAS-normalized REE pattern (Fig. 7−6), Ce in these sample are in trivalent form by XANES analysis (Fig. 7−8). The reduction of Ce during the diagenesis was also reported for chert in Tamba-Mino-Ashio Belt (Takahashi et al., 2000b). They showed positive Ce anomalies in chert samples and the absence of tetravalent Ce using XANES analysis. Therefore, the positive Ce anomaly shown in the Mn carbonate sample can be

explained by the reduction of MnO_2 to Mn^{2+} or $MnCO_3$. As described above, MnO_2 deposits oxidize Ce into tetravalent state and subsequently should initially exhibit a positive Ce anomaly. The initial formation of MnO_2 deposits followed by the reduction under the bicarbonate-rich condition would lead to the presence of a positive Ce anomaly with reduced form of Ce. In the case of Mn deposit consisting of quartz, rhodochrosite, and Mn oxides in the Katsuyama section, Inuyama area, Tamba-Mino-Ashio Belt showed presence of positive Ce anomalies and the enrichment of Cu, Pb, W, and Zn in Mn layer (Komuro and Wakita, 2005). As the Mn nodule in the Katsuyama section is a stratiform deposit interbedded chert according to Komura and Waktia (2005), they considered that the input of oxic water into the deep ocean floor to form the bedded Mn deposits at the Katsuyama section. Nakagawa et al. (2011) summarized bedded Mn deposits in the accretionary complexes of Japan and explained that Mn ores in the Tamba-Mino-Ashio Belt originated from Mn nodules or crusts followed by the low-grade metamorphism through subduction-accretion processes. These previous studies, however, may not be the case for our study, because the Mn carbonate collected in this study is not in bedded form but nodular appearance incorporated in siliceous mudstone.

Microscopic observation shows that no radiolarian shells were preserved outside of Mn carbonate grains (Fig. 7−3A, B). If Mn carbonate is formed due to the reduction from MnO_2 nodules or crusts *in situ*, radiolarian shells can be moved during the dissolution and re-deposition process. If such process occurred, radiolarian shells are expected to be bridged between two or more grains of rhodochrosite, which was not the case in this study. The exactly same observation was already documented by both Fujihara (2009) and Minoura et al. (1991). Therefore, the microscopic observation strongly suggests that rhodochrosite grains did not develop in the host rock any longer after the primary formation. The Y/Ho ratio shown in the PAAS-normalized REE pattern of Mn carbonate could support the primary formation of rhodochrosite. Generally, normalized Y/Ho ratios of marine Fe/Mn deposits are smaller than 1 (e.g., Bau et al., 1996; Hein et al., 1987; Takahashi et al., 2007), whereas those of seawater, hydrothermal fluids, and limestones are larger than 1 (e.g., Alibo and Nozaki, 1999;

Douville et al., 1999; Frimmel, 2009; Nothdurft et al., 2004). The larger Y abundance than Ho is also observed carbonate phase of Mn carbonate. The REE pattern after the leaching further verifies the primary formation of rhodochrosite. If rhodochrosite grains are secondarily formed followed by the reduction from MnO_2, a positive Ce anomaly is expected to occur in the carbonate phase. However, no distinct positive Ce anomaly was observed in the carbonate phase of Mn carbonate (Fig. 7−7). In addition, the leaching experiment shows that the residual phase, mainly composed of clay minerals, dominates the REE in the bulk Mn carbonate. The total REE concentration of hydrogenetic Fe/Mn deposits are typically high; some data showed that total lanthanoid concentration was higher than 1000 ppm (e.g., Bau et al., 1996; Hein et al., 1987; Nath et al., 1992). These facts do not support the primary formation of MnO_2 followed by the reduction to $MnCO_3$. The possibility of a primary formation of hydrothermal Fe/Mn deposits, which lacks positive Ce anomaly, can also be neglected due to the absence of a positive Eu anomaly (Figs. 7−6 and 7−7). Furthermore, if MnO_2 was formed primarily, $\delta^{142}Ce$ value is expected to be lower than that observed because preferential adsorption of lighter Ce was observed in the adsorption experiment (Chapter 3). Taking into account all the observational and experimental results, we suggest that Mn carbonate nodules surrounded by siliceous mudstones studied here primarily forms rhodochrosite followed by the incorporation of clays in the matrix which has the positive Ce anomaly during or after the settlement of the depositional site (Fig. 7–12). It is interesting to consider why such formative conditions of rhodochrosite *in situ* specifically appeared in the deep-sea ocean floor without the input of clay minerals in the limited areas where the radiolarian test of the Jurassic accretionary complexes of the Norhtern Chichibu, Tamba-Mino-Ashio and North Kitakami belt were sufficiently deposits.

7.6 Conculusions

Geochemical investigations on Mn carbonate nodules interbedded in red siliceous mudstone of the Tamba-Mino-Ashio Belt were performed. Microscopic observation showed the authigenic rhodochrosite and numerous radiolarian shells

without any clay minerals, and the spherule of rhodochrosite is abraded in consideration with the preserved condition of radiolarians. Radiolarian faunas from both the Mn carbonate nodule and their host rocks are correlative to the same Bajocian age of Middle Jurassic, but the host red siliceous mudstones are somewhat younger than the Mn nodule. These two evidences are explained by the facts that (i) spherules of rhodochrosite developed to involve radiolarian test at first at the depositional site without clay minerals and (ii) these isolated spherules moved to the depositional site of red siliceous mudstone where clay minerals are present. XRD analysis confirmed the existence of rhodochrosite and quartz in Mn carbonate. The bulk rock REE pattern normalized by PAAS showed the positive Ce anomaly, whereas XANES analysis showed Ce in Mn carbonate exists as trivalent state. In consideration with the REE pattern after the leaching and the occurrence state of rhodochrosite spherules in the Mn nodule, the best explanation of Mn nodule formation so far is that rhodochrosite is primarily formed and subsequently transferred to the different site where siliceous mudstone was deposited. Stable isotope ratio of Ce in Mn carbonate nodule support the suggestion.

Table 7−1. REE abundances (mg/kg) of siliceous mud and Mn carbonate determined using ICP-MS.

	SMa	SMb	Mn carbonate
Y	14.6	9.44	19.4
La	19.6	12.0	8.38
Ce	52.7	34.2	23.5
Pr	4.37	2.85	1.91
Nd	16.7	11.1	7.52
Sm	3.21	2.19	1.65
Eu	0.536	0.394	0.351
Gd	2.68	1.87	1.80
Tb	0.451	0.315	0.347
Dy	2.74	1.86	2.49
Ho	0.560	0.362	0.581
Er	1.81	1.10	1.96
Tm	0.268	0.161	0.291
Yb	1.93	1.10	1.93
Lu	0.293	0.157	0.293

Note siliceous (a) denotes siliceous mudstone locating above the Mn carbonate, whiereas siliceous (b) denotes that locating below.

Table 7–2. Stable isotope ratios of Ce in siliceous mud and Mn carbonate.

	Single	Duplicate	Triplicate	Mean	Deviation (2σ)
Mn carbonate	0.758	0.611	0.591	0.649	0.189
SMa	0.051	0.231	0.146	0.164	0.078
SMb	0.143	0.194	0.205	0.202	0.058

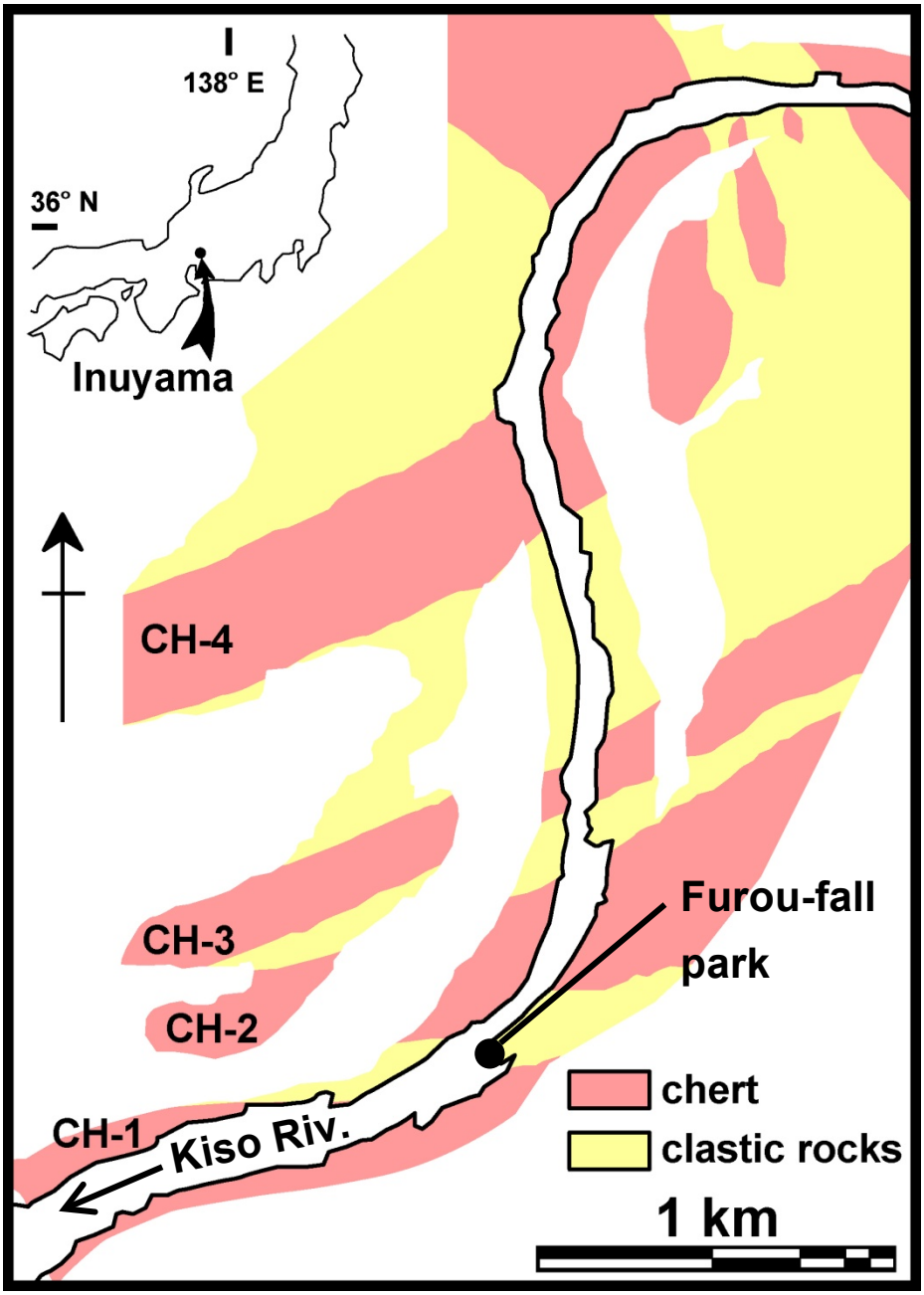

Fig. 7−1. Geological map of Inuyama area (after Yao, 1980).

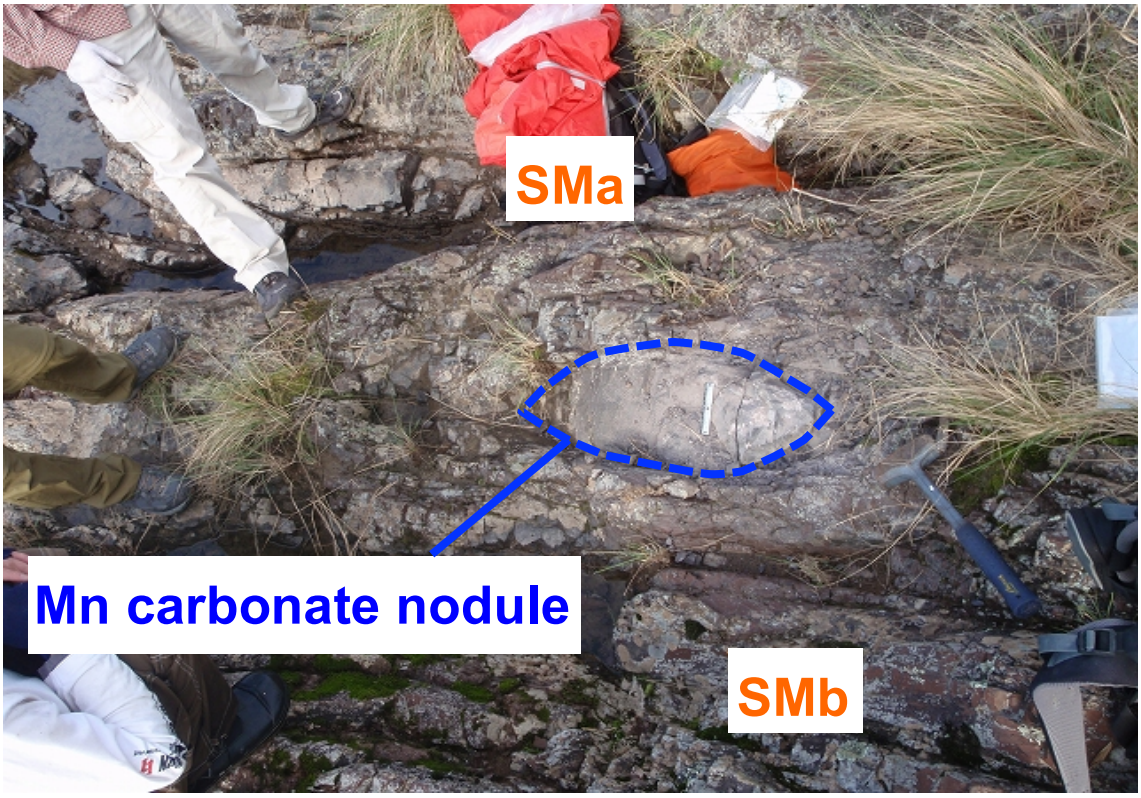

Fig. 7−2. Photograph showing the outcrop of Mn carbonate nodule and the host red siliceous mudstone. Two circles in the photograph denote the location where siliceous mudstones were collected. The length of hammer shown at the lower right of the Mn carbonate nodule is 40 cm.

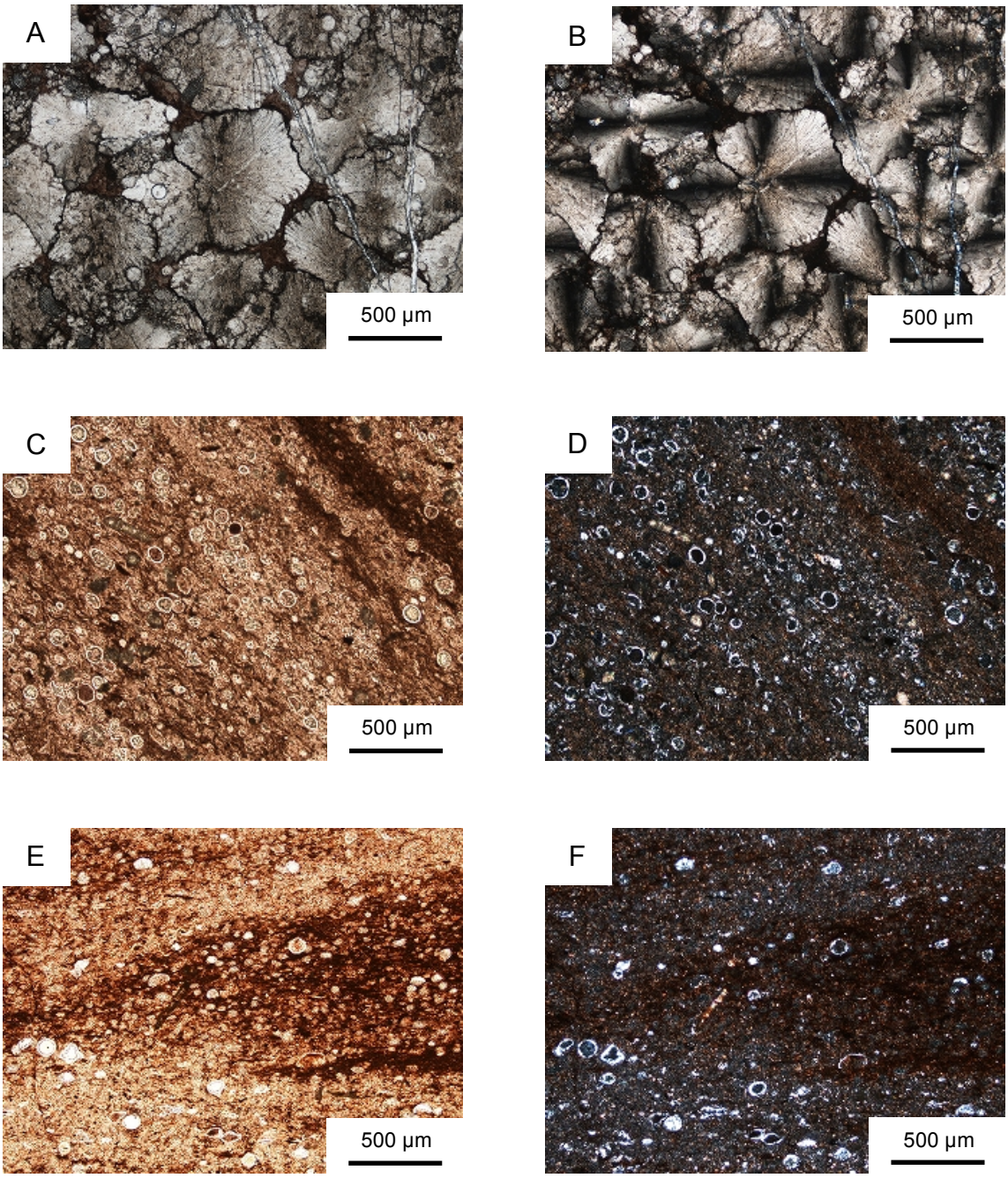

Fig. 7−3. Microscopic photographs of the thin section of Mn carbonate (A, B), overlain siliceous mudstone (SMa; C, D), and underlain siliceous mudstone (SMb; E, F) the Mn carbonate. (A), (C), and (E) are plane polarized photographs, while (B), (D), and (F) are crossed polarized. Bar denotes the 500 μm.

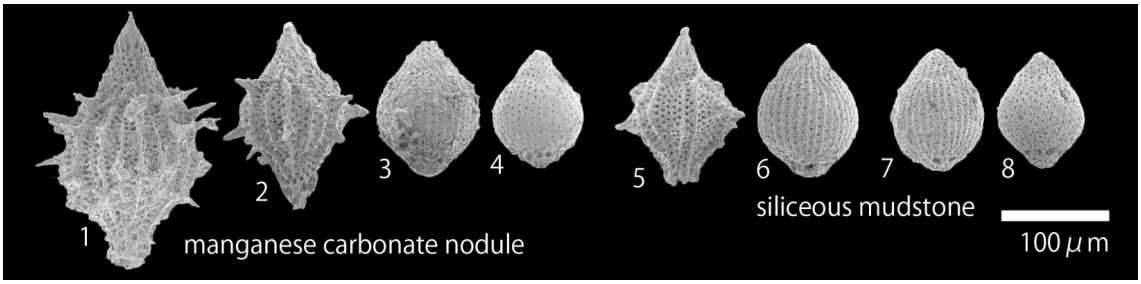

Fig. 7−4. Age determinable radiolarians from the Mn carbonate nodule (4.1.-4.4), the SMb (4.5 and 4.6) and SMa (4.7 and 4.8). 1. *Unuma echinatus* Ichikawa et Yao; 2. and 5. *Unuma* aff. *echinatus* Ichikawa et Yao; 3, 6 and 7. *Striatojaponocapsa plicarum plicarum* (Yao) sensu Hatakeda et al. (2007); 4. and 8. *Japonocapsa fusiformis* (Yao).

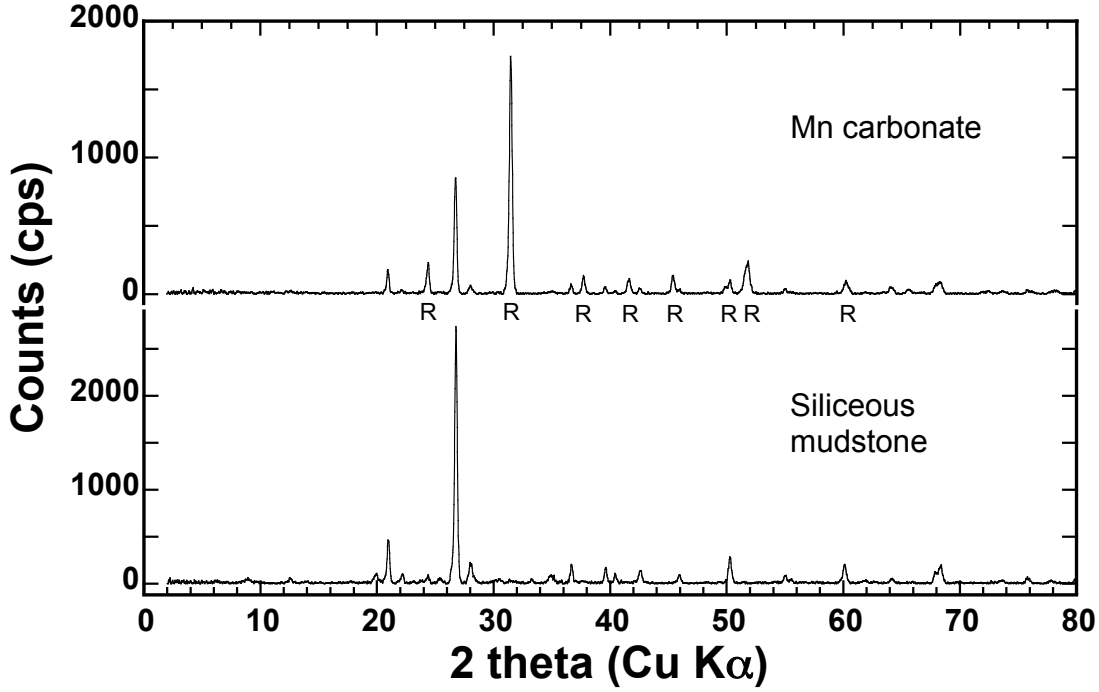

Fig. 7−5. XRD pattern after subtracting the background. Note that R corresponds to the peak of rhodochrosite.

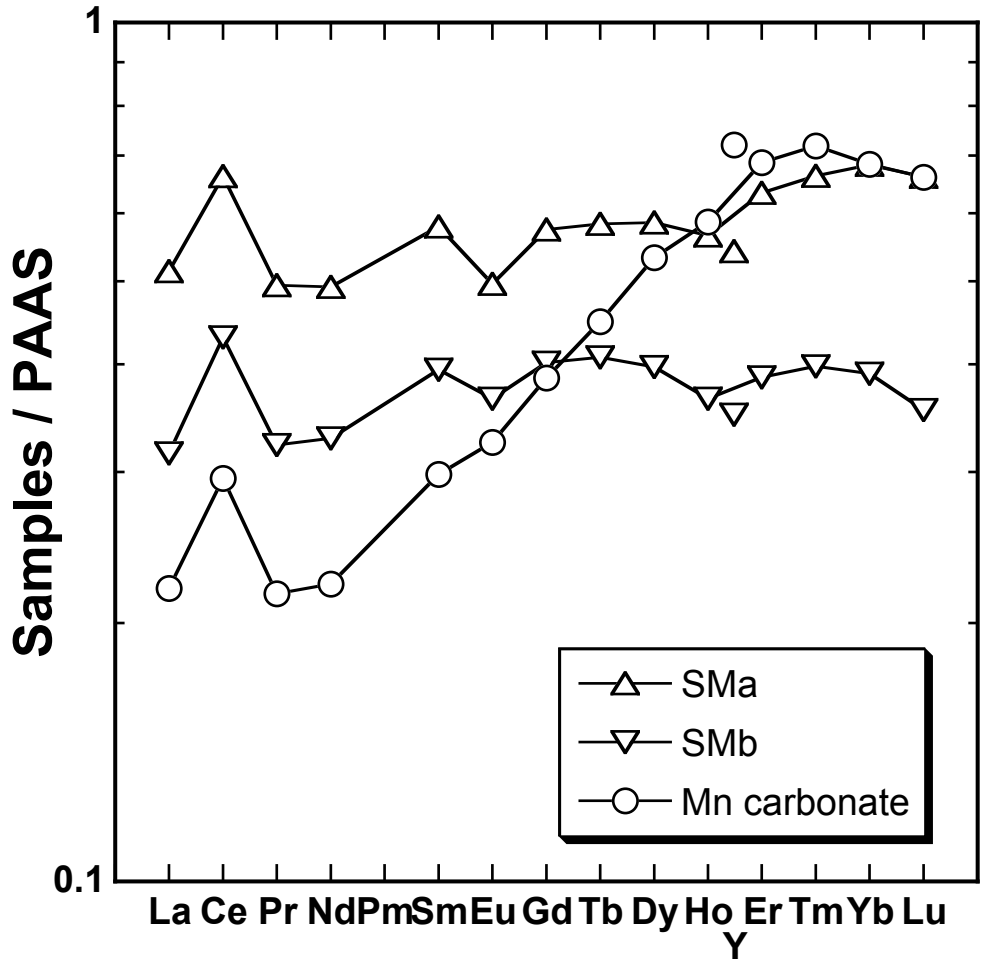

Fig. 7−6. PAAS-normalized REE patterns of siliceous mudstones and Mn carbonate nodule.

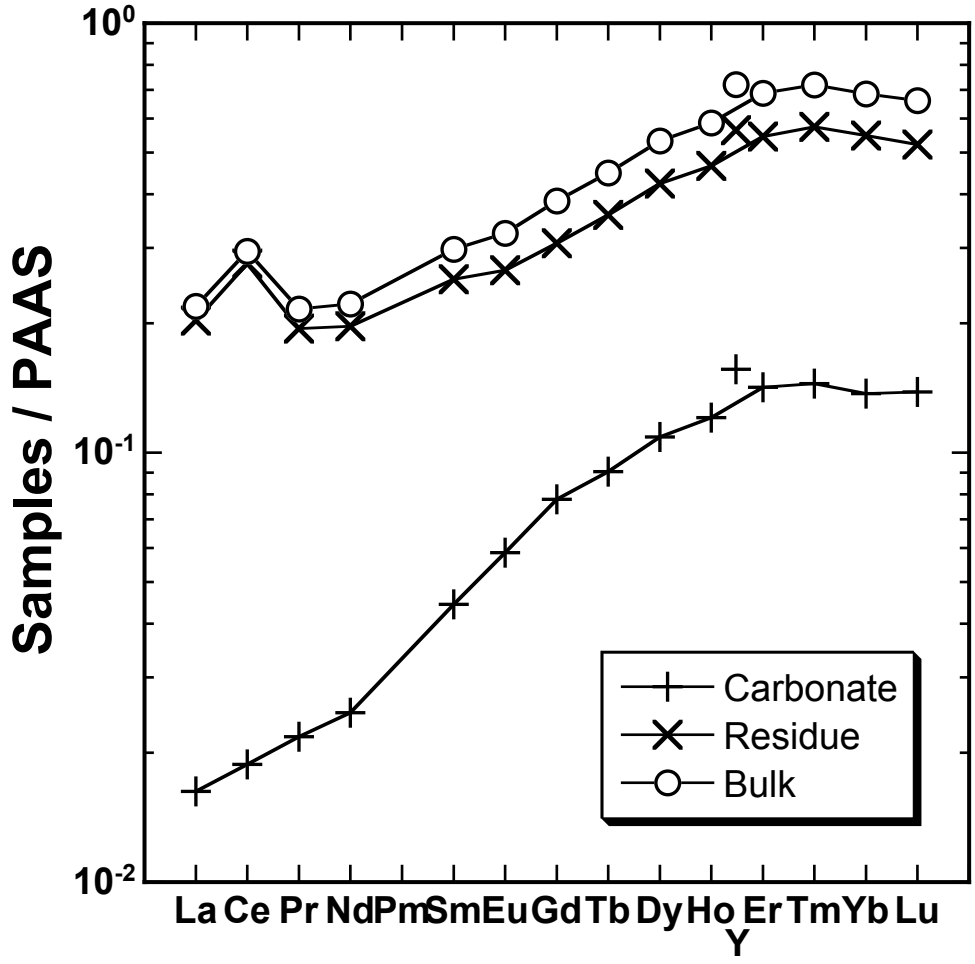

Fig. 7−7. PAAS-normalized REE pattern of Mn carbonate nodule after sequential leaching.

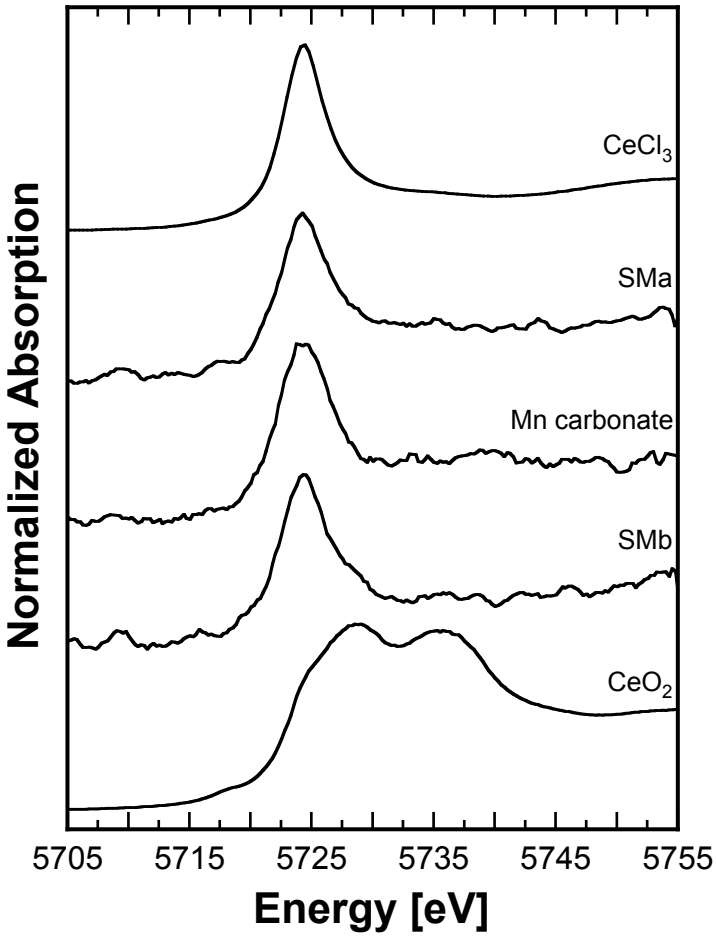

Fig. 7−8. Ce L_{III}-edge XANES spectra of samples and standards ($CeCl_3$ and CeO_2).

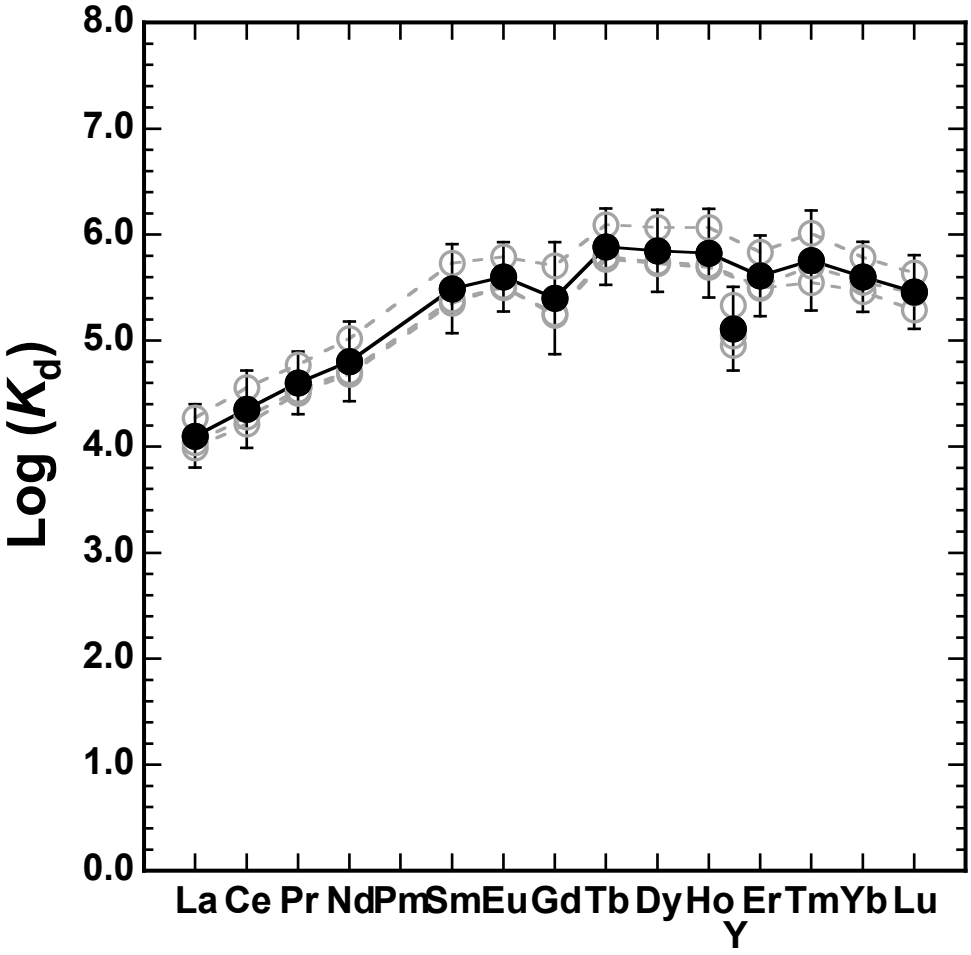

Fig. 7−9. REE distribution coefficient on synthesized $MnCO_3$. Error bar denotes deviation of triplicate experiments. Gray symbols indicate the results of each experiment.

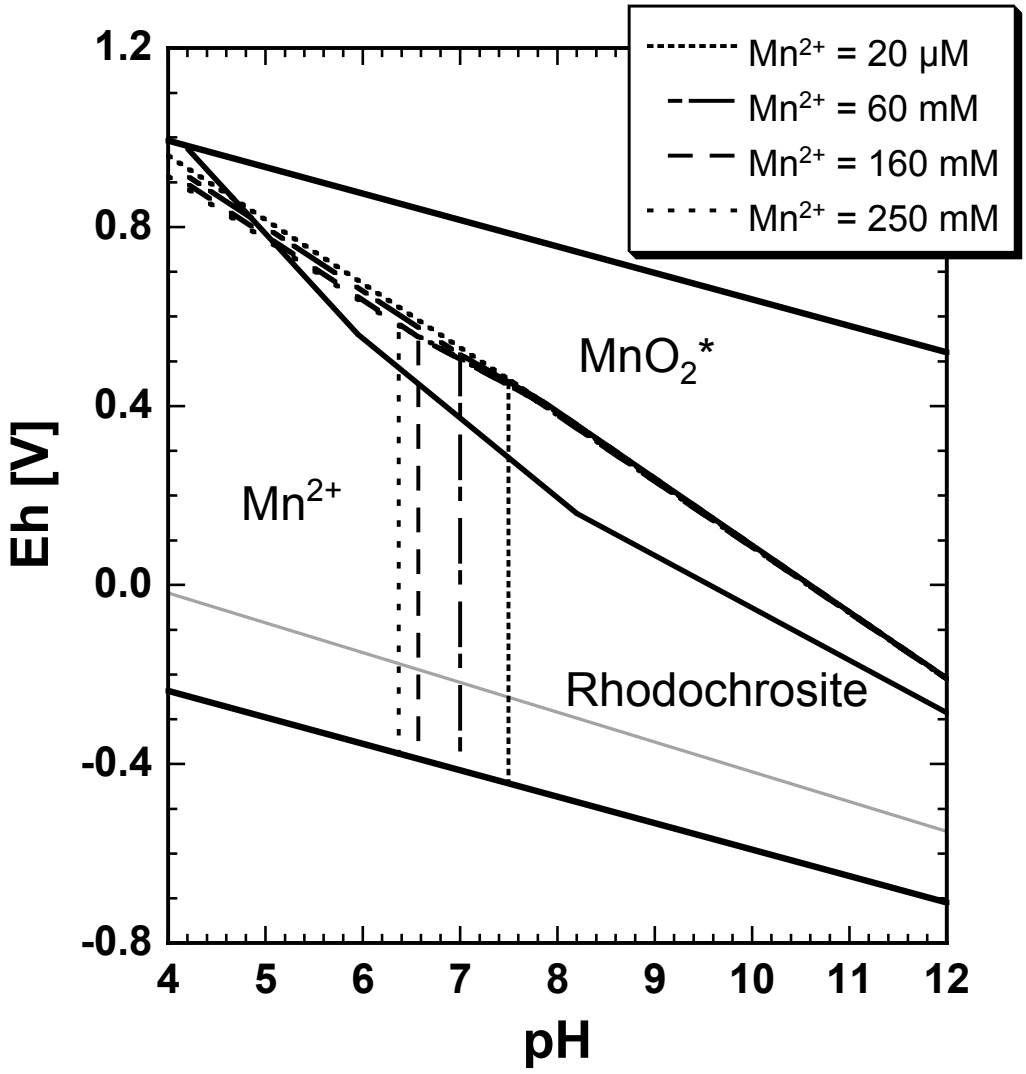

Fig. 7−10. Thermodynamic calculation of Eh-pH field of Mn species (dashed lines) with soluble/insoluble boundary of 1 pM Ce^{3+} (solid line). Solid gray line suggests H_2S/SO_4^{2-} boundary. Minerals included in MnO_2* are birnessite, todorokite, manganite, and hausumannite.

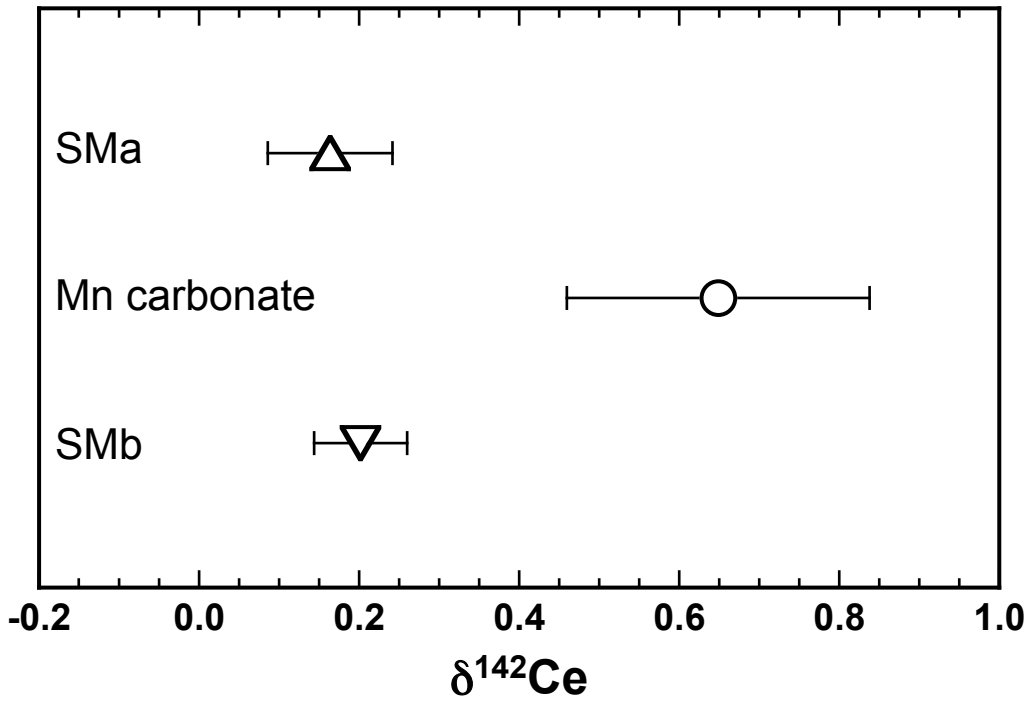

Fig. 7−11. Stable isotope ratios of Ce. Bars denotes analytical uncertainty of triplicate.

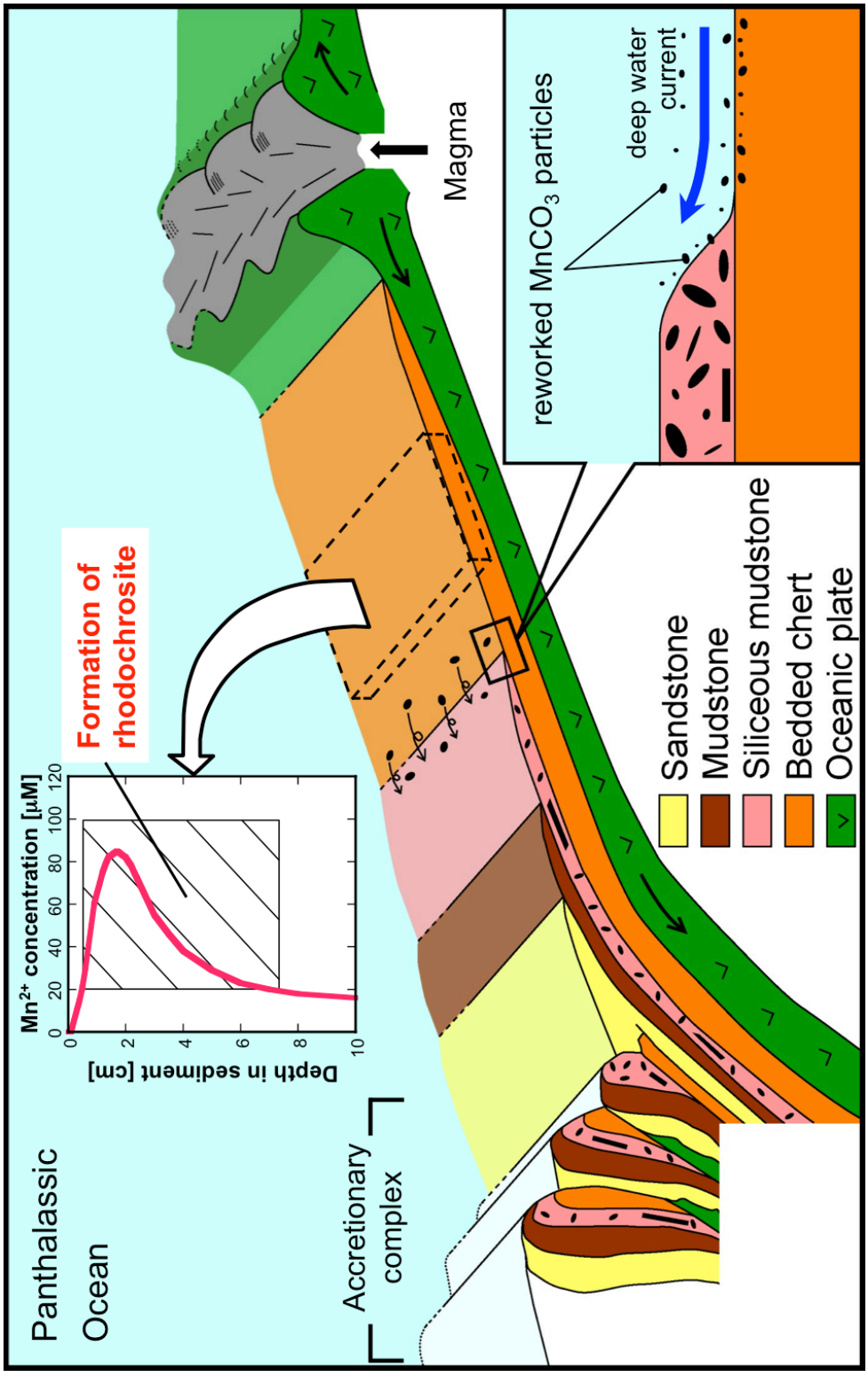

Fig. 7−12. Schematic illustration of the formation process of Mn carbonate nodule studied here. Dissolved Mn^{2+} concentration profile in deep sea sediment is a model result of Wang and Van Cappellen (1996).

Chapter 8

Late Triassic compositional changes of aeolian dusts in the pelagic Panthalassa: Response to the continental climatic change

8.1 Chapter introduction

8.1.1 Carnian pluvial event

The Triassic geologic period dawned with the Permian/Triassic mass extinction event (e.g., Raup and Sepkoski, 1982; Kump, 2003), and biofacies were recovered (e.g., Hallam and Wignall, 1997; Chen and Benton, 2012). It is thought that the relatively stable climate during the Triassic was controlled by the "Megamonsoon" or maximum strength of monsoonal circulation generated by the existence of the Pangea supercontinent and the surrounding Panthalassic Oceans (Kutzbach and Gallimore, 1989; Parrish, 1993). However, it has been suggested that a drastic climate change involving very humid conditions occurred during the Carnian stage of the Late Triassic (Simms and Ruffell, 1989, 1990). This event was initially indicated by the interrupted growth of the carbonate platform in the Northern Alps (Schlager and Schöllnberger, 1974). The widespread development of sandstones and the elevated kaolinite contents in southern England were explained by a climate with warmer temperatures and high humidity (Simms and Ruffell, 1989, 1990). This event, called the Carnian pluvial event (CPE: Simms and Ruffell, 1990), occurred during the middle to late Carnian according to the biostratigraphy (Hornung and Brandner, 2005; Rigo et al., 2007).

In addition to the climatic factor, the biotic crisis was an important factor associated with the CPE (e.g., Schlager and Schöllnberger, 1974; Simms and Ruffell, 1989; Simms et al., 1994; Benton, 2004; Furin et al., 2006). The extinction or turnover of some marine taxa, such as ammonites, crinoids, conodonts, bivalves, and bryozoa, was observed during this period (Simms and Ruffell, 1989, 1990; Simms et al., 1994). Meanwhile, calcareous nannoplankton was also observed in the Carnian (Erba, 2006). From the early Carnian to the late Norian, Tethyan radiolarian fauna became dominant in the Boreal ecosystem and formed mixed fauna in Siberia (Bragin et al., 2012),

which most likely was related to climatic warming in association with the CPE. These observations mean that the CPE is an important environmental event relevant to the origins of paleocoenosis in the Mesozoic Era.

Three possible causes are proposed to explain the CPE: (i) tectonic activity (Hornung and Brandner, 2005; Kozur and Bachmann, 2010), (ii) volcanic eruptions (Furin et al., 2006; Greene et al. 2009), and (iii) the peak of the Megamonsoon owing to the supercontinent−superocean setting (Parrish, 1993; Colombi and Parrish, 2008). The Cimmerian Micro-Continent, located at the northern margin of the Tethys realm, collided with the Eurasian plate during the formation of the Neotethys Ocean (Stampfli and Kozur, 2006). The uplift related to this collision enhanced the monsoonal circulation in the Tethys realm (Hornung and Brandner, 2005; Kozur and Bachmann, 2010). It is noteworthy that the CPE was approximately coincident with the large igneous province that was dated by the precise determination of $^{206}Pb/^{238}U$ in the Wrangellia Terrane (Furin et al., 2006). Geochemical analysis indicated that the large oceanic plateau derived from the depleted plume-type mantle source formed during a brief interval (225−231 Ma; Greene et al., 2009) at the eastern Panthalassa (Jones et al., 1977). Meanwhile, the depositional environment, characterized on the basis of the plant taphofacies of the Ischigualasto Formation in the southwest Pangea, suggested an increase in rainfall caused by the maximal development of the Megamonsoon during the middle Carnian (Colombi and Parrish, 2008).

Two important factors can be used to identify the cause of the CPE. First, the extent of the CPE remains unclear. A temporal demise of the carbonate platforms and a climate with high humidity were suggested in several areas around the Tethys realm, such as (i) Northwest Tethys (Northern Calcareous Alps, Southern Alps, southern England (1, 2, and 3 in Fig. 8−1, respectively); Schlager and Schöllnberger, 1974; Simms and Ruffell, 1989, 1990; Hornung and Brandner, 2005; Hornung et al., 2007a; Roghi et al., 2010 and references therein), (ii) northern Tethys (4 in Fig. 8−1; Donofrio, 1991), (iii) southeastern Tethys (5 in Fig. 8−1; Martini et al., 2000), (iv) northeastern Tethys (6 in Fig. 8−1; Lehrmann et al., 2005), and (v) southern Tethys (7 in Fig. 8−1; Hornung et al., 2007b). The increased amounts of rainfall have also been reported from

several areas other than the Tethys realm, such as western Pangea (8 and 9 in Fig. 8−1; Prochnow et al., 2006; Colombi and Parrish, 2008) and the Boreal region (10 and 11 in Fig. 8−1; Hochuli and Vigran, 2010; Bragin et al., 2012). Although these observations suggest that the CPE affected large areas of Pangea, the studies that were performed only regarded shallow oceans or land-sections (Fig. 8−1). Second, owing to tectonic deformation, a few lithologically continuous sections throughout the Carnian are present in the Tethys realm. In particular, the northward movement of the Cimmerian Micro-Continent continued and resulted in the closure of the Paleotethys and the opening of the Neotethys (Golonka, 2007). This requires a piecing together of fragmented information about the order of stratification, which resulted in an incomplete understanding of the CPE.

This study aims to reveal the pelagic sedimentary response to the Carnian climate changes by analyzing cherts collected from the successive sequence in the Tamba-Mino-Ashio Belt, Japan. This biostratigraphic study of the pelagic sediments deposited during the late Triassic has some implications for the CPE that have not been reported previously. In addition, deep-sea pelagic sediments can provide the most stable continuous section. The iron (Fe) species in the chert samples were the focus of the current study because of their potential for use as a paleo-redox tracer. For the first time, the X-ray absorption fine structure (XAFS) analysis of Fe was used as an alternative method to determine the iron species in chert samples. Despite the potential usefulness for the estimation of the paleo-redox condition, the identification of Fe-bearing minerals in chert is not easy due to the small amounts of Fe present in chert (e.g., Murray et al., 1991; Murray, 1994). Although ^{57}Fe Mössbauer spectroscopy can distinguish Fe-bearing minerals, such as hematite, goethite, and pyrite, further detailed classification, such as the type of clay minerals incorporated in chert, is difficult because Mössbauer spectroscopy shows only the peaks of paramagnetic Fe^{2+} and/or Fe^{3+} (Matsuo et al., 2002; Sato et al., 2011). Natural samples can contain mixtures of clays. For example, both chlorite and illite can be present in chert, while ^{57}Fe Mössbauer spectroscopy shows peaks corresponding to paramagnetic Fe^{2+}. In addition, in ^{57}Fe Mössbauer spectra, the peaks corresponding to pyrite and paramagnetic Fe^{3+},

from clay minerals and/or hydrated Fe^{3+} oxides (Manning and Ash, 1979), are very close to each other, and the interpretation of the spectra requires an assumption of the existence of either pyrite or paramagnetic Fe^{3+}. In this respect, XAFS is a powerful tool to analyze the Fe-bearing minerals in chert samples.

8.1.2 Clay minerals and aeolian dust

Clay minerals in pelagic sediments can reflect the weathering processes and the palaeoenvironmental conditions, such as climate, redox, and sea level variations (e.g., Ruffell et al., 2002; Ahlberg et al., 2003; Dera et al., 2009; Rostási et al., 2011). Among the clay minerals, illite and chlorite form during the initial stage of chemical weathering, typically under dry and cool condition, while smectite and kaolinite form in the advanced stage of weathering, typically under warm and humid conditions (Chamley, 1989; Weaver, 1989; Fürsich et al., 2005). Although metamorphism can alter mineral compositions, the identification of clays can act as a sensitive indicator of the palaeoenvironment.

Clay minerals are brought to the pelagic zone mainly as aeolian dusts or aerosols. In the case of the modern environment, most dusts originate in arid areas, such as North Africa, the Arabian peninsula, and eastern Asia (e.g., Maher et al., 2010). The influence of dust on the climate includes not only the direct effect of scattering and absorbing the solar and the terrestrial radiation but also the indirect effect of acting as cloud condensation nuclei. In addition, taking into account the large global depositional flux of dust to the oceans (0.3−2 Pg yr^{-1}; Mahowald et al., 2005; Zender et al., 2005), dust delivered to the oceans supplies macronutrients (phosphate, nitrate, and silica) and micronutrients (Fe, Zn, and Cd) that can fertilize the marine ecosystem and indirectly affect the climate. For example, Martin (1990) hypothesized that the change in the atmospheric CO_2 during glacial and interglacial periods can be controlled by the supply of Fe dust to the oceans because glacial periods are believed to be much dustier than interglacial periods (e.g., Petit et al., 1981; Kohfeld and Harrison, 2001). In addition, Fe has been identified as a limiting factor for phytoplankton growth in

high-nutrient low-chlorophyll (HNLC) regions (Martin and Fitzwater, 1988), and dusts from eastern Asia are considered to be major sources of Fe in the North Pacific HNLC regions (Duce and Tindale, 1991). Thus, the study of clays delivered to the pelagic environment as dusts is important for the knowledge of biological productivity. As in the modern case, dusts should play a similar role in the palaeoenvironment. Therefore, this study provides new information for the CPE that occurred in the Late Triassic period.

8.2 Geological setting

Bedded chert samples analyzed in this study were collected from the "Section R" (Sugiyama, 1997) continuous lithologic succession in the Tamba-Mino-Ashio Belt, a Paleozoic-Mesozoic accretionary complex in the Inuyama area in central Japan (Fig. 8−2). In the Inuyama area, Triassic-Jurassic bedded chert and clastic rock sequences form thrust pile structures, and the sections are called CH-1, CH-2, CH-3, and CH-4 in structurally ascending order (Yao et al., 1980). The sedimentary complex in this area formed by accretionary processes at shallow depths (Kimura and Hori, 1993) and has been classified into a very lower diagenetic zone based on the illite crystallinity (Otsuka and Watanabe, 1992). A paleomagnetic study was made of the bedded cherts from the Middle Triassic (Anisian) to the Lower Jurassic in the Inuyama area that was deposited in an equatorial region with a palaeolatitude between 10ºN and 10ºS (Ando et al., 2001).

Among the sections in the Inuyama area, we focused on Section R in CH-3 (35°24'18.6"N, 136°57'48.5"E; Fig. 8−2; Sugiyama, 1997). This section consists mainly of late Ladinian to late Carnian bedded red chert with a thickness of approximately 25 m, based on the radiolarian biostratigraphy (Sugiyama, 1997), and a small amount of white chert is intercalated at approximately 1.2, 4.3, and 22 m from the lower part of the section (Fig. 8−3). In Section R, there are two lithologic types of bedded chert (Imoto, 1984). The B-type bedded chert shows a clear repetition of distinct siliceous and muddy layers at levels of several centimeters. The F-type

(fine-grained quartz) bedded chert has boundaries that are indistinct due to amalgamation. In this study, the F-type chert is further divided into relatively Si-rich and Si-normal components.

We divided Section R into 6 units based on the colors and types of the bedded chert (Fig. 8−3). The lower part of this section, which consists of B-type bedded chert with siliceous layers (several cm in thickness) and muddy layers (several mm in thickness), is unit 1. The total thickness of unit 1 was approximately 4 m. Two massive white chert layers existed at the middle and upper parts of this unit. Field observations indicate that the color of the chert at the lower part of this section (beneath the lowest white chert) gradually became greenish. In this unit, we identified 130 single chert layers and named them "R1-X". The capital letter R identifies the samples collected from Section R, the number between 1 and 6 correspond to the unit, and the last letter indicates the number of samples collected from each unit. The F-type bedded chert with thickness of 6 m constituted unit 2. The F-type bedded chert with a thickness of 6 m constituted unit 2. The F-type bedded chert with the colored tone laminae and thickness of 3 m composed unit 3. The boundary between units 1 and 2 was transitional, while the boundary between units 2 and 3 was distinguished by colored laminae. In unit 3, the Si-normal parts correspond to the violet-colored laminae. In contrast to the B-type bedded chert, the identification of the single layer in the F-type chert was indistinct owing to amalgamation. Unit 4 was composed of three layers of bedded chert (R4-1, R4-2, and R4-3) and a layer of violet-colored siliceous mudstone (R4-4), which corresponded to the horizon of CS-1 in Sugiyama (1997). The boundary between units 3 and 4 was distinct. Above the siliceous mudstone layer, 70 single layers of B-type bedded chert appeared again in unit 5. The boundary between units 4 and 5 was also distinct, while the boundary between units 5 and 6 was transitional. Unit 6 consisted of F-type bedded chert without the lamina observed in unit 3 but with a narrow band of white chert.

8.3 Analytical methods

8.3.1 Major element analysis

The SiO_2 and P_2O_5 compositions of the cherts were determined using a PANalytical Epsilon5 energy dispersive XRF (EDXRF). Other major elements, such as Al_2O_3, CaO, Fe_2O_3, K_2O, MgO, MnO, Na_2O, and TiO_2, were determined using an ICP-AES (Thermo Scientific, iCAP 6000) after the samples were digested in a mixture of HF, $HClO_4$, and HNO_3. The accuracy and the precision of these measurements were better than 5%, as estimated from the reported values of a reference rock JCh-1 (chert; Imai et al., 1996) and the repeated measurements of chert samples.

8.3.2 XAFS analysis

XAFS is a powerful tool used to determine the electronic structure and the neighboring elements from X-ray absorption. The XAFS spectrum is divided into two energy regions: X-ray absorption near edge structure (XANES) and extended X-ray absorption edge structure (EXAFS). The former gives information about electronic states (valence) and the symmetry of the coordination environment. The latter is sensitive to the local structure of the center atom absorbing the incident X-ray (Fe in this case), including the interatomic distances and coordination numbers of the neighboring atoms. Although the origins of XANES and EXAFS differ, both methods enable us to identify the chemical species of the center atom or the mineral in a sample.

8.3.2.1 Iron K-edge XANES

In this study, the Fe K-edge (7111 eV) XANES spectra were measured at the BL-12C of Photon Factory (PF; Tsukuba, Japan) and at the BL-01B1 of SPring-8 (Hyogo, Japan). The XANES spectra obtained in these two beamlines were identical. Prior to the measurements, the X-ray energy was calibrated with the pre-edge peak maximum of hematite at 7114 eV. The XANES spectra of the reference materials, pyrite, fayalite, chlorite, hornblende, illite, smectite, magnetite, goethite, and hematite,

were measured in transmission mode, while the spectra of the chert samples were measured in fluorescence mode using a 19-element germanium (Ge) semiconductor detector. Clay minerals, including illite (IMt-1), smectite (SWy-2), and chlorite (CCa-2), were obtained from the Source Clays Repository of the Clay Mineral Society, USA. After dry sieving, clay standards with grain sizes smaller than 20 μm were obtained. Minerals such as fayalite (Fe_2SiO_4), pyrite (FeS_2), and hornblende were obtained from Nichika Inc. (Kyoto, Japan). Magnetite (Fe_3O_4) was obtained from Wako Pure Chemical Industries Ltd. Goethite and hematite were synthesized following the method of Schwertmann and Cornell (2000). The measurements were conducted at ambient pressure and temperature. The XANES spectra were analyzed using REX2000 software (Rigaku Co. Ltd.). The contributions of the various Fe species in each sample were estimated by linear combination fitting (LCF) of each XANES spectrum with the spectra of the reference materials. The LCF was conducted using no more than three minerals in the energy range of 7100–7200 eV. The quality of the fit was given by the residual value, the goodness-of-fit parameter *R*, defined by

$$R = \frac{\sum[x_{obs}(\mathrm{E}) - x_{\mathrm{cal}}(\mathrm{E})]^2}{\sum[x_{obs}(\mathrm{E})]^2} \qquad (8\text{–}1)$$

where $\chi_{obs}(E)$ and $\chi_{cal}(E)$ are the experimental and calculated absorption coefficients at a given energy (E), respectively. A smaller R value means a better fit in the LCF procedure.

8.3.2.2 Iron K-edge EXAFS

To confirm and enhance the reliability of the XANES-LCF, Fe K-edge EXAFS spectra were measured at BL-12C of PF or BL-01B1 of SPring-8. The EXAFS spectra were measured for the R1-1, R2-2, R2-3 (Si-normal), R3-4 (Si-normal, Si-rich), R4-1, R4-3, R4-4, and R5-1 areas in Section R. The EXAFS spectra of the reference materials, pyrite, chlorite, hornblende, illite, smectite, magnetite, ferrihydrite, goethite, and hematite, were measured in the transmission mode, while the spectra of chert samples were measured in the fluorescence mode using a 19-element Ge

semiconductor detector. The measurements were conducted at ambient pressure and temperature. The EXAFS spectra were analyzed using Athena software (Ravel and Newville, 2005). The energy unit was transformed from eV to $Å^{-1}$ to produce the EXAFS function $\chi(k)$, where k ($Å^{-1}$) is the photoelectron wave vector. The k^3-weighted EXAFS spectra were also fitted using the LCF of the reference materials in a k range of 2–11.5 $Å^{-1}$, depending on the spectral quality, by minimizing the residual of the fit, which was given by the goodness-of-fit parameter R, defined by

$$R = \frac{\sum[x_{obs}(k) - x_{\mathrm{cal}}(k)]^2}{\sum[x_{obs}(k)]^2} \qquad (8\text{–}2).$$

Similar to Eq. 8–1, $\chi_{\mathrm{obs}}(k)$ and $\chi_{\mathrm{cal}}(k)$ are the experimental and calculated absorption coefficients at a given k, respectively, and a smaller R value means a better fit in the LCF procedure.

8.3.2.3 Valence state analysis on Fe

Iron K-edge XANES has a pre-edge feature showing the oxidation state and the coordination environment of an Fe atom. The pre-edge is located approximately 15-20 eV before the main K-edge of the XANES peak (Waychunas et al. 1983) and is related to the electronic transitions from 1s to 3d and 4d, which are quadrupolar and dipolar transitions, respectively (Dräger et al., 1988). The shape and the amplitude of the pre-edge reflect the variation of the electronic transitions, i.e., the pre-edge is highly sensitive to Fe-bearing materials.

The pre-edge peak analysis was performed following the procedure reported by Wilke et al. (2001) and Giuli et al. (2002). The contribution of the edge jump was extracted from the background, which was fitted using a spline function to interpolate before and after several eV of the pre-edge (Fig. 8–4A). After the subtraction of the background related to the edge jump, the normalized pre-edge was fitted with a combination of three Gaussian functions, and the centroid position of the peak was defined as the weighted average of the three centroid energies of the Gaussian

functions (Fig. 8–4B). Three Fe-bearing minerals, fayalite (divalent), magnetite (valence state of 2.67), and hematite (trivalent), were used as standard materials to prepare the calibration curve for the centroid position against the valence state (Fig. 8–4C). The calibration line can be used to obtain the average oxidation state of Fe if all of the Fe species are six-coordinated compounds, which is generally accepted for natural Fe species (Wilke et al., 2001).

8.4 Results

8.4.1 Major element compositions

The results for the major element compositions are listed in Table 8–1. All of the samples, except for R4-4, contained over 90 wt.% SiO_2. In contrast, the Fe concentration as Fe_2O_3 in cherts is low, on average 0.66 wt.%, and varying from 0.06 to 2.04 wt.%. The chert samples from Section R showed similar Fe/Al ratios from 0.4 to 0.7 with an average of 0.57. Only one sample, R4-3, exhibited an Fe/Al ratio above 1. Figure 8–5 shows a ternary diagram based on the Al_2O_3, Fe_2O_3 (total), and MnO compositions that is used to estimate the formation environment of chert (Adachi et al., 1986). All of the samples, except for R4-3, were plotted within the area of non-hydrothermal origin. Although R4-3 was plotted at the rim of the non-hydrothermal region in the ternary diagram, its value was far outside of the hydrothermal origin. This means that the contribution of its hydrothermal origin can be ignored, which allows us to treat this sample as being similar to the other cherts.

8.4.2 Iron K-edge XANES

The Fe K-edge XANES spectra of the reference materials used in the LCF are shown in Fig. 8–6A, while the spectra of the chert samples with the fitting results listed in Table 8–2 are shown in Figs. 8–6. Samples containing chlorite, such as R1-1, R2-2, and R6-3 (r), showed a sharp peak at approximately 7126 eV and a shoulder at 7121 eV. In contrast, samples with major contributions from hematite gave spectra with a

two-step peak and larger absorbance at the right side of the peak (7132 eV).

All the red cherts require hematite with illite and/or smectite to fit the measured spectra. The best estimate of the mineral composition of the white chert (R2-2) is chlorite and hornblende. The best LCF result for R1-1, green chert, is obtained with the combination of chlorite, hornblende, and illite, although it could contain hematite due to the transitional change of color from red to green at the outcrop. Only one sample, R4-4, requires magnetite to fit the measured spectrum, while several samples from upper part of the Section R contain goethite.

8.4.3 Iron K-edge EXAFS

The k^3-weighted Fe K-edge EXAFS spectra of the reference materials used in the EXAFS-LCF are shown in Fig. 8–7A. The EXAFS spectra of selected chert samples with fitting results are listed in Table 8–3, and the contributions of each mineral composition are shown in Figs. 8–8B and 8–8C. Although some samples show several small fluctuations at higher k regions, the noise is small enough to observe several characteristics. The k-space spectrum of R4-3 showed clear similarity to that of hematite. The other spectra except for R1-1 and R2-2 were similar to that of R4-3, such as large negative amplitude at k = 7 and 9, but showed slightly different structures. For example, R2-3 had a small shoulder at k = 5.6 that corresponds to the presence of a small amount of chlorite, while the flat peak around k = 6 for R4-4 reflects the presence of a larger amount of smectite. In contrast, the EXAFS oscillations in the spectra of R1-1 and R2-2 were different from those of the red cherts, and slightly shifted to the left side compared to the other chert samples, which also can be due to the presence of chlorite. A positive amplitude for the white and green cherts at k = 5.6 corresponds to that of chlorite.

It should be noted that the EXAFS-LCF showed different end-member mineral compositions from those of XANES-LCF for R1-1, R2-2, R3-4 (both Si-rich and Si-normal), R4-1, R4-3, and R5-1. In the case of R4-3, goethite, which is required to achieve the better fit based on the XANES-LCF, is not necessarily among the

end-member minerals in the EXAFS-LCF. In the cases of the green and the white cherts, the XANES-LCF required hornblende. However, the EXAFS fitting needed magnetite instead of hornblende for a better fit. It is interesting that the end-member mineral composition is almost the same for the green and the white cherts.

8.4.4 Valence state analysis

The result of the valence analysis based on the pre-edge analysis is also shown in Table 8–2. Figure 8–8 shows the relationship between the Al-normalized Fe concentration and the average valence state of Fe along the geologic column. Except for one sample (R4-3), the Fe/Al ratios were almost constant irrespective of their color and type. This means that the source of chert can be constant through the Carnian. The sample with the high Fe/Al ratio exhibited the highest value for the average valence state of Fe beyond the analytical error. Most of the red chert had an average valence state of 2.5−2.6, although the LCF analysis showed the existence of hematite (Fe^{3+}) in the red chert. The white (R2-2) and the green cherts (R1-1), which were free of hematite, had a larger amount of reduced Fe. Because the average Fe valence state in the red cherts is almost constant through Section R, the degree of alteration can be similar except for R1-1 at the lowermost part of the studied section.

8.5 Discussion

8.5.1 Fe-bearing minerals determined using XAFS

The XANES-LCF results showed that all the red cherts contained hematite and clay minerals such as chlorite, illite, or smectite, while the white and the green cherts did not contain hematite. The red chert can reflect the existence of hematite, as indicated by Matsuo et al. (2002) and Sato et al. (2011). Clay minerals incorporated into chert can be an important source of Fe because our analysis shows that all the samples collected from Section R contain some clay minerals. The difference between the red and the violet colored cherts cannot be reflected in their mineral compositions

in XANES analysis. A mineral in the white and the green chert is also not clearly identified by XANES analysis. However, the absence of hematite, which was further confirmed by EXAFS analysis, can be the major factor that controls the color of the white and the green colored chert (Matsuo et al., 2002). Regarding the EXAFS analysis, the red chert, especially R4-3 from the middle part of the Section R, showed k-space spectra that were similar to those of hematite. This means that hematite can be incorporated in chert in particulate form because, if Fe forms bonds with Si via O, then the Fe-O-Si bond should have a different EXAFS oscillation from that of the Fe-O-Fe bond, which is not the case in these samples. The EXAFS-LCF showed the existence of chlorite in the R2-3 (Si-normal) sample having the largest amount of chlorite among the red cherts according to XANES analysis. Although Sato et al. (2011) suggested the possible presence of chlorite in chert samples, this type of identification of clay minerals is difficult using ^{57}Fe Mössbauer spectroscopy, showing the effectiveness of XAFS as an alternative tool to identify the Fe minerals in cherts.

The notable result obtained by the EXAFS analysis is that, except for R2-3 (Si-normal), the end-member mineral compositions are different from those estimated by XANES-LCF. This difference can be due to the similarity of the XANES spectra of the reference materials. The absorption peaks of some reference materials, such as chlorite, hornblende, magnetite, and goethite, are located at similar positions (Fig. 8–6A). The absorption peaks of illite and smectite are also located at similar energies. In contrast to XANES spectra, the k^3-weighted EXAFS spectra of the reference materials show different shapes that are sufficient to distinguish each contribution. A comparison between the XANES and the EXAFS results is summarized in Table 8–4. In the case of the green and the white cherts (R1-1 and R2-2, respectively), the absence of hornblende was estimated, although the XANES analysis required hornblende to achieve the minimum fitting error. Meanwhile, magnetite, which is not included in XANES-LCF, is needed to attain the better EXAFS fit. At least for the green chert, the presence of magnetite is preferred because the field observations showed that the color of R1-1 gradually changed from red to green, which may reflect alteration during the diagenesis as suggested by Sato et al. (2011). Thus, the XANES-LCF for the white and

the green cherts with end-member minerals determined by EXAFS-LCF was performed. A small increase in the fitting error (less than twofold) in the XANES-LCF using the minerals determined by the EXAFS is observed for the green chert. The assumption of hornblende can be caused by the similarity of the XANES spectra for hornblende and magnetite. On the other hand, an almost threefold increase in the fitting error is obtained for the white chert when performing XANES-LCF with minerals determined by EXAFS. Because the quality of the EXAFS spectrum of the white chert is poor due to the small abundance of Fe, the fitting result was not good compared to the other samples. Similar to the green and the white cherts, the reexaminations of the XANES-LCF using minerals determined by EXAFS was also performed. As shown in Table 8–4, the XANES-LCF without assuming goethite could not achieve the minimum fitting error, but a significant increase in the fitting error was not observed by omitting goethite from the end-member minerals except for R6-1 from the late Carnian period. This suggests that goethite may not be contained in the red cherts of Section R. Samples that were estimated to contain chlorite by the best XANES-LCF (R3-4 and R4-1) also showed a significant increase in the fitting error when the LCF was performed by assuming the mineral composition determined by EXAFS-LCF. This suggests that (i) the sensitivity to the X-ray energy for XANES-LCF provides different mineral combinations than EXAFS results or (ii) other Fe-bearing minerals, for which we did not measure the XAFS as reference material spectra, may be incorporated into the white chert.

8.5.2 Changes in mineral composition through Section R from Ladinian to Carnian

Applying the results listed in Table 8–4, the stratigraphic changes in the Fe-bearing mineral compositions are summarized in Fig. 8–9. Except for an R2-3 (Si-rich) sample from 5.6 m from the bottom of Section R, early Carnian, the contribution of chlorite to Fe-bearing minerals in the red cherts is not greater than 20%. The gradual decrease of the chlorite abundance is observed at the lower part of Section R corresponding to the late Ladinian. In the unit 2 of the early Carnian, the chlorite

composition also decreased successively toward the upper part of the unit. Compared to the upper part of unit 2, a slight increase in chlorite is observed from R3-2, at the middle part of unit 3. From the middle to the upper part of unit 3, the chlorite abundance gradually decreased again and was absent from R3-3. Instead of the absence of chlorite, smectite appears from R3-3 toward R5-2 in the middle to late Carnian. Neither chlorite nor smectite are observed from the middle part of the unit 5 (R5-3) to the lower part of the unit 6 (R6-2). The chlorite is, once again, observed in the uppermost sample (R6-3) in the late Carnian. As a whole, the relatively stable mineral composition shown in unit 2 at the early Carnian is significantly disturbed from the upper part of unit 3 to the lower part of unit 5, and returns from the middle part of unit 6.

According to the presence and/or absence of chlorite and smectite, the red cherts from the Section R can be divided into three parts: (i) those with relatively stable mineral compositions (chlorite + illite + hematite) observed in cherts from the early to the middle Carnian, (ii) the abrupt absence of chlorite and the presence of smectite from the middle Carnian, and (iii) the recovery of the mineral composition in R6-3 in the late Carnian. In general, chlorite and illite form under dry and cool conditions, whereas smectite forms under humid and warm conditions (Chamley, 1989; Weaver, 1989; Fürsich et al., 2005). Although chlorite can also form by hydrothermal alteration, the Al-Fe-Mn ternary diagram discards the possibility of a hydrothermal origin (Fig. 8–5). There is also the possibility that diagenesis is the source of the chlorite because the chrolitization (and also the illitization) of smectite can occur owing to diagenetic alteration (e.g., Morad et al., 2000). However, average valence state of Fe in red cherts is almost consistent and higher than that of slightly altered green chert (R1-1), suggesting that the diagenesis is not significant for these samples (Fig. 8–8). In any case, our notable results show that the mineral composition of the chert dramatically changed from the middle of the Section R, which were proven to correspond to the middle Carnian. The change in mineral composition can be closely related to the climate conditions (Chamley, 1989; Weaver, 1989; Fürsich et al., 2005), and we discuss Carnian environmental changes in the following section.

8.5.3 Implication for Carnian environment

Drastic environmental changes related to the CPE, such as a humid climate and the related demise of the carbonate platform, have been reported from the middle Carnian strata located around the Tethys realm (e.g., Schlager and Schöllnberger, 1974; Simms and Ruffell, 1989, 1990; Donofrio, 1991; Hornung and Brandner, 2005; Lehrmann et al., 2005; Hornung et al., 2007a, 2007b; Roghi et al., 2010; and references therein), Western Pangea (Prochnow et al., 2006; Colombi and Parrish, 2008), and the Boreal region (Hochuli and Vigran, 2010; Bragin et al., 2012). The maximization of the monsoon circulation in the Late Triassic was presumed to be associated with the two events that occurred at the Colorado Plateau located in westernmost equatorial Pangea and Australia at the higher latitudes of Southeast Pangea (Parrish, 1993). If the trade wind was enhanced by the strengthened monsoon (Kutzbach and Gallimore, 1989; Parrish, 1993; Colombi and Parrish, 2008), then the amount of mineral dust transported to the pelagic ocean should have increased. A wet climate due to the increased precipitation around the source regions of the dust could decrease the dust provision. The stratigraphic variation of the mineral composition observed in the current study can reflect dry or wet conditions in Pangea.

According to model simulations of the surface winds (Kutzbach and Gallimore, 1989), dust delivered to the depositional area of chert examined in our study largely originated in western Pangea (Fig. 8–1). A multi-proxy paleosol study on continental deposits created in a fluvial environment that was located between 5° and 15°N of the paleoequator during the Triassic showed increased amounts of rainfall in the middle Carnian and returned to semiarid conditions by the Carnian−Norian boundary (8 in Fig. 8–1; Prochnow et al., 2006). A taphonomy study of the plants on the terrigenous site located between 40° and 45°S of the paleoequator during the Triassic also showed increasing humidity during the middle Carnian and a return to the dry seasonal climate (9 in Fig. 8–1; Colombi and Parrish, 2008). On the basis of combining these two previous studies performed along the western Pangea with the surface wind simulation, it is expected that the mineral composition in the pelagic environment can record the variation from a dry to a wet climate followed by the return to a dry climate.

The stratigraphic changes in the mineral composition shown in the Section R can be considered as follows. First, the relatively stable mineral compositional ratios shown in the cherts from unit 2 to the middle part of unit 3 at the early to middle Carnian were deposited before the CPE under dry climate conditions (Fig. 8–10A). Second, the sudden disappearance of chlorite and the presence of smectite observed from upper part of unit 3 to the lower part of unit 5 occurred by means of increasing amounts of rainfall, corresponding to the CPE period (Fig. 8–10B). The primary formation of chlorite should decrease, whereas smectite should form due to the increasing humidity in the continental area. In addition, increased precipitation around the source region should decrease the dust provided to the pelagic environment. Finally, the appearance of chlorite and the recovery of the mineral composition ratios observed in R6-3 at the late Carnian reflect the return to a dry climate similar to the climate prior to the CPE (Fig. 8–10C). Therefore, the change in the mineral composition observed from the middle to the late Carnian pelagic chert greatly responds to climate changes on the Pangea.

Kozur and Bachman (2010) suggested that the duration of the CPE was 0.7–0.8 myr based on chronological data from the northwestern Tethys. Meanwhile, the mean depositional rate of the Triassic bedded chert in the Inuyama area was estimated to be 1.6–2.1 mm/kyr (Ikeda et al., 2010). The average duration of one chert-mudstone couplet was assumed to be approximately 20 kyr. The thickness of chert, which includes smectite (R3-3 to R5-2), is 875 mm. Assuming that the CPE began at the middle of R3-2 and R3-3 and continued until the midpoint between R5-2 and R5-3, the total thickness deposited during the CPE is calculated to be 1.82 m. Although the identification of a single chert layer was difficult for F-type bedded chert in unit 3, we verified 14 and 28 couplets of chert-muddy layers from R5-1 to R5-2 and from R5-2 to R5-3, respectively. Given that the CPE continued until a time that was intermediate between R5-2 and R5-3, the duration of the wet climate in unit 5 is calculated to be 0.56 myr with a thickness of 1.16 m. If this relationship is extrapolated to the total thickness of the estimated CPE period (1.82 m), the duration is calculated to be 0.88 myr. The calculated duration of the CPE period is almost consistent with the previous

estimate by Kozur and Bachman (2010), suggesting that the stratigraphic change in Fe-bearing mineral composition observed in the current study reflects continental climate change.

The input of Fe-bearing clay minerals, namely chlorite, illite, and smectite, to the ocean might also play an important role for the biological productivity, which is strongly controlled by the input of dissolved mineral nutrients (e.g., Herring, 2002). Our analysis showed that illite was mostly included in the cherts through Section R. The primary form of chlorite was observed from the low to the middle (units 1−3) and the uppermost (R6-3) part of Section R, while smectite was observed from the middle to the upper part (Fig. 8–9). Interestingly, the deposition of F-type chert is roughly consistent with the supply of primary formed chlorite, while the B-type chert occurs when there is a lack of chlorite. The lower part of unit 1 may be exceptional because the cherts with greenish color most likely are altered, which is reflected by the average valence state of Fe (Fig. 8–8). It is generally suggested that the solubility of Fe increases when the mineral Fe content decreases (e.g., Journet et al., 2008; Trapp et al., 2010). In other words, Fe incorporated in clay minerals or feldspar has greater solubility than Fe in (hydr-)oxides such as hematite. In the case of these chert samples, F-type chert is believed to be deposited under conditions of greater biological productivity than B-type chert (Sugiyama, 1997). Thus, it is possible that the mineralogical composition of these cherts corresponds to the types that can be reflected by the biological productivity. Trace element analysis, such as Sr and Ba, can provide evidence for contemporaneous biological productivity.

8.6 Conclusions

This study attempted to determine the Fe species in chert samples using XAFS analysis. The XANES analysis showed that all the red chert contained hematite, while the green and the white cherts did not. The incorporation of chlorite is suggested for some of the red, the green, and the white cherts, which is further confirmed by EXAFS analysis. The average valence state of Fe is lower in the green and the white cherts

than in the red chert, which can be due to the reduction of hematite.

The stratigraphic change in the Fe-bearing minerals was observed at the middle Carnian, and it is suggested that (i) the relatively stable mineral compositional ratios observed from unit 2 to the middle part of unit 3 corresponding to the early to middle Carnian reflect dry climate conditions in the source region, (ii) the significant perturbation in the mineral composition suddenly observed from the upper part of unit 3 to lower part of unit 5 at the middle Carnian reflects wet climate conditions known as the CPE, and (iii) the appearance of chlorite and the recovery of mineral composition ratios observed in R6-3 at the late Carnian indicate the return to dry climate conditions similar to those prior to the CPE. In consideration with the modern ocean environment, the increased input of reduced Fe in chlorite or smectite affects the biological productivity. Although additional data such as trace element analysis may be necessary, this study shows that the drastic but brief environmental change in the continental area is preserved in the pelagic chert samples.

Table 8–1. Major element compositions (%) of chert samples collected in this study.

Samples	SiO_2	TiO_2	Al_2O_3	Fe_2O_3 *	MnO	MgO	CaO	Na_2O	K_2O	P_2O_5	Total	Fe/Al
R6-3 (Si-rich)	97.3	0.026	0.731	0.332	0.021	0.098	0.223	0.214	0.166	0.096	99.22	0.45
R6-3 (Si-normal)	93.2	0.064	1.44	0.804	0.043	0.132	0.030	0.489	0.497	0.114	96.85	0.56
R6-2 (Si-rich)	97.1	0.033	0.739	0.423	0.045	0.108	0.028	0.198	0.296	0.084	99.05	0.57
R6-2 (Si-normal)	93.3	0.078	1.68	0.908	0.091	0.144	0.035	0.434	0.748	0.085	97.48	0.54
R6-1	94.6	0.057	1.39	0.764	0.069	0.130	0.033	0.411	0.599	0.082	98.11	0.55
R5-3	92.4	0.079	1.80	1.12	0.082	0.134	0.038	0.509	0.840	0.088	97.11	0.62
R5-2	94.5	0.069	1.44	0.838	0.021	0.117	0.032	0.355	0.640	0.078	98.11	0.58
R5-1	93.6	0.077	1.56	1.06	0.024	0.119	0.035	0.464	0.655	0.071	97.70	0.68
R4-4	85.8	0.160	3.16	1.55	0.037	0.162	0.048	0.836	1.55	0.071	93.36	0.49
R4-3	91.4	0.071	1.59	2.04	0.032	0.114	0.039	0.476	0.800	0.070	96.59	1.29
R4-2	92.9	0.083	1.73	0.879	0.050	0.115	0.042	0.491	0.844	0.070	97.22	0.51
R4-1	93.8	0.052	1.26	0.577	0.028	0.573	0.040	0.340	0.619	0.447	97.70	0.46
R3-4 (Si-rich)	97.2	0.031	0.721	0.331	0.031	0.096	0.024	0.248	0.282	0.083	99.07	0.46
R3-4 (Si-normal)	94.5	0.058	1.22	0.693	0.116	0.115	0.031	0.479	0.510	0.091	97.84	0.57
R3-3 (Si-rich)	98.2	0.020	0.49	0.251	0.012	0.134	0.027	0.161	0.197	0.105	99.60	0.51
R3-3 (Si-normal)	93.2	0.086	1.61	0.886	0.025	0.307	0.042	0.470	0.796	0.204	97.58	0.55
R3-2 (Si-rich)	99.1	0.010	0.264	0.108	0.004	0.096	0.023	0.050	0.093	0.047	99.80	0.41
R3-2 (Si-normal)	95.8	0.054	1.03	0.527	0.015	0.119	0.029	0.325	0.460	0.097	98.50	0.51
R3-1 (Si-rich)	98.6	0.017	0.454	0.201	0.007	0.095	0.027	0.099	0.187	0.085	99.75	0.44
R3-1 (Si-normal)	96.0	0.049	0.970	0.556	0.016	0.122	0.032	0.277	0.428	0.097	98.57	0.57
R2-5 (Si-rich)	98.7	0.013	0.357	0.223	0.008	0.081	0.023	0.104	0.134	0.080	99.71	0.62
R2-5 (Si-normal)	97.8	0.026	0.548	0.357	0.009	0.097	0.023	0.148	0.225	0.084	99.35	0.65
R2-4 (Si-rich)	98.7	0.013	0.351	0.217	0.010	0.100	0.024	0.099	0.124	0.090	99.76	0.62
R2-4 (Si-normal)	95.8	0.053	1.04	0.651	0.018	0.116	0.025	0.282	0.406	0.086	98.45	0.63
R2-3 (Si-rich)	97.3	0.028	0.691	0.389	0.022	0.103	0.029	0.206	0.279	0.104	99.12	0.56
R2-3 (Si-normal)	96.0	0.048	0.977	0.639	0.033	0.127	0.036	0.293	0.402	0.092	98.65	0.65
R2-2	99.3	0.005	0.127	0.060	0.012	0.056	0.010	0.031	0.037	0.058	99.66	0.48
R2-1 (Si-rich)	98.9	0.015	0.353	0.208	0.071	0.080	0.018	0.061	0.143	0.044	99.88	0.59
R2-1 (Si-normal)	95.0	0.058	1.24	0.753	0.102	0.105	0.031	0.328	0.528	0.086	98.27	0.61
R1-3	93.1	0.084	1.87	0.957	0.041	0.149	0.043	0.412	0.928	0.090	97.63	0.51
R1-2	93.3	0.077	1.65	1.00	0.073	0.160	0.042	0.422	0.775	0.113	97.56	0.61
R1-1	94.5	0.064	1.44	0.673	0.024	0.148	0.033	0.311	0.624	0.129	97.93	0.47

* Total Fe as Fe_2O_3

Table 8–2. The LCF result of Fe K-edge XANES and valence state analysis.

	Py	Fa	Chl	Hbl	Ill	Sm	Mag	Goet	Hem	*R* (%)	Valence
R6-3 (Si-rich)			14		53				33	0.009	2.54
R6-3 (Si-normal)			4		49				47	0.008	2.56
R6-2 (Si-rich)					37				63	0.010	2.60
R6-2 (Si-normal)					41			18	41	0.008	2.57
R6-1					28			38	34	0.008	2.59
R5-3					33			23	44	0.010	2.71
R5-2					29	15			56	0.007	2.55
R5-1			17			29			53	0.010	2.50
R4-4					42		25		33	0.015	2.42
R4-3					19			31	50	0.008	2.85
R4-2					53	26			21	0.011	2.59
R4-1			20			57			23	0.010	2.49
R3-4 (Si-rich)			26			37			37	0.014	2.53
R3-4 (Si-normal)			23			35			42	0.013	2.55
R3-3 (Si-rich)					57			18	25	0.008	2.72
R3-3 (Si-normal)					37	17			46	0.008	2.52
R3-2 (Si-rich)			9		50				41	0.008	2.46
R3-2 (Si-normal)			3		61				36	0.008	2.54
R3-1 (Si-rich)			14		46				40	0.010	2.49
R3-1 (Si-normal)			18		33				49	0.011	2.51
R2-5 (Si-rich)			8		49				43	0.008	2.65
R2-5 (Si-normal)			3		45				52	0.007	2.58
R2-4 (Si-rich)			18		38				44	0.008	2.52
R2-4 (Si-normal)			7		42				51	0.007	2.61
R2-3 (Si-rich)			29		33				38	0.014	2.47
R2-3 (Si-normal)			29		26				45	0.015	2.55
R2-2			35	65						0.012	2.28
R2-1 (Si-rich)			16		32				52	0.009	2.40
R2-1 (Si-normal)			19		37				44	0.010	2.60
R1-3			9		42				49	0.010	2.55
R1-2			23		29				48	0.014	2.52
R1-1			37	36	27					0.012	2.30

Py: pyrite; Fa: fayalite; Cho: choorite; Ill: illite; Sm: smectite; Mag: magnetite; Goet: goethite; Hem: hematite

Note that *R* (%) is calculated using Eq. 8–1.

Table 8–3. The LCF results of Fe K-edge EXAFS.

	Py	Fa	Chl	Hbl	Ill	Sm	Mag	Goet	Hem	*R* (%)
R5-1						42	5		53	0.134
R4-4						57	3		40	0.092
R4-3					36				64	0.041
R4-1					50	14			36	0.056
R3-4 (Si-rich)					28	38			34	0.177
R3-4 (Si-normal)					27	34			39	0.112
R2-3 (Si-normal)			15		45				40	0.055
R2-2			50		33		17			0.172
R1-1			52		32		16			0.092

Py: pyrite; Fa: fayalite; Cho: choorite; Ill: illite; Sm: smectite; Mag: magnetite; Goet: goethite; Hem: hematite

Note that *R* (%) is calculated using Eq. 8–2.

Table 8–4. Comparison between XANES- and EXAFS-LCF.

	Py	Fa	Chl	Hbl	Ill	Sm	Mag	Goet	Hem	*R* (%)	Note
R6-2 (Si-rich)					39			15	46	0.008	(a)
					38				62	0.009	(d)
R6-2 (Si-normal)					42			19	39	0.007	(a)
					40				60	0.009	(d)
R6-1					27			37	36	0.008	(a)
					35				65	0.019	(d)
R5-3					33			23	44	0.008	(a)
					32				68	0.010	(d)
R5-2					37			15	48	0.008	(a)
					36				64	0.009	(d)
R5-1			17			29			53	0.010	(a)
						42	5		53	0.134	(b)
						6	50		44	0.021	(c)
R4-4					40		27		33	0.015	(a)
						57	3		40	0.092	(b)
						7	57		36	0.019	(c)
R4-3					19			31	50	0.008	(a)
					36				64	0.041	(b)
					16				84	0.012	(c)
R4-1			20			57			23	0.010	(a)
					50	14			36	0.056	(b)
					69	10			21	0.027	(c)
R3-4 (Si-rich)			26			37			37	0.014	(a)
					28	38			34	0.177	(b)
					72	4			24	0.031	(c)
R3-4 (Si-normal)			23			35			42	0.013	(a)
					27	34			39	0.112	(b)
					69	5			26	0.030	(c)
R3-3 (Si-rich)					57			18	25	0.008	(a)
					56				44	0.010	(d)
R2-3 (Si-normal)			29		26				45	0.015	(a)
			15		45				40	0.055	(b)
R2-2			35	65						0.012	(a)
			50		33		17			0.172	(b)
			52		1		47			0.035	(c)
R1-1			37	36	27					0.012	(a)
			52		32		16			0.092	(b)
			46		25		29			0.017	(c)

Py: pyrite; Fa: fayalite; Cho: choorite; Ill: illite; Sm: smectite; Mag: magnetite; Goet: goethite; Hem: hematite

Note the best LCF results based on the XANES analysis, (b): the best LCF results based on the EXAFS analysis, (c) XANES-LCF based on the mineral compositions determined by EXAFS-LCF, and (d): XANES-LCF without goethite.

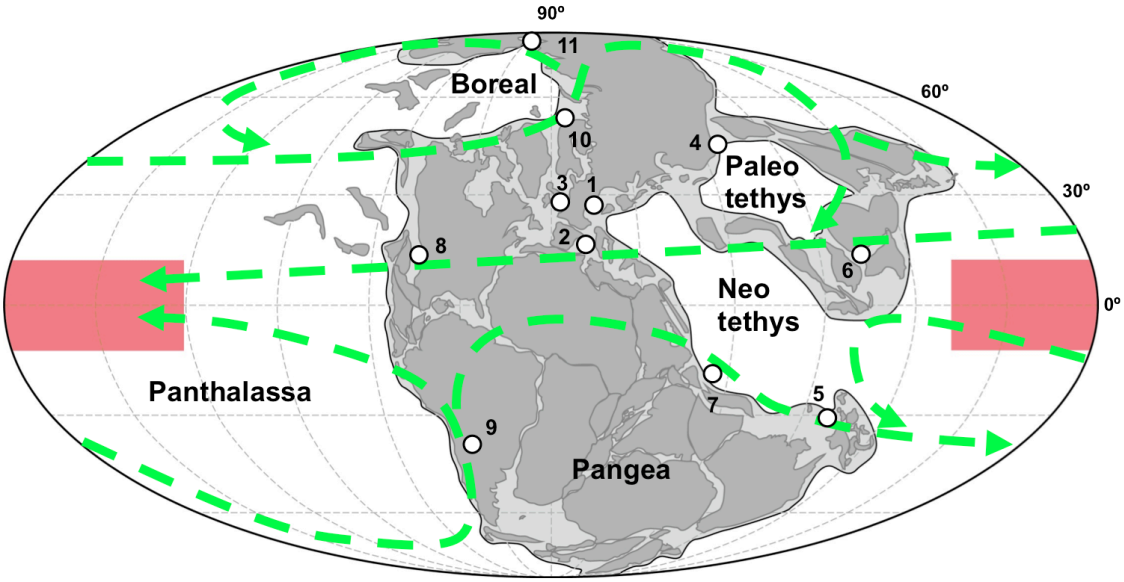

Fig. 8–1. The paleogeography of the Late Triassic modified after Scotese (2004) and Golonka (2007). The light gray area with solid black lines denotes shallow sea. The circles denote areas where the studies of the CPE have been performed, and the numbers show each study as follows: 1: Northern Calcareous Alps (Schlager and Schöllnberger, 1974; Hornung and Brandner, 2005; Roghi et al., 2010); 2: Southern Alps (Hornung et al., 2007a); 3: North Curry Sandstone Member and Arden Sandstone Member (Simms and Ruffell, 1989, 1990); 4: Aghdarband, NE Iran (Donofrio, 1991); 5: Parautochthonous Complex, Timor (Martini et al., 2000); 6: Yangtze platform, South China (Lehrmann et al., 2005); 7: Spiti Valley, Northern Indian Himalaya (Hornung et al., 2007b); 8: paleosols from Chinle Formation (Prochnow et al., 2006); 9: Ischigualasto Formation (Colombi and Parrish, 2008); 10: core samples from Barents sea (Hochuli and Vigran, 2010); 11: Sheina and Tikhaya Reka Formations in Kotel'nyi Island (Bragin et al., 2012). The red area indicates the estimated depositional area of the chert samples used in this study (Ando et al., 2001), and the dashed arrows suggest the simulated surface winds by Kutzbach and Gallimore (1989).

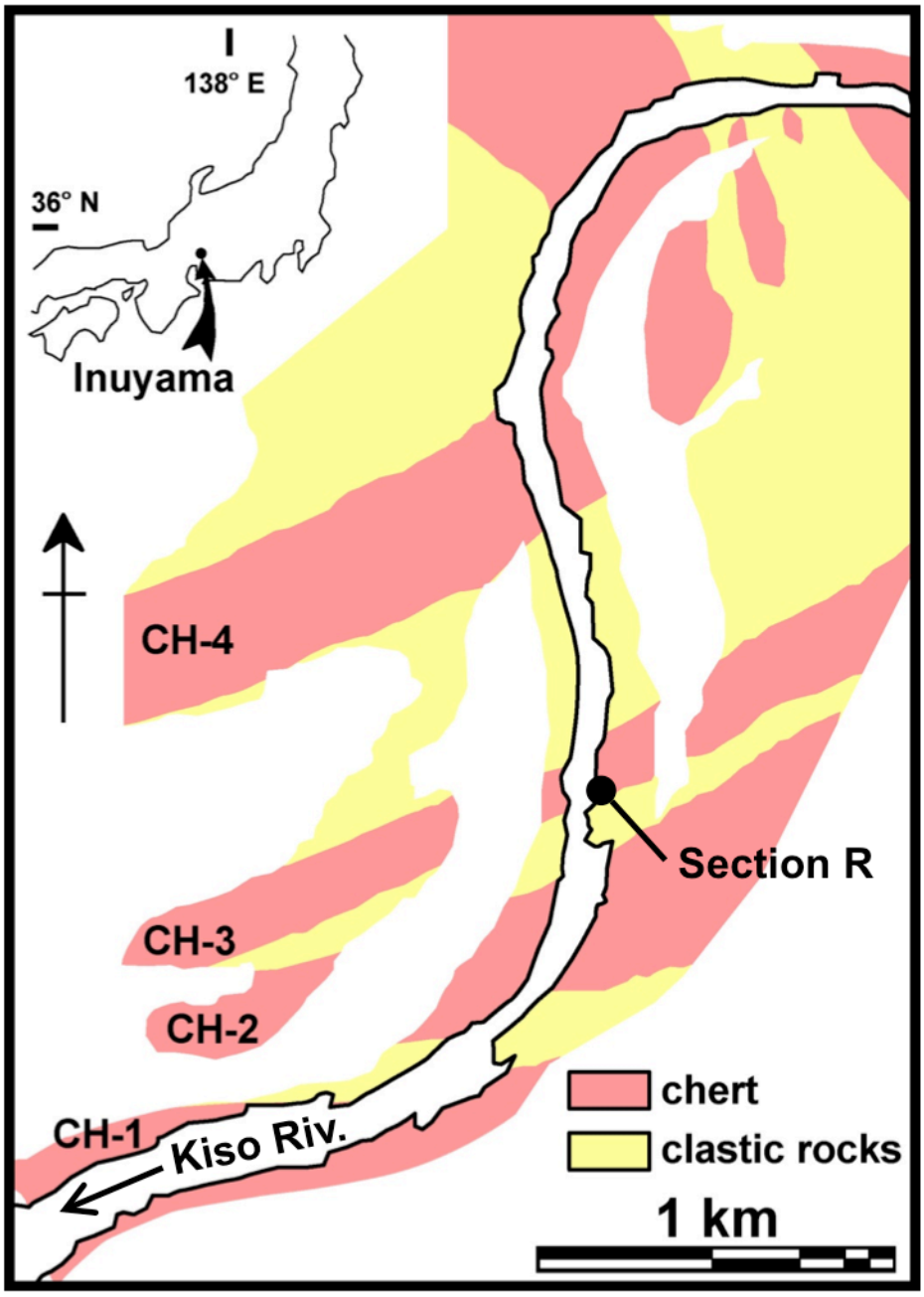

Fig. 8–2. Geological map of the Inuyama area, Central Japan (after Yao, 1980).

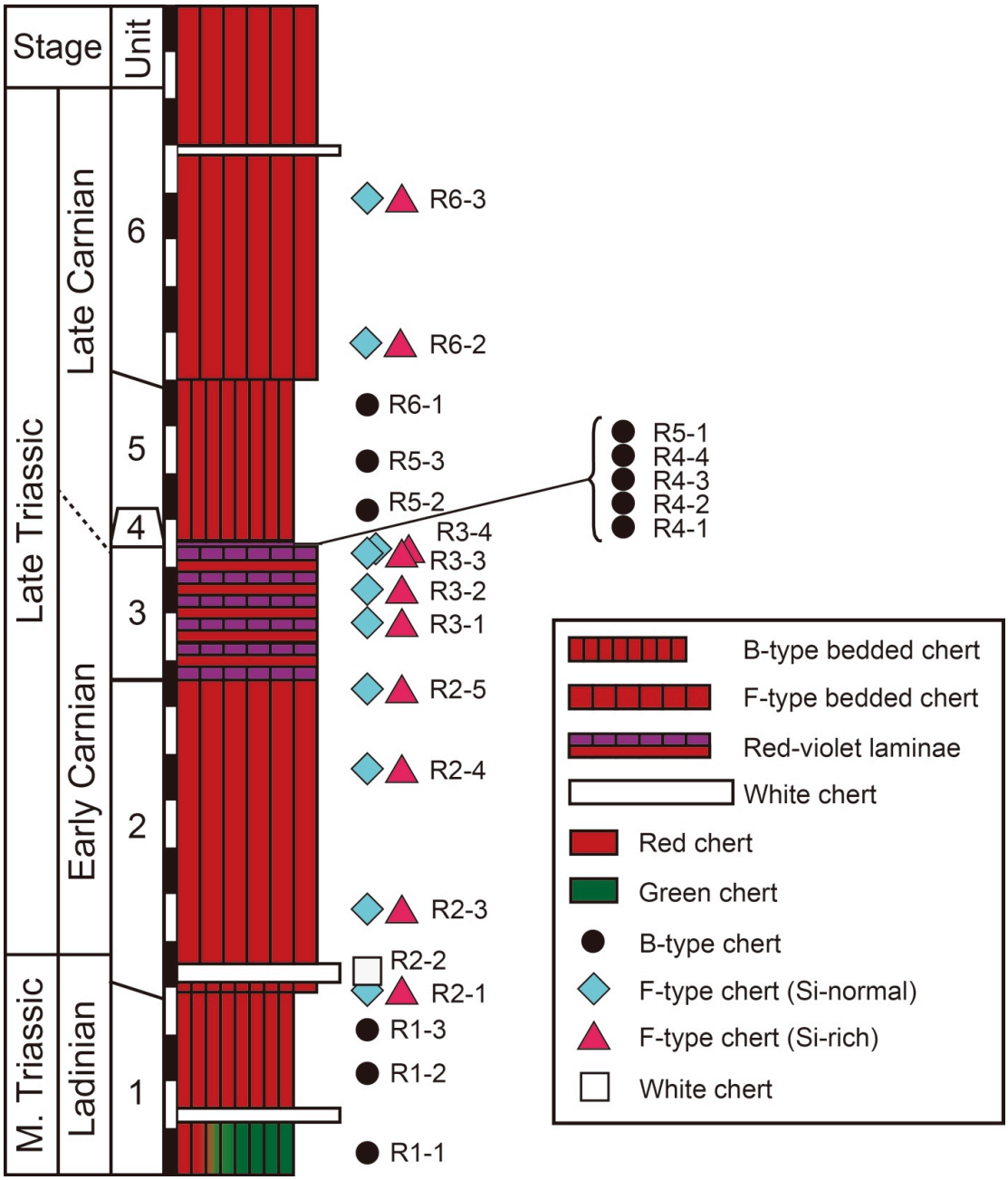

Fig. 8–3. Geological column of Section R with sample names.

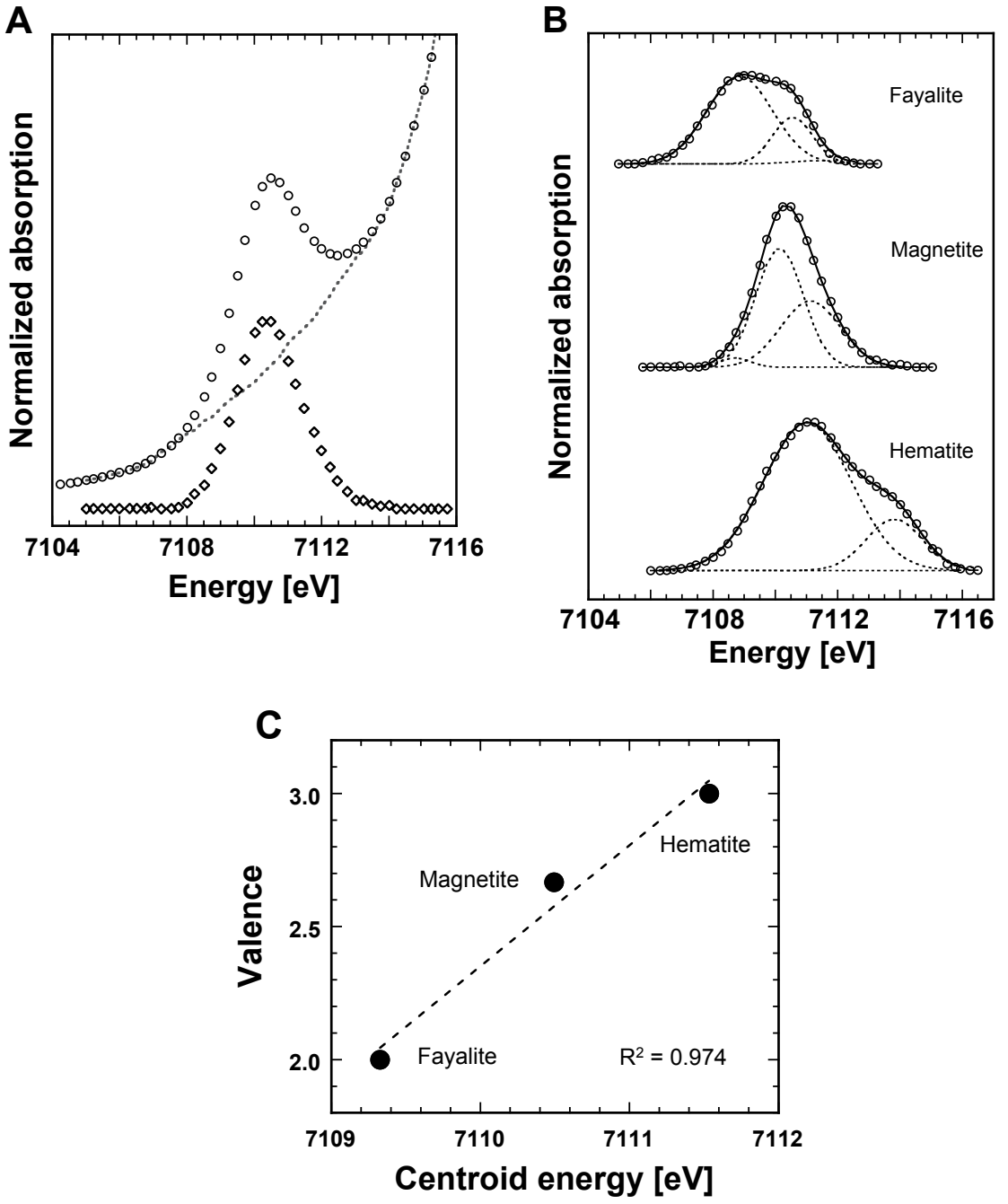

Fig. 8–4. (A) Magnification of the pre-edge. The circle denotes the measured absorbance, the dotted line shows the background spectrum calculated using a spline function, and the quarry is the normalized absorbance. (B) Pre-edge analysis of three standards. The circle denotes the normalized absorbance, the dotted line shows the Gaussian functions, and solid line is the sum of the Gaussian functions. (C) Calibration curve for the valence calculation.

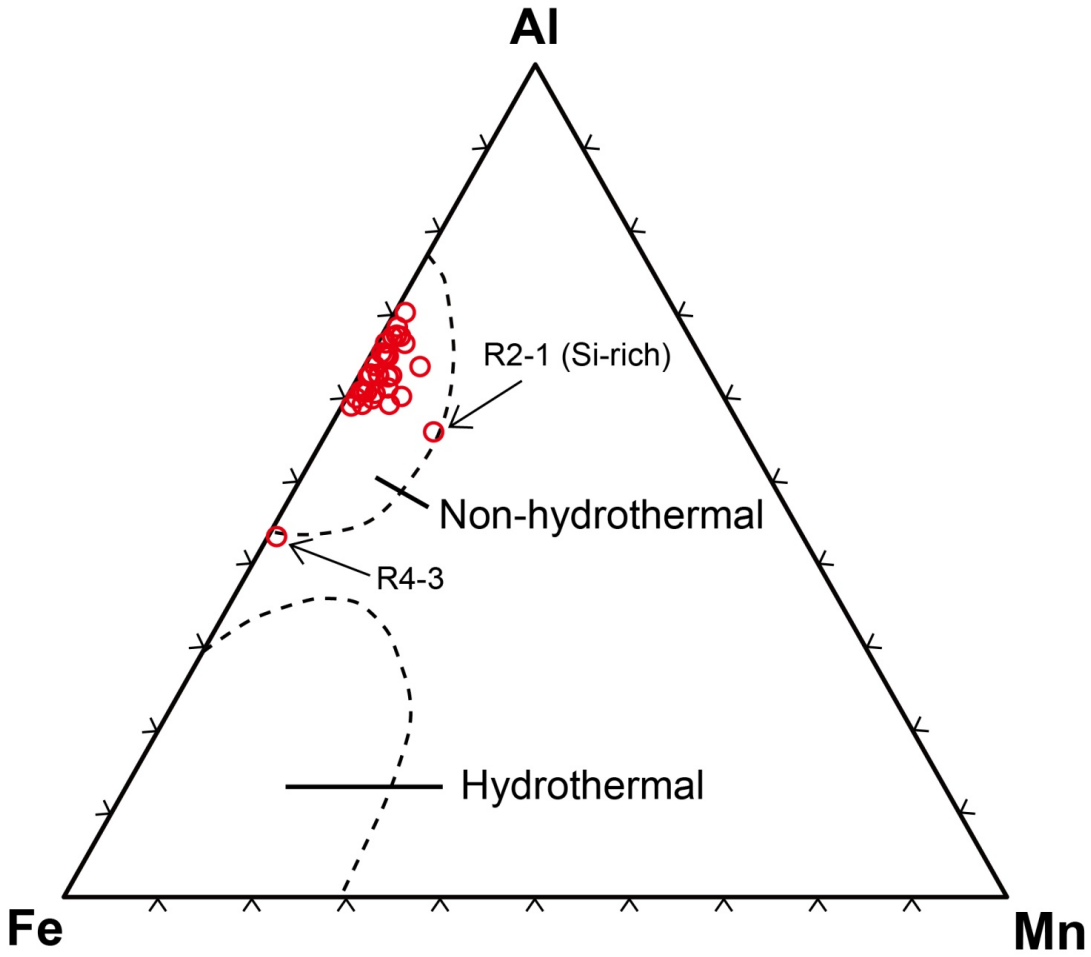

Fig. 8–5. Ternary diagram used to estimate the formation environment of chert (after Adachi et al., 1986).

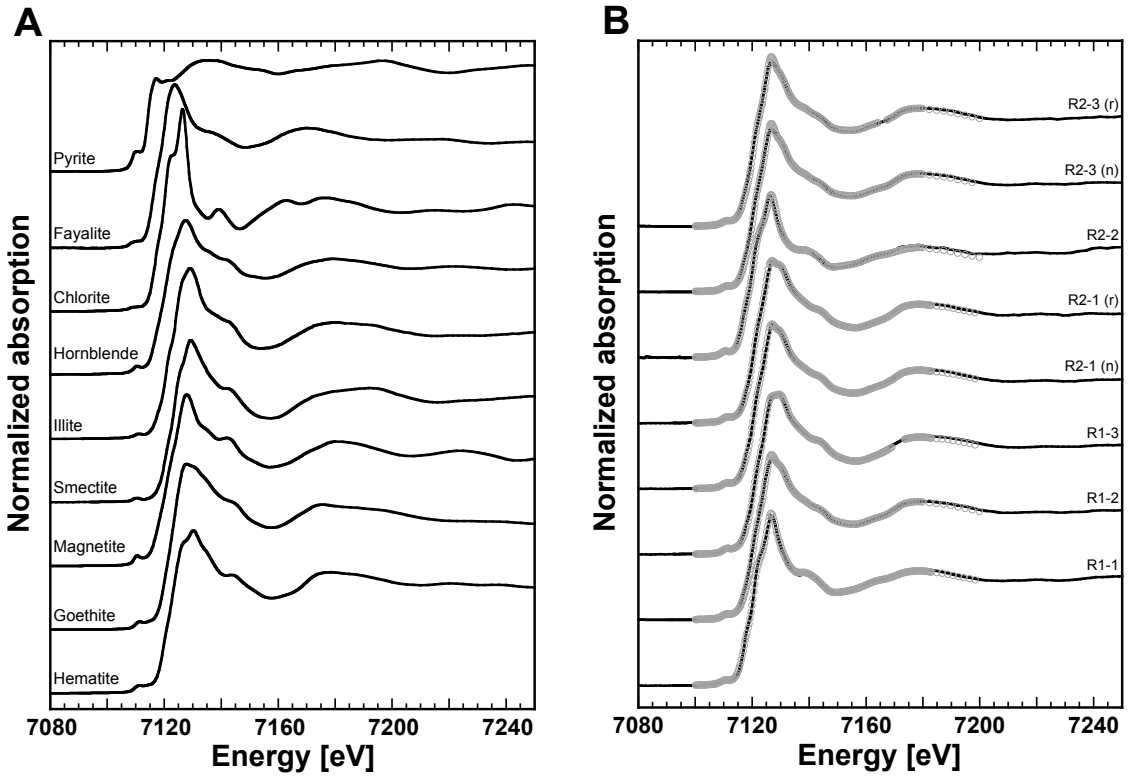

Fig. 8–6. Iron K-edge XANES spectra of (A) standard minerals used to fit the measured chert samples and (B)–(E) chert samples analyzed in this study. The solid black line denotes the measured spectra, and the gray circle shows results from the fit using the parameters listed in Table 8–2. Note that (n) denotes the Si-normal part of F-type chert.

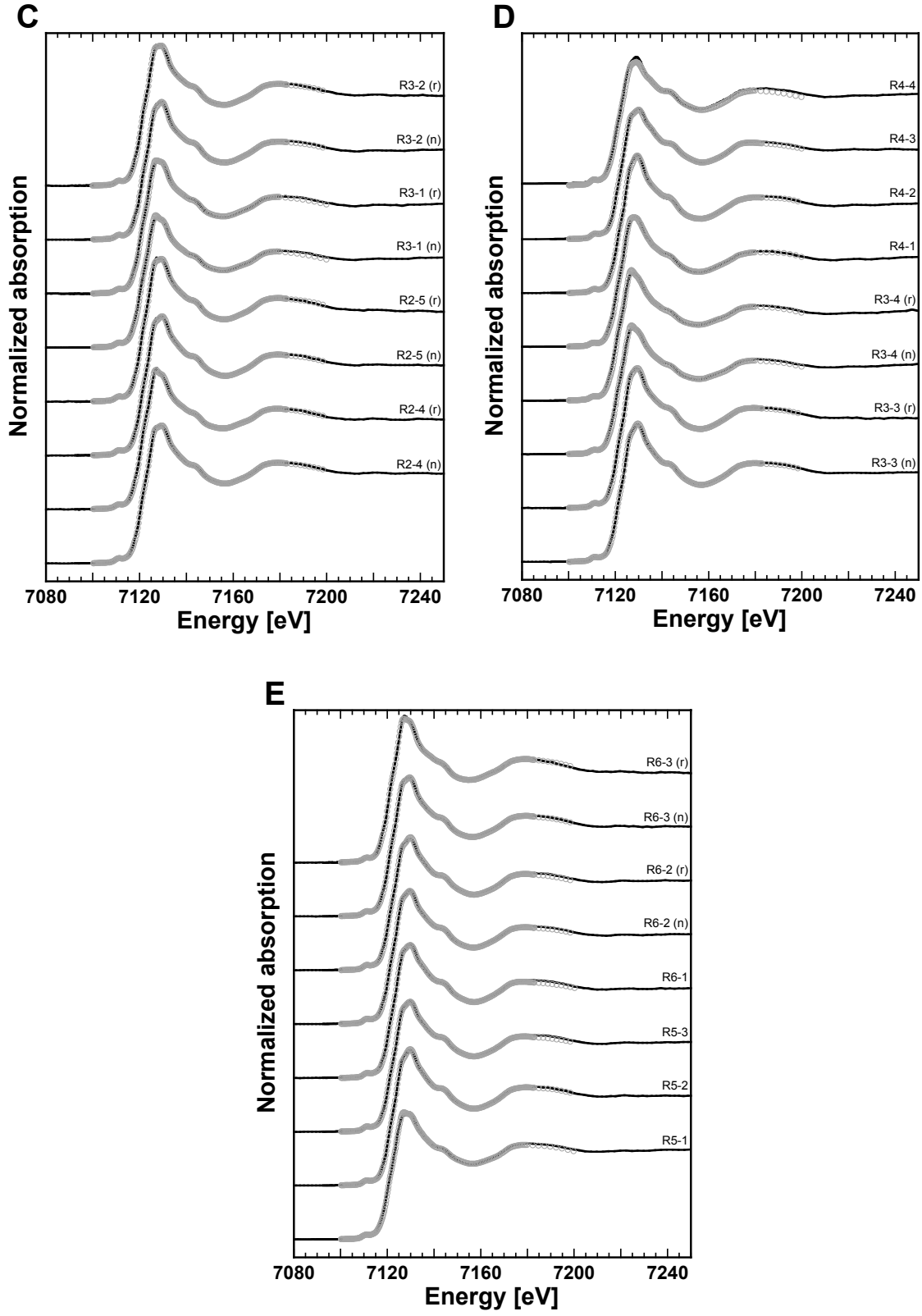

Fig. 8–6. (continued)

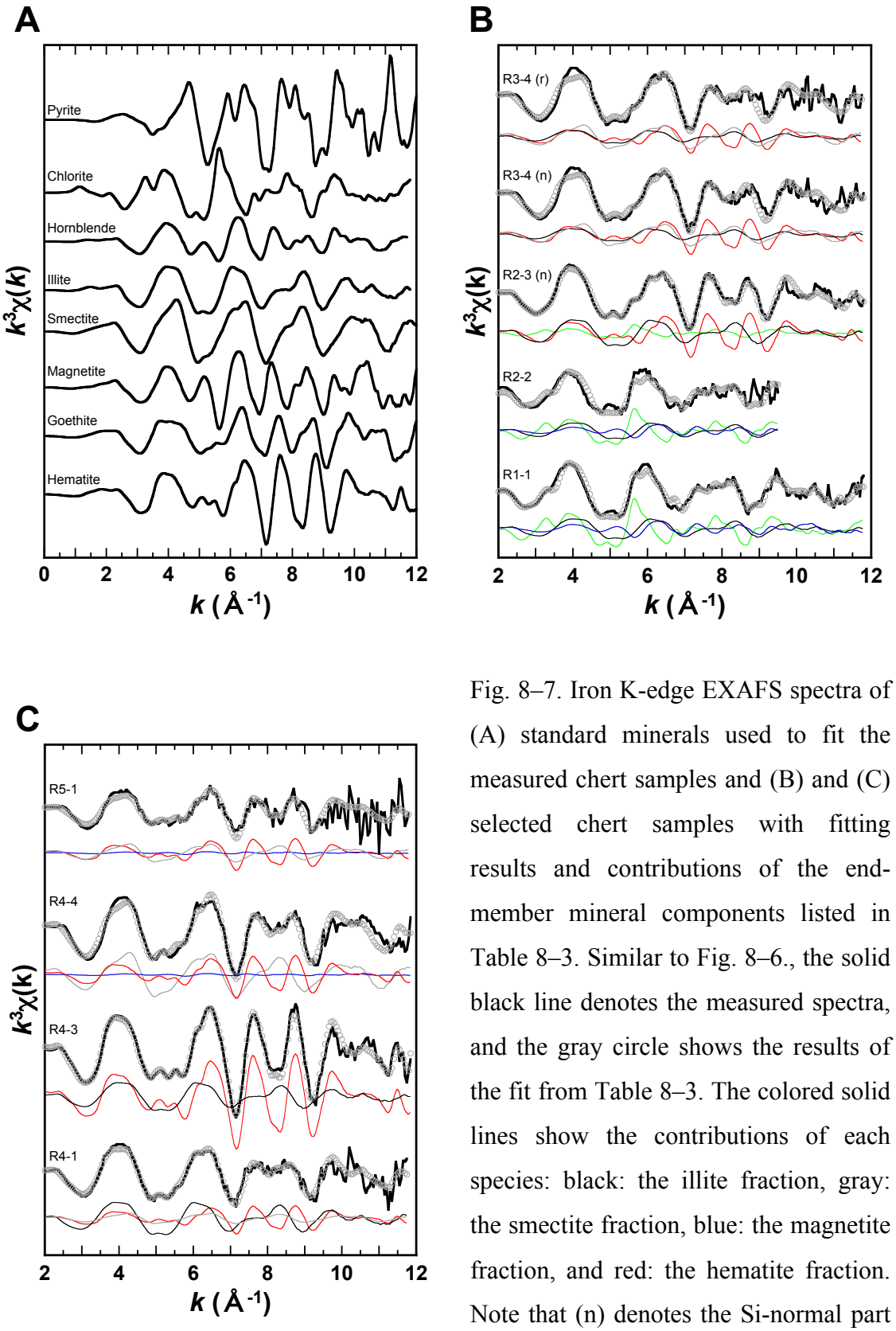

Fig. 8–7. Iron K-edge EXAFS spectra of (A) standard minerals used to fit the measured chert samples and (B) and (C) selected chert samples with fitting results and contributions of the end-member mineral components listed in Table 8–3. Similar to Fig. 8–6., the solid black line denotes the measured spectra, and the gray circle shows the results of the fit from Table 8–3. The colored solid lines show the contributions of each species: black: the illite fraction, gray: the smectite fraction, blue: the magnetite fraction, and red: the hematite fraction. Note that (n) denotes the Si-normal part of F-type chert.

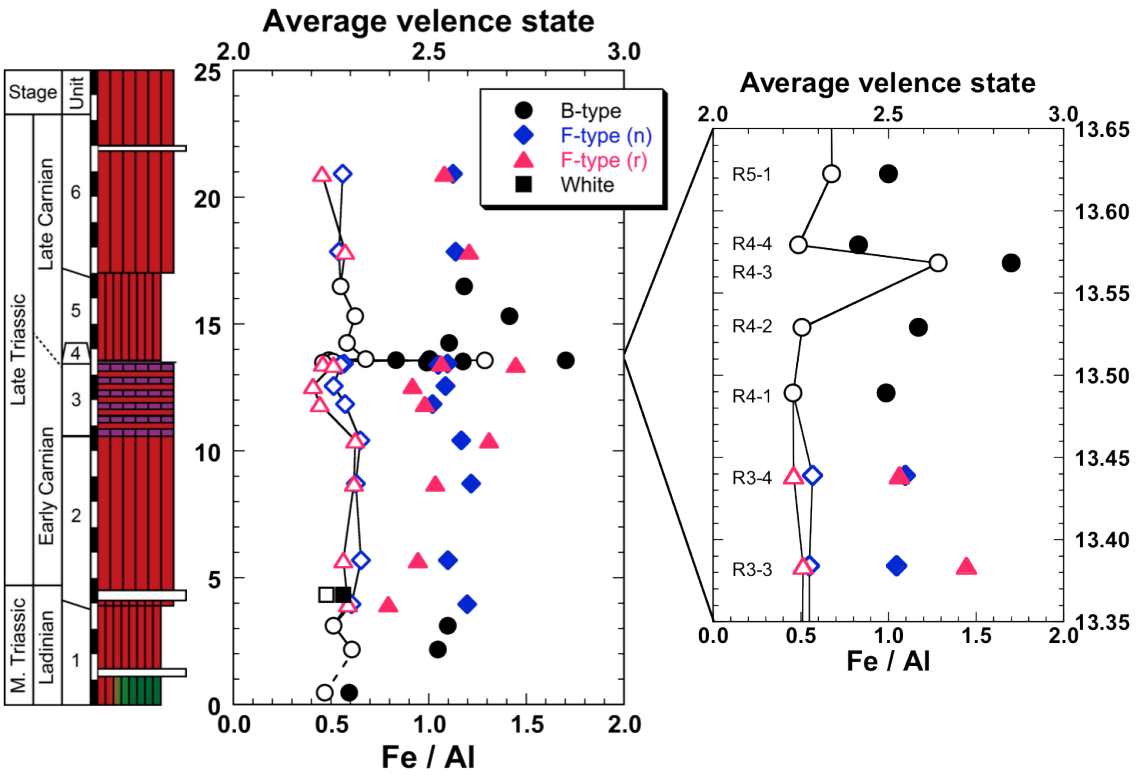

Fig. 8–8. The relationship between the Fe/Al compositional ratio and the average valence state of Fe along the geologic column. The open symbols with solid lines show the Fe/Al ratios corresponding to the lower column, while the filled symbols without a line show the average valence state of Fe corresponding to the upper column. Note that (n) and (r) denote the Si-normal and the Si-rich parts of F-type chert, respectively.

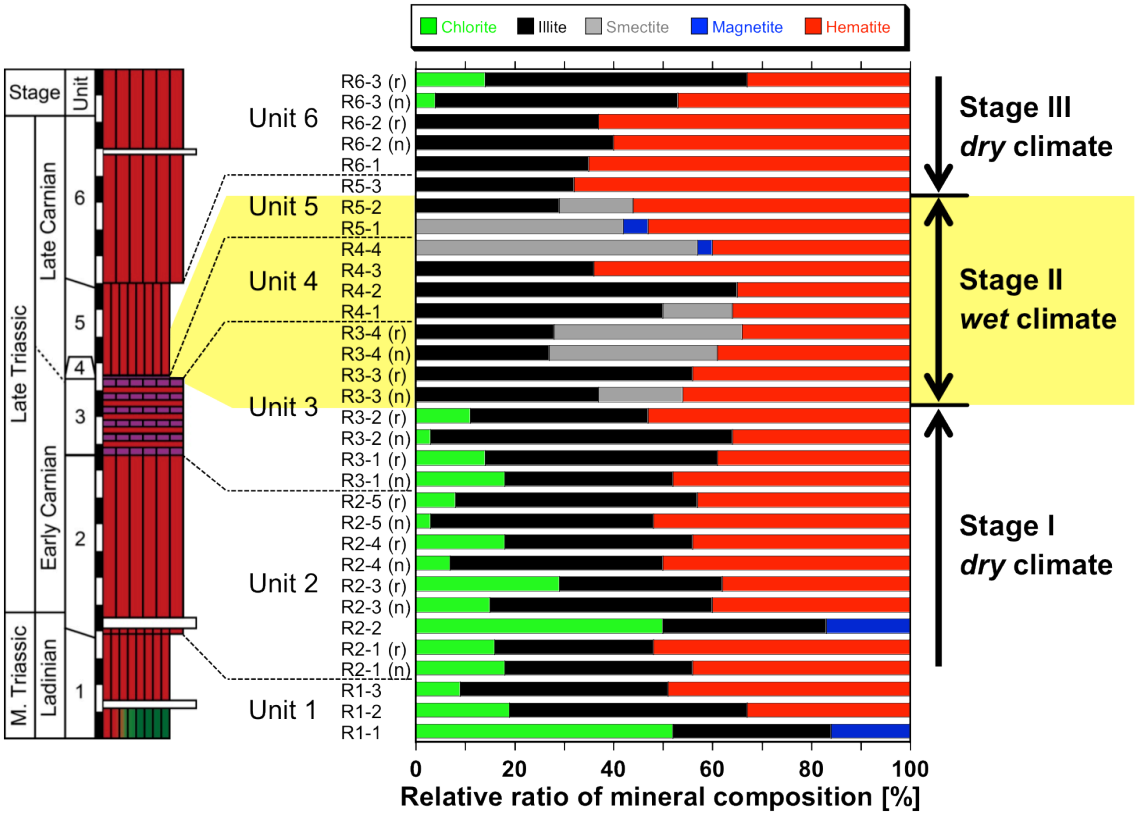

Fig. 8–9. Summary of XANES- and EXAFS-LCF results for chert samples collected from Section R. The mineral composition determined by EXAFS-LCF prevailed over tne XANES-LCF results. Note that (n) and (r) denote the Si-normal and the Si-rich parts of F-type chert, respectively.

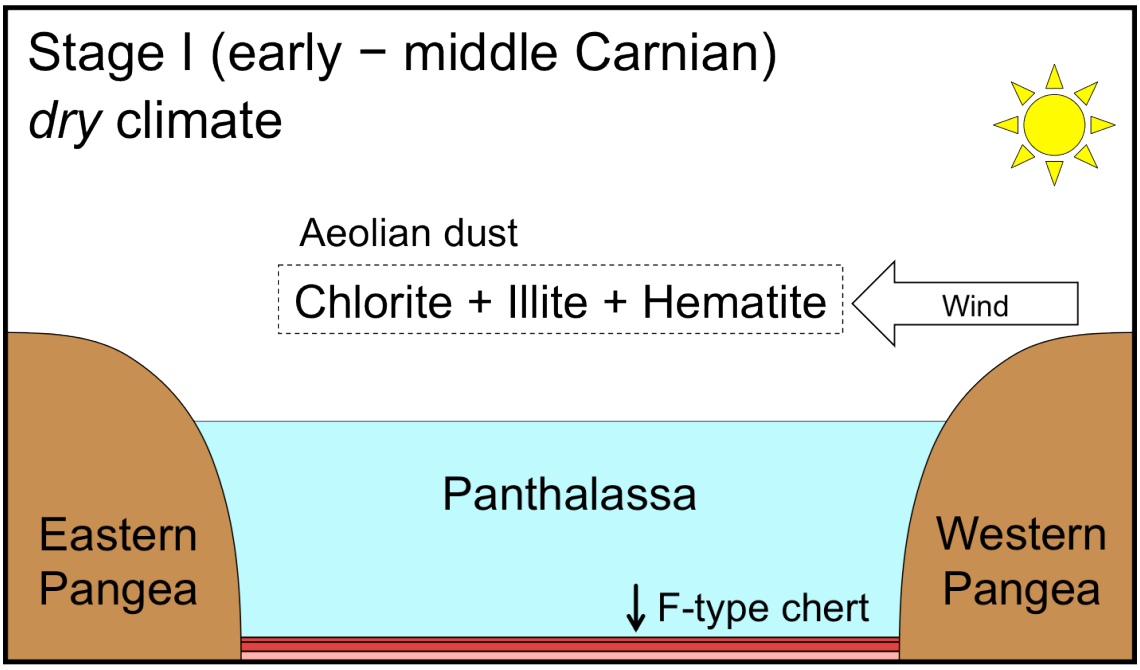

Fig. 8–10. Schematic illustrations through the Carnian pelagic environment. (A) Before the CPE period and corresponding to stage I in Fig. 8–9. The climate in the continental area was dry, which resulted in the supply of chlorite, illite, and hematite to the ocean.

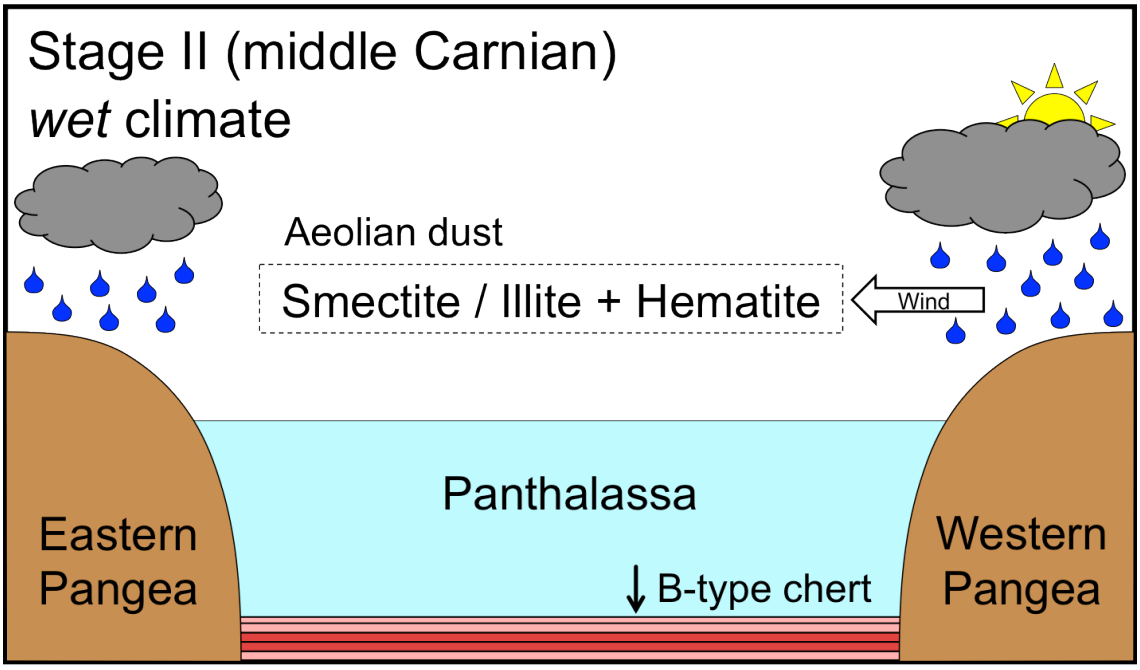

Fig. 8–10. Schematic illustrations through the Carnian pelagic environment (continued). (B) The CPE period corresponding to stage II in Fig. 8–9. The increased precipitation resulted in the primary formation of smectite instead of chlorite in the source area. It is expected that the amount of dust delivered to the ocean decreased relative to the pre-CPE period.

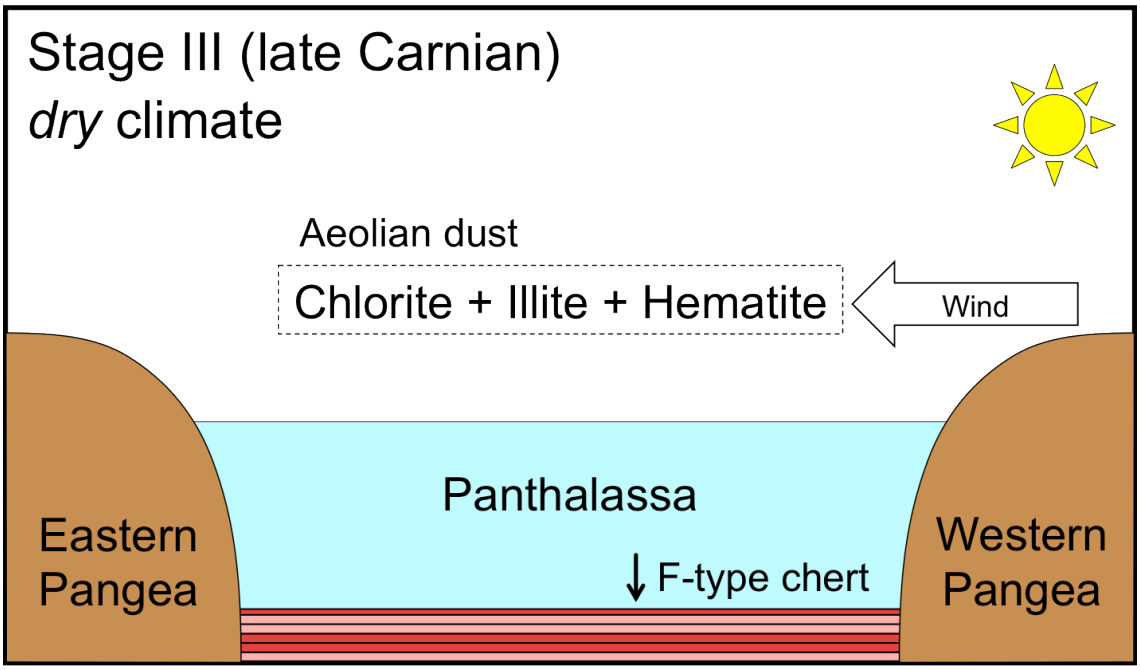

Fig. 8–10. Schematic illustrations through the Carnian pelagic environment (continued). (C) The post CPE period corresponding to stage III in Fig. 8–9. The continental environment recovered totally and resembled the period prior to the CPE, which resulted in the supply of the chlorite + illite + hematite combination. The amount of dust was larger than during the CPE period (B). The pink sediment shows B-type bedded chert, while the red color denotes F-type chert.

Chapter 9

Iron and sulfur species in deep-sea pelagic chert determined by XAFS: Implication for the gradual recovery from oceanic acidification during the Toarcian Ocean Anoxic Event (T-OAE)

9.1 Chapter introduction

In the Jurassic period, the Early Toarcian oceanic anoxic event (T-OAE) has been suggested by the negative excursion of carbon isotopic ratios ($\delta^{13}C$) observed in marine organic and inorganic matters (e.g., Jenkyns and Clayton, 1986; Schouten et al., 2000; Kemp et al., 2005), marine carbonate (e.g., Sælen et al., 2000; Röhl et al., 2001), and terrestrial plants (Hesselbo et al., 2000; 2007) (Fig. 9−1). In addition to the $\delta^{13}C$ excursion, organic carbon burial has been suggested to globally increase (Jenkyns, 1988; Jenkyns et al., 2002). It has been suggested that the ^{12}C enrichment in the carbon cycle is caused by the catastrophic release of methane dissociated from methane hydrate (Hesselbo et al., 2000; Kemp et al., 2005), which could be triggered by the large scale eruptions in the Karoo-Ferrar basaltic province (Pálfy and Smith, 2000). The event is associated with the increase in the atmospheric CO_2 (McElwain et al., 2005), sudden rise in seawater palaeotemperatures (Bailey et al., 2003; Rosales et al., 2004), 4- to 8-fold increase in global weathering rates (Cohen et al., 2004; Waltham and Gröcke, 2006), which resulted in seawater acidification prior to and during the T-OAE (Hermoso et al., 2012), and the mass extinction of terrestrial (Benton, 1995) and marine organisms (Harries and Little, 1999; Bucefalo et al., 2002). Not only the carbon cycle, widespread marine anoxia significantly perturbed sulfur cycle and a modeling estimated that marine sulfate concentrations were 4 to 8 mM (Gill et al., 2011).

Although several studies have been performed so far, these studies mainly focused on the isotopic ratios and modeling, and discussion based on the speciation of redox-sensitive elements has not sufficiently been performed. Iron-57 Mössbauer spectroscopy can distinguish Fe-bearing minerals such as hematite, goethite, pyrite, etc. (e.g., Sato et al., 2009). The Mössbauer spectroscopy can also show the existence of

paramagnetic Fe^{2+} and/or Fe^{3+}, but detailed classification, namely kind of clay minerals incorporated in chert, is difficult. In particular in ^{57}Fe Mössbauer spectroscopy, the peaks of pyrite and that of paramagnetic Fe^{3+}, originated from clay minerals and/or hydrated Fe^{3+} oxides (Manning and Ash, 1979), locate very close each other, which requires an assumption of the existence of either pyrite or paramagnetic Fe^{3+}. This fact means that if pyrite and Fe^{3+}-bearing minerals coexisted in samples, identification of each contribution is difficult.

In this study, therefore, X-ray absorption fine structure (XAFS) analysis was used to determine the iron (Fe) and sulfur (S) species in chert samples collected from the Tamba-Mino-Ashio Belt of Japan. Similar to the Mössbauer spectroscopy, XAFS is a nondestructive analysis, which requires only a small amount of sample (less than 100 mg). XAFS is highly element-selective analysis because an element has its specific absorption edge in the X-ray region, which enables us to determine Fe species if the Fe concentration in the sample is above a few dozens of ppm. Highly element-sensitive property also enables to determine the multi-element of the same sample as will be performed in this study.

9.2 Samples and Methods

9.2.1 Chert samples

Bedded chert samples analyzed in this study were collected from the Tamba-Mino-Ashio Belt, a Paleozoic-Mesozoic accretionary complex in Inuyama area, central Japan (Fig. 9−2). In this area, Triassic-Jurassic bedded chert and clastic rocks sequence forms thrust pile structure and the section is called as CH-1, CH-2, CH-3, and CH-4 in structurally ascending order (Yao et al., 1980).

Black and gray cherts were collected from Katsuyama section located in the northern part of Inuyama area. The biostratigraphy of this section has been well studied (Hori, 1990, 1993, 1997; Takeuchi, 2001; Matsuoka, 2004) and revealed that the section consists of lower Triassic to lower Jurassic bedded chert with thickness of >100 m (Hori, 1993; Matsuoka et al., 1994). Black chert which is suggested to be deposited during

T-OAE (Gröcke et al., 2011) and gray cherts which have deposited before and after the black chert, named as gray (E) and gray (W) respectively, were collected from this section.

9.2.2 Major element analysis

Major compositions of black and gray cherts collected from Katsuyama section were determined using a Rigaku ZSX-101e X-ray fluorescence spectrometer (XRF). About 2 g of powdered chert sample was mixed with a flux composed of 20% $Li_2B_4O_7$ and 80% $LiBO_2$ (Johnson-Matthy, Spectro flux 100B). Samples and flux were placed into an agate mortar with 0.6 g of $LiNO_3$ serving as an oxidant. After the homogenization, the material was put into a platinum crucible and melted at 1200 ºC. After the melting for 6 min., the crucible was placed on a cooling fan, which made a glass bead. Since chert samples used here can be enriched in organic materials, powdered cherts were heated at 980 ºC before the mixing with flux, which enabled to determine the loss of ignition (LOI). Analytical conditions using XRF were 50 kV accelerating voltage and 50 mA beam current with rhodium K_α, L_α, and $L_{\beta1}$, and tungsten K_α and L_α sources. Accuracy and precision of these measurements were better than 3%, as estimated from the reported analysis of a reference rock JCh-1 (chert; Imai et al., 1996) and the repeated measurements of all the chert samples, respectively.

9.2.3 XAFS analysis

XAFS is a powerful method to determine the electronic structure and neighboring element using the absorption of X-ray. The XAFS spectrum is divided into two energy regions: X-ray absorption near edge structure (XANES) and extended X-ray absorption fine structure (EXAFS). The former gives information of electronic state (valence) and symmetry of coordination environment. The latter is sensitive to local structure of the center atom absorbing the incident X-ray (= Fe and S in this case) including such as interatomic distances and coordination numbers of neighboring atoms. Both XANES and EXAFS, though their origins are different, enable us to identify the

chemical species of the center atom, or the mineral if the atom forms certain mineral in the samples.

9.2.3.1 Iron K-edge XANES

In this study, Fe K-edge (7111 eV) XANES spectra were measured at BL-01B1 at SPring-8 (Hyogo, Japan). Prior to the measurements, the X-ray energy was calibrated with the pre-edge peak maximum of hematite at 7114 eV. XANES spectra of reference materials, pyrite, fayalite, chlorite, hornblende, illite, magnetite, goethite, and hematite, were measured in transmission mode, whereas those of chert samples were measured in fluorescence mode using a 19-element germanium (Ge) semiconductor detector. The measurements were conducted under ambient pressure and temperature. Obtained XANES spectra were analyzed using a REX2000 software (Rigaku Co. Ltd.). Contribution of various Fe species to each sample was estimated by calculating the XANES spectra of the unknown samples by the linear combination fitting (LCF) of the spectra of known reference materials. The LCF was conducted using no more than three minerals in the energy ranges of 7100–7180 eV. The quality of the fit was given by the residual value, the goodness-of-fit parameter *R*, defined

$$R = \frac{\sum[x_{obs}(\mathrm{E}) - x_{\mathrm{cal}}(\mathrm{E})]^2}{\sum[x_{obs}(\mathrm{E})]^2} \qquad (9-1)$$

where $\chi_{\mathrm{obs}}(E)$ and $\chi_{\mathrm{cal}}(E)$ are the experimental and calculated absorption coefficients at a given energy (E), respectively. The smaller R value means the better fit in the LCF procedure.

9.2.3.2 Iron K-edge EXAFS

To confirm and enhance the reliability of LCF, Fe K-edge EXAFS spectra were measured at BL-12C at Photon Factory (PF; Tsukuba, Japan). EXAFS spectra of reference materials, pyrite, chlorite, hornblende, illite, magnetite, goethite, and hematite, were measured in transmission mode, whereas those of chert samples were measured in

fluorescence mode using a 19-element Ge semiconductor detector. The measurements were conducted under ambient pressure and temperature. Obtained EXAFS spectra were analyzed using Athena software (Ravel and Newville, 2005). The energy unit was transformed from eV to $Å^{-1}$ to produce the EXAFS function $\chi(k)$, where k ($Å^{-1}$) is the photoelectron wave vector. The k^3-weigted EXAFS spectra were also fitted using LCF of reference materials at a k range of 2-10.2 $Å^{-1}$, by minimizing the residual of the fit which was also given by the residual value, the goodness-of-fit parameter R, defined by

$$R = \frac{\sum[x_{obs}(k) - x_{\text{cal}}(k)]^2}{\sum[x_{obs}(k)]^2} \qquad (9-2).$$

9.2.3.3 Sulfur K-edge XANES

Sulfur K-edge (2470 eV) XANES spectra were measured at BL-9A at PF. To minimize attenuation of incident X-rays by air, we enclosed the experimental apparatus in a chamber containing He gas. The X-ray energy was calibrated with the absorption peak maximum of elemental sulfur at 2470 eV. XANES spectra of reference materials, pyrrohotite, pyrite, native S, Na_2SO_3, $(NH_4)_2SO_4$, and gypsum, were measured in transmission mode, whereas those of chert samples were measured in fluorescence mode using a Lytle detector. Similar to Fe K-edge XANES, obtained spectra were analyzed using the REX2000 software (Rigaku Co. Ltd.). Contribution of various S species to each sample was calculated by the Lorentzian Function and arctangent based on the procedure performed by Waldo et al. (1991) and Vairavamurthy et al. (1994).

9.3 Results

9.3.1 Major elements

The results of major element compositions determined using XRF are listed in Table 9−1. As expected, all the samples are composed of a large amount of SiO_2 (> 95 wt.%). Black chert contained largest amount of Al, whereas the least amount of total Fe, resulted in the lowest Fe/Al ratio among the samples. Meanwhile, Fe/Al ratio of gray

(W) deposited next to the black chert had the highest Fe/Al ratio. The LOI of gray (E) which deposited before the black chert was the smallest among the chert samples analyzed here. The low Fe/Al ratio and high LOI observed in the black chert suggests the increased input of Al due to the increase in global weathering and burial of organic materials. These results harmonize with the T-OAE characteristics (Jenkyns, 1988; Jenkyns et al., 2002; Cohen et al., 2004; Waltham and Gröcke, 2006).

9.3.2 Iron K-edge XANES

The Fe K-edge XANES spectra of reference materials used in LCF are shown in Fig. 9−3A. XANES spectra of black and gray cherts are shown in Fig. 9−3B with fitting results and contributions of each fraction are listed in Table 9−2. The spectra of chert samples were similar with each other, meaning that the Fe-bearing minerals in these cherts are almost identical. The characteristics of these spectra resemble that of pyrite, particularly, absorbance does not decrease significantly after the absorption maximum. Interestingly, the absorption maximum of chert samples and pyrite are slightly different. The largest absorption of black chert was observed at 7127.7 eV, whereas that of gray cherts was at 7131.8 eV. These energies slightly shifted to the left side compared to pyrite (7135.0 eV), suggests the existence of other Fe minerals in black and gray cherts. Surprisingly, the best LCF was achieved when assuming the contribution of goethite in black and gray cherts (Table 9−2). The abundance of goethite in the black chert was estimated to be 49%, whereas those of gray (E) and (W) cherts were 26 and 47%, respectively. The minerals in black and gray cherts are further discussed later based on the EXAFS results.

9.3.3 Iron K-edge EXAFS

The k^3-weighted Fe K-edge EXAFS spectra of reference materials used in LCF are shown in Fig. 9−4A, and those of chert samples are shown in Fig. 9−4B with fitting results and contribution of each fraction are listed in Table 9−2. EXAFS spectra of black and gray cherts evidently showed the similarity to that of pyrite which clearly

shows different spectra from other minerals. Pyrite had the larger EXAFS oscillation than other minerals and showed signature of splitting peaks at k = 6 and 8 ($Å^{-1}$). In addition, only pyrite showed positive amplitude at k = 4.7, which gives clear distinction between pyrite and Fe^{3+}-bearing minerals. Thus, pyrite should be the main component for black and gray cherts. The EXAFS-LCF confirmed that 75% and 100% of Fe-bearing minerals were pyrite and in black and gray cherts, respectively. It should be noted that EXAFS-LCF showed different end-member mineral compositions from those of XANES-LCF. In the case of the black chert, the smallest R value was obtained by assuming pyrite, goethite, and magnetite which was not included by XANES analysis. Meanwhile, EXAFS-LCF required only pyrite to obtain the smallest R value for gray chert.

9.3.4 Sulfur K-edge XANES

Sulfur K-edge XANES spectra of reference materials are shown in Fig. 9−5A. All the samples were dominated by reduced form of S as S_2^{2-} corresponding to the pyrite (FeS_2) (Table 9−3, Fig. 9−5B). This result is consistent with the Fe K-edge results. The FeS fraction was not present in our analysis. Surprisingly, both black and gray cherts showed peaks at 2480.5 eV which suggest the slight (less than 10%) existence of oxidized S (S^{6+}). The mole fraction of sulfide/sulfate ratio becomes larger in the order of gray (E) > black > gray (W).

9.4 Discussion

9.4.1 Mineral composition of cherts

Black and gray cherts collected from Katsuyama section shows the existence of pyrite with blackish color. Therefore, pyrite can play a role to make the color of chert darker. Although XANES spectra may not be sufficient to identify the difference between black and gray cherts, the important results we obtained is the fact that XANES spectra of black and gray cherts show similarity with pyrite. As described in Section

9.3.2, if pyrite is not a main mineral in black and gray cherts, XANES spectra should show much sharper peak in the XANES region with lower absorption around 7200 eV. This result clearly indicates that pyrite is the major Fe-bearing mineral in dark colored chert at least collected in the current study, though XANES-LCF suggests that the half of Fe species in the black chert was goethite. Compared to the XANES analysis, EXAFS-LCF shows higher abundance of pyrite in black and gray cherts (Table 9−2). EXAFS oscillation of gray chert only requires pyrite to achieve the smallest R value. Although the lower region (< 4 Å), which can be affected by the XANES oscillation, of EXAFS spectra does not fit well, the higher region shows clear similarity with pyrite (Fig. 9−4B). The notable result is that both XANES and EXAFS do not show the existence of clay minerals such as illite in black and gray cherts. The different results obtained between XANES- and EXAFS-LCF mean that almost all the Fe incorporated in the gray chert composed of pyrite. However, small amount of Fe can be (i) slightly oxidized during the weathering, and/or (ii) composed of Fe^{3+} adsorbed on organic matters. The identification of Fe^{3+} component in pyrite-rich material is important, since it is difficult to determine the Fe^{3+} component using the ^{57}Fe Mössbauer spectroscopy (e.g., Sato et al., 2011).

The dominance of pyrite with slight existence of oxidized form of Fe is also supported by the S K-edge XANES (Table 9−3, Fig. 9−5B). Our estimation suggests that more than 90% of S exist as pyrite. It should be noted that the smallest presence of oxidized sulfur (sulfate as S^{6+}) is obtained from gray (E), while the largest abundance of S^{6+} is estimated for gray (W). Based on the geology and paleontology at the Katsuyama section (e.g., Matsuoka et al., 1994), the bedded chert has become younger toward the western direction, and thus the youngest chert examined in this paper is gray (W) whereas the oldest one is gray (E). Therefore, the most reducing environment is not suggested to be achieved during the deposition of the black chert.

9.4.2 Implications for T-OAE

Our S K-edge XANES indicates gradual recovery of reducing condition from

gray (E), thorough black, to gray (W). The darker color can reflect the increasing depositional rate of organic materials as suggested by the higher LOI compared to the gray cherts, which can be related to the higher weathering rate and resulted in the release of oxygen. The increase in oxygen concentration triggered by the tectonic factor is also suggested to occur at Precambrian Era (DesMarais, 1992; Campbell and Allen, 2008). These studies suggested that collisions between continents cause to form higher mountains which were rapidly eroded as a source of large amounts of nutrients into the ocean. The increased sedimentation rate led to the burial of organic matters (and pyrite), which was not subject to degradation by the reaction with the free oxygen (O_2). As a result, O_2 produced by algae and cyanobacteria which were increased by the enhanced input of nutrients was released to the atmosphere. Part of this assumption is supported by the molecular biological evidence that the open ocean planktonic algae started to be diversified at ca. 175 Ma as algal symbionts to radiolarians (See Fig. 3 of Decelle et al., 2012). This kind of tectonic control on the carbon burial and release of O_2 is also suggested for modern environment at Himalayan orogeny (Derry and France-Lanord, 1996; France-Lanord and Derry, 1997; Galy et al., 2007).

The continental weathering is suggested to increase from deposition of gray (E) to black cherts based on the Fe/Al ratios and LOI, while rapidly decreased to the black to gray (W) cherts (Table 9−1). If this is the case, the most reducing environment is expected to observe form black chert. Although more reducing environment is suggested for black chert than gray (W) chert, S K-edge XANES shows the smallest contribution of sulfate fraction from gray (E) chert (Table 9−3; Fig. 9−5B).

Another possibility to explain the increasing contribution of sulfate fraction in the order of gray (E) > black > gray (W) is the recovery, or neutralization of seawater, from seawater acidification. Recently, Hermoso et al. (2012) showed that high pCO_2 levels led to the seawater acidification prior to and during the Early Toarcian $\delta^{13}C$ excursion. Assuming that the T-OAE maximum occurred when the black chert deposited, recovery from seawater acidification is consistent with our S XANES data. As shown in Eh-pH diagrams, the boundary between pyrite and sulfate or hematite draws diagonally right down curve (Figs. 9−6). These facts mean that, under the same

redox condition, the increase in pH results in the formation of oxidized form of S and Fe. Therefore, increasing contribution of sulfate fraction along with the depositional order of cherts suggests that gradual recovery from oceanic acidification occurred during the T-OAE.

9.5 Conclusions

The attempt to determine the Fe and S species in chert samples using XAFS analysis was performed. Iron K-edge XANES and EXAFS analysis showed large contribution of pyrite, which was confirmed by S K-edge XANES. The EXAFS oscillation of black chert showed slight contribution of oxidized form of Fe-bearing minerals, which was difficult to identify using the ^{57}Fe Mössbauer spectroscopy analysis. The increasing in the sulfate contribution was observed from S K-edge XANES along with the depositional order. It is suggested that the data reflected the gradual recovery from oceanic acidification during the T-OAE.

Table 9−1. Major element compositions (%) of chart samples.

Samples	SiO_2	TiO_2	Al_2O_3	$Fe_2O_3^*$	MnO	MgO	CaO	Na_2O	K_2O	P_2O_5	Total	LOI	Fe/Al
Gray (W)	96.8	0.033	0.860	1.59	0.023	0.071	0.055	0.025	0.18	0.022	99.50	1.50	1.85
Black	98.6	0.052	1.40	0.515	0.004	0.141	0.086	0.026	0.32	0.046	100.80	1.51	0.37
Gray (E)	99.6	0.027	0.754	0.729	0.007	0.056	0.304	0.025	0.14	0.213	101.50	0.98	0.97

* Total Fe as Fe_2O_3

Table 9−2. The LCF result of Fe K-edge XANES and EXAFS.

	Py	Fa	Chl	Hbl	Ill	Mag	Goet	Hem	*R* (%)
Gray (W) (XANES)	53						47		0.028
Black (XANES)	51						49		0.024
Gray (E) (XANES)	74						26		0.029
Gray (W) (EXAFS)	100								0.092
Black (EXAFS)	75					9	16		0.174

Py: pyrite; Fa: fayalite; Cho: choorite; Ill: illite; Sm: smectite; Mag: magnetite; Goet: goethite; Hem: hematite

Table 9−3. Contribution of S species.

	Pyrrohotite	Pyrite	+4	+6
Gray (W)		93.4		6.6
Black		94.2		5.8
Gray (E)		96.9		3.1

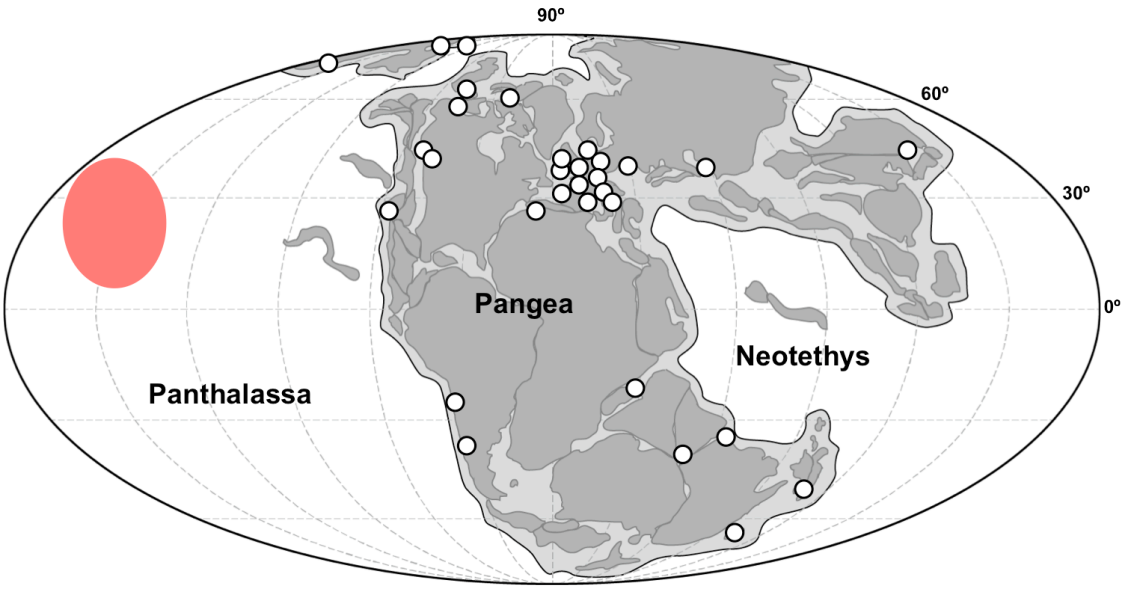

Fig. 9−1. Early Jurassic palaeogeographical map showing the global distribution of previously reported T-OAE. The palaeogeographical map is after Scotese (2007). Locations of the T-OAEs are based mainly on Jenkens (1988), Jenkyns et al. (2002), and Cohen et al. (2007). The red area indicates the estimated depositional area of the chert samples used in this study (Ando et al., 2001).

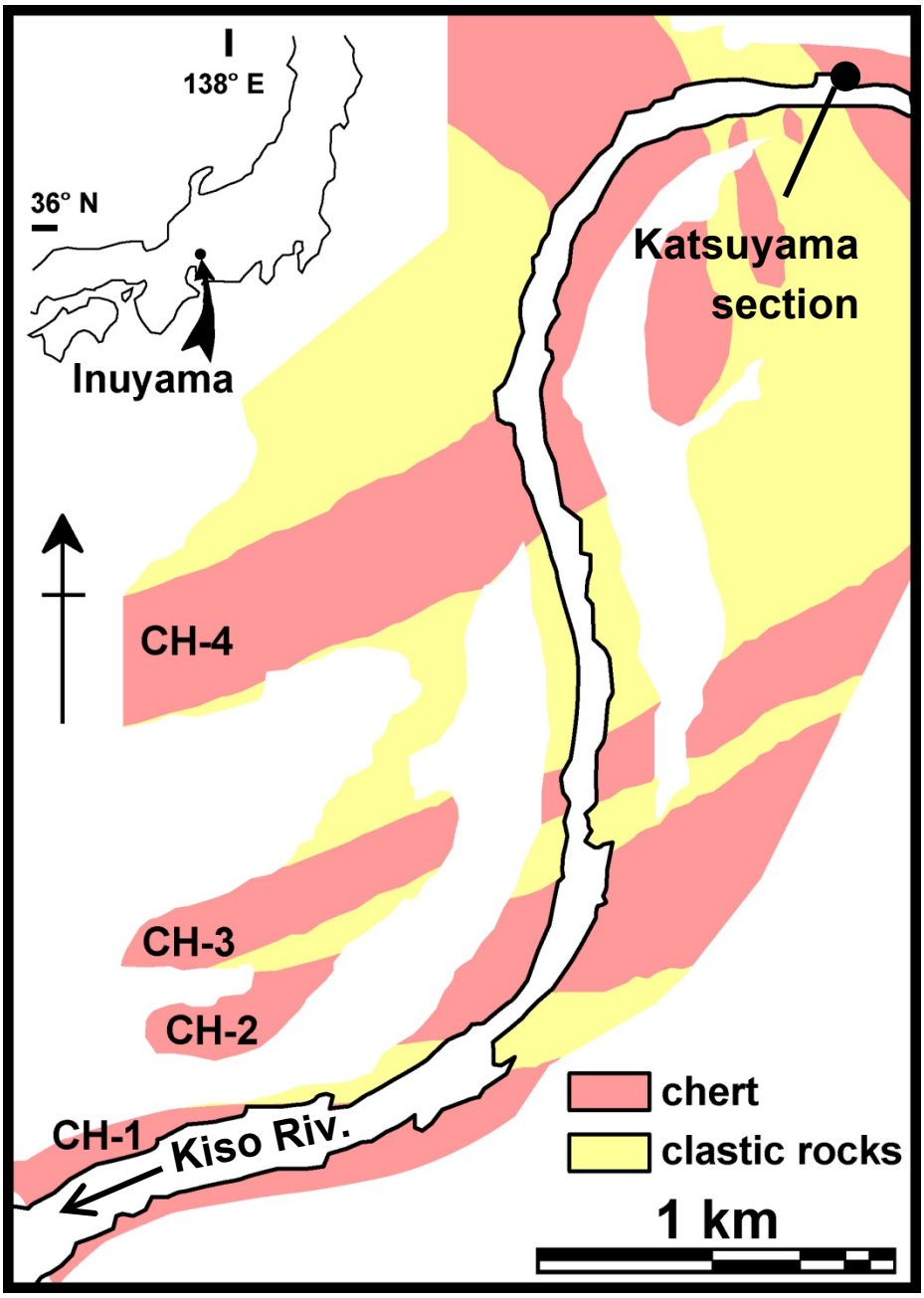

Fig. 9−2. Geological map of Inuyama area (after Yao, 1980).

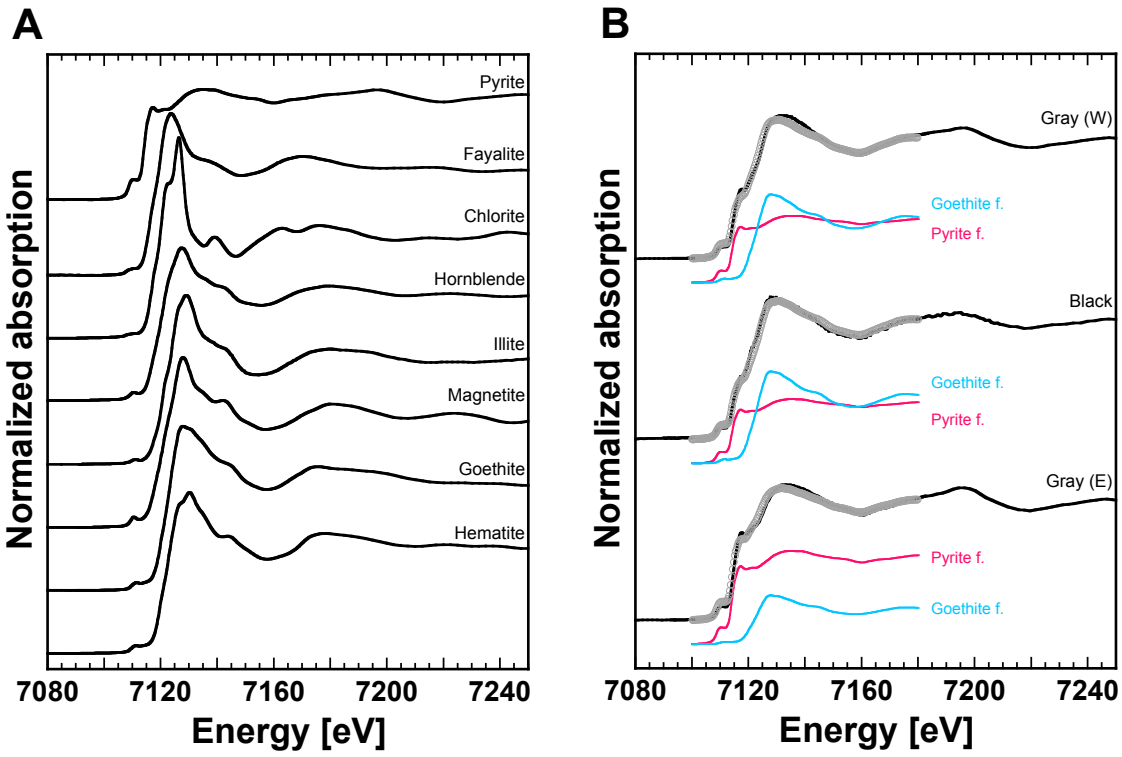

Fig. 9−3. Iron K-edge XANES spectra of (A) standard minerals used to fit the measured chert samples and (B) chert samples collected from Katsuyama section. Solid line denotes measured spectra and blue circle shows fitting results using the parameters listed in Table 9−2. Contribution of each fraction is also shown.

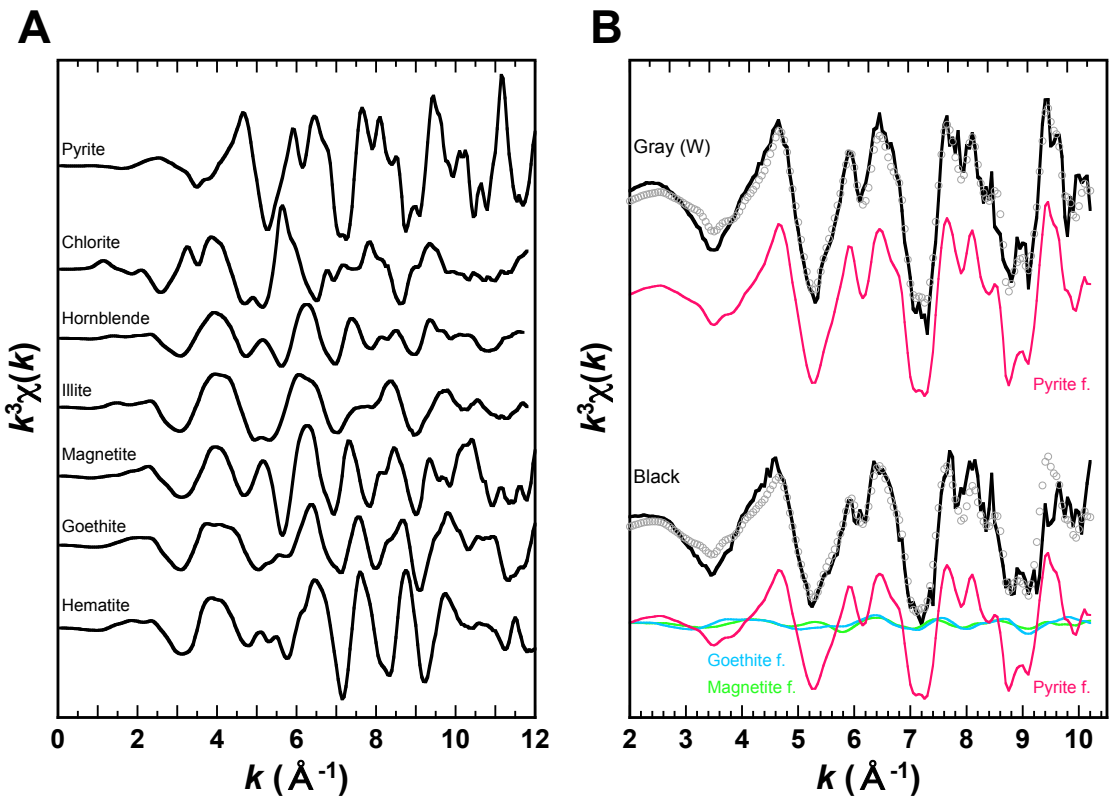

Fig. 9−4. Iron K-edge EXAFS spectra of (A) standard minerals used to fit the measured chert samples and (B) chert samples with fitting results and contributions of each mineral components listed in Table 9−2.

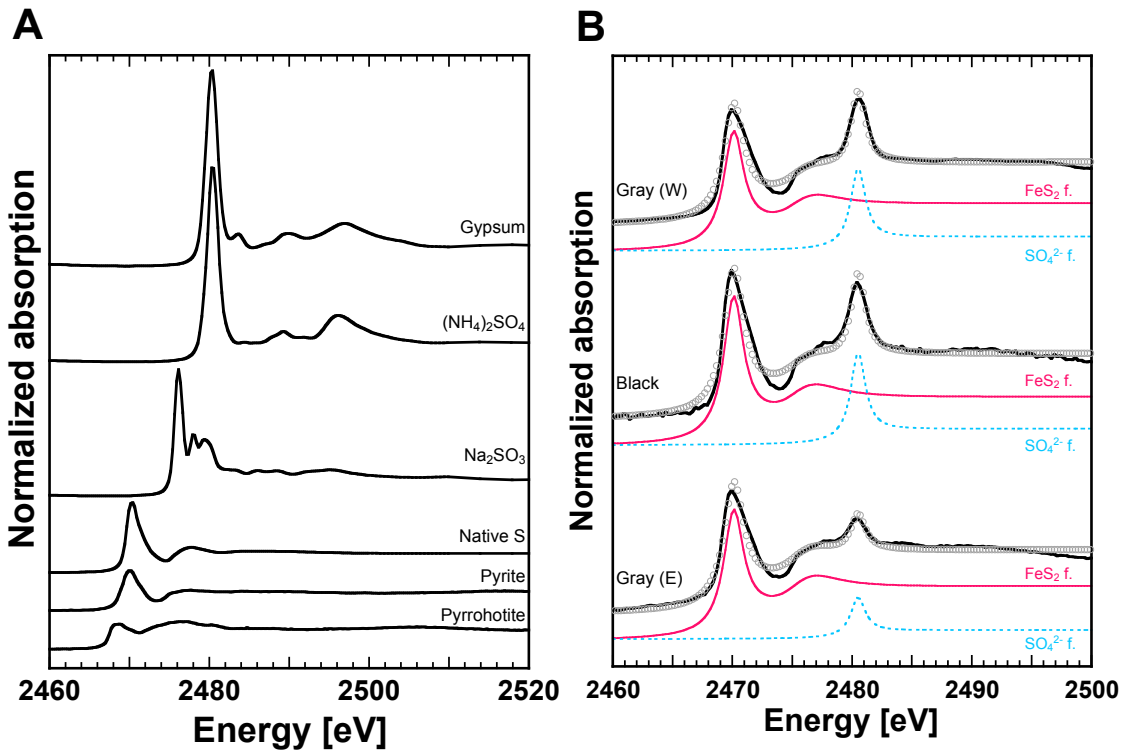

Fig. 9−5. Sulfur K-edge XANES spectra of (A) standard minerals used to fit the measured chert samples and (B) chert samples with fitting results and contributions of various oxidation states of S species listed in Table 9−3.

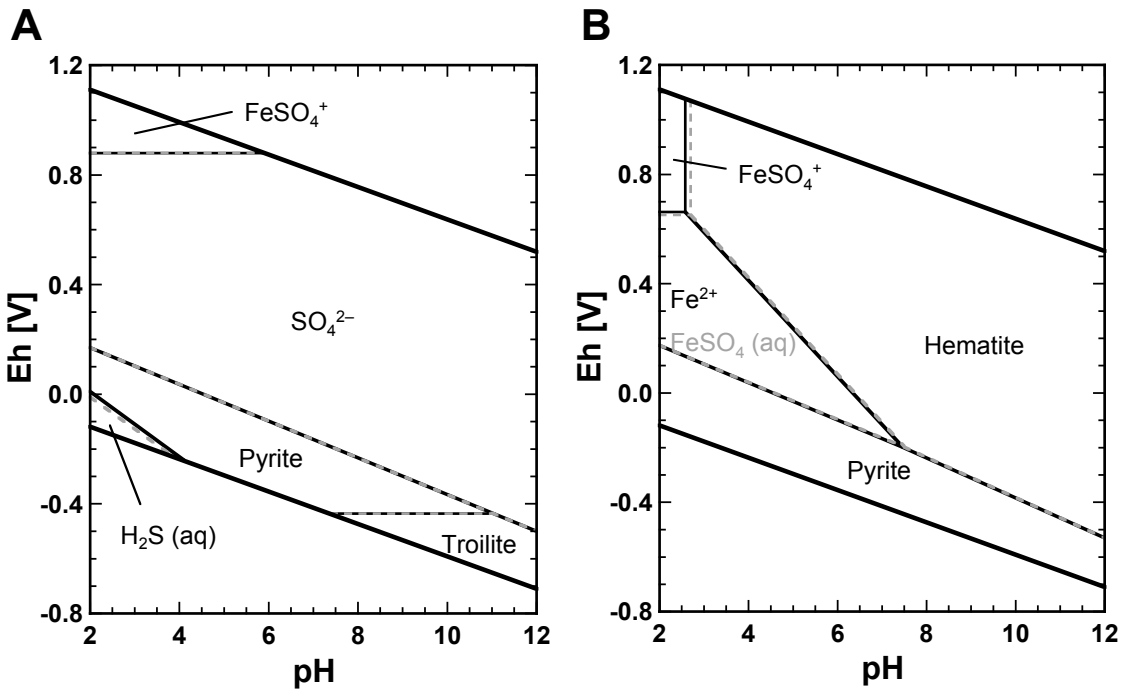

Fig. 9−6. Eh-pH diagram of (A) S and (B) Fe under 25 ºC, 1 atm using the Geochemist's Workbench (GWB, Volume 6; Bethke, 2006). In both diagrams, concentration of Fe^{2+} and HCO_3^- were fixed at 1 μM and 2.25 mM, respectively. Meanwhile, SO_4^{2-} concentration was varied from 4 mM (shown as black solid lines) to 8 mM (gray dashed lines). Only the soluble Fe species changed from Fe^{2+} to $FeSO_4$ (aq) by the increase of SO_4^{2-} concentration.

Chapter 10

Conclusions

After the first discovery of Y in 1794, it had taken 113 years for separation of the naturally occurring REEs (Chapter 1). The chemical properties make REE the most unique geochemical tool to discuss the origin and reaction processes that samples had experienced. Establishment of the REE pattern in 1962 by A. Masuda has greatly contributed to the development of REE geochemistry (Masuda, 1962). Despite of the progress in this half a century, there are a couple of scientific fields that are still unclear or have not been studied. This PhD thesis focused on these fields.

In Chapter 2, the cause of positive Eu anomaly during the water-rock interaction which is still under discussion was investigated using synthesized basalts. Larger abundance of REEs was released from basalt that crystallized out plagioclase and augite to low salinity water compared to the 0.7 M NaCl solution. The REE fraction became larger with increasing water-rock interaction temperature. The basalt containing plagioclase and augite released larger abundances of REEs than the basaltic glass irrespective of any solution conditions, which can be due to the heterogeneous compositions of elements in the former particles. Since Eu/Eu* values were smaller when basalts contacted with 0.7 M NaCl solution, it is suggested that the possible positive Eu anomaly caused by the formation of stable Cl complex was less effective in this experiment. The Eu/Eu* values became larger with increasing reaction temperature when ultra-pure water was used, which can be applied to the water-rock reaction thermometer under low salinity condition.

In Chapters 3 and 4, stable isotopic fractionation of REEs during adsorption was investigated for the first time. In Chapter 3, three data consisting of Ce—abundance, stable isotope ratio, and chemical state—were provided for the first time. The REE distribution coefficient pattern combined with Ce L_{III}-edge XANES spectra suggested that Ce is not oxidized by ferrihydrite, but is oxidatively scavenged by δ-MnO_2, as expected from the Eh–pH diagrams. The degree of isotopic fractionation of Ce between

the liquid and solid phases increases as the redox condition becomes more oxic in the following order: adsorption without oxidation, Ce(IV) precipitation, and oxidative adsorption (incorporation). In particular, the latter two processes were distinguished by the Ce stable isotope ratio, and cannot be discerned using the Ce anomaly alone. It is expected that applying Ce geochemistry to Precambrian BIFs and carbonates in future research will lead to a better understanding of the paleo-redox state of the ancient oceans. However, this result was inconsistent with the studies reported for cations (Balistrieri et al., 2008) and did not follow the most important rule governing the equilibrium isotopic fractionation (Bigeleisen and Mayer, 1947). Therefore, the isotopic fractionation of neighboring REEs was examined to compare the fractionation data with that of Ce in Chapter 4. Adsorption experiments with Nd and Sm on ferrihydrite and δ-MnO_2 were performed again to determine the factors governing equilibrium isotopic fractionation among REEs. Heavier isotopes of Nd and Sm were found to be enriched in the solid phase. EXAFS analyses showed that shortening of REE–O bonds during adsorption was the governing factor responsible for equilibrium isotopic fractionation of Nd and Sm. In contrast, the coordination structures of adsorbed La, Ce, and Pr were more distorted than those of their aqua ions. This comparison among the REEs enables us to improve our understanding of the cause of such stable isotopic fractionation. The distorted adsorbed structure and the stability of hydrated species leads to lighter-isotope enrichment in the solid phase for Ce (and is also expected for La) adsorbed on ferrihydrite. In-depth analysis of the coordination environment, revealed by EXAFS analyses, was important to determining the mechanisms behind equilibrium isotopic fractionation. It is possible that the systematic isotopic fractionation over the REE series could be a new geochemical tool to study REE behavior during water−rock interaction in natural systems. These studies developed new possibilities for REE geochemistry and the cause of stable isotopic fractionation for heavy elements.

In Chapter 5, an interesting subject that has long been neglected in REE geochemistry although it certainly has a lot of potential, REEs in crude oil, was examined. This study provided complete REE patterns of crude oil for the first time and showed that (i) REE in crude oils can reflect their source rocks and sediments, and (ii)

REE in crude oils mainly form carboxyl and phenolate complexes, which induce a larger partition of REE into the crude oil relative to the coexisting water. However, the retention of carboxyl group in crude oil is generally unusual, since it can be decomposed during the maturation process. In Chapter 6, therefore, the maturation process was examined by measuring REE concentration in oil samples without containing carboxyl group collected from 5 oil fields in Japan and performing a laboratory experiment simulating the release of REE from organic phase during the oil maturation. The REE abundance of oils without containing carboxyl group was more than three orders of magnitude lower than those showing existence of the carboxyl group (Chapter 5). REE distribution experiment showed that REEs adsorbed on humic acid were released to the solid phase in association with the decrease of the concentration of carboxyl group. A comparison between oils with or without containing carboxyl group suggests that approximately 16 g of total REEs are released during the production of a barrel of crude oil. As such, studies in Chapters 5 and 6 bring a new possibility on the fusion of organic and inorganic geochemistry.

Studies performed from Chapters 2 to 6, which showed new possibilities for REE geochemistry, are linked to the Chapters 8 and 9 via Chapter 7. In Chapter 7, Mn carbonate nodules interbedded in red siliceous mudstone of the Tamba-Mino-Ashio Belt was investigated with the combination of geochemical and geological methods. Microscopic observation showed the authigenic rhodochrosite and numerous radiolarian shells without any clay minerals, and the spherule of rhodochrosite is abraded in consideration with the preserved condition of radiolarians. Radiolarian faunas from both the Mn carbonate nodule and their host rocks are correlative to the same Bajocian age of Middle Jurassic, but the host red siliceous mudstones are somewhat younger than the Mn nodule suggested by the radiolarian age. These two evidences are explained by the facts that (i) spherules of rhodochrosite developed to involve radiolarian test at first at the depositional site without clay minerals and (ii) these isolated spherules moved to the depositional site of red siliceous mudstone where clay minerals are present. XRD analysis confirmed the existence of rhodochrosite and quartz in Mn carbonate. The bulk rock REE pattern normalized by PAAS showed the positive Ce anomaly, whereas

XANES analysis showed Ce in Mn carbonate exists as trivalent state. In consideration with the REE pattern after the leaching and the occurrence state of rhodochrosite spherules in the Mn nodule, the best explanation of Mn nodule formation so far is that rhodochrosite is primarily formed and subsequently transferred to the different site where siliceous mudstone was deposited. In addition, δ^{142}Ce value of Mn carbonate nodule was enriched in heavier isotopes than that of siliceous mudstone beyond the analytical uncertainty. Since the experimental study performed in Chapter 3 showed that the lighter Ce was preferentially adsorbed on δ-MnO_2, the heavier isotope enrichment in the nodule can decline the possibility of the primary formation of MnO_2 with following alteration. This Chapter successfully showed a possible application of stable isotope ratio to geological study.

The rest of the thesis, Chapters 8 and 9, showed that the XAFS analysis is a powerful geochemical tool to determine the Fe species in chert samples and brings a new perception for geological study. The first attempt to determine Fe species in chert samples using XAFS analysis was performed in Chapter 8. The XANES analysis showed that all the red chert contained hematite, while the green and the white cherts did not. The incorporation of chlorite is suggested for some of the red, the green, and the white cherts, which is further confirmed by EXAFS analysis. The average valence state of Fe is lower in the green and the white cherts than in the red chert, which can be due to the reduction of hematite. The stratigraphic change in the Fe-bearing minerals was observed at the middle Carnian, and it is suggested that (i) the relatively stable mineral compositional ratios observed from unit 2 to the middle part of unit 3 corresponding to the early to middle Carnian reflect dry climate conditions in the source region, (ii) the significant perturbation in the mineral composition suddenly observed from the upper part of unit 3 to lower part of unit 5 at the middle Carnian reflects wet climate conditions known as the CPE, and (iii) the appearance of chlorite and the recovery of mineral composition ratios observed in R6-3 at the late Carnian indicate the return to dry climate conditions similar to those prior to the CPE. In consideration with the modern ocean environment, the increased input of reduced Fe in chlorite or smectite affects the biological productivity. This study shows that the drastic but brief

environmental change in the continental area is preserved in the pelagic chert samples. In Chapter 9, the Fe and S species in chert samples were determined using XAFS analysis. Iron K-edge XANES and EXAFS analyses showed large contribution of pyrite, which was confirmed by S K-edge XANES. The EXAFS oscillation of black chert showed slight contribution of oxidized form of Fe-bearing minerals, which was difficult to identify using the ^{57}Fe Mössbauer spectroscopy analysis. The increasing in the sulfate contribution was observed from S K-edge XANES along with the depositional order. It is suggested that the data reflected the gradual recovery from oceanic acidification during the T-OAE. As such, the application of XAFS for chert samples to determine the chemical species is a very important and powerful tool to study the paleoenvironment. In addition, as performed in Chapter 7, it is possible that the application of stable isotope ratio brings another evidence to confirm the suggestions given by the XAFS analysis.

In this decade, widespread development of ICP-MS makes several researchers misunderstood that “REE geochemistry is over”. However, studies performed in Chapters 2 to 6 in this PhD thesis clearly deny this misunderstanding. The thesis also indicates that the method performed in these Chapters is a useful and powerful tool to clarify the paleoenvironment. To have a “micro” perspective is important for geochemistry, whereas a point of “macro” view is necessary for geology. I would like to emphasize that either “micro” or “macro” is not a choice but both “micro” and “macro” should be combined together to unveil the mystery of Earth (and Planetary) Systems Science (Fig. 10–1).

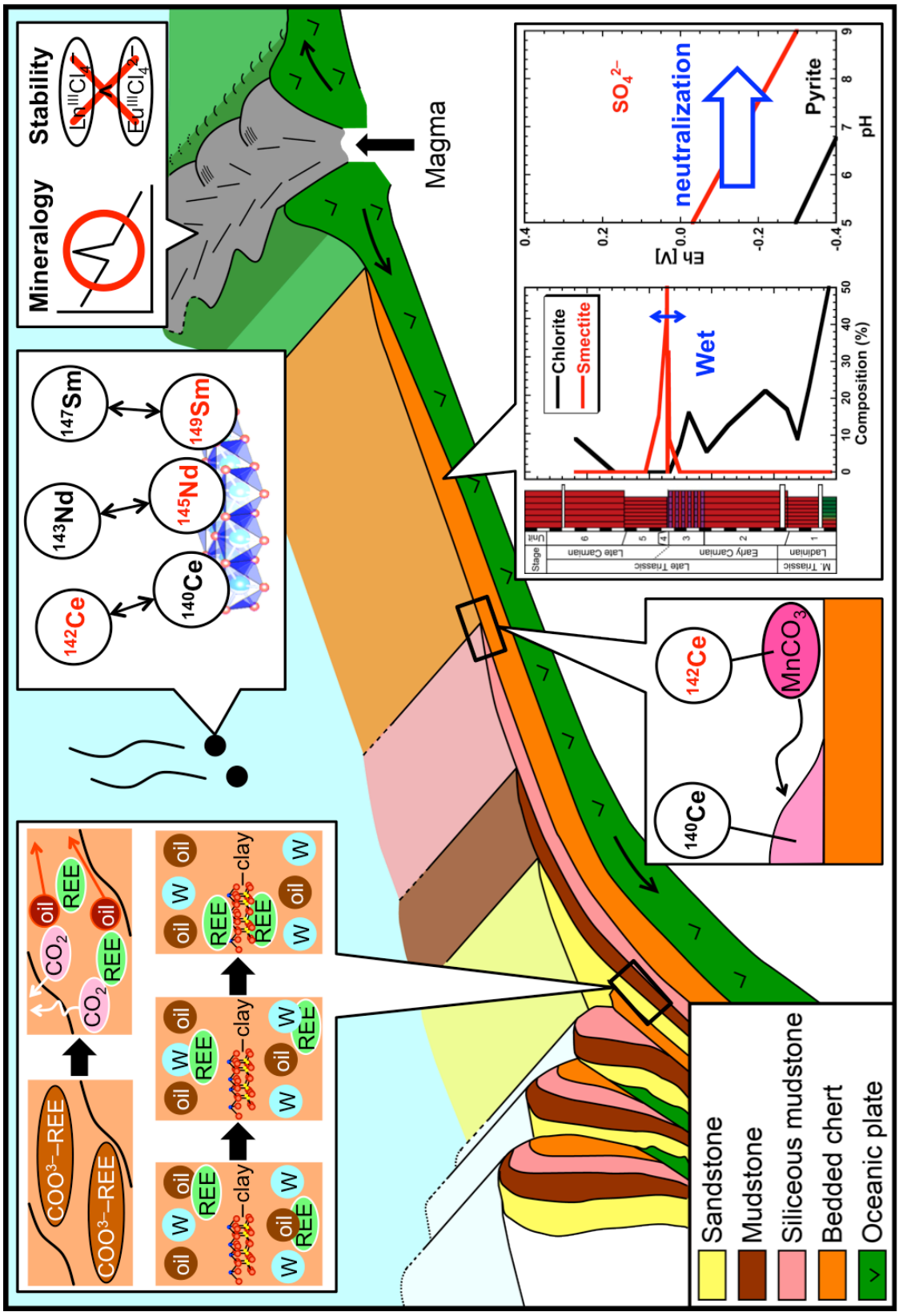

Fig. 10–1. Schematic illustration of the concluding of the PhD thesis.

Appendix

A comprehensive geochemical study on mud volcanoes in the Junggar Basin, Northwestern China

1 Introduction

Mud volcanoes, which are characterized by the release of mud, water, and gases, are found all over the world, particularly in compressional tectonic settings such as in accretionary complexes along subduction zones (Dimitrov, 2002, 2003; Kholodov, 2002; Kopf, 2002). Similar to magmatic volcanoes, the release of fluids from mud volcanoes may occur during the quiescent phase or the eruptive periods. Mud, water, and gases typically ascend through conduits from pressurized reservoirs (e.g., Kopf, 2002). Dimitrov (2002) summarized the factors controlling the occurrence of mud volcanoes: (i) recent tectonic activity, particularly compressional regime; (ii) rapid loading of rocks due to fast sedimentation, accretion, or overthrusting; (iii) active hydrocarbon generation; and (iv) existence of thick, fine-grained, soft sediments deep in the sedimentary succession. The main factor of mud volcano formation is considered to be a gravitative instability in low-density sediments below the high-density rocks induced by fast sedimentation. Gravitative instability provides mud diapirism, i.e., the intrusion of shale or clay into overburdened sediments.

Methane is commonly a dominant component in emitted gases from mud volcanoes (e.g., Dimitrov, 2002, 2003; Etiope and Milkov, 2004), with an average concentration of 90.6% (v/v) (Etiope et al., 2009a). The methane flux from mud volcanoes to the atmosphere is estimated to be between 10.3 and 12.6 Tg y^{-1} (Dimitrov, 2002), 5−10 Tg y^{-1} (Etiope and Klusman, 2002), 5 Tg y^{-1} (Dimitrov, 2003), and 6−9 Tg y^{-1} (Etiope and Milkov, 2004), and more recently, 10−20 Tg y^{-1} (Etiope et al., 2011). These estimates suggest that mud volcanoes represent an important natural source of atmospheric methane considered in global greenhouse gas emission inventories (Etiope, 2010).

More than 76% of terrestrial mud volcanoes release thermogenic methane

(Etiope et al., 2009a), suggesting that gases released from mud volcanoes can be related to petroleum seepage system. On the other hand, $\delta^{13}C$ values of CO_2 released from mud volcanoes vary to a large degree (−20 to +25‰ VPDB), suggesting that anaerobic biodegradation occurs (Etiope et al., 2009b). Anaerobic biodegradation of oil and natural gas is described to be mostly limited to shallow reservoirs, generally shallower than 2000 m where temperature is below 60−80 °C (Pallasser, 2000; Feyzullayev and Movsumova, 2001). Etiope et al. (2009b) showed that the reservoir depth of Azerbaijan mud volcanoes releasing ^{13}C-enriched CO_2 ($\delta^{13}C$ values of CO_2 are larger than +5‰ VPDB) is shallower than 2000 m, while the reservoir depth of mud volcanoes releasing smaller $\delta^{13}C$ values of CO_2 (−20 to ±0‰ VPDB) is deeper than 2000 m up to 6000 m. However, they noted that anaerobic biodegradation of petroleum may take place at shallower depths above the deep non-biodegraded reservoir occurring along the seepage channels of the mud volcano system. In any case, such kind of information is insufficient, but needed to better understanding of mud volcano seepage system and microbial activities.

This paper presents geochemical data of mud, water, and gases discharged from mud volcanoes along the southern margin of the Junggar Basin in northwestern China to reveal their origin. Detailed studies on mud volcanoes in this region have been required for the lack of proper documentation. In addition, there are few studies on any mud volcanoes located along the coast, in the sea, or even onshore, based on the systematic analyses of the three components, namely, mud, water, and gas (e.g., Kopf et al., 2003; Lavrushin et al., 1996).

In the current study, several analyses were conducted to determine the origin of mud, water, and gas. For the mud, major and trace element compositions, including rare earth elements (REE), were determined and compared with the reported values of moraine samples from the northern Tianshan Mountains (Chang et al., 2000). The concentrations of major elements, REE, and isotopic compositions of hydrogen and oxygen were determined to understand the origin of water. Concentrations of the major component and their carbon and hydrogen isotope compositions were analyzed to evaluate the origin of the gases.

2 Geological setting

There are two large sedimentary basins in Xinjiang Province, northwestern China, Junggar Basin in the north and Tarim Basin in the south, which are separated by the Tianshan Mountains (Fig. A−1). There are several mud volcanoes along the southern margin of the Junggar Basin (Fu et al., 2007). According to Nansheng et al. (2008), the southern part of the Junggar Basin is underlain by 16 km thick sedimentary rocks deposited since Permian. The rocks are folded and faulted, especially in the Tianshan side of the Junggar Basin due to the orogenic activity of the Tianshan Mountains (Avouac et al., 1993). Due to the absence of igneous activity, the heat flow of the southern part of the basin is low, around 35 mW/m^2, and the geothermal gradient of the investigated area obtained by oil-testing and well-logging data is about 18 ºC/km with uncertainty ±1 ºC/km (Nansheng et al., 2008). Quaternary conglomerates, such as moraine, overlie the large part of the basin, including the study area (Avouac et al., 1993). Evaporite occurs around the study area (Ma et al., 2010).

The Junggar Basin is also well known for hosting crude oil (e.g., Carroll, 1998; Song et al., 2004; Nakada et al., 2010; Zheng et al., 2010). The Dushanzi oil field produces crude oil from Cretaceous and Tertiary reservoirs and lies outside the depositional limits of Upper Permian shales (Graham et al., 1990). Clayton et al. (1997) collected low maturity crude oil at Dushanzi oil field from Oligocene formation in the depth 3644−3656 m.

3 Mud volcano description

Mud volcanoes studies here are located in the cities of Wusu and Dushanzi, Xinjiang Uyghur Autonomous Region, northwest China. The locations of mud volcanoes are shown in Fig. A−1 and Table A−1. Sites 1−4 are located in the rural area south of Wusu City where many mud pies, flat mud extrusive feature (more than 20 in 1 km^2), with a gentle discharge of mud and gas, are found on a slope of a mountain range (Fig. A−2). Sites 6 and 7 are “twin” mud volcanoes located in the mountainous region about 8 km east from sites 1−4. Although samples were not collected, another mud pie

was identified about 1 km northwest from sites 6 and 7. Sites 8 and 9, situated near the Dushanzi oil refineries, are called Dushanzi mud volcanoes, which were discovered in July, 1995 (Wang et al., 1997) (Fig. A−2). Three mud pools were observed around site 9. Sites 1−4 are pie-shaped mud volcanoes, whereas sites 6−9 are cone-shaped (Figs. A−2I and J). Among the sites, site 7 is the highest mud volcano with a height of about 10 m (Figs. A−2F and J).

The crater sizes are listed in Table A−1. Among eight mud volcanoes, only the crater of site 6 is a true circle, while others are elliptical in shape (Table A−1 and Fig. A−2). As seen in Figs. A−2A, D, and E, some of the mud in the crater became dried. Those dried-up areas were not counted into the size. Therefore, in the past, the crater size of sites 1, 4, and 6 could have been larger than the present size.

Oil seepages were observed at sites 2, 3, 6, 7, 8, and 9. Among them, the largest abundance of oil is discharged at site 9, probably owing to its close location to the Dushanzi oil field. All the mud volcanoes were in the quiescent period with some visible degassing, as evidenced by bubbling in the craters and mud pools.

4 Sampling and analytical methods

4.1 Sampling

Mud, water, and gas samples were collected at each mud volcano. Surface organic soil samples near the mud volcanoes outside the mud flow were also collected for comparison (three, four, and one samples from sites 1−4, 6−7, and 8−9, respectively). Muddy water was collected directly from the crater of mud volcanoes. One fraction of the water was filtrated on site using 0.45 μm membrane filters (hydrophilic PTFE, ADVANTEC®), as used by Hensen et al. (2007). This filter allows a good separation of clay from water. The microbial activities were small enough not to affect the composition of water, because the composition did not change over the analytical error on repeated measurements for several time spans. After filtration, the water was further divided into two parts: one part was acidified to 2 wt.% nitric acid solution for the analyses of REE, and the remaining fraction without acid was used for

the analyses of major ions. About 10 ml of acid-free water sample was placed into bottles with no head space remaining for isotope analysis. Another fraction of water was not filtrated but was brought back to the laboratory for centrifugation into mud and water. Gases discharged from the muddy water in the crater were collected by an inverted funnel connected to a syringe and a silicon tube equipped with a stop-cock. After collecting the gases, the stop-cock was closed. Subsequently, the gases in the syringe were transferred to a glass bottle already evacuated using a tip-pierced needle.

4.2 Analytical methods

Temperature, pH, Eh, conductivity, and dissolved oxygen in muddy water were directly measured on site using handylab multi 12 (SCHOTT, Germany), a portable in-situ measuring instrument. The accuracies were 0.5% for conductivity and dissolved oxygen, whereas those for temperature, pH, and Eh were ±0.1 °C, ±0.01 pH unit, and ±1 mV, respectively. Alkalinity of the acid-free water sample was also determined on site by titration of 0.100 M and 0.0100 M HCl solution with 1% precision. In the laboratory, muddy water samples were centrifuged for 20 min at 2000 rpm to be separated into mud and water. Mineralogy of the mud samples was determined by a Rigaku MultiFlex X-ray diffractometer (XRD). XRD analyses were also conducted for clay fractions separated by elutriation to identify clay minerals better. Major and trace element compositions of mud and surface soils were determined using a Rigaku ZSX-101e X-ray fluorescence spectrometer (XRF). Analytical conditions were 50 kV accelerating voltage and 50 mA beam current with rhodium K_α, L_α, and $L_{\beta1}$, and tungsten K_α and L_α sources. REE concentrations of mud and surface soils were determined using inductively coupled plasma mass spectrometry (ICP-MS) (Agilent 7500) after the digestion of the samples in a mixture of HF, $HClO_4$, and HCl (Takahashi et al., 2002a). Accuracy and precision of the XRF analysis were better than 5%, whereas those of the REE obtained using ICP-MS were better than 3%, as estimated from the reported values of a standard rock JSl-1 (slate; Imai et al., 1995) and the repeated measurements of our samples.

Major cations (i.e., Na^+, Ca^{2+}, and Mg^{2+}) in the water samples were measured using cation chromatography (JASCO), whereas K^+ was measured using atomic absorption spectrometry (AA-646, Shimadzu). Major anions (i.e., F^-, Cl^-, Br^-, NO_3^-, and SO_4^{2-}) were measured using anion chromatography (Shimadzu). Analytical accuracy and precision of the major cations and anions were better than 5%. The δD values of water were measured using Thermo-Fisher Scientific DELTA plus XL (SI Science Co.) with an analytical error of ±1.0‰. The $\delta^{13}C$ and $\delta^{18}O$ of carbonate in the mud samples, and the $\delta^{18}O$ of water and $\delta^{13}C$ of dissolved carbonate in the water samples were measured using the Finnigan MAT Delta Plus mass spectrometer interfaced with Gas Bench II (Hori et al., 2009). Analytical uncertainties for $\delta^{13}C$ and $\delta^{18}O$ of carbonate in the mud samples were ±0.15 and ±0.19‰, respectively, whereas those in the water samples were ±0.04 and ±0.18‰, respectively. REE concentrations in water were determined using ICP-MS (Agillent 7500) after preconcentration using a column loaded with cation exchange resin (AG50W-X8; Takahashi et al., 2002a) because their concentrations were lower than the ppt level in water.

Concentrations and $\delta^{13}C$ of methane, ethane, and carbon dioxide in gas samples were measured at Hokkaido University using a continuous-flow gas chromatography (Agilent 6890) connected to an isotope-ratio mass spectrometry (Thermo Finnigan MAT 252) system (GC/IRMS). Analytical accuracy of the concentrations of CH_4 and CO_2 was better than 1%, whereas that of C_2H_6 was better than 5%. Analytical precision of the concentrations of CH_4, CO_2, and C_2H_6 was better than 5%. Analytical error of $\delta^{13}C$ of CH_4 and CO_2 was ±0.3‰, whereas that of C_2H_6 was ±0.7‰. Details of the method for isotopic composition were given in Tsunogai et al. (2002). The N_2 and O_2 concentrations of gas samples were also measured with 1% accuracy and 5% precision for both analyses.

The δD values of methane and ethane were measured at G.G. Hatch Isotope Laboratories, University of Ottawa. Calibration and normalization were conducted by the online combustion of two international standards (i.e., NGS1-8559 and NGS2-8560) and one internal standard. Methane and ethane were isolated by GC using a PoraBOND Q column (27.5 m long, 10 μm film thickness, 2 ml min^{-1} flow at −15 °C) on an HP

6890 gas chromatograph interfaced to a XP Finnigan-Mat IRMS. Precision of δD analysis was ±2‰. Concentrations of H_2, C_3 and C_4 of the gas samples were determined using a Shimadzu GC-14B (Sumika Chemical Analysis Service Co.) with an analytical error of 2%. The detection limits of H_2, C_3, and C_4 were 30, 0.3, and 0.3 ppmv, respectively. Hereafter, all stable isotope compositions are expressed in the conventional delta (δ) notation, defined as per mil (‰) deviation from the reference standard VSMOW for hydrogen and oxygen, and VPDB for carbon.

5 Results

5.1 Mud and surface soils

Results of the XRD analysis show that all the mud samples contain albite, calcite, chlorite, illite, mica, quartz, and smectite (Table A−2). Anorthite and kaolinite are found in some samples. All samples contain high SiO_2, 58−65 wt.% and Al_2O_3, 13−23 wt.% (Table A−3). Mud samples collected from sites 6 and 7 contain high Fe_2O_3 (total) and MnO. Concentrations of the major elements in mud and surface soil are normalized to the reported values of moraine samples from the northern Tianshan Mountains (Chang et al., 2000) (Fig. A−3). Major element concentrations, except for Ca, show similar values to those of moraine samples (Fig. A−3).

REE concentrations in mud and surface soil samples are reported in Table A−4. They are normalized to an average upper continental crust (UCC) (Taylor and McLennan, 1985) as shown in Fig. A−4A. All samples are depleted in light-REE (LREE) with variation at Ce and Eu (i.e., Ce and Eu anomalies, respectively), whereas they are all almost flat in heavy-REE (HREE). REE normalized to the average values of moraines from the northern Tianshan Mountains (Chang et al., 2000) are almost flat with positive Eu anomalies, except for a mud sample at site 9 (Fig. A−4B).

Major and trace element concentrations (Table A−3) are normalized to the average UCC and are plotted in Fig. A−5. Elements are arranged from left to right in the order of increasing abundance in the average Mesozoic-Cenozoic greywacke (Condie, 1993) relative to UCC (Fig. A−5). Although the abundance of elements on the left side

varies widely, elements on the right side, especially after Si, show gradual enrichment.

5.2 Water

Table A−5 lists the pH, Eh, temperature, conductivity, salinity, dissolved oxygen, alkalinity, concentration of major components (i.e., F^-, Cl^-, Br^-, NO_3^-, SO_4^{2-}, K^+, Na^+, Ca^{2+}, and Mg^{2+}), δD, and $\delta^{18}O$ isotope compositions for water and $\delta^{13}C$ for dissolved carbonate. The concentrations of almost all ions in the water from mud volcanoes are higher than those of river water.

The δD values of all water samples collected from mud volcanoes are between −57.1 and −99.2‰, and the $\delta^{18}O$ values for muddy water range from −1.0 to −5.7‰. On the other hand, the $\delta^{18}O$ value of river water (−10.6‰) at site 5 is much smaller than that of muddy water, though the δD value of river water at the site (−71.2‰) is within the range of those collected from mud volcanoes. In the δD and $\delta^{18}O$ diagram (Fig. A−6), the water at site 5 lies on the meteoric water line and is plotted in the field of North Xinjiang meteoric waters (Wei and Gasse, 1999). In comparison, muddy waters show an ^{18}O shift from meteoric waters. Moreover, data on muddy waters from sites 1−4 form a parallel regression line with the meteoric water line. Samples collected from sites 6 and 7 lie slightly on the right side of the regression line of sites 1−4, whereas sites 8 and 9 lie on the left side. The $\delta^{13}C$ values of dissolved carbonate are within the range of +35.6 to −23.3‰.

Although REE abundances in the water samples are variable, most samples are rich in HREE with positive Ce and Eu anomalies (Table A−6 and Fig. A−7). However, the river water sample at site 5 shows an HREE-depleted pattern with a negative Ce anomaly (Fig. A−7).

Dia et al. (1999) suggested that alkalinity records the reactions with carbonates and silicates, whereas Cl^- is sensitive to diagenetic processes and seawater interaction. In addition, Na and K can characterize the contribution from dissolution of host rock and/or leaching from clay minerals. In Na/Cl versus Alk/Cl (Fig. A−8A) and K/Cl versus Alk/Cl (Fig. A−8B) diagrams, water samples collected from the mud volcanoes

are plotted in three separated areas: (i) sites 1−4, (ii) sites 6 and 7, and (iii) sites 8 and 9.

5.3 Gas

Similar to other mud volcanoes in the world (e.g., Dimitrov, 2002, 2003; Etiope and Milkov, 2004; Etiope et al., 2009a), methane is the main component of gases emitted from the Xinjiang mud volcanoes (Table A−7). In Table A−7, all compositional data were corrected for air contamination. Raw analyses showed that the contamination of O_2 was 11.9, 3.2, 3.5, 3.6, 3.7, and 9.3% for sites 2, 4, 6, 7, 8, and 9, respectively. Given that the concentrations of methane and ethane collected from mud volcanoes are more than 10^4 higher than those of atmospheric value, the correction was not conducted for the $\delta^{13}C$ of both methane and ethane. On the other hand, the concentration of atmospheric CO_2 is about 385 ppmv (Keeling et al., 2009). This means that the $\delta^{13}C_{CO2}$ value of gases from mud volcanoes can be largely affected by air contamination because of a small difference in the concentrations between atmospheric CO_2 and CO_2 from mud volcanoes. Therefore, a re-calculation was conducted for the CO_2 concentration and $\delta^{13}C_{CO2}$ values by supposing that the atmospheric $\delta^{13}C_{CO2}$ values are about −8.5‰ (Keeling et al., 2005). Corrections for the concentration and isotope ratio of CO_2 were carried out using the following equation by assuming that original O_2 concentration is zero:

$$CO_{2\text{-cor.}} = (100 \times CO_{2\text{-meas.}}) - (O_2 \times CO_{2\text{-air}}) / (100 - O_2) \qquad \text{(A−1)}$$

where $CO_{2\text{-cor.}}$, $CO_{2\text{-meas.}}$, and $CO_{2\text{-air}}$ represent corrected CO_2, measured CO_2, and reported atmospheric CO_2 values, respectively, for both concentration and isotope ratio of carbon, while O_2 denotes measured raw concentration of O_2.

The $\delta^{13}C$ values of methane and ethane at each site are similar at around −40‰ and −30‰, respectively, whereas those of carbon dioxide are variable. Hydrogen gas was detected in the samples collected from sites 2, 4, 6, and 7. Although the H_2 concentration in the sample collected at site 4 was less than 100 ppm, further quantitative analysis was difficult because of its small peak. The intensities of the H_2 peaks at sites 2, 6, and 7 are much smaller than that in the gas sample collected at site 4.

The "Bernard ratio" $C_1/(C_2+C_3)$ versus $\delta^{13}C_1$ and C_2 diagrams show that all the samples are plotted in the thermogenic field (Fig. A−9). The values of $\delta^{13}C$ and δD for CH_4 also fall into the field of thermogenic origin, especially thermogenic gas related to petroleum field, following the Schoell plot (Schoell, 1983) (Fig. A−10).

6 Discussion

6.1 Origin of mud

The mud samples show major element compositions similar to moraines in the Tianshan Mountains (Fig. A−3); thus, mud and moraine likely have a similar source. The moraine forms as a mechanical mixture of basement rocks during glaciations (Chang et al., 2000). The wide variations of CaO are most likely explained by the different contents of calcite, semiquantitatively detected by the XRD patterns (Table A−2). Major element concentrations of mud samples collected from the "twin" mud volcanoes (i.e., sites 6 and 7) are similar, which confirms that they originated from the same source and ascended through separate vents or conduits. Mud samples collected from sites 6 and 7 also contain greater abundances of Fe_2O_3 (total), MnO, and P_2O_5 than those from other sites. The difference between the abundances of sites 6−7 and those from other samples is not only due to their source rocks, but also to an extensive water-rock interaction, which will be discussed in Section 6.2.

Mud and soils show similar normalized REE patterns (Fig. A−4), indicating that the mud originated from similar sedimentary rocks in this area, except for the sample at site 9. REE patterns normalized to the moraines collected from northern Tianshan Mountains (Chang et al., 2000) show flat patterns, except for Ce and Eu anomalies (Fig. A−4B). The Eu anomalies may be a result of the different abundances of plagioclase between moraines and our samples. In Fig. A−4B, a negative Eu anomaly is observed only for mud at site 9. This result suggests that the source layer of site 9 can be different from that of other sites or mixed with different rocks, which have less abundance of plagioclase in the paths during ascending.

Figure A−4 shows that the elements arranged on the right side are enriched,

where the order of the plots is similar to that in the Mesozoic and Cenozoic sandstones (Cutten et al., 2006). When a similar plot is made using North American Shale Composite (NASC; Gromet et al., 1984), the pattern shows enrichment in the right side, suggesting that typical sedimentary rocks can show such pattern. Furthermore, it has been reported that some igneous rocks present a pattern with enrichment toward the right side (e.g., Kawano et al., 2006). However, the absence of igneous rocks and the wide occurrence of Mesozoic and Cenozoic sedimentary rocks in this area (Avouac et al., 1993; Nansheng et al., 2008), combined with the definition that mud comes from shale (Kopf, 2002), suggest that the source of mud in Xinjiang mud volcanoes can be Mesozoic or Cenozoic shale. The folded shale layer can be fractionated into mud due to the extensive water-rock interaction (Section 6.2.). Although the patterns of mud in Figs. A−4A and A−4B are nearly identical, mud collected from site 9 shows a clear difference from those of other sites in the abundance of Ba. This result also supports the fact that the mud at site 9 originated from a layer different from that of other sites or mixed with another layer.

6.2 Origin of the water and suggestion for water-rock interaction

All the water samples from the mud volcanoes are rich in Na^+ and Cl^- when compared to other ions; this is commonly observed in water from mud volcanoes (e.g., Dia et al., 1999; Hensen et al., 2007; Lavrushin et al., 1996; You et al., 2004). However, a more detailed comparison on the composition of water suggests that the concentrations of these ions are lower than those from other mud volcanoes, whereas other cations, such as Ca^{2+} and Mg^{2+}, have similar concentrations as those in other sites. This kind of saline water is observed from a petroleum field (Kharaka and Hanor, 2003), which is also the case in our samples. In addition, the presence of evaporites in the area may contribute to the increased salinity. Similar concentrations of other cations, except for Na^+, can be obtained from the extensive water-rock interactions in the system of Xinjiang mud volcanoes. At several sites, the concentrations of Ca^{2+} and Mg^{2+} in water samples collected from mud volcanoes are lower than those from the river, which

suggest that the concentration of these cations may be decreased due to the precipitation through the cooling process during or after ascending. The calculation using PHREEQC (Parkhurst, 1995) with the WATEQ4F database (Ball and Nordstrom, 1991) shows that all water samples are saturated with calcite and dolomite, except for the sample collected at site 6. The water sample collected at site 6 is supersaturated with dolomite and is slightly undersaturated with calcite.

The δD values of water from the mud volcanoes are almost identical to those of the reported local meteoric water (Wei and Gasse, 1999); hence, water from the mud volcanoes originates from meteoric water (Fig. A−6). However, it should be noted that the water is not limited to "present" meteoric water, but includes "fossil" meteoric water as well. It is suggested that the origin of the saline water associated with oil and gas is "fossil" meteoric water that experienced isotope exchange reactions during migration among the sedimentary strata and water-rock interaction (Clayton et al., 1966). Moreover, $\delta^{18}O$ shift from the meteoritic line in Fig. A−6 is larger at sites 6 and 7 and smaller at sites 8 and 9 pair relative to the sites 1−4 group. This fact suggests that the degree of water-rock interaction is greater at sites 6−7 and lower at sites 8−9 compared with those at sites 1−4. Oxygen isotope fractionation between water and calcite is used to calculate the equilibrium temperature following the equation of O'Neil et al. (1969):

$$10^3 \ln\alpha = 2.78(10^6/T^2) - \delta^{18}O_{water} + 3.39 \qquad \text{(A−2)}$$

where $10^3 \ln\alpha$ is $\delta^{18}O_{calcite} - \delta^{18}O_{water}$, T is the temperature in Kelvin, and δ is in VSMOW value. The mean calculated temperature among sites 1–4, 6–7, and 8–9 is 95, 127, and 81 °C, respectively, which is consistent with the degree of $\delta^{18}O$ shift.

REE patterns of the water also suggest that the water samples were subjected to the water-rock interaction (Fig. A−7). The positive Ce anomalies in water can occur through the formation of soluble Ce(IV)-carbonate species in alkaline water with high carbonate content (Möller and Bau, 1993). Stability fields of the Ce species on an Eh-pH diagram (Brookins, 1988) show that Ce(IV) is the predominant species in all the water samples. Positive Eu anomalies shown in the REE patterns are likely produced by the dissolution of anorthite (Byrne and Sholkovitz, 1996) or, at least, plagioclase, which

contains Ca^{2+}. This mechanism can be the reason why anorthite is only detected in the mud samples collected from sites 1 and 7 using XRD analysis (Table A−2). The detection of anorthite in the mud samples seems to contradict the positive Eu anomaly observed in the water samples. However, even a partial dissolution of anorthite can produce a positive Eu anomaly in the aqueous phase, due to the considerably higher concentration of Eu in plagioclase than Sm and Gd, the neighboring elements of Eu (e.g., Schnetzler and Philpotts, 1970; Pride and Muecke, 1981). Moreover, the incorporation of other strata during the ascent of mud close to the surface cannot be ruled out with regard to the detection of anorthite at sites 1 and 7. Although the positive Eu anomaly is suggested to be found specifically in hydrothermal water (Byrne and Sholkovitz, 1996), the actual temperature range needed to cause a positive Eu anomaly in water samples during water-rock interaction is unclear at present. However, Minami et al. (1995) showed that a small positive Eu anomaly (Eu/Eu* = 1.1) could only be found in water in contact with basalt at 70 °C, not in the samples at 20 °C (Minami et al., 1995). This result implies that a relatively higher temperature (over 70 °C) is required to induce a positive Eu anomaly in water during water-rock interaction.

Another evidence of water-rock interaction is supported by the compositional ratios of major ions. Alk/Cl and Na/Cl ratios of water collected from sites 6 and 7 are higher than those from sites 1−4, 8, and 9 (Fig. A−8A). K/Cl ratios of water collected from sites 6 and 7 are also higher than those from other sites (Fig. A−8B). These results indicate that the degrees of reaction between water and minerals (i.e., carbonates and silicates) at sites 6 and 7 are greater than those at other sites (Dia et al., 1999). CaO and SiO_2 concentrations of the mud collected from sites 6 and 7 are actually smaller than those from other sites (Table A−3). This finding is supported further by the Ti-normalized major element ratios of the mud samples (Fig. A−11). Ti concentration cannot vary to a larger degree before and after the water-rock interaction because Ti is an immobile element (Pearce and Cann, 1973; Hill et al., 2000). The Ti-normalized ratios clearly indicate the depletions of Si and Ca in the mud samples collected from sites 6 and 7. Moreover, Ti-normalized abundances of Fe and Mn are larger than those of sites that may be related to the difference in the degree of water-rock interactions

(Fig. A−11). The evidence suggests that the extensive reactions between mud and water at sites 6 and 7 are consistent with the result of ^{18}O shift for water and with the calculated temperature using $\delta^{18}O$ of calcite and water (Fig. A−6). Although there are slight differences, variations in the composition of water reflect the degree of interaction with mud and vice versa.

Interestingly, Alk/Cl, Na/Cl, and K/Cl ratios of water collected from sites 8 and 9 are nearly identical irrespective of the large difference in concentrations among these elements between the two sites (Table A−5), probably owing to the result of the dilution by meteoric water at surface. Although the δD values of water collected from sites 8 and 9 are almost identical, $\delta^{18}O$ of water at site 8 is larger than that at site 9 (Table A−5), which also supports the idea that the water at site 9 is diluted by meteoric water to a large degree. The finding of dilution by meteoric water at site 9 can cause a problem, since the temperature of water-rock interaction is calculated using oxygen isotopic fractionation as described above (Eqn. A−2). However, the calculated temperature at site 8 is 83 °C, which is lower than those of sites 1−4 and 6−7. This fact suggests that the degree of ^{18}O shift is consistent with other evidences, namely, compositional ratio (Figs. A−8) and Ti-normalized ratio (Fig. A−11). Therefore, the most extensive water-rock interaction occurred at sites 6−7, while weakest interaction occurred at sites 8−9.

6.3 Origin of gas

Methane is the main component of gases released from the Xinjiang mud volcanoes as shown in Table A−7. Moreover, methane and ethane in gases are suggested to be predominantly of thermogenic origin by the diagrams of $C_1/(C_2+C_3)$ versus $\delta^{13}C_1$ and $\delta^{13}C_2$ (Figs. A−9). As suggested by the "Schoell plot," which is $\delta^{13}C_1$ versus δD_1 (Fig. A−10), the gases released from Xinjiang mud volcanoes are associated with petroleum.

Next, $\delta^{13}{}_{CO2}$ values and inverse of CO_2 concentrations in the gas phases are shown in Fig. A−12, where some $\delta^{13}C$ values of the gas collected from Xinjiang mud

volcanoes are markedly shifted to larger values compared to those of thermogenic origin (Jenden et al., 1993). This heavier shift is considered to be caused by a secondary microbial effect. A two end-member mixing model seems to be inappropriate to explain the scattered data shown in Fig. A−12, suggesting that the complicated and heterogeneous processes that gases has experienced. The possible process that can explain the large variations in $\delta^{13}C$ values are as follows.

First, thermogenic kerogen decarboxylation should be considered because hydrocarbons are of thermogenic origin (Figs. A−9 and A−10). Kerogen decarboxylation reaction during source maturation shows a trend of increasing $\delta^{13}C_{CO2}$ with increasing CO_2 concentration (Jenden et al., 1993; Pallasser, 2000). The $\delta^{13}C_{CO2}$ values of two samples collected from sites 1 and 4 are in the area of the natural thermogenic $\delta^{13}C_{CO2}$ value, which ranges from −25 to −5‰ (Jenden et al., 1993; Kotarba, 2001; Hosgormez et al., 2008). The $\delta^{13}C_{CO2}$ value of a sample collected from site 9 also lies on the upper limit of the natural thermogenic $\delta^{13}C$ value.

Second, anaerobic biodegradation of crude oil can be considered to explain the large $\delta^{13}C_{CO2}$ values. Oil biodegradation is suggested by high C_2/C_3 and i-C_4/n-C_4 ratios (Pallasser, 2000; Waseda and Iwano, 2008). High C_2/C_3 and i-C_4/n-C_4 ratios are identified in our samples, thus supporting oil biodegradation. An isotopic effect of the oil biodegradation results in the increase in $\delta^{13}C$ of residual CO_2, which can easily exceed +10‰ (Pallasser, 2000; Waseda and Iwano, 2008). This phenomenon also shows a trend of increasing $\delta^{13}C_{CO2}$ with increasing CO_2 concentration. The difference between kerogen decarboxylation and oil biodegradation is that the latter shows a steeper slope in Fig. A−12 and causes a larger shift of $\delta^{13}C_{CO2}$ values.

Oil biodegradation includes the following CO_2 reduction:

$$CO_2 + 4H_2 \rightarrow CH_4 + 2H_2O \qquad \text{(A−3)}.$$

The reaction is also associated with a large kinetic isotope effect. The more the reaction proceeds with decreasing CO_2 concentration, the more ^{13}C is enriched in residual CO_2. The reaction is supported by the presence of H_2 gas. The largest concentration of H_2 among all the sites is found at site 4, where an almost pure thermogenic origin is

suggested for methane through its lowest $\delta^{13}C_{CO2}$ value, implying that the reaction (A−3) is ongoing. Smaller H_2 peaks are found in the chromatograms at sites 2, 6, and 7. This finding shows that the microbes use H_2 gas for the reaction, resulting in the enrichment of $\delta^{13}C_{CO2}$ value for these samples.

Regarding the variation in $\delta^{13}C_{CO2}$ values, although sites 1−4 are close to one another with similar compositions of mud and water, the gas sample at site 2 has a higher $\delta^{13}C$ value compared with those at other sites (sites 1 and 4), as shown in Fig. A−12. This observation suggests that $\delta^{13}C_{CO2}$ reflects the degree of microbial activity in the vents at shallow levels closer to the surface. Our data are consistent with the variable carbon isotope compositions of CO_2 in other mud volcanoes. Etiope et al. (2009b) reported highly variable $\delta^{13}C_{CO2}$ in different vents in individual mud volcanoes and pointed out that CO_2 reduction associated with oil biodegradation seems to occur at a depth shallower than the main gas reservoir, probably along the seepage system.

While the $\delta^{13}C_{CO2}$ values suggest secondary methanogenic activity, the hydrocarbons emitted from the mud volcanoes are plotted in the field of thermogenic origin in the "Bernard diagram" (Fig. A−9) and "Schoell plot" (Fig. A−10; Schoell, 1983). Note that the concentrations of CH_4 are much larger than those of CO_2 in gases released from the mud volcanoes, and the addition of CH_4 by microbial effects seems to be negligible. Furthermore, Milkov (2010) reported that the secondary microbial CH_4 is likely to show a $\delta^{13}C_1$ value similar to that of thermogenic gas. Therefore, a dramatic change in $\delta^{13}C$ values is observed for CO_2 by oil biodegradation and CO_2 reduction, whereas these reactions do not cause a significant $\delta^{13}C$ change for hydrocarbons.

6.4 Depths of the water-rock interaction and gas reservoir in the Xinjiang mud volcanoes

Results of the δD and $\delta^{18}O$ values of water indicate that the water is subjected to extensive water-rock interaction (Fig. A−6). In addition, the positive Eu anomalies shown in the REE patterns of the water samples from mud volcanoes (Fig. A−7) imply anorthite dissolution, which commonly occurs at high temperature as seen in

hydrothermal water systems (Byrne and Sholkovitz, 1996). As discussed in Section 6.2., the positive Eu anomaly in the water caused by the reaction with rocks can occur when the temperature is above 70 ºC (Minami et al., 1995). If we use 70 ºC as the possible lowest temperature of water-rock interaction, the depth is calculated to be deeper than 3060 ±175 m from the surface, considering that (i) the geothermal gradient of the investigated area is 18 ±1 ºC/km (Nansheng et al., 2008) and (ii) the surface temperature is 15 ºC.

In general, however, the reservoir of saline fossil waters related to petroleum is deeper than that of gas and crude oil due to their density variations. At the Dushanzi oil field, which is close to sites 8–9, Oligocene crude oil is collected from the depth of 3644−3656 m beneath the surface (Clayton et al., 1997). Therefore, if we apply 81 °C as the lowest temperature for the water-rock interaction calculated from oxygen isotope ratio, the depth is about 3670 ±200 m, slightly deeper than the reservoir of oil at Dushanzi mud volcanoes (sites 8 and 9). In addition, the water-rock interaction occurs deeper than 3670 m for sites 1–4 and 6–7 due to the higher calculated temperature.

Considering that the gases released from mud volcanoes can be related to the petroleum reservoir (Fig. A−10) and that generally the gas reservoir is above the petroleum reservoir, the thermogenic gas released from Xinjiang mud volcanoes would be derived from about 3600 m beneath the surface. This depth, 3600 m, is greater than those of other mud volcanoes releasing ^{13}C-enriched CO_2 (Pallasser, 2000; Etiope et al., 2009b). Such greater depth can be related to the geology of the Junggar Basin. The Junggar Basin is covered by very thick sediments, and its geothermal gradient is lower than that of the average continental crust especially in the western and southern margins of the basin (Avouac et al., 1993; Nansheng et al., 2008).

Assuming that the (i) surface temperature is 15 °C, (ii) average geothermal gradient of the area is 18 ±1 °C /km (Nansheng et al., 2008), and (iii) depth of the gas reservoir is 3600 m, the temperature of the gas reservoir is calculated to be 79.8 ±3.6 °C. If the depth of the gas reservoir is 3640 m, slightly above the petroleum reservoir, the temperature is calculated to be 80.5 ±3.6 °C. These calculations suggest that the

temperature of the gas reservoir in Xinjiang mud volcanoes is within the highest range of 60–80 °C, where anaerobic biodegradation can occur in other mud volcanoes (Pallasser, 2000; Etiope et al. 2009b), or slightly higher than the suggested temperature range.

The depth of oil biodegradation, including CO_2 reduction reactions occurring in this area, can be shallower than the reservoir depth of the gas. The shallower depth of oil biodegradation can be supported by the heterogeneous $\delta^{13}C_{CO2}$ values observed among sites 1, 2, and 4, which would have the same reservoir due to their close locations and similarities, as shown in other data. Etiope et al. (2009b) implied the possibility that the deep reservoir of thermogenic gas associated with secondary microbial activity in shallow depth. This study reinforces the presence of deep reservoir for thermogenic gas followed by the secondary microbial activity which occurs in the vents above the reservoir (Fig. A−13).

7 Conclusions

This study provides, for the first time, a data set of mud, water, and gas released from mud volcanoes in northwestern China. Major and trace element compositions of mud suggest that the mud can originate from Mesozoic or Cenozoic shale. The origin of water is suggested to be fossil meteoric water which has experienced interactions with rock. Thermogenic methane dominates the composition of gas.

Taking into account the petroleum reservoir around the mud volcanoes, the reservoir depth of gas can be about 3600 m. As suggested by the geothermal gradient of studied area, the water-rock interaction occurs deeper than 3670 ±200 m. The oil biodegradation occurs at a shallower depth along the seepage system of the mud volcanoes which caused large isotopic change for CO_2. This study provides an example of terrestrial mud volcanoes that release thermogenic gas from very deep sedimentary layers, followed by microbial activities which occur in the vents above the reservoir.

Table A−1. Coordinates, altitude, and size on the mud volcanoes investigated in this study.

	site 1	site 2	site 3	site 4	site 5	site 6	site 7	site 8	site 9
latitude (N)	44° 11' 00.5"	44° 10' 58.0"	44° 10' 57.7"	44° 10' 57.0"	44° 12' 55.9"	44° 11' 19.4"	44° 11' 19.9"	44° 18' 18.6"	44° 18' 32.1"
longitude (E)	84° 23' 20.5"	84° 23' 15.6"	84° 23' 14.0"	84° 23' 12.3"	84° 24' 11.1"	84° 29' 34.6"	84° 29' 35.5"	84° 50' 46.9"	84° 51' 15.8"
altitude (m)	1280	1273	1272	1271	902	1171	1174	964	841
size of crater (m)	2.4 × 2.0	1.1 × 0.9	1.1 × 0.95	1.3 × 3.8		diameter 1.1	3 × 2.4	0.6 × 0.4	0.5 × 0.5

Size of the crater is represented by “length × width.” (Site 5: river water)

Table A−2. Mineral compositions of the mud sample.

	Site 1	Site 2	Site 3	Site 4	Site 6	Site 7	Site 8	Site 9
Ab	D	D	D	D	D	D	D	D
An	D	N. D.	N. D.	N. D.	N. D.	D	N. D.	N. D.
Calc	D	D	T	T	T	T	D	D
Chl	D	D	D	D	D	D	D	D
Illite	D	D	D	D	D	D	D	D
Kaol	D	D	D	D	D	N. D.	N. D.	N. D.
Mica	D	D	D	D	D	D	D	D
Qtz	D	D	D	D	D	D	D	D
Smec	D	D	D	D	D	D	D	D
other	N. D.	N. D.	N. D.	N. D.	Verm	Verm	N. D.	N. D.

Ab: albite; An: anorthite; Calc: calcite; Chl: Chlorite; Kaol: kaolinite; Qtz: quartz; Smec: smectite; Verm: vermiculite. D: major mineral in the XRD pattern; T: minor mineral in the XRD pattern. N. D. means minerals not determined.

Table A−3. Chemical compositions of mud and soils determined by XRF.

	Soil a	Soil b	Soil c	Mud Site 1	Mud Site 2	Mud Site 3	Mud Site 4	Soil d	Soil e	Soil f	Soil g	Mud Site 6	Mud Site 7	Soil h	Mud Site 8	Mud Site 9
SiO_2	63.9	63.4	64.2	59.5	59.4	60.5	64.7	61.1	58.0	61.5	61.8	58.7	58.8	63.4	56.8	58.5
TiO_2	0.774	0.748	0.806	0.783	0.738	0.858	0.812	0.672	0.884	1.079	1.112	0.971	0.961	0.653	0.821	0.734
Al_2O_3	17.4	13.9	17.3	18.4	18.0	19.9	18.9	13.4	16.6	21.5	23.1	21.8	21.6	15.2	20.7	17.5
$Fe_2O_3^*$	6.79	5.06	6.36	7.33	6.93	8.52	6.44	4.69	12.6	8.81	7.80	10.5	10.5	5.35	7.28	6.63
MnO	0.142	0.108	0.178	0.139	0.087	0.188	0.111	0.095	0.233	0.101	0.102	0.291	0.211	0.113	0.084	0.100
MgO	2.50	2.87	2.13	3.22	4.18	2.61	2.07	2.78	1.30	2.18	2.12	2.26	2.22	2.73	3.98	3.38
CaO	3.41	9.57	2.28	3.82	5.17	1.93	0.885	10.5	7.09	0.789	0.518	1.51	1.52	7.39	3.65	5.58
Na_2O	2.39	2.62	2.85	3.30	2.05	2.35	2.51	2.44	1.50	1.91	1.16	1.31	1.85	1.83	2.35	2.19
K_2O	3.02	2.48	3.42	3.22	3.30	2.81	2.94	2.60	2.25	2.60	2.82	2.76	2.75	3.07	3.62	3.14
P_2O_5	0.231	0.184	0.216	0.221	0.229	0.249	0.190	0.170	0.095	0.202	0.148	0.355	0.353	0.224	0.163	0.166
Total	100.61	100.94	99.73	99.92	100.11	99.93	99.51	98.47	100.56	100.72	100.62	100.54	100.68	99.95	99.47	97.93
LOI (%)	8.73	9.10	5.75	9.67	11.0	8.87	6.81	8.04	9.82	7.74	7.16	10.7	10.8	9.86	8.97	12.4
Sc	17.2	15.7	16.3	18.6	18.0	17.9	15.0	16.7	22.5	20.1	22.0	20.7	20.6	16.6	20.9	17.4
V	132	105	115	141	136	156	133	95.8	127	168	174	192	194	106	270	246
Cr	71.6	70.9	49.4	85.1	86.6	75.3	65.2	62.2	76.1	89.9	90.5	80.8	84.1	67.9	105	82.6
Co	16.4	13.9	17.1	18.5	15.8	18.0	15.9	13.3	13.8	25.8	25.8	22.1	21.1	15.2	18.4	14.2
Ni	42.4	35.3	32.9	51.8	51.8	45.7	36.0	31.5	33.8	54.5	55.9	53.5	54.1	38.1	49.1	38.4
Cu	58.6	54.1	66.2	54.1	53.2	51.7	50.8	32.9	64.9	53.9	44.9	61.6	63.7	35.1	54.7	51.5
Zn	97.0	78.1	98.8	69.7	90.3	105	98.5	76.8	116	125	121	120	116	81.8	78.9	82.2
Ga	20.9	17.7	21.6	24.3	22.4	25.3	24.5	16.3	21.0	25.7	29.6	27.1	27.8	18.3	26.6	22.3
Rb	112	94.4	116	124	122	112	111	99.0	83.8	100	108	111	109	119	155	126
Sr	332	409	315	456	543	430	244	483	282	225	143	293	279	375	434	384
Zr	245	363	236	173	169	226	246	265	236	243	246	244	243	234	164	173
Nb	11.8	13.1	12.6	12.4	12.1	12.1	11.7	11.8	10.1	13.2	12.9	12.3	12.1	12.1	14.7	12.5
Cs	4.19	3.51	6.21	8.14	18.8	9.08	15.8	2.90	5.05	4.8	10.3	18.1	6.18	1.61	10.5	10.1
Ba	613	570	697	562	522	620	572	533	1029	594	829	774	762	596	812	2034
Hf	6.52	7.67	6.14	4.84	5.51	5.60	7.09	6.57	5.72	7.03	6.22	6.43	5.94	5.89	4.42	4.51
W	0.360	4.50	4.19	4.18	2.39	1.36	2.14	1.08	2.47	1.05	2.36	0.05	2.24	2.68	1.66	1.13
Pb	18.6	10.7	24.0	9.80	21.2	24.9	22.2	16.9	19.9	17.4	21.8	23.0	23.3	21.4	12.4	8.65
Th	14.6	17.6	16.1	18.0	17.1	17.4	16.5	15.7	12.1	12.6	12.7	17.6	15.8	14.1	15.3	14.8
U	3.65	2.70	3.33	3.74	4.52	2.93	3.31	3.42	1.87	2.65	2.98	3.27	2.94	3.08	4.18	4.35

Amounts of oxides are in wt.%, whereas the elements listed below Sc are in mg/kg. *Total iron as Fe_2O_3. LOI denotes loss on iginition.

Note that soil a−c are surface soil samples collected around the mud volcanoes are located at sites 1−4; soil d−g are collected at around sites 6 and 7; and soil h is collected at around sites 8 and 9.

Table A−4. REE abundances (mg/kg) of mud and soil samples determined using ICP-MS and $\delta^{13}C$ and $\delta^{18}O$ of carbonate in the mud samples.

	Soil a	Soil b	Soil c	Mud Site 1	Mud Site 2	Mud Site 3	Mud Site 4	Soil d	Soil e	Soil f	Soil g	Mud Site 6	Mud Site 7	Soil h	Mud Site 8	Mud Site 9
Y	23.6	23.0	31.0	21.6	19.0	25.1	24.7	21.4	26.2	24.6	28.7	29.2	30.1	21.2	23.6	19.4
La	30.5	33.7	32.9	24.1	22.6	34.1	23.2	26.4	24.0	25.2	29.5	31.0	31.3	26.7	27.4	21.4
Ce	75.7	73.3	76.9	60.5	53.1	79.1	54.5	55.1	50.9	64.0	75.4	82.5	78.2	57.8	54.7	43.3
Pr	8.00	7.76	7.79	6.04	5.80	8.25	5.76	5.78	5.82	6.68	7.91	8.50	8.07	6.11	6.48	5.15
Nd	34.1	32.3	33.7	25.5	24.4	35.5	24.4	24.1	24.9	28.9	34.3	37.2	35.2	25.9	24.3	19.5
Sm	7.03	6.70	7.22	5.48	5.07	7.45	5.08	5.05	5.26	6.07	7.41	7.98	7.52	5.48	4.98	4.03
Eu	1.36	1.25	1.42	1.11	1.00	1.46	1.00	0.969	1.16	1.34	1.62	1.66	1.55	1.10	0.924	0.583
Gd	6.55	6.50	7.23	5.35	4.91	6.99	4.84	4.96	5.47	5.87	7.17	7.67	7.40	5.33	4.40	3.60
Tb	1.03	1.02	1.14	0.857	0.769	1.11	0.778	0.791	0.900	0.944	1.15	1.22	1.16	0.847	0.773	0.646
Dy	5.93	5.73	6.58	5.03	4.35	6.37	4.55	4.57	5.53	5.56	6.84	7.10	6.76	4.98	4.53	3.63
Ho	1.18	1.16	1.34	1.01	0.869	1.29	0.910	0.927	1.12	1.13	1.40	1.45	1.36	1.00	0.913	0.764
Er	3.50	3.42	3.99	3.00	2.60	3.84	2.73	2.74	3.32	3.39	4.22	4.35	4.10	3.02	2.75	2.21
Tm	0.508	0.487	0.570	0.429	0.373	0.544	0.392	0.389	0.481	0.483	0.606	0.628	0.576	0.421	0.394	0.331
Yb	3.34	3.26	3.76	2.91	2.51	3.71	2.62	2.61	3.16	3.24	4.09	4.20	3.93	2.87	2.63	2.11
Lu	0.503	0.478	0.563	0.437	0.378	0.545	0.396	0.386	0.475	0.495	0.618	0.634	0.604	0.429	0.404	0.326
Ce/Ce*	1.11	1.03	1.10	1.15	1.06	1.07	1.08	1.02	0.98	1.12	1.13	1.16	1.12	1.03	0.94	0.94
Eu/Eu*	0.94	0.89	0.92	0.96	0.94	0.95	0.95	0.91	1.02	1.06	1.05	1.00	0.98	0.96	0.93	0.72
ΣREE	203	200	216	163	148	215	156	156	159	178	211	225	218	163	159	127
$\delta^{13}C$	N.A.	N.A.	N.A.	+1.1	-3.8	+6.1	-1.1	N.A.	N.A.	N.A.	N.A.	+15.7	+15.6	N.A.	-0.60	+0.91
$\delta^{18}O$	N.A.	N.A.	N.A.	+25.0	+26.2	+20.1	+23	N.A.	N.A.	N.A.	N.A.	+19.9	+20.6	N.A.	+24.7	+25.5

$Ce/Ce^* = Ce_N / \sqrt{La_N \times Pr_N}$, $Eu/Eu^* = Eu_N / \sqrt{Sm_N \times Gd_N}$ where N denotes the UCC normalized values.

Note that soil a−c are surface soil samples collected around the mud volcanoes located at sites 1−4; soil d−g are collected around sites 6 and 7; and soil h is collected at around sites 8 and 9. Note also that $\delta^{13}C$ values are in ‰ VPDB, whereas $\delta^{18}O$ values are in ‰ VSMOW. N. A. means that samples not analyzed isotope ratios.

Table A−5. Chemical characteristics of water samples.

	site 1	site 2	site 3	site 4	site 5	site 6	site 7	site 8	site 9
pH	8.78	8.40	8.65	9.16	8.43	7.35	7.80	7.75	8.08
Eh (mV)	-119	-86	-100	-127	-9	-28	-54	-50	-69
temperature (°C)	9.40	9.40	10.4	8.70	11.6	15.2	22.0	11.8	12.2
conductivity (mS/cm)	11.6	11.6	12.7	11.3	0.506	6.03	7.80	18.5	5.56
salinity (‰)	6.7	6.4	7.2	6.3	0.0	3.2	3.0	10.7	2.9
dissolved O_2 (ppm)	0.60	0.86	0.39	0.38	0.72	0.82	0.75	0.55	0.46
F^- (mM)	0.02	0.02	0.02	0.01	0.02	0.03	0.02	0.02	0.02
Cl^- (mM)	109	105	101	92.3	0.84	32.3	33.5	180	72.4
Br^- (mM)	0.26	0.26	0.25	0.26	0.01	0.09	0.09	0.47	0.35
NO_3^- (mM)	0.32	1.06	0.35	0.61	0.10	0.29	0.50	0.25	1.13
SO_4^{2-}* (mM)	0.49	1.32	2.00	3.56	2.46	3.69	1.06	9.98	3.55
Alk (mM)	71.0	71.0	60.0	56.7	2.00	53.0	53.0	10.0	10.0
Na^+ (mM)	145	154	145	143	1.26	75.6	80.4	193	73.1
K^+ (mM)	0.15	0.23	0.24	0.25	0.09	0.51	0.66	0.41	0.22
Ca^{2+} (mM)	0.26	0.48	0.36	0.09	3.04	0.29	0.32	6.75	0.93
Mg^{2+} (mM)	0.69	3.70	0.87	0.33	0.85	4.09	5.95	10.93	4.09
δD (‰ VSMOW)	-67.1	-78.8	-83.1	-82.1	-71.2	-77.5	-99.2	-57.1	-57.3
$\delta^{18}O$ (‰ VSMOW)	-1.5	-2.5	-3.0	-3.0	-10.6	-1.0	-4.6	-3.2	-5.7
$\delta^{13}C$ (‰ VPDB)	12.4	16.9	3.2	-3.7	-23.3	35.6	33.3	27.6	2.3

* Total sulfur as SO_4.

Note that the δD and $\delta^{18}O$ values represent the isotope ratio of water, and $\delta^{13}C$ represents the isotope ratio of dissolved carbonate in water. (Site 5: river water. Other sites: water from mud volcanoes)

Table A−6. REE concentrations (ng/L) in the water samples.

	Site 1	Site 2	Site 3	Site 4	Site 5	Site 6	Site 8
Y	57.9	90.7	18.2	55.4	14.2	44.5	6.43
La	36.5	126	5.77	8.32	9.94	5.61	1.93
Ce	142	299	12.0	27.2	21.1	14.1	4.38
Pr	10.3	27.2	1.15	2.44	2.77	1.53	0.379
Nd	41.2	110	5.08	10.5	11.4	6.17	1.50
Sm	9.87	25.3	1.80	3.18	2.26	1.47	0.254
Eu	8.51	17.9	10.6	6.75	0.796	1.52	0.554
Gd	9.69	23.2	2.78	4.05	2.65	2.26	0.369
Tb	1.61	3.73	0.308	0.814	0.347	0.511	0.095
Dy	9.38	18.6	2.22	6.36	1.83	4.03	0.693
Ho	2.02	3.54	0.545	1.71	0.357	1.10	0.195
Er	6.65	10.2	1.86	6.49	1.01	3.74	0.602
Tm	1.09	1.35	0.306	1.22	0.122	0.630	0.109
Yb	8.61	9.31	2.35	9.97	0.662	4.39	0.662
Lu	1.36	1.35	0.394	1.67	0.093	0.790	0.128
Ce/Ce*	1.67	1.16	1.06	1.38	0.92	1.09	1.17
Eu/Eu*	4.09	3.46	22.26	8.83	1.53	3.91	8.51
ΣREE	347	767	65.4	146	69.6	92.3	18.3

$Ce/Ce^* = Ce_N / \sqrt{La_N \times Pr_N}$, $Eu/Eu^* = Eu_N / \sqrt{Sm_N \times Gd_N}$ where N denotes the UCC normalized values. (Site 5: river water. Other sites: water from mud volcanoes)

Table A−7. Concentrations and stable isotope compositions of the gas samples.

	Site 1	Site 2	Site 4	Site 6	Site 7	Site 8	Site 9
Gas composition (Vol. %)							
N_2	N. D.	0.5	5.6	5.8	6.2	0.8	15.7
CH_4	91.6	89.0	89.6	81.5	80.4	92.6	75.8
C_2H_6	8.3	10.1	8.5	5.4	6.2	6.2	7.7
C_3H_8	0.002	0.004	0.1	0.002	0.02	0.6	1.0
Gas composition (ppmv)							
i-C_4	< 1	< 1	9.8	< 1	0.9	400	1390
n-C_4	2.4	4.5	120	1.6	3.5	1430	2540
CO_2*	1950	4970	973	1360	1740	4450	3060
$\delta^{13}C$ (‰ VPDB)							
CH_4*	–45.9	–43.7	–42.4	–40.7	–39.7	–40.5	–38.6
C_2H_6	–28.1	–26.9	–28.1	–30.8	–28.4	–27.9	–27.2
CO_2*	–8.0	+16.2	–11.5	+21.1	+24.6	+29.8	–4.8
δD (‰ VSMOW)							
CH_4*	–229	–244	–227	–252	–264	–229	–242
C_2H_6	–143	–180	–223	–183	–203	–194	–181

*The effect of air contamination is corrected.

N. D. means not detected.

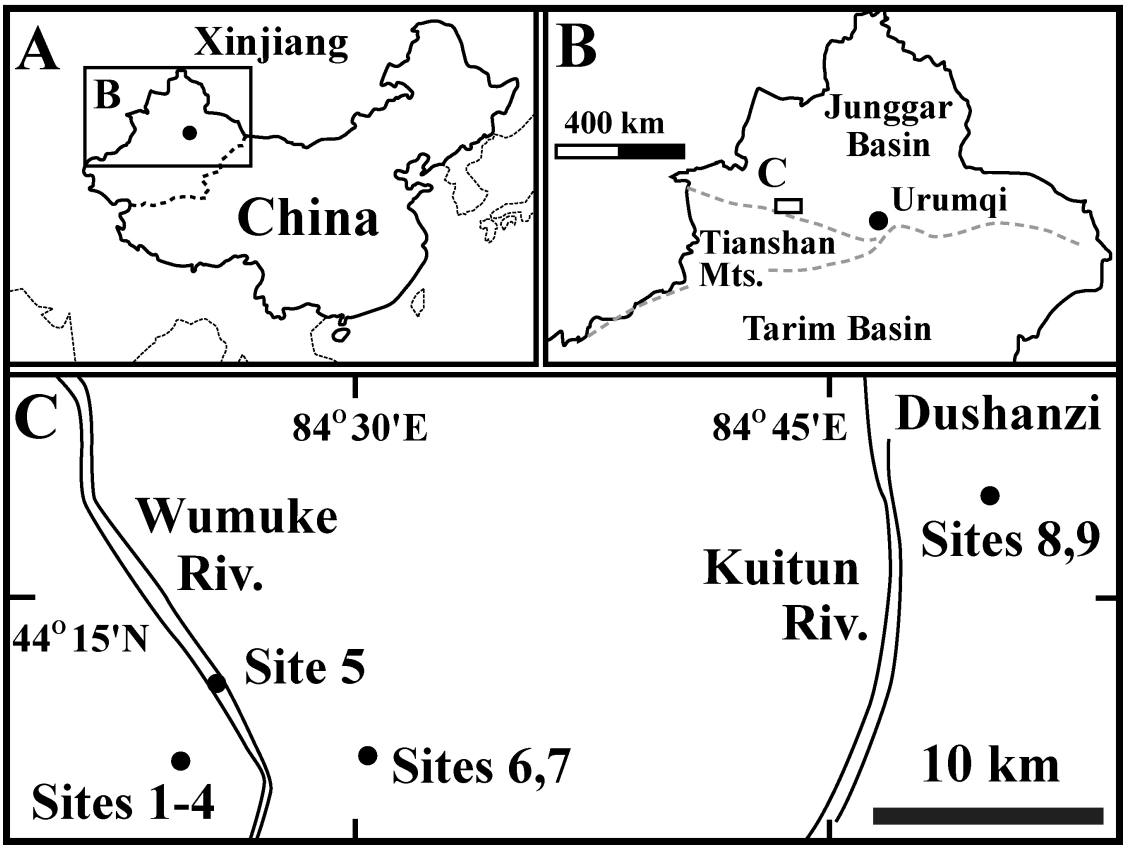

Fig. A−1. Schematic map of sampling locations. Map A depicts the whole of China; the dashed line represents the border of the Xinjiang Uyghur Autonomous Region. Map B depicts three quarters of Xinjiang; the dashed line represents the Tianshan Mountains. Location of a square marked on map B is enlarged on map C. Site 9 is situated near the Dushanzi District.

Fig. A−2. Photographs of the studied mud volcanoes. A−H: Crater of the mud volcanoes at sites 1−9, respectively. Length and width of craters are given in Table A−1. I: Panoramic view of site 6; J: “Twin” mud volcanoes at sites 6 (right) and 7 (left).

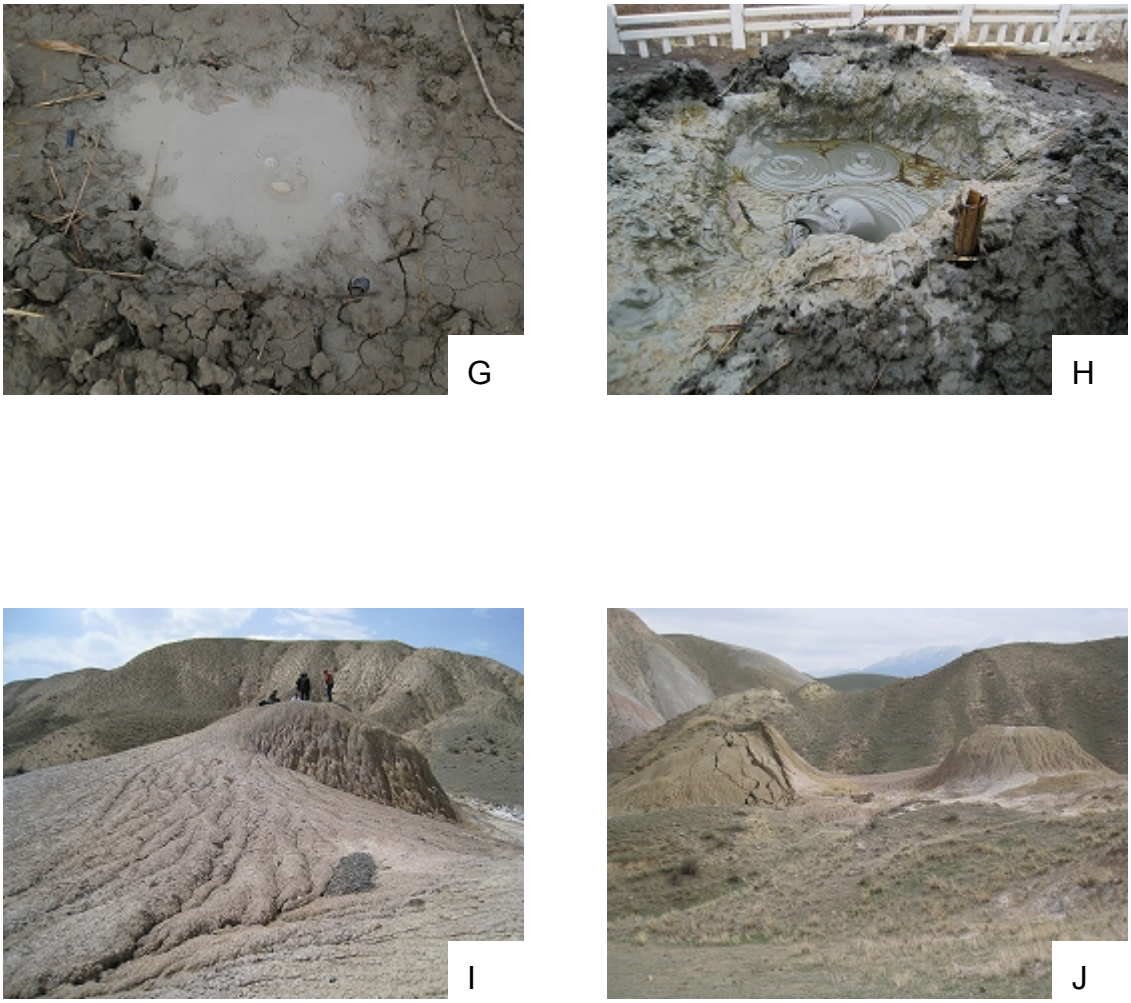

Fig. A−2. Photographs of the studied mud volcanoes (continued).

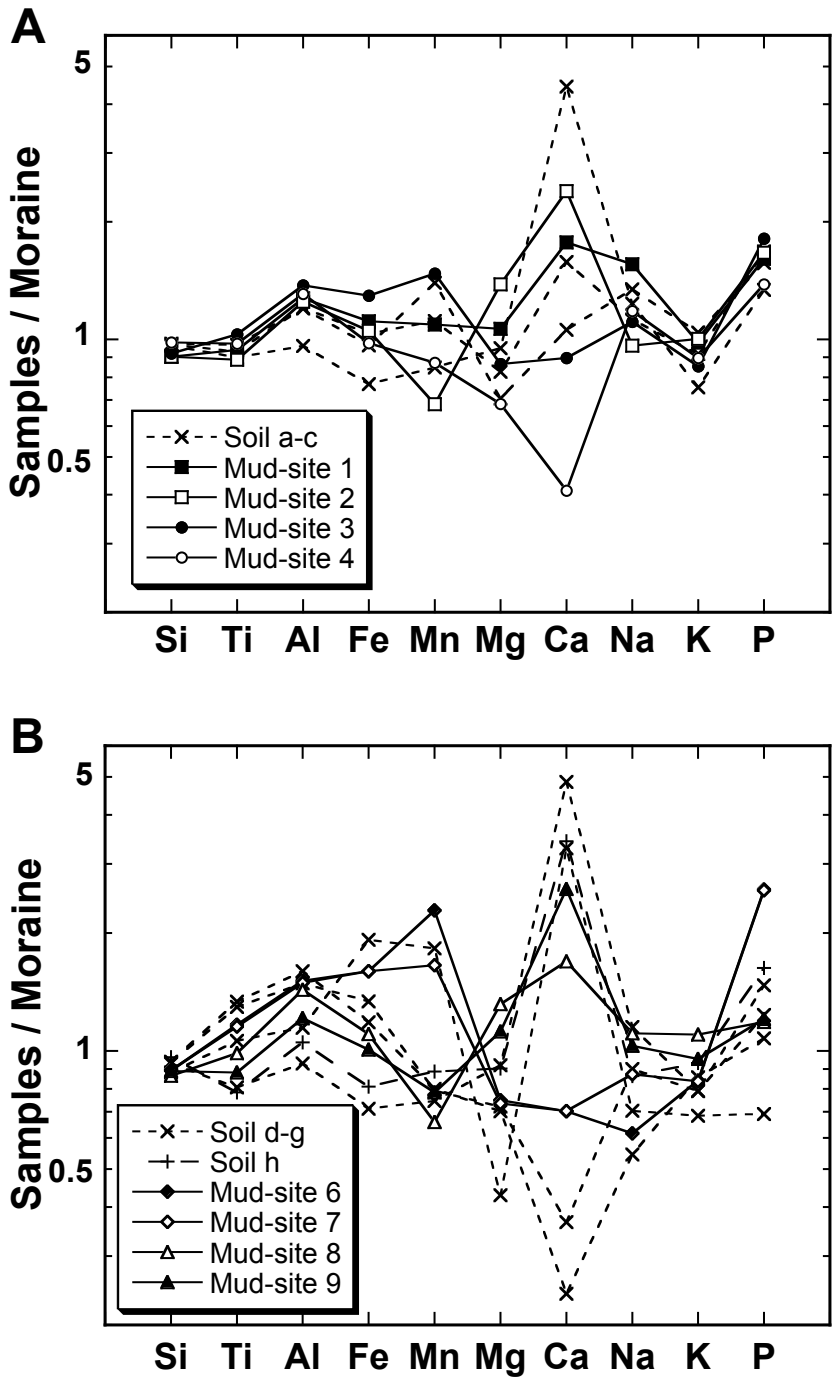

Fig. A−3. Major element abundances of mud and surface soils collected around the mud volcanoes normalized to the moraine collected from the northern Tianshan Mountains (Chang et al., 2000). (A) Sites 1−4; (B) Sites 6−9. Note that soil a−c are the surface soil samples collected around the mud volcanoes located at sites 1−4; soil d−g are collected at around sites 6 and 7; and soil h is collected at around sites 8 and 9.

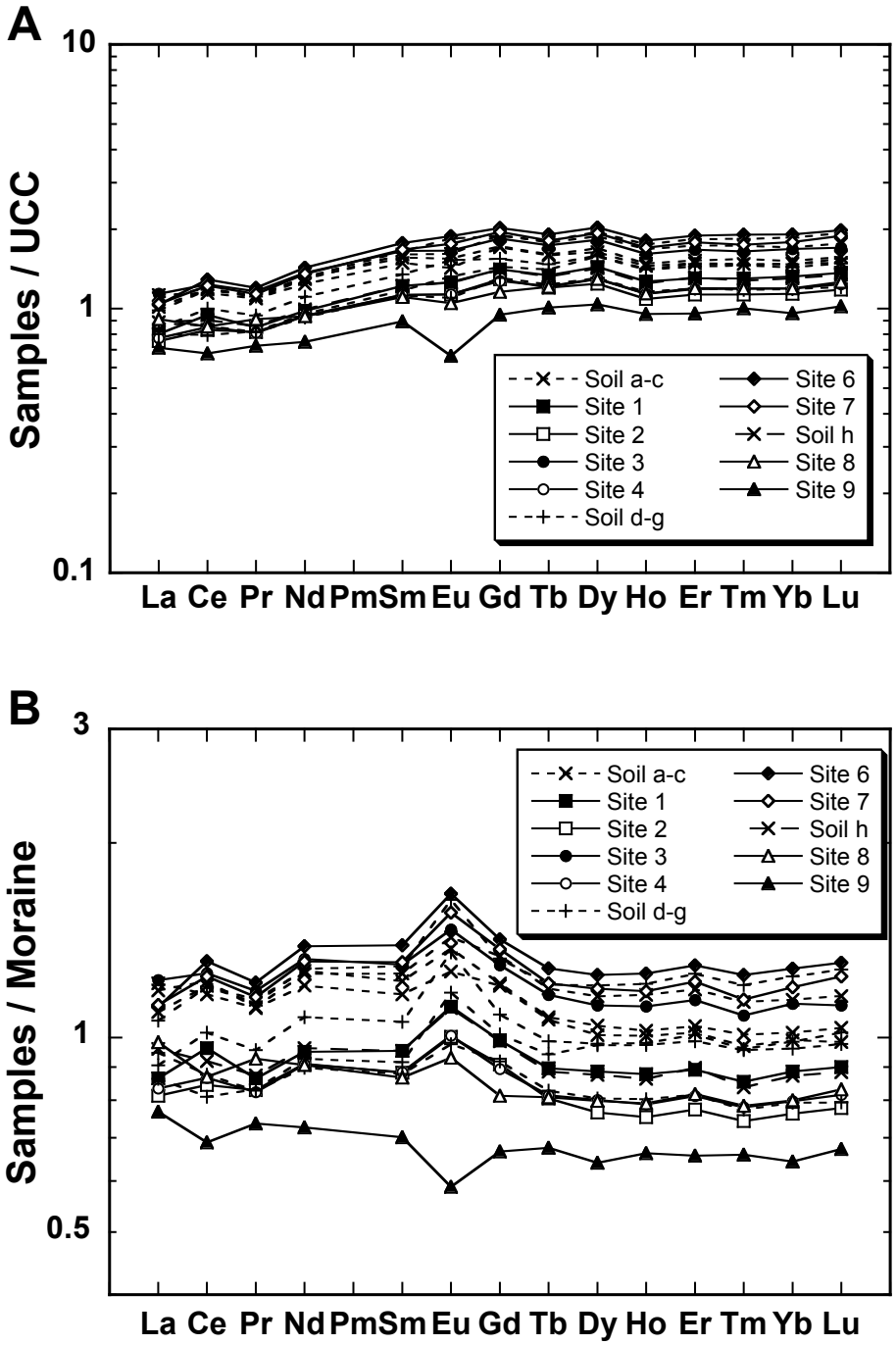

Fig. A−4. REE patterns of mud and surface soils collected around the mud volcanoes normalized to (A) UCC (Taylor and McLennan, 1985) and (B) moraine (Chang et al., 2000). Note that soil a−c are the surface soil samples collected around the mud volcanoes located at sites 1−4; soil d−g are collected at around sites 6 and 7; and soil h is collected at around sites 8 and 9.

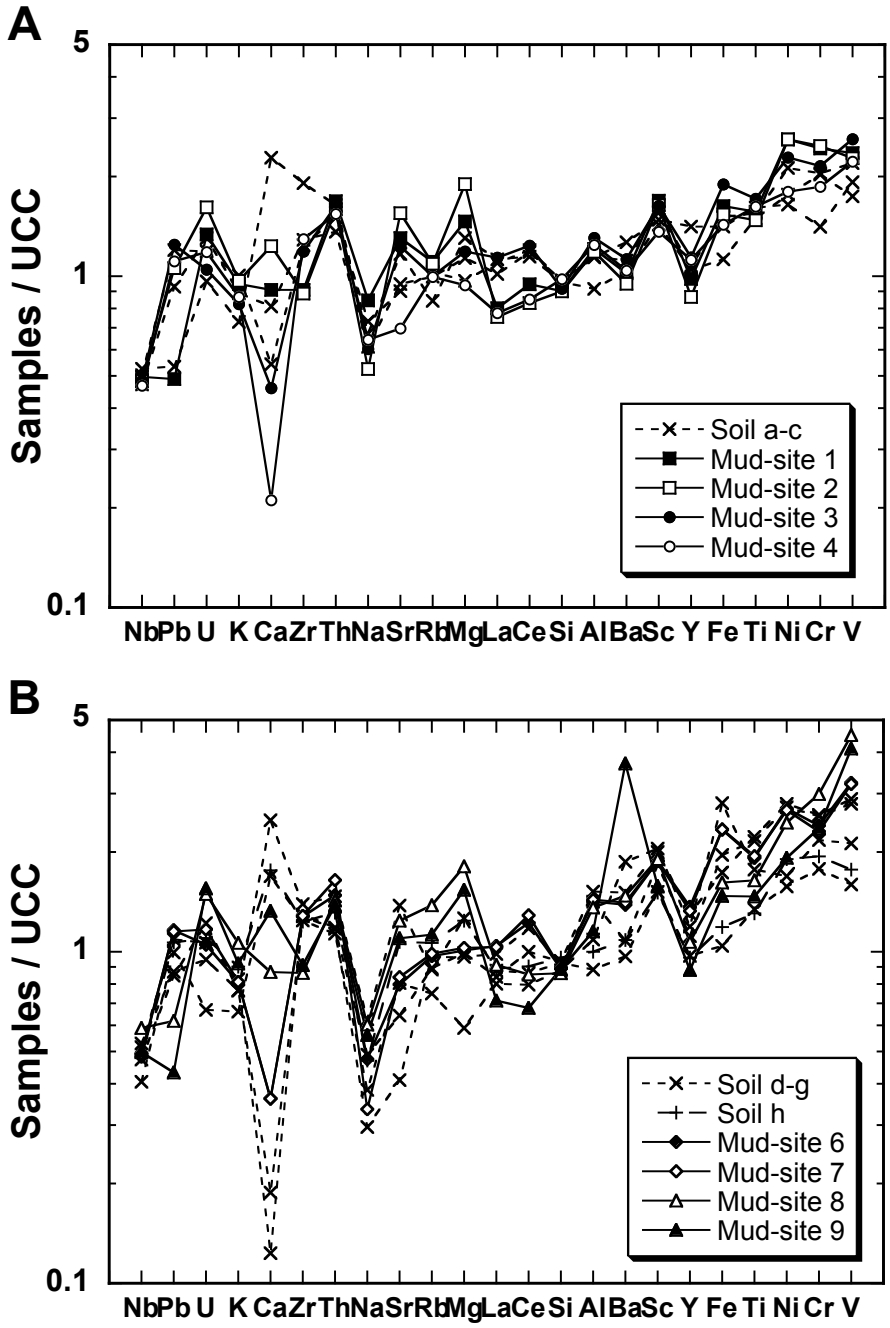

Fig. A−5. Compositions of mud and soils normalized against the UCC (Taylor and McLennan, 1985). Elements are arranged from left to right in the order of increasing abundance in the average Mesozoic-Cenozoic greywacke. (A) Sites 1−4; (B) Sites 6−9. Note that soil a−c are the surface soil samples collected around the mud volcanoes located at sites 1−4; soil d−g are collected at around sites 6 and 7; and soil h is collected at around sites 8 and 9.

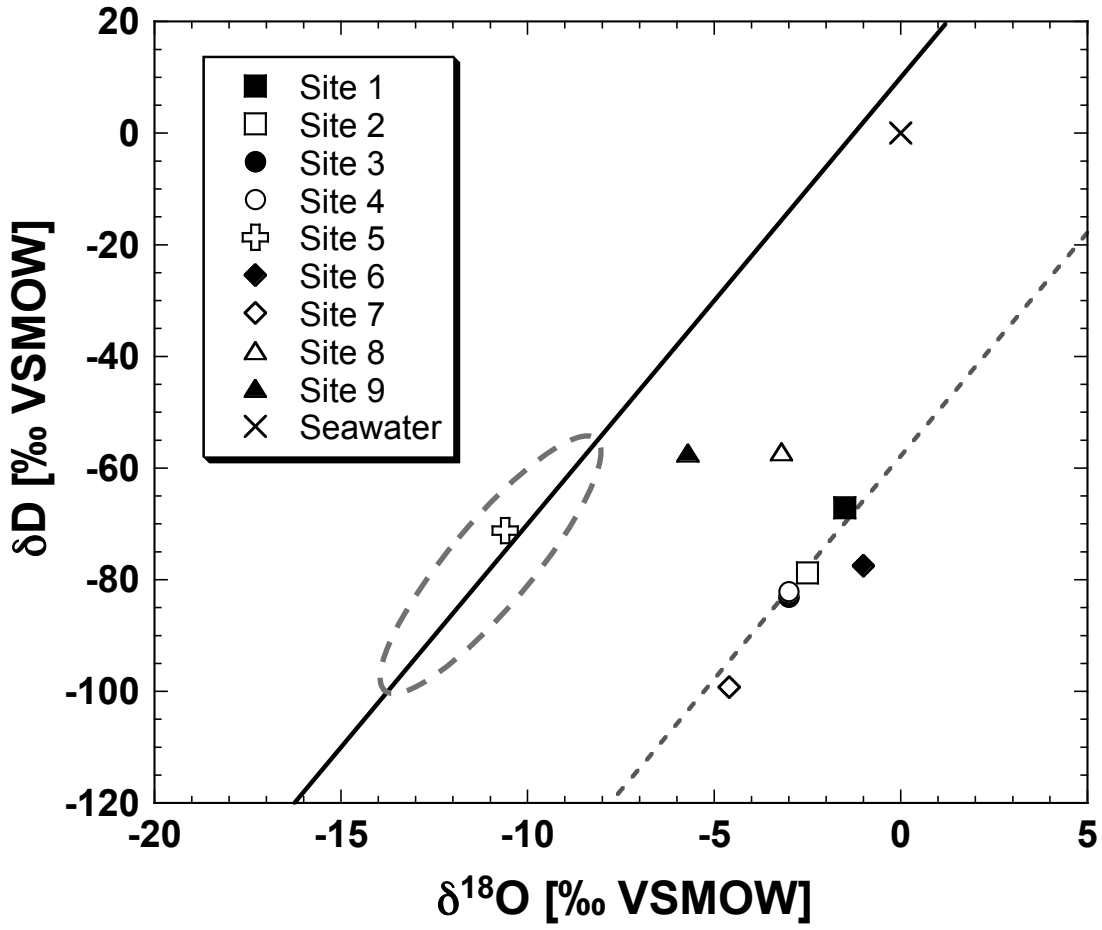

Fig. A−6. Comparison of δD and $\delta^{18}O$ values among muddy water, river water (site 5), and seawater. Solid line: the meteoric water line; dashed line: line passing through sites 1−4 and parallel to the meteoric water line; and dashed ellipse: field for the meteoric water in northern Xinjiang (Wei and Gasse, 1999).

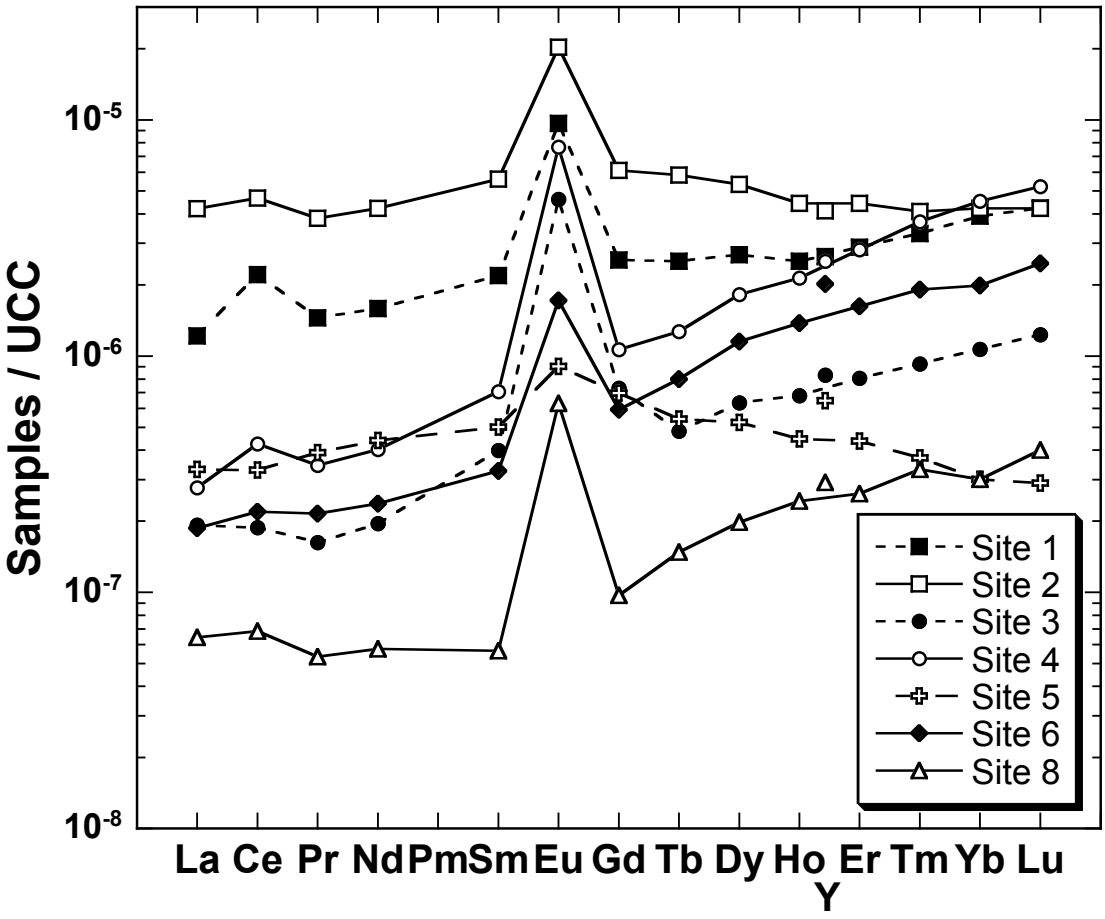

Fig. A−7. UCC-normalized REE pattern of water samples. (Site 5: river water; Other sites: water from mud volcanoes)

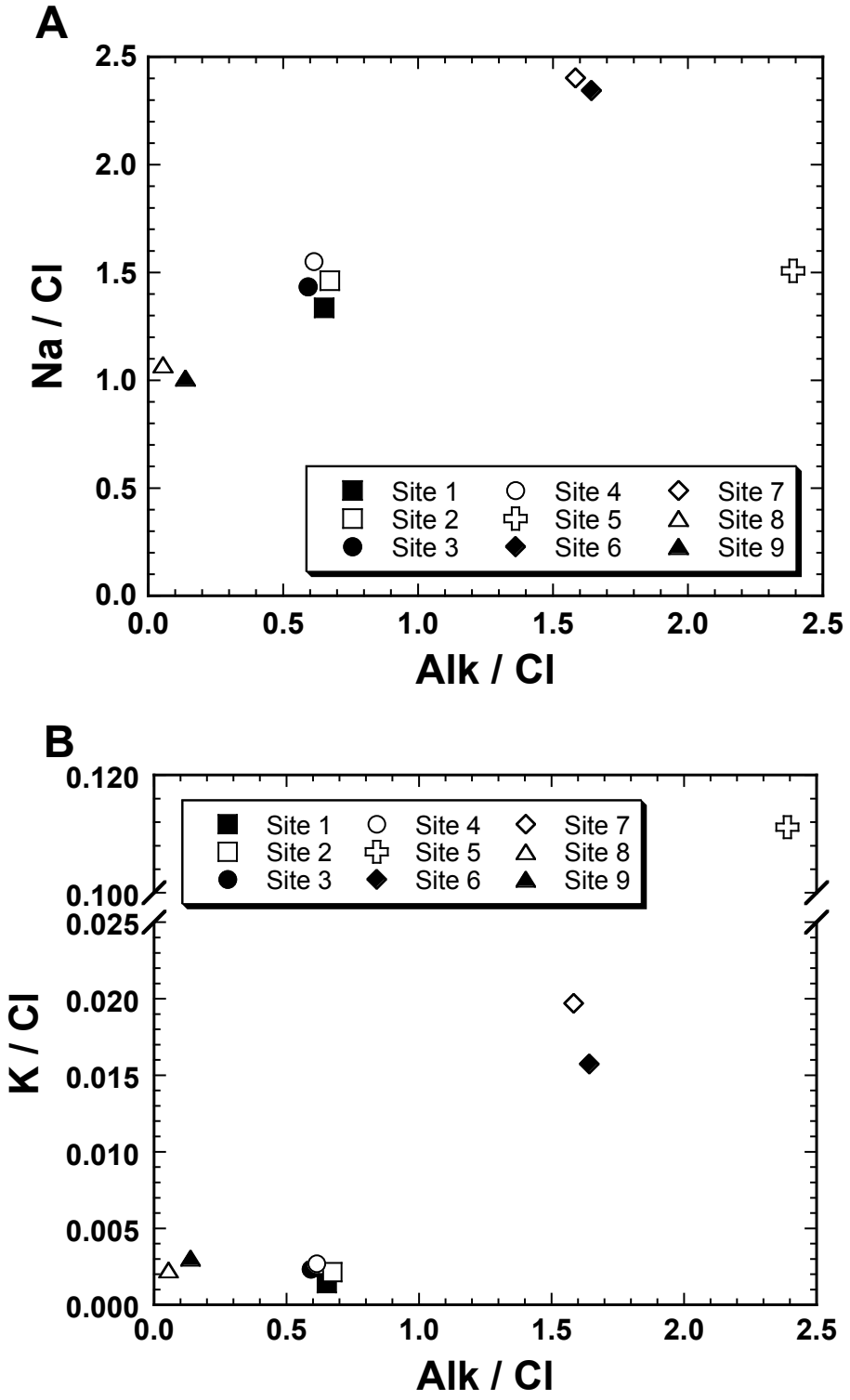

Fig. A−8. Comparison of the composition of water among muddy water, river water and seawater. (A) Na/Cl vs. Alk/Cl; (B) K/Cl vs. Alk/Cl. (Site 5: river water; Other sites: water from mud volcanoes)

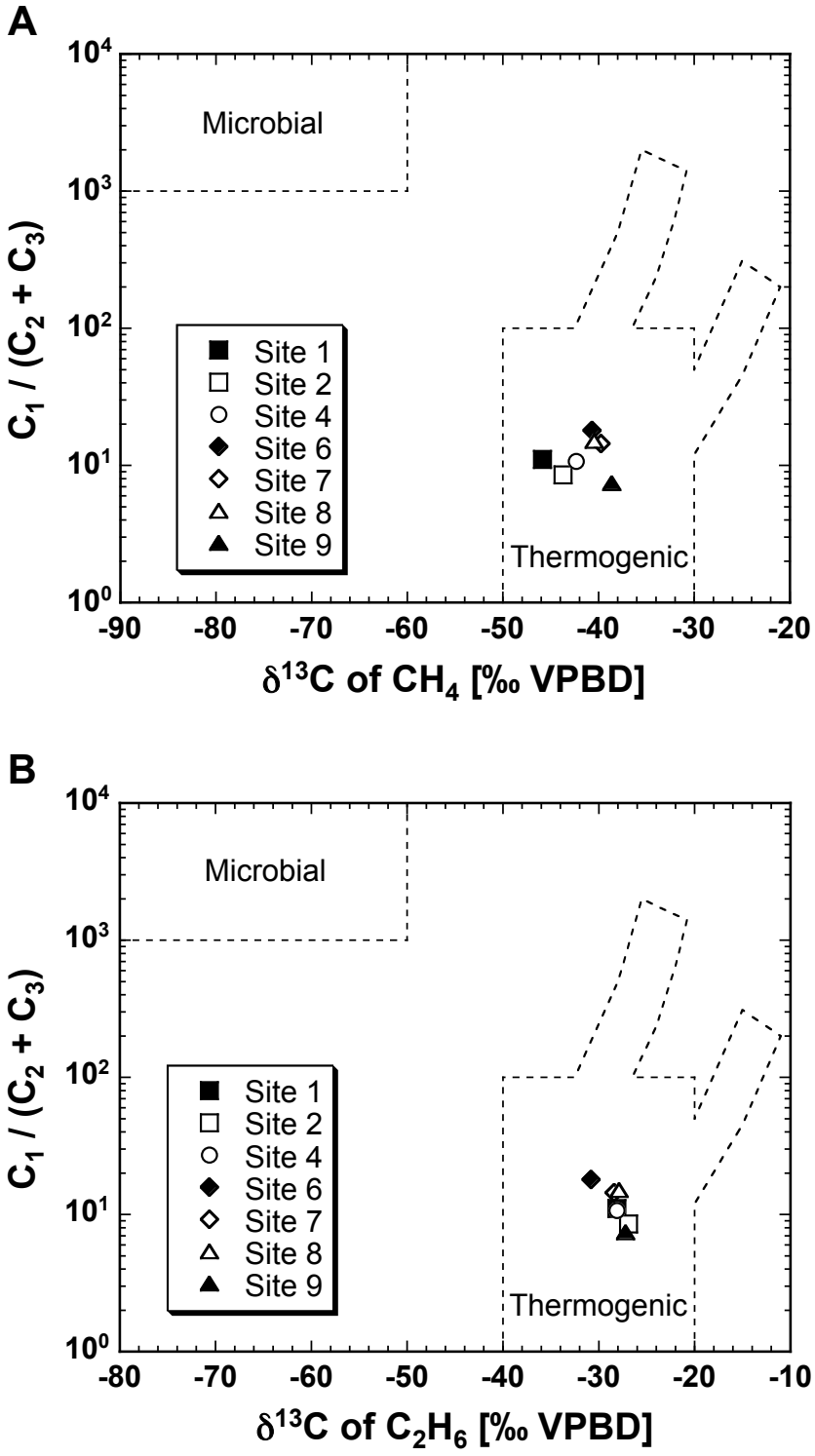

Fig. A−9. Relationship between "Bernard diagram," i.e., $C_1/(C_2+C_3)$ and $\delta^{13}C$ values of (A) methane and (B) ethane in gas samples.

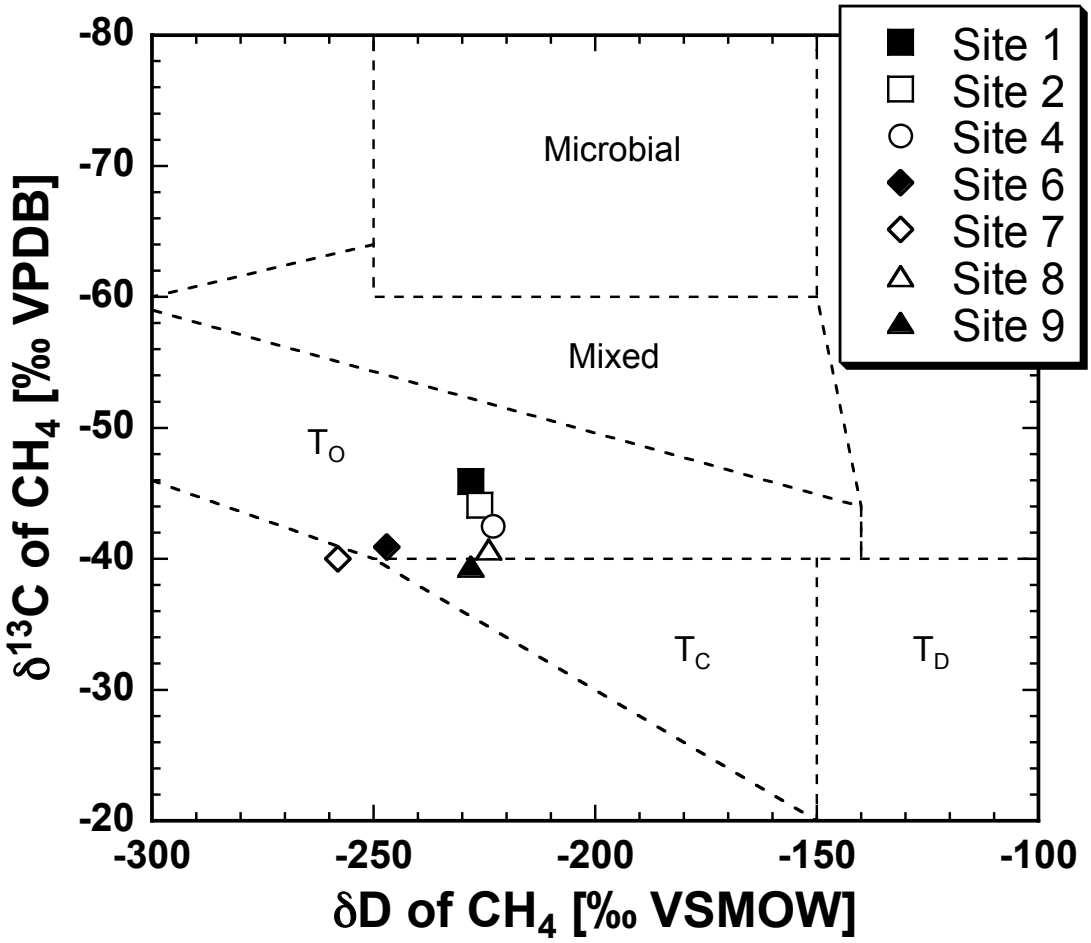

Fig. A−10. Relationship between δD and $\delta^{13}C$ of methane based on the discrimination diagram by Schoell (1983), for the classification of thermogenic and microbial natural gas. T_O, T_C, and T_D denotes thermogenic with oil, thermogenic with condensate, and dry thermogenic, respectively.

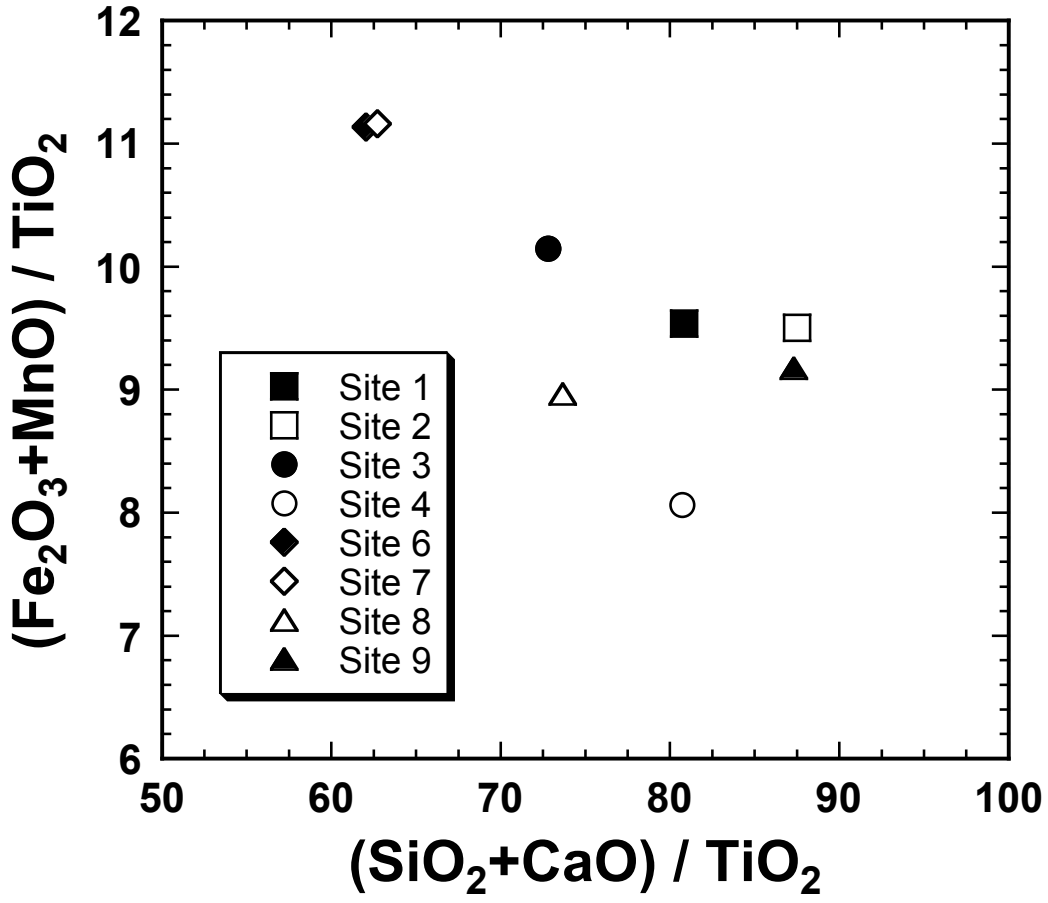

Fig. A−11. Ti-normalized major element ratio of the mud samples. The samples trending from the bottom right to the top left show that the depletion of Si and Ca reflects the enrichment of Fe and Mn.

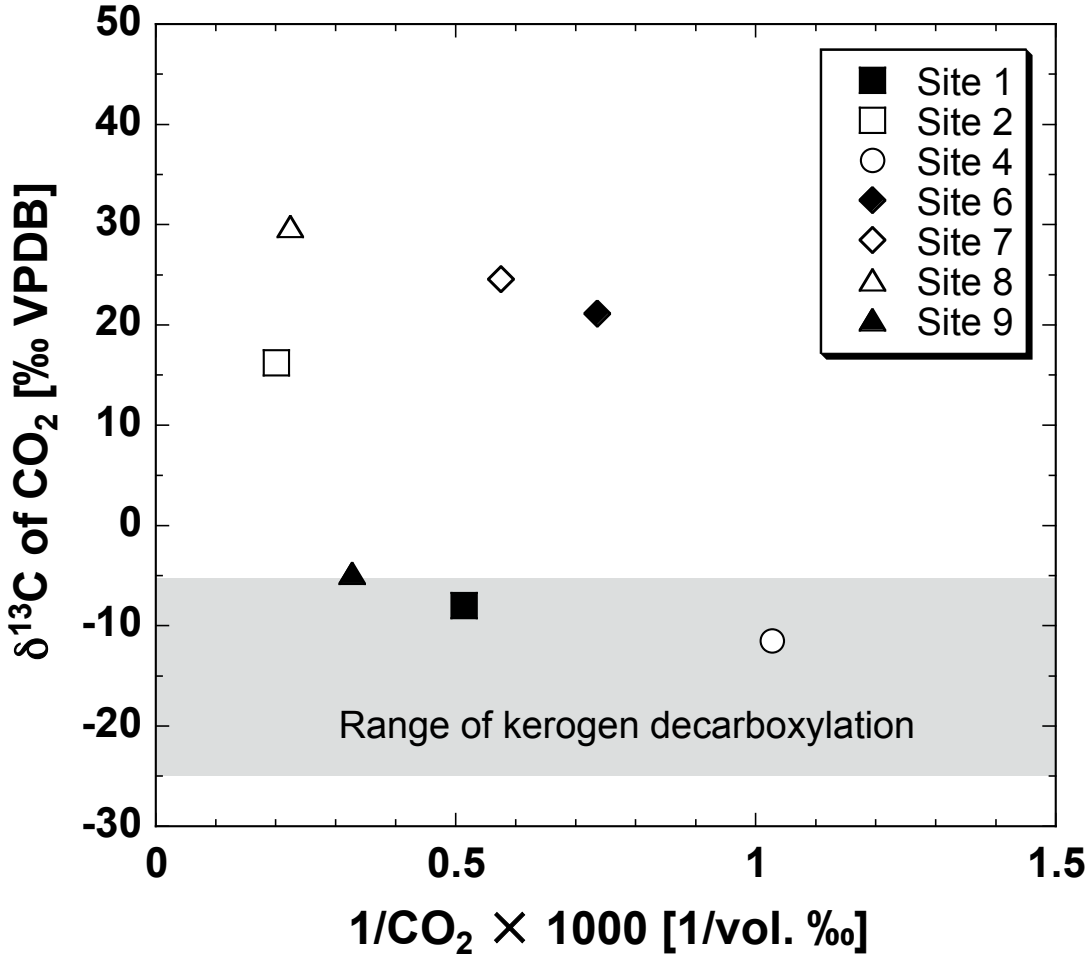

Fig. A−12. Relationship between $\delta^{13}C$ values of CO_2 and inverse of CO_2 concentrations in the gas phase. Note that the effect of air contamination is corrected based on the concentration of O_2. Colored area shows ranges of $\delta^{13}C$ values of CO_2 originated from natural thermogenic CO_2 (Jenden et al. 1993; Kotarba, 2001; Hosgormes et al., 2008).

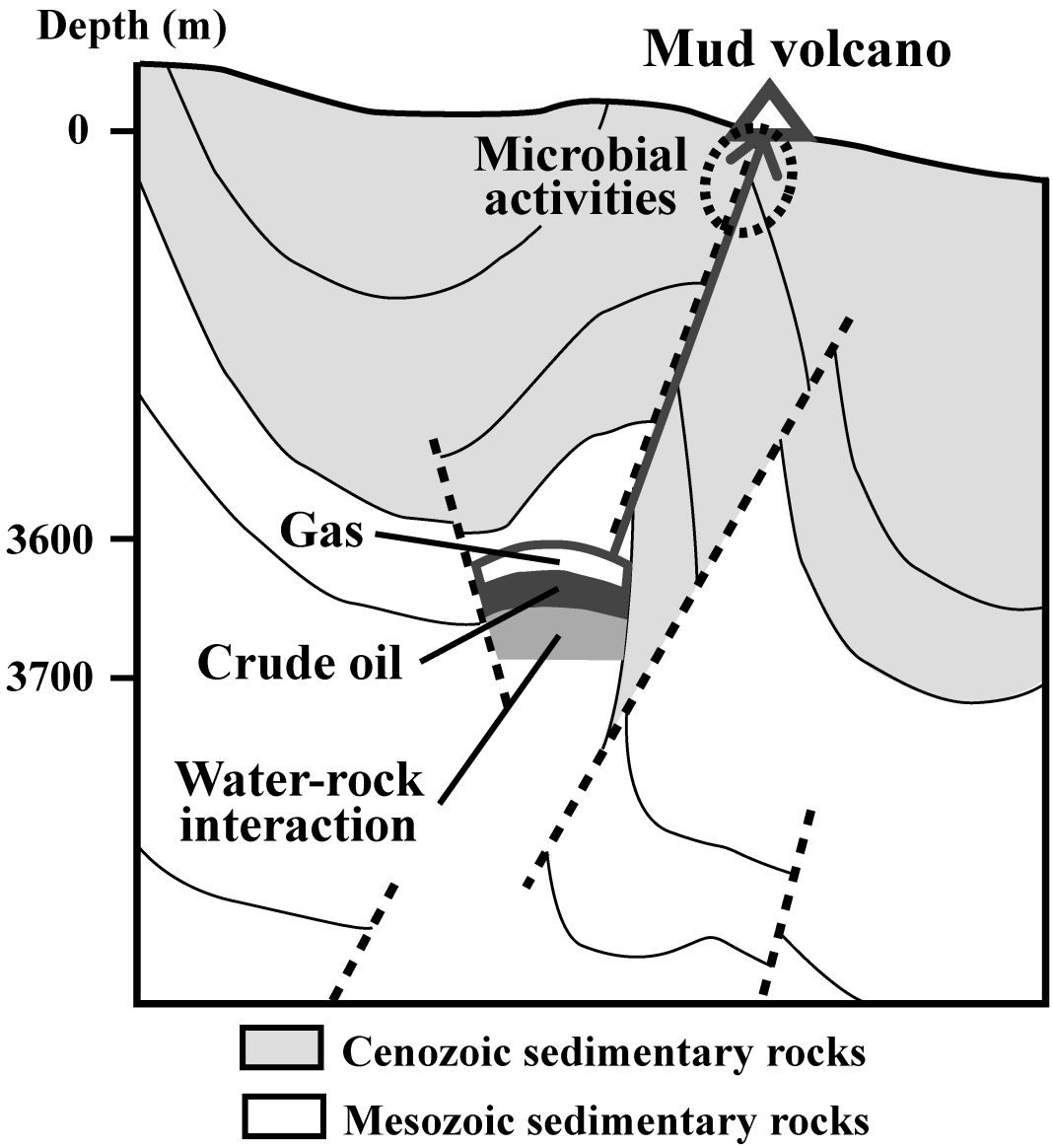

Fig. A−13. Schematic illustration of the origin of mud volcanoes in the study area. Cross section map is based on Avouac et al. (1993). Dashed line represents the faults.

References

Adachi, M., Yamamoto, K., Sugisaki, R. (1986) Hydrothermal chert and associated siliceous rocks from the Northern Pacific: their geological significance as indication of ocean ridge activity. *Sediment. Geol.* **47**, 125–148.

Ahlberg, A., Olsson, I., Šimkevičius, P. (2003) Triassic–Jurassic weathering and clay mineral dispersal in basement areas and sedimentary basins of southern Sweden. *Sediment. Geol.* **161**, 15–29.

Akinlua, A., Torto, N., Ajayi, T. R. (2008) Determination of rare earth elements in Niger Delta crude oils by inductively coupled plasma-mass spectrometry. *Fuel* **87**, 1469–1477.

Albani, A. E., Bengtson, S., Canfield, D. E., Bekker, A., Macchiarelli, R., Mazurier, A., Hammarlund, E. U., Boulvais, P., Dupuy, J.-J., Fontaine, C., Fürsich, F. T., Gauthier-Lafaye, F., Janvier, P., Javaux, E., Ossa, F. O., Pierson-Wickmann, A.-C., Riboulleau, A., Sardini, P., Vachard, D., Whitehouse, M., Meunier, A. (2010) Large colonial organisms with coordinated growth in oxygenated environments 2.1 Gyr ago. *Nature* **466**, 100–104.

Alibo, D. S., Nozaki, Y. (1999) Rare earth elements in seawater: Particle association, shale-normalization, and Ce oxidation. *Geochim. Cosmochim. Acta* **63**, 363–372.

Allen, D. E., Seyfried, W. E., Jr. (2005) REE controls in ultramafic hosted MOR hydrothermal systems: An experimental study at elevated temperature and pressure. *Geochim. Cosmochim. Acta* **69**, 675–683.

Anbar A. D. (2004) Molybdenum stable isotopes: observations, interpretations and directions. In *Geochemistry of Non-Traditional Stable Isotopes*. vol. **55** (eds. C. M. Johnson, B. L. Beard, F. Albarède). Mineralogical Society of America and Geochemical Society, Washington. pp. 429–454.

Anbar A. D., Rouxel O. (2007) Metal stable isotopes in paleoceanography. *Annu. Rev. Earth Planet. Sci.* **35**, 717–746.

Anbar, A. D., Duan, Y., Lyons, T. W., Arnold, G. L., Kendall, B., Creaser, R. A., Kaufman, A. J., Gordon, G. W., Scott, C., Garvin, J., Buick, R. (2007) A whiff of

oxygen before the Great Oxidation Event? *Science* **317**, 1903–1906.

Anders, E., Grevesse, N. (1989) Abundances of the elements: Meteoritic and solar. *Geochim. Cosmochim. Acta* **53**, 197–214.

Ando, A., Kodama, K., Kojima, S. (2001) Low-latitude and Southern Hemisphere origin of Anisian (Triassic) bedded chert in the Inuyama area, Mino terrane, central Japan. *J. Geophys. Res.* **106**, 1973–1986.

Aplin, A. (1984) Rare earth element geochemistry of Central Pacific ferromanganese encrustations. *Earth Planet. Sci. Lett.* **71**, 13–22.

Arakawa, R. (1998) Middle Jurassic radiolaria assemblages from manganese dioxide nodules, Kuzuu area of Ashio terrane, central Japan. *Bull. Tochigi Pref. Museum* **15**, 51–76. (In Japanese with English abstract)

Avouac, J. P., Tapponnier, P., Bai, M., You, H., Wang, G. (1993) Active thrusting and folding along the northern Tien Shan and late Cenozoic rotation of the Tarim relative to Dzungaria and Kazakhstan. *J. Geophys. Res*. **98**, 6755−6804.

Bach, W., Roberts, S., Vanko, D. A., Binns, R. A., Yeats, C. J., Craddock, P. R., Humphris, S. E. (2003) Controls of fluid chemistry and complexation on rare-earth element contents of anhydrite from the Pacmanus subseafloor hydrothermal system, Manus Basin, Papua New Guinea. *Miner. Depos*. **38**, 916−935.

Bailey, T. R., Rosenthal, Y., McArthur, J. M., van de Schootbrugge, B., Thirlwall, M. F. (2003) Paleoceanographic changes of the Late Pliensbachian-Early Toarcian interval: a possible link to the genesis of an Oceanic Anoxic Event. *Earth Planet. Sci. Lett*. **212**, 307–320.

Balci N., Bullen T. D., Witte-Lien K., Shanks W. C., Motelica M., Mandernack K. W. (2006) Iron isotope fractionation during microbially stimulated Fe(II) oxidation and Fe(III) precipitation. *Geochim. Cosmochim. Acta* **70**, 622–639.

Ball, J. W., Nordstrom, D. K. (1991) User's manual for WATEQ4F, with revised thermodynamic data base and test cases calculating speciation of major, trace and redox elements in natural waters. *USGS Open-file Report*, 91–183.

Balistrieri L. S., Borrok D. M., Wanty R. B., Ridley W. I. (2008) Fractionation of Cu and Zn isotopes during adsorption onto amorphous Fe(III) oxyhydroxide: Experimental mixing of acid rock drainage and ambient river water. *Geochim. Cosmochim. Acta* **72**, 311–328.

Barling J., Anbar A. D. (2004) Molybdenum isotope fractionation during adsorption by manganese oxides. *Earth Planet. Sci. Lett.* **217**, 315–329.

Barling J., Arnold G. L., Anbar A. D. (2001) Natural mass-dependent variations in the isotopic composition of molybdenum. *Earth Planet. Sci. Lett.* **193**, 447–457.

Bau, M. (1991) Rare-earth element mobility during hydrothermal and metamorphic fluid rock interaction and the significance of the oxidation-state of europium. *Chem. Geol*. **93**, 219–230.

Bau, M. (1993) Effects of syn- and post-depositional processes on the rare-earth element distribution in Precambrian iron-formations. *Eur. J. Mineral.* **5**, 257–267.

Bau, M. (1996) Controls on the fractionation of isovalent trace elements in magmatic and aqueous systems: evidence from Y/Ho, Zr/Hf, and lanthanide tetrad effect. *Contrib. Mineral. Petrol.* **123**, 323–333.

Bau, M. (1999) Scavenging of dissolved yttrium and rare earths by precipitating iron oxyhydroxide: Experimental evidence for Ce oxidation, Y-Ho fractionation, and lanthanide tetrad effect. *Geochim. Cosmochim. Acta* **63**, 67–77.

Bau, M., Dulski, P. (1996a) Distribution of yttrium and rare-earth elements in the Penge and Kuruman iron-formations, Transvaal Supergroup, South Africa. *Precambrian Res.* **79**, 37–55.

Bau, M., Koschinsky, A. (2009) Oxidative scavenging of cerium on hydrous Fe oxide: Evidence from the distribution of rare earth elements and yttrium between Fe oxides and Mn oxides in hydrogenetic ferromanganese crusts. *Geochem. J.* **43**, 37–47.

Bau, M., Koschinsky, A., Dulski, P., Hein, J. R. (1996) Comparison of the partitioning behaviours of yttrium, rare earth elements, and titanium between hydrogenetic marine ferromanganese crusts and seawater. *Geochim. Cosmochim. Acta* **60**,

1709–1725.

Bau, M., Usui, A., Pracejus, B., Mita, N., Kanai, Y., Irber, W., Dulski, P. (1998) Geochemistry of low-temperature water–rock interaction: evidence from natural waters, andesite, and iron–oxyhydroxide precipitates at Nishiki-numa iron-spring, Hokkaido, Japan. *Chem. Geol.* **151**, 293–307.

Beard B. L., Johnson C. M. (2004) Fe isotope variations in the modern and ancient Earth and other planetary bodies. In *Geochemistry of Non-Traditional Stable Isotopes*. vol. **55** (eds. C. M. Johnson, B. L. Beard, F. Albarède). Mineralogical Society of America and Geochemical Society, Washington. pp. 319–357.

Benton, M. J. (2004) Origin and relationships of Dinosauria, in: Weishampel, D.B., Dodson, P., Osmólska, H (Eds.), *The Dinosauria*. University of California Press, Berkeley, pp. 7–19.

Bethke, C. M. (2006) The Geochemist's Workbench Release 6.0 GWB Reaction Modeling Guide. Rockwater, Inc., Golden, CO.

Bigeleisen, J., Mmayer, M. G. (1947) Calculation of equilibrium constants for isotopic exchange reactions. *J. Chem. Phys.* **15**, 261–267.

Bragin, N. Y., Konstantinov, A. G., Sobolev, E. S. (2012) Upper Triassic stratigraphy and paleobiogeography of Kotel'nyi Island (New Siberian Islands). *Stratigr. Geo. Correl.* **20**, 541–566.

Braun, J. J., Pagel, M., Muller, J. P., Bilong, P., Michard, A., Guillet, B. (1990) Cerium anomalies in lateritic profiles. *Geochim. Cosmochim. Acta* **54**, 781–795.

Brookins, D. G. (1988) Eh-pH Diagrams for Geochemistry. Springer-Verlag. pp. 176.

Bruland, K. W., Lohan, M. C. (2003) Controls of trace metals in seawater. In: Holland, H. D., Turekeian, K. K. (Eds.) *Treatise on geochemistry*, vol. **6**. Elsevier, Amsterdam, pp. 23–47.

Butler I. B., Archer C., Vance D., Oldroyd A., Rickard D. (2005) Fe isotope fractionation on FeS formation in ambient aqueous solution. *Earth and Planetary Science Letters*, **236**, 430–442.

Byrne, R. H., Kim, K. H. (1990) Rare earth element scavenging in seawater. *Geochim.*

Cosmochim. Acta **54**, 2645–2656.

Byrne, R. H., Sholkovitz, E. R. (1996) Marine chemistry and geochemistry of the lanthanides. *Handbook on the Physics and Chemistry of Rare Earth*. Vol. 23 (Gschneidner, K. A., Jr., Eyring, L., eds.), 497–593, Elsevier Science B.V.

Cacaly, S., Marechal, C., Juillot, F., Guyot, F., Benedetti, M. (2004) Zn isotopes fractionation upon sorption and precipitation. *Geochim. Cosmochim. Acta* **68**, A366.

Calvert, S. E., Price, N. B., (1970) Composition of manganese nodules and manganese carbonates from Loch Fynn, Scotland. *Contrib. Mineral. Petrol.* **29**, 215–233.

Campbell I. H., Allen, C. M. (2008) Formation of supercontinents linked to increase in atmospheric oxygen. *Nature Geosci.* **1**, 554–558.

Carroll, A. R. (1998) Upper Permian lacustrine organic facies evolution, Southern Junggar Basin, NW China. *Org. Geochem.* **28**, 649−667.

Catling D., Claire M. (2005) How Earths atmosphere evolved to an oxic state: a status report. *Earth Planet. Sci. Lett.* **237**, 1–20.

Chamley, H. (1989) Clay Sedimentology. Springer-Verlag, Berlin Heidelberg. pp. 623.

Chang, Q., Mishima, T., Yabuki, S., Takahashi, Y., Shimizu, H. (2000) Sr and Nd isotope ratios and REE abundances of moraines in the mountain areas surrounding the Taklimakan Desert, NW China. *Geochem. J.* **34**, 407−427.

Chen, Z.-Q., Benton, M. J. (2012) The timing and pattern of biotic recovery following the end-Permian mass extinction. *Nature Geosci.* **5**, 375–383.

Choppin, G. R. (2002) Covalency in f-element bonds. *J. Alloys Compd.* **344**, 55–59.

Clayton, R. E., Hudson-Edwards, K. A., Houghton, S. L. (2005) Isotopic effects during Cu adsorption onto goethite. *Geochim. Cosmochim. Acta* **69**, A216.

Clayton, R. N., Friedman, I., Graf, D. L., Mayeda, T. K., Meents, W. F., Shimp, N. F. (1966) The origin of saline formation waters 1. Isotopic composition. *J. Geophis. Res.* **71**, 3869−3882.

Clayton, J. L., Yang, J., King, J. D., Lillis, P. G., and Warden, A. (1997) Geochemistry of oils from Junggar Basin, northwest China. *AAPG Bull.* **81**, 1926–1944.

Cleve, P. T. (1879a) Sur deux nouveaux éléments dans l'erbine. *C. R. Acad. Sci.* **88**, 478−481.

Cleve, P. T. (1879b) Sur le scandium. *C. R. Acad. Sci.* **89**, 419–422.

Cohen, A. S., Coe, A. L., Harding, S. M., Schwark, L. (2004) Osmium isotope evidence for the regulation of atmospheric CO_2 by continental weathering, *Geology* **32**, 157–160.

Cohen, A. S., Coe, A. L., Kemp, D. B. (2007) The Late Palaeocene–Early Eocene and Toarcian (Early Jurassic) carbon isotope excursions: a comparison of their time scales, associated environmental changes, causes and consequences. *J. Geol. Soc.* **164**, 1093–1108.

Colombi, C. E., Parrish, J. T. (2008) Late Triassic Environmental evolution in Southwestern Pangea: plant taphonomy of the Ischigualasto Formation. *Palaios* **23**, 778–795.

Condie, K. C. (1993) Chemical composition and evolution of the upper continental crust: Contrasting results from surface samples and shales. *Chem. Geol.* **104**, 1−37.

Connelly, N. G., Damhus, T., Hartshorn, R. M., Hutton, A. T. (2005) Nomenclature of Inorganic Chemistry IUPAC Recommendations 2005. In: The Royal Society of Chemistry, pp. 377.

Cordey, F. (1998) Radiolaires des complexes d'accrétion de la Cordillère Canadienne (Colombie-Britannique). *Bull. Geol. Sur. Can.* **509**, 1–209.

Criss, R. E. (1999) Principles of stable isotope distribution. *Oxford University Press*, Inc., New York. pp. 254.

Crosby, H. A., Johnson, C. A., Roden, E. E., Beard, B. L. (2005) Coupled Fe(II)- Fe(III) electron and atom exchange as a mechanism for Fe isotope fractionation during dissimilatory iron oxide reduction. *Environ. Sci. Technol.* **39**, 6698–6704.

Cutten, H. N. C., Korsch, R. J., Roser, B. P. (2006) Using geochemical fingerprinting to determine transpressive fault movement history: Application to the New Zealand Alpine Fault. *Tectonics* **25**, TC4014.

De Baar, H. J. W, Bacon, M. P., Brewer, P. G., Bruland, K. W. (1985) Rare earth elements in the Pacific and Atlantic Oceans. *Geochim. Cosmochim. Acta* **49**, 1943–1959.

De Baar, H. J. W, German, R. C., Elderfield, H., Van Gaans, P. (1988) Rare earth elements distributions in anoxic waters of the Cariaco Trench. *Geochim. Cosmochim. Acta* **52**, 1203–1219.

de Boisbaudran, L. P. E. (1879) Nouvelles raies spectrales observées dans des substances extradites de la samarskite. *C. R. Acad. Sci.* **88**, 322–324.

de Boisbaudran, L. P. E. (1886a) Le Yα de M. de Marignac est définitivement nomme gadolinium. *C. R. Acad. Sci.* **102**, 902.

de Boisbaudran, L. P. E. (1886b) L'homine (ou terre X de M. Soret) contient au moins deux radicaux métalliques. *C. R. Acad. Sci.* **102**, 1003–1005.

Decelle, J., Probert, I., Bittner, L., Desdevises, Y., Colin, S., de Vargas, C., Gali, M., Simo, R., Not, F. (2012) An original mode of symbiosis in open ocean plankton. *Proc. Natl. Acad. Sci. U. S. A.* **109**, 18000–18005.

De Carlo, E. H., McMurtry, G. M. (1992) Rare-earth element geochemistry of ferromanganese crusts from the Hawaiian Archipelago, Central Pacific. *Chem. Geol.* **95**, 235–250.

de Laeter J. R., Böhlke J. K., De Bièvre P., Hidaka H., Peiser H. S., Rosman K. J. R., Taylor P. D. P. (2003) Atomic weights of the elements: Review 2000 (IUPAC Technical Report). *Pure Appl. Chem.*, 75, 683–799.

De La Rocha C. L., Brzezinski M. A., DeNiro M. J. (2000) A first look at the distribution of the stable isotopes of silicon in natural waters. *Geochim. Cosmochim. Acta* **64**, 2467–2477.

Denarçay, E.-A. (1896) Sur un nouvel élément contenu dans les terres rares voisines du samarium. *C. R. Acad. Sci.* **122**, 728–730.

Denarçay, E.-A. (1901) Sur un nouvel élément l'europium. *C. R. Acad. Sci.* **132**, 1484–1486.

Dera, G., Pellenard, P., Neige, P., Deconinck, J.-F., Pucéat, E., Dommergues, J.-L.

(2009) Distribution of clay minerals in Early Jurassic Peritethyan seas: Palaeoclimatic significance inferred from multiproxy comparisons. *Palaeogeogr. Palaeoclimatol. Palaeoecol.* **271**, 39–51.

Derry, L. A., France-Lanord, C. (1996) Neogene growth of the sedimentary organic carbon reservoir. *Paleoceanography* **11**, 267–275.

DesMarais, D. J. (1992) Tectonic control of the crustal organic carbon reservoir during the Precambrian. *Chem. Geol.* **114**, 303–314.

Desheng, L. (1996) Basic characteristics of oil and gas basins in China. *J. Asian Earth Sci.* **13**, 299–304.

Dia, A. N., Castrec-Rouelle, M., Boulegue, J., Comeau, P. (1999) Trinidad mud volcanoes: Where do the expelled fluids come from? *Geochim. Cosmochim. Acta* **63**, 1023−1038.

Dimitrov, L. I. (2002) Mud volcanoes-the most important pathway for degassing deeply buried sediments. *Earth-Sci. Rev.* **59**, 49−76.

Dimitrov, L. I. (2003) Mud volcanoes-a significant source of atmospheric methane. *Geo-Mar. Lett.* **23**, 155−161.

Donofrio, D. A. (1991) Radiolaria and Porifera Spiculae from the Upper Triassic of Aghdarband (NE-Iran). In: Ruttner, A.W. (Ed.), *The Triassic of Aghdarband, AqDarband NE-Iran, and its Pre-Triassic Frame* **38**. Abhandlungen der Geologischen Bundesanstalt, pp. 205–223.

Douville, E., Bienvenu, P., Charlou, J. L., Donval, J. P., Fouquet, Y., Appriou, P., Gamo, T. (1999) Yttrium and rare earth elements in fluids from various deep-sea hydrothermal systems. *Geochim. Cosmochim. Acta* **63**, 627–643.

Dräger, G., Frahm, R., Materlik, G., Brümmer, O. (1988) On the multipole character of the X-ray transitions in the pre-edge structure of Fe K absorption spectra: An experimental study. *Phys. Status Solidi B* **146**, 287–294.

Duce, R. A., Tindale, N. W. (1991) Atmospheric transport of iron and its deposition in the ocean. *Limnol. Oceanogr.* **36**, 1715–1726.

Elderfield, H., Greaves, M. J. (1982) The rare-earth elements in sea-water. *Nature* **296**,

214−219.

Elderfield, E. H., Hawkesworth, C. J., Greaves, M. J., Calvert, S. E. (1981) Rare earth element geochemistry of oceanic ferromanganese nodules and associated sediments. *Geochim. Cosmochim. Acta* **45**, 513–528.

Ellis A. S., Johnson T. M., Bullen T. D. (2002) Chromium isotopes and the fate of hexavalent chromium in the environment. *Science* **295**, 2060–2062.

Ellis, A. S., Johnson, T. M., Bullen, T. D. (2004) Using chromium stable isotope ratios to quantify Cr(VI) reduction: lack of sorption effects. *Environ. Sci. Technol*. **38**, 3604–3607.

Erba, E. (2006) The first 150 million years history of calcareous nannoplankton: Biosphere–geosphere interactions. *Palaeogeogr. Palaeoclimatol. Palaeoecol.* **232**, 237–250

Etiope, G. (2010) Geological methane. In: Reay, D., Smith, P., van Amstel, A. (Eds.), *Methane and Climate Change*. Earthscan, London (Chapter 4).

Etiope, G., Klusman, R. W. (2002) Geologic emissions of methane to the atmosphere. *Chemosphere* **49**, 777−789.

Etiope, G., Milkov, A. V. (2004) A new estimate of global methane flux from onshore and shallow submarine mud volcanoes to the atmosphere. *Environ. Geol.* **46**, 997−1002.

Etiope, G., Feyzullayev, A., Baciu, C. L. (2009a) Terrestrial methane seeps and mud volcanoes: a global perspective of gas origin. *Mar. Pet. Geol.* **26**, 333−344.

Etiope, G., Feyzullayev, A., Milkov, A. V., Waseda, A., Mizobe, K., Sun, C. H. (2009b) Evidence of subsurface anaerobic biodegradation of hydrocarbons and potential secondary methanogenesis in terrestrial mud volcanoes. *Mar. Pet. Geol.* **26**, 1692−1703.

Etiope, G., Nakada, R., Tanaka, K., Yoshida, N. (2011) Gas seepage from Tokamachi mud volcanoes, onshore Niigata Basin (Japan): Origin, post-genetic alterations and CH_4-CO_2 fluxes. *Appl. Geochem*. **26**, 348−359.

Farquhar, J., Bao, H. M., Thiemens, M., (2000) Atmospheric influence of Earth's

earliest sulfur cycle. *Science* **289**, 756–758.

Feyzullayev, A., Movsumova, U. (2001) About the origin of isotopically heavy CO_2 in gases of Azerbaijan mud volcanoes. *Azerb. Geol*. **6**, 96−105 (in Russian).

Fleet, A. J. (1984) Aqueous and sedimentary geochemistry of the rare earth elements. In: P. Henderson (Editor), Rare Earth Element Geochemistry, *Elsevier, Amsterdam*, pp. 343–373.

Foster, A. L., Brown, G. E., Parks, G. A. (2003) X-ray absorption fine structure study of As(V) and Se(IV) sorption complexes on hydrous Mn oxides. *Geochim. Cosmochim. Acta* **67**, 1937–1953.

France-Lanord, C., Derry, L. A. (1997) Organic carbon burial forcing of the carbon cycle from Himalayan erosion. *Nature* **390**, 65–67.

Frei, R., Gaucher, C., Poulton, S. W., Canfield, D. E. (2009) Fluctuations in Precambrian atmospheric oxygenation recorded by chromium isotopes. *Nature* **461**, 250–253.

Frimmel, H. E. (2009) Trace element distribution in Neoproterozoic carbonates as palaeoenvironmental indicator. *Chem. Geol.* **258**, 338–353.

Fryer, B. J. (1977) Rare earth evidence in iron-formations for changing Precambrian oxidation states. *Geochim. Cosmochim. Acta* **41**, 361–367.

Fu, B. H., Zheng, G. D., Ninomiya, Y., Wang, C. Y., Sun, G. (2007) Mapping hydrocarbon-induced mineralogical alterations in the northern Tian Shan using ASTER multispectral data. *Terra Nova* **19**, 225–231.

Fu, F., Akagi, T., Shinotsuka, K. (1998) Distribution pattern of rare earth elements in fern: Implication for intake of fresh silicate particles by plants. *Biol. Trace Elem. Res*. **64**, 13–26.

Fujihara, T. (2009) Difference in radiolarian ages of Middle Jurassic manganese carbonate nodules and their host rocks in the Mino Terrane: Implications for the origin of manganese carbonate micro-spherules. *News Osaka Micropaleontol.* **14**, 413–432. (in Japanese with English abstract)

Fujii T., Yamamoto T., Nishizawa K., Inagawa J., Gunji K., Watanabe K. (1998)

Separation of samarium isotopes by a crown ether. *Solvent Extr. Ion Exch.* **16**, 985–999.

Fujii T., Yamamoto T., Inagawa J., Gunji K., Watanabe K., Nishizawa K. (2000) Nuclear size and shape effect in chemical isotope enrichment of neodymium using dicyclohexano-18-crown-6. *Solvent Extr. Ion Exch.* **18**, 1155–1166.

Fujinaka, K., Kato, Y., (2005) Radiolarian age of red chert from the Kunimiyama ferromanganese deposit in the Northern Chichibu Belt, central Shikoku. *Resour. Geol.* **55**, 353–356.

Fujioka, N., Saga, H. (1980) Boundary of the Takinoue Formation and the Poronai Group in the MITI NANPORO well, Hokkaido, Japan. *J. Japan. Acco. Petrol. Technol.* **45**, 193–201.

Fürsich, F. T., Singh, I. B., Joachimski, M., Krumm, S., Schlirf, M., Schlirf, S. (2005) Palaeoclimate reconstructions of the Middle Jurassic of Kachchh (western India): an integrated approach based on palaeoecological, oxygen isotopic, and clay mineralogical data. *Palaeogeogr. Palaeoclimatol. Palaeoecol.* **217**, 289–309.

Furin, S., Preto, N., Rigo, M., Roghi, G., Gianolla, P., Crowley, J. L., Bowring, S. A. (2006) High-precision U-Pb zircon age from the Triassic of Italy: Implications for the Triassic time scale and the Carnian origin of calcareous nannoplankton and dinosaurs. *Geology* **34**, 1009–1012.

Gadolin, J. (1794) Undersökning af en svart tung Stenart ifrån Ytterby Stenbrott i Roslagen. *K. Vetenskaps-akad. nya handl.* **15**, 137–155.

Galy, V., France-Lanord, C., Beyssac, O., Faure, P., Kudrass, H., Palhol, F. (2007) Efficient organic carbon burial in the Bengal fan sustained by the Himalayan erosion system. *Nature* **450**, 407–410.

Galy, A., Pokrovsky, O. S., Schott, J. (2002) Ge-isotopic fractionation during its sorption on goethite: an experimental study. *Geochim. Cosmochim. Acta* **66**, A259.

German, C.R., Elderfield, H., (1989) Rare earth elements in Saanich Inlet, British Columbia, a seasonally anoxic basin. *Geochim. Cosmochim. Acta* **53**, 2561–

2571.

Gill, B.C., Lyons, T.W., Jenkyns, H.C. (2011) A global perturbation to the sulfur cycle during the Toarcian Oceanic Anoxic Event. *Earth Planet. Sci. Lett.* **312**, 484–496.

Giuli, G., Pratesi, G., Cipriani, C., Paris, E. (2002) Iron local structure in tektites and impact glasses by extended X-ray absorption fine structure and high-resolution X-ray absorption near-edge structure spectroscopy. *Geochim. Cosmochim. Acta* **66**, 4347–4353.

Goldberg, T., Archer, C., Vance, D., Poulton, S. (2009) Mo isotope fractionation during adsorption to Fe (oxyhydr)oxides. *Geochim. Cosmochim. Acta* **73**, 6502–6516.

Goldberg, E. D., Smith, R. H., Koide, M., Schmitt, R. A. (1963) Rare earth distributions in marine environment. *J. Geophys. Res*. **68**, 4209–4217.

Golonka, J. (2007) Late Triassic and Early Jurassic palaeogeography of the world. *Palaeogeogr. Palaeoclimatol. Palaeoecol.* **244**, 297–307.

Graham, S. A., Brassell, S., Carroll, A. R., Xiao, X., Demaison, G., Mcknight, C. L., Liang, Y., Chu, J., Hendrix, M. S. (1990) Characteristics of selected petroleum source rocks, Xinjiang Uygur Autonomous Region, northwest China. *AAPG Bull*. **74**, 493−512.

Grandjean-Lécuyer, P., Feist, R., Albarède, F. (1993) Rare earth elements in old biogenic apatite. *Geochim. Cosmochim. Acta* **57**, 2507–2514.

Greene, A. R., Scoates, J. S., Weis, D., Nixon, G. T., Kieffer, B. (2009) Melting history and magmatic evolution of basalts and picrites from the accreted Wrangellia oceanic plateau, Vancouver Island, Canada. *J. Petrol.* **50**, 467–505.

Gromet, L. P., Silver, L. T. (1983) Rare earth element distributions among minerals in a granodiorite and their petrogenetic implications. *Geochim. Cosmochim. Acta* **47**, 925–939.

Gromet, L. P., Dymek, R. F., Haskin, L. A., Korotev, R. L., (1984) The 'North American shale composite': Its compilation, major and trace element characteristics. *Geochim. Cosmochim. Acta* **48**, 2469–2482.

Gussone N., Böhm F., Eisenhauer A., Dietzel M., Heuser A., Teichert B. M. A., Reitner

J., Wörheide G., Dullo W.-C. (2005) Calcium isotope fractionation in calcite and aragonite. *Geochim. Cosmochim. Acta* **69**, 4485–4494.

Hallam, A., Wignall, P. B. (1997) Mass extinctions and their aftermath. Oxford University Press, Oxford. pp. 320.

Halliday A. N., Lee D.-C., Christensen J. N., Rehkämper M., Yi W., Luo X, Hall C. M., Ballentine C. J., Pettke T., Stirling C. (1998) Applications of multiple collector-ICPMS to cosmochemistry, geochemistry, and paleoceanography. *Geochim. Cosmochim. Acta* **62**, 919–940.

Hanson, G. N. (1980) Rare Earth Elements in Petrogenetic Studies of Igneous Systems. *Ann. Rev. Earth Planet Sci.* **8**, 371–406.

Hasan, M. U., Ali, M. F., Bukhari, A. (1983) Structural characterization of Saudi Arabian heavy crude oil by n.m.r. spectroscopy. *Fuel* **62**, 518–523.

Haskin, L. A., Paster, T. P. (1979) Geochemistry and mineralogy of the rare earth elements. in: *Handbook on the physics and chemistry of rare earth*. (eds. Gschneidner, K.A.Jr., Eyring, L.), **3**. Elsevier, Amsterdam, pp. 1–80.

Hatakeda, K., Suzuki, N., Matsuoka, A. (2007) Quantitative morphological analyses and evolutionary history of the Middle Jurassic polycystine radiolarian genus Striatojaponocapsa Kozur. *Mar. Micropal.* **63**, 39–56.

Hattori, I. (1988) Radiolarian fossils from manganese nodules at the upper reach of the Tarumigawa in the Nanjo massif, Fukui Prefecture, central Japan, and the tectonic significance of the northwestern Mino Terrane. *Bull. Fukui Municipal Museum Natural History* **35**, 55–101. (In Japanese with English abstract)

Hein, J. R., Fleishman, C. L., Morgenson, L. A., Bloomer S. H., Stern R. J. (1987) Submarine ferromanganese deposits from the Mariana and Volcano Volcanic Arcs, West Pacific. *USGS Open File Report* 87–281.

Henderson, P. (1984) Rare Earth Element Geochemistry. *Elsevier, Amsterdam* pp. 510.

Hensen, C., Nuzzo, M., Hornibrook, E., Pinherio, L. M., Bock, B., Magalhaes, V. H., Bruckmann, W. (2007) Sources of mud volcano fluids in the Gulf of Cadiz-indications for hydrothermal imprint. *Geochim. Cosmochim. Acta* **71**,

1232−1248.

Herbert, B. E., Bertsch, P. M. (1995) Characterization of dissolved and colloidal organic matter in soil solution: a review. In: *Carbon Forms and Functions in Forest Soils*. McFee, W. W., Kelly, J. M. (Eds.), pp. 63−88. Madison, WI: Soil Science Society of America.

Hermoso, M., Minoletti, F., Rickaby, R. E. M., Hesselbo, S. P., Baudin, F., Jenkyns, H.C. (2012) Dynamics of a stepped carbon-isotope excursion: ultra high-resolution study of Early Toarcian environmental change. *Earth Planet. Sci. Lett*. **319–320**, 45–54.

Herring, P., 2002. The Biology of the Deep Oecan. Oxford Univ. Press. pp. 314.

Hesselbo, S. P., Gröcke, D. R., Jenkyns, H. C., Bjerrum, C., Farrimond, P., Morgans Bell, H., Green, O. (2000) Massive dissociation of gas hydrate during a Jurassic oceanic anoxic event, *Nature* **406**, 392–395.

Hesselbo, S. P., Jenkyns, H. C., Duarte, L., Oliveira, L. C. (2007) Carbon-isotope record of the Early Jurassic (Toarcian) Oceanic Anoxic Event from fossil wood and marine carbonate (Lusitanian Basin, Portugal), *Earth Planet. Sci. Lett.* **253**, 455–470.

Hill, I. G., Worden, R. H., Meighan, I. G. (2000) Yttrium: The immobility-mobility transition during basaltic weathering. *Geology* **28**, 923−926.

Hirata, T., Shimizu, H., Akagi, T., Sawatari, H., Masuda, A. (1988) Precise determination of rare earth elements in geological standard rocks by inductively coupled plasma source mass spectrometry. *Anal. Sci.* **4**, 637−643.

Hisinger, W., Berzelius, J. J. (1804) Cerium: ein neuer Metall aus einer Schwedischen Steinart, Bastnäs Tungstein gennant. *Neues Allgemeines J. Chem.* **2**, 397−418.

Hochuli, P. A., Vigran, J. O. (2010) Climate variations in the Boreal Triassic — Inferred from palynological records from the Barents Sea. *Palaeogeogr. Palaeoclimatol. Palaeoecol.* **290**, 20–42.

Hogdahl, O. T., Melson, S., Bowen, V. T. (1968) Neutron activation analysis of lanthanoid elements in sea water. In: Advances in Chemistry Series. Baker, R. A.

(Ed.), American Chemical Society, Vol. 73, Washington, DC. pp. 308–325.

Hori, R. S. (1990) Lower Jurassic radiolarian zones of SW Japan. *Trans. Proc. Palaeon. Soc. Japan N.S.* **159**, 562–586.

Hori, S. R. (1993) Toarcian Oceanic Event in deep-sea sediments. *Bull. Geol. Surv. Japan* **44**, 555–570. (in Japanese with English abstract)

Hori, S. R. (1997) The Toarcian radiolarian even in bedded cherts from southwest Japan. *Mar. Micropaleontol.* **30**, 159–169.

Hori, N., Wakita, K. (2006) Early Middle Jurassic (late Aalenian) radiolarian assemblage in a manganese nodule from the Northern Chichibu Belt in the Ino area, Kochi Prefecture, Southwest Japan. *J. Asian Earth Sci.* **27**, 45–60.

Hori, M., Takashima, C., Matsuoka, J., Kano, A. (2009) Carbon and oxygen stable isotopic measurements of carbonate and water samples using mass spectrometer with gas bench. *Bul. Grad. Sch. Soc. Cultur. Stud. Kyushu Univ.* **15**, 51−57. (in Japanese)

Hornung, T., Brandner, R. (2005) Biochronostratigraphy of the Reingraben Turnover (Hallstatt Facies Belt): Local black shale events controlled by regional tectonics, climatic change and plate tectonics. *Facies* **51**, 460–479.

Hornung, T., Brandner, R., Krystyn, L., Joachimski, M. M., Keim, L. (2007a) Multistratigraphic constraints on the NW Tethyan “Carnian Crisis”. In: Lucas, S.G., Spielmann, J.A. (Eds.), *The Global Triassic*, New Mexico Museum of Natural History and Science Bulletin, **41**, pp. 59–67.

Hornung, T., Krystyn, L., Brandner, R. (2007b) Tethys-wide mid-Carnian (Upper Triassic) carbonate productivity decline: evidence for the Alpine Reingraben Event from Spiti (Indian Himalaya)? *J. Asian Earth Sci.* **30**, 285–302.

Hosgormez, H., Etiope, G., Yalçin, M. N. (2008) New evidence for a mixed inorganic and organic origin of the Olympic Chimaera fire (Turkey): a large onshore seepage of abiogenic gas. *Geofluids* **8**, 263−273.

Hu, Z., Bertram, S., Kaindl, G. (1994) X-ray-absorption study of PrO_2 at high pressure. *Phys. Rev. B* **49**, 39–43.

Icopini G. A., Anbar A. D., Ruebush S. S., Tien M., Brantley S. L. (2004) Iron isotope fractionation during microbial reduction of iron: The importance of adsorption. *Geology* **32**, 205–208.

Ikeda, M., Tada, R., Sakuma, H. (2010) Astronomical cycle origin of bedded chert: A middle Triassic bedded chert sequence, Inuyama, Japan. *Earth Planet. Sci. Lett.* **297**, 369–378.

Imai, N., Terashima, S., Itoh, S., Ando, A. (1995) 1994 compilation values for GSJ reference samples, "Igneous rock series". *Geochem. J.* **29**, 91–95.

Imai, N., Terashima, S., Itoh, S., Ando, A. (1996) 1996 compilation of analytical data on nine GSJ geochemical reference samples, “sedimentary rock series”. *Geostandard. Newslett.* **20**, 165–216.

Imoto, N. (1984) Late Paleozoic and Mesozoic cherts in the Tamba Belt, Southwest Japan. Part 1. *Bull. Kyoto Univ. Edu. Series B* **65**, 15–40.

Jenden, P. D., Hilton, D. R., Kaplan, I. R., Craig, H. (1993) Abiogenic hydrocarbons and mantle helium in oil and gas fields. In: Howell, D. (Ed.), *The Future of Energy Gases*, vol. 1570. USGS, pp. 31−35.

Jenkyns, H. C. (1988) The Early Toarcian (Jurassic) Anoxic Event - stratigraphic, sedimentary, and geochemical evidence. *Am. J. Sci.* **288**, 101–151.

Jenkyns, H. C., Clayton, C. J. (1986) Black shales and carbon isotopes in pelagic sediments from the Tethyan Lower Jurassic, *Sedimentology* **33**, 87–106.

Jenkyns, H. C., Jones, C. E., Gröcke, D. R., Hesselbo, S. P., Parkinson, D. N. (2002) Chemostratigraphy of the Jurassic System: applications, limitations and implications for palaeoceanography. *J. Geol. Soc. Lond.* **159**, 351–378.

Johannesson, K. H., Stetzenbach, K. J., Hodge, V. F., Lyons, W. B. (1996) Rare earth elements complexation behavior in circumneutral pH groundwaters: assessing the role of carbonate and phosphate ions. *Earth Planet. Sci. Lett.* **139**, 305–319.

Johnson C. M., Beard B. L., Albarède F. (2004b) *Geochemistry of non-traditional stable isotopes*. Mineralogical Society of America and Geochemical Society, Washington, pp. 454.

Johnson, C. M., Bear, B. L., Roden, E. E. (2008) The iron isotope fingerprints of redox and biogeochemical cycling in modern and ancient Earth. *Annu. Rev. Earth Planet. Sci.* **36**, 457–493.

Johnson C. M., Beard B. L., Roden E. E., Newman D. K., Nealson K. H. (2004a) Isotopic constraints on biogeochemical cycling of Fe. In *Geochemistry of Non-Traditional Stable Isotopes*. vol. 55 (eds. C. M. Johnson, B. L. Beard, F. Albarède). Mineralogical Society of America and Geochemical Society, Washington. pp. 359–408.

Johnson T. M., Bullen T. D. (2004) Mass-Dependent Fractionation of Selenium and Chromium Isotopes in Low-Temperature Environments. In *Geochemistry of Non-Traditional Stable Isotopes*. vol. 55 (eds. C. M. Johnson, B. L. Beard, F. Albarède). Mineralogical Society of America and Geochemical Society, Washington. pp. 289–318.

Johnson, T. M., Herbel, M. J., Bullen, T. D., Zawislanski, P. T. (1999) Selenium isotope ratios as indicators of selenium sources and oxyanion reduction. *Geochim. Cosmochim. Acta* **63**, 2775−2783.

Jones, D. L., Silberling, N. J., Hillhouse, J. (1977) Wrangellia-A displaced terrane in northwestern North America. *Can. J. Earth Sci.* **14**, 2565–2577.

Journet, E., Desboeufs, K. V., Caquineau, S., Colin, J.-L. (2008) Mineralogy as a critical factor of dust iron solubility. *Geophys. Res. Lett.* **35**, L07805.

Juillot F., Maréchal C., Ponthieu M., Cacaly S., Morin G., Benedetti M., Hazemann J. L., Proux O., Guyot F. (2008) Zn isotopic fractionation caused by sorption on goethite and 2- Lines ferrihydrite. *Geochim. Cosmochim. Acta* **72**, 4886–4900.

Kaindl, G., Schmiester, G., Sampathkumaran, E. V., Wachter, P. (1988) Pressure-induced changes in L_{III} X-ray-absorption near-edge structure of CeO_2 and CeF_4: Relevance to 4f-electronic structure. *Phys. Rev. B* **38**, 10174−10177.

Kashiwabara, T., Takahashi, Y., Tanimizu, M., Usui, A. (2011) Molecular-scale mechanisms of distribution and isotopic fractionation of molybdenum between seawater and ferromanganese oxides. *Geochim. Cosmochim. Acta* **75**, 5762–5784.

Kato, S. (1992) Petroleum geology of the Omaezaki distinct, Shizuoka Prefecture – Hydrocarbon potential in fore-arc basins. *J. Japanese Asso. Petrol. Technol.* **57**, 45−52. (in Japanese with English abstract)

Kato, S., Waseda, A., Nishita, H., and Iwano, H. (2009) Geochemistry of crude oils and gases from mud volcanoes and their vicinities in the Higashi-Kubiki area, Niigata Prefecture. *J. Geogr.* **118**, 455–471 (in Japanese with English abstract).

Kato, Y., Yamaguchi, K. E., Ohmoto, H. (2006) Rare earth elements in Precambrian banded iron formations: Secular changes of Ce and Eu anomalies and evolution of atmospheric oxygen. In: *Evolution of Early Earth's Atmosphere, Hydrosphere, and Biosphere−Constraints from Ore Deposits*. Kesler, S.E., Ohmoto, H. (Eds.), Geological Society of America, Boulder, Colorado, pp. 269–289.

Kawabe, I. (1992) Lanthanide tetrad effect in the Ln3 + ionic radii and refined spin-paring energy theory. *Geochem. J.* **26**, 309–335.

Kawabe, I. (1999a) Hydration change of aqueous lanthanide ions and tetrad effects in lanthanide(III)– carbonate complexation. *Geochem. J.* **33**, 267–275.

Kawabe I. (1999b) Thermochemical parameters for solution of lanthanide(III) ethylsulphate and trichloride hydrate series: Tetrad effects and hydration change in aqua Ln^{3+} ion series. *Geochem. J.* **33**, 249−265.

Kawabe, I., Kitahara, Y., Naito, K. (1991) Non-chondritic yttrium/holmium ratio and lanthanide tetrad effect observed in Pre-Cenozoic limestones. *Geochem. J.* **25**, 31–41.

Kawabe I., Ohta A., Ishii S., Tokumura M., Miyauchi K. (1999a) REE partitioning between Fe-Mn oxyhydroxide precipitates and weakly acid NaCl solutions: Convex tetrad effect and fractionation of Y and Sc from heavy lanthanides. *Geochem. J.* **33**, 167–179.

Kawabe, I., Ohta, A., Miura, N. (1999b) Distribution coefficients of REE between Fe oxyhydroxide precipitates and NaCl solutions affected by REE-carbonate complexation. *Geochem. J.* **33**, 181–197.

Kawano, Y., Akiyama, M., Ikawa, T., Roser, B. P., Imaoka, T., Ishioka, J., Yuhara, M.,

Hamamoto, T., Hayasaka, Y., Kagami, H. (2006) Whole rock geochemistry and Sr isotopic compositions of Phanerozoic sedimentary rocks in the Inner Zone of the Southwest Japan Arc. *Gondwana Res*. **9**, 126−141.

Keeling, C. D., Bollenbacher, A. F., Whorf, T. P. (2005) Monthly atmospheric $^{13}C/^{12}C$ isotopic ratios for 10 SIO stations. In: *Trends: A Compendium of Data on Global Change*. Carbon Dioxide Information Analysis Center, Oak Ridge National Laboratory, U.S. Department of Energy, Oak Ridge, TN, http://cdiac.ornl.gov/trends/co2/iso-sio/iso-sio.html.

Keeling, R. F., Piper, S. C., Bollenbacher, A. F., Walker, J. S. (2009) Atmospheric carbon dioxide record from Mauna Loa. In: *Trends: A Compendium of Data on Global Change*. Carbon Dioxide Information Analysis Center, Oak Ridge National Laboratory, U.S. Department of Energy, Oak Ridge, TN, http://cdiac.ornl.gov/trends/co2/sio-mlo.html.

Kemp, D. B., Coe, A. L., Cohen, A. S., Schwark, L. (2005) Astronomical pacing of methane release in the Early Jurassic period, *Nature* **437**, 396–399.

Kharaka, Y. K., Hanor, J. S. (2003) Deep Fluids in the Continents: I. Sedimentary Basins. Treatise on Geochemistry, Vol 5. Drever, J. I. (Ed.). pp. 605. Elsevier, Amsterdam, p.499−540

Kholodov, V. N. (2002) Mud volcanoes, their distribution regularities and genesis: communication 1. mud volcanic provinces and morphology of mud volcanoes. *Lithol. Miner. Resour.* **37**, 197−209.

Kimura, K. Hori, R. (1993) Offscraping accretion of Jurassic chert-clastic complexes in the Mino-Tamba Belt, central Japan. *J. Struct. Geol.* **15**, 145–161.

Klaproth, M. H. (1803) Neues Metall (New Metal). *Neues Allgemeines J. Chem.* **1**, 462–463.

Klein, E. M. (2003) Geochemistry of the igneous oceanic crust: in Rudnick, RL, ed., *The crust*. Oxford, Elsevier-Pergamon, Treatise on Geochemistry, v. 3, pp. 433–464.

Klinkhammer, G. P., Elderfield, H., Edmond, J. M., Mitra, A. (1994) Geochemical

implications of rare earth elements patterns in hydrothermal fluids from mid-ocean ridges. *Geochim. Cosmochim. Acta* **58**, 5105−5113.

Klinkhammer, G., Elderfield, H., Hudson, A. (1983) Rare earth elements in seawater near hydrothermal vents. *Nature* **305**, 185−188.

Kobayashi, I., Tateishi, M., Yoshioka, T., Shimazu, M. (1991) Geology of the Nagaoka District. Quadrangle Series, Scale 1:50,000. *Geol. Serv. Japan.* (In Japanese with English abstract).

Kohfeld, K. E., Harrison, S. P. (2001) DIRTMAP: the geological record of dust. *Earth-Sci. Rev.* **54**, 81–114.

Komuro, K., Wakita, K. (2005) Chemical Profiles across a Jurassic Stratiform Manganese Deposit at Katsuyama in the Mino Terrane of Central Japan: Implications for Depositional Environment, Diagenetic Metal Redistribution and Paleoceanography. *Resour. Geol.* **55**, 321–336.

Komuro, K., Yamaguchi, K., Kajiwara, Y. (2005) Chemistry and sulfur isotopes in a chert-dominant sequence around the stratiform manganese deposit of the Noda-Tamagawa Mine, Northern Kitakami Terrane, Northeast Japan: implication for paleoceanographic environmental setting. *Resour. Geol.* **55**, 337–351.

Kopf, A. J. (2002) Significance of mud volcanism. *Rev. Geophys.* **40**, 1−52.

Kopf, A., Deyhle, A., Lavrushin, V. Y., Polyak, B. G., Gieskes, J. M., Buachidze, G. I., Wallmann, K., Eisenhauer, A. (2003) Isotopic evidence (He, B, C) for deep fluid and mud mobilization from mud volcanoes in the Caucasus continental collision zone. *Int. J. Earth Sci*. **92**, 407−425.

Koschinsky, A., Halbach, P. (1995) Sequential leaching of marine ferromanganese precipitates: genetic implications. *Geochim. Cosmochm. Acta* **59**, 5113–5132.

Kotarba, M. J. (2001) Composition and origin of coalbed gases in the Upper Silesian and Lublin basins, Poland. *Org. Geochem*. **32**, 163−180.

Kozur, H. W., Bachmann, G. H. (2010) The middle Carnian Wet Intermezzo of the Stuttgart Formation (Schilfsandstein), Germanic Basin. *Palaeogeogr. Palaeoclimatol. Palaeoecol.* **290**, 107–119.

Krebs, R. E. (2006) The history and use of our Earth's chemical elements: A reference guide, Second edition. Greenwood Press, Westport, Conn., pp. 448.

Kump, L. R. (2003) The geochemistry of mass extinction. In: Mackenzie, F.T. (Ed.), Sediments, Diagenesis, and Sedimentary Rocks. *Treatise of Geochemistry*, **7**, Elsevier-Pergamon, Amsterdam, pp. 351–367.

Kutzbach, J. E., Gallimore, R. G. (1989) Pangaean climates: Megamonsoons of the megacontinent. *J. Geophys. Res.* **94**, 3341–3357.

Lavrushin, V. Y., Polyak, B. G., Prasolov, R. M., Kamenskii, I. L. (1996) Sources of material in mud volcano products (based on isotopic, hydrochemical, and geological data). *Lithol. Miner. Resour.* **31**, 557−578.

Lee, K. Y. (1985) Geology of the petroleum and coal deposits in the Junggar (Zhungaer) basin, Xinjiang Uygur Zizhiqu, northwest China. *U.S.G.S. Open-File Repor*t 85−230.

Lehrmann, D. J., Enos, P., Jonathan, L. P., Montgomery, P., Wei, J., Yu, Y., Xiao, J., Orchard, M. (2005) Permian and Triassic depositional history of the Yangtze platform and Great Bank of Guizhou in the Nanpanjiang basin of Guizhou and Guangxi, south China. *Albertiana* **33**, 149–169.

Lemarchand E., Schott J., Gaillardet J. (2007) How surface complexes impact boron isotope fractionation: Evidence from Fe and Mn oxides sorption experiments. *Earth Planet. Sci. Lett.* **260**, 277–296.

Lipin, B. R., McKay, G. A. (1989) Geochemistry and mineralogy of rare earth elements. *Rev. Mineral.* **21**, pp.348.

Lord, C. J. (1991) Determination of trace metals in crude oil by inductively coupled plasma mass spectrometry with microemulsion sample introduction. *Anal. Chem.* **63**, 1594–1599.

Luo, Y-R., Byrne, R. H. (2004) Carbonate complexation of yttrium and the rare earth elements in natural waters. *Geochim. Cosmochim. Acta* **68**, 691−699.

Ma, L-C., Liu, C-L., Jiao, P-C., Chen, Y-Z. (2010) A preliminary discussion on geological conditions and indicator pattern of potash deposits in typical playas of

Xinjiang. *Mineral Deposits* **29**, 593−601 (in Chinese).

Maher, B. A., Prospero, J. M., Mackie, D., Gaiero, D., Hesse, P. P., Balkanski, Y. (2010) Global connections between aeolian dust, climate and ocean biogeochemistry at the present day and at the last glacial maximum. *Earth-Sci. Rev.* **99**, 61–97.

Mahowald, N. M., Baker, A. R., Bergametti, G., Brooks, N., Duce, R. A., Jickells, T. D., Kubilay, N., Prospero, J. M., Tegen, I. (2005) Atmospheric global dust cycle and iron inputs to the ocean. *Glob. Biogeochem. Cycle.* **19**, GB4025.

Manceau, A., Drits, V. A., Silverster, E., Bartoli, C, Lanson, B. (1997) Structural mechanism of Co^{2+} oxidation by the phyllomanganate buserite. *Am. Mineral.* **82**, 1150−1175.

Manceau, A., Nagy, K. L., Marcus, M. A., Lanson, M., Geoffroy, N., Jacquet, T., Kirpichtchikova, T. (2008) Formation of metallic copper nanoparticles at the soil-root interface. *Environ. Sci. Technol.* **42**, 1766−1772.

Manning, P. G., Ash, L. A. (1979) Mössbauer spectral studies of pyrite, ferric and high-spin ferrous distributions in sulfide-rich sediments from Moira Lake, Ontario. *Can. Mineral.* **17**, 111–115.

Maréchal C. N., Télouk P., Albarède F. (1999) Precise analysis of copper and zinc isotopic compositions by plasma-source mass spectrometry. *Chem. Geol.* **156**, 251–273.

Marginac, J. C. G. (1878) Sur l'ytterhine, nouvelle terre contenue dans la gadolinite. Compt. *C. R. Acad. Sci.* **87**, 578–581.

Marginac, J. C. G. (1880) Sur les terres de la samarskite. *C. R. Acad. Sci.* **89**, 899–903.

Marinsky, J. A., Glendenin, L. E., Coryell, C. D. (1947) The chemical identification of radioisotopes of neodymium and of element 61. *J. Am. Chem. Soc.* **69**, 2781–2785.

Marquez, E. J., Aitchison, J. C., Zamoras, L. R. (2006) Upper Permian to middle Jurassic radiolarian assemblages of Busuanga and surrounding islands, Palawan, Philippines, In: Baumgartner, P.O., De Wever, P., Aitchison, J.C. (Eds.),

Radiolaria – Siliceous plankton through time, Proceedings of the Tenth Meeting of the International Association of Radiolarian Palaeontologists, Eclogae Geologicae Helvetiae, **99**, pp. S101–S125.

Marshall, J. L., Marshall, V. R. (2001) Rediscovery of the elements: Ytterby Gruva (Ytterby Mine). *J. Chem. Edu.* **78**, 1343–1444.

Martin, J. H. (1990) Glacial-interglacial CO_2 change: The iron hypothesis. *Paleoceanography* **5**, 1–13

Martin, J. H., Fitzwater, S. E. (1988) Iron deficiency limits phytoplankton growth in the north-east Pacific subarctic. *Nature* **331**, 341–343.

Martin, W. C., Hagan, L., Rearder, J., Sugar, J. (1974) Ground levels and ionization potentials for lanthanide and actinide atoms and ion. *J. Phys. Chem. Ref. Data* **3**, 771–780.

Martini, R., Zaninetti, L., Villeneuve, M., Corne´e, J.-J., Krystyn, L., Cirilli, S., De Wever, P., Dumitrica, P., Harsolumakso, A. (2000) Triassic pelagic deposits of Timor: palaeogeographic and sealevel implications. *Palaeogeogr. Palaeoclimatol. Palaeoecol.* **160**, 123–151.

Masatani, K. (1980) Conditions of oil generation zone in Hokkaido, Japan. *J. Japan. Asso. Petrol. Technol.* **45**, 393-404.

Mason T. F. D., Weiss D. J., Chapman J. B., Wilkinson J. J. Tessalina S. G., Spiro B., Horstwood M. S. A., Spratt J., Coles B. J. (2005) Zn and Cu isotopic variability in the Alexandrinka volcanic-hosted massive sulphide (VHMS) ore deposit, Urals, Russia. *Chem. Geol.* **221**, 170–187.

Masuda A. (1962) Regularities in variation of relative abundances of lanthanide elements and an attempt to analyze separation index patterns of some minerals. *J. Earth Sei. Nagoya Univ*. **10**, 173−187.

Masuda, A. (1966) Lanthanides in basalts of Japan with three distinct types. *Geochem. J.* **1**, 11−26.

Masuda, A. (2003) Reminiscence and dream. *Chikyukagaku* **37**, 31−41. (in Japanese)

Masuda, A., Ikeuchi, Y. (1979) Lanthanoid tetrad effect observed in

marine-environment. *Geochem. J.* **13**, 19−22.

Masuda, A., Kawakami, O., Dohmoto, Y., Takenaka, T. (1987) Lanthanide tetrad effects in nature: two mutually opposite types, W and M. *Geochem. J.*, **21**, 119–124.

Matsuo, M., Kubo, K., Isozaki, Y. (2002) Mössbauer spectroscopic study on characterization of iron in the Permian to Triassic deep-sea chert from Japan, in: Thomas, M.F., Williams, J.M., Gibb, T.C. (Eds.), *Hyperfine Interactions (C)*, Springer Netherlands, pp. 435–438.

Matsuoka, A. (1995) Jurassic and Lower Cretaceous radiolarian zonation in Japan and in the western Pacific. *Isl. Arc* **4**, 140–153.

Matsuoka, A. (2004) Toarcian (Early Jurassic) radiolarian fauna from the Nanjo Massif in the Mino Terrane, central Japan. *News Osaka Micropaleontol. Spec.* **13**, 69–87

Matsuda, T., Isozaki, Y. (1991) Well-documented travel history of Mesozoic pelagic chert in Japan: from remote ocean to subduction zones. *Tectonics* **10**, 475–499.

Matsuoka, A., Hori, R., Kuwahara, K., Hiraishi, M., Yao, A., Ezaki, Y., (1994) Triassic-Jurassic radiolanan-bearing sequences in the Mino Terrane, central Japan. InterRad VII Field Excursion II (Mesozoic), Organ. Committee of InterRad VII, Osaka, 1994, pp. 19–61.

Matsuoka, A., Yamakita, S., Sakakibara, M., Hisada, K. (1998) Unit division for the Chichibu Composite Belt from a view point of accretionary tectonics and geology of western Shikoku, Japan. *J. Geol. Soc. Japan* **104**, 634–653 (in Japanese with English abstract)

McElwain, J. C., Wade-Murphy, J., Hesselbo, S. P. (2005) Changes in carbon dioxide during an oceanic anoxic event linked to intrusion into Gondwana coals, *Nature* **435**, 479–482.

McLennan, S. M. (1989) Rare earth elements in sedimentary rocks: Influence of provenance and sedimentary processes. *Rev. Min.* **21**, 169–200.

Michard, A., Albarède, F., Michard, G., Minster, J. F., Charlou, J. L. (1983) Rare-earth elements and uranium in high-temperature solutions from East Pasific Rise

hydrothermal vent fluid (13 °N). *Nature* **303**, 795−797.

Milkov, A. V. (2010) Methanogenic biodegradation of petroleum in the West Siberian Basin (Russia): significance for formation of giant Cenomanian gas pools. *AAPG Bull*. **94**, 1485−1541.

Minami, M., Matsuda, N., Masuda, A. (1995) Experimental studies on behaviors of lanthanides in interaction between water and basaltic rock grains. *Proc. Jpn. Acad. Ser. B-Phys. Biol. Sci.* **71**, 10–14.

Minoura, K., Nakaya, S., Takemura, A. (1991) Origin of manganese carbonates in Jurassic red shale, central Japan. *Sedimentology* **38**, 137–152.

Möller, P. and Bau, M. (1993) Rare-earth patterns with positive cerium anomaly in alkaline waters from Lake Van, Turkey. *Earth Planet. Sci. Lett.* **117**, 671–676.

Möller, P., Dulski, P., Bau, M. (1994) Rare-earth element adsorption in a seawater profile above the East Pacific Rise. *Chem. Erde-Geochem*. **54**, 129–149.

Morad, S., Ketzer, J. M., De Ros, L. F. (2000) Spatial and temporal distribution of diagenetic alterations in siliciclastic rocks: implications for mass transfer in sedimentary basins. *Sedimentology* **47**, 95–120.

Mosander, C. G. (1839) Lantan, ein neues Metall. *Ann. Phy. Chem.* **46**, 648–649.

Mosander, C. G. (1842) Något om Cer och Lanthan. *Förhandlingar vid de Skandinaviske naturforskarnes tredje möte (Stockholm)* **3**, 387–398.

Mosander, C. G. (1843) On the new metals, Lanthanium and Didymium, which are associated with Cerium; and on Erbium and Terbium, new metals associated with Yttria. *Philos. Mag.* **23**, 241–254.

Moseley, M. A. (1913) The high-frequency spectra of the elements. *Philos. Mag.* **26**, 1024–1034.

Moseley, M. A. (1914) The high-frequency spectra of the elements Pert II. *Philos. Mag.* **27**, 703–713.

Moynier F., Pichat S., Pons M.-L., Fike D., Balter V., Albarède F. (2009) Isotopic fractionation and transport mechanisms of Zn in plants. *Chem. Geol.* **267**, 125–130.

Murakami, T., Utsunomiya, S., Imazu, Y., Prasad, N. (2001) Direct evidence of late Archean to early Proterozoic anoxic atmosphere from a product of 2.5 Ga old weathering. *Earth Planet. Sci. Lett.* **184**, 523–528.

Murray, R. W. (1994) Chemical criteria to identify the depositional environment of chert: general principles and applications. *Sediment. Geol.* **90**, 213–232.

Murray, R. W., Tenbrink, M. R. B., Gerlach, D. C., Russ, G. P., Jones, D. L. (1991) Rare-earth, major, and trace-elements in chert from the Franciscan complex and Monterey group, California; Assessing REE sources to fine-grained marine-sediments. *Geochim. Cosmochim. Acta* **55**, 1875−1895.

Nagai H. (1986) Jurassic Eucyrtidiellum (Radiolaria) from central Japan. *Bull. Nagoya Univ. Museum* **2**, 1–21.

Nagai, H. (1989) Supersonic vibration effect on the surface texture of Jurassic Eucyrtidiellum (Radiolaria). *Bull. Nagoya Univ. Museum* **5**, 1–9.

Nagai, H., Mizutani, S. (1990) Jurassic *Eucyrtidiellum* (Radiolaria) in the Mino Terrane. *Trans. Proc. Palaeontol. Soc. Japan, New Series* **159**, 587–602.

Nakada, R., Takahashi, Y., Tanimizu, M. (2013) Isotopic and speciation study on cerium during its solid-water distribution with implication for Ce stable isotope as a paleo-redox proxy. *Geochim. Cosmochim. Acta* **103**, 49–62.

Nakada, R., Takahashi, Y., Zheng, G., Yamamoto, Y., Shimizu, H. (2010) Abundances of rare earth elements in crude oils and their partitions in water. *Geochem. J.*, **44**, 411–418.

Nakagawa, M., Santosh, M., Maruyama, S. (2009) Distribution and mineral assemblages of bedded manganese deposits in Shikoku, Southwest Japan: implications for accretion tectonics. *Gondwana Res.* **16**, 609–621.

Nakagawa, M., Santosh, M., Maruyama, S. (2011) Manganese formations in the accretionary belts of Japan: Implications for subduction–accretion process in an active convergent margin. *J. Asian Earth Sci.* **42**, 208–222.

Nansheng, Q., Zhihuan, Z., Ershe, X. (2008) Geothermal regime and Jurassic source rock maturity of the Junggar Basin, northwest China. *J. Asian Earth Sci.* **31**,

464−478.

Nath, B. N., Balaram, V., Sudhakar, M., Plüger, W. L. (1992) Rare earth element geochemistry of ferromanganese deposits from the Indian Ocean. *Mar. Chem.* **38**, 185–208.

Nielsen S. G., Mar-Gerrison S., Gannoun A., LaRowe D., Klemm V., Halliday,A. N., Burton K., Hein J. R. (2009) Thallium isotope evidence for a permanent increase in marine organic carbon export in the early Eocene. *Earth Planet. Sci. Lett.* **278**, 297–307.

Nilson, L. F. (1879) Sur l'ytterbine, terre nouvelle de M. Marignac. *C. R. Acad. Sci.* **88**, 642–647.

Nishizono, Y., Sato, T., Murata, M. (1997) A revised Jurassic radiolarian zonation for the South Belt of the Chichibu Terrane, western Kyushu, southwest Japan. *Mar. Micropaleontol.* **30**, 117–138.

Nordstrom, D. K., Plummer, L. N. Langmuir, D., Busenberg, E., May, H. M. (1990) Revised chemical equilibrium data for major water-mineral reactions and their limitations. In: *Chemical modeling of aqueous systems II*, Melchior, D. C. and Bassett, R. L. (Eds.). Am. Chem. Soc. Ser. **416**, pp. 398−413.

Nothdurft, L. D., Webb, G. E., Kamber, B. S. (2004) Rare earth element geochemistry of Late Devonian reefal carbonates, Canning Basin, Western Australia: confirmation of seawater REE proxy in ancient limestones. *Geochim. Cosmochim. Acta* **68**, 263–283.

Nozaki, T., Nakamura, K., Osawa, H., Fujinaga, K., Kato, Y. (2005) Geochemical features and tectonic setting of greenstones from Kunimiyama, Northern Chichibu Belt, central Japan. *Resour. Geol.* **55**, 301–310.

O'Day, P. A., Rehr, J. J., Zabinsky, S. I., Brown, G. E. (1994) Extended X-ray absorption fine structures (EXAFS) analysis of disorder and multiple scattering in complex crystalline solids. *J. Am. Chem. Soc*. **116**, 2938−2949.

Ohta, A., Kawabe, I. (2000) Theoretical study of tetrad effects observed in REE distribution coefficients between marine Fe–Mn deposit and deep seawater, and

in REE(III)–carbonate complexation constants. *Geochem. J.* **34**, 455–473.

Ohta, A., Kawabe, I. (2001) REE(III) adsorption onto Mn oxides (δ-MnO_2) and Fe oxyhydroxide: Ce(III) oxidation by δ-MnO_2. *Geochim. Cosmochim. Acta* **65**, 695−703.

Ohta, A., Kagi, H., Nomura, M., Tsuno, H., Kawabe, I. (2009) Coordination study of rare earth elements on Fe oxyhydroxide and Mn dioxides: Part II. Correspondence of structural change to irregular variations of partitioning coefficients and tetrad effect variations appearing in interatomic distances. *Am. Mineral* **94**, 476−486.

O'Neil, J. R. (1986) Theoretical and experimental aspects of isotopic fractionation. *Rev. Mineral*. **16**, 1−40.

O'Neil, J. R., Clayton, R. N. and Mayeda, T. K. (1969) Oxygen isotope fractionation in divalent metal carbonates. *J. Chem. Phys*. **51**, 5547−5558.

Otsuka, T., Watanabe, K. (1992) Illite crystallinity and low-grade metamorphism of Pelitic rocks in the Mino Terrane, central Japan. *The memoirs of the Geological Society of Japan* **38**, 135–145. (in Japanese with English abstract)

Ozawa, A., Suda, Y. (1980) Geological map of Japan 1:200,000, Akita and Oga. *Geol. Serv. Japan.* (In Japanese with English abstract).

Pálfy, J., Smith, P. L. (2000) Synchrony between Early Jurassic extinction, oceanic anoxic event, and the Karoo-Ferrar flood basalt volcanism, *Geology* **28**, 747–750.

Pallasser, R. J. (2000) Recognising biodegradation in gas/oil accumulations through the $\delta^{13}C$ compositions of gas components. *Org. Geochem.* **31**, 1363−1373.

Parkhurst, D. L. (1999) User's Guide to PHREEQC—A Computer Program for Speciation, Reaction-Path, Adjective Transport, and Inverse Geochemical Calculation. *Water-Resources Investigation Report, 95–4227* (Lakewood, Colorado).

Parrish, J. T. (1993) Climate of the supercontinent Pangea. *J. Geol.* **101**, 215–233.

Pavlov, A. A., Kasting, J. F. (2002) Mass-independent fractionation of sulfur isotopes in Archean sediments: strong evidence for an anoxic Archean atmosphere.

Astrobiology **2**, 27–41.

Pearce, J. A., Cann, J. R. (1973) Tectonic setting of basic volcanic rocks determined using trace element analysis. *Earth Planet. Sci. Lett*. **19**, 290–300.

Pedersen, T. F., Price, N. B. (1982) The geochemistry of manganese carbonate in Panama Basin sediments. *Geochim. Cosmochim. Acta* **46**, 59–68.

Peppard, D. F., Mason, G. W., Lewey, S. (1969) A tetrad effect in the liquid-liquid extraction ordering of lanthanides(III). *J. Inorg. Nucl. Chem*. **31**, 2271–2272.

Petit, J.-R., Briat, M., Royer, A. (1981) Ice age aerosol content from East Antarctic ice core samples and past wind strength. *Nature* **293**, 391–394.

Piepgras, D. J., Jacobsen, S. B. (1992) The behavior of rare earth elements in seawater: precise determinations of variations in the North Pacific water column. *Geochim. Cosmochim. Acta* **56**, 1851–1862.

Piepgras, D. J., Wasserburg, G. J., Dasch, E. J. (1979) Isotopic composition of Nd in different ocean masses. *Earth Planet. Sci. Lett*. **19**, 223–236.

Piper, D. Z. (1974) Rare-earth elements in sedimentary cycle – Summary. *Chem. Geol.* **14**, 285−304.

Pokrovsky O. S., Viers J., Freydier R. (2005) Zn stable isotope fractionation during its adsorption on oxides and hydroxides. *J. Colloid Interface Sci.* **291**, 192–200.

Pride, C., Muecke, G. K. (1981) Rare earth element distributions among coexisting granulite facies minerals, Scourian complex, NW Scotland. *Contrib. Mineral Petrol*. **76**, 463–471.

Prochnow, S. J., Nordt, L. C., Atchley, S. C., Hudec, M. R. (2006) Multi-proxy paleosol evidence for Middle and Late Triassic climate trends in eastern Utah. *Palaeogeogr. Palaeoclimatol. Palaeoecol.* **232**, 53–72.

Pupier, E., Duchene, S., Toplis, M. J. (2008) Experimental quantification of plagioclase crystal size distribution during cooling of a basaltic liquid. *Contrib. Mineral. Petrol.* **155**, 555−570.

Raup, D. M., Sepkoski, J. J. (1982) Mass extinction in the marine fossil record. *Science* **215**, 1501–1503.

Ravel, B., Newville, M. (2005) Athena, artemis, hephaestus: data analysis for X-ray absorption spectroscopy using IFEFFIT. *J. Synchrot. Radiat.* **12**, 537–541.

Rehkämper M., Frank M., Hein J. R., Halliday A. (2004) Cenozoic marine geochemistry of thallium deduced from isotopic studies of ferromanganese crusts and pelagic sediments. *Earth Planet. Sci. Lett.* **219**, 77–91.

Rehkämper M., Frank M., Hein J. R., Porcelli D., Halliday A., Ingri J., Liebetrau V. (2002) Thallium isotope variations in seawater and hydrogenetic, diagenetic, and hydrothermal ferromanganese deposits. *Earth Planet. Sci. Lett.* **197**, 65–81.

Rigo, M., Preto, N., Roghi, G., Tateo, F., Mietto, P. (2007) A rise in the Carbonate Compensation Depth of western Tethys in the Carnian: deep-water evidence for the Carnian Pluvial Event. *Palaeogeogr. Palaeoclimatol. Palaeoecol.* **246**, 188–205.

Rogers, R. R., Swisher, C. C., III, Sereno, P. C., Monetta, A. M., Forster, C. A., Martinez, R. N. (1993) The Ischigualasto tetrapod assemblage (Late Triassic, Argentina) and $^{40}Ar/^{39}Ar$ dating of dinosaur origins. *Science* **260**, 794–797.

Roghi, G., Gianolla, P., Minarelli, L., Pilati, C., Preto, N. (2010) Palynological correlation of Carnian humid pulses throughout western Tethys. *Palaeogeogr. Palaeoclimatol. Palaeoecol.* **290**, 89–106.

Röhl, H.-J., Röhl, A.S., Oschmann, W., Frimmel, A., Schwark, L. (2001) The Posidonia Shale (Lower Toarcian) of SW-Germany: an oxygendepleted ecosystem controlled by sea level and palaeoclimate. *Palaeogeogr. Palaeoclimatol. Palaeoecol.* **169**, 27–52.

Rosales, I., Quesada, S., Robles, S. (2004) Paleotemperature variations of Early Jurassic seawater recorded in geochemical trends of belemnites from the Basque-Cantabrian basin, northern Spain. *Palaeogeogr. Palaeoclim. Palaeoecol.* **203**, 253–275.

Rostási, Á., Raucsik, B., Varga, A. (2011) Palaeoenvironmental controls on the clay mineralogy of Carnian sections from the Transdanubian Range (Hungary). *Palaeogeogr. Palaeoclimatol. Palaeoecol.* **300**, 101–112.

Rouxel O., Ludden J., Fouquet Y. (2003) Antimony isotope variations in natural systems and implications for their use as geochemical tracers. *Chem. Geol.* **200**, 25–40.

Ruffell, A., McKinley, J. M., Worden, R. H. (2002) Comparison of clay mineral stratigraphy to other proxy palaeoclimate indicators in the Mesozoic of NW Europe. *Phil. Trans. R. Soc. A* **360**, 675–693.

Sato, T., Isozaki, Y., Matsuo, M. (2009) Redox conditions of the deep ocean in the late Neoproterozoic–early Paleozoic: ^{57}Fe Mossbauer spectroscopic study on deepsea pelagic chert. *J. Geol. Soc. Japan* **115**, 391–399 (in Japanese with English abstract).

Sato, T., Isozaki, Y., Shouzugawa, K., Matsuo, M. (2011) ^{57}Fe Mössbauer spectroscopic analysis of deep-sea pelagic chert: Effect of secondary alteration with respect to paleo-redox evaluation. *J. Asian Earth Sci.* **42**, 1403–1410.

Sælen, G., Tyson, R. V., Telnæs, N., Talbot, M. R. (2000) Contrasting watermass conditions during deposition of the Whitby Mudstone (Lower Jurassic) and the Kimmeridge Clay (Upper Jurassic) formations, UK. *Palaeogeogr. Palaeoclimatol. Palaeoecol.* **163**, 163–196.

Schauble, E. A. (2004) Applying stable isotope fractionation theory to new systems. *Rev. Mineral. Geochem*. **55**, 65–111.

Schauble E.A. (2007) Role of nuclear volume in driving equilibrium stable isotope fractionation of mercury, thallium, and other very heavy elements. *Geochim. Cosmochim. Acta* **71**, 2170–2189.

Schlager, W., Schöllnberger, W. (1974) Das Prinzip stratigraphischer Wenden in der Schichtfolge der Nördlichen Kalkalpen. *Mitt. Geol. Gesell. Wien* **66–67**, 165–193. (in Germany with English abstract)

Schmitt, R. A., Smith, R. H., Lasch, J. E., Mosen, A. W., Olehy, D. A., Vasilevskis, J. (1963) Abundance of the fourteen rare earth elements, scandium and yttrium in meteoritic and terrestrial matter. *Geochim. Cosmochim. Acta* **27**, 577–623.

Schnetzler, C. C., Philpotts, J. A. (1970) Partition coefficients of rare-earth elements

between igneous matrix material and rock-forming mineral phenocrysts–II. *Geochim. Cosmochim. Acta* **34**, 331–340.

Schnitzer, M. (1972) Chemical, spectroscopic and thermal methods for the classification and characterization of humic substances. In: *Proceeding of International Meeting on Humic Substances*. pp. 293–307. Nieuwersluis, Wageningen.

Schoell, M. (1983) Genetic characterization of natural gases. *AAPG Bull.* **67**, 2225−2238.

Schouten, S., van Kaam-Peters, H. M. E., Rijpstra, W. I. C., Schoell, M., Damsté, J. S. S. (2000) Effects of an oceanic anoxic event on the stable carbon isotopic composition of early 20 Toarcian carbon, *Am. J. Sci.* **300**, 1–22.

Schwertmann, U., Cornell, R. M. (2000) *Iron Oxides in the Laborator*. 2nd ed., Wiley-VCH, 103 pp.

Scotese, C. R. (2004) A continental drift flipbook. *J. Geol.* **112**, 729–741.

Shannon, R. D. (1976) Revised effective ionic raddi and systematic studies of interatomic distances in halides and chalcogenides. *Acta Cryst.* **A32**, 751–767.

Sharma, B. K., Adhvaryu, A., Perez, J. M., Erhan, A. Z. (2008) Effects of hydroprocessing on structure and properties of base oil using NMR. *Fuel Process. Technol.* **89**, 984–991.

Shen J. J.-S., Lee T., Chang C.-T. (1994) Lanthanum isotopic composition of meteoritic and terrestrial matter. *Geochim. Cosmochim. Acta* **58**, 1499–1506.

Shibata, S-N., Tanaka, T., Yamamoto, K. (2006) Crystal structure control of the dissolution of rare earth elements in water-mineral interactions. *Geochem. J.* **40**, 437–446.

Shimizu, H., Masuda, A. (1977) Cerium in chert as an indication of marine environment of its formation. *Nature* **266**, 346−348.

Simms, M. J., Ruffell, A. H. (1989) Synchroneity of climatic change and extinctions in the Late Triassic. *Geology* **17**, 265–268.

Simms, M. J., Ruffell, A. H. (1990) Climatic and biotic change in the late Triassic. *J. Geol. Soc.* **147**, 321–327.

Simms, M.J., Ruffel, A.H., Johnson, L.A. (1994) Biotic and climatic changes in the Carnian (Triassic) of Europe and adjacent areas. in: Fraser, N.C., Sues, H.-D. (Eds.), In the Shadow of the Dinosaurs: Early Mesozoic Tetrapods, Cambridge University Press, pp. 352–365.

Skulan, J. L., Beard, B. L., Johnson, C. M. (2002) Kinetic and equilibrium Fe isotope fractionation between aqueous Fe(III) and hematite. *Geochim. Cosmochim. Acta* **66**, 2995−3015.

Smith, R. M., Martell, A. E. (1987) Critical stability constants, enthalpies and entropies for the formation of metal complexes of aminopolycarboxylic acids and carboxylic acids. *Sci. Total Environ.* **64**, 125−147.

Soldatov, A. V., Ivanchenko, T. S., Longa, S. D., Kotani, A., Iwamoto, Y., Bianconi, A. (1994) Crystal-structure effects in the Ce L_3-edge X-ray absorption spectrum of CeO_2: multiple-scattering resonances and many-body final states. *Phys. Rev. B* **50**, 5074−5080.

Song, Y., Dai, J., Xia, X., Qin, S. (2004) Genesis and distribution of natural gas in the foreland basins of China. *J. Petrol. Sci. and Engineer.* **41**, 21−29.

Stampfli, G., Kozur, H. W. (2006) Europe from the Variscan to the Alpine cycles. In: Gee, D.G., Stephenson, R.A. (Eds.), *European Lithosphere Dynamics*, pp. 57–82.

Suzuki, N., Ogane, K. (2004) Paleoceanographic affinities of radiolarian faunas in late Aalenian time (Middle Jurassic) recorded in the Jurassic accretionary complex of Japan. *J. Asian Earth Sci.* **23**, 343–357.

Suzuki, N., Kojima, S., Kano, H., Yamakita, S., Misaki, A., Ehiro, M., Otoh, S., Kurihara, T., Aoyama, M. (2005) Permian radiolarian faunas from chert in the Khabarovsk Complex, Far East Russia and the age of each lithologic unit of the Khabarovsk Complex. *J. Paleontol.* **79**, 686–700.

Suzuki, N., Ehiro, M., Yoshihara, K., Kimura, Y., Kawashima, G., Yoshimoto, H., Nogi, T. (2007) Geology of the Kuzumaki-Kamaishi Subbelt of the North Kitakami Belt (a Jurassic accretionary complex), Northeast Japan: Case study of the Kawai-Yamada area, eastern Iwate Prefecture. *Bull. Tohoku Univ. Museum* **6**,

103–174.

Sugiyama, K. (1997) Triassic and Lower Jurassic radiolarian biostratigraphy in the siliceous claystone and bedded chert units of the southeastern Mino Terrane, Central Japan. *Bull. Mizunami Fossil Museum* **24**, 79–193.

Sverjenski, D. A. (1984) Europium redox equilibria in aqueous solution. *Earth. Planet. Sci. Lett*. **67**, 70–78.

Takahashi, Y., Châtellier, X., Hattori, K. H., Kato, K., Fortin, D. (2005) Adsorption of rare earth elements onto bacterial cell walls and its implication for REE sorption onto natural microbial mats. *Chem. Geol*. **219**, 53–67.

Takahashi, Y., Manceau, A., Geoffroy, N., Marcus, M. A., Usui, A. (2007) Chemical and structural control of the partitioning of Co, Ce, and Pb in marine ferromanganese oxides. *Geochim. Cosmochim. Acta* **71**, 984–1008

Takahashi, Y., Sakami, H., Nomura, M. (2002b). Determination of the oxidation state of cerium in rocks by Ce L_{III}-edge X-ray absorption near-edge structure. *Anal. Chim. Acta* **468**, 345–354.

Takahashi, Y., Shimizu, H., Kagi, H., Yoshida, H., Usui, A., Nomura, M. (2000b) A new method for the determination of Ce^{III}/Ce^{IV} ratios in geological materials; application for weathering, sedimentary and diagenetic processes. *Earth Planet. Sci. Lett.* **182**, 201–207.

Takahashi, Y., Shimizu, H., Usui, A., Kagi, H., Nomura, M. (2000a) Direct observation of tetravalent cerium in ferromanganese nodules and crusts by X-ray-adsorption near-edge structure (XANES). *Geochim. Cosmochim. Acta* **64**, 2929–2935.

Takahashi, Y., Tada, A., Shimizu, H. (2004) Distribution Pattern of rare earth ions between water and montmorillonite and its relation to the sorbed species of the ions. *Anal. Sci.* **20**, 1301–1306.

Takahashi, Y., Yoshida, H., Sato, N., Hama, K., Yusa, Y., Shimizu, H. (2002a) W- and M-type tetrad effects in REE patterns for water–rock systems in the Tono uranium deposit, central Japan. *Chem. Geol*. **184**, 311–335.

Takeda, K., Arikawa, Y. (2005) Determination of rare earth elements in petroleum by

ICP-MS. *Bunseki Kagaku* **54**, 939–943. (In Japanese with English abstract).

Takeuchi, M. (2001) Morphologic study of multicyrtid Nassellaria (Radiolaria) from the Lower Jurassic bedded cherts in the Inuyama Area, Mino Terrane, Central Japan, *News Osaka Micropal.* **12**, 181–189.

Tanaka, K., Ohta, A., Kawabe, I. (2004) Experimental REE partitioning between calcite and aqueous solution at 25 °C and 1 atm: constraints on the incorporation of seawater REE into seamount-type limestones. *Geochem. J.* **38**, 19–32.

Tanaka, K., Takahashi, Y., Shimizu, H. (2008) Local structure of Y and Ho in calcite and its relevance to Y fractionation from Ho in partitioning between calcite and aqueous solution. *Chem. Geol.* **248**, 104–113.

Tanimizu M., Araki Y., Asaoka S., Takahashi Y. (2011) Determination of natural isotopic variation in antimony using inductively coupled plasma mass spectrometry for an uncertainty estimation of the standard atomic weight of antimony. *Geochem. J*. **45**, 27–32.

Taylor, S. T., McLennan, S. M. (1985) The Continental Crust: Its Composition and Evolution. Blackwell Scientific Publications pp. 312.

Taylor, S. T., McLennan, S. M. (1988) The significance of the rare earths in geochemistry and cosmochemistry. In Handbook on the Physics and Chemistry of Rare Earth (eds. Gschneidner, K.A.Jr., Eyring, L.). *Elsevier, Amsterdam* pp. 485−578.

Thomson, J., Higgs, N. C., Jarvis, I., Hydes, D. J., Colley, S., Wilson, T. R. S. (1986) The behaviour of manganese in Atlantic carbonate sediments. *Geochim. Cosmochim. Acta* **50**, 1807–1818.

Thorn, K. A., Folan, D. W., MacCarthy, P. (1989) Characterization of the international humic substances society standard and reference fulvic and humic acids by solution state carbon-13 (^{13}C) and hydrogen-1 (^{1}H) nuclear magnetic resonance spectrometry. US Geological Survey, Water-Resource Investigation Report 89–4196, pp. 93.

Tipping. E. (1994) WHAM–A chemical wquilibrium model and computer code for

waters, sediments and soils incorporating a discrete site / electrostatic model of ion-binding by humic substances. *Comput. Geosci.* **20**, 973–1023.

Tipping, E. (2002) *Cation Binding by Humic Substances*. Cambridge University Press, Cambridge.

Tomaru, H., Lu, Z., Fehn, U., and Muramatsu, Y. (2009) Origin of hydrocarbons in the Green Tuff region of Japan: ^{129}I results from oil field brines and hot springs in the Akita and Niigata Basins. *Chem. Geol.* **264**, 221–231.

Toyoda, K., Nakamura, Y., Masuda, A. (1990) Rare earth elements of Pacific pelagic sediments. *Geochim. Cosmochim. Acta* **54**, 1093–1103.

Trapp, J. M., Millero, F. J., Prospero, J. M. (2010) Trends in the solubility of iron in dust-dominated aerosols in the equatorial Atlantic trade winds: Importance of iron speciation and sources, *Geochem. Geophys. Geosyst.* **11**, Q03014.

Tsuchi, R. (1961) On the late Neogene sediments and molluscs in the Tokai region, with notes on the geologic history of the Pacific coast of Southwest Japan. *Japan. J. Geol. Geogr.* **32**, 437–56 (in Japanese with English abstract).

Tsunogai, U., Yoshida, N., Gamo, T. (2002) Carbon isotopic evidence of methane oxidation through sulfate reduction in sediment beneath cold seep vents on the seafloor at Nankai Trough. *Mar. Geol.* **187**, 145−160.

Tsutsuki, K., Kuwatsuka, S. (1978) Chemical studies on soli humic acids. II. Composition of oxygen containing functional groups of humic acids. *Soil Sci. Plant Nutr*., **24**, 547–560.

Ujiie, H. (1962) Geology of Sagara–Kakegawa sedimentary basin in central Japan. *Science Reports of the Tokyo Kyoiku Daigaku* **8**, 123–88 (in Japanese with English abstract).

Urbain, M. G. (1907) Un nouvel élément, le lutécium, résultant du dédoublement de l'ytterbium de Marignac. *C. R. Acad. Sci.* **145**, 759–762.

Vairavamurthy, A., Zhou, W., Eglinton, T., Manowitz, B. (1994) Sulfonates: A novel class of organic sulfur compounds in marine sediments. *Geochim. Cosmochim. Acta* **58**, 4681–4687.

von Welsbach, A. C. (1885) Die zerlegung des didymus in seine elemente. *Monatsh. Chem.* **6**, 477–491.

von Welsbach, A. C. (1908) Die zerlegung des ytterbiums in seine elemente. *Monatsh. Chem.* **29**, 181–225.

Waldo, G. S., Carlson, R. M. K., Moldowan, J. M., Peters, K. E., Penner-Hahn, J. E. (1991) Sulfur speciation in heavy petroleums: Information from X-ray absorption near-edge structure. *Geochim. Cosmochim. Acta* **55**, 801–814.

Waltham, D., Gröcke, D. R. (2006) Non-uniqueness and interpretation of the seawater $^{87}Sr/^{86}Sr$ curve. *Geochim. Cosmochim. Acta* **70**, 384–394.

Wang, Y., Van Cappellen, P. (1996) A multicomponent reactive transport model of early diagenesis: application to redox cycling in coastal marine sediments. *Geochim. Cosmochim. Acta* **60**, 2993–3014.

Wang, Y. L., Liu, Y.-G., Schmitt, R. A. (1986) Rare earth element geochemistry of South Atlantic deep sea sediments: Ce anomaly change at ~54 My. *Geochim. Cosmochim. Acta* **50**, 1337–1355.

Wang, D., Maowei, L., Men, L., Xiaomin, D. (1997) A preliminary study on eruption of the mud volcano in Dusanzi, Xinjiang. *Seismol. Geol.* **19**, 14–16. (in Chinese)

Waseda, A., Iwano, H. (2008) Characterization of natural gases in Japan based on molecular and carbon isotope compositions. *Geofluids* **8**, 286−292.

Wasylenki, L. E., Weeks, C. L., Bargar, J. R., Spiro, T. G., Hein, J. R., Anbar, A. D. (2011) The molecular mechanism of Mo isotope fractionation during adsorption to birnessite. *Geochim. Cosmochim. Acta* **75**, 5019–5031.

Watanabe, T., Yui, S., Kato, A. (1970) Bedded manganese deposits in Japan, a review. In: Tatsumi, T. (Ed), *Volcanism and Ore Genesis*. University of Tokyo Press, Tokyo, pp. 119–141.

Waychunas, G. A., Apted, M. J., Brown, G. E. (1983) X-ray K-edge absorption spectra of Fe minerals and model compounds: Near edge structure. *Phys. Chem. Miner.* **10**, 1–9.

Weaver, C. E. (1989) Clays, Muds and Shales. *Dev. Sedimentol.* **44** Elsevier,

Amsterdam. pp. 819.

Wei, K., Gasse, F. (1999) Oxygen isotope in lacustrine carbonates of West China revisited: implications for post glacial changes in summer monsoon circulation. *Quat. Sci. Rev.* **18**, 1315−1334.

Weyer, S., Schwieters, J. (2003) High precision Fe isotope measurements with high mass resolution MC-ICPMS. *Int. J. Mass Spectrom.* **226**, 355−368.

Wieser, M. E., Schwieters, J. (2005) The development of multiple collector mass spectrometry for isotope ratio measurements. *Int. J. Mass Spectrom.* **242**, 97−115.

Wilke, M., Farges, F., Petit, P. E., Brown, G. E., Martin, F. (2001) Oxidation state and coordination of Fe in minerals: An Fe K-XANES spectroscopic study. *Am. Miner.* **86**, 714–730.

Wright J., Schrader H., Holser W.T. (1987) Paleoredox variations in ancient oceans recorded by rare earth elements in fossil apatite. *Geochim. Cosmochim. Acta* **51**, 631–644.

Xu, H.L., Shen, J.W., and Zhou, X.W. (2006) Geochemistry of geopressured hydrothermal waters in the Niigata sedimentary basin, Japan. *Isl. Arc* **15**, 199–209.

Yaita, T., Tachimori, S. (1996) Study of solvent extraction of lanthanide(III) with tetra(p-)tolymethylene dipphosphine dioxide (TTMDPDO) from a nitric acid solution. *Radiochim. Acta* **73**, 27–33.

Yao, A. (1972) Radiolarian fauna from the Mino belt in the northern part of the Inuyama area, central Japan. part 1. Spongosaturnalids. *J. Geosci. Osaka City Univ.* **15**, 21–64.

Yao, A. (1997) Faunal change of early-middle Jurassic radiolarians. *News Osaka Micropaleontol.* **10**, 155–182. (in Japanese with English abstract)

Yao, A., Matsuda, T., Isozaki, Y. (1980) Triassic and Jurassic radiolarians from the Inuyama area, central Japan. *J. Geosci. Osaka City Univ.* **23**, 135–154.

Yamakita, S., Hori, R. S. (2009) Early Jurassic radiolarians from a carbonate nodule in the Northern Chichibu Belt in western central Shikoku, Southwest Japan. *News*

Osaka Micropaleontol. **14**, 497–505. (Japanese with English abstract)

Yamamoto, Y., Takahashi, Y., Shimizu, H. (2009) Speciation of iron in humic substances by X-ray absorption fine structure and its effect on the complexation between humic substances and trace metal ions. *Chem. Lett.* **38**, 278–279.

Yamamoto, Y., Takahashi, Y., Shimizu, H. (2010) Systematic change in relative stabilities of REE-humic complexes at various metal loading levels. *Geochem. J.* **44**, 39–63.

Yoshimura, T. (1969) Supplement to ‘‘Manganese ore deposits of Japan’’, Part II. *Sci. Rep. Fac. Sci. Kyushu Univ. Geol.* **9**, 487–1004 (in Japanese).

Yoshizaki, M., Shibuya, T., Suzuki, K., Shimizu, K., Nakamura, K., Takai, K., Omori, S., Maruyama, S. (2009) H_2 generation by experimental hydrothermal alteration of komatiitic glass at 350 °C and 500 bars: A preliminary result from on-going experiment. *Geochem. J.* **43**, e17–e22.

You, C., Gieskes, J. M., Lee, T, Yui, T., Chen, H. (2004) Geochemistry of mud volcano fluids in the Taiwan accretionary prism. *Appl. Geochem.* **19**, 695−707.

Zabinsky, S. I., Rehr, J. J., Ankudinov, A., Albers, R. C., Eller, M. J. (1995) Multiple-scattering calculations of X-ray-adsorption sprctra. *Phys. Rev. B*, **52**, 2995–3009.

Zender, C. S., Miller, R. L. L., Tegen, I. (2005) Quantifying mineral dust mass budgets: Terminology, constraints, and current estimates, *Eos, Trans. Amer. Geophys. Union* **85**, 509–512.

Zhang, L., Zhao, Y., Jin, Z., Bai, G., Yang, L. (2009) Geochemical characteristics of rare earth elements in petroleum and their responses to mantle-derived fluid: an example from the Dongying Depression, East China. *Energy Explor. Exploit.* **27**, 47–68.

Zheng, G. D., Fu, B. H., Takahashi, Y., Kuno, A., Matsuo, M., Zhang, J. D. (2010) Chemical speciation of redox sensitive elements during hydrocarbon leaching in the Junggar Basin, Northwest China. *J. Asia Earth Sci.,* **39**, 713–723.

Acknowledgements

I really appreciate the numerous amounts of valuable scientific comments, encouragements, and supports given by **Prof. Yoshio Takahashi** throughout my study period. I respect his passion and attitude toward the science. I express my sincere appreciation to him.

I am grateful to **Dr. Masaharu Tanimizu**, vise supervisor, for his help in the stable isotopic measurement. I also appreciate his comments, suggestions, and encouragements. I learned a lot from his stern attitude toward the science.

I would like to express my thanks to the following researchers: **Dr. Katsuhiko Suzuki**, **Dr. Takazo Shibuya**, and **Dr. Motoko Yoshizaki** for their help in hydrothermal experiment and basalt synthesis, which is described in Chapter 2. Also, encouragements and helpful advice given by them have been so precious. I also would like to express my thanks to **Dr. Shinsuke Kawagucci**, **Dr. Kentaro Nakamura**, **Dr. Kenji Shimizu**, **Dr. Ken Takai**, **Dr. Yuichiro Ueno**, and **Prof. Shigenori Maruyama** for their encouragements and lots of scientific advice during my stay in Yokosuka.

I would like to thank **Dr. Andrew Gault** for his comments that improved the study describe in Chapter 4 greatly.

I am grateful to **Dr. Susumu Kato**, **Dr. Amane Waseda**, **Mr. Fumiaki Okumura**, and **JAPEX Co. Ltd.** for their provision of oil samples and permission on our publishing data. Special thanks to **Mr. Yukie Ishikawa** and **Mr. Shinkichi Ogawa** for their manuduction at Nagaoka-Higashiyama oil field. Also special thanks to **Sagara oil field's park** for their provision of crude oil.

I also would like to express my thanks to **Dr. Noritoshi Suzuki**, **Dr. Satoshi Takahashi**, **Mr. Kazuhiro Ogawa**, and **Mr. Taka'aki Shirai** for their helpful advice, worthful scientific comments, and encouragements. Studies described in Chapters 7, 8, and 9 were achieved by their cooperation.

I appreciate the advice and encouragements given by **Dr. Urumu Tsunogai**, **Dr. Guodong Zheng**, and **Prof. Keiko H. Hattori** for the study described in the Appendix.

Analysis using FE-SEM and measurement of ^{13}C-NMR were performed by the help of **Dr. Makoto Maeda** and **Mr. Hitoshi Fujitaka**, respectively at the Natural Science Center for Basis Research and Development (N-BARD), Hiroshima University.

The study described in Chapter 2 was supported by "Trans-crustal Advection and In-situ reaction of Global sub-seafloor Aquifer (TAIGA) project". Particularly, travel charge and cost of staying in Yokosuka needed to do the hydrothermal experiment described in Chapter 2 were supported by "TAIGA Mentorship on Research and Education (T-MORE)".

The study described in Chapter 3 was performed with the approval of the High Energy Accelerator Research Organization (KEK-PF, Proposal No. 2008G691 and 2010G072) and the Japan Synchrotron Radiation Research Institute (JASRI, Proposal No. 2010B1347, 2010B1295, and 2011B1279).

The study described in Chapter 4 was performed with the approval of the JASRI (Proposal Nos. 2010B1347, 2010B1295, and 2011B1279).

The study described in Chapter 7 was performed with the approval of the KEK-PF (Proposal No. 2011G197).

The study described in Chapter 8 was performed with the approval of the KEK-PF (Proposal No. 2011G644, 2012G111) and the JASRI (Proposal No. 2012B1221, 2013A1613).

The study described in Chapter 9 was performed with the approval of the KEK-PF (2012G111) and JASRI (Proposal No. 2012B1221).

Some traveling fees to attend international conferences were supported by "Financial support for sending graduate students overseas" by Graduate School of Science, Hiroshima University, and JSPS "Institutional program for Young Researcher Overseas Visits".

In addition, I really appreciate the research fellowship (DC1) by JSPS awarded for 3 years.

I appreciate the comments and suggestions given by following reviewers and editors of my papers: **Dr. Michael Bau**, **Dr. Aline Dia**, **Dr. Giuseppe Etiope**, **Dr. Ron Fuge**, **Dr. Juske Horita**, **Dr. Sune Nielsen**, **Dr. Mark Rehkämper**, **Dr. Derek Vance**, **Dr. Koshi Yamamoto**, and some anonymous reviewers. Though some of it was critical, their comments greatly improved my paper.

Scientific advice and encouragements given by seniors and faculties in Department of Earth and Planetary Systems Science, Hiroshima University were also grateful. Also, I would like to express my sincere thanks to **Ms. Akiko Ito**, **Ms. Chikako Kobayashi**, **Ms. Noriko Miyoshi**, and **Ms. Satomi Yanaka** (the office in the department and laboratory) for their great many support.

I would like to thank laboratory members and **Mr. Shintaro Azuma** and **Mr. Kosuke Kimura**. Daily discussion with them was really exciting.

I am grateful to **Prof. Hiroshi Shimizu** who had been my supervisor for two years since I was an undergraduate school student. His introduction of rare earth element geochemistry had greatly changed my perspective on geochemistry.

I wish to express my sincere appreciation to my parents.

In the end, again, I express my gratitude to all the people above, and I would like to close this PhD thesis. Thank you very much.

公表論文

(1) R. Nakada, Y. Takahashi, G. Zheng, Y. Yamamoto, H. Shimizu (2010)
Abundances of rare earth elements in crude oils anf their partitions in water.
Geochemical Journal, 44 (5), 411−418.

(2) R. Nakada, Y. Takahashi, U. Tsunogai, G. Zheng, H. Shimizu, K.H. Hattori (2011)
A geochemical study on mud volcanoes in the Junggaer Basin, China.
Applied Geochemistry, 26 (7), 1065−1076.

(3) R. Nakada, Y. Takahashi (2013)
Thermogenic Methane with Secondary Alteration in Gases Released from Terrestrial Mud Volcanoes.
Hydrocarbon (Edited by V. Kutcherov and A. Kolesnikov), 29−42.

(4) R. Nakada, Y. Takahashi, M. Tanimizu (2013)
Isotopic and speciation study on cerium during its solid-water distribution with implication for Ce stable isotope as a paleo-redox proxy.
Geochimica et Cosmochimica Acta, 103, 49−62.

(5) R. Nakada, M. Tanimizu, Y. Takahashi (2013)
Difference in the stable isotopic fractionations of Ce, Nd, and Sm during adsorption on iron and manganese oxides and its interpretation based on their local structures.
Geochimica et Cosmochimica Acta, 121, 105−119.

Geochemical Journal, Vol. 44, pp. 411 to 418, 2010

Abundances of rare earth elements in crude oils and their partitions in water

RYOICHI NAKADA,[1] YOSHIO TAKAHASHI,[1]* GUODONG ZHENG,[2] YUHEI YAMAMOTO[3] and HIROSHI SHIMIZU[1]

[1]Department of Earth and Planetary Systems Science, Graduate School of Science, Hiroshima University, Higashi-Hiroshima, Hiroshima 739-8526, Japan
[2]Key Laboratory of Petroleum Resources Research, Institute of Geology and Geophysics, Chinese Academy of Sciences, 382 West Donggang Road, Lanzhou 730000, China
[3]Tono Geoscientific Research Unit, Geological Isolation Research and Development Directorate, Japan Atomic Energy Agency (JAEA), Mizunami, Gifu 509-6132, Japan

(*Received November 10, 2009; Accepted April 5, 2010*)

Patterns of the entire range of REE in crude oils and coexisting water, collected from mud volcanoes in Xinjiang Province of China, are reported here for the first time. Crude oils show light REE enriched patterns with flat or depleted patterns in heavy REE, when normalized to chondrite. The REE concentrations in crude oils are larger than those in coexisting water by a factor of more than one hundred. Considering the hydrophobicity of oil and the high ionic characteristics of REE, it is strongly suggested that REE form complexes with ligands present in the crude oils. Based on the ^{13}C NMR spectroscopy, it is found that small amounts of phenol and carboxyl groups are contained in the crude oil samples, which could possibly provide complexing sites for REE. REE patterns of crude oils are similar to those of coexisting mud samples collected from the same mud volcanoes, which suggests that the REE in crude oils are derived from rocks and sediments where crude oils were generated.

Keywords: rare earth elements, crude oil, partition coefficient, NMR, Junggar Basin

INTRODUCTION

Rare earth elements (REE) show similar chemical properties with each other, because the outermost electron orbits are same. Their chemical similarities induce systematic partition in various natural systems. Consequently, relative abundances of REE, namely REE pattern, reflect chemical processes occurring in various systems on the earth. These properties enables REE pattern to be a useful effective geochemical tracer (Henderson, 1984). Recently, Zhang *et al*. (2009) suggested that REE patterns of crude oils could provide genetic information on the oils, while Akinlua *et al*. (2008) noted that REE contents of oils are useful in the classification of oils. However, the existing quantum of REE data of crude oil samples is still insufficient. Complete REE patterns are neither reported by Akinlua *et al*. (2008) nor by Takeda and Arikawa (2005). Here we report REE abundances measured in crude oils from the Xingiang Province, China to provide more data towards the building of a database on REE abundances of crude oils.

A correct interpretation of the chemical state of REE in crude oils is necessary to ascertain genetic processes and provenances of the oils. Further it controls the shape of REE patterns which depends on the REE partition of species between the aqueous and the solid phases (Byrne and Kim, 1990; Takahashi *et al*., 2005; Yamamoto *et al*., 2010). For example, complexation with carbonate ions induces a preferential distribution of heavy-REE (HREE) into the aqueous phase (e.g., Byrne and Sholkovitz, 1996; Johannesson *et al*., 1996). Thus, it is expected that REE distribution between crude oil and water phase involves the information of REE species incorporated into the crude oil. Consequently, REE abundances were measured in both crude oils and coexisting water.

SAMPLES AND METHODS

Samples

Samples of crude oils along with their coexisting muddy water were collected from the mud volcanoes along the southern margin of the Junggar Basin in Xinjiang Uyghur Autonomous Region of China. The Xinjiang Province can be divided into two sedimentary basins, the Junggar Basin in the north and the Tarim Basin, south of the Tianshan Mountains. The Xinjiang Province is well known for its large oil deposits (e.g., Lee, 1985; Desheng, 1996), and several oil fields occur along the margin of these basins. There are several active mud volcanoes along the south margin of the Junggar Basin

*Corresponding author (e-mail: ytakaha@hiroshima-u.ac.jp)

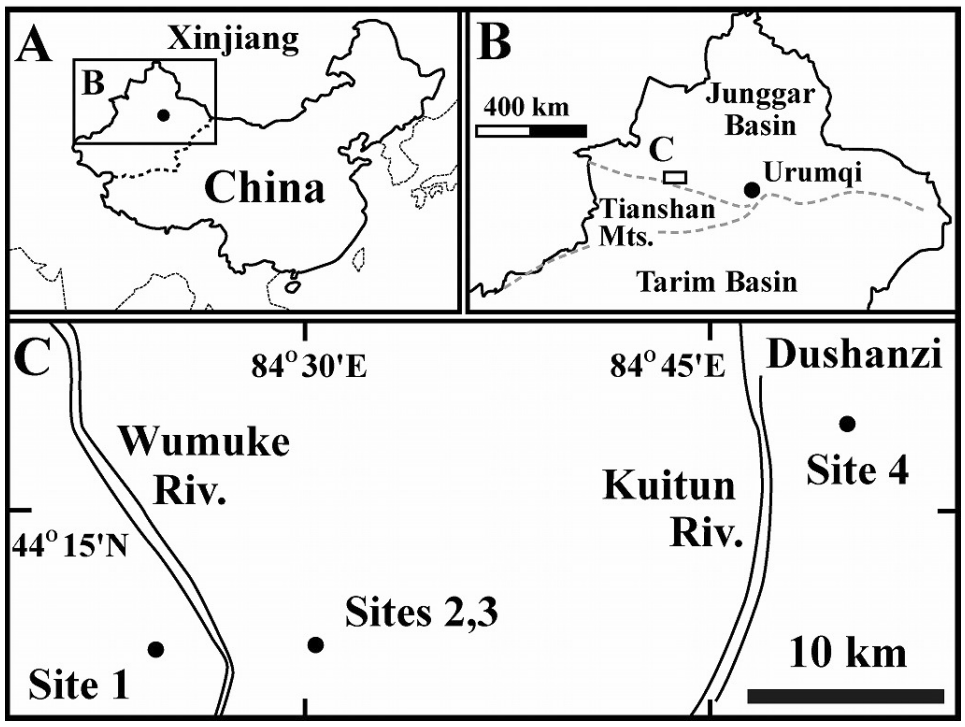

Fig. 1. Schematic map of sampling locations. Map A depicts entire China and the dashed line represents the border of Xinjiang Uyghur Autonomous Region. Map B depicts three quarters of Xinjiang and the dashed lines represent Tianshan Mountains. Location of a square marked on map B is enlarged to map C. Site 4 is situated near Dushanzi District.

(Fu *et al*., 2007), erupting gas, oil, water and mud. Samples were collected from four sites along the southern margin of the Junggar Basin (Fig. 1). Site 1 is located in an area where many mud pies, flat mud extrusive feature, discharge mud and gas. Sites 2 and 3 are "twin" mud volcanoes which are located in a mountainous region, while site 4 is situated near the Dushanzi refineries. Oil slick and crude oil were seen in all sites studied here. Samples of muddy water were collected directly from the crater of mud volcanoes, and were filtrated on site by 0.45 μm membrane filters. After filtration, samples were acidified to 2 wt.% nitric acid solution to prevent the precipitation of Fe and REE. Samples of crude oils were centrifuged for 20 minutes at 2,000 rpm to separate oil from water and mud. Previous studies (e.g., Clayton *et al*., 1997) indicate that crude oil samples that we collected in the Dushanzi area have relatively lower maturity with predominance of saturated hydrocarbons relative to aromatics and non-hydrocarbons.

Analytical methods

To determine the molecular structure of sampled crude oils, nuclear magnetic resonance (NMR) spectroscopy was conducted on carbon atom (^{13}C NMR) for samples from sites 2 and 4 using a JEOL ECA600 at the Natural Science Center for Basic Research and Development (N-BARD), Hiroshima University. The NMR spectra for other crude oils could not be obtained due to the low amount of collected samples. CHNS analysis was not possible because the weight of the oil could not be correctly measured due to the volatilization of volatile components.

The difficulty in measuring the concentrations of REE in crude oils lies in the separation of REE from crude oils (Akinlua *et al*., 2008; Takeda and Arikawa, 2005). If organic matter is not perfectly decomposed, the residual organic matter can have harmful effects on the measurement of REE by inductively coupled plasma mass spectrometry (ICP-MS); (i) introduction of organic matter into the ICP-MS leads to the formation of carbon-containing ions such as C^{2+}, CO^{2+} and ArC^{+} (Lord, 1991); (ii) some carbon-bearing materials can be deposited at the interface into the mass spectrometer of the ICP-MS; (iii) high viscosity and boiling point of crude oils lower their atomization efficiency. Thus, a complete decomposition of organic matter is necessary to determine the concentration of REE in crude oils. In this study, about 0.1 g of weighed crude oil was decomposed by heating (at *ca*. 180°C) for a week in 68 wt.% HNO_3 solution in a Teflon vessel with a screw cap. After evaporation, the organic matter was thoroughly digested using H_2SO_4 (at *ca*. 230°C). The samples were evaporated again at 230°C and

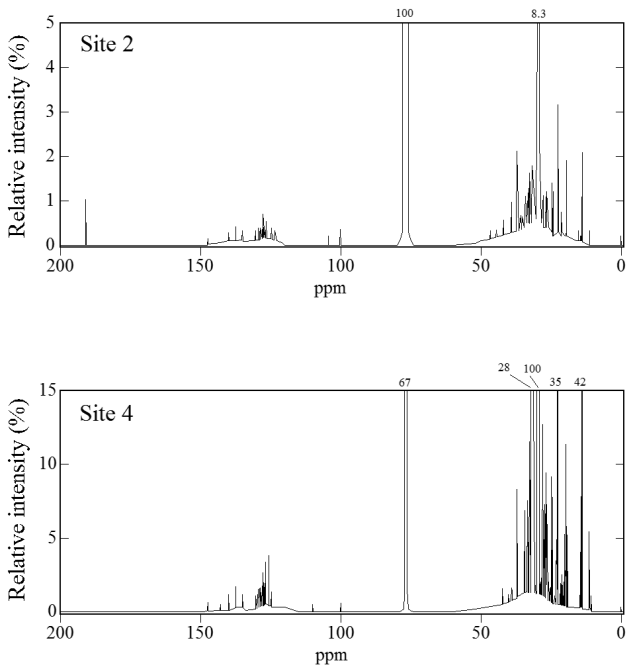

Fig. 2. ^{13}C NMR spectra of crude oil samples at sites 2 and 4. The numbers at the top of the figures indicate the relative intensities of the peaks presently out of range of the figures.

finally dissolved in 2 wt.% HNO_3 and analyzed using an Agilent 7500 ICP-MS. In this study, Y was also determined as well as the lanthanoids. The loss of REE during decomposition, evaporation and redissolution processes is negligible as suggested by results from rock samples treated in the same way (Takahashi *et al*., 2002).

The REE concentrations in water samples were also determined by ICP-MS. Since concentrations of some REE in groundwater are generally lower than ppt level, REE were pre-concentrated using a column (diameter 1.0 cm, length: 10 cm) loaded with a cation exchange resin AG50W-X8 (Takahashi *et al*., 2002). About 250 mL of weighed sample was introduced into the column. Major cations were eluted by 2 M HCl solutions and REE were eluted by 40 mL of 6 M HCl solution. The eluted solution containing REE was evaporated and redissolved by 2 wt.% HNO_3 solution, which was used for the REE determination by ICP-MS. In addition, total organic carbon (TOC) in water samples was determined using a TOC analyzer (TOC-V_{CSH}; Shimadzu). Abundance of iron (Fe) in water samples was determined using an ICP-atomic emission spectrometry (ICP-AES; SII Nano Technology).

Results

The ^{13}C NMR spectra of two samples (sites 2 and 4) show several peaks from 10 to 60 ppm, around 77 ppm and from 120 to 150 ppm. These peaks, often observed in crude oils (Hasan *et al*., 1983; Sharma *et al*., 2008) can be ascribed to the presence of functional groups of aliphatic carbons (0–70 ppm), formyl groups (77 ppm) and aromatic carbons (110–160 ppm), respectively (Fig. 2). In addition, we observed peaks at 145 ppm for crude oil samples collected at sites 2 and 4, which suggest the presence of phenol groups (Thorn *et al*., 1989). A peak at 191 ppm observed in a crude oil sample from site 2 is due to the presence of a carboxyl group.

Table 1. REE concentrations (μg/g) in crude oil samples

Element	Site 1	Site 2	Site 3	Site 4
Y	22.8	337	1350	242
La	33.6	288	861	386
Ce	66.6	662	2150	843
Pr	7.91	59	278	102
Nd	30.1	233	1140	397
Sm	6.52	47.2	182	84.4
Eu	1.55	11.2	38.2	16.7
Gd	5.70	44.4	166	74.6
Tb	1.01	8.1	32.4	12.0
Dy	5.31	48.0	187	62.2
Ho	1.08	10.1	39.2	11.0
Er	3.23	32.8	125	29.3
Tm	0.446	4.74	17.9	3.45
Yb	2.98	32.4	124	21.0
Lu	0.437	4.93	18.4	2.77
∑REE	189	1820	6710	2290

The REE concentrations in crude oil samples have been normalized to a CI chondrite (Anders and Grevesse, 1989; Table 1, Fig. 3a). Light-REE (LREE) enrichment is observed in all the REE patterns of crude oils. Flat heavy-REE (HREE) patterns are observed for oil samples collected from sites 1, 2 and 3, while HREE-depleted pattern is observed for that collected from site 4. The former three samples from sites 1 to 3 have convex patterns in the Gd–Tb–Dy–Ho span, i.e., M-type effect shown in the third tetrad (Masuda *et al*., 1987). The concentrations of REE collected from site 3 are the highest among all collected crude oils, while site 1 has the lowest REE concentrations. Although the concentrations of REE have wide variations among each site, such a variation can be caused by different abundances of functional groups in crude oils (Zhang *et al*., 2009). All the crude oil samples showed negative Eu anomalies, whereas no distinct Ce anomalies were found.

The concentrations of REE in coexisting water were also determined and have been normalized to the CI chondrite (Anders and Grevesse, 1989; Table 2, Fig. 3b). The chondrite-normalized REE pattern for water sample of site 1 is enriched in LREE, while that for water collected at site 2 shows a V-shaped pattern (Fig. 3b). Both

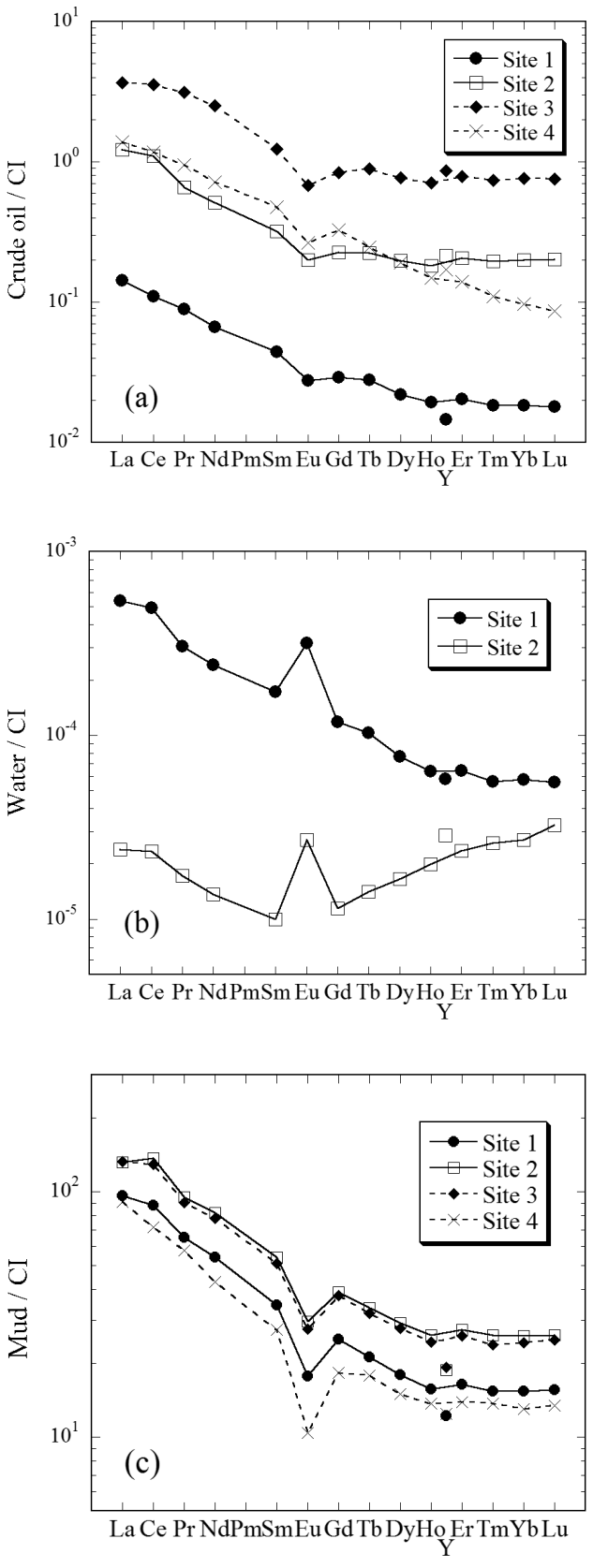

Fig. 3.

REE patterns have distinct positive Eu and small positive Ce anomalies, respectively. The results of XRD analysis of mud samples showed that the mud contained feldspars. Thus, the positive Eu anomalies shown in the REE patterns can be induced by the dissolution of anorthite (Byrne and Sholkovitz, 1996), while the positive Ce anomalies can be related to the formation of Ce(IV)-carbonate species in alkaline water with a high carbonate content (Möller and Bau, 1993). Actually, according to the classification of the "true Ce anomaly" suggested by Bau and Dulski (1996), water sample collected at site 1 exhibits positive Ce anomaly. On the other hand, water sample collected at site 2 shows negative La anomaly, suggesting the presence of M-type tetrad effect as seen in the upward concave curve in the La–Ce–Pr–Nd span in the REE patterns (e.g., Bau, 1996; Takahashi *et al*., 2002). The REE concentrations in mud and surface soil samples have been normalized to the CI chondrite (Anders and Grevesse, 1989; Table 3, Fig. 3c). All samples are rich in LREE, typical for sedimentary rocks, with negative Eu anomalies with Eu/Eu* varying from 0.47 to 0.68.

DISCUSSION

Comparison of REE abundances in crude oils with previous reports

Previous reports on REE abundances in crude oils (Akinlua *et al*., 2008; Takeda and Arikawa, 2005) mostly provided patterns of LREE, but not the complete REE patterns. Total REE abundances reported by Akinlua *et al*. (2008) and Takeda and Arikawa (2005) are less than 3 ng/g. Recently, Zhang *et al*. (2009) reported REE patterns for crude oils, which show a zigzag structure with enrichments of Nd, Eu, Tb, Ho, Tm and Lu in all their crude oil samples except one. They suggested that the enrichment of MREE with an even number of f electrons and the enrichment of HREE in crude oils result from higher stability constants of organic complexes with these elements. However, such zigzag REE patterns can be an analytical artifact, because the odd numbered REE generally occur in lower concentrations, often well below the detection limit of available instruments. Our report of complete REE patterns of crude oils is thus important, since resolution of the fine structure of REE patterns allows us to estimate the REE species in the samples. Total REE abundances of the crude oil samples showing zigzag patterns in Zhang *et al*. (2009) are less than 30 μg/g, while

Fig. 3. Chondrite-normalized REE patterns of (a) crude oil, (b) water and (c) mud samples collected at mud volcanoes in Xinjiang Province, China. REE concentrations of CI chondrite are taken from Anders and Grevesse (1989).

Table 2. REE concentrations (ng/L), pH, alkalinity (mM), calculated CO_3^{2-} concentrations (mM), TOC (mg/L) and concentration of iron (μg/L) in water samples

Element	Site 1	Site 2
Y	90.7	44.5
La	126	5.61
Ce	299	14.1
Pr	27.2	1.53
Nd	110	6.17
Sm	25.3	1.47
Eu	17.9	1.52
Gd	23.2	2.26
Tb	3.73	0.511
Dy	18.6	4.03
Ho	3.54	1.10
Er	10.2	3.74
Tm	1.35	0.630
Yb	9.31	4.39
Lu	1.35	0.790
∑REE	767	92.3
pH	8.40	7.35
Alkalinity	71	53
CO_3^{2-}	70	48
TOC	7.20	6.54
Fe	4.52	3.85

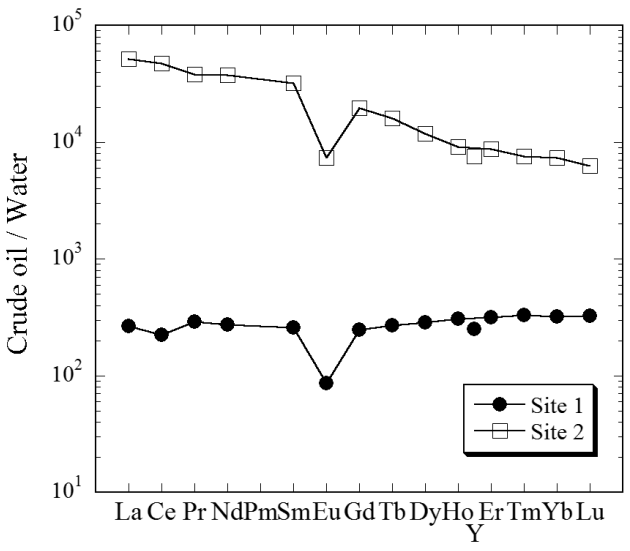

Fig. 4. Partition coefficients between crude oil and water.

the sample with smooth pattern contains more than 140 μg/g (Zhang *et al*., 2009). Compared with the Zhang *et al*. (2009) data, our crude oil samples have higher REE abundances (except for Y), *ca*. 160, 1500, 5360, 2050 μg/g for sites 1, 2, 3 and 4, respectively (Table 1).

REE complexes in crude oils

It must be noted that concentrations of REE in crude oils are much larger than those in water. The preferential REE partitioning into the crude oil rather than water suggests that REE form neutral species and complexes with organic matter in the oil phase, because crude oil is hydrophobic and REE have high ionic properties. ^{13}C NMR spectra of crude oils collected from the sites 2 and 4 demonstrate the presence of aliphatic carbons, formyl group, aromatic carbons and phenol groups. Furthermore, the crude oil collected from site 2 shows a peak at 191 ppm, which indicates the presence of carboxyl group (Fig. 2). The phenol and carboxyl groups can act as binding sites for metal cations, similarly to metal complexation in humic substances (Tipping, 2002). Thus, it is suggested that the large partition of REE into crude oil relative to water can be caused by the formation of complexes with these ligands occurring in crude oils.

The evidence that REE form complexes with ligands in the oils is supported by the M-type tetrad in the Gd–Tb–Dy–Ho span observed for some of our oil samples. It has been often reported that M-type tetrad is observed in complex formation of REE with ligands such as found in the complexation with extractant in organic phases in liquid-liquid extraction system (Peppard *et al*., 1969; Yaita and Tachimori, 1996; Yamamoto *et al*., 2010). In addition, the differences observed in the REE patterns between crude oils collected from sites 2 and 4 could be due to the presence of different REE complexes they are bound to.

Partition coefficients of REE between crude oil and water

REE partition coefficients between crude oil and water were calculated for samples from sites 1 and 2, where both phases were collected. Partition coefficient patterns show that the coefficients for the samples collected from site 2 are higher than those of the samples collected from site 1 by more than an order of magnitude, with negative Eu anomalies presented in both patterns (Fig. 4). If REE in both phases were in equilibrium, the degree of Eu anomalies would be expected to be similar between oil and water phases, which obviously is not the case. Our results suggest that although the two phases are in contact, the REE partition between oil and water is not at equilibrium. The strong binding of REE in the oil phase perhaps inhibits the redistribution of REE into the water phase. This might also explain the large discrepancy of the partition coefficients calculated in samples collected from sites 1 and 2.

To evaluate the complexation of REE in the oil phase, it is better to obtain partition of REE in the oil phase relative to free REE ions in water. The partition coefficient

Table 3. REE abundances (mg/kg) of mud and rocks determined using ICP-MS

Element	Rock (i)	Mud Site 1	Rock (ii)	Mud Site 2	Mud Site 3	Rock (iii)	Mud Site 4
Y	23.6	19.0	28.7	29.2	30.1	21.2	19.4
La	30.5	22.6	29.5	31.0	31.3	26.7	21.4
Ce	75.7	53.1	75.4	82.5	78.2	57.8	43.3
Pr	8.00	5.80	7.91	8.50	8.07	6.11	5.15
Nd	34.1	24.4	34.3	37.2	35.2	25.9	19.5
Sm	7.03	5.07	7.41	7.98	7.52	5.48	4.03
Eu	1.36	1.00	1.62	1.66	1.55	1.10	0.583
Gd	6.55	4.91	7.17	7.67	7.40	5.33	3.60
Tb	1.03	0.769	1.15	1.22	1.16	0.847	0.646
Dy	5.93	4.35	6.84	7.10	6.76	4.98	3.63
Ho	1.18	0.869	1.40	1.45	1.36	1.00	0.764
Er	3.50	2.60	4.22	4.35	4.10	3.02	2.21
Tm	0.508	0.373	0.606	0.628	0.576	0.421	0.331
Yb	3.34	2.51	4.09	4.20	3.93	2.87	2.11
Lu	0.503	0.378	0.618	0.634	0.604	0.429	0.326
Ce/Ce*	1.16	1.11	1.18	1.22	1.18	1.09	0.99
Eu/Eu*	0.61	0.61	0.68	0.64	0.63	0.62	0.47
∑REE	203	148	211	225	218	163	127

$Ce/Ce^* = Ce_{CN}/\sqrt{La_{CN} \times Pr_{CN}}$, $Eu/Eu^* = Eu_{CN}/\sqrt{Sm_{CN} \times Gd_{CN}}$ where CN means chondrite normalized values.
Note that rock (i) is a sedimentary rock sample collected around mud volcanoes locate site 1, rock (ii) is collected around sites 2 and 3, and rock (iii) is collected around site 4.

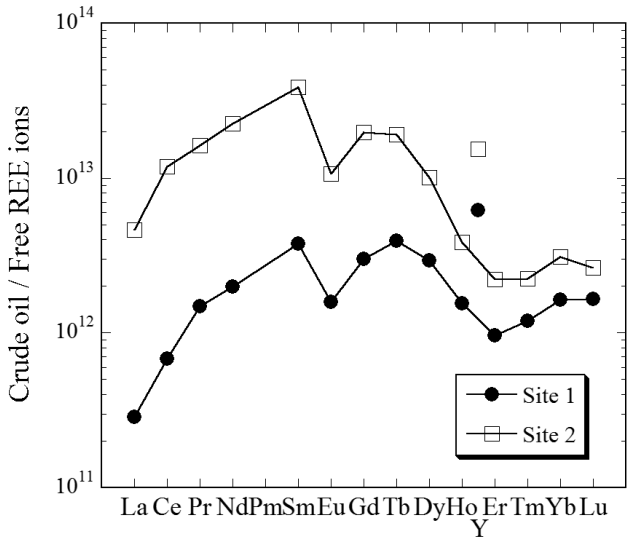

Fig. 5. Partition coefficients between crude oil and free REE ions in water.

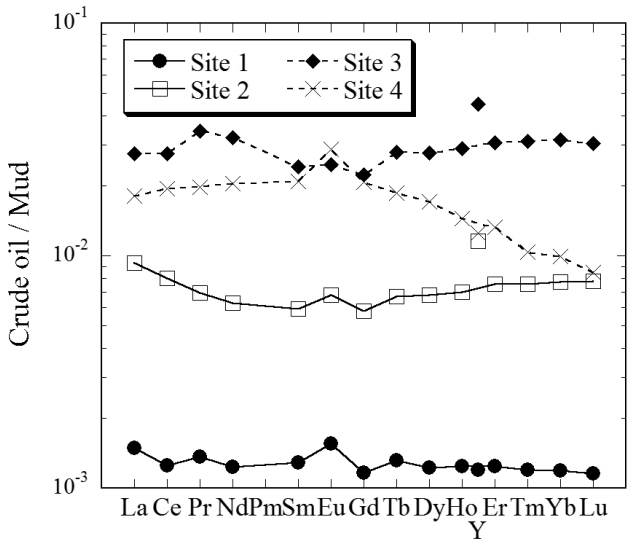

Fig. 6. Coexisting mud-normalized REE patterns of crude oils.

of REE in the oils phase to free ions in the aqueous phase can be directly compared with the stability constants (β) of REE with known ligands (=L^{z-}) formulated for free REE ions (=Ln^{3+}) as $\beta_{REE\text{-}L} = [Ln\text{–}L^{(3-z)+}]/([Ln^{3+}][L^{z-}])$. A speciation calculation using the Windermere Humic Aqueous Model (WHAM; Tipping, 1994) was conducted to determine the free REE ions in our water samples. Intrinsic stability constant (log K_{MA}) values of REE and humic complexes were obtained from Yamamoto *et al.* (2010). We assumed that humic acid constitutes 50% of the total organic carbon and that all iron dissolved in the water is bound to humic acid as Fe(III) (Herbert and Bertsch, 1995; Yamamoto *et al.*, 2009). Based on the concentrations of free REE ions, we reevaluated the parti-

tion coefficient of REE into oil phase normalized by free REE ions in the water. A relatively high pH and a large content of carbonate ions in the water samples (Table 2) can lead to lower fractions of free REE ions for the heavier REE. Although a complete equilibrium of REE between oil and water phases may not be attained, the REE partition coefficients to free REE ions in water phase clearly show enrichments for Sm and Lu (Fig. 5). Such a trend is known for the stability constants of REE with carboxylic acids (Smith and Martell, 1987), which were detected in our crude oil samples by ^{13}C NMR spectra. It is most likely that the complexation of REE with these ligands induces larger partitions of REE into crude oils relative to the water phase.

Origin of REE in crude oil

The REE patterns of the crude oils were compared with those of coexisting mud (Table 3; Fig. 6). Samples of crude oils collected from sites 1, 2 and 3 show flat mud-normalized REE patterns, while the crude oil collected from site 4 shows an HREE-depleted pattern. The flat patterns suggest that REE in crude oils principally inherit those in coexisting mud which originates from surrounding sedimentary rocks. The HREE depletion observed at sample collected from site 4 in Fig. 6 can be due to the lower abundances of HREE in crude oil itself shown in Fig. 3a, since REE patterns of mud samples erupted from mud volcanoes were very similar among all sites (Table 3). The absence of carboxyl groups, as discussed above, can cause the depletion of HREE in the oil samples. Thus, we speculate that REE in crude oil sample collected from site 4 is also derived originally from sediments.

Difference of Y/Ho ratio shown in Fig. 6 can be caused by the difference of their source reservoirs, in particular REE abundances in water contacted with oil in each reservoir. Although the Y/Ho ratios of mud samples are almost the same in a range from 20.1 to 25.4 (Fig. 3c), the ratio varies greatly among water samples with the ratio of 25.6 for site 1 while 40.5 for site 2 (Fig. 3b). Water-rock interactions can induce the increase of Y/Ho ratio in water relative to the original rock source to various extents depending on the degree of water-rock interaction (Bau, 1996; Takahashi *et al*., 2002). Since REE abundances in water primarily affect REE abundances in oils, the Y/Ho ratio in oil can be variable depending on the ratio in water in each system. In addition, water-rock interaction causes positive Eu anomalies in water samples, which in turn induces positive Eu anomaly in the oil normalized to mud as shown in Fig. 6. The degree of Eu anomaly is also dependent on the water-rock interaction in each system. Thus, both Y/Ho ratio and degree of Eu anomaly are variable among different samples (Fig. 6).

The cerium anomaly, which is often observed in plants (Fu *et al*., 1998) or in marine organic matters (e.g., Fleet, 1984), is absent in our crude oil samples. If REE in crude oils are originated from the precursors of oils such as the plants and the marine organic matters, it is most likely that REE patterns of the crude oils have Ce anomalies, which is obviously not the case in our samples. This implies that REE in our crude oil samples are originated from those in surrounding rocks during diagenetic processes associated to the maturation of the crude oils.

Conclusions

The study of REE abundance patterns in crude oils and coexisting water and mud samples from the Xingiang Province, China, brought to the following conclusions:

(1) REE in crude oils derived from their source rocks and sediments;

(2) REE in crude oils mainly form carboxylate and phenolate complexes, which induce a larger partition of REE into the crude oil relative to the coexisting water phase.

Due to a lack of reported data of REE in crude oils, the present study can constitute a preliminary database which may contribute to understand the genetic processes of maturation of hydrocarbons.

Acknowledgments—This study was partially supported by China National Key Basic Research and Development Program (2009CB219506) and a grant-in-aid for scientific research from Japan Society for the Promotion of Science (JSPS). The measurement of ^{13}C NMR was made using JEOL ECA600 at the Natural Science Center for Basic Research and Development (N-BARD), Hiroshima University. Speciation study of REE in oil samples was conducted by X-ray absorption fine structure in Photon Factory in Tsukuba, Japan (2008G683), but effective data were not obtained. The authors are grateful to two reviewers, Prof. M. Bau and one anonymous, for giving us constructive comments.

References

Akinlua, A., Torto, N. and Ajayi, T. R. (2008) Determination of rare earth elements in Niger Delta crude oils by inductively coupled plasma-mass spectrometry. *Fuel* **87**, 1469–1477.

Anders, E. and Grevesse, N. (1989) Abundances of the elements: Meteoritic and solar. *Geochim. Cosmochim. Acta* **53**, 197–214.

Bau, M. (1996) Controls on the fractionation of isovalent trace elements in magmatic and aqueous systems: evidence from Y/Ho, Zr/Hf, and lanthanide tetrad effect. *Contrib. Mineral. Petrol.* **123**, 323–333.

Bau, M. and Dulski, P. (1996) Distribution of yttrium and rare-earth elements in the Penge and Kuruman iron-formations, Transvaal Supergroup, South Africa. *Precambrian Res.* **79**, 37–55.

Byrne, R. H. and Kim, K. H. (1990) Rare earth element scav-

enging in seawater. *Geochim. Cosmochim. Acta* **54**, 2645–2656.
Byrne, R. H. and Sholkovitz, E. R. (1996) Marine chemistry and geochemistry of the lanthanides. *Handbook on the Physics and Chemistry of Rare Earth*, Vol. 23 (Gschneidner, K. A., Jr. and Eyring, L., eds.), 497–593, Elsevier Science B.V.
Clayton, J. L., Yang, J., King, J. D., Lillis, P. G. and Warden, A. (1997) Geochemistry of oils from Junggar Basin, northwest China. *AAPG Bull*. **81**, 1926–1944.
Desheng, L. (1996) Basic characteristics of oil and gas basins in China. *J. Asian Earth Sci*. **13**, 299–304.
Fleet, A. J. (1984) Aqueous and sedimentary geochemistry of the rare earth elements. *Rare Earth Element Geochemistry* (Henderson, P., ed.), 343–373, Elsevier, Amsterdam.
Fu, B., Zheng, G., Ninomiya, Y., Wang, C. and Sun, G. (2007) Mapping hydrocarbon-induced mineralogical alterations in the northern Tian Shan using ASTER multispectral data. *Terra Nova* **19**, 225–231.
Fu, F., Akagi, T. and Shinotsuka, K. (1998) Distribution pattern of rare earth elements in fern: Implication for intake of fresh silicate particles by plants. *Biol. Trace Elem. Res*. **64**, 13–26.
Hasan, M. U., Ali, M. F. and Bukhari, A. (1983) Structural characterization of Saudi Arabian heavy crude oil by n.m.r. spectroscopy. *Fuel* **62**, 518–523.
Henderson, P. (1984) *Rare Earth Element Geochemistry*. Elsevier, Amsterdam, 510 pp.
Herbert, B. E. and Bertsch, P. M. (1995) Characterization of dissolved and colloidal organic matter in soil solution: a review. *Carbon Forms and Functions in Forest Soils* (McFee, W. W. and Kelly, J. M., eds.), 63–88, Soil Science Society of America, Madison, WI, U.S.A.
Johannesson, K. H., Stetzenbach, K. J., Hodge, V. F. and Lyons, W. B. (1996) Rare earth elements complexation behavior in circumneutral pH groundwaters: assessing the role of carbonate and phosphate ions. *Earth Planet. Sci. Lett*. **139**, 305–319.
Lee, K. Y. (1985) Geology of the petroleum and coal deposits in the Junggar (Zhungaer) basin, Xinjiang Uygur Zizhiqu, northwest China. U.S.G.S. Open-File Report 85-230.
Lord, C. J. (1991) Determination of trace metals in crude oil by inductively coupled plasma mass spectrometry with microemulsion sample introduction. *Anal. Chem*. **63**, 1594–1599.
Masuda, A., Kawakami, O., Dohmoto, Y. and Takenaka, T. (1987) Lanthanide tetrad effects in nature: two mutually opposite types, W and M. *Geochem. J*., **21**, 119–124.
Möller, P. and Bau, M. (1993) Rare-earth patterns with positive cerium anomaly in alkaline waters from Lake Van, Turkey. *Earth Planet. Sci. Lett*. **117**, 671–676.
Peppard, D. F., Mason, G. W. and Lewey, S. (1969) A tetrad effect in the liquid-liquid extraction ordering of lanthanides(III). *J. Inorg. Nucl. Chem*. **31**, 2271.
Sharma, B. K., Adhvaryu, A., Perez, J. M. and Erhan, A. Z. (2008) Effects of hydroprocessing on structure and properties of base oil using NMR. *Fuel Process. Technol*. **89**, 984–991.
Smith, R. M. and Martell, A. E. (1987) Critical stability constants, enthalpies and entropies for the formation of metal complexes of aminopolycarboxylic acids and carboxylic acids. *Sci. Total Environ*. **64**, 125–147.
Takahashi, Y., Yoshida, H., Sato, N., Hama, K., Yusa, Y. and Shimizu, H. (2002) W- and M-type tetrad effects in REE patterns for water-rock systems in the Tono uranium deposit, central Japan. *Chem. Geol*. **184**, 311–335.
Takahashi, Y., Châtellier, X., Hattori, K. H., Kato, K. and Fortin, D. (2005) Adsorption of rare earth elements onto bacterial cell walls and its implication for REE sorption onto natural microbial mats. *Chem. Geol*. **219**, 53–67.
Takeda, K. and Arikawa, Y. (2005) Determination of rare earth elements in petroleum by ICP-MS. *Bunseki Kagaku* **54**, 939–943 (in Japanese with English abstract).
Thorn, K. A., Folan, D. W. and MacCarthy, P. (1989) Characterization of the international humic substances society standard and reference fulvic and humic acids by solution state carbon-13 (^{13}C) and hydrogen-1 (^{1}H) nuclear magnetic resonance spectrometry. US Geological Survey, Water-Resource Investigation Report 89-4196, pp. 93.
Tipping. E. (1994) WHAM—A chemical equilibrium model and computer code for waters, sediments and soils incorporating a discrete site/electrostatic model of ion-binding by humic substances. *Comput. Geosci*. **20**, 973–1023.
Tipping, E. (2002) *Cation Binding by Humic Substances*. Cambridge Univ. Press, Cambridge.
Yaita, T. and Tachimori, S. (1996) Study of solvent extraction of lanthanide(III) with tetra(p-)tolymethylene dipphosphine dioxide (TTMDPDO) from a nitric acid solution. *Radiochim. Acta* **73**, 27–33.
Yamamoto, Y., Takahashi, Y. and Shimizu, H. (2009) Speciation of iron in humic substances by X-ray absorption fine structure and its effect on the complexation between humic substances and trace metal ions. *Chem. Lett*. **38**, 278–279.
Yamamoto, Y., Takahashi, Y. and Shimizu, H. (2010) Systematic change in relative stabilities of REE-humic complexes at various metal loading levels. *Geochem. J*. **44**, 39–63.
Zhang, L., Zhao, Y., Jin, Z., Bai, G. and Yang, L. (2009) Geochemical characteristics of rare earth elements in petroleum and their responses to mantle-derived fluid: an example from the Dongying Depression, East China. *Energy Explor. Exploit*. **27**, 47–68.

Volume 26, issue 7, July 2011 ISSN 0883-2927

ELSEVIER

Applied Geochemistry

JOURNAL OF THE INTERNATIONAL ASSOCIATION OF GEOCHEMISTRY

Continued on outside back cover

Applied Geochemistry 26 (2011) 1065–1076

Contents lists available at ScienceDirect

Applied Geochemistry

journal homepage: www.elsevier.com/locate/apgeochem

A geochemical study on mud volcanoes in the Junggar Basin, China

Ryoichi Nakada [a,*], Yoshio Takahashi [a], Urumu Tsunogai [b], Guodong Zheng [c], Hiroshi Shimizu [a], Keiko H. Hattori [d]

[a] Department of Earth and Planetary Systems Science, Graduate School of Science, Hiroshima University, Higashi-Hiroshima, Hiroshima 739-8526, Japan
[b] Division of Earth and Planetary Sciences, Graduate School of Science, Hokkaido University, Kita-10 Nishi-8, Kita-ku, Sapporo 060-0810, Japan
[c] Key Laboratory of Petroleum Resources Research, Institute of Geology and Geophysics, Chinese Academy of Sciences, 382 West Donggang Road, Lanzhou 730000, China
[d] Department of Earth Science, University of Ottawa, Ottawa, ON, Canada K1N 6N5

ARTICLE INFO

Article history:
Received 22 November 2010
Accepted 11 March 2011
Available online 21 March 2011
Editorial handling by R. Fuge

ABSTRACT

A comprehensive study was performed to characterize, for the first time, the mud, water, and gases released from onshore mud volcanoes located in the southern margin of the Junggar Basin, northwestern China. Chemical compositions of mud, along with the geology of the basin, suggest that a source of the mud is Mesozoic or Cenozoic shale. Oxygen and H isotope compositions of the released water suggest a local meteoric origin. Combined with the positive Eu anomalies of the water, a large ^{18}O shift of the water suggests extensive interaction with rocks. Gases discharged from the mud volcanoes are predominantly thermogenic hydrocarbons, and the high $\delta^{13}C$ values (>+20‰ VPDB) for CO_2 gases and dissolved carbonate in muddy water suggest secondary methanogenesis with CO_2 reduction after oil biodegradation.

The enrichments of Eu and ^{18}O in water and the low thermal gradient of the area suggest that the water–rock interactions possibly occur deeper than 3670 ± 200 m. On the other hand, considering the relationship to the petroleum reservoir around the mud volcanoes, the depth of the gases can be derived from about 3600 m, a depth that is greater than that generally estimated for reservoirs whose gas is characterized by ^{13}C-enriched CO_2. Oil biodegradation with CO_2 reduction likely occurs at a shallower depth along the seepage system of the mud volcano. The results contribute to the worldwide data set of gas genesis in mud volcanoes. Moreover, they further support the concept that most terrestrial mud volcanoes release thermogenic gas produced in very deep sediments and may be early indicators of oil biodegradation, an important problem in the petroleum industry.

1. Introduction

Mud volcanoes, which are characterized by the release of mud, water and gases, are found all over the world, particularly in compressional tectonic settings such as in accretionary complexes along subduction zones (Dimitrov, 2002, 2003; Kholodov, 2002; Kopf, 2002). Similar to magmatic volcanoes, the release of fluids from mud volcanoes may occur during the quiescent phase or the eruptive periods. Mud, water, and gases typically ascend through conduits from pressurized reservoirs (e.g., Kopf, 2002). Dimitrov (2002) summarized the factors controlling the occurrence of mud volcanoes: (i) recent tectonic activity, particularly a compressional regime; (ii) rapid loading of rocks due to fast sedimentation, accretion, or overthrusting; (iii) active hydrocarbon generation; and (iv) existence of thick, fine-grained, soft sediments deep in the sedimentary succession. The main factor of mud volcano formation is considered to be a gravity instability in low-density sediments below the high-density rocks induced by fast sedimentation. Gravity instability provides mud diapirism, i.e., the intrusion of shale or clay into overburdened sediments.

Methane is commonly a dominant component in emitted gases from mud volcanoes (e.g., Dimitrov, 2002, 2003; Etiope and Milkov, 2004), with an average concentration of 90.6% (v/v) (Etiope et al., 2009a). The CH_4 flux from mud volcanoes to the atmosphere is estimated to be between 10.3 and 12.6 Tg a^{-1} (Dimitrov, 2002), 5–10 Tg a^{-1} (Etiope and Klusman, 2002), 5 Tg a^{-1} (Dimitrov, 2003), and 6–9 Tg a^{-1} (Etiope and Milkov, 2004), and more recently, 10–20 Tg a^{-1} (Etiope et al., 2011). These estimates suggest that mud volcanoes represent an important natural source of atmospheric CH_4 to be considered in global greenhouse gas emission inventories (Etiope, 2010).

More than 76% of terrestrial mud volcanoes release thermogenic CH_4 (Etiope et al., 2009a), suggesting that gases can be related to a petroleum seepage system. On the other hand, $\delta^{13}C$ values of CO_2 released from mud volcanoes vary to a large degree (−20‰ to +25‰ VPDB), with positive values due to reduction of

* Corresponding author. Tel.: +81 82 424 7460; fax: +81 82 424 0735.
E-mail address: ryo-nakada@hiroshima-u.ac.jp (R. Nakada).

0883-2927/$ - see front matter © 2011 Elsevier Ltd. All rights reserved.
doi:10.1016/j.apgeochem.2011.03.011

CO_2 (originally derived by kerogen decarboxylation) after hydrocarbon biodegradation (Etiope et al., 2009b). Anaerobic biodegradation of oil and natural gas has been identified to be mostly limited to shallow reservoirs, generally shallower than 2000 m where temperature is below 60–80 °C (Pallasser, 2000; Feyzullayev and Movsumova, 2001). Etiope et al. (2009b) showed that the reservoir depth of Azerbaijan mud volcanoes releasing ^{13}C-enriched CO_2 ($\delta^{13}C_{CO2}$ > +5‰ VPDB) is shallower than 2000 m, while the reservoir depth of mud volcanoes releasing lower $\delta^{13}C_{CO2}$ values (−20‰ to ±0‰ VPDB) is deeper than 2000 m up to 6000 m. However, they noted that anaerobic biodegradation of petroleum may take place at shallower depths above the deep non-biodegraded reservoir occurring along the seepage channels of the mud volcano system.

This paper presents geochemical data on mud, water, and gases discharged from mud volcanoes along the southern margin of the Junggar Basin in northwestern China to reveal their origin. Detailed studies on mud volcanoes in this region are needed due to a lack of proper documentation. In addition, there are few studies on any mud volcanoes located along the coast, in the sea, or even onshore, based on the systematic analyses of the three components, namely, mud, water, and gas (e.g., Kopf et al., 2003; Lavrushin et al., 1996).

In the current study, several analyses were conducted to determine the origin of mud, water, and gas. For the mud, major and trace element compositions, including rare earth elements (REE), were determined and compared with the reported values of moraine samples from the northern Tianshan Mountains (Chang et al., 2000). The concentrations of major elements, REE, and isotopic compositions of H and O were determined to understand the origin of water. Concentrations of the major component and their C and H isotope compositions were analyzed to evaluate the origin of the gases.

2. Geological setting

There are two large sedimentary basins in Xinjiang Province, northwestern China, Junggar Basin in the north and Tarim Basin in the south, which are separated by the Tianshan Mountains (Fig. 1). Several mud volcanoes occur along the southern margin of the Junggar Basin (Fu et al., 2007). According to Nansheng et al. (2008), the southern part of the Junggar Basin is underlain by 16 km of thick sedimentary rocks deposited since the Permian. The rocks are folded and faulted, especially on the Tianshan side of the Junggar Basin due to the orogenic activity of the Tianshan Mountains (Avouac et al., 1993). Due to the absence of igneous activity, the heat flow of the southern part of the basin is low, around 35 mW/m^2, and the geothermal gradient of the investigated area, obtained by oil-testing and well-logging data, is about 18 °C/km with an uncertainty of ±1 °C/km (Nansheng et al., 2008). Quaternary conglomerates, such as moraines, overlie a large part of the basin, including the study area (Avouac et al., 1993). Evaporites occurs around the study area (Ma et al., 2010).

The Junggar Basin is also well known for hosting crude oil (e.g., Carroll, 1998; Song et al., 2004; Nakada et al., 2010; Zheng et al., 2010). The Dushanzi oil field produces oil from Cretaceous and Tertiary reservoirs and lies outside the depositional limits of the Upper Permian shales (Graham et al., 1990). Clayton et al. (1997) collected low maturity oil at Dushanzi oil field from an Oligocene formation at a depth of 3644–3656 m.

3. Mud volcano description

Mud volcanoes studied here are located in the cities of Wusu and Dushanzi, Xinjiang Uyghur Autonomous Region, NW China. The locations of mud volcanoes are shown in Fig. 1 and Table 1. Sites 1–4 are located in the rural area south of Wusu City where many mud pies, flat mud extrusive feature (more than 20 in 1 km^2), with a gentle discharge of mud and gas, are found on a slope of a mountain range (Photographs can be found in Fig. A1 in Supplementary material). Sites 6 and 7 are "twin" mud volcanoes located in the mountainous region about 8 km east of sites 1–4. Although samples were not collected, another mud pie was identified about 1 km NW of sites 6 and 7. Sites 8 and 9, situated near the Dushanzi oil refineries, are called Dushanzi mud volcanoes, which were discovered in early 1950's (Zheng et al., 2010) and the last big eruption occurred in July, 1995 (Wang et al., 1997) (Fig. A1). Three mud pools were observed around site 9. Sites 1–4 are pie-shaped mud volcanoes, whereas sites 6–9 are

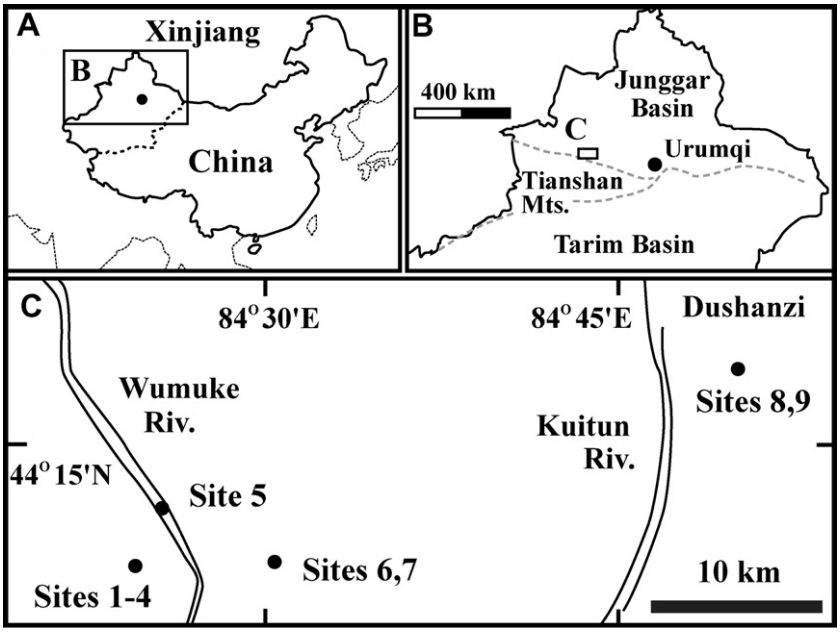

Fig. 1. Location map. Dashed line in (A) represents the border of the Xinjiang Uyghur Autonomous Region. Dashed line in (B) represents the Tianshan Mountains. Location of a square marked on map B is enlarged on map C. Site 9 is situated near the Dushanzi District.

Table 1
Coordinates, altitude, and size of the mud volcanoes investigated in this study.

	Site 1	Site 2	Site 3	Site 4	Site 5	Site 6	Site 7	Site 8	Site 9
Latitude (N)	44°11′00.5″	44°10′58.0″	44°10′57.7″	44°10′57.0″	44°12′55.9″	44°11′19.4″	44°11′19.9″	44°18′18.6″	44°18′32.1″
Longitude (E)	84°23′20.5″	84°23′15.6″	84°23′14.0″	84°23′12.3″	84°24′11.1″	84°29′34.6″	84°29′35.5″	84°50′46.9″	84°51′15.8″
Altitude (m)	1280	1273	1272	1271	902	1171	1174	964	841
Size of crater (m)	2.4 × 2.0	1.1 × 0.9	1.1 × 0.95	1.3 × 3.8		Diameter 1.1	3 × 2.4	0.6 × 0.4	0.5 × 0.5

Size of the crater is represented by "length × width" (site 5: river water).

cone-shaped [Fig. A1(i) and (j)]. Site 7 is the highest mud volcano with a height of about 10 m [Fig. A1(f) and (j)].

Table 2
Mineral composition of the mud samples.

	Site 1	Site 2	Site 3	Site 4	Site 6	Site 7	Site 8	Site 9
Ab	D	D	D	D	D	D	D	D
An	D	N. D.	N. D.	N. D.	N. D.	D	N. D.	N. D.
Calc	D	D	T	T	T	T	D	D
Chl	D	D	D	D	D	D	D	D
Illite	D	D	D	D	D	D	D	D
Kaol	D	D	D	D	D	N. D.	N. D.	N. D.
Mica	D	D	D	D	D	D	D	D
Qtz	D	D	D	D	D	D	D	D
Smec	D	D	D	D	D	D	D	D
Other	N. D.	N. D.	N. D.	N. D.	Verm	Verm	N. D.	N. D.

Ab: albite; An: anorthite; Calc: calcite; Chl: Chlorite; Kaol: kaolinite; Qtz: quartz; Smec: smectite; Verm: vermiculite.
D: major mineral in the XRD pattern; T: minor mineral in the XRD pattern. N. D.: minerals not determined.

The crater sizes are listed in Table 1. Of 8 mud volcanoes, only the crater of site 6 is a true circle, while others are elliptical in shape (Table 1 and Fig. A1). As seen in Fig. A1(a), (d) and (e), some of the mud in the crater has become dried. Those dried-up areas were not counted into the size. Therefore, in the past, the crater size of sites 1, 4, and 6 could have been larger.

Oil seepages were observed at sites 2, 3, 6, 7, 8 and 9. Among them, the largest abundance of oil is discharged at site 9, probably due to its location close to the Dushanzi oil field. All the mud volcanoes were in a quiescent period with some visible degassing, as evidenced by bubbling in craters and mud pools.

4. Sampling and analytical methods

4.1. Sampling

Mud, water, and gas samples were collected at each mud volcano. Surface organic soil samples near the mud volcanoes outside

Table 3
Chemical compositions of mud and soils determined by XRF.

	Soil a	Soil b	Soil c	Mud Site 1	Mud Site 2	Mud Site 3	Mud Site 4	Soil d	Soil e	Soil f	Soil g	Mud Site 6	Mud Site 7	Soil h	Mud Site 8	Mud Site 9
SiO_2	63.9	63.4	64.2	59.5	59.4	60.5	64.7	61.1	58.0	61.5	61.8	58.7	58.8	63.4	57.8	58.5
TiO_2	0.774	0.748	0.806	0.783	0.738	0.858	0.812	0.672	0.884	1.08	1.11	0.971	0.961	0.653	0.821	0.734
Al_2O_3	17.4	13.9	17.3	18.4	18.0	19.9	18.9	13.4	16.6	21.5	23.1	21.8	21.6	15.2	19.7	17.5
Fe_2O_3[a]	6.79	5.06	6.36	7.33	6.93	8.52	6.44	4.69	12.6	8.81	7.80	10.5	10.5	5.35	7.38	6.63
MnO	0.142	0.108	0.178	0.139	0.087	0.188	0.111	0.095	0.233	0.101	0.102	0.291	0.211	0.113	0.084	0.100
MgO	2.50	2.87	2.13	3.22	4.18	2.61	2.07	2.78	1.30	2.18	2.12	2.26	2.22	2.73	3.98	3.38
CaO	3.41	9.57	2.28	3.82	5.17	1.93	0.885	10.5	7.09	0.789	0.518	1.51	1.52	7.39	3.65	5.58
Na_2O	2.39	2.62	2.85	3.30	2.05	2.35	2.51	2.44	1.50	1.91	1.16	1.31	1.85	1.83	2.35	2.19
K_2O	3.02	2.48	3.42	3.22	3.30	2.81	2.94	2.60	2.25	2.60	2.82	2.76	2.75	3.07	3.62	3.14
P_2O_5	0.231	0.184	0.216	0.221	0.229	0.249	0.190	0.170	0.095	0.202	0.148	0.355	0.353	0.224	0.163	0.166
Total	100.56	100.94	99.74	99.93	100.08	99.92	99.56	98.45	100.55	100.67	100.68	100.46	100.77	99.96	99.55	97.92
LOI (%)	8.73	9.10	5.75	9.67	11.0	8.87	6.81	8.04	9.82	7.74	7.16	10.7	10.8	9.86	8.97	12.4
Sc	17.2	15.7	16.3	18.6	18.0	17.9	15.0	16.7	22.5	20.1	22.0	20.7	20.6	16.6	20.9	17.4
V	132	105	115	141	136	156	133	95.8	127	168	174	192	194	106	270	246
Cr	71.6	70.9	49.4	85.1	86.6	75.3	65.2	62.2	76.1	89.9	90.5	80.8	84.1	67.9	105	82.6
Co	16.4	13.9	17.1	18.5	15.8	18.0	15.9	13.3	13.8	25.8	25.8	22.1	21.1	15.2	18.4	14.2
Ni	42.4	35.3	32.9	51.8	51.8	45.7	36.0	31.5	33.8	54.5	55.9	53.5	54.1	38.1	49.1	38.4
Cu	58.6	54.1	66.2	54.1	53.2	51.7	50.8	32.9	64.9	53.9	44.9	61.6	63.7	35.1	54.7	51.5
Zn	97.0	78.1	98.8	69.7	90.3	105	98.5	76.8	116	125	121	120	116	81.8	79.9	82.2
Ga	20.9	17.7	21.6	24.3	22.4	25.3	24.5	16.3	21.0	25.7	29.6	27.1	27.8	18.3	26.6	22.3
Rb	112	94.4	116	124	122	112	111	99.0	83.8	100	108	111	109	119	155	126
Sr	332	409	315	456	543	430	244	483	282	225	143	293	279	375	434	384
Zr	245	363	236	173	169	226	246	265	236	243	246	244	243	234	164	173
Nb	11.8	13.1	12.6	12.4	12.1	12.1	11.7	11.8	10.1	13.2	12.9	12.3	12.1	12.1	14.7	12.5
Cs	4.19	3.51	6.21	8.14	18.8	9.08	15.8	2.90	5.05	4.8	10.3	18.1	6.18	1.61	10.5	10.1
Ba	613	570	697	562	522	620	572	533	1030	594	829	774	762	596	812	2030
Hf	6.52	7.67	6.14	4.84	5.51	5.60	7.09	6.57	5.72	7.03	6.22	6.43	5.94	5.89	4.42	4.51
W	<1.19	4.50	4.19	4.18	2.39	1.36	2.14	<1.19	2.47	<1.19	2.36	<1.19	2.24	2.68	1.66	<1.19
Pb	18.6	10.7	24.0	9.80	21.2	24.9	22.2	16.9	19.9	17.4	21.8	23.0	23.3	21.4	12.4	8.65
Th	14.6	17.6	16.1	18.0	17.1	17.4	16.5	15.7	12.1	12.6	12.7	17.6	15.8	14.1	15.3	14.8
U	3.65	2.70	3.33	3.74	4.52	2.93	3.31	3.42	1.87	2.65	2.98	3.27	2.94	3.08	4.18	4.35

Amounts of oxides are in wt.%, whereas the elements listed below Sc are in mg/kg.
LOI denotes loss on ignition.
Note that soil a–c are surface soil samples collected around the mud volcanoes located at sites 1–4; soil d–g were collected around sites 6 and 7; and soil h was collected around sites 8 and 9.
[a] Total iron as Fe_2O_3.

the mud flow were also collected for comparison (three, four and one samples from sites 1–4, 6–7, and 8–9, respectively). Muddy water was collected directly from the crater of mud volcanoes. One fraction of the water was filtered on site using 0.45 μm membrane filters (hydrophilic PTFE, ADVANTEC®), as used by Hensen et al. (2007). This filter allows a good separation of clay from water. Microbial activities were minor enough not to affect the composition of water, because the composition did not change over the analytical error on repeated measurements for several time spans. After filtration, the water was further divided into two parts: one part was acidified to 2 wt.% HNO_3 for the analyses of REE, and the remaining fraction without acid was used for the analyses of major ions. About 10 mL of acid-free water sample was placed into bottles with no head space remaining, for isotope analysis. Another fraction of water was not filtered but was brought back to the laboratory for centrifugation into mud and water. Gases discharged from the muddy water in the crater were collected by an inverted funnel connected to a syringe and a silicon tube equipped with a stop-cock. After collecting the gases, the stop-cock was closed. Subsequently, the gases in the syringe were transferred to a glass bottle already evacuated using a tip-pierced needle.

4.2. Analytical methods

Temperature, pH, Eh, conductivity, and dissolved O_2 in muddy water were directly measured on site using handylab multi 12 (SCHOTT, Germany), a portable in situ measuring instrument. The accuracies were 0.5% for conductivity and dissolved O_2, whereas those for temperature, pH, and Eh were ±0.1 °C, ±0.01 pH unit, and ±1 mV, respectively. Alkalinity of the acid-free water sample was also determined on site by titration with 0.100 M and 0.0100 M HCl solutions with 1% precision. In the laboratory, muddy water samples were centrifuged for 20 min at 2000 rpm to be separated into mud and water. Mineralogy of the mud samples was determined by a Rigaku MultiFlex X-ray diffractometer (XRD). XRD analyses were also conducted for clay fractions separated by elutriation to identify clay minerals better. Major and trace element compositions of mud and surface soils were determined using a Rigaku ZSX-101e X-ray fluorescence spectrometer (XRF). Analytical conditions were 50 kV accelerating voltage and 50 mA beam current with Rh K_α, L_α, and $L_{\beta1}$, and W K_α and L_α sources. REE concentrations of mud and surface soils were determined using inductively coupled plasma mass spectrometry (ICP-MS) (Agilent 7500) after the digestion of the samples in a mixture of HF, $HClO_4$ and HCl (Takahashi et al., 2002). Accuracy and precision of the XRF analyses were better than 5%, whereas those of the REE obtained using ICP-MS were better than 3%, as estimated from the reported values of a reference rock JSl-1 (slate; Imai et al., 1995) and the repeated measurements of samples.

Major cations (i.e., Na^+, Ca^{2+} and Mg^{2+}) in the water samples were measured using cation chromatography (JASCO), whereas K^+ was measured using atomic absorption spectrometry (AA-646, Shimadzu). Major anions (i.e., F^-, Cl^-, Br^-, NO_3^- and SO_4^{2-}) were measured using anion chromatography (Shimadzu). Analytical accuracy and precision of the major cations and anions were better than 5%. The δD values of water were measured using a Thermo-Fisher Scientific DELTA plus XL (SI Science Co.) with an analytical error of ±1.0‰. The $\delta^{13}C$ and $\delta^{18}O$ of carbonate in the mud samples, and the $\delta^{18}O$ of water and $\delta^{13}C$ of dissolved carbonate in the water samples were measured using the Finnigan MAT Delta Plus mass spectrometer interfaced with a Gas Bench II (Hori et al., 2009). Analytical uncertainties for $\delta^{13}C$ and $\delta^{18}O$ of carbonate in the mud samples were ±0.15‰ and ±0.19‰, respectively, whereas those in the water samples were ±0.04‰ and ±0.18‰, respectively. REE concentrations in water were determined using ICP-MS (Agilent 7500) after preconcentration using a column loaded with cation exchange resin (AG50W-X8; Takahashi et al., 2002) because their concentrations were lower than the ng/L level in water.

Concentrations and $\delta^{13}C$ of CH_4, C_2H_6, and CO_2 in gas samples were measured at Hokkaido University using a continuous-flow gas chromatograph (Agilent 6890) connected to an isotope-ratio mass spectrometer (Thermo Finnigan MAT 252) system (GC/IRMS). Analytical accuracy for the measurements of CH_4 and CO_2 was better than 1%, whereas that of C_2H_6 was better than 5%. Analytical precision for CH_4, CO_2, and C_2H_6 was better than 5%. Analytical error for $\delta^{13}C$ in CH_4 and CO_2 was ±0.3‰, whereas that of C_2H_6 was ±0.7‰. Details of the method for isotopic composition have been given in Tsunogai et al. (2002). The N_2 and O_2 concentrations of gas samples were also measured with 1% accuracy and 5% precision for both.

The δD values of CH_4 and C_2H_6 were measured at G.G. Hatch Isotope Laboratories, University of Ottawa. Calibration and normalization were conducted by the online combustion of two international standards (i.e., NGS1-8559 and NGS2-8560) and one internal standard. Methane and C_2H_6 were isolated by GC using a PoraBOND Q column (27.5 m long, 10 μm film thickness, 2 ml min^{-1} flow at −15 °C) on an HP 6890 gas chromatograph interfaced to a XP Finnigan-Mat IRMS. Precision of δD analysis was ±2‰. Concentrations of H_2, C_3 and C_4 of the gas samples were determined using a Shimadzu GC-14B (Sumika Chemical Analysis Service Co.) with an analytical error of 2%. The detection limits of H_2, C_3 and C_4 were 30, 0.3, and 0.3 ppmv, respectively. Hereafter, all stable isotope compositions are expressed in the conventional delta (δ) notation, defined ‰ deviation from the reference standard VSMOW for H and O, and VPDB for C.

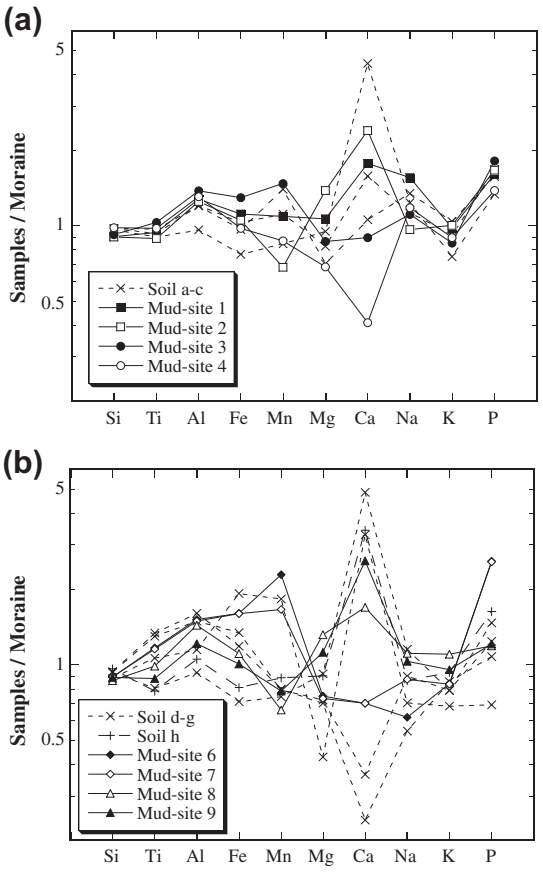

Fig. 2. Major element abundances of mud and surface soils collected around the mud volcanoes normalized to the moraine collected from the northern Tianshan Mountains (Chang et al., 2000). (a) Sites 1–4; (b) sites 6–9. Note that soils a–c are the surface soil samples collected around the mud volcanoes located at sites 1–4; soil d–g were collected at around sites 6 and 7; and soil h was collected around sites 8 and 9.

Table 4
REE abundances (mg/kg) of mud and rocks determined using ICP-MS and $\delta^{13}C$ and $\delta^{18}O$ of carbonate in the mud samples.

	Soil a	Soil b	Soil c	Mud Site 1	Mud Site 2	Mud Site 3	Mud Site 4	Soil d	Soil e	Soil f	Soil g	Mud Site 6	Mud Site 7	Soil h	Mud Site 8	Mud Site 9
Y	23.6	23.0	31.0	21.6	19.0	25.1	24.7	21.4	26.2	24.6	28.7	29.2	30.1	21.2	23.6	19.4
La	30.5	33.7	32.9	24.1	22.6	34.1	23.2	26.4	24.0	25.2	29.5	31.0	31.3	26.7	27.4	21.4
Ce	75.7	73.3	76.9	60.5	53.1	79.1	54.5	55.1	50.9	64.0	75.4	82.5	78.2	57.8	54.7	43.3
Pr	8.00	7.76	7.79	6.04	5.80	8.25	5.76	5.78	5.82	6.68	7.91	8.50	8.07	6.11	6.48	5.15
Nd	34.1	32.3	33.7	25.5	24.4	35.5	24.4	24.1	24.9	28.9	34.3	37.2	35.2	25.9	24.3	19.5
Sm	7.03	6.70	7.22	5.48	5.07	7.45	5.08	5.05	5.26	6.07	7.41	7.98	7.52	5.48	4.98	4.03
Eu	1.36	1.25	1.42	1.11	1.00	1.46	1.00	0.969	1.16	1.34	1.62	1.66	1.55	1.10	0.924	0.583
Gd	6.55	6.50	7.23	5.35	4.91	6.99	4.84	4.96	5.47	5.87	7.17	7.67	7.40	5.33	4.40	3.60
Tb	1.03	1.02	1.14	0.857	0.769	1.11	0.778	0.791	0.900	0.944	1.15	1.22	1.16	0.847	0.773	0.646
Dy	5.93	5.73	6.58	5.03	4.35	6.37	4.55	4.57	5.53	5.56	6.84	7.10	6.76	4.98	4.53	3.63
Ho	1.18	1.16	1.34	1.01	0.869	1.29	0.910	0.927	1.12	1.13	1.40	1.45	1.36	1.00	0.913	0.764
Er	3.50	3.42	3.99	3.00	2.60	3.84	2.73	2.74	3.32	3.39	4.22	4.35	4.10	3.02	2.75	2.21
Tm	0.508	0.487	0.570	0.429	0.373	0.544	0.392	0.389	0.481	0.483	0.606	0.628	0.576	0.421	0.394	0.331
Yb	3.34	3.26	3.76	2.91	2.51	3.71	2.62	2.61	3.16	3.24	4.09	4.20	3.93	2.87	2.63	2.11
Lu	0.503	0.478	0.563	0.437	0.378	0.545	0.396	0.386	0.475	0.495	0.618	0.634	0.604	0.429	0.404	0.326
Ce/Ce*	1.11	1.03	1.10	1.15	1.06	1.07	1.08	1.02	0.98	1.12	1.13	1.16	1.12	1.03	0.94	0.94
Eu/Eu*	0.94	0.89	0.92	0.96	0.94	0.95	0.95	0.91	1.02	1.06	1.05	1.00	0.98	0.96	0.93	0.72
ΣREE	203	200	216	163	148	215	156	156	159	178	211	225	218	163	159	127
$\delta^{13}C$	N. A.	N. A.	N. A.	+1.1	−3.8	+6.1	−1.1	N. A.	N. A.	N. A.	N. A.	+15.7	+15.6	N. A.	−0.6	+0.9
$\delta^{18}O$	N. A.	N. A.	N. A.	+25.0	+26.2	+20.1	+23.0	N. A.	N. A.	N. A.	N. A.	+19.9	+20.6	N. A.	+24.7	+25.5

$Ce/Ce^* = Ce_N/\sqrt{La_N \times Pr_N}$, $Eu/Eu^* = Eu_N/\sqrt{Sm_N \times Gd_N}$ where *N* denotes the UCC normalized values.
Note that soil a–c are surface soil samples collected around the mud volcanoes located at sites 1–4; soil d–g were collected around sites 6 and 7; and soil h was collected around sites 8 and 9. Note also that $\delta^{13}C$ values are in ‰ VPDB, whereas $\delta^{18}O$ values are in ‰ VSMOW. N. A. means non analyzed isotope ratios.

5. Results

5.1. Mud and surface soils

Results of the XRD analysis show that all the mud samples contain albite, calcite, chlorite, illite, mica, quartz and smectite (Table 2). Anorthite and kaolinite are found in some samples. All samples contain high SiO_2, 58–65 wt.% and Al_2O_3, 13–23 wt.% (Table 3). Mud samples collected from sites 6 and 7 contain high Fe_2O_3 (total) and MnO. Concentrations of the major elements in mud and surface soil are normalized to the reported values of moraine samples from the northern Tianshan Mountains (Chang et al., 2000) (Fig. 2).

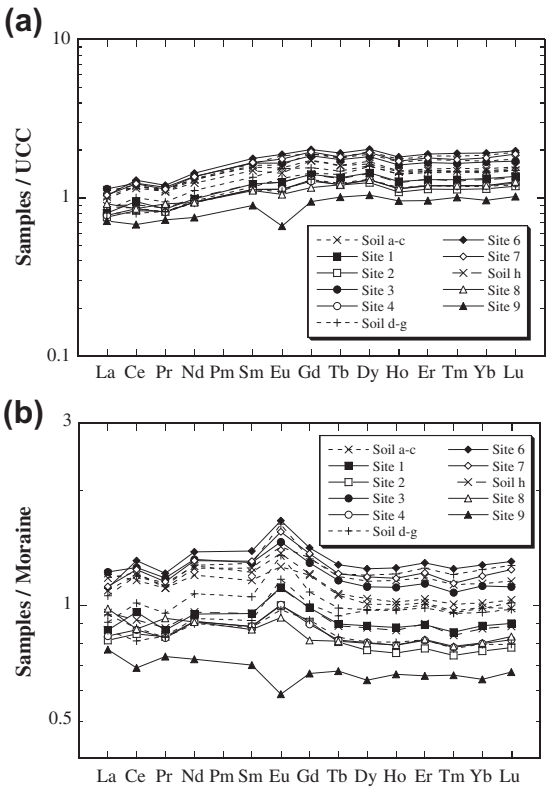

Fig. 3. REE patterns of mud and surface soils collected around the mud volcanoes normalized to (a) UCC (Taylor and McLennan, 1985) and (b) moraine (Chang et al., 2000). Note that soil a–c are the surface soil samples collected around the mud volcanoes located at sites 1–4; soil d–g were collected at around sites 6 and 7; and soil h was collected around sites 8 and 9.

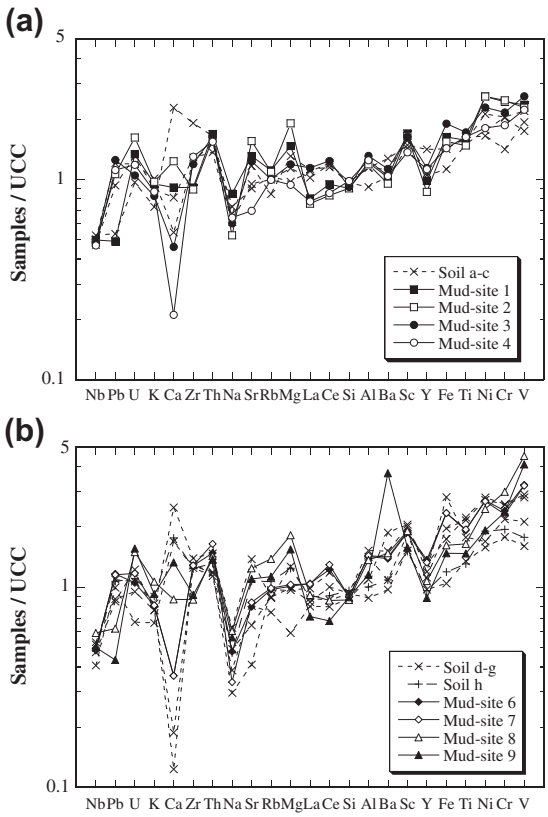

Fig. 4. Composition of mud and soils normalized against the UCC (Taylor and McLennan, 1985). Elements are arranged from left to right in the order of increasing abundance in the average Mesozoic–Cenozoic greywacke. (a) Sites 1–4; (b) sites 6–9. Note that soil a–c are the surface soil samples collected around the mud volcanoes located at sites 1–4; soil d–g were collected at around sites 6 and 7; and soil h was collected around sites 8 and 9.

Table 5
Chemical characteristics of water samples.

	Site 1	Site 2	Site 3	Site 4	Site 5	Site 6	Site 7	Site 8	Site 9
pH	8.78	8.40	8.65	9.16	8.43	7.35	7.80	7.75	8.08
Eh (mV)	−119	−86	−100	−127	−8.8	−28	−54	−50	−69
Temperature (°C)	9.4	9.4	10.4	8.7	11.6	15.2	22.0	11.8	12.2
Conductivity (mS/cm)	11.6	11.6	12.7	11.3	0.506	6.03	7.8	18.5	5.56
Salinity (‰)	6.7	6.4	7.2	6.3	0.0	3.2	3.0	10.7	2.9
Dissolved O_2 (ppm)	0.60	0.86	0.39	0.38	0.72	0.82	0.75	0.55	0.46
F^- (mM)	0.02	0.02	0.02	0.01	0.02	0.03	0.02	0.02	0.02
Cl^- (mM)	109	105	101	92.3	0.84	32.3	33.5	180	72.4
Br^- (mM)	0.26	0.26	0.25	0.26	0.01	0.09	0.09	0.47	0.35
NO_3^- (mM)	0.32	1.06	0.35	0.61	0.10	0.29	0.50	0.25	1.13
SO_4^{2-} (mM)[a]	0.49	1.32	2.00	3.56	2.46	3.69	1.06	9.98	3.55
Alk (mM)	71.0	71.0	60.0	56.7	2.00	53.0	53.0	10.0	10.0
Na^+ (mM)	145	154	145	143	1.26	75.6	80.4	193	73.1
K^+ (mM)	0.15	0.23	0.24	0.25	0.09	0.51	0.66	0.41	0.22
Ca^{2+} (mM)	0.26	0.48	0.36	0.09	3.04	0.29	0.32	6.75	0.93
Mg^{2+} (mM)	0.69	3.70	0.87	0.33	0.85	4.09	5.95	10.9	4.09
δD (‰ VSMOW)	−67.1	−78.8	−83.1	−82.1	−71.2	−77.5	−99.2	−57.1	−57.3
$\delta^{18}O$ (‰ VSMOW)	−1.5	−2.5	−3.0	−3.0	−10.6	−1.0	−4.6	−3.2	−5.7
$\delta^{13}C$ (‰ VPDB)	+12.4	+16.9	+3.2	−3.7	−23.3	+35.6	+33.3	+27.6	+2.3

[a] Total sulfur as SO_4. Note that the δD and $\delta^{18}O$ values represent the isotope ratio of water, and $\delta^{13}C$ represents the isotope ratio of dissolved carbonate in water. (Site 5: river water. Other sites: water from mud volcanoes.)

Major element concentrations, except for Ca, show similar values to those of moraine samples (Fig. 2).

REE concentrations in mud and surface soil samples are reported in Table 4. They are normalized to an average upper continental crust (UCC) (Taylor and McLennan, 1985) as shown in Fig. 3a. All samples are depleted in light-REE (LREE) with variation at Ce and Eu (i.e., Ce and Eu anomalies, respectively), whereas they are all almost flat in heavy-REE (HREE). REE normalized to the average values of moraines from the northern Tianshan Mountains (Chang et al., 2000) are almost flat with positive Eu anomalies, except for a mud sample at site 9 (Fig. 3b).

Major and trace element concentrations (Table 3) are normalized to the average UCC and are plotted in Fig. 4. Elements are arranged from left to right in the order of increasing abundance in the average Mesozoic–Cenozoic greywacke (Condie, 1993) relative to UCC (Fig. 4). Although the abundance of elements on the left side varies widely, elements on the right side, especially after Si, show gradual enrichment.

5.2. Water

Table 5 lists the pH, Eh, temperature, conductivity, salinity, dissolved O_2, alkalinity, concentration of major components (i.e., $F^-, Cl^-, Br^-, NO_3^-, SO_4^{2-}, K^+, Na^+, Ca^{2+}$ and Mg^{2+}), δD and $\delta^{18}O$ isotope compositions for water and $\delta^{13}C$ for dissolved carbonate. The concentrations of almost all ions in the water from mud volcanoes are higher than those of river water.

The δD values of all water samples collected from mud volcanoes are between −57.1‰ and −99.2‰, and the $\delta^{18}O$ values for muddy water range from −1.0‰ to −5.7‰. On the other hand, the $\delta^{18}O$ value of river water (−10.6‰) at site 5 is much smaller than that of muddy water, though the δD value of river water at the site (−71.2‰) is within the range of those collected from mud volcanoes. In the δD and $\delta^{18}O$ diagram (Fig. 5), the water at site 5 lies on the meteoric water line and is plotted in the field of North Xinjiang meteoric waters (Wei and Gasse, 1999). In comparison, muddy waters show an ^{18}O shift from meteoric waters. Moreover, data on muddy waters from sites 1 to 4 form a parallel regression line with the meteoric water line. Samples collected from sites 6 and 7 lie slightly to the right of the regression line for sites 1–4, whereas sites 8 and 9 lie on the left side. The $\delta^{13}C$ values of dissolved carbonate are within the range +35.6‰ to −23.3‰.

Although REE abundances in the water samples are variable, most samples are rich in HREE with positive Ce and Eu anomalies (Table 6 and Fig. 6). However, the river water sample at site 5 shows a HREE-depleted pattern with a negative Ce anomaly (Fig. 6).

Dia et al. (1999) suggested that alkalinity records the reactions with carbonates and silicates, whereas Cl^- is sensitive to diagenetic processes and seawater interaction. In addition, Na and K can characterize the contribution from dissolution of host rock and/or leaching from clay minerals. In Na/Cl versus Alk/Cl (Fig. 7a) and K/Cl versus Alk/Cl (Fig. 7b) diagrams, water samples collected from the mud volcanoes plot in three separated areas: (i) sites 1–4, (ii) sites 6 and 7, and (iii) sites 8 and 9.

5.3. Gas

Similar to other mud volcanoes in the world (e.g., Dimitrov, 2002, 2003; Etiope and Milkov, 2004; Etiope et al., 2009a), CH_4 is the main component of gases emitted from the Xinjiang mud volcanoes (Table 7). In Table 7, all compositional data were corrected

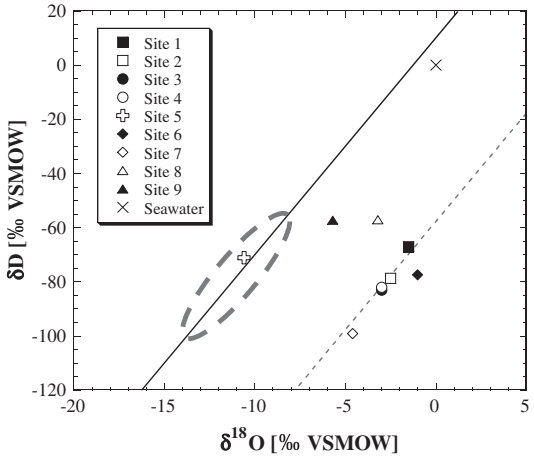

Fig. 5. Comparison of δD and $\delta^{18}O$ values in muddy water, river water (site 5), and seawater. Solid line: the meteoric water line; dashed line: line passing through sites 1–4 and parallel to the meteoric water line; and dashed ellipse: field for meteoric water in northern Xinjiang (Wei and Gasse, 1999).

Table 6
REE concentrations (ng/L) in the water samples.

	Site 1	Site 2	Site 3	Site 4	Site 5	Site 6	Site 8
Y	57.9	90.7	18.2	55.4	14.2	44.5	6.43
La	36.5	126	5.77	8.32	9.94	5.61	1.93
Ce	142	299	12.0	27.2	21.1	14.1	4.38
Pr	10.3	27.2	1.15	2.44	2.77	1.53	0.379
Nd	41.2	110	5.08	10.5	11.4	6.17	1.50
Sm	9.87	25.3	1.80	3.18	2.26	1.47	0.254
Eu	8.51	17.9	4.06	6.75	0.796	1.52	0.554
Gd	9.69	23.2	2.78	4.05	2.65	2.26	0.369
Tb	1.61	3.73	0.308	0.814	0.347	0.511	0.095
Dy	9.38	18.6	2.22	6.36	1.83	4.03	0.693
Ho	2.02	3.54	0.545	1.71	0.357	1.10	0.195
Er	6.65	10.2	1.86	6.49	1.01	3.74	0.602
Tm	1.09	1.35	0.306	1.22	0.122	0.630	0.109
Yb	8.61	9.31	2.35	9.97	0.662	4.39	0.662
Lu	1.36	1.35	0.394	1.67	0.093	0.790	0.128
Ce/Ce*	1.67	1.16	1.06	1.38	0.92	1.09	1.17
Eu/Eu*	4.09	3.46	22.3	8.83	1.53	3.91	8.51
ΣREE	347	767	65.4	146	69.6	92.3	18.3

$Ce/Ce^* = Ce_N/\sqrt{La_N \times Pr_N}$, $Eu/Eu^* = Eu_N/\sqrt{Sm_N \times Gd_N}$ where N denotes the UCC normalized values. (Site 5: river water. Other sites: water from mud volcanoes.)

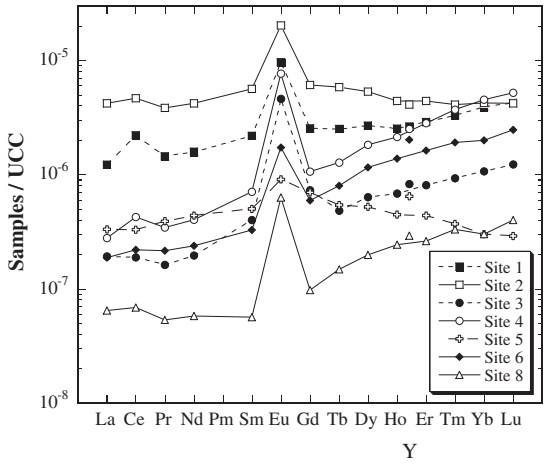

Fig. 6. UCC-normalized REE pattern of water samples. (Site 5: river water; Other sites: water from mud volcanoes).

for air contamination. Raw analyses showed that the contamination with O_2 was 11.9%, 3.2%, 3.5%, 3.6%, 3.7%, and 9.3% for sites 2, 4, 6, 7, 8 and 9, respectively. Given that the concentrations of CH_4 and C_2H_6 collected from mud volcanoes are more than 10^4 times higher than those of atmospheric values, the correction was not conducted for the $\delta^{13}C$ of both CH_4 and C_2H_6. On the other hand, the concentration of atmospheric CO_2 is about 385 ppmv (Keeling et al., 2009). This means that the $\delta^{13}C_{CO2}$ value of gases from mud volcanoes can be greatly affected by air contamination because of the small difference in the concentrations between atmospheric CO_2 and CO_2 from mud volcanoes. Therefore, a re-calculation was conducted for CO_2 concentration and $\delta^{13}C_{CO2}$ values by supposing that the atmospheric $\delta^{13}C_{CO2}$ values are about −8.5‰ (Keeling et al., 2005). Corrections for the concentration and isotope ratio of CO_2 were carried out using the following equation, by assuming that the original O_2 concentration is zero:

$$CO_{2-cor.} = (100 \times CO_{2-meas.}) - (O_2 \times CO_{2-air})/(100 - O_2) \quad (1)$$

where $CO_{2\text{-cor.}}$, $CO_{2\text{-meas.}}$, and $CO_{2\text{-air}}$ represent corrected CO_2, measured CO_2, and reported atmospheric CO_2 values, respectively, for both concentration and isotope ratio of C, while O_2 denotes measured raw concentration of O_2.

The $\delta^{13}C$ values of CH_4 and C_2H_6 at each site are similar at around −40‰ and −30‰, respectively, whereas those of CO_2 are variable. Hydrogen gas was detected in the samples collected from sites 2, 4, 6 and 7. Although the H_2 concentration in the sample collected at site 4 was less than 100 ppm, further quantitative analysis was difficult because of its small peak. The intensities of the H_2

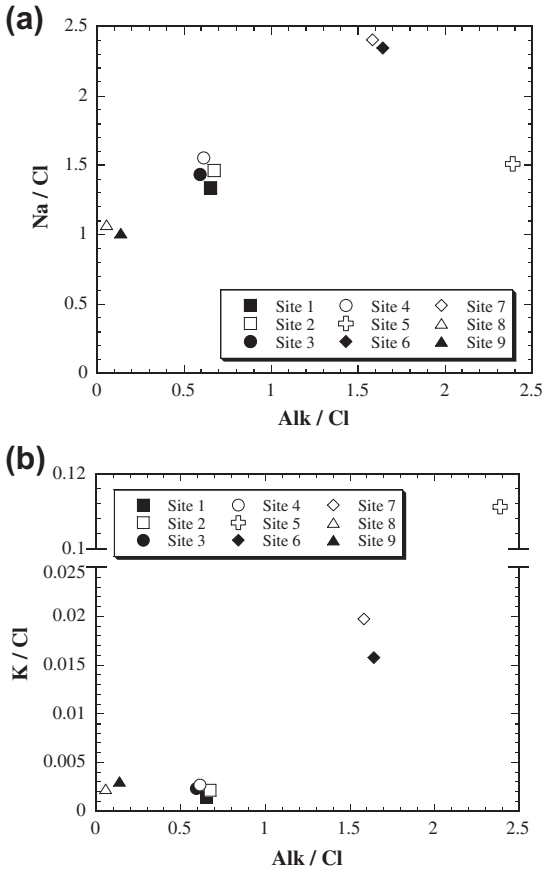

Fig. 7. Comparison of the composition of water in muddy water, river water and seawater. (a) Na/Cl versus Alk/Cl; (b) K/Cl versus Alk/Cl. (Site 5: river water; Other sites: water from mud volcanoes.)

Table 7
Concentrations and stable isotope compositions of gas.

	Site 1	Site 2	Site 4	Site 6	Site 7	Site 8	Site 9
Gas composition (vol.%)							
N_2	N. D.	0.5	5.6	5.8	6.2	0.8	15.7
CH_4	91.6	89.0	89.6	81.5	80.4	92.6	75.8
C_2H_6	8.3	10.1	8.5	5.4	6.2	6.2	7.7
C_3H_8	0.002	0.004	0.1	0.002	0.02	0.6	1.0
Gas composition (ppmv)							
i-C_4	<1	<1	9.8	<1	0.9	400	1390
n-C_4	2.4	4.5	120	1.6	3.5	1430	2540
CO_2	1950	4970	973	1360	1740	4450	3060
$\delta^{13}C$ (‰ VPDB)							
CH_4	−45.9	−43.7	−42.4	−40.7	−39.7	−40.7	−38.6
C_2H_6	−28.1	−26.9	−28.1	−30.8	−28.4	−27.9	−27.2
CO_2	−8.0	+16.2	−11.5	+21.1	+24.6	+29.8	−4.8
δD (‰ VSMOW)							
CH_4	−229	−244	−227	−252	−264	−229	−242
C_2H_6	−143	−180	−223	−183	−203	−194	−181

The effect of air contamination is corrected.
N. D. means not detected.

peaks at sites 2, 6 and 7 are much smaller than that in the gas sample collected at site 4.

The "Bernard ratio" $C_1/(C_2 + C_3)$ versus $\delta^{13}C_1$ and C_2 diagrams show that all the samples plot in the thermogenic field (Fig. 8). The values of $\delta^{13}C$ and δD for CH_4 also fall into the field of thermogenic origin, especially thermogenic gas related to the petroleum field, following the Schoell plot (Schoell, 1983) (Fig. 9).

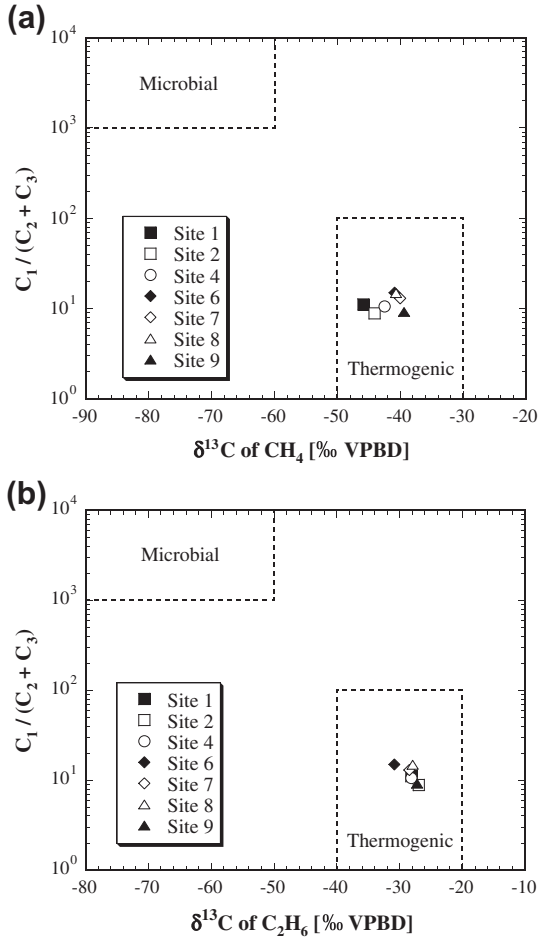

Fig. 8. Relationship between $C_1/(C_2 + C_3)$ and $\delta^{13}C$ values of (a) methane and (b) ethane in gas samples.

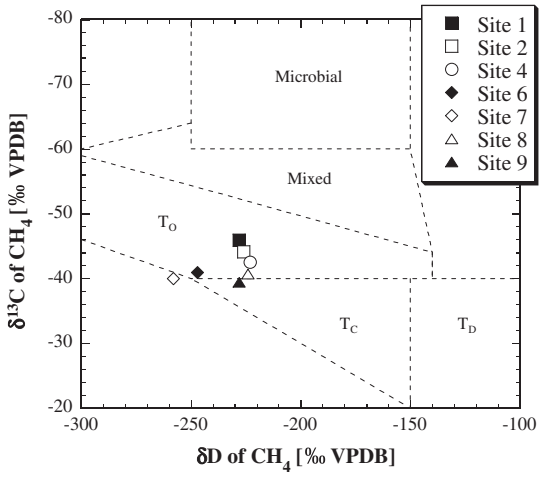

Fig. 9. Relationship between δD and $\delta^{13}C$ of methane based on the discrimination diagram by Schoell (1983), for the classification of thermogenic and microbial natural gas. T_O, T_C, and T_D denote thermogenic with oil, thermogenic with condensate, and dry thermogenic, respectively.

6. Discussion

6.1. Origin of mud

The mud samples show major element compositions similar to moraines in the Tianshan Mountains (Fig. 2); thus, mud and moraine likely have a similar source. The moraine forms as a mechanical mixture of basement rocks during glaciations (Chang et al., 2000). The wide variations of CaO are most likely explained by the different contents of calcite, semiquantitatively detected by XRD patterns (Table 2). Major element concentrations of mud samples collected from the "twin" mud volcanoes (i.e., sites 6 and 7) are similar, which confirms that they originated from the same source and ascended through separate vents or conduits. Mud samples collected from sites 6 and 7 also contain greater abundances of Fe_2O_3 (total), MnO and P_2O_5 than those from other sites. The difference between the abundances of sites 6–7 and those from other samples is not only due to their source rocks, but also to extensive water–rock interaction, which will be discussed in Section 6.2.

Mud and soils show similar normalized REE patterns (Fig. 3), indicating that the mud originated from similar sedimentary rocks in this area, except for the sample at site 9. REE patterns normalized to the moraines collected from northern Tianshan Mountains (Chang et al., 2000) show flat patterns, except for Ce and Eu anomalies (Fig. 3b). The Eu anomalies may be a result of the different abundances of plagioclase between moraines and the samples. In Fig. 3b, a negative Eu anomaly is observed only for mud at site 9. This result suggests that the source layer of site 9 may be different from that of other sites or mixed with different rocks, which are less abundance in plagioclase along the ascent paths.

Fig. 4 shows that the elements arranged on the right side are enriched, where the order of the plots is similar to that in the Mesozoic and Cenozoic sandstones (Cutten et al., 2006). A similar plot using North American Shale Composite (NASC; Gromet et al., 1984), shows a pattern of enrichment on the right side, suggesting that typical sedimentary rocks can show such a pattern. Furthermore, it has been reported that some igneous rocks have a pattern of enrichment toward the right side (e.g., Kawano et al., 2006). However, the absence of igneous rocks and the wide occurrence of Mesozoic and Cenozoic sedimentary rocks in this area (Avouac et al., 1993; Nansheng et al., 2008), combined with the definition that mud comes from shale (Kopf, 2002), suggest that the source of mud in Xinjiang mud volcanoes is Mesozoic or Cenozoic shale. The folded shale layer can be converted into mud due to extensive water–rock interaction (Section 6.2). Although the patterns of mud in Fig. 4a and b are nearly identical, mud collected from site 9 shows a clear difference from those of other sites in the abundance of Ba. This result also supports the fact that the mud at site 9 originated from a different layer from that of other sites or from a mixture of layers.

6.2. Origin of the water and water–rock interaction

All the water samples from the mud volcanoes are rich in Na^+ and Cl^- when compared to other ions; this is commonly observed in water from mud volcanoes (e.g., Dia et al., 1999; Hensen et al., 2007; Lavrushin et al., 1996; You et al., 2004). However, a more detailed comparison of the composition of water suggests that the concentrations of these ions are lower than those from other mud volcanoes, whereas some cations, such as Ca^{2+} and Mg^{2+}, have similar concentrations to those of other sites. This kind of saline

water is observed from a petroleum field (Kharaka and Hanor, 2003), which is also the case in the present samples. In addition, the presence of evaporites in the area may contribute to the increased salinity. Similar concentrations of other cations, except for Na^+, can be obtained from the extensive water–rock interactions in the system of the Xinjiang mud volcanoes. At several sites, the concentrations of Ca^{2+} and Mg^{2+} in water samples collected from mud volcanoes are lower than those from the river, which suggest that the concentration of these cations may be decreased due to precipitation through the cooling process during or after ascent. The calculation using PHREEQC (Parkhurst, 1995) with the WATEQ4F database (Ball and Nordstrom, 1991) shows that all water samples are saturated with calcite and dolomite, except for the sample collected at site 6. The water sample collected at site 6 is supersaturated with dolomite and is slightly undersaturated with calcite.

The δD values of water from the mud volcanoes are almost identical to those of the reported local meteoric water (Wei and Gasse, 1999); hence, water from the mud volcanoes originates from meteoric water (Fig. 5). However, it should be noted that the water is not limited to "present day" meteoric water, but also includes "fossil" meteoric water. It is suggested that the origin of the saline water associated with oil and gas is "fossil" meteoric water that experienced isotope exchange reactions during migration through the sedimentary strata and water–rock interaction (Clayton et al., 1966). Moreover, the $\delta^{18}O$ shift from the meteoritic line in Fig. 5 is larger at sites 6 and 7 and smaller at sites 8 and 9 relative to those of sites 1–4. This fact suggests that the degree of water–rock interaction is greater at sites 6 and 7 and lower at sites 8 and 9 compared with those at sites 1–4. Oxygen isotope fractionation between water and calcite is used to calculate the equilibrium temperature following the equation of O'Neil et al. (1969):

$$10^3 \ln \alpha = 2.78(10^6/T^2) - \delta^{18}O_{water} + 3.39 \quad (2)$$

where $10^3 \ln \alpha$ is $\delta^{18}O_{calcite} - \delta^{18}O_{water}$, T is the temperature in Kelvin, and δ is in VSMOW value. The mean calculated temperature of sites 1–4, 6 and 7, and 8 and 9 is 95, 127 and 81 °C, respectively, which is consistent with the degree of $\delta^{18}O$ shift.

REE patterns of the water also suggest that the water samples were subjected to water–rock interaction (Fig. 6). A positive Ce anomalies in water can occur through the formation of soluble Ce(IV)-carbonate species in alkaline water with high carbonate content (Möller and Bau, 1993). Stability fields of the Ce species on an Eh–pH diagram (Brookins, 1988) show that Ce(IV) is the predominant species in all the water samples. Positive Eu anomalies shown in the REE patterns are likely produced by the dissolution of anorthite (Byrne and Sholkovitz, 1996) or, at least, plagioclase, which contains Ca^{2+}. This mechanism may be the reason why anorthite is only detected in the mud samples collected from sites 1 and 7 using XRD analysis (Table 2). The detection of anorthite in the mud samples seems to contradict the positive Eu anomaly observed in the water samples. However, even a partial dissolution of anorthite can produce a positive Eu anomaly in the aqueous phase, due to the considerably higher concentration of Eu in plagioclase than Sm and Gd, the neighboring elements of Eu (e.g., Schnetzler and Philpotts, 1970; Pride and Muecke, 1981). Moreover, the incorporation of other strata close to the surface during the ascent of mud cannot be ruled out with regard to the detection of anorthite at sites 1 and 7. Although the positive Eu anomaly is suggested to be found specifically in hydrothermal water (Byrne and Sholkovitz, 1996), the actual temperature range needed to cause a positive Eu anomaly in water samples during water–rock interaction is unclear at present. However, Minami et al. (1995) showed that a small positive Eu anomaly ($Eu/Eu^* = 1.1$) could only be found in water in contact with basalt at 70 °C, not in the samples at 20 °C (Minami et al., 1995). This result implies that a relatively high temperature (over 70 °C) is required to induce a positive Eu anomaly in water during water–rock interaction.

Another evidence of water–rock interaction is supported by the compositional ratios of major ions. Alk/Cl and Na/Cl ratios of water collected from sites 6 and 7 are higher than those from sites 1–4, 8 and 9 (Fig. 7a). Potassium/Cl ratios of water collected from sites 6 and 7 are also higher than those from other sites (Fig. 7b). These results indicate that the degree of reaction between water and minerals (i.e., carbonates and silicates) at sites 6 and 7 are greater than those at other sites (Dia et al., 1999). The CaO and SiO_2 concentrations of the mud collected from sites 6 and 7 are actually lower than those from other sites (Table 3). This finding is supported further by the Ti-normalized major element ratios of the mud samples (Fig. A2, Supplementary material). Titanium concentrations would not vary to a large degree before and after water–rock interaction because Ti is an immobile element (Pearce and Cann, 1973; Hill et al., 2000). The Ti-normalized ratios clearly indicate depletion of Si and Ca in the mud samples collected from sites 6 and 7. Moreover, Ti-normalized abundances of Fe and Mn are larger than those of sites where there is a difference in the degree of water–rock interaction (Fig. A2). The evidence suggests that extensive reactions between mud and water at sites 6 and 7 are consistent with the result of ^{18}O shift for water and with the calculated temperature using $\delta^{18}O$ of calcite and water (Fig. 5). Although there are slight differences, variations in the composition of water reflect the degree of interaction with mud and vice versa.

Interestingly, Alk/Cl, Na/Cl, and K/Cl ratios of water collected from sites 8 and 9 are nearly identical irrespective of the large difference in concentrations among these elements between the two sites (Table 5), probably due to dilution by meteoric water at surface. Although the δD values of water collected from sites 8 and 9 are almost identical, $\delta^{18}O$ of water at site 8 is greater than that at site 9 (Table 5), which also supports the idea that the water at site 9 is diluted by meteoric water to a large degree. The finding of dilution by meteoric water at site 9 may cause a problem, since the temperature of water–rock interaction is calculated using O isotopic fractionation as described above (Eq. (2)). However, the calculated temperature at site 8 is 83 °C, which is lower than those of sites 1–4 and, 6 and 7. This fact suggests that the degree of ^{18}O shift is consistent with other evidence, namely, compositional ratio (Fig. 7) and the Ti-normalized ratios (Fig. A2). Therefore, the most extensive water–rock interaction occurred at sites 6 and 7, while weakest interaction occurred at sites 8 and 9.

6.3. Origin of gas

Thermogenic hydrocarbons are the main component of gases released from the Xinjiang mud volcanoes (Table 7 and Figs. 8 and 9). However, considering only thermogenic gas would be difficult to explain the large variations in $\delta^{13}C$ values of CO_2. The $\delta^{13}C_{CO2}$ values and inverse of CO_2 concentrations in the gas phases are shown in Fig. 10, where some $\delta^{13}C$ values of the gas collected from Xinjiang mud volcanoes are markedly shifted to greater values compared to those of thermogenic origin (Jenden et al., 1993). This heavier shift is considered to be caused by a secondary microbial effect. A two end-member mixing model seems to be inappropriate to explain the scattered data shown in Fig. 10, suggesting that the gases experienced complicated and heterogeneous processes. The possible processes that can explain the large variations in $\delta^{13}C$ values are as follows.

First, thermogenic kerogen decarboxylation should be considered because the hydrocarbons are of thermogenic origin (Figs. 8 and 9). The kerogen decarboxylation reaction during source maturation shows a trend of increasing $\delta^{13}C_{CO2}$ with increasing

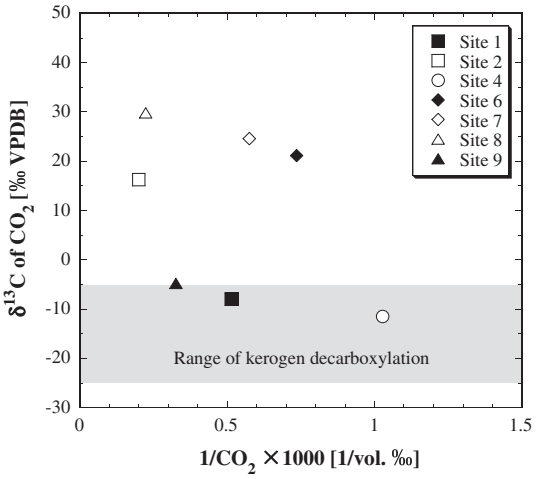

Fig. 10. Relationship between $\delta^{13}C$ values of CO_2 and inverse of CO_2 concentrations in the gas phase. Colored area shows ranges of $\delta^{13}C$ values of CO_2 originating from natural thermogenic CO_2 (Jenden et al., 1993; Kotarba, 2001; Hosgormez et al., 2008).

CO_2 concentration (Jenden et al., 1993; Pallasser, 2000). The $\delta^{13}C_{CO2}$ values of two samples collected from sites 1 and 4 are in the area of the natural thermogenic $\delta^{13}C_{CO2}$ value, which ranges from −25‰ to −5‰ (Jenden et al., 1993; Kotarba, 2001; Hosgormez et al., 2008). The $\delta^{13}C_{CO2}$ value of a sample collected from site 9 also lies on the upper limit of the natural thermogenic $\delta^{13}C$ value.

Second, anaerobic biodegradation of crude oil can be considered to explain the large $\delta^{13}C_{CO2}$ values. Oil biodegradation is suggested by high C_2/C_3 and i-C_4/n-C_4 ratios (Pallasser, 2000; Waseda and Iwano, 2008). High C_2/C_3 and i-C_4/n-C_4 ratios are identified in the samples, thus supporting oil biodegradation. An isotopic effect of the oil biodegradation results in the increase in $\delta^{13}C$ of residual CO_2, which can easily exceed +10‰ (Pallasser, 2000; Waseda and Iwano, 2008). This phenomenon also shows a trend of increasing $\delta^{13}C_{CO2}$ with increasing CO_2 concentration. The difference between kerogen decarboxylation and oil biodegradation is that the latter shows a steeper slope in Fig. 10 and causes a larger shift of $\delta^{13}C_{CO2}$ values.

Oil biodegradation can be followed by CO_2 reduction:

$$CO_2 + 4H_2 \rightarrow CH_4 + 2H_2O. \quad (3)$$

The reaction is also associated with a large kinetic isotope effect. The more the reaction proceeds with decreasing CO_2 concentration, the more ^{13}C is enriched in residual CO_2. The reaction is supported by the presence of H_2 gas. The largest concentration of H_2 of all the sites is found at site 4, where an almost pure thermogenic origin is suggested for CH_4 due to its low $\delta^{13}C_{CO2}$ value, implying that reaction (3) is ongoing. Smaller H_2 peaks are found in the chromatograms at sites 2, 6 and 7. This finding shows that the microbes use H_2 gas for the reaction, resulting in the enrichment of $\delta^{13}C_{CO2}$ value for these samples.

Regarding the variation in $\delta^{13}C_{CO2}$ values, although sites 1–4 are close to one another with similar compositions of mud and water, the gas sample at site 2 has a higher $\delta^{13}C$ value compared with those at other sites (sites 1 and 4), as shown in Fig. 10. This suggests that $\delta^{13}C_{CO2}$ reflects the degree of microbial activity in the vents at shallow levels closer to the surface. The data are consistent with the variable C isotope compositions of CO_2 in other mud volcanoes. Etiope et al. (2009b) reported highly variable $\delta^{13}C_{CO2}$ in different vents in individual mud volcanoes and pointed out that CO_2 reduction associated with oil biodegradation seems to occur at a depth shallower than the main gas reservoir, probably along the seepage system.

While the $\delta^{13}C_{CO2}$ values suggest secondary methanogenic activity, the hydrocarbons emitted from the mud volcanoes plot in the field of thermogenic origin in the "Bernard diagram" (Fig. 8) and "Schoell plot" (Fig. 9; Schoell, 1983). Note that the concentrations of CH_4 are much higher than those of CO_2 in gases released from the mud volcanoes, and the addition of CH_4 from microbial action seems to be negligible. Furthermore, Milkov (2010) has reported that secondary microbial CH_4 is likely to show a $\delta^{13}C_1$ value similar to that of thermogenic gas. Therefore, a dramatic change in $\delta^{13}C$ values is observed for CO_2 due to oil biodegradation and CO_2 reduction, whereas these reactions do not cause a significant $\delta^{13}C$ change for hydrocarbons.

6.4. Depths of the water–rock interaction and gas reservoir in the Xinjiang mud volcanoes

Results for δD and $\delta^{18}O$ values of water indicate that the water is subjected to extensive water–rock interaction (Fig. 5). In addition, the positive Eu anomalies shown in the REE patterns of the water samples from mud volcanoes (Fig. 6) imply anorthite dissolution, which commonly occurs at high temperature as seen in hydrothermal water systems (Byrne and Sholkovitz, 1996). As discussed in Section 6.2, the positive Eu anomaly in the water caused by the reaction with rocks occurs when the temperature is above 70 °C (Minami et al., 1995). If 70 °C is used as the possible lowest temperature of water–rock interaction, the depth is calculated to be deeper than 3060 ± 175 m from the surface, considering that (i) the geothermal gradient of the investigated area is 18 ± 1 °C/km (Nansheng et al., 2008) and (ii) the surface temperature is 15 °C.

In general, however, the reservoir of saline fossil waters related to petroleum is deeper than that of gas and crude oil due to their density variations. At the Dushanzi oil field, which is close to sites 8–9, Oligocene crude oil is collected from a depth of 3644–3656 m beneath the surface (Clayton et al., 1997). Therefore, if 81 °C is taken as the lowest temperature for the water–rock interaction calculated from the O isotope ratio, the depth is about 3670 ± 200 m, slightly deeper than the reservoir of oil at the Dushanzi mud volcanoes (sites 8 and 9). In addition, the water–rock interaction occurs deeper than 3670 m for sites 1–4 and 6–7 from the higher calculated temperature.

Considering that the gases released from the mud volcanoes can be related to the petroleum reservoir (Fig. 9) and that generally the gas reservoir is above the petroleum reservoir, the thermogenic gas released from Xinjiang mud volcanoes would be derived from about 3600 m beneath the surface. This depth, 3600 m, is greater than those of other mud volcanoes releasing ^{13}C-enriched CO_2 (Pallasser, 2000; Etiope et al., 2009b). Such a greater depth could be related to the geology of the Junggar Basin. The Junggar Basin is covered by very thick sediments, and its geothermal gradient is lower than that of the average continental crust especially in the western and southern margins of the basin (Avouac et al., 1993; Nansheng et al., 2008).

Assuming that the (i) surface temperature is 15 °C, (ii) average geothermal gradient of the area is 18 ± 1 °C/km (Nansheng et al., 2008), and (iii) depth of the gas reservoir is 3600 m, the temperature of the gas reservoir is calculated to be 79.8 ± 3.6 °C. This calculation suggests that the temperature of the gas reservoir in Xinjiang mud volcanoes is within the highest range of 60–80 °C, where anaerobic biodegradation has been shown to occur in other mud volcanoes (Pallasser, 2000; Etiope et al., 2009b), or slightly higher than the suggested temperature range.

The depth of oil biodegradation, including CO_2 reduction reactions occurring in this area, may be shallower than the reservoir

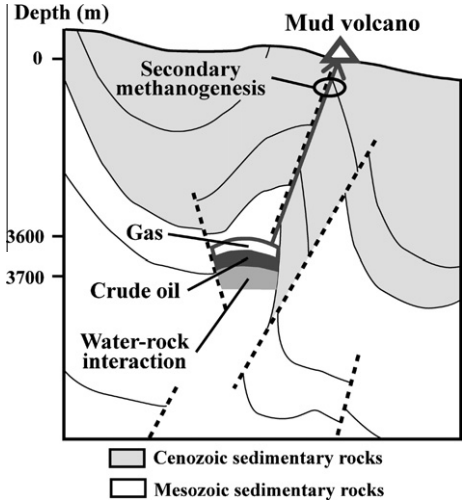

Fig. 11. Schematic illustration of the origin of mud volcanoes in the study area. Cross section is based on Avouac et al. (1993). Dashed line represents the faults which were interpreted from seismic reflection studies (see Avouac et al., 1993 and references therein).

depth of the gas. The shallower depth of oil biodegradation is supported by the heterogeneous $\delta^{13}C_{CO2}$ values observed for sites 1, 2 and 4, which would have the same reservoir due to their close proximity and similarities, as shown by other data. Etiope et al. (2009b) implied the possibility that a deep reservoir of thermogenic gas can be associated with secondary microbial activity at shallow depth. This study reinforces the model which considers a deep reservoir with thermogenic gas and secondary microbial activity likely occurring along the seepage system, which often includes minor gas accumulations, above the main deep reservoir (Fig. 11).

7. Conclusions

This study provides, for the first time, a data set of mud, water, and gas released from mud volcanoes in northwestern China. Major and trace element compositions of mud suggest that the mud originates from Mesozoic or Cenozoic shale. The origin of water is suggested to be fossil meteoric water which has experienced interaction with rock. Thermogenic CH_4 dominates the composition of gas.

Taking into account the petroleum reservoir around the mud volcanoes, the reservoir depth of gas may be about 3600 m. As suggested by the geothermal gradient of the studied area, the water–rock interaction occurs deeper than 3670 ± 200 m. Oil biodegradation and secondary methanogenesis occur at shallower depth along the seepage system of the mud volcanoes which caused large isotopic changes in CO_2. This study provides an example of terrestrial mud volcanoes that release thermogenic gas from very deep sedimentary layers, followed by microbial activity which occurs in the seepage system, probably including minor gas pools above the main reservoir.

Acknowledgements

This study was partially supported by the National Natural Science Foundation of China (Grant No. 41020124002) and the CAS/SAFEA International Partnership Program for Creative Research Teams (2010-1013). This study was also supported by the grants-in-aid for scientific research from the Ministry of Education, Culture, Sports, Science and Technology of Japan, including the "TAIGA" project, which was accepted as a Scientific Research on Innovative Areas. We would like to thank anonymous reviewers for their constructive comments and suggestions which have greatly improved this manuscript.

Appendix A. Supplementary material

Supplementary data associated with this article can be found, in the online version, at doi:10.1016/j.apgeochem.2011.03.011.

References

Avouac, J.P., Tapponnier, P., Bai, M., You, H., Wang, G., 1993. Active thrusting and folding along the northern Tien Shan and late Cenozoic rotation of the Tarim relative to Dzungaria and Kazakhstan. J. Geophys. Res. 98, 6755–6804.
Ball, J.W., Nordstrom, D.K., 1991. User's manual for WATEQ4F, with revised thermodynamic data base and test cases calculating speciation of major, trace and redox elements in natural waters. US Geol. Surv. Open-File Rep., 91–183.
Brookins, D.G., 1988. Eh–pH Diagrams for Geochemistry. Springer-Verlag.
Byrne, R.H., Sholkovitz, E.R., 1996. Marine Chemistry and Geochemistry of the Lanthanides. Handbook on the Physics and Chemistry of Rare Earths, vol. 23, pp. 497–593.
Carroll, A.R., 1998. Upper Permian lacustrine organic facies evolution, Southern Junggar Basin, NW China. Org. Geochem. 28, 649–667.
Chang, Q., Mishima, T., Yabuki, S., Takahashi, Y., Shimizu, H., 2000. Sr and Nd isotope ratios and REE abundances of moraines in the mountain areas surrounding the Taklimakan Desert, NW China. Geochem. J. 34, 407–427.
Clayton, R.N., Friedman, I., Graf, D.L., Mayeda, T.K., Meents, W.F., Shimp, N.F., 1966. The origin of saline formation waters 1. Isotopic composition. J. Geophys. Res. 71, 3869–3882.
Clayton, J.L., Yang, J., King, J.D., Lillis, P.G., Warden, A., 1997. Geochemistry of oils from the Junggar Basin, Northwest China. Am. Assoc. Petrol. Geol. Bull. 81, 1926–1944.
Condie, K.C., 1993. Chemical composition and evolution of the upper continental crust: contrasting results from surface samples and shales. Chem. Geol. 104, 1–37.
Cutten, H.N.C., Korsch, R.J., Roser, B.P., 2006. Using geochemical fingerprinting to determine transpressive fault movement history: application to the New Zealand Alpine Fault. Tectonics 25, TC4014.
Dia, A.N., Castrec-Rouelle, M., Boulegue, J., Comeau, P., 1999. Trinidad mud volcanoes: where do the expelled fluids come from? Geochim. Cosmochim. Acta 63, 1023–1038.
Dimitrov, L.I., 2002. Mud volcanoes – the most important pathway for degassing deeply buried sediments. Earth-Sci. Rev. 59, 49–76.
Dimitrov, L.I., 2003. Mud volcanoes – a significant source of atmospheric methane. Geo-Mar. Lett. 23, 155–161.
Etiope, G., 2010. Geological methane. In: Reay, D., Smith, P., van Amstel, A. (Eds.), Methane and Climate Change. Earthscan, London (Chapter 4).
Etiope, G., Klusman, R.W., 2002. Geologic emissions of methane to the atmosphere. Chemosphere 49, 777–789.
Etiope, G., Milkov, A.V., 2004. A new estimate of global methane flux from onshore and shallow submarine mud volcanoes to the atmosphere. Environ. Geol. 46, 997–1002.
Etiope, G., Feyzullayev, A., Baciu, C.L., 2009a. Terrestrial methane seeps and mud volcanoes: a global perspective of gas origin. Mar. Pet. Geol. 26, 333–344.
Etiope, G., Feyzullayev, A., Milkov, A.V., Waseda, A., Mizobe, K., Sun, C.H., 2009b. Evidence of subsurface anaerobic biodegradation of hydrocarbons and potential secondary methanogenesis in terrestrial mud volcanoes. Mar. Pet. Geol. 26, 1692–1703.
Etiope, G., Nakada, R., Tanaka, K., Yoshida, N., 2011. Gas seepage from Tokamachi mud volcanoes, onshore Niigata Basin (Japan): origin, post-genetic alterations and CH_4–CO_2 fluxes. Appl. Geochem. 26, 348–359.
Feyzullayev, A., Movsumova, U., 2001. About the origin of isotopically heavy CO_2 in gases of Azerbaijan mud volcanoes. Azerb. Geol. 6, 96–105 (in Russian).
Fu, B.H., Zheng, G.D., Ninomiya, Y., Wang, C.Y., Sun, G., 2007. Mapping hydrocarbon-induced mineralogical alterations in the northern Tian Shan using ASTER multispectral data. Terra Nova 19, 225–231.
Graham, S.A., Brassell, S., Carroll, A.R., Xiao, X., Demaison, G., Mcknight, C.L., Liang, Y., Chu, J., Hendrix, M.S., 1990. Characteristics of selected petroleum source rocks, Xinjiang Uygur Autonomous Region, northwest China. Am. Assoc. Petrol. Geol. Bull. 74, 493–512.
Gromet, L.P., Dymek, R.F., Haskin, L.A., Korotev, R.L., 1984. The 'North American shale composite': its compilation, major and trace element characteristics. Geochim. Cosmochim. Acta 48, 2469–2482.
Hensen, C., Nuzzo, M., Hornibrook, E., Pinherio, L.M., Bock, B., Magalhaes, V.H., Bruckmann, W., 2007. Sources of mud volcano fluids in the Gulf of Cadiz-indications for hydrothermal imprint. Geochim. Cosmochim. Acta 71, 1232–1248.
Hill, I.G., Worden, R.H., Meighan, I.G., 2000. Yttrium: the immobility–mobility transition during basaltic weathering. Geology 28, 923–926.
Hori, M., Takashima, C., Matsuoka, J., Kano, A., 2009. Carbon and oxygen stable isotopic measurements of carbonate and water samples using mass spectrometer with gas bench. Bull. Graduate School of Social and Cultural Studies, Kyushu Univ., vol. 15, pp. 51–57 (in Japanese).

Hosgormez, H., Etiope, G., Yalçin, M.N., 2008. New evidence for a mixed inorganic and organic origin of the Olympic Chimaera fire (Turkey): a large onshore seepage of abiogenic gas. Geofluids 8, 263–273.
Imai, N., Terashima, S., Itoh, S., Ando, A., 1995. 1994 Compilation values for GSJ reference samples, "Igneous rock series". Geochem. J. 29, 91–95.
Jenden, P.D., Hilton, D.R., Kaplan, I.R., Craig, H., 1993. Abiogenic hydrocarbons and mantle helium in oil and gas fields. In: Howell, D. (Ed.), The Future of Energy Gases, vol. 1570. Geological Survey, US, pp. 31–35.
Kawano, Y., Akiyama, M., Ikawa, T., Roser, B.P., Imaoka, T., Ishioka, J., Yuhara, M., Hamamoto, T., Hayasaka, Y., Kagami, H., 2006. Whole rock geochemistry and Sr isotopic compositions of Phanerozoic sedimentary rocks in the Inner Zone of the Southwest Japan Arc. Gondwana Res. 9, 126–141.
Keeling, C.D., Bollenbacher, A.F., Whorf, T.P., 2005. Monthly atmospheric $^{13}C/^{12}C$ isotopic ratios for 10 SIO stations. In: Trends: A Compendium of Data on Global Change. Carbon Dioxide Information Analysis Center, Oak Ridge National Laboratory, US Department of Energy, Oak Ridge, TN. <http://www.cdiac.ornl.gov/trends/co2/iso-sio/iso-sio.html>.
Keeling, R.F., Piper, S.C., Bollenbacher, A.F., Walker, J.S., 2009. Atmospheric carbon dioxide record from Mauna Loa. Trends: A Compendium of Data on Global Change. Carbon Dioxide Information Analysis Center, Oak Ridge National Laboratory, US Department of Energy, Oak Ridge, TN. <http://www.cdiac.ornl.gov/trends/co2/sio-mlo.html>.
Kharaka, Y.K., Hanor, J.S., 2003. Deep fluids in the continents: I. sedimentary basins. In: Drever, J.I. (Ed.), Surface and Ground Water, Weathering, Erosion and Soils, vol. 5. Holland, H.G., Turekian, K.K., (Exec. Eds.), Treatise on Geochemistry. Elsevier, pp. 499–540.
Kholodov, V.N., 2002. Mud volcanoes, their distribution regularities and genesis: communication 1. Mud volcanic provinces and morphology of mud volcanoes. Lithol. Miner. Resour. 37, 197–209.
Kopf, A.J., 2002. Significance of mud volcanism. Rev. Geophys. 40, 1–52.
Kopf, A., Deyhle, A., Lavrushin, V.Y., Polyak, B.G., Gieskes, J.M., Buachidze, G.I., Wallmann, K., Eisenhauer, A., 2003. Isotopic evidence (He, B, C) for deep fluid and mud mobilization from mud volcanoes in the Caucasus continental collision zone. Int. J. Earth Sci. 92, 407–425.
Kotarba, M.J., 2001. Composition and origin of coalbed gases in the Upper Silesian and Lublin basins, Poland. Org. Geochem. 32, 163–180.
Lavrushin, V.Y., Polyak, B.G., Prasolov, R.M., Kamenskii, I.L., 1996. Sources of material in mud volcano products (based on isotopic, hydrochemical, and geological data). Lithol. Miner. Resour. 31, 557–578.
Ma, L.-C., Liu, C.-L., Jiao, P.-C., Chen, Y.-Z., 2010. A preliminary discussion on geological conditions and indicator pattern of potash deposits in typical playas of Xinjiang. Miner. Deposits 29, 593–601 (in Chinese).
Milkov, A.V., 2010. Methanogenic biodegradation of petroleum in the West Siberian Basin (Russia): significance for formation of giant Cenomanian gas pools. Am. Assoc. Petrol. Geol. Bull. 94, 1485–1541.
Minami, M., Matsuda, N., Masuda, A., 1995. Experimental studies on behaviors of lanthanides in interaction between water and basaltic rock grains. Proc. Jpn. Acad. Ser. B – Phys. Biol. Sci. 71, 10–14.
Möller, P., Bau, M., 1993. Rare-earth patterns with positive cerium anomaly in alkaline waters from Lake Van, Turkey. Earth Planet. Sci. Lett. 117, 671–676.
Nakada, R., Takahashi, Y., Zheng, G., Yamamoto, Y., Shimizu, H., 2010. Abundances of rare earth elements in crude oils and their partitions in water. Geochem. J. 44, 411–418.
Nansheng, Q., Zhihuan, Z., Ershe, X., 2008. Geothermal regime and Jurassic source rock maturity of the Junggar Basin, northwest China. J. Asian Earth Sci. 31, 464–478.
O'Neil, J.R., Clayton, R.N., Mayeda, T.K., 1969. Oxygen isotope fractionation in divalent metal carbonates. J. Chem. Phys. 51, 5547–5558.
Pallasser, R.J., 2000. Recognising biodegradation in gas/oil accumulations through the $\delta^{13}C$ compositions of gas components. Org. Geochem. 31, 1363–1373.
Parkhurst, D.L., 1995. User's Guide to PHREEQC—A Computer Program for Speciation, Reaction-Path, Adjective Transport, and Inverse Geochemical Calculation. US Geol. Surv. Water-Resour. Invest. Rep., 95-4227.
Pearce, J.A., Cann, J.R., 1973. Tectonic setting of basic volcanic rocks determined using trace element analysis. Earth Planet. Sci. Lett. 19, 290–300.
Pride, C., Muecke, G.K., 1981. Rare earth element distributions among coexisting granulite facies minerals, Scourian complex, NW Scotland. Contrib. Mineral. Petrol. 76, 463–471.
Schnetzler, C.C., Philpotts, J.A., 1970. Partition coefficients of rare-earth elements between igneous matrix material and rock-forming mineral phenocrysts–II. Geochim. Cosmochim. Acta 34, 331–340.
Schoell, M., 1983. Genetic characterization of natural gases. Am. Assoc. Petrol. Geol. Bull. 67, 2225–2238.
Song, Y., Dai, J., Xia, X., Qin, S., 2004. Genesis and distribution of natural gas in the foreland basins of China. J. Petrol. Sci. Eng. 41, 21–29.
Takahashi, Y., Yoshida, H., Sato, N., Hama, K., Yusa, Y., Shimizu, H., 2002. W- and M-type tetrad effects in REE patterns for water–rock systems in the Tono uranium deposit, central Japan. Chem. Geol. 184, 311–335.
Taylor, S.T., McLennan, S.M., 1985. The Continental Crust: Its Composition and Evolution. Blackwell Scientific Publications.
Tsunogai, U., Yoshida, N., Gamo, T., 2002. Carbon isotopic evidence of methane oxidation through sulfate reduction in sediment beneath cold seep vents on the seafloor at Nankai Trough. Mar. Geol. 187, 145–160.
Wang, D., Li, M.W., Li, M., Dai, X.M., 1997. A preliminary study on eruption of the mud volcano in Dusanzi, Xinjiang. Seismol. Geol. 19, 14–16 (in Chinese).
Waseda, A., Iwano, H., 2008. Characterization of natural gases in Japan based on molecular and carbon isotope compositions. Geofluids 8, 286–292.
Wei, K., Gasse, F., 1999. Oxygen isotope in lacustrine carbonates of West China revisited: implications for post glacial changes in summer monsoon circulation. Quater. Sci. Rev. 18, 1315–1334.
You, C., Gieskes, J.M., Lee, T., Yui, T., Chen, H., 2004. Geochemistry of mud volcano fluids in the Taiwan accretionary prism. Appl. Geochem. 19, 695–707.
Zheng, G.D., Fu, B.H., Takahashi, Y., Kuno, A., Matsuo, M., Zhang, J.D., 2010. Chemical speciation of redox sensitive elements during hydrocarbon leaching in the Junggar Basin, Northwest China. J. Asian Earth Sci. 39, 713–723.

Chapter 2

Thermogenic Methane with Secondary Alteration in Gases Released from Terrestrial Mud Volcanoes

Ryoichi Nakada and Yoshio Takahashi

Additional information is available at the end of the chapter

http://dx.doi.org/10.5772/48232

1. Introduction

Mud volcanoes are surface expressions of mud accompanied by water and gas originated from deep underground. They are found all over the world. The locations of mud volcanoes resemble magmatic volcanoes, that is, they are concentrated in areas of compressional tectonic settings such as accretionary complexes and subduction zones (Dimitrov, 2002, 2003; Kholodov, 2002; Kopf, 2002). Recent developments in seismic exploration and seafloor imaging have led to the discovery of mud volcanoes not only onshore, but also offshore. The fact that mud volcanoes are found along the compressional area suggests that eruptions are related to the occurrence of volcanic and earthquake activity. Mud extrusion is a phenomenon wherein fluid-rich, fine-grained sediments accompanying the gases ascend within a lithologic succession through conduits from pressurized reservoirs because of their buoyancy. The factors controlling the occurrence of mud volcanoes are considered to be (i) recent tectonic activity, particularly in a compressional regime; (ii) rapid loading of rocks due to fast sedimentation, accretion, or overthrusting; (iii) active hydrocarbon generation; and (iv) existence of thick, fine-grained, soft sediments deep in the sedimentary succession (Dimitrov, 2002). The main factor in mud volcano formation is considered to be a gravitative instability in low-density sediments below high-density rocks induced by fast sedimentation.

The major differences between mud volcano and normal (magmatic) volcano are as follows: (i) mud volcano only releases, as suggested by its name, mud associated with water, whereas magmatic volcano releases ash and high-temperature lava; and (ii) most of the gases released from the former are methane (CH_4), whereas the latter releases CO_2 and N_2, except for water vapor. With regard to difference (i), one may think that the mud volcano is

not serious as a natural disaster. On the contrary, in Indonesia for example, more than 30,000 people lost their homes due to the eruption of mud (Mazzini et al., 2007). The eruption of an enormous amount of mud (170,000 m^3 per day at the maximum) with the temperature close to 100 ºC buried the Sidoarjo village in Northeast Java (Mazzini et al., 2007). Thus, it is important to understand the eruption mechanism from the view of the disaster caused by the eruption. Difference (ii) is also important, considering that CH_4 has a larger global warming potential than CO_2 (IPCC, 2001). According to the IPCC report (2001), the global warming potential of CH_4 is 62 times higher than that of CO_2 in 20 years and 23 times higher in 100 years. The reported CH_4 concentration released from mud volcanoes all over the world shows that CH_4 dominates more than 90% for most mud volcanoes (Table 1). Furthermore, even if mud volcanoes are in the quiescent period, they constantly release gases into the atmosphere. Considering that magmatic volcanoes are not active in the quiescent period, the consecutive release of CH_4 from mud volcanoes is potentially an important problem. Therefore, understanding the source, abundance, and cause of CH_4 release from mud volcanoes is necessary to evaluate the global warming and potential resource as energy.

Both the concentration and CH_4 flux from mud volcanoes to the atmosphere are important. Thus far, several estimates for global emission have been done, including 10.3 Tg y^{-1} to 12.6 Tg y^{-1} (Dimitrov, 2002), 5 Tg y^{-1} to 10 Tg y^{-1} (Etiope and Klusman, 2002), 5 Tg y^{-1} (Dimitrov, 2003), and 6 Tg y^{-1} to 9 Tg y^{-1} (Etiope and Milkov, 2004). The estimates include several assumptions that can have large uncertainty in their flux estimation because it is almost impossible to determine the quantity of CH_4 released from each mud volcano on Earth. More recently, it has also been reported that gases from mud volcanoes not only originate from visible bubbling in the crater of mud volcanoes but also from soils around mud volcanoes. For example, Etiope et al. (2011) performed flux measurements from soils around mud volcanoes in Japan and showed that total output from soils is comparable with that from vents in the mud volcanoes. Their calculation suggests that global CH_4 flux from mud volcanoes is between 10 and 20 Tg y^{-1} (Etiope et al., 2011). These estimates mean that mud volcanoes represent an important natural source of atmospheric CH_4 considered in global greenhouse gas emission inventories.

Understanding the origin of CH_4, namely, microbial origin from acetate fermentation, microbial from carbonate reduction, thermogenic, and inorganic, provides information on the process and environment responsible for its generation. The interpretation of the origins of gas is generally based on its stable carbon and hydrogen isotopes ($\delta^{13}C$ and δD, respectively), and on the chemical composition of its gaseous alkanes (C_1–C_4; methane, ethane, propane, and butane). In particular, identifying the gas source is accomplished by plotting the stable carbon isotope ratio of C_1 ($\delta^{13}C_1$) versus the light gas composition (Bernard et al., 1978), and the $\delta^{13}C_1$ versus δD_1 (Schoell, 1983). Post-genetic alterations that can affect isotopic and molecular composition of gas should also be considered. The processes include (i) aerobic and anaerobic microbial oxidation of CH_4, (ii) abiogenic oxidation, (iii) isotopic fractionation by diffusion, (iv) molecular fractionation by advection, (v) gas mixing, and (vi) anaerobic biodegradation of petroleum and secondary

methanogenesis. In this respect, both the chemical and isotopic compositions of hydrocarbons and of CO_2 can be useful. In this chapter, we attempt to improve our understanding of the origin of gases released from terrestrial mud volcanoes and seepages by summarizing published data. Further knowledge will allow researchers to use seepage gases as a tracer for hydrocarbon reservoirs and as an indicator of geodynamic processes, hazards, and importance in global changes.

2. Database

The database used in this chapter includes all terrestrial mud volcanoes and other seeps for which all the following parameters are reported: CH_4 stable isotopes ($\delta^{13}C_1$ and δD_1), compositional ratio of hydrocarbons [$C_1/(C_2 + C_3)$], and concentration and stable carbon isotope ratio of CO_2. The data which satisfy these restrictions are listed in Table 1. From more than 200 data, only 27 data from five countries consisted of all five parameters: 14 mud volcanoes from Azerbaijan, 7 from China, 1 from Georgia, 2 from Japan, and 3 from Turkmenistan; all other data lacked at least one parameter (Valyaev et al., 1985; Etiope et al., 2011; Nakada et al., 2011). Numerous studies have reported on at least one of the parameters above and/or the data of gases collected from the same mud volcanoes in different periods. However, the discussion should be performed using all the parameters above reported in one study, because (i) gases released from mud volcanoes have a complicated history, including secondary alterations, and (ii) compositions and stable isotope ratio can be fluctuated with time even in the same vent. Meanwhile, data from peats, recent sediments in freshwater environments, anthropogenically induced seeps from coal mines, coal-bed CH_4 production, and submarine mud volcanoes are not considered.

3. Results and discussion

3.1. The "Bernard" and "Schoell" diagrams

All the data listed in Table 1 are plotted in the "Bernard" and "Schoell" diagrams, namely, $\delta^{13}C_1$ versus $C_1/(C_2 + C_3)$ (Bernard et al., 1978; Faber and Stahl, 1984), and $\delta^{13}C_1$ versus δD_1 (Schoell, 1983). The former plot, which is widely used for the discrimination of thermogenic and microbial C_1, was originally developed by Bernard et al. (1978) through their analysis of hydrocarbons from Texas shelf and slop sediments. In 1984, Faber and Stahl collected sediment samples from the North Sea and modified the Bernard plot by adding the maturation trends of type II and type III kerogen. Figure 1 shows that all the gases released from mud volcanoes in China and Japan fall within or close to the thermogenic field. One of three data in Turkmenistan also falls within the thermogenic field, while two data from Turkmenistan and Georgia are in the intermediate region of the thermogenic and microbial fields. The rest of the data, all from Azerbaijan and one-third from Turkmenistan, fall in the region A, an ambiguous sector above the thermogenic field and right to the microbial. Gases from mud volcanoes do not appear to originate from microbial activities. However, gases

from mud volcanoes in Azerbaijan, Italy, Papua New Guinea, and Russia (Taman Peninsula) fall in the microbial area (Valyaev et al., 1985; Baylis et al., 1997; Etiope et al., 2007). The data listed in Table 1 are selected ones that show all five parameters described in the previous section. Hence, the data lacking in other parameters, such as δD_1 or $\delta^{13}C_{CO2}$, are not considered in the present work. Then, it should be noted that not all the gases released from mud volcanoes are of thermogenic origin.

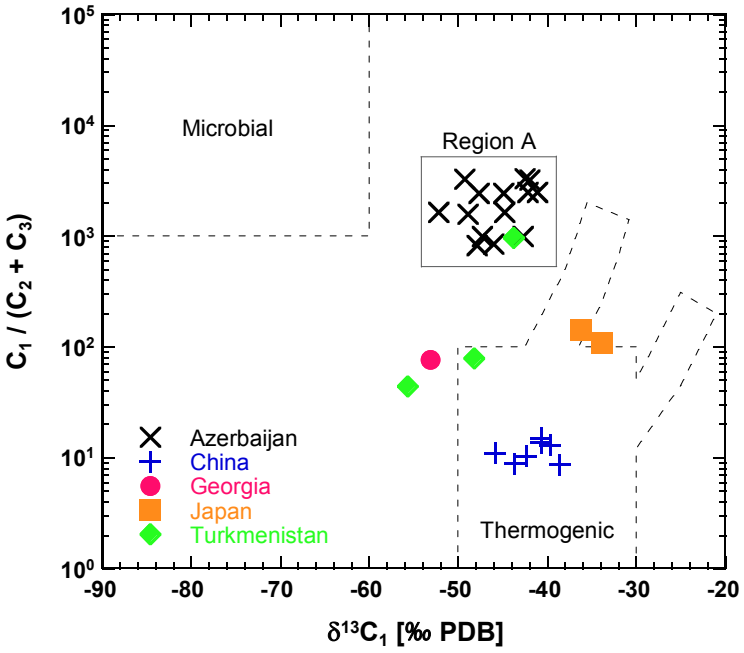

Figure 1. Carbon isotope ratio of CH_4 vs. hydrocarbon molecular composition diagram (Bernard plot; Bernard et al., 1978).

The "Schoell" plot, developed by Schoell (1983) through a summary of the genetic characterization of natural gases from several basins and areas including Gulf of Mexico, German Molasse, and Vienna (references therein), also shows that the data summarized here do not fall in the microbial field (Fig. 2). Likewise, no data are plotted in the dry thermogenic field (T_D). Most of the data fall in the thermogenic field associated with oil or the mixed field. The gases collected in Japan were plotted in the thermogenic field with condensate. Similar to the discussion for the Bernard diagram, the data selected in this work do not cover all the reported data on gases released from mud volcanoes. Actually, gases released from mud volcanoes in Papua New Guinea and Italy fall in the microbial field (Baylis et al., 1997; Etiope et al., 2007). However, until now, any combination of $\delta^{13}C_1$ and δD_1 is not reported for the gas samples that fall on the dry thermogenic area released from mud volcano, though gases from water seeps and dry seeps sometimes fall on the dry thermogenic field (Etiope et al., 2006; 2007, Greber et al., 1997).

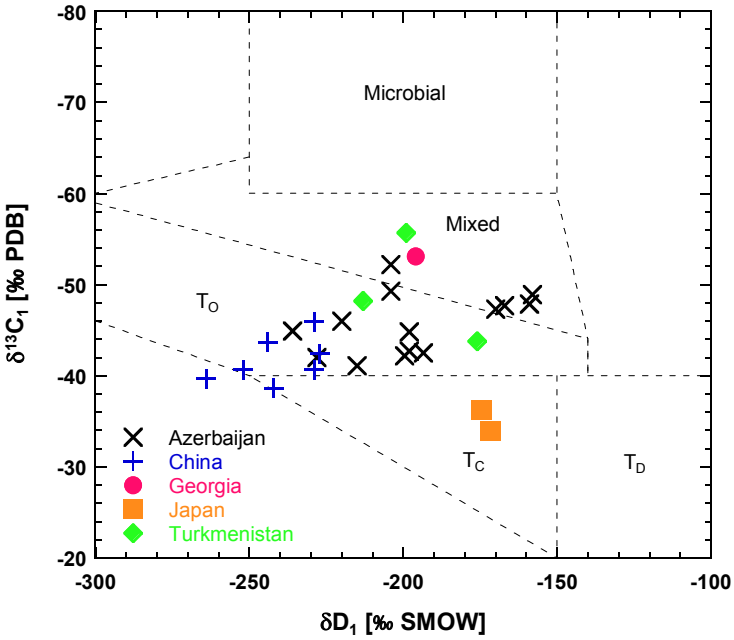

Figure 2. Carbon and hydrogen isotope diagram of CH_4 (Schoell plot; Schoell, 1983); To: thermogenic with oil; Tc: thermogenic with condensate; T_D: dry thermogenic.

The above figures suggest that thermogenic hydrocarbons are the main component of gases released from mud volcanoes. Considering that about half the gases from Azerbaijan fall in the thermogenic field in the Schoell plot, the reason gases plotted in region A in the Bernard diagram may be due to the fact that mixing between thermogenic and microbial or compositional ratio of hydrocarbons changed during post-genetic alteration. Considering $\delta^{13}C_1$ values alone, gases from Azerbaijan can be regarded as thermogenic, whereas Bernard ratios, namely, $C_1/(C_2 + C_3)$, are in the range of microbial origin. Therefore, it can be natural to consider that the data indicate mixing of the gases with two origins. When combining the origins, however, both Bernard ratios and $\delta^{13}C_1$ values are high enough to assume mixing between thermogenic and microbial, because the mixing trend generally tracks high $\delta^{13}C_1$ value with low Bernard ratio to low $\delta^{13}C_1$ value with high Bernard ratio and vise versa. This empirical rule suggests that gases from Georgia and one-third from Turkmenistan are regarded as tracking the mixing trend. On the other hand, gases from Azerbaijan and another one-third from Turkmenistan are not tracking the mixing trend, suggesting that the gases plotted in region A are not due to the mixing of thermogenic and microbial components. The data fall in region A in the Bernard diagram, therefore indicating post-genetic alteration such as (i) aerobic and anaerobic microbial oxidation of CH_4, (ii) abiogenic oxidation, and (iii) anaerobic biodegradation of petroleum and secondary methanogenesis. In this respect, discussion using only isotope and compositional ratios of hydrocarbon is not sufficient; CO_2 data provide useful information.

3.2. Large variation in $\delta^{13}C_{CO2}$ from mud volcanoes

In contrast to the $\delta^{13}C_1$ values, $\delta^{13}C_{CO2}$ from mud volcanoes show a large variation, from -36.9‰ to +29.8‰ (Table 1). Furthermore, the $\delta^{13}C_{CO2}$ values of the gases from Azerbaijan and China, which were plotted on a narrow range in the Bernard diagram, varied to a large degree. The $\delta^{13}C_1$ values of Azerbaijan show a variation of 11.1‰ (from -52.2‰ to -41.1‰), whereas the variation of $\delta^{13}C_{CO2}$ values is 51‰ (from -36.9‰ to +14.1‰). Similar to Azerbaijan, gases from seven mud volcanoes in China show a small variation in $\delta^{13}C_1$ (7.3‰, from -45.9‰ to -38.6‰) and a large variation in $\delta^{13}C_{CO2}$ (41.3‰, from -11.5‰ to +29.8‰). Besides the data selected there, similar characteristics also present in other reported data of gas released from mud volcanoes. Seven mud volcanoes in Georgia have a variation of 14.4‰ in $\delta^{13}C_1$ values and a 28.7‰ variation of $\delta^{13}C_{CO2}$ (Valyaev et al., 1985). Six vents of a mud volcano in Italy have a range of $\delta^{13}C_1$ in 4.3‰ with 29.1‰ variation of $\delta^{13}C_{CO2}$ values (Favara et al., 2001). Thirteen mud volcanoes with 20 reported isotopic ratios in Russia (Taman Peninsula) show a variation of 31.3‰ in $\delta^{13}C_1$ and a variation of 41.9‰ in $\delta^{13}C_{CO2}$ (Valyaev et al., 1985; Lavrushin et al., 1996). Twelve mud volcanoes with 15 vents in Trinidad display a variation of 21.6‰ in $\delta^{13}C_1$ and a 32.4‰ variation in $\delta^{13}C_{CO2}$ (Deville et al., 2003). Turkmenistan, with six available data of mud volcanoes, shows a variation of 12.5‰ in $\delta^{13}C_1$ with 32.1‰ variation in $\delta^{13}C_{CO2}$ (Valyaev et al., 1985). Eleven reported data from Ukraine show a 16.8‰ variation in $\delta^{13}C_1$ and a 40.9‰ variation in $\delta^{13}C_{CO2}$ (Valyaev et al., 1985). Seven mud volcanoes in Taiwan, in contrast, display a variation of 27.3‰ in $\delta^{13}C_1$ with 17.3‰ in $\delta^{13}C_{CO2}$ (Etiope et al., 2009). These facts clearly indicate that terrestrial mud volcanoes show a large variation in the isotopic ratio of CO_2, though most of their $\delta^{13}C_1$ values are within a thermogenic range.

In general, the $\delta^{13}C_{CO2}$ value ranges from -25‰ to -5‰ for natural thermogenic and/or kerogen decarboxylation (Jenden et al., 1993; Kotarba, 2001; Hosgormez et al., 2008). In addition, Jenden et al. (1993) suggested that the upper limit of $\delta^{13}C_{CO2}$ value due to the alteration of marine carbonates is +5‰. Therefore, CO_2 released from mud volcanoes with $\delta^{13}C_{CO2}$ value above that threshold can be called ^{13}C-enriched CO_2. Surprisingly, 14 mud volcanoes in the 28 listed in Table 1 release ^{13}C-enriched CO_2. Considering the 134 mud volcanoes described in the previous paragraph (data not shown), 66 (49%) of them show the ^{13}C-enriched value.

Before assessing the relationship between ^{13}C-enriched CO_2 and composition and isotopes of carbon in hydrocarbon gas, it is necessary to note that a large variability of the $\delta^{13}C_{CO2}$ value can be found within a mud volcano, both in space (gas samples from different vents) and in time (same vents analyzed in different time). For example, according to Nakada et al. (2011), four mud volcanoes (sites 1–4) are located very close to one another. The chemical compositions of mud and water, as well as relative abundances and stable isotopes of various hydrocarbons, are very similar. In particular, sites 2 to 4 are located within a 500 m distance, suggesting that their reservoir can be the same. Among these sites, however, only a gas released from site 2 has ^{13}C-enriched CO_2 (+16.2‰), whereas CO_2 from sites 1 and 4 are within a range of kerogen decarboxylation, -8.0‰ and -11.5‰, respectively (gases from site

Name	$\delta^{13}C_1$	δD_1	$\delta^{13}C_{CO2}$	CH_4 (%)	CO_2 (%)	$C_1/(C_2+C_3)$	Reference
Azerbaijan							
Airantekyan	–44.9	–236	+13.9	96.9	3.04	2423	Valyaev et al. (1985)
Akhtarma Pashaly	–47.9	–159	–7.2	99.1	0.68	825	Valyaev et al. (1985)
Chukhuroglybozy	–41.1	–215	+1.7	99.5	0.42	2488	Valyaev et al. (1985)
Dashgil	–42.2	–200	–6.4	99.0	0.93	2476	Valyaev et al. (1985)
Galmas	–47.7	–167	+13.7	97.4	2.06	2435	Valyaev et al. (1985)
Goturlyg	–42.7	–198	–15.4	98.9	0.99	989	Valyaev et al. (1985)
Gyrlykh	–49.3	–204	+0.6	98.4	1.54	3280	Valyaev et al. (1985)
Inchabel	–48.9	–158	–30.9	94.4	5.53	1573	Valyaev et al. (1985)
Kichik Kharami	–52.2	–204	+0.4	98.7	1.20	1646	Valyaev et al. (1985)
Shikhikaya	–47.3	–170	–36.9	98.9	0.99	989	Valyaev et al. (1985)
Shikhzagirli (Ilanly)	–42.5	–194	+0.1	99.1	0.81	3302	Valyaev et al. (1985)
Shokikhan	–42.0	–228	+13.8	96.7	3.30	3222	Valyaev et al. (1985)
Zayachya Gora (a)	–44.8	–198	+10.5	99.0	0.81	1647	Valyaev et al. (1985)
Zaakhtarma	–46.0	–220	+14.1	93.8	6.14	852	Valyaev et al. (1985)
China							
site 1	–45.9	–229	–8.0	91.6	0.20	11	Nakada et al. (2011)
site 2	–43.7	–244	+16.2	89.0	0.50	9	Nakada et al. (2011)
site 4	–42.4	–227	–11.5	89.6	0.10	10	Nakada et al. (2011)
site 6	–40.7	–252	+21.1	81.5	0.14	15	Nakada et al. (2011)
site 7	–39.7	–264	+24.6	80.4	0.17	13	Nakada et al. (2011)
site 8	–40.7	–229	+29.8	92.6	0.45	14	Nakada et al. (2011)
site 9	–38.6	–242	–4.8	75.8	0.31	9	Nakada et al. (2011)
Georgia							
Tyulkitapa	–53.1	–196	+5.9	89.0	10.86	77	Valyaev et al. (1985)
Japan							
Kamou	–33.9	–172	+10.9	95.4	2.91	108	Etiope et al. (2011)
Murono vent2	–36.2	–175	+28.3	93.7	5.62	144	Etiope et al. (2011)
Turkmenistan							
Keimir	–48.2	–213	–25.2	95.3	0.89	79	Valyaev et al. (1985)
Kipyashii Bugor	–43.8	–176	+6.9	96.8	2.79	968	Valyaev et al. (1985)
Ak-Patlauk	–55.7	–199	–16.2	94.2	3.67	44	Valyaev et al. (1985)

Table 1. Selected data of composition and stable isotope ratio of CH_4 and CO_2.

3 were not collected). Another example can be given by mud volcanoes in Japan. Kato et al. (2009) reported that the $\delta^{13}C_{CO2}$ value of gas released from the Murono mud volcano in August 2004 was +30.8‰. Mizobe (2007) showed that the value of the same mud volcano in May 2005 was +19.2‰ and in June 2006 was +21.2‰. Etiope et al. (2011) reported the value of the same mud volcano was +28.32‰ in May 2010. In contrast, the variation observed in $\delta^{13}C_1$ value of the Murono mud volcano reported in these papers was -33.1‰ to -36.2‰. These observations mean that the different vents of a mud volcano can be related to different circulation systems and/or post-genetic processes, and possibly different source pools or reservoirs. Some of the large Azerbaijan mud volcanoes show oil-saturated structures in some vents while others do not. This finding means that mud volcano systems may not be uniform, but can be structured in different systems and isolated blocks.

However, the variation of $\delta^{13}C_{CO2}$ with time for the same vent suggests that CO_2 carbon isotopes are intrinsically unstable and can be affected by multiple gas–water–rock interactions. According to the estimation by Pallasser (2000), however, the dissolution effect is limited in the carbon isotope enrichments of up to 5‰, suggesting that the main enrichment is due to biochemical fractionation related to secondary methanogenesis.

Figure 3 shows that ^{13}C-enriched CO_2 has no relation with CO_2 concentrations. Hypothetical end-members were assumed in the figure at 30% CO_2 with a carbon isotope ratio of 10‰ and 25% CO_2 with $\delta^{13}C_{CO2}$ of 30‰ for fermentation of hydrocarbon oxidation products, and 0% CO_2 with carbon isotope ratio of -20‰ and 0.5% CO_2 with $\delta^{13}C_{CO2}$ of 0‰ for thermogenic (Jeffrey et al., 1991). The observed data are distributed following the mixing trend between CO_2-rich gas produced by fermentation and CO_2-poor thermogenic gas. The two trend lines appear compatible with a mixing model and, therefore, with the presence of a residual CO_2 related to secondary methanogenesis and anaerobic biodegradation.

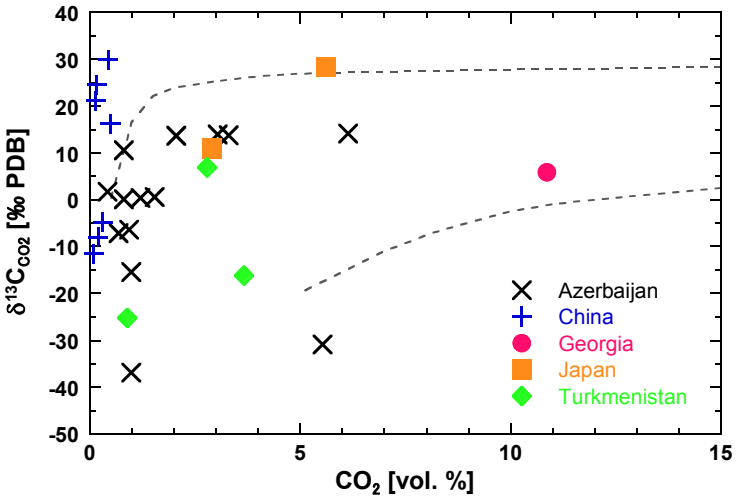

Figure 3. Relationship between $\delta^{13}C_{CO2}$ and CO_2 concentration. The 2 lines refer to a mixing trend similar to the model by Jeffrey et al. (1991).

3.3. CH_4 versus CO_2

The relationship between $\delta^{13}C$ of CH_4 and CO_2 is shown in Fig. 4. The ^{13}C-enriched CO_2 seems to occur preferentially in thermogenic CH_4, where $\delta^{13}C_1$ values are within a range of -50‰ to -30‰. In other words, this relationship seems to have a correlation; the gases showing a low $\delta^{13}C_1$ value have a low $\delta^{13}C_{CO2}$ value while a high $\delta^{13}C_1$ value corresponds to a high $\delta^{13}C_{CO2}$ value. This observation can imply that the light $\delta^{13}C_1$ in the few mud volcanoes (although data are not shown here, gases from Azerbaijan, Italy, Papua New Guinea, and Taman Peninsula fall in the microbial area in the Bernard diagram) with microbial gas is not due to secondary methanogenesis, but simply to primary methanogenesis. On the other

hand, thermogenic gas with ^{13}C-enriched CO_2 maintains its high $\delta^{13}C_1$ value, indicating that $\delta^{13}C_1$ value is not perturbed by the secondary microbial gas. The $\delta^{13}C_1$ value does not vary to a large degree by post-genetic alteration because the amount of secondary microbial CH_4 is small compared with that of the pre-existing thermogenic gas.

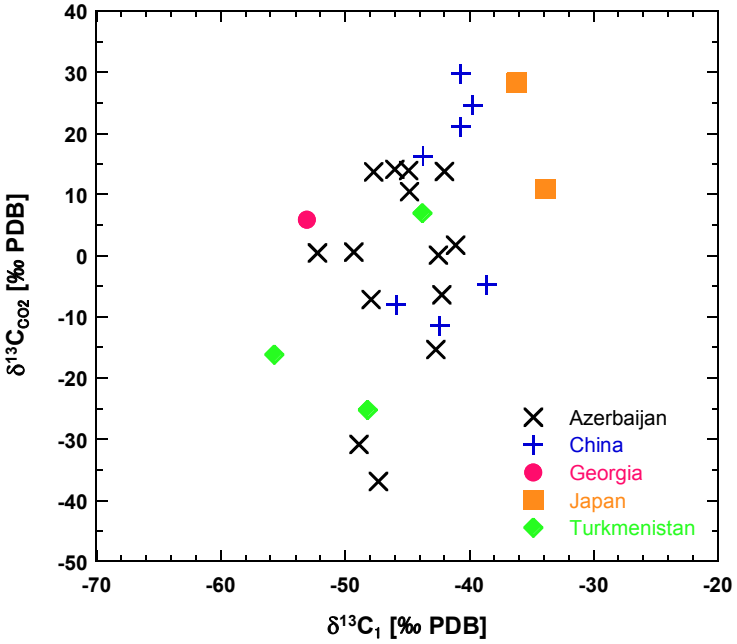

Figure 4. Relationship between carbon isotopes of CH_4 and CO_2.

However, the post-genetic alteration can lead to a significant change in their concentration and isotopic composition for CO_2. Oil biodegradation, one of the post-genetic alterations followed by CO_2 reduction, is described as follows:

$$CO_2 + 4H_2 \rightarrow CH_4 + 2H_2O. \quad (1)$$

This reaction is associated with a large kinetic isotope effect, meaning that the more the reaction proceeds with decreasing CO_2 concentration, the more ^{13}C is enriched in residual CO_2. Considering that CO_2 is a minor component of gases released from mud volcanoes, the concentration and isotopic composition of CO_2 can largely be affected by the reaction. The isotope effect of oil biodegradation results in the increase in $\delta^{13}C$ of residual CO_2, which can easily exceed +10‰ (Pallasser, 2000; Waseda and Iwano, 2008). Occurrence of oil biodegradation is suggested by the high C_2/C_3 and i-C_4/n-C_4 ratios (Pallasser, 2000; Waseda and Iwano, 2008) and/or by the presence of H_2 gas. For example, all these characteristics are identified in the gases released from mud volcanoes in China, which show a large variation in $\delta^{13}C_{CO2}$ as described above (Nakada et al., 2011). The increase of C_2/C_3 ratio due to oil biodegradation also leads to an increase of Bernard ratio, meaning that a gas sample plotted

on the Bernard diagram will move in an upward direction. Thus, gases that fall in region A, which is geometrically above the thermogenic field in the Bernard diagram (Fig. 1), can be subject to the post-genetic alteration including biodegradation.

3.4. Depth of the reservoir and ^{13}C-enriched CO_2

The anaerobic biodegradation of oil and natural gas has been document to be mostly limited to shallow reservoirs, generally shallower than 2000 m with temperature below 60 ºC to 80 ºC (Pallasser, 2000; Feyzullayev and Movsumova, 2001). For example, the depth of petroleum reservoirs in the South Caspian Basin is shallower than 2000 m if the data are confined to the gas showing ^{13}C-enriched CO_2 (Fig. 5; after Etiope et al., 2009). This observation suggests that mud volcanoes showing anaerobic biodegradation signals will be linked with shallow reservoirs, while mud volcanoes without anaerobic biodegradation will more likely be produced by deeper reservoirs. Anaerobic biodegradation of petroleum and subsequent secondary methanogenesis, however, can also take place at shallower depths even above the deep reservoir along the seepage channels of the mud volcano system.

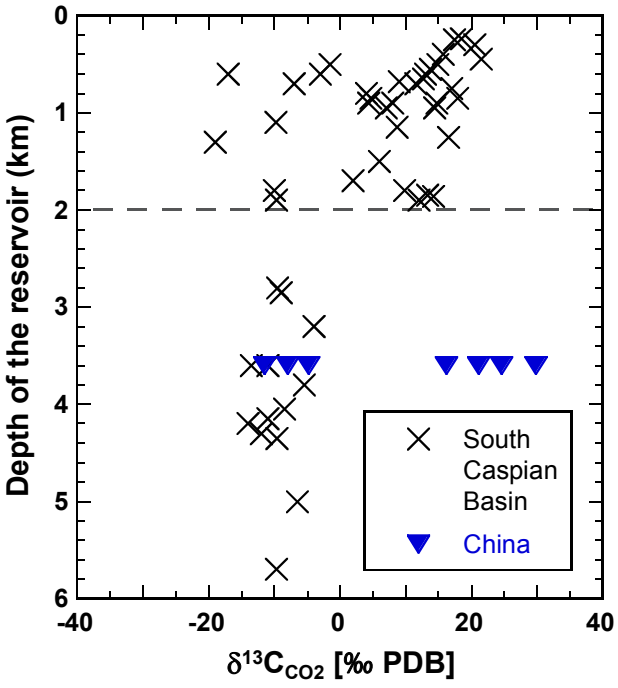

Figure 5. Carbon isotopic ratios of CO_2 vs. reservoir depth in the South Caspian Basin and China.

Recently, Nakada et al. (2011) showed that the reservoir depth of mud volcanoes in Xinjiang Province, China, is deeper than 3600 m, though some of the volcanoes release ^{13}C-enriched CO_2. The province hosts a large abundance of petroleum; therefore, many oil-testing wells are made in the province, leading to the knowledge of geothermal gradient and depth of oil reservoir. Nakada et al. (2011) calculated the equilibrium temperature of oxygen isotope fractionation between water and calcite in mud, indicating that the temperature where the water–rock interaction is occurring is 81 ºC for mud volcanoes located close to the Dushanzi oil field. Assuming the mean geothermal gradient of the area is 18 ±1 ºC/km (Nansheng et al., 2008) and that the surface temperature is 15 ºC, the depth of the chamber with the temperature of 81 ºC is calculated to be 3670 ±200 m. The calculated depth is slightly deeper than the oil reservoir at the Dushanzi field (3644 m–3656 m; Clayton et al., 1997). However, considering that the reservoir of saline fossil waters related to petroleum is generally deeper than that of oil and gas due to the difference in density, the calculation by Nakada et al. (2011) was surprisingly well consistent with the observation by Calyton et al. (1997). Then, Nakada et al. (2011) estimated the depth of gas reservoir at about 3600 m by considering that (i) the gases released from the mud volcanoes in the area were thermogenic gas associated with oil and (ii) the gas reservoir is generally located above the petroleum reservoir. The depth of 3600 m is greater than those previously reported for mud volcanoes releasing ^{13}C-enriched CO_2, such as those in South Caspian Basin. Thus, the secondary microbial effect that can occur at a relatively shallower depth must be considered separately from the initial thermogenic source in the field in China. Therefore, Nakada et al. (2011) clearly showed that the anaerobic biodegradation of petroleum can take place at a shallower depth. This result strengthens the model that considers a deep reservoir with thermogenic gas and secondary microbial activity occurring along the seepage system above the main deep reservoir.

4. Summary

Terrestrial mud volcanoes release a dominant abundance of thermogenic CH_4 related to the activities in relatively deep reservoirs, most of which are in petroleum seepage systems. Maturated petroleum associated with gas and water pressurizes the reservoir, causing gas and water to ascend preferentially through faults (Nakada et al., 2011). Some post-genetic secondary processes can alter the chemical and isotopic composition of the gases. Among these processes, some mixing, molecular fractionation, and particularly, secondary methanogenesis related to subsurface biodegradation of petroleum seem to be significant in changing the chemical and isotopic composition of gases released from mud volcanoes. Mud volcanoes show highly variable $\delta^{13}C_{CO2}$ values even within the same mud volcanoes, such that ^{13}C-enriched CO_2 can be found in some vents and not in others nearby, or not systematically changed in the same vent, meaning that ^{13}C-enriched CO_2 is, therefore, not an uncommon characteristic. The association of anaerobic biodegradation can depend on the type of microbial communities and physicochemical conditions of the reservoir.

Author details

Ryoichi Nakada* and Yoshio Takahashi
Department of Earth and Planetary Systems Science, Graduate School of Science, Hiroshima University, Higashi-Hiroshima, Hiroshima, Japan

Acknowledgement

R. N. is a Research Fellow of the Japan Society of the Promotion of Science. We thank Prof. Guodong Zheng (Chinese Academy of Sciences) for his suggestions throughout this study.

5. References

Baylis, S.A., Cawley, S.J., Clayton, C.J., Savell, M.A. (1997) The origin of unusual gas seeps from onshore Papua New Guinea. *Mar. Geol.*, 137, 109–120.

Bernard, B.B., Brooks, J.M., Sackett, W.M. (1978) Light hydrocarbons in recent Texas continental shelf and slope sediments. *J. Geophys. Res.*, 83, 4053–4061.

Capozzi, R., Picotti, V. (2002) Fluid migration and origin of a mud volcano in the Northern Apennines (Italy): the role of deeply rooted normal faults. *Terranova*, 14, 363–370.

Clayton, J. L., Yang, J., King, J. D., Lillis, P. G., and Warden, A. (1997) Geochemistry of oils from the Junggar Basin, Northwest China. *AAPG Bull.*, 81, 1926–1944.

Deville, E., Battani, A., Griboulard, R., Guerlais, S.H., Herbin, J.P., Houzay, J.P., Muller, C., Prinzhofer, A. (2003) Mud volcanism origin and processes. New insights from Trinidad and the Barbados Prism. In: Van Rensbergen, P., Hillis, R.R., Maltman, A.J., Morley, C. (Eds.), Surface Sediment Mobilization. Special Publication of the Geological Society (London), vol. 216, pp. 475–490.

Dimitrov, L. I. (2002) Mud volcanoes-the most important pathway for degassing deeply buried sediments. *Earth-Sci. Rev.*, 59, 49–76.

Dimitrov, L. I. (2003) Mud volcanoes-a significant source of atmospheric methane. *Geo-Mar. Lett.*, 23, 155–161.

Etiope, G. and Klusman, R. W. (2002) Geologic emissions of methane to the atmosphere. *Chemosphere*, 49, 777–789.

Etiope, G. and Milkov, A. V. (2004) A new estimate of global methane flux from onshore and shallow submarine mud volcanoes to the atmosphere. *Environ. Geol.*, 46, 997–1002.

Etiope, G., Papatheodorou, G., Christodoulou, D., Ferentinos, G., Sokos, E., Favali, P. (2006) Methane and hydrogen sulfide seepage in the NW Peloponnesus petroliferous basin (Greece): origin and geohazard. *AAPG Bull.*, 90, 701–713.

Etiope, G., Martinelli, G., Caracausi, A., Italiano. F. (2007) Methane seeps and mud volcanoes in Italy: gas origin, fractionation and emission to the atmosphere. *Geophys. Res. Lett.*, 34, L14303.

* Corresponding Author

Etiope, G., Feyzullayev, A., Milkov, A. V., Waseda, A., Mizobe, K. and Sun, C. H. (2009) Evidence of subsurface anaerobic biodegradation of hydrocarbons and potential secondary methanogenesis in terrestrial mud volcanoes. *Mar. Pet. Geol.*, 26, 1692–1703.

Etiope, G., Nakada, R., Tanaka, K., and Yoshida, N. (2011) Gas seepage from Tokamachi mud volcanoes, onshore Niigata Basin (Japan): Origin, post-genetic alterations and CH_4–CO_2 fluxes. *Appl. Geochem.*, 26, 348–359.

Faber, E., Stahl, W. (1984) Geochemical surface exploration for hydrocarbons in the North Sea. *AAPG Bull.*, 68, 363–386.

Favara, R., Gioia, C., Grassa, F., Inguaggiato, S., Proietto, F., Valenza, M. (2001) Studio geochimico delle manifestazioni fluide della riserva naturale integrale "Macalube di Aragona". *Nat. Sicil.*, 25, 137–154 (in Italian).

Feyzullayev, A. and Movsumova, U. (2001) About the origin of isotopically heavy CO_2 in gases of Azerbaijan mud volcanoes. *Azerb. Geol.*, 6, 96–105 (in Russian).

Greber, E., Leu, W., Bernoulli, D., Schumacher, M.E., Wyss, R. (1997) Hydrocarbon provinces in the Swiss southern Alps—a gas geochemistry and basin modeling study. *Mar. Pet. Geol.*, 14, 3–25.

Hosgormez, H., Etiope, G., and Yalçin, M. N. (2008) New evidence for a mixed inorganic and organic origin of the Olympic Chimaera fire (Turkey): a large onshore seepage of abiogenic gas. *Geofluids*, 8, 263–273.

Intergovernmental Panel on Climate Change (2001) Houghton, J.T., Ding, Y., Griss, D.J., Noguer, M., van der Linden, P.J., Dai, X., Maskell, K., Johnson, C.A. (Eds), Climate Change 2001: The scientific basis. Cambridge Univ PressCambridge, UK, pp. 881

Jeffrey, A.W.A., Alimi, H.M., Jenden, P.D. (1991) Geochemistry of the Los Angeles Basin oil and gas systems. In: Biddle, K.T. (Ed.), Active Margin Basins. AAPG Memoir, vol. 52, pp. 197–219.

Jenden, P. D., Hilton, D. R., Kaplan, I. R., Craig, H. (1993) Abiogenic hydrocarbons and mantle helium in oil and gas fields. In: Howell, D. (Ed.), The Future of Energy Gases, vol. 1570. USGS, pp. 31–35.

Kato, S., Waseda, A., Nishita, H., Iwano, H. (2009) Geochemistry of crude oils and gases from mud volcanoes and their vicinities in the Higashi-Kubiki area, Niigata Prefecture. *Journal of Geography*, 118, 455–471 (In Japanese with English abstract).

Kholodov, V. N. (2002) Mud volcanoes, their distribution regularities and genesis: communication 1. mud volcanic provinces and morphology of mud volcanoes. *Lithol. Miner. Resour.*, 37, 197–209.

Kopf, A. J. (2002) Significance of mud volcanism. *Rev. Geophys.*, 40, 1–52.

Kotarba, M. J. (2001) Composition and origin of coalbed gases in the Upper Silesian and Lublin basins, Poland. *Org. Geochem.*, 32, 163–180.

Lavrushin, V. Y., Polyak, B. G., Prasolov, R. M. and Kamenskii, I. L. (1996) Sources of material in mud volcano products (based on isotopic, hydrochemical, and geological data). *Lithol. Miner. Resour.*, 31, 557–578.

Mazzini, A., Svensen, H., Akhmanov, G. G., Aloisi, G., Planke, S., Malthe-Sørenssen, A., and Istadi, B. (2007) Triggering and dynamic evolution of the LUSI mud volcano, Indonesia. *Earth Planet. Sci. Lett.*, 261, 375–388.

Mizobe, K. (2007) Geochemical characteristics of natural gases from mud volcanoes in Tokamachi City, Niigata Prefecture. Master Thesis, Graduate School of Science and Engineering, Yamaguchi University, pp. 44.

Nakada, R., Takahashi, Y., Tsunogai, U., Zheng, G., Shimizu, H., and Hattori, K. H. (2011) A geochemical study on mud volcanoes in the Junggar Basin, China. *Appl. Geochem.*, 26, 1065–1076.

Nansheng, Q., Zhihuan, Z. and Ershe, X. (2008) Geothermal regime and Jurassic source rock maturity of the Junggar Basin, northwest China. *J. Asian Earth Sci.*, 31, 464–478.

Pallasser, R. J. (2000) Recognising biodegradation in gas/oil accumulations through the $\delta^{13}C$ compositions of gas components. *Org. Geochem.*, 31, 1363–1373.

Schoell, M. (1983) Genetic characterization of natural gases. *AAPG Bull.*, 67, 2225–2238.

Valyaev, B.M., Grinchenko, Y.I., Erokhin, V.E., Prokhorov, V.S., Titkov, G.A. (1985) Isotopic composition of gases from mud volcanoes. *Lithol. Miner. Resour.*, 20, 62–75.

Waseda, A., Iwano, H. (2008). Characterization of natural gases in Japan based on molecular and carbon isotope compositions. *Geofluids*, 8, 286–292.

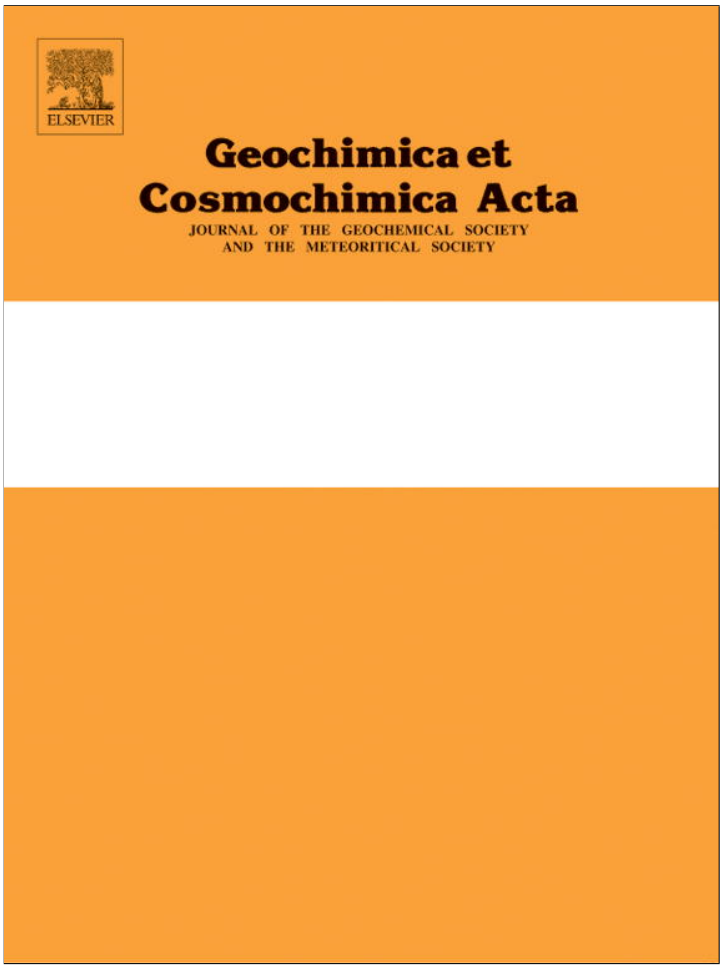

(This is a sample cover image for this issue. The actual cover is not yet available at this time.)

Available online at www.sciencedirect.com

SciVerse ScienceDirect

Geochimica et Cosmochimica Acta 103 (2013) 49–62

Geochimica et Cosmochimica Acta

www.elsevier.com/locate/gca

Isotopic and speciation study on cerium during its solid–water distribution with implication for Ce stable isotope as a paleo-redox proxy

Ryoichi Nakada [a,*], Yoshio Takahashi [a,b,c], Masaharu Tanimizu [a,b]

[a] *Department of Earth and Planetary Systems Science, Graduate School of Science, Hiroshima University, Higashi-Hiroshima, Hiroshima 739-8526, Japan*

[b] *Kochi Institute for Core Sample Research, Japan Agency for Marine-Earth Science and Technology (JAMSTEC), Monobe 200, Nankoku, Kochi 783-8502, Japan*

[c] *Key Laboratory of Petroleum Resources, Institute of Geology and Geophysics, Chinese Academy of Sciences, 382 Donggang Road, Lanzhou 730000, China*

Received 15 May 2012; accepted in revised form 26 October 2012; Available online 5 November 2012

Abstract

Cerium (Ce) has anomalously high or low concentrations relative to its neighboring elements, lanthanum (La) and praseodymium (Pr), because of its chemical properties; this phenomenon is known as the Ce anomaly. This redox-sensitive property of Ce allows the estimation of the redox state of paleo-ocean environments and the evolution of the atmosphere. However, a consideration of only the relative abundance of Ce may lead to an incomplete understanding of its oxidation process. In the current study, three important geochemical parameters, namely, abundance, stable isotope ratio, and chemical speciation, were obtained for Ce to derive more information from the Ce anomaly. In our adsorption experiments, the distribution pattern of rare earth elements (REEs) suggests the oxidative scavenging of Ce by δ-MnO_2. This finding is further supported by the presence of Ce(IV), as detected by the X-ray absorption near-edge structure (XANES) spectra, which is in agreement with previous studies. However, the REE distribution pattern combined with the XANES spectra of the Ce adsorbed on ferrihydrite indicated that Ce may not have been oxidized by ferrihydrite in the Ce/ferrihydrite system during our experimental period. Assuming equilibrium fractionation, the mean isotopic fractionation factors between the liquid and solid phases (α_{Lq-So}) of (i) Ce adsorbed on ferrihydrite, (ii) spontaneous precipitation of Ce, and (iii) Ce adsorbed on δ-MnO_2 were 1.000145 (±0.000022), 1.000196 (±0.000031), and 1.000411 (±0.000079), respectively. These results indicate that the degree of isotopic fractionation of Ce between the liquid and solid phases becomes larger as the redox condition becomes more oxic in the following order: adsorption without oxidation < spontaneous precipitation < oxidative adsorption. Previously, the appearance of the Ce anomaly and/or XANES analysis constituted the only tool available for exploring the redox state. This study, however, suggests that the stable isotope ratio of Ce can be used to clearly distinguish spontaneous precipitation from oxidative adsorption on δ-MnO_2, that occur under more oxic conditions than the Ce(III)/Ce(IV) boundary. Although similar experiments need to be done in a system more similar to natural systems, our results suggest that the combination of the stable isotope ratio and chemical state of Ce can be used to classify the redox condition into three stages based on Ce geochemistry, thereby offering a powerful tool for exploring redox conditions in paleo-ocean environments.

* Corresponding author. Tel.: +81 82 424 7460; fax: +81 82 424 0735.
E-mail address: ryo-nakada@hiroshima-u.ac.jp (R. Nakada).

0016-7037/$ - see front matter © 2012 Elsevier Ltd. All rights reserved.
http://dx.doi.org/10.1016/j.gca.2012.10.045

1. INTRODUCTION

Cerium (Ce), one of the rare earth elements (REEs), has the unique characteristic of being able to form tetravalent cations under oxic conditions, whereas the other REEs are stable in a trivalent state. Although Ce(IV) carbonate species are soluble (Möller and Bau, 1993), Ce is relatively insoluble in seawater compared with other REEs following the oxidation from Ce(III) to Ce(IV), due to the low solubility of Ce(IV). Two formation processes for the oxidation of Ce(IV) are possible. The first is oxidation after adsorption onto a solid phase, namely, oxidative adsorption, which may occur on manganese oxide (e.g., Taylor and McLennan, 1988; Takahashi et al., 2000, 2007). The other process is oxidation in the liquid phase followed by precipitation as $Ce(OH)_4$ or CeO_2 (De Baar et al., 1988; German and Elderfield, 1989; Braun et al., 1990). Given these chemical properties, an anomalously high or low concentration of Ce relative to its neighboring elements, lanthanum (La) and praseodymium (Pr), known as a positive or negative Ce anomaly, respectively, is often observed in REE abundance patterns following the generation of Ce(IV) (Henderson, 1984). This redox-sensitive property allows the estimation of the redox state of a paleo-ocean environment (e.g., Shimizu and Masuda, 1977; Wang et al., 1986; Wright et al., 1987; Murray et al., 1991) and the study of the redox evolution of the atmosphere (e.g., Fryer, 1977; Murakami et al., 2001; Kato et al., 2006).

In seawater, REEs are adsorbed on various types of suspended matter and solid phases. In particular, marine ferromanganese deposits show large positive Ce anomalies in their REE patterns (e.g., Piper, 1974; Elderfield et al., 1981; Bau et al., 1996). Large negative Ce anomalies in REE patterns are observed in seawater as a counterpart to these positive anomalies (e.g., Elderfield and Greaves, 1982; Piepgras and Jacobsen, 1992; Möller et al., 1994). The positive Ce anomalies in marine ferromanganese oxides are possibly caused by the oxidative adsorption of Ce (Takahashi et al., 2000, 2007). Takahashi et al. (2007) showed that the chemical state of Ce in marine ferromanganese deposits is tetravalent, regardless of the formation environment, namely, hydrogenetic, diagenetic, and hydrothermal. In addition, adsorption experiments have suggested the oxidation of Ce by δ-MnO_2 (Takahashi et al., 2000; Ohta and Kawabe, 2001). The Eh–pH diagram indicates that the Mn^{2+}/MnO_2 boundary is located at a higher Eh level than that of Ce^{3+}/CeO_2 (Brookins, 1988; Fig. 1A). These facts support the suggestion that Mn oxides can act as an oxidant for Ce(III), indicating that the oxidative adsorption of Ce on Mn oxides can generate a positive Ce anomaly. Meanwhile, the $Fe^{2+}/Fe(OH)_3$ boundary is located at an Eh level lower than the Ce^{3+}/CeO_2 boundary (Brookins, 1988; Fig. 1A), indicating that $Fe(OH)_3$ may be less powerful in oxidizing Ce into CeO_2, as suggested by previous studies (De Carlo and McMurtry, 1992; Kawabe et al., 1999; Takahashi et al., 2007). However, Kato et al. (2006) summarized the REE pattern of Precambrian banded iron formations (BIFs) and showed that both positive and negative Ce anomalies were observed regardless of their formation age. Surprisingly, although some Precambrian BIFs may have undergone recent weathering or post-depositional alteration (e.g., Bau, 1993), some Archean BIFs show positive Ce anomalies. If Mn oxides are necessary to generate positive Ce anomalies, it is questionable whether Mn oxides existed in ancient periods when the atmospheric oxygen level was estimated to be less than 10^{-5} atm (e.g., Pavlov and Kasting, 2002; Catling and Claire, 2005).

Recently, Bau and Koschinsky (2009) suggested the oxidative scavenging of Ce by Fe hydroxides, following leach-

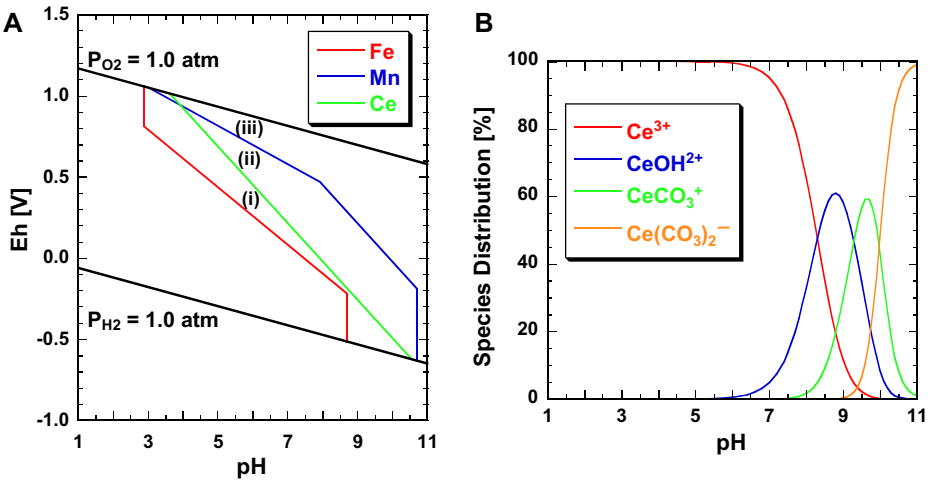

Fig. 1. (A) Eh–pH diagram for Fe, Mn, and Ce in the system metal–H–O at 25 °C. The red line represents the soluble–insoluble boundary for Fe (soluble species: Fe^{2+} and Fe^{3+}; insoluble species: $Fe(OH)_3$ and $Fe(OH)_2$). The green line represents the boundary between Ce^{3+} (soluble) and CeO_2 (insoluble). The blue line represents the soluble–insoluble boundary for Mn (soluble species: Mn^{2+}; insoluble species: MnO_2, MnO, Mn_3O_4, and $Mn(OH)_2$). In this calculation, the concentrations of both Fe and Mn are 10^{-6} M, and that of Ce is 10^{-10} M. (B) Calculated species distribution of Ce under the experimental conditions. The data for REE–carbonate complexation constants were obtained from Luo and Byrne (2004), and the equilibrium constants of the carbonate species were obtained from Nordstrom et al. (1990). (For interpretation of the references to color in this figure legend, the reader is referred to the web version of this article.)

ing experiments with a hydrogenetic ferromanganese crust. Furthermore, Bau (1999) performed scavenging experiments and demonstrated oxidative scavenging of Ce by Fe hydroxide, especially at lower pH ($pH \leqslant 4.6$). Their result suggested that discussions relying only on the Eh–pH diagram would be risky if applied to the natural environment. All these findings imply that the geochemical processes responsible for the occurrence of Ce anomalies are not fully understood, and that any discussion based only upon the intensity of the Ce anomaly will have limitations. Therefore, alternative and quantitative evidence is needed to fully determine the cause of Ce anomalies.

In this study, we examine the Ce stable isotope ratio as an alternative geochemical tool that may have better resolution in discerning redox conditions. This study aims to provide information on the relationship between redox conditions and the mass-dependent isotope fractionation of the Ce stable isotope ratio. More information on redox conditions in the paleo environment may be obtained if fractionations of the Ce stable isotope respond differently to different geochemical processes as follows: (i) adsorption of Ce^{3+} without oxidation; (ii) precipitation as CeO_2 or $Ce(OH)_4$; and (iii) oxidative scavenging on Mn oxide (corresponding to fields (i), (ii), and (iii), respectively, in Fig. 1A). To date, several geochemical (isotopic) tracers have been introduced to clarify paleo-redox conditions, such as $\Delta^{33}S$, $\delta^{56}Fe$, $\delta^{53}Cr$, and Mo isotopes (e.g., Farquhar et al., 2000; Anbar et al., 2007; Johnson et al., 2008; Frei et al., 2009). However, most of these indicators are sensitive only under low atmospheric oxygen conditions, indicating that geochemical tracers that are useful after the great oxidation event (c.a. 2.2 Ga) are lacking. Therefore, the stable isotopic fractionation of Ce may be used as an alternative tool sensitive to suboxic conditions. Speciation analysis of Ce in the solid phase has also been examined by X-ray absorption near-edge structure (XANES) and extended X-ray absorption fine structure (EXAFS) analyses to support the determination of redox conditions, thereby providing data on the oxidation state of Ce in the solid phase and quantitative information about the distance to neighboring atoms and the coordination number (CN), respectively. This study includes three parameters for Ce that are important in inorganic geochemistry: abundance (degree of the Ce anomaly); the Ce stable isotope ratio; and the chemical speciation of Ce. This study was confined to a lower pH region ($pH = 5$) where the aqua complex is stable, to focus on the Ce isotopic fractionation from an aqua complex of Ce^{3+} as the first step (Fig. 1B).

2. EXPERIMENTAL

2.1. REE adsorption experiment

Synthetic ferrihydrite was prepared by dissolving 40 g $Fe(NO_3)_3$ in 500 mL ultrapure water. KOH solution was then added to the $Fe(NO_3)_3$ solution and pH was adjusted to between 7 and 8 (Schwertmann and Cornell, 2000). δ-MnO_2 was prepared by mixing equal volumes of a 30 mM $MnCl_2$ solution with a 20 mM $KMnO_4$ solution at pH 10 (Foster et al., 2003). Both precipitates were washed several times in ultrapure water, and then freeze-dried. The precipitates were freeze-dried to allow use of the same materials for various experiments in this study (adsorption experiments, isotopic study, and XAFS measurements), and to avoid the change of their crystal structure before and/or during the measurement of EXAFS spectra. Identification of both minerals was conducted with an X-ray diffractometer (Multi Flex, Rigaku Co. Ltd.) and Fe and Mn K-edge EXAFS at BL-12C at the Photon Factory (Tsukuba, Japan).

A standard REE solution (Spex Certiprep., USA) containing all REEs, except promethium (Pm), at a concentration of 10.0 mg/L each was placed in plastic bottles with 100 mg ferrihydrite or 30 mg δ-MnO_2 for the solid phase. In the REE/ferrihydrite system, 1 mL REE solution and 10 mL ultrapure water served as a liquid phase, whereas 6 mL REE solution with 1 mL ultrapure water was mixed in the REE/δ-MnO_2 system. Diluted NaOH and HCl solutions were used to adjust the pH to 5.00 ± 0.05, where REE is dissolved as hydrated free ion in water without the formation of a REE carbonate and/or a hydroxide complex. Ionic strength was not considered in this study because our primary aim was to understand Ce isotopic fractionation under the simplest conditions. Notably, in our experiment, the Ce^{3+} aqua complex dominated the Ce species in the liquid phase (Fig. 1B). The suspension was stirred for 6 h at 25 °C using a shaking apparatus, based on findings that the apparent distribution coefficients of La, Ce, gadolinium (Gd), and lutetium (Lu) are almost constant from 3 to 130 h (Ohta and Kawabe, 2001). This finding indicated that 6 h is a sufficient time to reach equilibrium. At the end of the experimental period, the liquid phase was separated from the solid phase by filtration using a hydrophilic PTFE filter (0.2 μm; ADVANTEC).

The filtrate was acidified with HNO_3 to obtain a final concentration of 2 wt% for the determination of the REE concentration using an inductively coupled plasma mass spectrometer (ICP-MS; Agilent 7700). Indium (In) and bismuth (Bi) were also added at a concentration of 1 μg/L as internal standards. The precision of the ICP-MS measurement was better than 1% for all the REEs, except for erbium (Er) (1.7%), as calculated from repeated measurements. The distribution coefficient (K_d) of a REE between the liquid and solid phases is defined as

$$K_d\ (\mathrm{L/g}) = \frac{[\mathrm{REE}]_{init} - [\mathrm{REE}]_{fil}}{c \times [\mathrm{REE}]_{fil}} \quad (1)$$

where $[REE]_{fil}$ is the REE concentration in the filtrate and $[REE]_{init}$ is the initial concentration of dissolved REE. c (g/L) denotes the ratio of the solid phase (ferrihydrite or δ-MnO_2, dry weight) to water, which was 0.0097 and 0.0040 g/L for adsorption on ferrihydrite and δ-MnO_2, respectively. The adoption of different solid–water ratios between ferrihydrite and δ-MnO_2 systems was necessary to obtain appropriate K_d values for the determination of isotopic fractionation factors. δ-MnO_2 exhibited much higher affinity for REE than ferrihydrite, so that, the REE concentrations remaining in the solution were lower than the detection limit of our measurement in the δ-MnO_2 system.

2.2. Adsorption and precipitation of Ce

A Ce(III)Cl_3 reagent (Wako, Japan) dissolved in ultrapure water was used to adsorb Ce on both ferrihydrite and δ-MnO_2. Various amounts of $CeCl_3$ solution were placed in plastic bottles with 100 mg ferrihydrite or 30 mg δ-MnO_2 for the solid phase. In this experiment, the amounts of the solid phase were fixed, whereas the Ce concentration was systematically changed to prepare samples with different adsorbed or precipitated fractions (the ratio of the adsorbed or precipitated Ce to the total Ce added into the system). The adsorbed fraction was 1 if all the Ce added into the system were adsorbed on the solid phase. For the REE adsorption experiment, the pH was adjusted to 5.00 ± 0.05 and the suspension was stirred for 6 h at 25 °C. At the end of the experimental period, the liquid phase was separated from the solid phase, as described in Section 2.1.

The liquid samples were acidified with 2 wt% HNO_3 to prevent Ce precipitation. Ferrihydrite was dissolved with 6 M HCl, and δ-MnO_2 was dissolved with 6 M HCl and H_2O_2. Both minerals were then finally dissolved in 0.5 M HCl solution, followed by the separation of Ce from Fe or Mn by cation exchange column chemistry. For the elution of Fe, 2.0 M HCl solution was passed through a column (length: 10 cm, diameter: 1.0 cm) loaded with cation exchange resin (Bio-Rad, AG50W-X8), whereas 2.0 M HNO_3 solution was used to elute Mn. Almost 100% (better than 99%) Ce was recovered by the elution using 6.0 M HCl solution, indicating that no isotopic fractionation occurred during the column chemistry. The Ce concentrations in both solid and liquid samples were determined using an ICP-MS (Agilent 7700). Procedural blanks in the experiments for Ce were checked using ultrapure water, which was below the detection limit (0.5 ng/kg).

Adsorption experiments under various elapsed times were also performed to examine whether isotopic equilibrium was attained. In this experiment, the adsorbed fraction was adjusted between 0.25 and 0.35 for the ferrihydrite system, and adjusted to 0.90–0.99 for the δ-MnO_2 system. In both systems, ionic strength was adjusted to 0.10 and 0.70 M by NaCl solution and pH was adjusted to 5.00 ± 0.05. The suspension was stirred for 24, 120, 168, and 240 h. The procedure after the experiment was similar to those previously described. In this experiment, Ce in the liquid phase was separated from Na using the cation exchange column before the measurement. After the elution of Na using 1.5 M HCl, more than 99% Ce was recovered by 6.0 M HCl.

Spontaneous precipitation of Ce(IV) from the $CeCl_3$ solution was induced at pH 5.00 ± 0.05 in an O_2 gas bubbling environment. The solutions were left for 1 week to obtain Ce(IV) precipitates. The precipitate obtained was recovered using a 0.2 μm hydrophilic PTFE filter (ADVANTEC). Various Ce concentrations in the initial solution (from 0.5% to 2%) were tested to prepare the Ce precipitates. The oxidation state of Ce in the precipitates was determined by Ce L_{III}-edge XANES (Section 2.4).

2.3. Isotopic analysis

Isotope ratios of Ce were determined at the Kochi Institute for Core Sample Research, Japan Agency for Marine-Earth Science and Technology (JAMSTEC) using a double-focusing multiple collector (MC) ICP-MS (Neptune, Thermo Fisher). The details of this instrument were previously described (Weyer and Schwieters, 2003; Wieser and Schwieters, 2005).

Ce has four stable isotope masses, namely, 136, 138, 140, and 142, with isotopic abundances of 0.19%, 0.25%, 88.45%, and 11.11%, respectively. Among these isotope masses, ^{140}Ce and ^{142}Ce abundances were determined using an MC-ICP-MS. ^{136}Ce and ^{138}Ce were not measured because their relative isotopic abundances are two orders of magnitude lower than those of ^{140}Ce and ^{142}Ce. The analyzed Ce solutions were diluted to concentrations of about 200 μg/L. During the measurements, the neodymium (Nd) on mass 146 was also monitored to estimate the influence of ^{142}Nd, which can interfere with ^{142}Ce. The signal of ^{146}Nd was negligible (<0.01% of the ^{142}Ce signal) for all samples and standard solutions, indicating that the isobaric interference by ^{142}Nd was negligible in this study. Furthermore, the ion signal of Ce as $^{140}Ce^{16}O$ was checked before the isotopic analysis. The CeO/Ce ratio was adjusted in the range of 5–8% (average: 6%) by decreasing the carrier gas flow rate.

The measured isotope ratio of $^{142}Ce/^{140}Ce$ was corrected using the samarium (Sm) doping technique in wet plasma mode. Among the Sm stable isotopes (144, 147, 148, 149, 150, 152, and 154), the relative abundances of ^{147}Sm and ^{149}Sm are similar at 14.99% and 13.82%, and do not interfere with Ce isotopes. Therefore, these two Sm isotopes were measured by adding a Sm standard solution (Wako, Japan) diluted to about 200 μg/L to the Ce solutions just before the Ce isotope analysis. No Sm signals were observed for all the samples before the doping with the Sm solution.

In the Sm doping technique, the observed $^{142}Ce/^{140}Ce$ isotope ratios were corrected based on an exponential law using the $^{147}Sm/^{149}Sm$ ratio of a reference Sm solution. The relationship between the observed and normalized isotope ratios of Ce and Sm is described by the following equations:

$$(^{142}Ce/^{140}Ce)_{norm} = (^{142}Ce/^{140}Ce)_{obs} \times (^{142}A/^{140}A)^{f_{Ce}} \quad (2)$$

$$(^{147}Sm/^{149}Sm)_{norm} = (^{147}Sm/^{149}Sm)_{obs} \times (^{147}A/^{149}A)^{f_{Sm}} \quad (3)$$

$$f_{Ce} = f_{Sm} \quad (4)$$

where f and A are the mass discrimination correction factor and the atomic masses of the Ce and Sm isotopes, respectively.

The isotopes measured using MC-ICP-MS were ^{140}Ce, ^{142}Ce, ^{146}Nd, ^{147}Sm, and ^{149}Sm. The $CeCl_3$ solution used in the adsorption experiment was employed as a standard solution that was analyzed every three or four samples. The isotope ratios are expressed in standard delta notation relative to the average standards, as shown in the following equation:

$$\delta^{142}Ce = \left[\frac{(^{142}Ce/^{140}Ce)_{sample}}{(^{142}Ce/^{140}Ce)_{CeCl_3}} - 1\right] \times 10^3. \quad (5)$$

The analytical uncertainty for the measurement was 0.064‰ (2σ), which was calculated from repeated analysis of the standard $CeCl_3$ solution ($n = 26$).

2.4. XAFS analysis

The Ce adsorption experiment was conducted again for both δ-MnO_2 and ferrihydrite under the same conditions, and the solid phases were filtrated using a 0.2 μm mixed cellulose filter (ADVANTEC). Immediately after filtration, the solid samples were packed into individual polyethylene bags, and then frozen. The Ce L_{III}-edge (5.723 keV) XANES was measured at BL-12C at the Photon Factory (Tsukuba, Japan). The Ce L_{III}-edge XANES spectra, which are sensitive to the covalent/ionic bond character and the oxidation state, were measured for the adsorbed samples in fluorescence mode using a 19-element germanium (Ge) semiconductor detector. The spontaneous precipitation of Ce and the three reference materials diluted by boron nitride powder, namely, $CeCl_3$, CeO_2, and $Ce(SO_4)_2$ were measured in transmission mode. The measurements were conducted under ambient pressure and temperature. The X-ray energy was calibrated with the first peak of CeO_2 at 5.723 keV. The Ce K-edge (40.453 keV) EXAFS spectra of the adsorbed samples and the standard materials, namely, $CeCl_3$ and CeO_2, were measured at BL-01B1 at SPring-8 (Hyogo, Japan). The K-edge EXAFS spectra, which provide quantitative information about the distance to the neighboring atoms and the CN, were also measured in fluorescence mode using a 19-element Ge semiconductor detector. The energy was calibrated with the first peak of CeO_2 at 40.453 keV. The repeated scans of XANES and EXAFS yielded identical spectra to one another, indicating that X-ray-induced redox change of Ce did not occur in our experiments.

Both XANES and EXAFS spectra were analyzed using the REX2000 software (Rigaku Co. Ltd.). The parameters generated by the FEFF 7.0 code (Zabinsky et al., 1995) were used for the EXAFS analysis. After extracting the EXAFS oscillation and its Fourier transform, the inversely Fourier-filtered data were analyzed using a standard curve-fitting method. The theoretical phase shifts and amplitude functions for the Ce–O, Ce–Ce, Ce–Fe, and Ce–Mn pairs employed in this fitting procedure were extracted from FEFF 7.0 (Zabinsky et al., 1995). Finally, the EXAFS spectrum in the whole k- and R- space ranges employed in the procedure was compared with the measured EXAFS spectrum in k- and R- spaces to confirm the good fitting of the measured to the simulated spectrum. Multiple scattering was initially included in this study, but was found to be a very weak contribution to the EXAFS spectra. The error estimates of the interatomic distance and CN obtained by the fitting were ±0.02 Å and ±20%, respectively (O'Day et al., 1994). The quality of the fit was given by the goodness-of-fit parameter R, defined by

$$R = \frac{\sum[\chi_{obs}(E) - \chi_{cal}(E)]^2}{\sum[\chi_{obs}(E)]^2} \quad (6)$$

where $\chi_{obs}(E)$ and $\chi_{cal}(E)$ are the experimental and calculated absorption coefficients at a given energy (E), respectively.

3. RESULTS

3.1. REE distribution patterns

The REE distribution patterns for the adsorption of REEs on ferrihydrite and δ-MnO_2 are shown in Fig. 2A. Both distribution patterns exhibited a convex M-type tetrad effect and smaller $\log K_d$(Y) than the $\log K_d$(Ho) values. These findings are consistent with a previous report by Ohta and Kawabe (2001). In addition, both patterns showed "apparent" positive Ce anomalies ($Ce/Ce^* > 1$). In this study, Ce/Ce^* is defined as

$$Ce/Ce^* = \frac{Ce}{\sqrt{La \times Pr}} \quad (7)$$

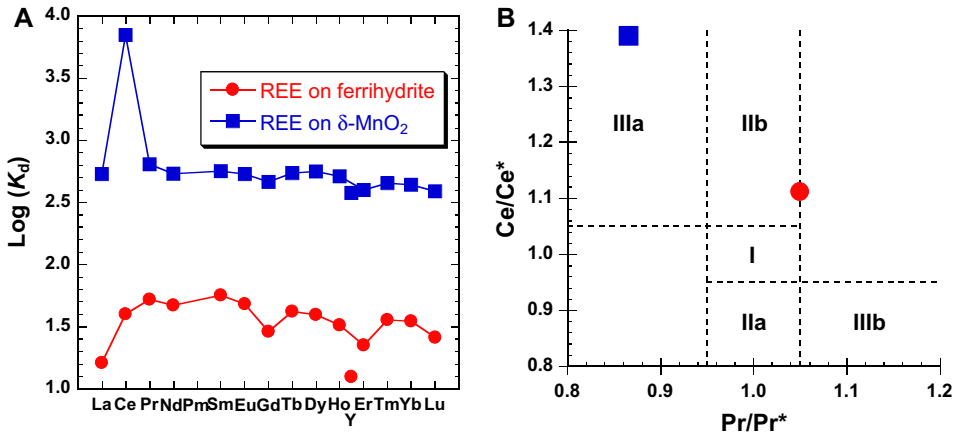

Fig. 2. (A) Distribution coefficient pattern of REEs between the liquid and solid phases. K_d is defined in the text (Eq. (1)). (B) Diagram to define "true Ce anomaly". Field I: neither Ce nor La anomaly; field IIa: positive La anomaly, no Ce anomaly; field IIb: negative La anomaly, no Ce anomaly; field IIIa: positive Ce anomaly; field IIIb: negative Ce anomaly. The legend is the same as that of 2A.

where the chemical symbol represents the $\log K_d$ value of the element. However, according to the "true" Ce anomaly defined by Bau and Dulski (1996), the distribution pattern of REEs adsorbed on δ-MnO_2 shows a positive Ce anomaly, whereas that of REEs on ferrihydrite shows a negative La anomaly (Fig. 2B). This result indicates that "apparent" positive Ce anomaly was caused by the presence of the M-type tetrad effect, and that Ce is not oxidized by Fe minerals, but is scavenged by Mn oxide through oxidation to Ce(IV) from the liquid phase. The formation of Ce(IV) was further supported by the XANES analysis, as will be discussed later.

3.2. Isotopic fractionation of Ce between the solid and liquid phases

First, the time dependence of the Ce isotopic data in the liquid phase was examined for the Ce/ferrihydrite and Ce/δ-MnO_2 systems (Fig. 3). Although the δ^{142}Ce values for the ferrihydrite system presented only a small fractionation, the values for the δ-MnO_2 system were fractionated to positive values, indicating that the lighter ^{140}Ce isotope was partitioned into the solid phase to a greater degree than the heavier ^{142}Ce. The variation of δ^{142}Ce values in the liquid phase was within the analytical uncertainty in this experimental period, both for the ferrihydrite and δ-MnO_2 systems, suggesting that isotopic equilibrium was attained within 6 h. The degree of isotopic fractionation did not vary with ionic strength.

The results of the isotopic fractionation of Ce during adsorption and spontaneous precipitation are presented in Table 1 and Fig. 4A (adsorption on ferrihydrite), B (spontaneous precipitation), and C (adsorption on δ-MnO_2), versus the fraction of total Ce adsorbed or precipitated. In Fig. 4, model lines for the equilibrium isotopic fractionation and the Rayleigh fractionation are shown as solid and dashed lines, respectively. As a constraint on the model

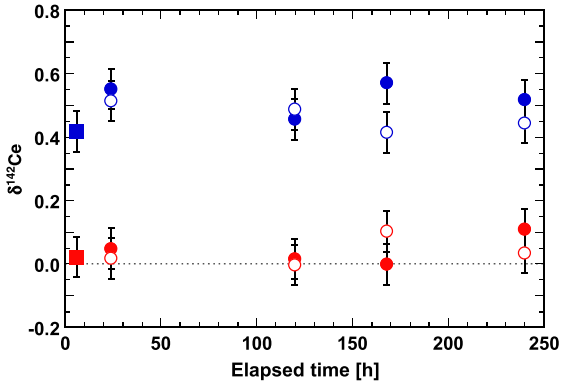

Fig. 3. Variation of δ^{142}Ce values in the liquid phase during the adsorption experiment at various elapsed times. Blue symbols: Ce/δ-MnO_2 system with adsorbed fraction of 0.90–0.99; red symbols: Ce/ferrihydrite system with adsorbed fraction of 0.25–0.35 (only a datum in 120 h, 0.70 M system was taken from the adsorbed fraction of 0.40); square symbols: data from Table 1; closed circles: ionic strength of 0.10 M; open circles: ionic strength of 0.70 M. (For interpretation of the references to color in this figure legend, the reader is referred to the web version of this article.)

Table 1
Isotope ratio and fractionation factor for Ce during adsorption and precipitation.

System	Fraction	δ^{142}Ce (Lq)	δ^{142}Ce (So)	α_{Lq-So}	Average
Ce/ferrihydrite	0.85	0.085	−0.073	1.000158	
	0.73	0.051	−0.089	1.000140	
	0.60	0.045	−0.089	1.000134	
	0.44	0.035	−0.106	1.000141	
	0.29	0.021	−0.139	1.000159	
	0.18	−0.001	−0.138	1.000137	1.000145 ±0.000022
Ce precipitation	0.12	0.045	−0.127	1.000173	
	0.09	0.033	−0.169	1.000202	
	0.06	0.020	−0.183	1.000203	
	0.03	0.000	−0.207	1.000207	1.000196 ±0.000031
Ce/δ-MnO_2	1.00	0.417	−0.004	1.000421	
	0.86	0.350	−0.065	1.000416	
	0.74	0.264	−0.163	1.000427	
	0.63	0.248	−0.219	1.000467	
	0.46	0.116	−0.238	1.000355	
	0.32	0.106	−0.272	1.000378	1.000411 ±0.000079

Note that deviations are expressed in 2σ values calculated from the respective α_{Lq-So} values.

lines, the δ^{142}Ce value for the solid phase should be 0‰ when the adsorbed or precipitated fraction is 1. By contrast, if all the Ce remains in the liquid phase, the δ^{142}Ce value for the liquid phase should not vary from that of the original $CeCl_3$ solution. The mean α_{Lq-So} value listed in Table 1 was used in calculating these model lines. In the table, the isotopic fractionation factor α between the liquid and solid phases was calculated as

$$\alpha_{Lq-So} = \frac{10^3 + \delta^{142}Ce_{Lq}}{10^3 + \delta^{142}Ce_{So}}. \quad (8)$$

In relation to the degree of isotopic fractionation between the liquid and solid phases in the three systems, the mean α_{Lq-So} value is largest when Ce is adsorbed on δ-MnO_2. For the spontaneous precipitation of Ce, although we could achieve only a low precipitation fraction, the mean α_{Lq-So} value was slightly higher than that of the Ce/ferrihydrite system.

3.3. XAFS spectra

The Ce L_{III}-edge (5.723 keV) XANES spectra of both Ce adsorbed on ferrihydrite and δ-MnO_2 measured at BL-12C at the Photon Factory (Tsukuba, Japan), along with results for certain reference materials, are shown in Fig. 5. The L_{III}-edge XANES spectrum of Ce precipitated from the same $CeCl_3$ solution is also shown. The shapes of the spectra revealed a clear distinction between trivalent and tetravalent Ce, that is, Ce(III) presents one sharp peak and Ce(IV) shows a two-humped peak. In addition, the indicated energy of the peak tops for Ce(III) and Ce(IV) differs. The results illustrate that Ce adsorbed on ferrihydrite was trivalent in our samples. By contrast, the two-

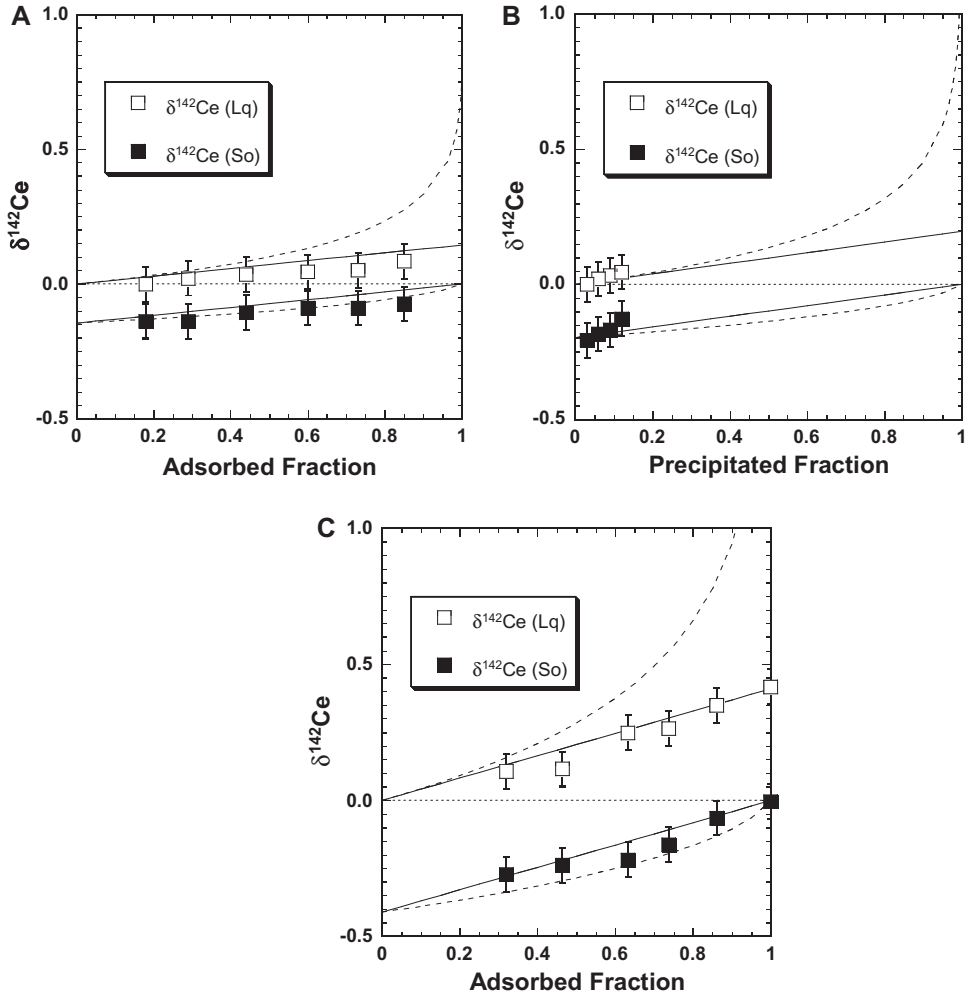

Fig. 4. Isotopic fractionation of Ce during (A) adsorption on ferrihydrite, (B) spontaneous precipitation, and (C) adsorption on δ-MnO_2, along with the adsorbed fraction in the system. Open squares represent the δ^{142}Ce values of the liquid phase, and closed squares represent the solid phase. The error bar indicates the analytical error calculated from repeated measurements of a standard solution. The solid lines correspond to a model of equilibrium fractionation and the dashed lines to a Rayleigh fractionation.

humped peak of the Ce L_{III}-XANES spectrum of Ce(III) adsorbed on δ-MnO_2 suggests that Ce was oxidized to the tetravalent state. This result is consistent with expectations based on the Eh–pH diagram (Fig. 1A).

Similar to the XANES spectra, the Ce K-edge EXAFS spectra can be classified into two groups based on their frequency patterns. The phase of EXAFS oscillation in the k-space for the $CeCl_3$ solution and the Ce adsorbed on ferrihydrite was shifted from the other three spectra, that is, spontaneous precipitation of Ce, Ce adsorbed on δ-MnO_2, and tetravalent CeO_2 reagent (Fig. 6A). The amplitude of the oscillation for the CeO_2 spectrum increased with the increase in k range. Difference among the spectra was also observed in the R-space after Fourier transformation (FT). The FT magnitude of the $CeCl_3$ solution and Ce on ferrihydrite showed one peak, whereas those of the spontaneous precipitation of Ce, Ce on δ-MnO_2, and CeO_2 showed two peaks (Fig. 6B). The first ($R + \Delta R = 1.75$) and second ($R + \Delta R = 3.5$) peaks correspond to the first and second coordination spheres, respectively. Oxygen is an element in the first coordination for all spectra. The second coordination can reflect the shell of Ce–Ce or Ce–Mn, indicating spontaneous precipitation and CeO_2 or Ce adsorbed on δ-MnO_2, respectively. The fitting results for the Fourier transform spectra are listed in Table 2. The bond length of Ce–O is approximately 2.52–2.53 Å for the $CeCl_3$ solution and the Ce/ferrihydrite system, whereas it is approximately 2.30 Å for the Ce precipitation, Ce/δ-MnO_2 system, and CeO_2 reagent. In the Ce/δ-MnO_2 system, a better-fitting result was obtained by assuming a Ce–Ce shell instead of a Ce–Mn shell. This process is discussed in Section 4.2.2.

4. DISCUSSION

4.1. Change in oxidation state during adsorption and precipitation

Given that a "true" positive Ce anomaly was not observed for the sample of Ce(III) adsorbed on ferrihydrite

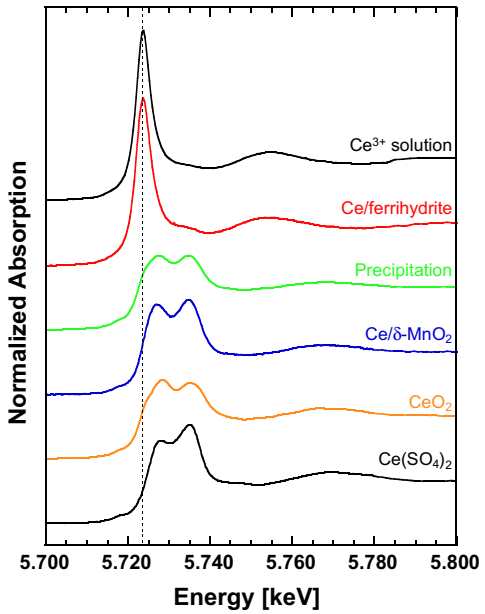

Fig. 5. Cerium L_{III}-edge XANES spectra of adsorption and reference materials (Ce^{3+} solution, CeO_2, and $Ce(SO_4)_2$). The dashed line runs through the peak top of Ce(III).

(Fig. 2), it is suggested that Ce was not oxidized by Fe minerals. By contrast, a large positive Ce anomaly was observed from the sample of Ce adsorbed on δ-MnO_2, suggesting that Ce was scavenged oxidatively for the liquid phase by Mn oxide (Fig. 2). Previously, this kind of REE pattern was used as the basis of discussions on the valence of Ce. Although the REE pattern can provide some indication as to whether Ce is trivalent or tetravalent, XANES spectra can provide the direct evidence on Ce oxidation state.

The Ce L_{III}-XANES spectrum clearly showed that the Ce adsorbed on ferrihydrite is trivalent, at least on the timescale considered in this study (Fig. 5). An important point from this result is that ferrihydrite does not oxidize Ce on the timescale of this study, as expected based on the Eh–pH diagram (Fig. 1A). This result is consistent with previous studies (De Carlo and McMurtry, 1992; Kawabe et al., 1999; Takahashi et al., 2007). Compared with leaching experiments (Bau and Koschinsky, 2009), the XANES data can provide more direct evidence and from these data it was clarified that oxidative scavenging of Ce does not occur by means of interaction with Fe minerals within the time range employed in this study. By contrast, Ce adsorbed on δ-MnO_2 was oxidized to a tetravalent state, which is consistent with the expectations based on the Eh–pH diagram (Fig. 1A) and as suggested in other studies (Takahashi et al., 2000, 2007; Ohta and Kawabe, 2001). This outcome is also consistent with the results of the REE adsorption experiment, which showed the positive Ce anomaly (Fig. 2). In addition, the XANES spectrum of the spontaneous precipitation of Ce also showed a two-humped peak, suggesting that Ce was oxidized by the bubbling of O_2 gas to a highly insoluble tetravalent state.

Although REE patterns and XANES spectra suggest whether Ce is trivalent or tetravalent, as shown in Figs. 2 and 5, the timing of oxidation, that is, whether Ce is oxidized during adsorption or in the water column before adsorption, cannot be clearly determined, which may be related to the isotopic fractionation found in our system. This issue is explored in the discussion in Section 4.2.

4.2. Stable isotopic fractionation of Ce between the solid and liquid phases

In this section, the isotopic fractionation based on the local structural data of Ce by XAFS is discussed in the framework of equilibrium isotopic fractionation. The attainment of the isotopic equilibrium is suggested because (i) the $\delta^{142}Ce$ values of the liquid phase with similar adsorbed fraction did not show isotopic variation against elapsed time (Fig. 3) and (ii) the isotopic fractionation of Ce during the adsorption experiment and the formation of spontaneous precipitate obeyed the model line of the equilibrium isotopic fractionation (Fig. 4). Although a study of natural ferromanganese nodules and crusts showed that the magnitude of Ce anomaly was kinetically controlled (Takahashi et al., 2007), the growth rate of natural ferromanganese crust is very slow, irrespective of the formation environments, compared with our experimental study. Thus, the reaction in the natural sample can be regarded as a pseudoequilibrium adsorption reaction over a short period, which can be treated by adsorption experiments in the laboratory, as conducted in this study.

The main factors controlling the degree of equilibrium isotopic fractionation are temperature, relative mass difference between isotopes (Bigeleisen and Mayer, 1947; O'Neil, 1986; Schauble, 2004). In addition, the heavier isotope preferentially partitions into stronger bonding sites relative to the weaker bonding site, including a higher oxidation state, highly covalent bonds, shorter bond lengths, low-spin electronic configurations, and a lower CN (Bigeleisen and Mayer, 1947; O'Neil, 1986; Schauble, 2004). Data for the chemical state of Ce before and after the adsorption experiment are necessary to clarify the reason for the Ce isotopic fractionation. This issue is discussed, along the Ce K-edge EXAFS spectra, below.

4.2.1. Coordination environment and isotopic fractionation: Ce/ferrihydrite and Ce precipitation systems

There are two main types of adsorbed species, namely, outer-sphere and inner-sphere surface complexes. The former species is adsorbed as hydrated species without direct bonding to the solid surface, whereas the latter shares oxygen between the adsorbed species and adsorbent surface. The absence of the second shell for the Ce/ferrihydrite system (Fig. 6B) suggests that Ce mainly forms an outer-sphere complex on the surface of ferrihydrite, which is in contrast to the clear second shell peak found in the Ce/δ-MnO_2 system (Fig. 6B). Moreover, the interatomic distance between Ce and first neighbor O, and the CN of the first shell, for the Ce^{3+} adsorbed on ferrihydrite are similar to those for the Ce^{3+} aqua complex (Table 2). These results show that the local coordination environment of Ce^{3+} adsorbed on ferrihydrite is similar to that of the Ce^{3+} aqua

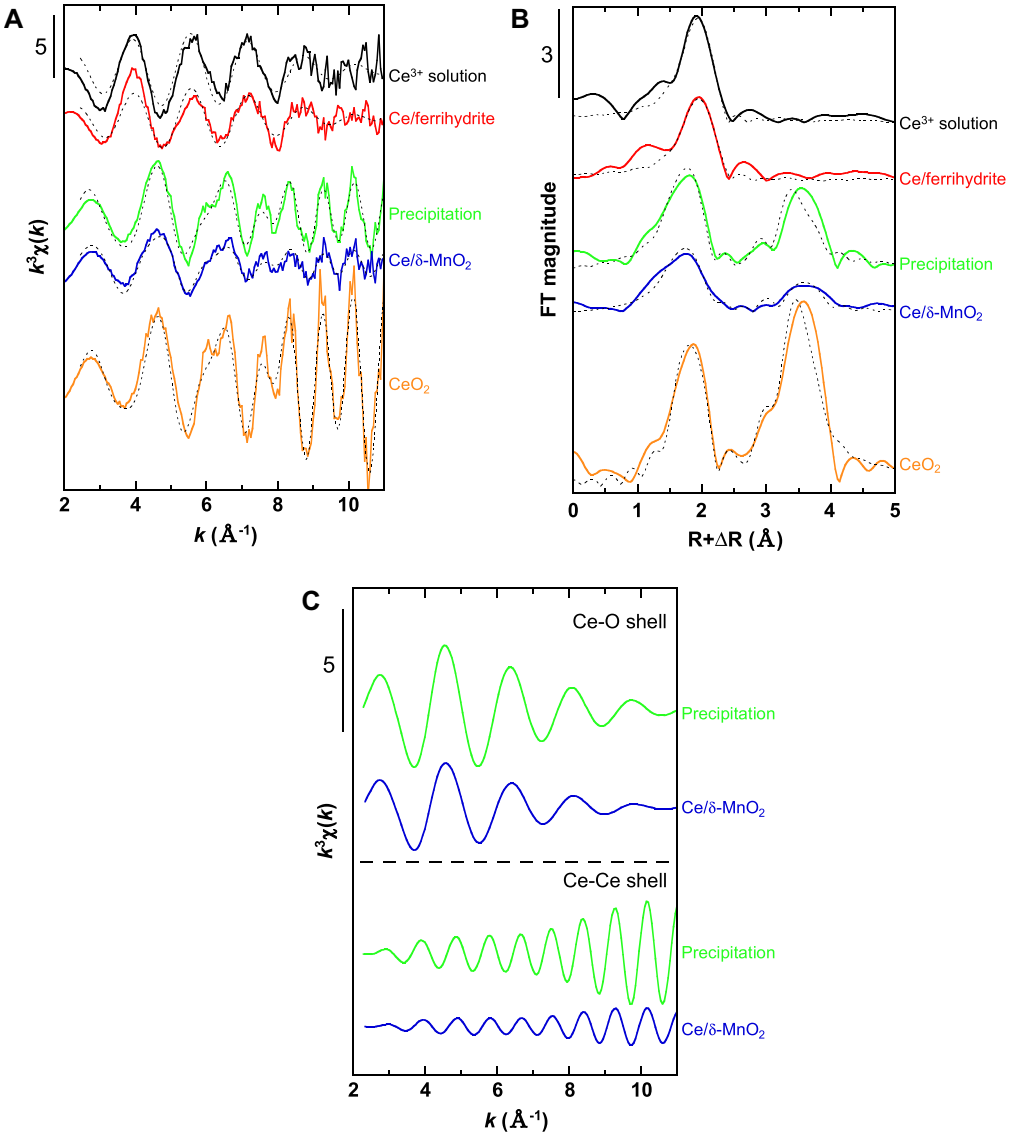

Fig. 6. (A) The k^3-weighted Ce K-edge EXAFS spectra of samples and reference materials (Ce^{3+} solution and CeO_2). (B) The radial structure functions of the samples and reference materials (Ce^{3+} solution and CeO_2). In both figures, the solid lines represent measured data, and the dashed lines represent fitting results. (C) Contributions of Ce–O and Ce–Ce shells in the k-space spectrum of the spontaneous precipitation of Ce and Ce adsorbed on δ-MnO_2.

Table 2
Fitting results of Fourier transform spectra.

System	Shell	CN		*R* (Å)		σ^2 (Å^2)	*R* factor (%)
Ce^{3+} solution	Ce–O	8.6	±1.3	2.521	±0.013	0.012	0.086
Ce/ferrihydrite (Ce/Fe = 0.0177)	Ce–O	7.5	±1.3	2.526	±0.014	0.013	0.056
Precipitation	Ce–O	8.4	±1.2	2.303	±0.014	0.015	6.3
	Ce–Ce	4.7	±1.1	3.846	±0.010	0.0058	
Ce/δ-MnO_2 (Ce/Mn = 0.0199)	Ce–O	6.5	±1.1	2.296	±0.019	0.019	9.5
	Ce–Ce	2.4	±1.3	3.850	±0.024	0.0085	
CeO_2	Ce–O	8.5	±1.2	2.335	±0.011	0.0094	4.7
	Ce–Ce	6.6	±2.0	3.855	±0.012	0.0022	

Note: CN denotes the coordination number, *R* (Å) denotes the distance from the center atom, σ: Debye–Waller factor, and the *R* factor (%) is the quality of fit (see Eq. (6)).

complex. By contrast, the local structure of Ce was changed from the aqua complex in the Ce-precipitation and Ce/δ-MnO_2 systems. For the isotopes, the degree of isotopic fractionation of Ce was the smallest for the ferrihydrite system among the three systems, which can be attributed to the similarity in local structure between the Ce adsorbed on ferrihydrite and the Ce aqua complex. Similar phenomena have been found in other adsorption systems. For example, molybdate forms an outer-sphere complex on ferrihydrite, indicating that the local structure of Mo does not vary in the system, and consistent with the small Mo isotopic fractionation in the ferrihydrite system (Goldberg et al., 2009). Therefore, the smallest isotopic fractionation for Ce in the Ce/ferrihydrite system, among the three systems, can be explained within the framework of equilibrium isotopic fractionation, that isotopic fractionation must be accompanied with changes in the local structure of the ion during the reaction (Bigeleisen and Mayer, 1947; O'Neil, 1986; Schauble, 2004).

In the Ce-precipitation system, $\delta^{142}Ce$ becomes larger for the Ce remaining in solution. The XANES spectra showed that Ce in the spontaneous precipitation was oxidized to Ce(IV), a higher oxidation state than Ce in Ce^{3+} solution (Fig. 3). Therefore, the bond length of Ce–O is shorter because of the increase in the charge, which is reflected in the EXAFS results for the Ce(IV) species (Table 2). Furthermore, in general, it is strongly expected that CN decreases as the ionic radius decreases, although the decrease is not clear from our results due to the large analytical uncertainty in CN. These results indicate that the factors controlling the isotopic fractionation of Ce cannot be attributed to the stronger bonding of Ce–O in the Ce(IV) precipitates or Ce(IV) (hydr)oxides relative to the aqua complex. Therefore, the preferential retention of the heavier isotope in the aqueous phase cannot be explained reasonably based on the structural data or on the rule of equilibrium isotopic fractionation, as discussed by Bigeleisen and Mayer (1947). However, in a manner analogous to the case for Ce, stable isotopic fractionation between aqueous Fe(III) and precipitated Fe(III) showed that Fe precipitation had a smaller $\delta^{56}Fe$ value than that of coexisting $Fe(III)_{aq}$ (Skulan et al., 2002; Balci et al., 2006), indicating that lighter isotopes can be partitioned into the solid phase when the precipitation occurs from aqueous solution. This fractionation is qualitatively consistent with the isotopic fractionation of Ce in the Ce-precipitation system.

4.2.2. Ce species incorporated into δ-MnO_2

The notable result obtained from the EXAFS spectra signatures was that the spectrum of the Ce adsorbed on δ-MnO_2 was similar to that of spontaneous precipitation of Ce (Fig. 6A). A study of natural ferromanganese crusts showed that the XANES spectra of the samples do not resemble $Ce(OH)_4$ (Takahashi et al., 2007), which was also observed in our XANES spectra. However, the EXAFS spectrum of Ce/δ-MnO_2 showed its similarity to that of $Ce(OH)_4$. This difference could be caused by the high concentration of Ce in our experiment compared with that of the real deep ocean, where the Ce concentration is several pmol/kg. In addition, the Fourier transform magnitude of the Ce adsorbed on δ-MnO_2 suggests that the interatomic distance of the second shell is similar to that for spontaneous precipitation of Ce, namely $Ce(OH)_4$ and CeO_2 (Fig. 6B). These findings suggest that the atom indicated in the second shell in the Ce/δ-MnO_2 system is not Mn but Ce. Assuming that the second neighboring atom is Mn, the interatomic distance between the center Ce and Mn is estimated as 4.113 ± 0.013 Å based on the EXAFS fitting; this value is even longer than the estimated values for the Ce–Ce shell (Table 2). The ionic radius at CN = 6 for Mn^{4+} (=0.530 Å; Shannon, 1976) is much smaller than that for Ce^{4+} (=0.870 Å), also suggesting that the assignment of Mn to the second shell is incorrect. Therefore, it is reasonable to expect that the atom at the second neighbor site in the Ce/δ-MnO_2 system is also Ce, indicating that Ce(IV) (hydr)oxide was formed at the surface of δ-MnO_2.

Although the EXAFS spectra in k-space showed similarities between the Ce/δ-MnO_2 system, Ce precipitation, and CeO_2, the relative intensity of the Ce–Ce peak at $R + \Delta R = 3.8$ Å in the R space decreased in the order of CeO_2 > Ce precipitation > Ce on δ-MnO_2 (Fig. 6B). In particular, the peak for Ce on δ-MnO_2 was much smaller than those for CeO_2 and Ce precipitation, as reflected in the CN of the Ce–Ce shell: 2.4 for Ce on δ-MnO_2 compared with 6.6 and 4.7, respectively, for CeO_2 and Ce precipitation (Table 2; note that the difference of the CN becomes larger if we assume the Debye–Waller factor for Ce–Ce is constant for the three species). In this case, the lower CN of Ce in the Ce/δ-MnO_2 system might be explained by the formation of nanoparticles of Ce(IV) (hydr)oxide, which has a lower CN value for the second neighboring Ce compared with the Ce bulk in CeO_2, as similarly observed in the K-edge EXAFS results for the Cu nanoparticles (Manceau et al., 2008). The smaller contributions of Ce–Ce shell in the Ce/δ-MnO_2 system compared to that of nanoparticles of $Ce(OH)_4$ in the k-space spectrum was also observed (Fig. 6C). Thus, the present results show that nanoparticles of Ce(IV) (hydr)oxide were formed in the Ce/δ-MnO_2 system. The Debye–Waller factor indicates that the degree of disorder of the coordination environment of Ce increases in the order of CeO_2 < Ce precipitation < Ce on δ-MnO_2 (Table 2), which is also compatible with the suggestion that Ce is present as nanoparticles of Ce(IV) (hydr)oxide on δ-MnO_2.

In addition to the EXAFS results, the formation of $Ce(OH)_4$ nanoparticles is also reflected in the XANES spectra of Ce in the Ce/δ-MnO_2 and Ce precipitation systems. The absorbance of Ce(IV) (hydr)oxide and CeO_2 is higher at first maxima and the two spectra have a shoulder (Fig. 5). These two features are attributed to many-body effects and to the covalent nature of the Ce–O–Ce bond (Kaindl et al., 1988; Hu et al., 1994; Soldatov et al., 1994; Takahashi et al., 2002, 2007). However, such shoulders were not observed in the spectra of the Ce adsorbed on the δ-MnO_2 and $Ce(SO_4)_2$ reagents because of the more ionic character of the Ce(IV)–O bond in these compounds (Takahashi et al., 2002). Alternatively, the absorbance of these two XANES spectra is higher at the second maxima (Fig. 5). The smaller the particle becomes, the greater the number of Ce–$(OH)_x$ bond becomes, leading to a decrease

in the number of Ce–O–Ce bonds that represents more covalent bonding (see Appendix Fig. A.1). An electronic polarization occurs when Ce forms a Ce–O–H bond, leading to a more ionic character. Therefore, the formation of Ce(IV) (hydr)oxide nanoparticles is responsible for both the EXAFS and XANES spectra.

The formation of nanoparticles probably occurred after the adsorption on δ-MnO_2 for the following reasons: (i) in the Co/δ-MnO_2 system, which behaves similarly to Ce in terms of the oxidative adsorption on δ-MnO_2, the oxidation of Co^{2+} to Co^{3+} occurred after the adsorption of Co^{2+} on δ-MnO_2 (Manceau et al., 1997); and (ii) the EXAFS spectrum of Ce on δ-MnO_2 differs from that of Ce in the spontaneous precipitation system. Based on these facts, it is suggested that Ce(III) is initially adsorbed on the δ-MnO_2 surface and Ce(III) is oxidized to Ce(IV) by δ-MnO_2 after the initial adsorption of Ce(III). The subsequent oxidation after the adsorption results in the formation of nanoparticles of Ce(IV) (hydr)oxide associated with δ-MnO_2.

4.2.3. Coordination environment and isotopic fractionation: Ce/δ-MnO_2 system

The relationship between Ce isotopic fractionation and Ce species in the Ce/δ-MnO_2 system is based on the Ce species on δ-MnO_2. The linear isotopic fractionation line in Fig. 4C shows that the system consisting of dissolved Ce(III), dissolved Ce(IV), Ce(III) adsorbed on δ-MnO_2, and Ce(IV) nanoparticles on δ-MnO_2 is at equilibrium. This observation indicates that Ce(IV) in the aqueous phase is also present and equilibrated with Ce(IV) nanoparticles in the solid phase, although the main pathway for the formation of Ce(IV) nanoparticles is the oxidation of Ce(III) after the adsorption of Ce(III) on δ-MnO_2, as suggested in the Section 4.2.2.

Here, we focus on the isotopic fractionation between aqueous Ce and $Ce(OH)_4$ nanoparticles on δ-MnO_2. Considering the very low solubility of Ce(IV), it is most likely that Ce(III) is the main species dissolved in the aqueous phase, whereas $Ce(OH)_4$ nanoparticles are the main Ce species in the solid phase. Thus, two fractionation pathways have to be considered if we assume equilibrium isotopic fractionation; that is, dissolved Ce(III) and $Ce(OH)_4$ nanoparticles are in equilibrium with both Ce(IV) in the aqueous phase and Ce(III) adsorbed on δ-MnO_2, respectively. The difference in the two pathways is the timing of the oxidation, specifically, whether Ce is oxidized in the aqueous phase or after the adsorption.

In the first pathway, the equilibrium isotopic fractionation between dissolved Ce(III) to the Ce(IV) nanoparticles on δ-MnO_2 through Ce(IV) in the aqueous phase (Dissolved Ce(III) ↔ Ce(OH)x in the solution ↔ $Ce(OH)_4$ nanoparticles on δ-MnO_2) is considered. Although it is difficult to predict the direction and degree of the equilibrium fractionation between aqueous Ce(III) and Ce(IV) precipitates theoretically, as suggested in Section 4.2.2, the results obtained for the Ce-precipitation system showed that the heavier isotope remains in the aqueous phase during the precipitation (Fig. 4B). However, our results show a much greater isotopic fractionation factor in the Ce/δ-MnO_2 system than in the Ce-precipitation system. Considering the large difference in the isotopic fractionation between the two systems, it is speculated that the formation of $Ce(OH)_4$ nanoparticles on δ-MnO_2 is the main reason for the larger isotopic fractionation in this system compared with the Ce-precipitation system. In considering the nanoparticles, the following points arise: (i) the coordination environment of Ce at the surface of the $Ce(OH)_4$ nanoparticles is different from that of the larger $Ce(OH)_4$ particles; and (ii) the $Ce(OH)_4$ nanoparticles have a much greater population of Ce at the surface compared with larger particles. These distorted structures of Ce in the nanoparticles might cause greater isotopic fractionation, as suggested by previous studies (Kashiwabara et al., 2011; Wasylenki et al., 2011).

In the second pathway, assuming the adsorbed Ce(III) as the intermediate species, possible isotopic fractionation between dissolved Ce(III) and Ce(III) adsorbed on δ-MnO_2 (Dissolved Ce(III) ↔ Ce(III) on δ-MnO_2 ↔ $Ce(OH)_4$ nanoparticles on δ-MnO_2) can be suggested based on equilibrium isotopic fractionation during the adsorption reaction. Ohta et al. (2009) reported local structures of La(III) and Pr(III) adsorbed on a δ-MnO_2 surface, where the bond lengths of La–O (=2.608 Å) and Pr–O (=2.558 Å) were larger than the respective corresponding La–O (=2.551 Å) and Pr–O (=2.489 Å) distances in their aqua complexes. It is highly likely, therefore, that the Ce(III)–O bond length adsorbed on δ-MnO_2 may be much greater than that of the Ce(III) aqua complex. These suggestions appear reasonable in the framework of equilibrium isotopic fractionation, as the results suggest that heavier Ce remains in the aqueous phase. In addition, Ohta et al. (2009) reported the bond length of REE–O in the REE/ferrihydrite system, stating that the REE–O distance increased in the order of REE^{3+} aqua complex < REE/ferrihydrite system < REE/δ-MnO_2 system. The larger difference in distance can explain the greater isotopic fractionation in the REE/δ-MnO_2 system compared with the REE/ferrihydrite system. The isotopic fractionation in the subsequent processes of Ce(III) oxidation on the δ-MnO_2 surface and the formation of Ce(IV) nanoparticles may be similar to that in the first case.

Therefore, it is reasonable to conclude that there is preferential adsorption of lighter Ce onto the solid phase, if we accept that (i) a heavier isotope remains in the aqueous phase in the Ce-precipitation system and (ii) equilibrium is attained in the Ce/δ-MnO_2 system, as suggested by Fig. 4C.

4.3. Application of XAFS and the Ce isotope ratio to geochemical samples

Given that the Ce/δ-MnO_2 system attains, at least apparently, equilibrium isotopic fractionation, the two reactions described in the Section 4.2.3 occur in the Ce/δ-MnO_2 system. It is strongly suggested that the initial reaction proceeds via the adsorption of Ce(III) on the δ-MnO_2 surface, followed by surface oxidation to Ce(IV). Final equilibrium was achieved in the Ce/δ-MnO_2 system. Oxidation at the δ-MnO_2 surface leads to the formation of $Ce(OH)_4$ nanoparticles on the surface. It was speculated that the formation of nanoparticles is related to the degree of isotopic fractionation in the Ce/δ-MnO_2 system, which is

significantly greater than that in the Ce-precipitation system. Although the reason for the large isotopic fractionation in the Ce/δ-MnO_2 system is not yet clear, the difference in the isotopic fractionation in the three systems (Ce spontaneous precipitation, Ce/ferrihydrite, and Ce/δ-MnO_2) suggests that the Ce stable isotope may be used as a new redox indicator.

Even with the recent development of XANES analysis, the previous discussion on redox conditions has only referred to the Ce(III)/Ce(IV) boundary. Although the Ce L_{III}-XANES spectra can show the mixing ratio of trivalency and tetravalency, which would be difficult to determine using only the size of the Ce anomaly, the situation has not changed significantly. Identifying the formation process of Ce(IV), that is, oxidative adsorption or oxidation in the liquid phase followed by precipitation, would enable more detailed discussion of the redox state. In this respect, the stable isotope ratio of Ce can give definitive data.

The isotopic fractionation of $\delta^{142}Ce$ between the liquid and solid phases is the lowest in the case of adsorption on ferrihydrite, which is not accompanied by the oxidation of Ce and occurs above the $Fe^{2+}/Fe(OH)_3$ boundary, below the Ce^{3+}/CeO_2 boundary in the Eh–pH diagrams (field (i) in Fig. 1A). For spontaneous precipitation of Ce, the $\delta^{142}Ce$ fractionation is greater than for Ce adsorbed on ferrihydrite, whereas it is less than that for Ce incorporated into δ-MnO_2. This situation occurs above the Ce^{3+}/CeO_2 boundary and below the Mn^{2+}/MnO_2 boundary, that is, in the relatively oxidative condition (field (ii) in Fig. 1A). Although the extent of $\delta^{142}Ce$ fractionation in these two cases is within analytical uncertainty, the size of the Ce anomaly and the XANES spectra data provide a clear distinction between adsorption without oxidation and spontaneous precipitation. The largest isotopic fractionation between the liquid and solid phases is observed when Ce is removed by δ-MnO_2 (field (iii) in Fig. 1A) via oxidative adsorption, which cannot be distinguished clearly from the spontaneous precipitation by the Ce anomaly and XANES data alone.

Thus, the combination of the Ce anomaly (and Ce oxidation state) and the stable isotope ratio of Ce may offer a powerful tool in detecting a consecutive variation from a reductive to an oxidative condition. This variation can be seen in geochemical samples such as Precambrian BIFs and carbonates, which may preserve redox information on paleo seawater when the Earth was under (i) a reductive condition, (ii) a moderately oxidative condition, or (iii) an oxidative condition. In addition, this method can be used to clarify the cause of the positive Ce anomaly seen in Archean BIFs (Kato et al., 2006), i.e. whether it is generated under moderately oxidative conditions (field (ii) in Fig. 1A) or oxidative conditions with the existence of Mn oxides (field (iii) in Fig. 1A). This combination could be especially useful for samples formed between 2.3 and 2.1 Ga. To date, the atmospheric O_2 level is believed to be below 10^{-5} PAL (present atmospheric level) until 2.3 Ga because of the appearance of sulfur mass-independent fractionation (Farquhar et al., 2000; Pavlov and Kasting, 2002). The presence of a eukaryote recently discovered in a 2.1 Ga black shale in Gabon (Albani et al., 2010) shows that an O_2 level greater than 1% PAL existed at that time. However, the lack of other evidence makes it difficult to discuss in detail the increase of atmospheric O_2 between these two time points. The combination of the stable isotope ratio and the Ce anomaly may enable a more precise estimation of the redox state of the paleo-ocean environment and the evolution of the atmosphere.

For example, if there is no Ce anomaly in Precambrian BIFs, it is expected that isotopic fractionation of Ce between a BIF and carbonate is small, as seen in the Ce/ferrihydrite system. Furthermore, as described above, such a condition is attained when the Eh–pH state is between the $Fe^{2+}/Fe(OH)_3$ and the Ce^{3+}/CeO_2 boundaries (field (i) in Fig. 1A), which generally corresponds to euxinic marine water. If a Ce anomaly is observed in a Precambrian BIF, analysis of the stable isotope ratio of Ce allows further investigation of whether the Ce(IV) is generated by spontaneous precipitation or by oxidative adsorption in the presence of a small amount of Mn oxide, which cannot be distinguished using other methods. If the Ce isotopic fractionation suggests that Mn oxide was present (but easily disappears due to the subsequent diagenetic process), the ocean at that time could be as oxic as it is today. It is therefore likely that the Ce isotope ratio will enable the determination of redox conditions more precisely than with a Ce anomaly alone. Although our study ultimately aims to use the Ce isotopic fractionation to understand the paleo-redox condition, the experiments were performed under low pH and high Ce concentration–conditions which are different from natural seawater. Thus, further studies are necessary more analogous to natural seawater conditions as follows: (i) Ce species in the aqueous phase must include dissolved complexes such as carbonate; (ii) experiments in the Ce/δ-MnO_2 system must be conducted at lower Ce concentration where the formation of $Ce(OH)_4$ nanoparticles is suppressed. However, the current study represents the first step in elucidating more quantitative redox information from Ce chemistry during adsorption reactions.

5. CONCLUSION

In this study, three data consisting of Ce—abundance, stable isotope ratio, and chemical state—were provided for the first time. The REE distribution coefficient pattern combined with Ce L_{III}-edge XANES spectra suggested that Ce is not oxidized by ferrihydrite, but is oxidatively scavenged by δ-MnO_2, as expected from the Eh–pH diagrams. The degree of isotopic fractionation of Ce between the liquid and solid phases increases as the redox condition becomes more oxic in the following order of adsorption: without oxidation, Ce(IV) precipitation, and oxidative adsorption (incorporation). In particular, the latter two processes were distinguished by the Ce stable isotope ratio, and cannot be discerned using the Ce anomaly alone. The difference between the two systems originated from the different Ce isotopes in the solid phase of a $Ce(OH)_4$ precipitate in the spontaneous Ce precipitation and $Ce(OH)_4$ nanoparticles in the Ce/δ-MnO_2 system. Although we have to continue similar studies in systems more similar to the natural marine environment (e.g., carbonate complex in

the aqueous phase, lower Ce concentration, etc.), it is expected that applying Ce geochemistry to Precambrian BIFs and carbonates in future research will lead to a better understanding of the paleo-redox state of the ancient oceans.

ACKNOWLEDGEMENTS

The speciation of Ce was performed with the approval of KEK-PF (Proposal No. 2008G691 and 2010G072) and JASRI (Proposal No. 2010B1347, 2010B1295, and 2011B1279). This study was supported by Grants in-aid for scientific research from the Ministry of Education, Culture, Sports, Science and Technology of Japan including the "TAIGA" project accepted as a Scientific Research on Innovative Areas, and by the JSPS Research Fellowships for Young Scientists. This study was also partially supported by Chinese Academy of Sciences Visiting Professorship for Senior International Scientists (Grant No. 2012T1Z0035) and National Natural Science Foundation of China (No. 41273112). The authors are grateful to the associate editor and three anonymous reviewers. Their suggestions and comments were very helpful in improving the manuscript.

APPENDIX A. SUPPLEMENTARY DATA

Supplementary data associated with this article can be found, in the online version, at http://dx.doi.org/10.1016/j.gca.2012.10.045.

REFERENCES

Albani A. E., Bengtson S., Canfield D. E., Bekker A., Macchiarelli R. and Mazurier A., et al. (2010) Large colonial organisms with coordinated growth in oxygenated environments 2.1 Gyr ago. *Nature* **466**, 100–104.

Anbar A. D., Duan Y., Lyons T. W., Arnold G. L., Kendall B. and Creaser R. A., et al. (2007) A whiff of oxygen before the Great Oxidation Event?. *Science* **317** 1903–1906.

Balci N., Bullen T. D., Witte-Lien K., Shanks W. C., Motelica M. and Mandernack K. W. (2006) Iron isotope fractionation during microbially stimulated Fe(II) oxidation and Fe(III) precipitation. *Geochim. Cosmochim. Acta* **70**, 622–639.

Bau M. (1993) Effects of syn- and post-depositional processes on the rare-earth element distribution in Precambrian iron-formations. *Eur. J. Mineral.* **5**, 257–267.

Bau M. (1999) Scavenging of dissolved yttrium and rare earths by precipitating iron oxyhydroxide: experimental evidence for Ce oxidation, Y-Ho fractionation, and lanthanide tetrad effect. *Geochim. Cosmochim. Acta* **63**, 67–77.

Bau M. and Dulski P. (1996) Distribution of yttrium and rare-earth elements in the Penge and Kuruman iron-formations, Transvaal Supergroup, South Africa. *Precambrian Res.* **79**, 37–55.

Bau M. and Koschinsky A. (2009) Oxidative scavenging of cerium on hydrous Fe oxide: evidence from the distribution of rare earth elements and yttrium between Fe oxides and Mn oxides in hydrogenetic ferromanganese crusts. *Geochem. J.* **43**, 37–47.

Bau M., Koschinsky A., Dulski P. and Hein J. R. (1996) Comparison of the partitioning behaviours of yttrium, rare earth elements, and titanium between hydrogenetic marine ferromanganese crusts and seawater. *Geochim. Cosmochim. Acta* **60**, 1709–1725.

Bigeleisen J. and Mayer M. G. (1947) Calculation of equilibrium constants for isotopic exchange reactions. *J. Chem. Phys.* **15**, 261–267.

Braun J. J., Pagel M., Muller J. P., Bilong P., Michard A. and Guillet B. (1990) Cerium anomalies in lateritic profiles. *Geochim. Cosmochim. Acta* **51**, 597.

Brookins D. G. (1988) *Eh–pH Diagrams for Geochemistry*. Springer-Verlag, pp. 176.

Catling D. and Claire M. (2005) How Earths atmosphere evolved to an oxic state: a status report. *Earth Planet. Sci. Lett.* **237**, 1–20.

De Baar H. J. W., German R. C., Elderfield H. and Van Gaans P. (1988) Rare earth elements distributions in anoxic waters of the Cariaco Trench. *Geochim. Cosmochim. Acta* **52**, 1203–1219.

De Carlo E. H. and McMurtry G. M. (1992) Rare-earth element geochemistry of ferromanganese crusts from the Hawaiian Archipelago, Central Pacific. *Chem. Geol.* **95**, 235–250.

Elderfield H. and Greaves M. J. (1982) The rare-earth elements in sea-water. *Nature* **296**, 214–219.

Elderfield E. H., Hawkesworth C. J., Greaves M. J. and Calvert S. E. (1981) Rare earth element geochemistry of oceanic ferromanganese nodules and associated sediments. *Geochim. Cosmochim. Acta* **45**, 513–528.

Farquhar J., Bao H. M. and Thiemens M. (2000) Atmospheric influence of Earth's earliest sulfur cycle. *Science* **289**, 756–758.

Foster A. L., Brown G. E. and Parks G. A. (2003) X-ray absorption fine structure study of As(V) and Se(IV) sorption complexes on hydrous Mn oxides. *Geochim. Cosmochim. Acta* **67**, 1937–1953.

Frei R., Gaucher C., Poulton S. W. and Canfield D. E. (2009) Fluctuations in Precambrian atmospheric oxygenation recorded by chromium isotopes. *Nature* **461**, 250–253.

Fryer B. J. (1977) Rare earth evidence in iron-formations for changing Precambrian oxidation states. *Geochim. Cosmochim. Acta* **41**, 361–367.

German C. R. and Elderfield H. (1989) Rare earth elements in Saanich Inlet, British Columbia, a seasonally anoxic basin. *Geochim. Cosmochim. Acta* **53**, 2561–2571.

Goldberg T., Archer C., Vance D. and Poulton S. (2009) Mo isotope fractionation during adsorption to Fe (oxyhydr)oxides. *Geochim. Cosmochim. Acta* **73**, 6502–6516.

Henderson P. (1984) *Rare Earth Element Geochemistry*. Elsevier, Amsterdam, pp. 510.

Hu Z., Bertram S. and Kaindl G. (1994) X-ray-absorption study of PrO_2 at high pressure. *Phys. Rev. B* **49**, 39–43.

Johnson C. M., Bear B. L. and Roden E. E. (2008) The iron isotope fingerprints of redox and biogeochemical cycling in modern and ancient Earth. *Annu. Rev. Earth Planet. Sci.* **36**, 457–493.

Kaindl G., Schmiester G., Sampathkumaran E. V. and Wachter P. (1988) Pressure-induced changes in L_{III} X-ray-absorption near-edge structure of CeO_2 and CeF_4: relevance to 4f-electronic structure. *Phys. Rev. B* **38**, 10174–10177.

Kashiwabara T., Takahashi Y., Tanimizu M. and Usui A. (2011) Molecular-scale mechanisms of distribution and isotopic fractionation of molybdenum between seawater and ferromanganese oxides. *Geochim. Cosmochim. Acta* **75**, 5762–5784.

Kato Y., Yamaguchi K. E. and Ohmoto H. (2006) Rare earth elements in Precambrian banded iron formations: secular changes of Ce and Eu anomalies and evolution of atmospheric oxygen. In *Evolution of Early Earth's Atmosphere, Hydrosphere, and Biosphere – Constraints from Ore Deposits* (eds. S. E. Kesler and H. Ohmoto). Geological Society of America, Boulder, Colorado, pp. 269–289.

Kawabe I., Ohta A. and Miura N. (1999) Distribution coefficients of REE between Fe oxyhydroxide precipitates and NaCl solutions affected by REE-carbonate complexation. *Geochem. J.* **33**, 181–197.

Luo Y.-R. and Byrne R. H. (2004) Carbonate complexation of yttrium and the rare earth elements in natural waters. *Geochim. Cosmochim. Acta* **68**, 691–699.

Manceau A., Drits V. A., Silverster E., Bartoli C. and Lanson B. (1997) Structural mechanism of Co^{2+} oxidation by the phyllomanganate buserite. *Am. Mineral.* **82**, 1150–1175.

Manceau A., Nagy K. L., Marcus M. A., Lanson M., Geoffroy N. and Jacquet T., et al. (2008) Formation of metallic copper nanoparticles at the soil–root interface. *Environ. Sci. Technol.* **42**, 1766–1772.

Möller P. and Bau M. (1993) Rare-earth patterns with positive cerium anomaly in alkaline waters from Lake Van Turkey. *Earth Planet. Sci. Lett.* **117**, 671–676.

Möller P., Dulski P. and Bau M. (1994) Rare-earth element adsorption in a seawater profile above the East Pacific Rise. *Chem. Erde Geochem.* **54**, 129–149.

Murakami T., Utsunomiya S., Imazu Y. and Prasad N. (2001) Direct evidence of late Archean to early Proterozoic anoxic atmosphere from a product of 2.5 Ga old weathering. *Earth Planet. Sci. Lett.* **184**, 523–528.

Murray R. W., Tenbrink M. R. B., Gerlach D. C., Russ G. P. and Jones D. L. (1991) Rare-earth, major, and trace-elements in chert from the Franciscan complex and Monterey group, California: assessing REE sources to fine-grained marine-sediments. *Geochim. Cosmochim. Acta* **55**, 1875–1895.

Nordstrom D. K., Plummer L. N., Langmuir D., Busenberg E. and May H. M. (1990) Revised chemical equilibrium data for major water–mineral reactions and their limitations. In *Chemical Modeling of Aqueous Systems II* (eds. D. C. Melchior and R. L. Bassett). *Am. Chem. Soc. Ser.* **416**, 398−413.

O'Day P. A., Rehr J. J., Zabinsky S. I. and Brown G. E. (1994) Extended X-ray absorption fine structures (EXAFS) analysis of disorder and multiple scattering in complex crystalline solids. *J. Am. Chem. Soc.* **116**, 2938–2949.

Ohta A. and Kawabe I. (2001) REE(III) adsorption onto Mn oxides (δ-MnO_2) and Fe oxyhydroxide: Ce(III) oxidation by δ-MnO_2. *Geochim. Cosmochim. Acta* **65**, 695–703.

Ohta A., Kagi H., Nomura M., Tsuno H. and Kawabe I. (2009) Coordination study of rare earth elements on Fe oxyhydroxide and Mn dioxides: Part II. Correspondence of structural change to irregular variations of partitioning coefficients and tetrad effect variations appearing in interatomic distances. *Am. Mineral* **94**, 476–486.

O'Neil J. R. (1986) Theoretical and experimental aspects of isotopic fractionation. *Rev. Mineral.* **16**, 1–40.

Pavlov A. A. and Kasting J. F. (2002) Mass-independent fractionation of sulfur isotopes in Archean sediments: strong evidence for an anoxic Archean atmosphere. *Astrobiology* **2**, 27–41.

Piepgras D. J. and Jacobsen S. B. (1992) The behavior of rare earth elements in seawater: precise determinations of variations in the North Pacific water column. *Geochim. Cosmochim. Acta* **56**, 1851–1862.

Piper D. Z. (1974) Rare-earth elements in sedimentary cycle – summary. *Chem. Geol.* **14**, 285–304.

Schauble E. A. (2004) Applying stable isotope fractionation theory to new systems. *Rev. Mineral. Geochem.* **55**, 65–111.

Schwertmann U. and Cornell R. M. (2000) *Iron Oxides in the Laboratory*, 2nd ed. Wiley-VCH, pp. 103.

Shannon R. D. (1976) Revised effective ionic radii and systematic studies of interatomic distances in halides and chalcogenides. *Acta Cryst.* **A32**, 751–767.

Shimizu H. and Masuda A. (1977) Cerium in chert as an indication of marine environment of its formation. *Nature* **266**, 346–348.

Skulan J. L., Beard B. L. and Johnson C. M. (2002) Kinetic and equilibrium Fe isotope fractionation between aqueous Fe(III) and hematite. *Geochim. Cosmochim. Acta* **66**, 2995–3015.

Soldatov A. V., Ivanchenko T. S., Longa S. D., Kotani A., Iwamoto Y. and Bianconi A. (1994) Crystal-structure effects in the Ce L_3-edge X-ray absorption spectrum of CeO_2: multiple-scattering resonances and many-body final states. *Phys. Rev. B* **50**, 5074–5080.

Takahashi Y., Shimizu H., Usui A., Kagi H. and Nomura M. (2000) Direct observation of tetravalent cerium in ferromanganese nodules and crusts by X-ray-adsorption near-edge structure (XANES). *Geochim. Cosmochim. Acta* **64**, 2929–2935.

Takahashi Y., Sakami H. and Nomura M. (2002) Determination of the oxidation state of cerium in rocks by Ce L_{III}-edge X-ray absorption near-edge structure. *Anal. Chim. Acta* **468**, 345–354.

Takahashi Y., Manceau A., Geoffroy N., Marcus M. A. and Usui A. (2007) Chemical and structural control of the partitioning of Co, Ce, and Pb in marine ferromanganese oxides. *Geochim. Cosmochim. Acta* **71**, 984–1008.

Taylor S. T. and McLennan S. M. (1988) The significance of the rare earths in geochemistry and cosmochemistry. In *Handbook on the Physics and Chemistry of Rare Earth* (eds. K. A. Gschneidner Jr. and L. Eyring). Elsevier, Amsterdam, pp. 485–578.

Wang Y. L., Liu Y.-G. and Schmitt R. A. (1986) Rare earth element geochemistry of South Atlantic deep sea sediments: Ce anomaly change at ~54 My. *Geochim. Cosmochim. Acta* **50**, 1337–1355.

Wasylenki L. E., Weeks C. L., Bargar J. R., Spiro T. G., Hein J. R. and Anbar A. D. (2011) The molecular mechanism of Mo isotope fractionation during adsorption to birnessite. *Geochim. Cosmochim. Acta* **75**, 5019–5031.

Weyer S. and Schwieters J. (2003) High precision Fe isotope measurements with high mass resolution MC-ICPMS. *Int. J. Mass Spectrom.* **226**, 355–368.

Wieser M. E. and Schwieters J. (2005) The development of multiple collector mass spectrometry for isotope ratio measurements. *Int. J. Mass Spectrom.* **242**, 97–115.

Wright J., Schrader H. and Holser W. T. (1987) Paleoredox variations in ancient oceans recorded by rare earth elements in fossil apatite. *Geochim. Cosmochim. Acta* **51**, 631–644.

Zabinsky S. I., Rehr J. J., Ankudinov A., Albers R. C. and Eller M. J. (1995) Multiple-scattering calculations of X-ray-adsorption spectra. *Phys. Rev. B* **52**, 2995–3009.

Associate editor: Derek Vance

ISSN 0016-7037
Volume 121
November 15, 2013

ELSEVIER

Geochimica et Cosmochimica Acta

JOURNAL OF THE GEOCHEMICAL SOCIETY
AND THE METEORITICAL SOCIETY

Volume 121 November 15, 2013

Articles

Continued on outside back cover

Available online at www.sciencedirect.com

ScienceDirect

Geochimica et Cosmochimica Acta 121 (2013) 105–119

Geochimica et Cosmochimica Acta

www.elsevier.com/locate/gca

Difference in the stable isotopic fractionations of Ce, Nd, and Sm during adsorption on iron and manganese oxides and its interpretation based on their local structures

Ryoichi Nakada [a,*], Masaharu Tanimizu [a,b], Yoshio Takahashi [a,b,c]

[a] *Department of Earth and Planetary Systems Science, Graduate School of Science, Hiroshima University, Higashi-Hiroshima, Hiroshima 739-8526, Japan*

[b] *Kochi Institute for Core Sample Research, Japan Agency for Marine-Earth Science and Technology (JAMSTEC), Monobe 200, Nankoku, Kochi 783-8502, Japan*

[c] *Key Laboratory of Petroleum Resources, Institute of Geology and Geophysics, Chinese Academy of Sciences, 382 Donggang Road, Lanzhou 730000, China*

Received 26 October 2012; accepted in revised form 12 July 2013; available online 24 July 2013

Abstract

Many elements have become targets for studies of stable isotopic fractionation with the development of various analytical techniques. Although several chemical factors that control the isotopic fractionation of heavy elements have been proposed, it remains controversial which properties are most important for the isotopic fractionation of elements. In this study, the stable isotopic fractionation of neodymium (Nd) and samarium (Sm) during adsorption on ferrihydrite and δ-MnO_2 was examined. This examination was combined with speciation analyses of these ions adsorbed on the solid phases by extended X-ray absorption fine structure (EXAFS) spectroscopy. Neodymium isotope ratios for Nd on ferrihydrite and δ-MnO_2 systems were, on average, 0.166‰ and 0.410‰ heavier than those of the liquid phase, which correspond to mean isotopic fractionation factors between the liquid and solid phases (α_{Lq-So}) of Nd on ferrihydrite and δ-MnO_2 of 0.999834 ($2\sigma = \pm 0.000048$) and 0.999590 ($2\sigma = \pm 0.000106$), respectively. Similarly, averaged Sm isotope ratios on ferrihydrite and δ-MnO_2 were 0.206‰ and 0.424‰ heavier than those of the liquid phase and the corresponding α_{Lq-So} values were 0.999794 (±0.000041) and 0.999576 (±0.000134), respectively. These results indicate that the directions of isotopic fractionation in the Nd and Sm systems are in contrast with that recently found for Ce(III) systems despite the similar chemical characteristics of rare earth elements.

EXAFS analyses suggest that the bond length of the first coordination sphere (REE–O bond) of Nd and Sm adsorbed on δ-MnO_2 is shorter than that of their aqua ions, although this was not clear for the ferrihydrite systems. The shorter bond length relative to the aqua ion is indicative of a stronger bond, suggesting that the equilibrium isotopic fractionation for the Nd and Sm systems can be governed by bond strength as has often been discussed for isotopic fractionation in solid–water adsorption systems. Meanwhile, EXAFS analyses of the Ce/ferrihydrite system showed a distorted structure for the first coordination sphere that was not observed for Ce^{3+} aqua ions. Such distortion was also observed for La adsorption on ferrihydrite and δ-MnO_2. In addition, previous studies have suggested a high stability of the hydrated state for La and Ce in terms of Gibbs free energy change. Thus, we suggest here that the difference in the stable isotopic fractionation for Ce (and predicted for La) vs. Nd and Sm can be explained by (i) the shorter bond lengths of adsorbed relative to dissolved species for Nd and Sm and (ii) the distorted structure of adsorbed Ce (and La) species and high stability of the aqua Ce ion.

* Corresponding author. Tel.: +81 82 424 7460; fax: +81 82 424 0735.
E-mail addresses: ryo-nakada@hiroshima-u.ac.jp (R. Nakada), ytakaha@hiroshima-u.ac.jp (Y. Takahashi).

0016-7037/$ - see front matter © 2013 Elsevier Ltd. All rights reserved.
http://dx.doi.org/10.1016/j.gca.2013.07.014

1. INTRODUCTION

The advent of multicollector-inductively coupled plasma-mass spectrometry (MC-ICP-MS), has enabled the study of the isotopic fractionation of heavy non-traditional elements (i.e., those heavier than sulfur), leading to a robust assessment of the behavior of elements such as silicon (Si) (De La Rocha et al., 2000), calcium (Ca) (Gussone et al., 2005), chromium (Cr) (Ellis et al., 2002; Frei et al., 2009), iron (Fe) (Beard and Johnson, 2004; Icopini et al., 2004; Johnson et al., 2004a), copper (Cu) (Maréchal et al., 1999; Mason et al., 2005), zinc (Zn) (Maréchal et al., 1999; Juillot et al., 2008; Moynier et al., 2009), selenium (Se) (Johnson et al., 1999; Johnson and Bullen, 2004), molybdenum (Mo) (Barling et al., 2001; Anbar, 2004; Barling and Anbar, 2004), antimony (Sb) (Rouxel et al., 2003), and thallium (Tl) (Rehkämper et al., 2002, 2004; Nielsen et al., 2009). Such work on the isotopic fractionation of heavy elements has provided a better understanding of ancient Earth and biogeochemical cycles (e.g., Halliday et al., 1998; Johnson et al., 2004b; Anbar and Rouxel, 2007), but despite the increasing attention given to the isotopic fractionation of heavy elements, the mechanisms controlling isotopic fractionation for some elements have yet to be clearly explained.

Elements that are present as cations in a solution, such as Fe, Cu, and Zn, have been shown to exhibit enrichment of the heavier isotopes on solid phases in adsorption experiments (Cacaly et al., 2004; Icopini et al., 2004; Clayton et al., 2005; Crosby et al., 2005; Pokrovsky et al., 2005; which are summarized in Balistrieri et al., 2008), whereas elements that form soluble oxyanions, such as germanium (Ge), Se, Sb, and Mo are subject to adsorption of lighter isotopes on Fe and/or Mn oxides (Johnson et al., 1999; Galy et al., 2002; Barling and Anbar, 2004; Ellis et al., 2004; Balistrieri et al., 2008; Tanimizu et al., 2011). Isotopic fractionation is not observed during adsorption of hexavalent Cr on goethite and γ-Al_2O_3 although Cr(VI) is dissolved as an oxyanion (Ellis et al., 2004). Major factors that control equilibrium isotopic fractionation include temperature, the relative mass difference between isotopes, and the nature and strength of the bonding environment (Bigeleisen and Mayer, 1947; O'Neil, 1986; Schauble, 2004). The degree of equilibrium isotopic fractionation usually decreases as the temperature increases, the factor of which is roughly equal to $1/T^2$ for most elements, whereas isotopic fractionation is greater for lighter elements owing to the larger relative mass differences among their isotopes. At equilibrium, the heavy isotope of an element is preferentially concentrated in the component where the element forms a stronger bond. The bond strength is greater for the species that have (i) shorter bond lengths; (ii) higher oxidation states; (iii) highly covalent bonds between atoms with similar electronegativities; and (iv) lower coordination numbers (CNs) (Criss, 1999; Schauble, 2004). These rules suggest that large equilibrium isotopic fractionations occur at low temperatures between substances with highly varying oxidation states, bond lengths, or CNs. Knowledge on whether the adsorption occurs via inner-sphere complexation (ions have direct bond with the surface of a solid phase) or outer-sphere complexation (ions do not have direct bond but are attracted by electrostatic force to a solid phase) can also be important for isotopic fractionation in elements such as Fe and Mo (e.g., Barling and Anbar, 2004; Butler et al., 2005). Although several possible causes of isotopic fractionation have been presented, the chemical property that has the greatest influence on bond strength remains unknown.

Nakada et al. (2013) recently showed that the stable isotopic fractionation of cerium (Ce) observed during adsorption on ferrihydrite and δ-MnO_2 cannot be explained by the isotopic fractionation mechanisms described above. Under their experimental conditions, Ce should be dissolved as a free cation, specifically, the Ce^{3+} aqua ion, which suggests that the heavier isotope of Ce should be concentrated in the solid phase according to the general observation of cation adsorption. In particular, Ce adsorption on δ-MnO_2 was accompanied by the oxidation of Ce(III) to Ce(IV) on the surface of the substrate, suggesting that the heavier Ce isotope should be concentrated in δ-MnO_2 because both the higher oxidation state and the resulting shorter bond length indicate a stronger chemical bond compared with the aqua Ce(III) ion in the liquid phase. However, it was found that the lighter Ce isotope was preferentially distributed to both ferrihydrite and δ-MnO_2, which is inconsistent with the studies reported for cations (Balistrieri et al., 2008). Nakada et al. (2013) explained this inconsistency by postulating that (i) Ce adsorbed on ferrihydrite possibly formed an outer-sphere complex and (ii) Ce adsorbed on δ-MnO_2 showed a distortion by the formation of $Ce(OH)_4$ nanoparticles. Whether these interpretations are adequate or not can be assessed by a comparison with the other REEs.

The current study aims to compare the isotopic fractionation data of Ce with neighboring rare earth elements (REEs) and presents results for stable isotopic fractionation of neodymium (Nd) and samarium (Sm) during adsorption on ferrihydrite and δ-MnO_2. Unfortunately, since praseodymium (Pr) is a monoisotopic element and promethium (Pm) only has radionuclides, stable isotope ratios of these elements cannot be measured. Although we also tried to measure the isotope ratio of lanthanum (La), we do not include La isotopic data, because repeated measurements (32 times) of the $LaCl_3$ solution used in the adsorption experiment showed an uncertainty of approximately 0.5‰ (2σ), which is better than that reported in the literature (Shen et al., 1994) but larger than the Ce isotopic fractionation observed during adsorption (Nakada et al., 2013). The relative mass difference of La isotopes ($^{139}La/^{138}La$) is about a half to that of Ce ($^{142}Ce/^{140}Ce$). As such, the isotopic fractionation of La during the adsorption is expected to be smaller than that of Ce, suggesting that the isotopic fractionation of La during adsorption cannot be precisely measured.

In spite of these difficulties, a systematic analysis of REE isotopic fractionation caused by adsorption on common mineral phases can offer insights into the geochemical behavior of REEs. For example, in seawater, REEs are adsorbed on various types of suspended matter and solid phases. It is noteworthy that Ce can behave differently than

other trivalent REEs owing to its oxidation to Ce(IV). Cerium is present in seawater at anomalously low concentrations relative to those of neighboring REEs, La and Pr (e.g., Elderfield and Greaves, 1982; Piepgras and Jacobsen, 1992; Möller et al., 1994), whereas Ce enrichment is observed in ferromanganese nodules (e.g., Piper, 1974; Elderfield et al., 1981; Bau et al., 1996). Although trivalent REEs have similar chemical properties, they can show systematic variations in their distributions to various natural samples as a function of the atomic number due to the lanthanide contraction (e.g., Henderson, 1984; Taylor and McLennan, 1988; Byrne and Sholkovitz, 1996). For instance, seawater is characterized by relative enrichment of heavy REE (HREE) compared with those in suspended particles due to their larger stability of carbonate complexes caused by the smaller ionic radii of HREE. Meanwhile, the high reactivity of REEs results in the short residence times of REEs in the ocean and low REE concentration in seawater (e.g., Elderfield and Greaves, 1982; Piepgras and Jacobsen, 1992; Möller et al., 1994). These observations suggest that the isotopic fractionation mechanisms may show a systematic variation among REEs due to the change in stabilities of adsorbed species over the REE series.

In this study, Fe and Mn oxides were used as an adsorptive medium, since marine ferromanganese deposits play a role as a major sink for REEs (e.g., Piper, 1974; Elderfield et al., 1981; Bau et al., 1996). K-edge extended X-ray absorption fine structure (EXAFS) spectroscopy analyses of these elements were conducted to determine their chemical speciation including coordination number (CN) and bond length for their adsorbed species, which were used to interpret the isotopic fractionation data. EXAFS analyses for La, Ce, and Pr were also included, though isotopic data are not available for La and Pr. The pH condition in this study was confined to the lower pH region (pH = 5), where the aqua ion is stable for REEs, to focus on the mass-dependent isotopic fractionation between the aqua ion and the adsorbed species and to compare the data with those reported for Ce in Nakada et al. (2013).

2. EXPERIMENTAL

2.1. Adsorption experiment

Synthetic ferrihydrite and δ-MnO_2 were used as adsorptive media. The procedure for the preparation of the synthetic ferrihydrite and δ-MnO_2 is detailed in Nakada et al. (2013) and follows the scheme of Schwertmann and Cornell (2000) for ferrihydrite and that of Foster et al. (2003) for δ-MnO_2. All experiments were performed in a manner similar to that described in Nakada et al. (2013). A $LaCl_3$, $NdCl_3$, or $SmCl_3$ reagent (purity of 99.9%; Wako, Japan) dissolved in ultrapure water was used for the adsorption experiments on ferrihydrite and δ-MnO_2. Similarly, an adsorption experiment for Pr on these minerals was performed using a 99.5% $PrCl_3$ reagent (Wako, Japan). For the adsorption experiments of Nd and Sm, 10 g of varying concentration of their solutions were poured into plastic bottles with 100 mg of ferrihydrite or 30 mg of δ-MnO_2 as the solid phase. In this experiment, both the amounts of the solid phase and the volume of the liquid phase were fixed, whereas the REE concentration in the solutions were systematically varied to prepare samples with different adsorbed fractions (the ratio of adsorbed REEs to total REEs added into the system: F_{ad}). In the case of the adsorption experiment for EXAFS measurement, about 10 g of solution containing 10 mg REE (Nd or Sm) were poured into plastic bottles with 250 mg of ferrihydrite or 100 mg of δ-MnO_2 as the solid phase.

The other experimental parameters, such as the pH and the experimental period, were identical to those reported in the study by Nakada et al. (2013). The pH was adjusted to 5.00 ± 0.05 with dilute NaOH and HCl solutions because the REE^{3+} aqua ion dominates the REE species in the liquid phase at pH = 5. Speciation calculations under the experimental condition showed that more than 99.5% of La, Ce(III), Pr, Nd, and Sm were dissolved as REE^{3+} aqua ions under our experimental condition. In the calculation, the data for REE–carbonate complexation constants were obtained from Luo and Byrne (2004), and the equilibrium constants of the carbonate species were obtained from Nordstrom et al. (1990). The suspension was stirred for 6 h at 25 °C at 130 rpm. At the end of the experiment, the liquid phase was separated from the solid phase by filtration using a 0.2 μm hydrophilic polytetrafluoroethylene filter (ADVANTEC).

2.2. Isotopic analysis

After the solid–water separation in the adsorption experiments, the liquid samples were acidified to 0.3 M HNO_3 to prevent the precipitation of REEs. The ferrihydrite was dissolved in 6 M HCl (ultrapure grade), while the δ-MnO_2 was dissolved in 6 M HCl and H_2O_2 (ultrapure grade). Both mineral digests were finally diluted to 0.5 M HCl, and the REEs were separated from Fe or Mn via column chemistry. For Fe elution, 15 g of 2.0 M HCl solution was passed through a column (4 cm long; 1.0 cm diameter) loaded with an AG 50W-X8 cation exchange resin (Bio-Rad); for Mn elution, 20 g of 2.0 M HNO_3 solution was used (elution curves are shown in Fig. EA1 in the Electronic annex). The column chemistry had been checked prior to the sample introduction using an ICP-MS (Agilent 7700) with precision better than 1%. Almost 100% (more than 99%) of the REEs were recovered by elution using a 6.0 M HCl solution, ensuring the absence of isotopic fractionation during the column chemistry. REE concentrations in both solid and liquid samples were determined with precision of 2% using an SPS3500 Series ICP-atomic emission spectrometer (SII NanoTechnology, Inc.) to determine F_{ad} and for the subsequent dilution prior to MC-ICP-MS analyses. Procedural blanks in the adsorption experiments (REE-free experiments), measured using ICP-MS, indicated that the ferrihydrite and δ-MnO_2 contained less than 10 pg of the REE, which corresponds to less than 0.01% of REE added in our experiments.

The isotope ratios of Nd and Sm were determined at the Kochi Institute for Core Sample Research, Japan Agency for Marine-Earth Science and Technology using a double-focusing MC-ICP-MS (NEPTUNE, Thermo Fisher

Scientific) previously described by Weyer and Schwieters (2003) and Wieser and Schwieters (2005). Sample solutions were introduced at 100 μL/min using a GE Micromist nebulizer (Glass Expansion, Australia) in free aspiration mode attached to a dual cyclonic/double Scott quartz glass spray chamber. The measurements were performed in low-resolution mode using an X-type skimmer cone. The typical operating conditions of the instrument are given in Table 1. The measured isotope ratios were corrected by an element doping technique. The doped element (Sm and Eu for Nd and Sm isotope measurements, respectively) used has a similar mass to the analyte and more than one stable isotope, and was added to the sample solutions immediately before MC-ICP-MS analysis. Through the element doping technique, the observed isotope ratios were corrected according to an exponential law using the isotope ratio of the doped solutions. The relationship between the observed and normalized isotope ratios is described by

$$R_{\text{a-norm}} = R_{\text{a-obs}} \times A_{\text{a}}^{f_{\text{analyte}}}, \quad (1)$$

$$R_{\text{d-norm}} = R_{\text{d-obs}} \times A_{\text{d}}^{f_{\text{dope}}}, \quad (2)$$

$$f_{\text{analyte}} = f_{\text{dope}}, \quad (3)$$

where R_{a} and R_{d} are the measured isotope ratios of the analyte and doping element, and f and A are the mass discrimination correction factor and the ratio of exact atomic masses of the analyte or doping isotope, respectively. The exact atomic masses were obtained from the IUPAC Technical Report by de Laeter et al. (2003). The REE chloride solutions used in the adsorption experiment were employed as the standard solution. The isotope ratios are expressed in a standard delta notation relative to the average standards, as described by

$$\delta(^{i}E)_{\text{S}} = [(R_{\text{S}}/R_{\text{RM}}) - 1] \times 10^{3}, \quad (4)$$

where R_{S} and R_{RM} are the isotope abundance ratios $n(^{i}E)/n(^{j}E)$ in a sample (S: also corresponds to $R_{\text{a-norm}}$) and a standard solution used in the adsorption experiment, respectively. The E represents the elements (Nd or Sm) and superscripts i and j denote heavy and light isotopes of the element, respectively.

Table 1
Typical instrumental operation conditions.

RF frequencies	27.12 MHz
RF power	1.2 kW forward, <1 W reflection
Fassel-type torch Ar gas flow rates	
Nebulizer	1.14 L/min
Auxiliary	0.70 L/min
Cool	15.7 L/min
Nebulizer	Glass Expansion Micromist
Spray chamber	Dual synchronic/double Scott glass chamber (ambient temperature)
Sample uptake	100 μL/min (free aspiration)
Cones	X-type skimmer cone
Ion energy	10,000 V
Extraction	2000 V
Pressures during operation	
ESA	$1.0–1.5 \times 10^{-5}$ Pa (9×10^{-6} Pa during standby)
Analyzer	$4–9 \times 10^{-7}$ Pa (4×10^{-7} Pa during standby)

A possible mass spectrometric interference in wet plasma mode is the REE-hydride, which can affect isotope ratio of another element, for example, ^{144}SmH on ^{145}Nd, ^{146}NdH on ^{147}Sm, and ^{148}NdH on ^{149}Sm. To reduce the variation in the hydride formation, the ratio between measuring and doping elements was fixed through the measurement. The contribution of hydride was estimated using 1000 μg/L Nd and Sm solutions. The NdH/Nd ratio estimated from the ion signal intensity at the mass number 151 as ^{150}NdH/^{150}Nd, was about 3×10^{-6}. Similarly, ^{154}SmH/^{154}Sm was measured as approximately 3×10^{-6}. Although the ^{150}NdH/^{150}Nd and ^{154}SmH/^{154}Sm ratios can be affected by contamination from ^{151}Eu and ^{155}Gd, respectively, measured the 151/150 and 155/154 ratios of 3×10^{-6}, were small enough to ignore. The ion signals of Nd as ^{145}Nd^{16}O and Sm as ^{147}Sm^{16}O were also checked before each isotopic analysis. The NdO/Nd and SmO/Sm ratios were adjusted to 1% on average by tuning the carrier gas flow rate.

The interferences generated by Sm impurities in Nd and Eu impurities in Sm (on Nd and Sm isotopic measurements, respectively) were also estimated before the addition of doping elements. We examined the contribution of ^{146}NdH and ^{147}Sm by measuring the ion signal intensity at the mass number 147 when introducing a 1000 μg/L Nd solution. The measured (^{146}NdH + ^{147}Sm)/^{146}Nd ratio was slightly higher than the ^{150}NdH/^{150}Nd ratio owing to the contribution of ^{147}Sm. Similarly, the intensity at the mass number 151 was measured when a 1000 μg/L Sm solution was introduced and the contribution of ^{151}Eu was estimated from the (^{150}SmH + ^{151}Eu)/^{150}Sm ratio by comparisonwith the ^{154}SmH/^{154}Sm ratio. The estimated amounts of Sm and Eu were less than 0.01% of Nd and Sm in each solution. Thus, the interferences from neighboring REE were negligible. In the following, the isotope measurement of each element is described in detail.

For the Nd isotopic analyses, ^{143}Nd, ^{145}Nd, and ^{146}Nd were measured simultaneously with the doping element isotopes ^{147}Sm and ^{149}Sm using the MC-ICP-MS. Samples and Nd standard solutions were diluted to about 200 μg/L, which corresponds to a ^{145}Nd signal of about 1.3 V. In contrast, the standard Sm solution (Wako, Japan) serving as a doping element was diluted to 100 μg/L, which provided a ^{147}Sm signal of about 2 V. The Nd isotope ratios are expressed as δ^{145}Nd and δ^{146}Nd when the isotope ratios of ^{145}Nd/^{143}Nd and ^{146}Nd/^{143}Nd correspond to R in Eq. (4). The determination of both δ^{145}Nd and δ^{146}Nd allows us to assess the accuracy of the measurement. In the natural environment, both mass-dependent and mass-independent (including nuclear-volume) isotopic fractionations occur. The mass-dependent isotope effect is due to differences in atomic weight, which implies that relative isotopic fractionations can be calculated for elements that have more than three stable isotopes. The relative isotopic fractionation assuming an equilibrium is calculated as

$$\delta^{145}Nd/\delta^{146}Nd = \frac{[1/(143+143)] - [1/(143+145)]}{[1/(143+143)] - [1/(143+146)]}, \quad (5)$$

where 143, 145, and 146 correspond to exact atomic masses of each Nd isotope. Therefore, mass-dependent fractionation of the two Nd isotope ratios is expected to follow

$$\delta^{145}Nd = 0.669 \times \delta^{146}Nd. \quad (6)$$

The analytical uncertainties in the measurement of the δ^{145}Nd and δ^{146}Nd value were 0.048‰ and 0.069‰ (2σ), respectively, as calculated from repeated analyses of the standard $NdCl_3$ solution ($n = 14$). In addition, Nd isotope measurements were performed twice by preparing one sample with a similar F_{ad} to confirm the quality of the experiment, and the results were the same within the analytical uncertainty.

For the Sm isotope measurements, ^{147}Sm, ^{149}Sm, and ^{152}Sm were measured simultaneously alongside the doping element isotopes ^{151}Eu and ^{153}Eu. The ion signals of ^{147}Sm and ^{151}Eu were about 1.4 and 3 V, respectively, using Sm and Eu standard (Wako, Japan) solutions that were respectively diluted to about 100 and 50 μg/L. During the measurement, ^{156}Gd was also monitored to estimate the influence of ^{152}Gd, which can interfere with ^{152}Sm. The ^{156}Gd signal was negligible (<0.001% of the ^{147}Sm signal) for all samples and standard solutions, which indicates that isobaric interferences by ^{152}Gd were negligible in this study. Similar to the case for Nd isotope ratios, two independent Sm isotope ratio can be determined, δ^{149}Sm and δ^{152}Sm, when R in Eq. (4) is ^{149}Sm/^{147}Sm and ^{152}Sm/^{147}Sm, respectively. Here, it is expected that

$$\delta^{149}Sm = 0.404 \times \delta^{152}Sm. \quad (7)$$

The analytical reproducibility for the measurements of the δ^{149}Sm and δ^{152}Sm value were 0.038‰ and 0.069‰ (2σ), respectively, as calculated from repeated analyses of the $SmCl_3$ standard solution ($n = 8$).

2.3. EXAFS analysis

Immediately after filtration, solid samples were packed into individual polyethylene bags and frozen. Lanthanum, Pr, Nd, and Sm K-edge EXAFS spectra, which provide quantitative information on neighboring atom distances and the CN, were measured at BL-01B1 of SPring-8 (Hyogo, Japan). For light REEs, such as La, Pr, Nd, and Sm, analysis of the K-edge EXAFS is more suitable than that of the L-edge EXAFS because (i) the L-edge for a lighter REE is subject to interferences by multi-electron excitation and (ii) the energy range applicable to EXAFS analysis is short because of the close energy gap between the L_{III} and L_{II} edges. Furthermore, measurement of the L_{III}-edge EXAFS spectra of Sm in fluorescence mode is severely affected by the Mn K-line in the Sm/δ-MnO_2 system. Thus, we employed K-edge EXAFS analysis to obtain information on the local coordination environment of La, Pr, Nd, and Sm adsorbed on ferrihydrite and δ-MnO_2. Prior to the measurement of samples, the monochromator was calibrated to the first inflection point for each element using the following standard compounds (diluted with boron nitride): $LaCl_3$ (38.938 keV), $PrCl_3$ (41.999 keV), Nd_2O_3 (43.578 keV), and $SmCl_3$ (46.856 keV). The K-edge EXAFS spectra of standard materials and chloride solutions used in the adsorption experiments were measured in transmission mode, whereas adsorbed samples were measured in fluorescence mode using a 19-element Ge semiconductor detector. Each sample was scanned several times to obtain the spectra with better statistics. Repeated EXAFS scans were identical, showing that any X-ray-induced alteration of the samples was unlikely in our experiments.

The EXAFS spectra were analyzed using REX2000 software (Rigaku Co. Ltd.) with parameters generated by the FEFF 7.0 code (Zabinsky et al., 1995). In addition to La, Pr, Nd, and Sm measured in this study, the EXAFS of the Ce^{3+} and Ce/ferrihydrite system measured by Nakada et al. (2013) was reanalyzed here. After extracting the EXAFS oscillations and its Fourier transform, the inversely Fourier-filtered data were analyzed using a standard curve-fitting method. The theoretical phase shifts and amplitude functions for the REE–O, REE–REE, REE–Fe, and REE–Mn shells employed in this fitting procedure were extracted from FEFF 7.0 (Zabinsky et al., 1995). In the fitting process, the threshold energy shifts of the first and second shells were constrained to be the same. Finally, the processed EXAFS spectra in the whole k- and R-space ranges employed in the fitting procedure were compared with the measured EXAFS spectra in k- and R-space to confirm that the fits developed for the processed spectra also provided good matches to the measured spectra. The uncertainty estimates for the interatomic distance and CN obtained from the fitting were ±0.02 Å and ±20%, respectively (O'Day et al., 1994). The quality of the fit was given by the goodness-of-fit parameter R (R-factor), defined as

$$R = \frac{\sum [\chi_{obs}(k) - \chi_{cal}(k)]^2}{\sum [\chi_{obs}(k)]^2} \quad (8)$$

where $\chi_{obs}(k)$ and $\chi_{cal}(k)$ are the experimental and calculated absorption coefficients at a given k, respectively. The multiple-scattering effect was initially included in the EXAFS analyses in this study, but was found to make a very weak contribution to the EXAFS spectra.

3. RESULTS

3.1. Isotopic fractionation

Table 2 lists the Nd isotope ratios expressed as delta notation of both solid and liquid samples after the adsorption experiments. The table gives both δ^{145}Nd and δ^{146}Nd, along with the initial weight in the adsorption experiment and adsorbed fraction (F_{ad}). The δ^{145}Nd and δ^{146}Nd values of the solid phase have positive values except for a datum with the highest F_{ad}, whereas all the values of the liquid phase are negative. This means that the heavier Nd isotopes were enriched in the solid phase, resulting in the liquid phase becoming enriched in lighter Nd isotopes. All the data fall on a straight line in a plot of δ^{145}Nd vs. δ^{146}Nd as expected from the theoretical calculation of Eq. (6) (solid line, Fig. EA2 in the Electronic annex), indicating that the measurements were performed well and no mass-indepen-

Table 2
Isotope ratio and fractionation factor for Nd and Sm during adsorption.

System	Initial (mg)[a]	F_{ad}[b]	δ1 (Lq)[c]	δ1 (So)[c]	δ2 (Lq)[c]	δ2 (So)[c]	α_{Lq-So}[d]	Average
Nd/ferrihydrite	0.05	0.86	−0.113	0.088	−0.156	0.147	0.999799	
	0.30	0.68	−0.079	0.102	−0.107	0.179	0.999819	
	1.00	0.32	−0.037	0.112	−0.030	0.181	0.999851	
	2.01	0.16	−0.029	0.126	−0.032	0.197	0.999845	
	3.21	0.08	−0.012	0.132	−0.028	0.207	0.999855	0.999834 ± 0.000048
Nd/δ-MnO_2	5.22	1.00	−0.466	0.001	−0.690	−0.001	0.999533	
	6.27	0.91	−0.395	0.064	−0.588	0.105	0.999541	
	7.51	0.77	−0.320	0.089	−0.477	0.140	0.999590	
	8.69	0.69	−0.250	0.112	−0.367	0.190	0.999638	
	10.2	0.57	−0.207	0.145	−0.298	0.231	0.999647	0.999590 ± 0.000106
Sm/ferrihydrite	0.32	0.62	−0.103	0.123	−0.227	0.326	0.999774	
	0.64	0.49	−0.092	0.135	−0.233	0.324	0.999773	
	1.07	0.34	−0.061	0.143	−0.165	0.327	0.999796	
	1.89	0.22	−0.036	0.157	−0.088	0.391	0.999806	
	3.04	0.10	−0.018	0.162	−0.044	0.393	0.999820	0.999794 ± 0.000041
Sm/δ-MnO_2	5.44	1.00	−0.479	0.005	−1.195	0.005	0.999516	
	6.74	0.89	−0.407	0.083	−0.999	0.155	0.999510	
	8.12	0.76	−0.305	0.115	−0.740	0.275	0.999580	
	9.34	0.66	−0.244	0.151	−0.615	0.345	0.999606	
	10.9	0.57	−0.186	0.143	−0.471	0.363	0.999671	0.999576 ± 0.000134

[a] Initial (mg) denotes initial amount of Nd and Sm in the adsorption experiments added into a 10 g of ultra-pure water.
[b] F_{ad} means the ratio of adsorbed fraction of REE to initial REE.
[c] δ1 and δ2 correspond to (i) δ^{145}Nd or δ^{149}Sm and (ii) δ^{146}Nd or δ^{152}Sm values, respectively.
[d] The definition of α is given by Eqs. (9) and (10) for Nd and Sm systems, respectively.

dent fractionation was observed. Given that the δ^{145}Nd and δ^{146}Nd values have a clear correlation, only the δ^{145}Nd data are discussed further. Fig. 1 shows the isotopic fractionation of Nd during the adsorption experiment, along with F_{ad} (Fig. 1A: adsorption on ferrihydrite; Fig. 1B: adsorption on δ-MnO_2). In the figure, the model lines for the equilibrium and Rayleigh fractionations are shown as solid and dashed lines, respectively (Fig. 1). In calculating these model lines, the mean α_{Lq-So}, which is the isotopic fractionation factor between the liquid and solid phases (Table 2), was calculated as

$$\alpha_{Lq-So} = \frac{10^3 + \delta^{145}Nd_{Lq}}{10^3 + \delta^{145}Nd_{So}} \quad (9)$$

The uncertainty in the mean α_{Lq-So} (Table 2) is the deviation (2σ) of five α_{Lq-So} values measured at various F_{ad}. The figure shows that both experimental systems are in accord with the line of equilibrium isotopic fractionation.

Table 2 also lists δ^{149}Sm and δ^{152}Sm of solid and liquid samples along with the initial concentration and F_{ad}. Similar to the case for Nd, heavier and lighter Sm isotopes were enriched in the solid and liquid phases, respectively. The clear correlation observed between δ^{149}Sm and δ^{152}Sm (Fig. EA3) indicates that mass-independent fractionation was not observed, and as such only δ^{149}Sm is discussed further. Fig. 1C and D show the isotopic fractionation of Sm during the adsorption experiment along with F_{ad} (Fig. 1C: adsorption on ferrihydrite; Fig. 1D: adsorption on δ-MnO_2) and the model lines for the equilibrium and Rayleigh fractionations. As in the case of the Nd system, the mean α_{Lq-So} is calculated as

$$\alpha_{Lq-So} = \frac{10^3 + \delta^{149}Sm_{Lq}}{10^3 + \delta^{149}Sm_{So}} \quad (10)$$

Similar to the case for the Nd system, the uncertainty in the mean α_{Lq-So} (Table 2) is the deviation (2σ) of five α_{Lq-So} values measured at various F_{ad}. The figure shows that the Sm system also follows the line of equilibrium isotopic fractionation.

3.2. EXAFS

In presenting EXAFS results, we include the results for La and Pr adsorbed on ferrihydrite and δ-MnO_2 and Ce on ferrihydrite for comparison. The La K-edge EXAFS spectra and radial structural function (RSF) obtained from the Fourier transform of the spectra are shown in Fig. 2. The dashed lines show the fitting result, from which we obtained the EXAFS parameters listed in Table 3. Assuming an oxygen atom in the first shell, the La–O bond lengths are approximately 2.56, 2.55, and 2.53 Å for the La^{3+} solution, La on ferrihydrite, and La on δ-MnO_2 systems, respectively (Table 3). However, as observed in the broader RSF of the La–O shell for La on ferrihydrite and δ-MnO_2 compared with La^{3+} solution, the La–O shell actually consists of two La–O shells. The pronounced dip at $k = 6.5$ ($Å^{-1}$) not only requires a La–Fe/Mn shell but also the negative amplitude of the La–O_1 and La–O_2 shell to obtain a better fit (Fig. 2A). The existence of two inner O shells for La was also suggested by Ohta et al. (2009). The La–O bond length is 2.56 Å for the La^{3+} solution, which is longer than the La–O_1 bonds of the La/ferrihydrite (2.45 Å) and the δ-MnO_2 systems (2.46 Å). The presence

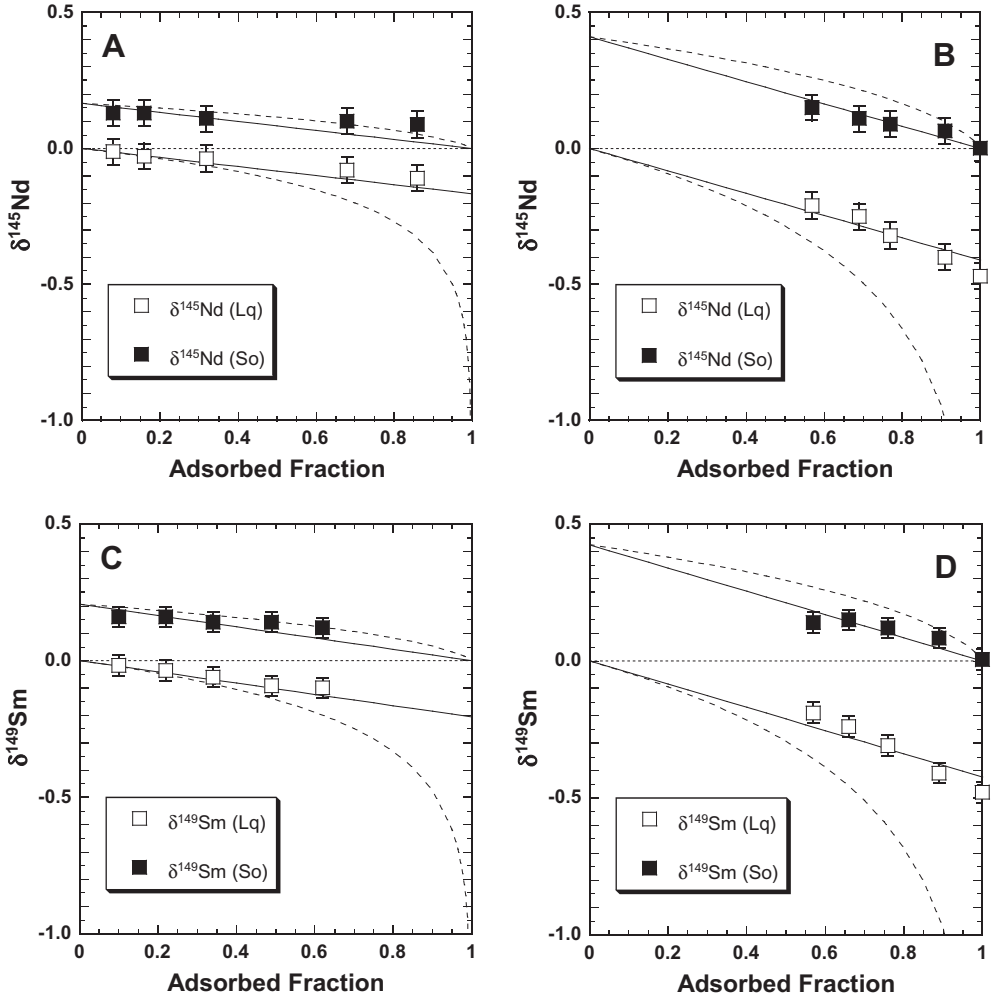

Fig. 1. Isotope ratios of the liquid and solid phases and adsorbed fractions (F_{ad}) obtained during adsorption experiments in the following systems: (A) Nd on ferrihydrite, (B) Nd on δ-MnO_2, (C) Sm on ferrihydrite, (D) Sm on δ-MnO_2. Open squares represent the $\delta^{145}Nd$ and $\delta^{149}Sm$ values of the liquid phase, and closed squares represent the solid phase. The error bar indicates the analytical uncertainty calculated from repeated measurements of a standard solution. Solid lines correspond to a model of equilibrium fractionation, while dashed lines correspond to Rayleigh fractionation.

of shorter bonds between La and the O atoms of the mineral surfaces is reasonable considering that the total CN ($= CN_1 + CN_2$) of the adsorbed species is smaller than the CN for hydrated La^{3+}.

The results of the re-examination of Ce K-edge EXAFS spectra and the RSF of the Ce^{3+} solution and Ce/ferrihydrite system are presented in Table 3 and Fig. 3. For comparison, the previous analysis assuming only one oxygen shell is also presented. The *k*-space EXAFS spectra show that a better fit was obtained when assuming two oxygen shells located at different distances (Fig. 3A), similar to that found for La. In the previous examination of the Ce/ferrihydrite system, the *R* factor (Eq. (8)) was 0.056% determined from the fitting in the range of $R + \Delta R = 1.47$–2.42 Å which covered the first shell only (Nakada et al., 2013). Although the *R* factor itself was worse in the current analysis, the factor was determined in the range of $R + \Delta R = 1.00$–4.00 Å. The comparison in the *k*-space spectra clearly showed the improvement in the new fitting (Fig. 3A).

The Pr K-edge EXAFS spectra and their Fourier transform magnitudes also suggest two shells of oxygen atoms located at different distances; that is, distortion in the first coordination sphere (Table 3; Fig. 4). Similar to the case for the La and Ce/ferrihydrite systems, the Pr–O_1 bond of the adsorbed species was shorter than for Pr^{3+} in solution. The CN value of REE–O is correlated with the bond length (Shannon, 1976), which is consistent with the low CN value for the Pr/δ-MnO_2 system ($CN_1 + CN_2 = 7.6 \pm 1.3$) compared with that of the aqua complex ($CN = 10.4 \pm 1.6$).

In contrast with the La, Ce(III), and Pr systems, distortions were not observed in the first coordination sphere of Nd adsorbed on ferrihydrite or δ-MnO_2 (Table 3; Fig. 5). In the δ-MnO_2 system, the CN of the first coordination sphere is smaller than that of Nd^{3+} solution beyond analytical uncertainty, whereas the CN is identical within the analytical uncertainty for the ferrihydrite system. The Nd–O bond length is about 2.49, 2.48, and 2.46 Å for the Nd^{3+} solution, Nd adsorbed on ferrihydrite, and Nd adsorbed on δ-MnO_2 systems, respectively.

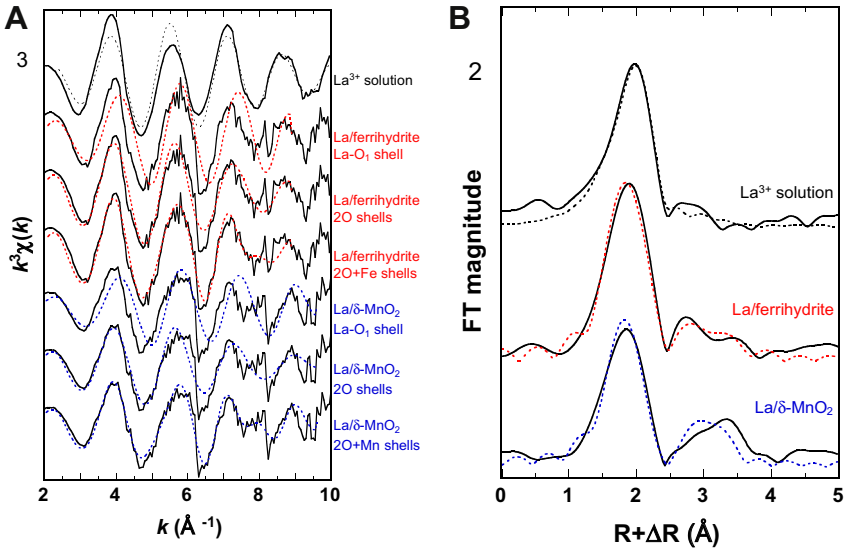

Fig. 2. (A) K^3-weighted La K-edge EXAFS spectra of samples and reference material (La^{3+} solution). The contributions of each shell are shown for La/ferrihydrite and δ-MnO_2 systems. (B) Radial structure functions (RSFs) of the samples and reference material (La^{3+} solution). In both figures, the solid lines represent the measurement data, and the dashed lines represent the fitting results.

Distorted coordination spheres were also not observed for the Sm systems (Table 3; Fig. 6). The Sm–O bond lengths in the ferrihydrite system and the Sm^{3+} solution are essentially identical (2.45 Å), whereas the Sm–O bond length in the δ-MnO_2 system is 2.41 Å, which is smaller than that of the aqua complex beyond the range of analytical uncertainty.

We also examined a possible formation of a distorted first coordination sphere for Nd and Sm (Table 3). Smaller *R* values were obtained by assuming two oxygen shells at different distances, however, in contrast with the La and Pr systems, the CN values for these systems differed by more than a factor of four ($CN(REE–O_2)/CN(REE–O_1) > 4.5$). The large differences between the two CNs suggest that the assumption of a distorted structure with two REE–O shells was not required to accurately fit the Nd and Sm EXAFS.

4. DISCUSSION

4.1. Isotopic fractionation between the liquid and solid phases

Similar to the case of Ce in Nakada et al. (2013), the isotopic fractionation for the Nd and Sm systems obeyed equilibrium fractionation. As for the degree of isotopic fractionation, adsorption in the ferrihydrite system showed less fractionation than that in the δ-MnO_2 system for Ce, Nd, and Sm. The most important result obtained in the Nd and Sm measurements was the preferential partitioning of heavier isotopes into the solid phases (Table 2, Fig. 1). This isotopic fractionation trend was different from that of Ce where it was reported that (i) Ce was not oxidized during adsorption on ferrihydrite, whereas Ce adsorbed on δ-MnO_2 was oxidized to the tetravalent state, and (ii) lighter isotope enrichment of the solid phase for Ce(III)/ferrihydrite may be accompanied with formation of an outer-sphere complex. Although Schauble (2007) suggested the possible enrichment of lighter Ce isotopes in reduced species during the $Ce^{3+} \rightarrow Ce^{4+}$ reaction may be due to nuclear-volume isotope fractionation, the Ce/ferrihydrite system was unaffected here by the oxidation reaction. A nuclear-volume driven effect was also reported for Nd and Sm (Fujii et al., 1998, 2000), but the current study shows that the $\delta^{145}Nd$ vs. $\delta^{146}Nd$ and $\delta^{149}Sm$ vs. $\delta^{152}Sm$ correlations are in accord with a purely mass-dependent isotope effect (Figs. EA2 and EA3), meaning that nuclear-volume driven fractionation was negligible in the experiments.

Fig. 7 summarizes α_{Lq-So} for the ferrihydrite and δ-MnO_2 systems with Ce, Nd, and Sm. The general trend previously observed for cations in the literature, such as Fe^{2+}, Cu^{2+}, and Zn^{2+}, suggests that heavier isotopes should be distributed in the solid phase during adsorption of REE^{3+} on metal oxides (e.g., Cacaly et al., 2004; Icopini et al., 2004; Clayton et al., 2005; Crosby et al., 2005; Pokrovsky et al., 2005; Balistrieri et al., 2008). Thus, it was found that Nd and Sm systems follow the expected trend but Ce does not. This isotopic fractionation contrasted with the Nd and Sm systems, indicating that a systematic change in a physicochemical factor among REEs (especially between Ce and Nd) is responsible for the different fractionations observed during the adsorption reactions. Even though REEs have similar chemical properties in a trivalent state, the direction of the isotopic fractionation can differ among light REEs (LREEs).

4.2. Coordination environment and isotopic fractionation

The most important rule governing stable isotopic fractionation is that the heavy isotopes of an element are concentrated in species with stronger bonds when two species with different bond lengths are in equilibrium (Bigeleisen

Table 3
Fitting results of EXAFS spectra for La, Ce, Pr, Nd, and Sm.

System	Shell	CN	R (Å)	σ^2 (Å^2)	R (%)
La^{3+} solution	La–O	12.5 ± 1.9	2.555 ± 0.012	0.011	0.57[c]
La/ferrihydrite[a]	La–O	8.3 ± 0.8	2.551 ± 0.019	0.010[†]	8.93[c]
	La–Fe	3.9 ± 0.5	3.513 ± 0.027	0.010[†]	10.1[d]
La/ferrihydrite[b]	La–O_1	3.5 ± 0.7	2.453 ± 0.020	0.010[†]	
	La–O_2	4.3 ± 0.8	2.548 ± 0.026	0.010[†]	0.68[c]
	La–Fe	3.5 ± 1.1	3.524 ± 0.030	0.010[†]	2.26[d]
La/δ-MnO_2[a]	La–O	5.9 ± 0.5	2.527 ± 0.016	0.009[†]	12.0[c]
	La–Mn	3.0 ± 0.8	3.506 ± 0.019	0.010[†]	15.7[d]
La/δ-MnO_2[b]	La–O_1	4.1 ± 0.7	2.459 ± 0.023	0.009[†]	
	La–O_2	2.7 ± 0.8	2.568 ± 0.021	0.009[†]	1.01[c]
	La–Mn	3.0 ± 1.0	3.528 ± 0.019	0.010[†]	4.25[d]
Ce^{3+} solution[f]	Ce–O	8.6 ± 1.3	2.521 ± 0.013	0.012	0.09[e]
Ce^{3+} solution	Ce–O	11.5 ± 0.9	2.535 ± 0.017	0.010	0.10[c]
Ce/ferrihydrite[f]	Ce–O	7.5 ± 1.3	2.526 ± 0.014	0.013	0.06[e]
Ce/ferrihydrite	Ce–O_1	4.7 ± 0.6	2.418 ± 0.022	0.011	
	Ce–O_2	5.3 ± 0.7	2.535 ± 0.025	0.010[†]	1.57[c]
	Ce–Fe	0.8 ± 0.3	3.531 ± 0.062	0.013	3.96[d]
Pr^{3+} solution	Pr–O	10.4 ± 1.6	2.500 ± 0.013	0.009	0.55[c]
Pr/ferrihydrite[a]	Pr–O	8.4 ± 1.5	2.472 ± 0.013	0.010[†]	10.4[c]
	Pr–Fe	1.1 ± 0.5	3.497 ± 0.028	0.010	13.3[d]
Pr/ferrihydrite[b]	Pr–O_1	4.4 ± 0.5	2.353 ± 0.027	0.010[†]	
	Pr–O_2	5.5 ± 0.5	2.499 ± 0.024	0.010[†]	2.23[c]
	Pr–Fe	0.9 ± 1.0	3.479 ± 0.047	0.009	6.16[d]
Pr/δ-MnO_2[a]	Pr–O	6.8 ± 0.5	2.431 ± 0.012	0.010[†]	2.61[c]
	Pr–Mn	2.0 ± 0.6	3.404 ± 0.059	0.010[†]	6.42[d]
Pr/δ-MnO_2[b]	Pr–O_1	3.7 ± 0.6	2.381 ± 0.018	0.010[†]	
	Pr–O_2	3.9 ± 0.8	2.481 ± 0.049	0.010[†]	1.71[c]
	Pr–Mn	0.7 ± 0.5	3.407 ± 0.053	0.010[†]	4.40[d]
Nd^{3+} solution	Nd–O	10.0 ± 1.5	2.487 ± 0.012	0.010	0.36[c]
Nd/ferrihydrite[a]	Nd–O	6.5 ± 1.1	2.484 ± 0.013	0.011	1.75[c]
	Nd–Fe	1.3 ± 0.4	3.342 ± 0.064	0.010[†]	2.96[d]
Nd/ferrihydrite[b]	Nd–O_1	0.8 ± 0.4	2.279 ± 0.043	0.010[†]	
	Nd–O_2	7.1 ± 0.6	2.494 ± 0.007	0.010[†]	1.00[c]
	Nd–Fe	1.4 ± 0.6	3.356 ± 0.024	0.010[†]	4.06[d]
Nd/δ-MnO_2[a]	Nd–O	5.7 ± 0.9	2.458 ± 0.012	0.010	7.99[c]
	Nd–Mn	1.0 ± 0.4	3.359 ± 0.068	0.010[†]	11.8[d]
Nd/δ-MnO_2[b]	Nd–O_1	1.1 ± 0.3	2.211 ± 0.022	0.010[†]	
	Nd–O_2	5.0 ± 0.5	2.490 ± 0.007	0.010[†]	1.16[c]
	Nd–Mn	0.9 ± 0.6	3.420 ± 0.041	0.010[†]	6.18[d]
Sm^{3+} solution	Sm–O	10.6 ± 1.5	2.445 ± 0.011	0.009	0.79[c]
Sm/ferrihydrite[a]	Sm–O	5.1 ± 0.8	2.447 ± 0.014	0.011	1.81[c]
	Sm–Fe	0.3 ± 0.4	3.337 ± 0.049	0.010	3.11[d]
Sm/ferrihydrite[b]	Sm–O_1	0.1 ± 1.2	2.264 ± 0.043	0.010[†]	
	Sm–O_2	5.4 ± 1.1	2.456 ± 0.024	0.010[†]	0.80[c]
	Sm–Fe	0.1 ± 0.9	3.352 ± 0.067	0.010[†]	2.26[d]
Sm/δ-MnO_2[a]	Sm–O	6.9 ± 1.0	2.413 ± 0.014	0.014	6.64[c]
	Sm–Mn	1.0 ± 1.4	3.349 ± 0.036	0.010[†]	8.80[d]
Sm/δ-MnO_2[b]	Sm–O_1	0.1 ± 0.2	2.143 ± 0.074	0.010[†]	
	Sm–O_2	4.7 ± 0.4	2.418 ± 0.007	0.010[†]	3.92[c]
	Sm–Mn	2.6 ± 0.6	3.373 ± 0.015	0.010[†]	5.55[d]

Note: CN denotes the coordination number; R (Å) denotes the distance from the center atom; σ is the Debye–Waller factor; R (%) is quality of fit (see Eq. (8)).

[a] Fitting results assuming one oxygen shell.
[b] Fitting results assuming two oxygen shells.
[c] Fitting from 1.00 to 2.50 Å in $R + \Delta R$ space.
[d] Fitting from 1.00 to 4.00 Å in $R + \Delta R$ space.
[e] Fitting from 1.42 to 2.43 Å in $R + \Delta R$ space.
[f] Fitting results reported in Nakada et al. (2013).
[†] The parameter was fixed in the EXAFS fitting.

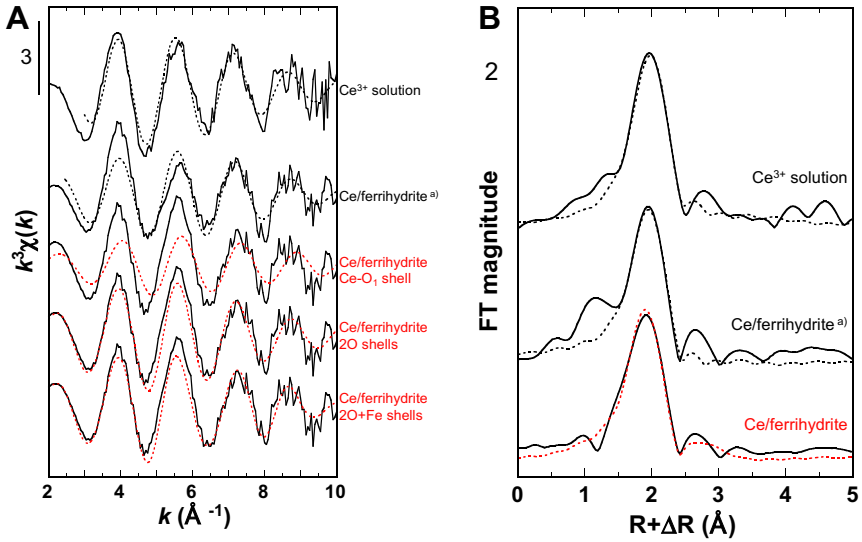

Fig. 3. (A) K^3-weighted Ce K-edge EXAFS spectra with the contributions of each shell and (B) RSF of the samples and reference material (Ce^{3+} solution). In both figures, the superscript (a) denotes the analysis performed by Nakada et al. (2013). The solid and dashed lines represent the measurement data and fitting results, respectively.

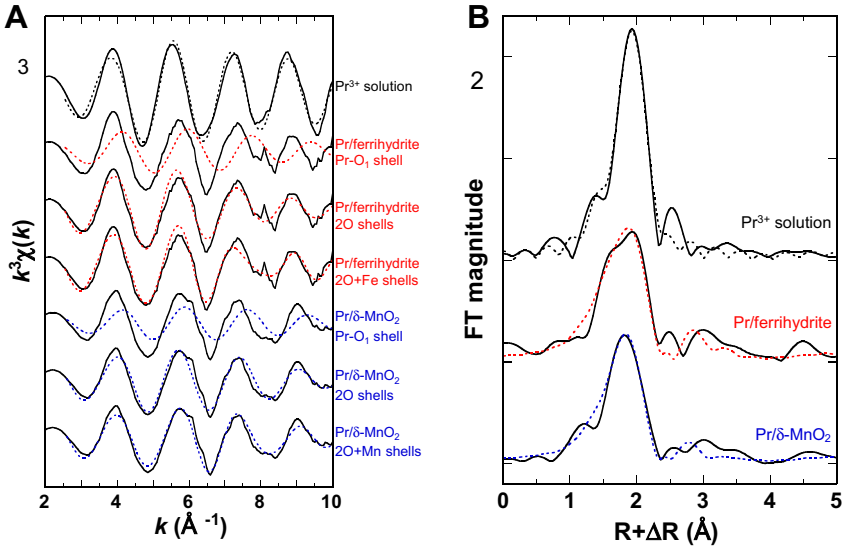

Fig. 4. (A) K^3-weighted Pr K-edge EXAFS spectra with the contributions of each shell and (B) RSF of the samples and reference material (Pr^{3+} solution). The solid and dashed lines represent the measurement data and fitting results, respectively.

and Mayer, 1947; O'Neil, 1986; Criss, 1999; Schauble, 2004). Considering that the REEs have similar chemical characteristics, the factors that control equilibrium isotopic fractionation may be considered similar among all trivalent REEs. The REEs examined in this study are in a trivalent state (except for Ce on δ-MnO_2), which indicates that isotopic fractionation is not caused by a redox change. In our results (Table 3), the CNs of REEs adsorbed on δ-MnO_2 were smaller than the CNs of the REE aqua ions, which is consistent with a shorter REE–O bond length in the REE/δ-MnO_2 system. The EXAFS spectra obtained for the Sm systems did not show large oscillations, which makes it difficult to discuss whether Sm forms an inner-sphere or outer-sphere complex. In the case of the Nd systems, inner-sphere complexes formed for both Nd adsorbed on ferrihydrite and δ-MnO_2 (Fig. 5), though the Nd/δ-MnO_2 system showed larger isotopic fractionation than the Nd/ferrihydrite system. Although it was not clear for the ferrihydrite systems, the smaller CN observed for the δ-MnO_2 systems and related shorter bond length was reflected in an increase in the ratio of inner-sphere to outer-sphere complexes. The increase of this ratio is consistent with the larger isotopic fractionation observed in the δ-MnO_2 systems. However, the precise determination of

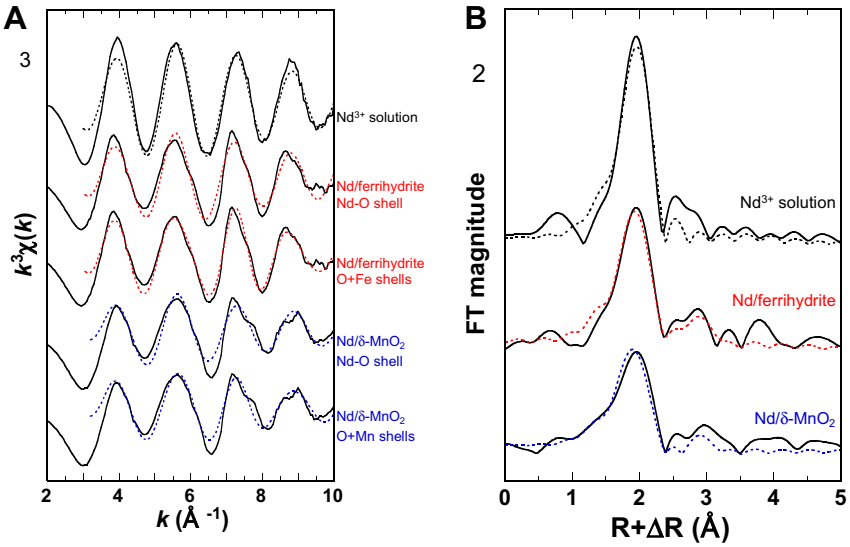

Fig. 5. (A) K^3-weighted Nd K-edge EXAFS spectra with the contributions of each shell and (B) RSF of the samples and reference material (Nd^{3+} solution). The solid and dashed lines represent the measurement data and fitting results, respectively.

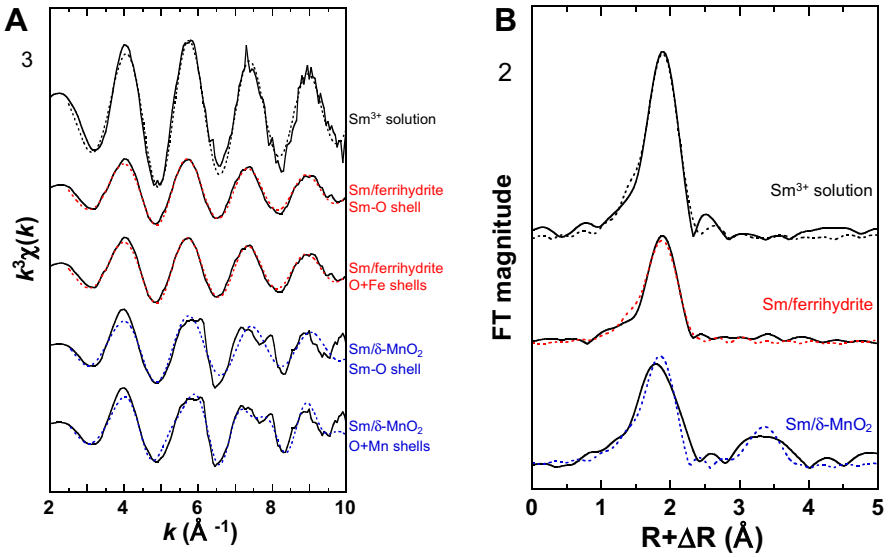

Fig. 6. (A) K^3-weighted Sm K-edge EXAFS spectra and (B) RSF of the samples and reference material (Sm^{3+} solution). The solid and dashed lines represent the measurement data and fitting results, respectively.

the CN, which is highly correlated with the Debye–Waller factor, was difficult in the EXAFS analyses, thus impeding discussion of the equilibrium isotopic fractionation of REEs based on the CN alone.

Hereafter, we focus on the interatomic distances of the REE–O bonds summarized in Fig. 8A. It should be noted that the interatomic distances for adsorbed La, Ce, and Pr are shown as weighted mean values based on CN_1 and CN_2 values. For the REE^{3+} aqua ions and ferrihydrite systems, the interatomic distance decreased as the atomic number increased, due to the lanthanide contraction. The lanthanide contraction was also observed for the δ-MnO_2 system except for Ce, which was oxidized to Ce(IV) during adsorption on δ-MnO_2. In Fig. 8B, the REE–O interatomic distances for the ferrihydrite and δ-MnO_2 systems are normalized to those of the REE^{3+} aqua ions. If this ratio is less than 1, the REE–O bond length has shortened due to adsorption of the REE on the Fe or Mn oxide surface. In the ferrihydrite system, the REE–O interatomic distances were almost identical (within analytical uncertainty) to those of the REE^{3+} aqua ions for Nd and Sm. In the δ-MnO_2 system, however, the REE–O distances were shorter than for the REE^{3+} solutions beyond analytical uncertainty. The shorter bond length indicates that REEs have stronger REE–O bonds during adsorption onto δ-MnO_2, thereby favoring the preferential enrichment of heavy iso-

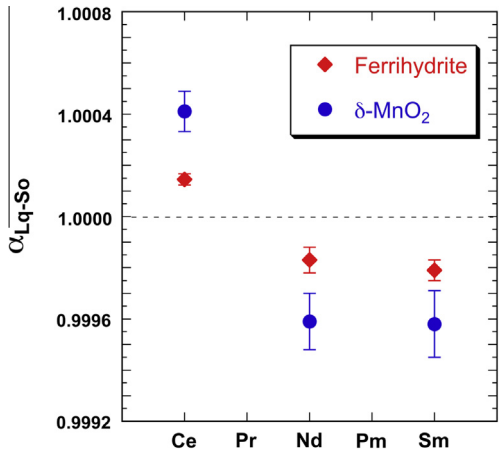

Fig. 7. Summary of factors of isotopic fractionation between liquid and solid phases (α_{Lq-So}) defined by Eqs (9) and (10). α_{Lq-So} values of the Ce system are cited from Nakada et al. (2013). By definition, $\alpha_{Lq-So} > 1$ indicates lighter-isotope enrichment in the solid phase. The error bar denotes the deviation (2σ) of five α_{Lq-So} values measured at various F_{ad}.

topes in the solid phase for these elements, as was observed for Nd and Sm in our isotopic measurements (Table 2, Figs. 1 and 7). Therefore, we propose that the interatomic distance between the REEs and the first coordinated atom (oxygen) is the main factor that affects the equilibrium isotopic fractionation of Nd and Sm. The larger isotopic fractionation observed for the δ-MnO_2 system compared with the ferrihydrite system is likely due to the shorter REE–O bond lengths of REE adsorbed on δ-MnO_2.

In the case of La, EXAFS analysis showed two oxygen shells in the first coordination sphere for both the ferrihydrite and δ-MnO_2 systems (Table 3, Fig. 2). A better fit was obtained by assuming two oxygen atoms at different distances in the first coordination sphere, suggesting that the coordination structure is more distorted than that of the La^{3+} aqua ion. The distorted structures of adsorbed La and Pr species found in this study and by Ohta et al. (2009) imply that the distortion is also expected to be observed in the first coordination sphere of the Ce/ferrihydrite system, as identified in this study. The enrichment of lighter isotopes (by ca. 0.15‰) in adsorbed Ce species can be related to the distorted structure of Ce on ferrihydrite. Although we were unable to resolve La isotope compositions at the required level of precision, the distortion seen in the first coordination sphere of the La/ferrihydrite and La/δ-MnO_2 systems suggests that a light isotope enrichment is to be expected for La in the solid phase.

Isotopic fractionation caused by a distorted adsorbed structure has also been reported for other elements. The formation of highly distorted bidendate complexes is thought to explain the light isotopic composition of adsorbed trigonal boron (Lemarchand et al., 2007). Juillot et al. (2008) found a smaller fractionation for octahedral Zn adsorbed to goethite relative to the free Zn^{2+} ion hydrated by six water molecules. They suggested that the distortion of the octahedral environment of Zn when sharing oxygens with Fe atoms may account for the small fractionation on goethite. A similar case was also reported for Mo systems (Kashiwabara et al., 2011; Wasylenki et al., 2011). These results are consistent with our observations for the isotopic fractionation of Ce.

Not only the species adsorbed on the solid phase but also the stability in the liquid phase can cause the contrasting stable isotopic fractionation. Kawabe (1999) compared the standard Gibbs free energy changes of the nonahydrated REE relative to isostructural $REE(H_2O)_8^{3+}$ species of REE^{3+} from La^{3+} to Gd^{3+}. The Gibbs free energy changes were reported to be −7.16, −5.27, −4.09, −3.02, −0.67, −0.17, and −0.06 kJ/mol for La^{3+}, Ce^{3+}, Pr^{3+}, Nd^{3+}, Sm^{3+}, Eu^{3+}, and Gd^{3+}, respectively. These results indicate that the hydrated state is extraordinarily stable in terms of both Gibbs free energy and enthalpy for La^{3+} and Ce^{3+} compared to Nd^{3+} and Sm^{3+}, which reflects stabilization by the formation of stronger chemical bonds in the compounds. This effect is suggested to be responsible for the much lower K_d, partition coefficient of REE between solid and liquid phases, of La^{3+} and Ce^{3+} adsorption on ferrihydrite and δ-MnO_2 compared with heavier REE^{3+} (Kawabe et al., 1999; Ohta and Kawabe, 2000). In other words, the

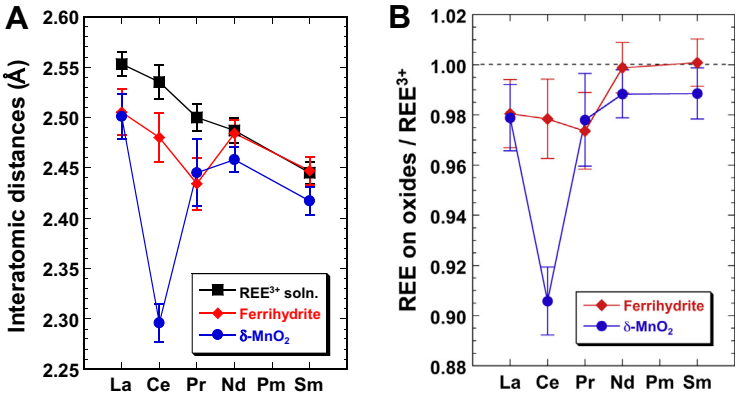

Fig. 8. (A) Summary of interatomic distances between REE–O bonds. Data for the Ce/δ-MnO_2 system are cited from Nakada et al. (2013). The interatomic distances of La/ferrihydrite, La/δ-MnO_2, Ce/ferrihydrite, Pr/ferrihydrite, and Pr/δ-MnO_2 are shown as weighted mean values. (B) REE–O bond lengths of adsorption systems (ferrihydrite and mδ-MnO_2) normalized to the bond length of the REE^{3+} aqua ion using the data shown in Fig. 8A. A ratio smaller than 1 indicates shortening of the bond length relative to the aqua ion.

lower stability of the adsorbed species is due to the higher stability of the hydrated species in the aqueous phase. The new results, which include a comparison among REEs, suggest that the factors governing the lighter isotope enrichment of Ce (and possibly La) on the solid phase are (i) the distorted structure of La^{3+}, Ce^{3+}, and Pr^{3+} adsorbed on the solid phases; and (ii) the higher stability of the hydrated species. We suggest that these anomalies for La and Ce in terms of thermodynamic and structural characteristics affect not only K_d but also the isotopic fractionation incurred during adsorption.

4.3. Geochemical implications

The results of this study suggest that REE partitioning between solid and aqueous phases can cause contrasting stable isotopic fractionation for Ce(III) vs. Nd and Sm. The contrasting fractionation of Ce vs. Nd and Sm may not be seen in other reactions such as magmatic processes without solid–water interactions, because the fractionation should occur with the change of coordination environment of the REE such as in an adsorption reaction. Adsorption reactions are important in the geochemical behavior of REEs at the Earth's surface, since REEs are readily adsorbed on various types of suspended matter and solid phases in rivers and seawater. In particular, our findings on the contrasting fractionation between Ce vs. Nd and Sm isotopes during adsorption on ferrihydrite and δ-MnO_2 can improve our understanding of REE behavior when considering that ferromanganese deposits are the major sink for REEs in the marine environment (e.g., Piper, 1974; Elderfield et al., 1981; Bau et al., 1996). In addition, the stable hydrated states of Ce^{3+} (and La^{3+}) can explain the preferential adsorption of lighter isotopes on the solid phase. Hence, the difference in the direction of the isotopic fractionations among LREEs is a new indicator of water–rock interactions inherent in the formation of natural REE-bearing samples.

However, the isotopic fractionation factor obtained in this study may be subject to change when a similar experiment is performed at higher pH depending on the dominance of different soluble species such as REE carbonate complexes. In addition, the possible occurrence of nuclear-volume isotope fractionation cannot be ignored in the natural environment. For example, according to Bigeleisen and Mayer (1947), mass dependent isotopic fractionation of Tl should be about 1/15th to that of Fe. In contrast, Rehkämper et al. (2002) showed approximately 2‰ fractionation for Tl isotopes between seawater and hydrogenetic Fe–Mn crusts. Thus, while the work presented here improves our knowledge of the processes behind systematic isotopic fractionation of selected REEs during adsorption on two common mineral phases, further work is required to elucidate the dominant mechanisms governing isotopic fraction of heavy elements in the natural environment.

5. CONCLUSIONS

Adsorption experiments with Nd and Sm on ferrihydrite and δ-MnO_2 were performed in this study to determine the factors governing equilibrium isotopic fractionation among REEs. Heavier isotopes of Nd and Sm were found to be enriched in the solid phase. EXAFS analyses showed that shortening of REE–O bonds during adsorption was the governing factor responsible for equilibrium isotopic fractionation of Nd and Sm. In contrast, the coordination structures of adsorbed La, Ce, and Pr were more distorted than those of their aqua ions. This comparison among the REEs enables us to improve our understanding of the cause of such stable isotopic fractionation. The distorted adsorbed structure and the stability of hydrated species leads to lighter-isotope enrichment in the solid phase for Ce (and is also expected for La) adsorbed on ferrihydrite. In-depth analysis of the coordination environment, revealed by EXAFS analyses, was important to determining the mechanisms behind equilibrium isotopic fractionation. It is possible that the systematic isotopic fractionation over the REE series could be a new geochemical tool which can be used to study REE behavior during water–rock interaction in natural systems.

ACKNOWLEDGEMENTS

We would like to thank Dr. Andrew Gault (Queen's University, Canada) for his comments that improved the manuscript greatly. Beam time for EXAFS analysis of the La, Pr, Nd, and Sm systems was performed with the approval of JASRI (Proposal Nos. 2010B1347, 2010B1295, and 2011B1279). This study was supported by the JSPS Research Fellowships for Young Scientists. The authors are grateful to Prof. Mark Rehkämper, AE of this manuscript, and anonymous reviewers for providing suggestions and comments that helped improve the manuscript.

APPENDIX A. SUPPLEMENTARY DATA

Supplementary data associated with this article can be found, in the online version, at http://dx.doi.org/10.1016/j.gca.2013.07.014.

REFERENCES

Anbar A. D. (2004) Molybdenum stable isotopes: observations, interpretations and directions. In *Geochemistry of Non-Traditional Stable Isotopes*, vol. 55 (eds. C. M. Johnson, B. L. Beard and F. Albarède). Mineralogical Society of America and Geochemical Society, Washington, pp. 429–454.

Anbar A. D. and Rouxel O. (2007) Metal stable isotopes in paleoceanography. *Annu. Rev. Earth Planet. Sci.* **35**, 717–746.

Balistrieri L. S., Borrok D. M., Wanty R. B. and Ridley W. I. (2008) Fractionation of Cu and Zn isotopes during adsorption onto amorphous Fe(III) oxyhydroxide: experimental mixing of acid rock drainage and ambient river water. *Geochim. Cosmochim. Acta* **72**, 311–328.

Barling J. and Anbar A. D. (2004) Molybdenum isotope fractionation during adsorption by manganese oxides. *Earth Planet. Sci. Lett.* **217**, 315–329.

Barling J., Arnold G. L. and Anbar A. D. (2001) Natural mass-dependent variations in the isotopic composition of molybdenum. *Earth Planet. Sci. Lett.* **193**, 447–457.

Bau M., Koschinsky A., Dulski P. and Hein J. R. (1996) Comparison of the partitioning behaviours of yttrium, rare earth elements, and titanium between hydrogenetic marine

ferromanganese crusts and seawater. *Geochim. Cosmochim. Acta* **60**, 1709–1725.

Beard B. L. and Johnson C. M. (2004) Fe isotope variations in the modern and ancient Earth and other planetary bodies. In *Geochemistry of Non-Traditional Stable Isotopes*, vol. 55 (eds. C. M. Johnson, B. L. Beard and F. Albarède). Mineralogical Society of America and Geochemical Society, Washington, pp. 319–357.

Bigeleisen J. and Mayer M. G. (1947) Calculation of equilibrium constants for isotopic exchange reactions. *J. Chem. Phys.* **15**, 261–267.

Butler I. B., Archer C., Vance D., Oldroyd A. and Rickard D. (2005) Fe isotope fractionation on FeS formation in ambient aqueous solution. *Earth Planet. Sci. Lett.* **236**, 430–442.

Byrne R. H. and Sholkovitz E. R. (1996) Marine chemistry and geochemistry of the lanthanides. In *Handbook on the Physics and Chemistry of Rare Earth*, vol. 23 (eds. , Jr.K. A. Gschneidner and L. Eyring). Elsevier Science B.V., pp. 497–593.

Cacaly S., Marechal C., Juillot F., Guyot F. and Benedetti M. (2004) Zn isotopes fractionation upon sorption and precipitation. *Geochim. Cosmochim. Acta* **68**, A366.

Clayton R. E., Hudson-Edwards K. A. and Houghton S. L. (2005) Isotopic effects during Cu adsorption onto goethite. *Geochim. Cosmochim. Acta* **69**, A216.

Criss R. E. (1999) *Principles of stable isotope distribution*. Oxford University Press, Inc., New York, p. 254.

Crosby H. A., Johnson C. A., Roden E. E. and Beard B. L. (2005) Coupled Fe(II)–Fe(III) electron and atom exchange as a mechanism for Fe isotope fractionation during dissimilatory iron oxide reduction. *Environ. Sci. Technol.* **39**, 6698–6704.

de Laeter J. R., Böhlke J. K., De Bièvre P., Hidaka H., Peiser H. S., Rosman K. J. R. and Taylor P. D. P. (2003) Atomic weights of the elements: Review 2000 (IUPAC Technical Report). *Pure Appl. Chem.* **75**, 683–799.

De La Rocha C. L., Brzezinski M. A. and DeNiro M. J. (2000) A first look at the distribution of the stable isotopes of silicon in natural waters. *Geochim. Cosmochim. Acta* **64**, 2467–2477.

Elderfield H. and Greaves M. J. (1982) The rare earth elements in seawater. *Nature* **296**, 214–219.

Elderfield H., Hawkesworth C. J., Greaves M. J. and Calvert S. E. (1981) Rare earth element geochemistry of oceanic ferromanganese nodules and associated sediments. *Geochim. Cosmochim. Acta* **45**, 513–528.

Ellis A. S., Johnson T. M. and Bullen T. D. (2002) Chromium isotopes and the fate of hexavalent chromium in the environment. *Science* **295**, 2060–2062.

Ellis A. S., Johnson T. M. and Bullen T. D. (2004) Using chromium stable isotope ratios to quantify Cr(VI) reduction: lack of sorption effects. *Environ. Sci. Technol.* **38**, 3604–3607.

Foster A. L., Brown G. E. and Parks G. A. (2003) X-ray absorption fine structure study of As(V) and Se(IV) sorption complexes on hydrous Mn oxides. *Geochim. Cosmochim. Acta* **67**, 1937–1953.

Frei R., Gaucher C., Poulton S. W. and Canfield D. E. (2009) Fluctuations in Precambrian atmospheric oxygenation recorded by chromium isotopes. *Nature* **461**, 250–253.

Fujii T., Yamamoto T., Nishizawa K., Inagawa J., Gunji K. and Watanabe K. (1998) Separation of samarium isotopes by a crown ether. *Solvent Extr. Ion Exch.* **16**, 985–999.

Fujii T., Yamamoto T., Inagawa J., Gunji K., Watanabe K. and Nishizawa K. (2000) Nuclear size and shape effect in chemical isotope enrichment of neodymium using dicyclohexano-18-crown-6. *Solvent Extr. Ion Exch.* **18**, 1155–1166.

Galy A., Pokrovsky O. S. and Schott J. (2002) Ge-isotopic fractionation during its sorption on goethite: an experimental study. *Geochim. Cosmochim. Acta* **66**, A259.

Gussone N., Böhm F., Eisenhauer A., Dietzel M., Heuser A., Teichert B. M. A., Reitner J., Wörheide G. and Dullo W.-C. (2005) Calcium isotope fractionation in calcite and aragonite. *Geochim. Cosmochim. Acta* **69**, 4485–4494.

Halliday A. N., Lee D.-C., Christensen J. N., Rehkämper M., Yi W., Luo X., Hall C. M., Ballentine C. J., Pettke T. and Stirling C. (1998) Applications of multiple collector-ICPMS to cosmochemistry, geochemistry, and paleoceanography. *Geochim. Cosmochim. Acta* **62**, 919–940.

Henderson P. (1984) *Rare Earth Element Geochemistry*. Elsevier, Amsterdam, p. 510.

Icopini G. A., Anbar A. D., Ruebush S. S., Tien M. and Brantley S. L. (2004) Iron isotope fractionation during microbial reduction of iron: the importance of adsorption. *Geology* **32**, 205–208.

Johnson C. M., Beard B. L. and Albarède F. (2004b) *Geochemistry of Non-traditional Stable Isotopes*. Mineralogical Society of America and Geochemical Society, Washington, p. 454.

Johnson C. M., Beard B. L., Roden E. E., Newman D. K. and Nealson K. H. (2004a) Isotopic constraints on biogeochemical cycling of Fe. In *Geochemistry of Non-Traditional Stable Isotopes*, vol. 55 (eds. C. M. Johnson, B. L. Beard and F. Albarède). Mineralogical Society of America and Geochemical Society, Washington, pp. 359–408.

Johnson T. M. and Bullen T. D. (2004) Mass-dependent fractionation of selenium and chromium isotopes in low-temperature environments. In *Geochemistry of Non-Traditional Stable Isotopes*, vol. 55 (eds. C. M. Johnson, B. L. Beard and F. Albarède). Mineralogical Society of America and Geochemical Society, Washington, pp. 289–318.

Johnson T. M., Herbel M. J., Bullen T. D. and Zawislanski P. T. (1999) Selenium isotope ratios as indicators of selenium sources and oxyanion reduction. *Geochim. Cosmochim. Acta* **63**, 2775–2783.

Juillot F., Maréchal C., Ponthieu M., Cacaly S., Morin G., Benedetti M., Hazemann J. L., Proux O. and Guyot F. (2008) Zn isotopic fractionation caused by sorption on goethite and 2-lines ferrihydrite. *Geochim. Cosmochim. Acta* **72**, 4886–4900.

Kashiwabara T., Takahashi Y., Tanimizu M. and Usui A. (2011) Molecular-scale mechanisms of distribution and isotopic fractionation of molybdenum between seawater and ferromanganese oxides. *Geochim. Cosmochim. Acta* **75**, 5762–5784.

Kawabe I. (1999) Thermochemical parameters for solution of lanthanide(III) ethylsulphate and trichloride hydrate series: tetrad effects and hydration change in aqua Ln^{3+} ion series. *Geochem. J.* **33**, 249–265.

Kawabe I., Ohta A., Ishii S., Tokumura M. and Miyauchi K. (1999) REE partitioning between Fe–Mn oxyhydroxide precipitates and weakly acid NaCl solutions: convex tetrad effect and fractionation of Y and Sc from heavy lanthanides. *Geochem. J.* **33**, 167–179.

Lemarchand E., Schott J. and Gaillardet J. (2007) How surface complexes impact boron isotope fractionation: evidence from Fe and Mn oxides sorption experiments. *Earth Planet. Sci. Lett.* **260**, 277–296.

Luo Y.-R. and Byrne R. H. (2004) Carbonate complexation of yttrium and the rare earth elements in natural waters. *Geochim. Cosmochim. Acta* **68**, 691–699.

Maréchal C. N., Télouk P. and Albarède F. (1999) Precise analysis of copper and zinc isotopic compositions by plasma-source mass spectrometry. *Chem. Geol.* **156**, 251–273.

Mason T. F. D., Weiss D. J., Chapman J. B., Wilkinson J. J., Tessalina S. G., Spiro B., Horstwood M. S. A., Spratt J. and

Coles () Zn and Cu isotopic variability in the Alexandrinka volcanic-hosted massive sulphide (VHMS) ore deposit, Urals, Russia. *Chem. Geol.* **221**, 170–187.

Möller P., Dulski P. and Bau M. (1994) Rare-earth element adsorption in a seawater profile above the East Pacific Rise. *Chem. Erde* **54**, 129–149.

Moynier F., Pichat S., Pons M.-L., Fike D., Balter V. and Albarède F. (2009) Isotopic fractionation and transport mechanisms of Zn in plants. *Chem. Geol.* **267**, 125–130.

Nakada R., Takahashi Y. and Tanimizu M. (2013) Isotopic and speciation study on cerium during its solid–water distribution with implication for Ce stable isotope as a paleo-redox proxy. *Geochim. Cosmochim. Acta* **103**, 49–62.

Nielsen S. G., Mar-Gerrison S., Gannoun A., LaRowe D., Klemm V., Halliday A. N., Burton K. and Hein J. R. (2009) Thallium isotope evidence for a permanent increase in marine organic carbon export in the early Eocene. *Earth Planet. Sci. Lett.* **278**, 297–307.

Nordstrom D. K., Plummer L. N., Langmuir D., Busenberg E. and May H. M. (1990) Revised chemical equilibrium data for major water-mineral reactions and their limitations. In *Chemical Modeling of Aqueous Systems II*, vol. 416 (eds. D. C. Melchior and R. L. Bassett). Am. Chem. Soc. Ser., pp. 398–413.

O'Day P. A., Rehr J. J., Zabinsky S. I. and Brown G. E. (1994) Extended X-ray absorption fine structures (EXAFS) analysis of disorder and multiple scattering in complex crystalline solids. *J. Am. Chem. Soc.* **116**, 2938–2949.

Ohta A. and Kawabe I. (2000) Theoretical study of tetrad effects observed in REE distribution coefficients between marine Fe–Mn deposit and deep seawater, and in REE(III)-carbonate complexation constants. *Geochem. J.* **34**, 455–473.

Ohta A., Kagi H., Nomura M., Tsuno H. and Kawabe I. (2009) Coordination study of rare earth elements on Fe oxyhydroxide and Mn dioxides: Part I. Influence of a multi-electron excitation on EXAFS analyses of La, Pr, Nd, and Sm. *Am. Mineral.* **94**, 467–475.

O'Neil J. R. (1986) Theoretical and experimental aspects of isotopic fractionation. In *Stable Isotopes in High Temperature Geological Processes*, vol. 16 (eds. J. W. Valley, , Jr.H. P. Taylor and J. R. O'Neil). Mineralogical Society of America, Washington, pp. 1–40.

Piepgras D. J. and Jacobsen S. B. (1992) The behavior of rare earth elements in seawater: precise determinations of variations in the North Pacific water column. *Geochim. Cosmochim. Acta* **56**, 1851–1862.

Piper D. Z. (1974) Rare-earth elements in sedimentary cycle – Summary. *Chem. Geol.* **14**, 285–304.

Pokrovsky O. S., Viers J. and Freydier R. (2005) Zn stable isotope fractionation during its adsorption on oxides and hydroxides. *J. Colloid Interface Sci.* **291**, 192–200.

Rehkämper M., Frank M., Hein J. R. and Halliday A. (2004) Cenozoic marine geochemistry of thallium deduced from isotopic studies of ferromanganese crusts and pelagic sediments. *Earth Planet. Sci. Lett.* **219**, 77–91.

Rehkämper M., Frank M., Hein J. R., Porcelli D., Halliday A., Ingri J. and Liebetrau V. (2002) Thallium isotope variations in seawater and hydrogenetic, diagenetic, and hydrothermal ferromanganese deposits. *Earth Planet. Sci. Lett.* **197**, 65–81.

Rouxel O., Ludden J. and Fouquet Y. (2003) Antimony isotope variations in natural systems and implications for their use as geochemical tracers. *Chem. Geol.* **200**, 25–40.

Schauble E. A. (2004) Applying stable isotope fractionation theory to new systems. In *Geochemistry of Non-Traditional Stable Isotopes*, vol. 55 (eds. C. M. Johnson, B. L. Beard and F. Albarède). Mineralogical Society of America and Geochemical Society, Washington, pp. 65–111.

Schauble E. A. (2007) Role of nuclear volume in driving equilibrium stable isotope fractionation of mercury, thallium, and other very heavy elements. *Geochim. Cosmochim. Acta* **71**, 2170–2189.

Schwertmann U. and Cornell R. M. (2000) *Iron Oxides in the Laboratory*, second ed. Wiley-VCH, p. 103.

Shannon R. D. (1976) Revised effective ionic radii and systematic studies of interatomic distances in halides and chalcogenides. *Acta Crystallogr.* **A32**, 751–767.

Shen J. J.-S., Lee T. and Chang C.-T. (1994) Lanthanum isotopic composition of meteoritic and terrestrial matter. *Geochim. Cosmochim. Acta* **58**, 1499–1506.

Tanimizu M., Araki Y., Asaoka S. and Takahashi Y. (2011) Determination of natural isotopic variation in antimony using inductively coupled plasma mass spectrometry for an uncertainty estimation of the standard atomic weight of antimony. *Geochem. J.* **45**, 27–32.

Taylor S. R. and McLennan S. M. (1988) The significance of the rare earths in geochemistry and cosmochemistry. In *Handbook on the Physics and Chemistry of Rare Earths*, vol. 11 (eds. , Jr.K. A. Gschneidner and L. Eyring). Elsevier, Amsterdam, pp. 485–578.

Wasylenki L. E., Weeks C. L., Bargar J. R., Spiro T. G., Hein J. R. and Anbar A. D. (2011) The molecular mechanism of Mo isotope fractionation during adsorption to birnessite. *Geochim. Cosmochim. Acta* **75**, 5019–5031.

Weyer S. and Schwieters J. B. (2003) High precision Fe isotope measurements with high mass resolution MC-ICPMS. *Int. J. Mass Spectrom.* **226**, 355–368.

Wieser M. E. and Schwieters J. B. (2005) The development of multiple collector mass spectrometry for isotope ratio measurements. *Int. J. Mass Spectrom.* **242**, 97–115.

Zabinsky S. I., Rehr J. J., Ankudinov A., Albers R. C. and Eller M. J. (1995) Multiple-scattering calculations of X-ray-absorption spectra. *Phys. Rev. B* **52**, 2995–3009.

Associate editor: Mark Rehkamper

参考論文

(1) G. Etiope, R. Nakada, K. Tanaka, N. Yoshida (2011)
Gas seepage from Tokamachi mud volcanoes, onshore Niigata Basin (Japan): Origin, post-genetic alterations and CH_4-CO_2 fluxes.
Applied Geochemistry, 26 (3), 348−359.

Volume 26, issue 3, March 2011 ISSN 0883-2927

ELSEVIER

Applied Geochemistry

JOURNAL OF THE INTERNATIONAL ASSOCIATION OF GEOCHEMISTRY

Continued on outside back cover

Applied Geochemistry 26 (2011) 348–359

Contents lists available at ScienceDirect

Applied Geochemistry

journal homepage: www.elsevier.com/locate/apgeochem

Gas seepage from Tokamachi mud volcanoes, onshore Niigata Basin (Japan): Origin, post-genetic alterations and CH_4–CO_2 fluxes

G. Etiope [a,*], R. Nakada [b], K. Tanaka [c], N. Yoshida [d]

[a] Istituto Nazionale di Geofisica e Vulcanologia, via V. Murata 605, 00143 Roma, Italy
[b] Dept. of Earth and Planetary Systems Science, Graduate School of Science, Hiroshima University, Japan
[c] Graduate School of Science and Engineering, Yamaguchi University, Japan
[d] Dept. of Environmental Chemistry & Engineering, Tokyo Institute of Technology, Japan

ARTICLE INFO

Article history:
Received 8 October 2010
Accepted 22 December 2010
Available online 28 December 2010
Editorial handling by R. Fuge

ABSTRACT

Methane and CO_2 emissions from the two most active mud volcanoes in central Japan, Murono and Kamou (Tokamachi City, Niigata Basin), were measured in from both craters or vents (macro-seepage) and invisible exhalation from the soil (mini- and microseepage). Molecular and isotopic compositions of the released gases were also determined. Gas is thermogenic ($\delta^{13}C_{CH4}$ from −32.9‰ to −36.2‰), likely associated with oil, and enrichments of ^{13}C in CO_2 ($\delta^{13}C_{CO2}$ up to +28.3‰) and propane ($\delta^{13}C_{C3H8}$ up to −8.6‰) suggest subsurface petroleum biodegradation. Gas source and post-genetic alteration processes did not change from 2004 to 2010. Methane flux ranged within the orders of magnitude of 10^1–10^4 g m^{-2} d^{-1} in macro-seeps, and up to 446 g m^{-2} d^{-1} from diffuse seepage. Positive CH_4 fluxes from dry soil were widespread throughout the investigated areas. Total CH_4 emission from Murono and Kamou were estimated to be at least 20 and 3.7 ton a^{-1}, respectively, of which more than half was from invisible seepage surrounding the mud volcano vents. At the macro-seeps, CO_2 fluxes were directly proportional to CH_4 fluxes, and the volumetric ratios between CH_4 flux and CO_2 flux were similar to the compositional CH_4/CO_2 volume ratio. Macro-seep flux data, in addition to those of other 13 mud volcanoes, supported the hypothesis that molecular fractionation (increase of the "Bernard ratio" $C_1/(C_2 + C_3)$) is inversely proportional to gas migration fluxes. The CH_4 "emission factor" (total measured output divided by investigated seepage area) was similar to that derived in other mud volcanoes of the same size and activity. The updated global "emission-factor" data-set, now including 27 mud volcanoes from different countries, suggests that previous estimates of global CH_4 emission from mud volcanoes may be significantly underestimated.

1. Introduction

Mud volcanoes in sedimentary basins are surface manifestations of underground pressurised fluids (gas and water) that may be linked to petroleum accumulations (oil and gas), even of commercial importance (e.g., Rhakmanov, 1987; Deville et al., 2003; Milkov, 2005; Etiope et al., 2009a). Mud volcanoes also represent a natural atmospheric source of CH_4, which is a powerful greenhouse gas (Dimitrov, 2003; Etiope and Milkov, 2004; Etiope et al., 2008). Gas origin has been assessed for many onshore and offshore mud volcanoes worldwide (e.g., Deville et al., 2003; Etiope et al., 2004a; 2007b; Yang et al., 2004; Stadnitskaia et al. 2008; Kikvadze et al., 2010; Sun et al., 2010). A global data-set of more than 140 onshore mud volcanoes from 12 countries shows that in 76% of cases gas is thermogenic, 20% mixed and only 4% microbial (Etiope et al., 2009a). This means that mud volcanism is generally associated with deep source rocks and hydrocarbons which have entered the catagenetic and oil window (temperatures typically above 60 °C; Hunt, 1996). Mud volcano gases can also exhibit signals of petroleum biodegradation, which is an important alteration process with major economic consequences for oil and gas production (Aitken et al., 2004; Pallasser, 2000). Gas associated with petroleum biodegradation processes has a typical fingerprint characterised by high C_2/C_3 (ethane/propane), ^{13}C enrichment in propane (C_3H_8), due to preferential degradation of C_3, and ^{13}C enrichment in CO_2 (positive $\delta^{13}C_{CO2}$ value) due to secondary methanogenesis which follows anaerobic biodegradation of heavy hydrocarbons (e.g., Pallasser, 2000; Etiope et al., 2009b). Recognizing these signals in mud volcanoes, or in other types of gas seeps, in frontier or unexplored areas, would, therefore, reveal the underground reservoir conditions without drilling.

The amount of gas released to the atmosphere, however, has been thoroughly measured only in a limited number of mud volcanoes: in Romania (Etiope et al., 2004a; Spulber et al., 2010),

* Corresponding author. Tel.: +39 0651860394.
E-mail address: etiope@ingv.it (G. Etiope).

0883-2927/$ - see front matter © 2010 Elsevier Ltd. All rights reserved.
doi:10.1016/j.apgeochem.2010.12.008

Azerbaijan (Etiope et al., 2004b; Kopf et al., 2009), Italy (Etiope et al., 2007b) and Taiwan (Yang et al., 2004; Chang et al., 2010; Chao et al., 2010). Flux measurements are generally based on closed-chamber methods and various techniques for determining the gas output from bubble plumes (e.g., flux-meters, inverted bottles). Only very approximate and indirect estimates are available for gas outputs during eruptions (e.g., Guliyev and Feizullayev, 1997). The CH_4 fluxes are typically expressed in mg m^{-2} d^{-1} (in analogy with other natural CH_4 sources or sinks), and in kg d^{-1} or ton a^{-1} for individual gas vents (point sources). The total gas emission from a mud volcano would then be the sum of all point sources (vents) plus the total output from diffuse seepage. The total emission divided by the seepage area gives the "emission factor": it is the key parameter typically used to extrapolate gas emissions from natural or anthropogenic sources on regional or global scale, e.g., for emission inventories of agricultural or natural ecosystems, as recommended by the air pollutant emission guidebook of the European Environment Agency (EMEP-EEA, 2009; Etiope et al., 2007a). For mud volcanoes, emission factors seem to range in the order of 10^2–10^3 ton km^{-2} a^{-1} (Etiope and Milkov, 2004; Etiope et al., 2008). Such a range, disaggregated for different sizes of mud volcanoes, was used to derive a global estimate of CH_4 emission of about 6–9 Mt a^{-1} (Etiope and Milkov, 2004). Differently from previous estimates (e.g., Dimitrov, 2003), this evaluation was the first based on direct flux measurements including the diffuse exhalation of gas around the mud volcano vents. Since the first flux surveys performed by closed-chamber method (Etiope et al., 2002) it was evident, in fact, that CH_4 is released to the atmosphere not only from the visible manifestations (=macro-seepage: craters, gryphons, bubbling pools), but also through a diffuse, invisible but widespread seepage from the ground (mud or soil), even at large distances (orders of tens of meters) from vents: such a seepage can be referred to as "miniseepage" and "microseepage" (Spulber et al., 2010). The three levels of seepage can be defined as follows:

(a) *Macro-seepage*: Localized gas flux from the vents of a gas or gas-oil seep (from bubbles in a pool, or high degassing from the ground, often flammable, focused in a small area); CH_4 flux is in the order of 10^3–10^6 mg m^{-2} d^{-1} or, in terms of output, may range from 10^{-2} to 10^3 ton a^{-1} from individual vents (e.g., Etiope, 2009); macro-seeps can have strong odors and induce abnormal snowmelt patterns.
(b) *Miniseepage*: Pervasive, medium–high gas flux (typically hundreds to thousands of mg m^{-2} d^{-1}), generally surrounding the macro-seeps but it can also be independent of seep occurrence; it can stress vegetation and flood the soil with gas.
(c) *Microseepage*: Pervasive, low CH_4 fluxes from soil (typically units up to hundreds of mg m^{-2} d^{-1}) more distant from seeps or independent of seep occurrence; it can induce the production in the soil of secondary carbonate from oxidizing CH_4, secondary mineralization and abnormal methanotrophic bacterial activity (R. Klusman, pers. comm.).

A wide literature shows that mud volcanoes always include all the three levels of seepage (e.g., Etiope et al., 2002; 2004a,b; 2007b; Hong and Yang, 2007; Spulber et al., 2010). In many cases, the CH_4 flux integrated throughout the large miniseepage and microseepage areas produces a total output that is comparable and often higher than that from macro-seepage (e.g., Etiope et al., 2004a,b; 2007b). The knowledge of the spatial extent and intensity of the diffuse seepage is therefore fundamental to refine

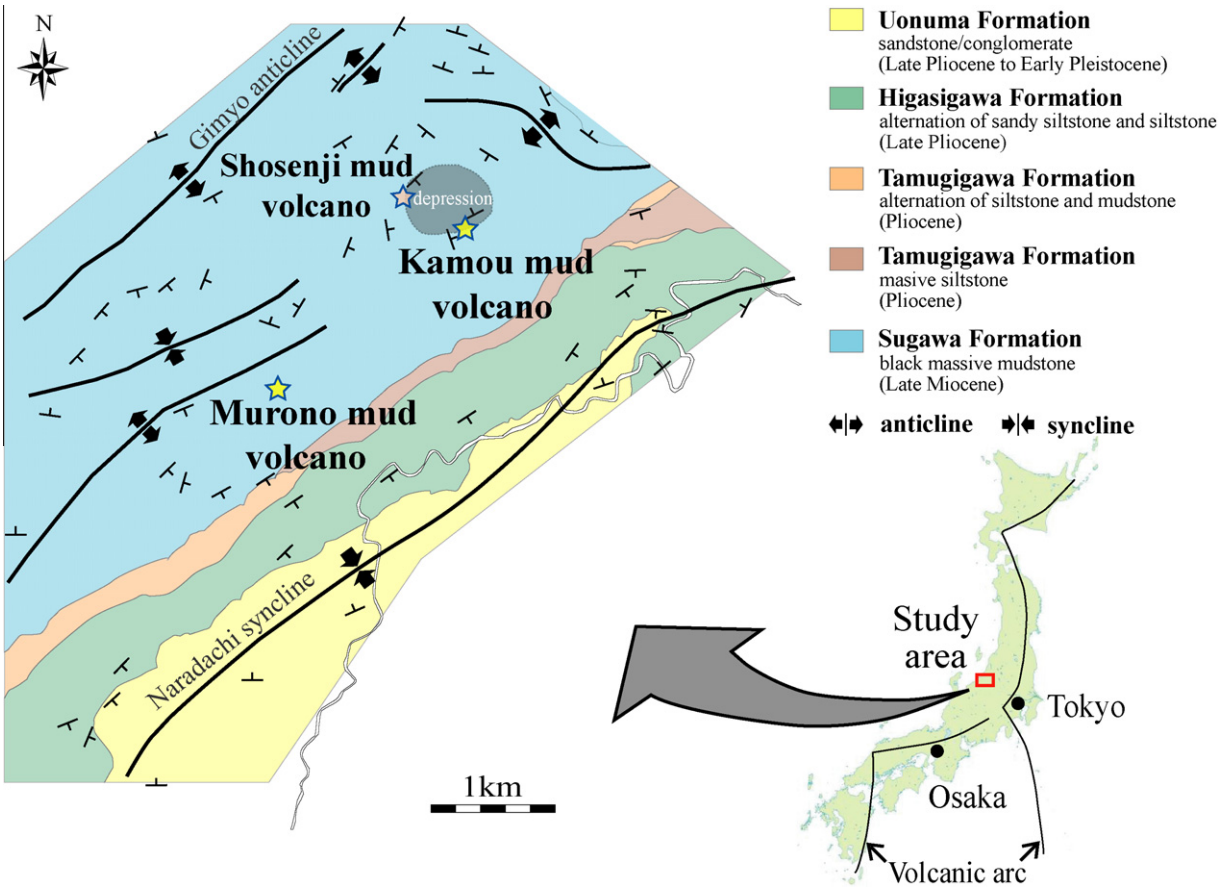

Fig. 1. Geologic map of the Murono and Kamou mud volcano area in the Niigata Basin, Japan (after Mizobe, 2007).

the "emission factors" data-set and derive improved global CH_4 emission estimates.

This paper contributes to this aim providing the results of a detailed gas flux investigation, coupled with a study of gas compositional and isotopic features, from the two main mud volcanoes in central Japan: Murono and Kamou, located near Tokamachi town, in the onshore Niigata petroliferous basin. These mud volcanoes have been the subject of several investigations on the origin of gas and erupted material (Mizobe, 2007; Kato et al., 2009), and on the geometry and size of the underground mud volcano system (Suzuki et al., 2009; Ishihara and Tanaka, 2009), but gas fluxes have never been measured. Methane and CO_2 flux data from macro-seepage and diffuse seepage acquired in May 2010 by the closed-chamber method are presented. Gas was also sampled and analysed for complete compositional and stable C ($\delta^{13}C_{CH4}$, $\delta^{13}C_{C2H6}$, $\delta^{13}C_{C3H8}$, $\delta^{13}C_{CO2}$) and H (δD_{CH4}) isotopic analysis. The following items are thus examined and discussed in this work:

1. Origin, and temporal variability of compositional and isotopic properties of the released gas, including enrichments of $\delta^{13}C$ in CO_2 and C_3H_8, as signals of subsurface petroleum biodegradation: the data has been compared with those acquired in 2004, 2005 and 2006 (Mizobe, 2007; Kato et al., 2009), and the first data on δD_{CH4} not determined previously, has been provided; this allows a more precise assessment of CH_4 origin (Schoell, 1983).
2. Spatial distribution of CH_4 and CO_2 flux from macro-seeps and soil, in order to assess the actual area affected by gas seepage, the total emission of gas into the atmosphere, and the "emission factor". Comparing CH_4/CO_2 flux ratio with the original CH_4/CO_2 compositional ratio provided a verification of the correctness of CH_4 and CO_2 flux values measured by two independent sensors.
3. Verification of the effect of gas flux in determining molecular fractionation (increase of the "Bernard ratio" $C_1/(C_2 + C_3)$ due to slow gas migration); macro-flux vs. $C_1/(C_2 + C_3)$ data of Murono and Kamou are compared with those of other 13 mud volcanoes from Italy, Romania and Taiwan.
4. Updating a global "emission-factor" data set and re-evaluation of the global estimate of CH_4 emission from mud volcanoes.

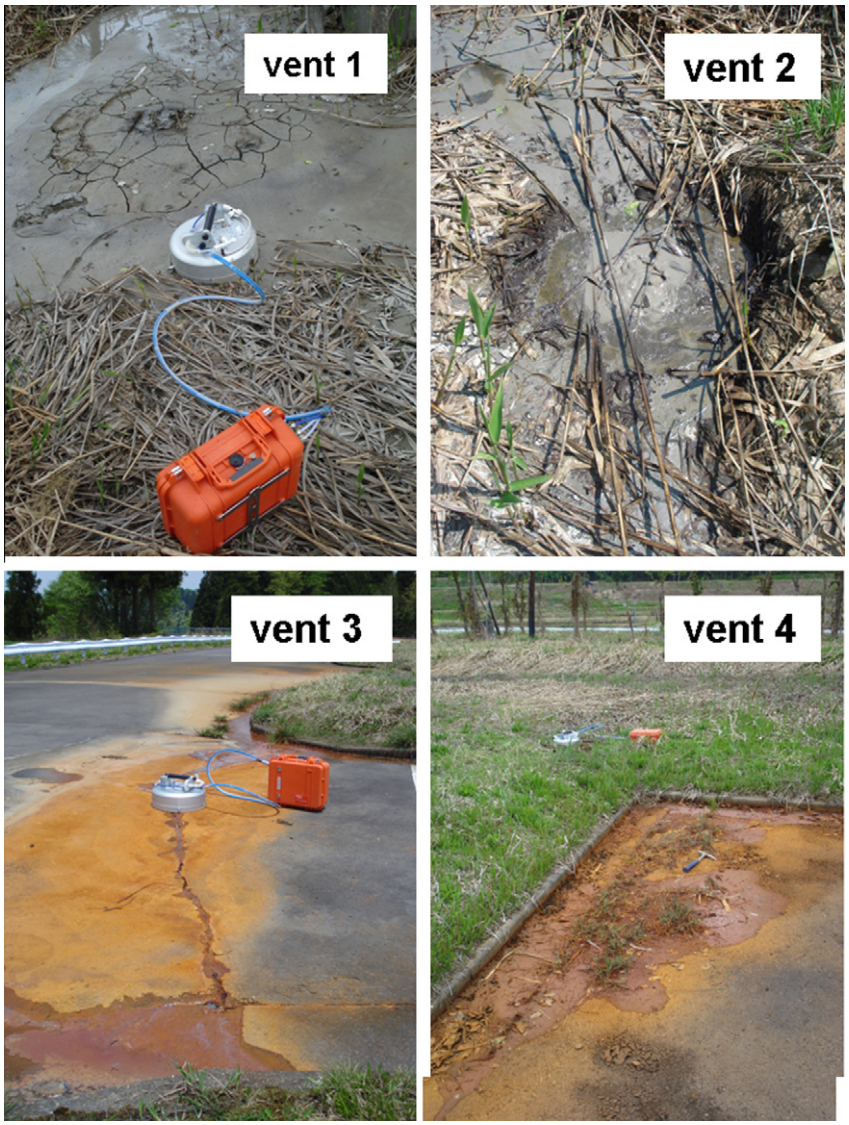

Fig. 2. Murono mud volcano; two mud craters (above) and two satellite vents on asphalt cracks (below). See Fig. 4 for location of the vents. Photographs on the left also show the closed-chamber system with CH_4 and CO_2 sensors in the red case.

2. Geologic setting and description of the mud volcanoes

The study area is located in the Tertiary sedimentary basin in Niigata Prefecture, within the back-arc region of Central Japan (Fig. 1). Niigata Basin is part of the wider Green Tuff belt of Honshu and is one of the most important petroleum (oil and gas) producing areas of Japan. The Green Tuff formation is associated with the opening of the Japan Sea, which occurred in the Early Miocene and was accompanied by large-scale volcanic activity. Commercial oil and gas accumulations are hosted in clastic and volcanic reservoirs, tuffaceous mudstones and rhyolite, while Miocene siliceous mudstones seem to be the main source rocks, with predominant Type II kerogen (Waseda and Iwano, 2008; Kato et al., 2009; Tomaru et al., 2009). Sodium–Cl-type geopressured fossil formation waters, related to the hydrocarbon reservoirs, are the source of numerous hot springs (Xu et al., 2006).

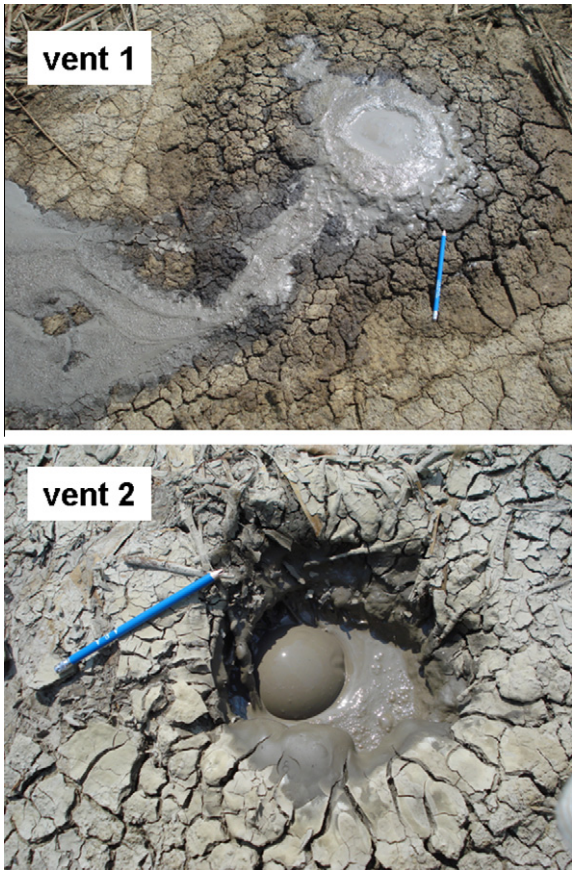

Fig. 3. Kamou mud craters. Their location in shown in Fig. 5.

In the Tokamachi area, massive mudstones 800 m thick belonging to the Late Miocene Sugawa Formation are widely distributed (Takeuchi et al., 2000). The Sugawa Formation is entirely folded with a NE–SW trending axis, and exhibits a wavelength of several tens of km. The mud volcanoes are all distributed in the upper horizon of the Sugawa Formation, in correspondence with anticline axes (Shinya and Tanaka, 2005; Ishihara and Tanaka, 2009). The other geological formations in the area include: (i) Pliocene Tamugigawa Formation (silt and sandstones), (ii) Late Pliocene Higashigawa Formation (siltstone and alternations of sandy siltstone) and (iii) Late Pliocene to Early Pleistocene Uonuma Formation (sandstone).

The two active mud volcanoes, Murono and Kamou, are about 10 km west of Tokamachi village. A third mud volcano in the Kamou area (Shosenji mud volcano) is inactive today; it was active at least about 38 ka BP, as estimated by the ^{14}C age (38,479 ± 820 a BP) of the charcoal intercalation in the swamp deposit overlying the erupted mud (Shinya and Tanaka, 2005). Kamou and Shosenji mud volcanoes are located at the margin of a wide structural depression (Fig. 1), probably a sort of caldera related to gas seepage. At Murono, groundwater, mud and gases are erupting at two bubbling craters, with a diameter of 2 m (vent 1) and 0.5 m (vent 2); natural gas is also seeping from cracks formed in the asphalt pavement along the road of a car test track that was built around the mud volcano; the crack-seepage mainly occurs in at least two sites (vents 3 and 4; Fig. 2 and 4). At Kamou, only two small mud craters, about 0.5 m in diameter, were found during

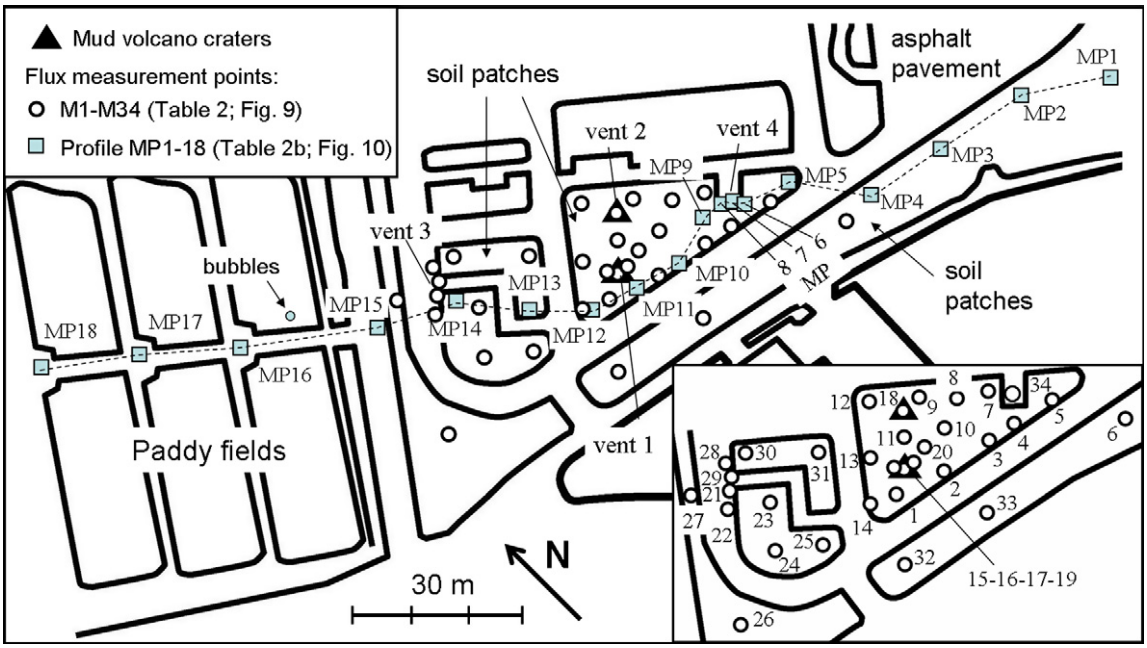

Fig. 4. Map of flux measurement points at Murono.

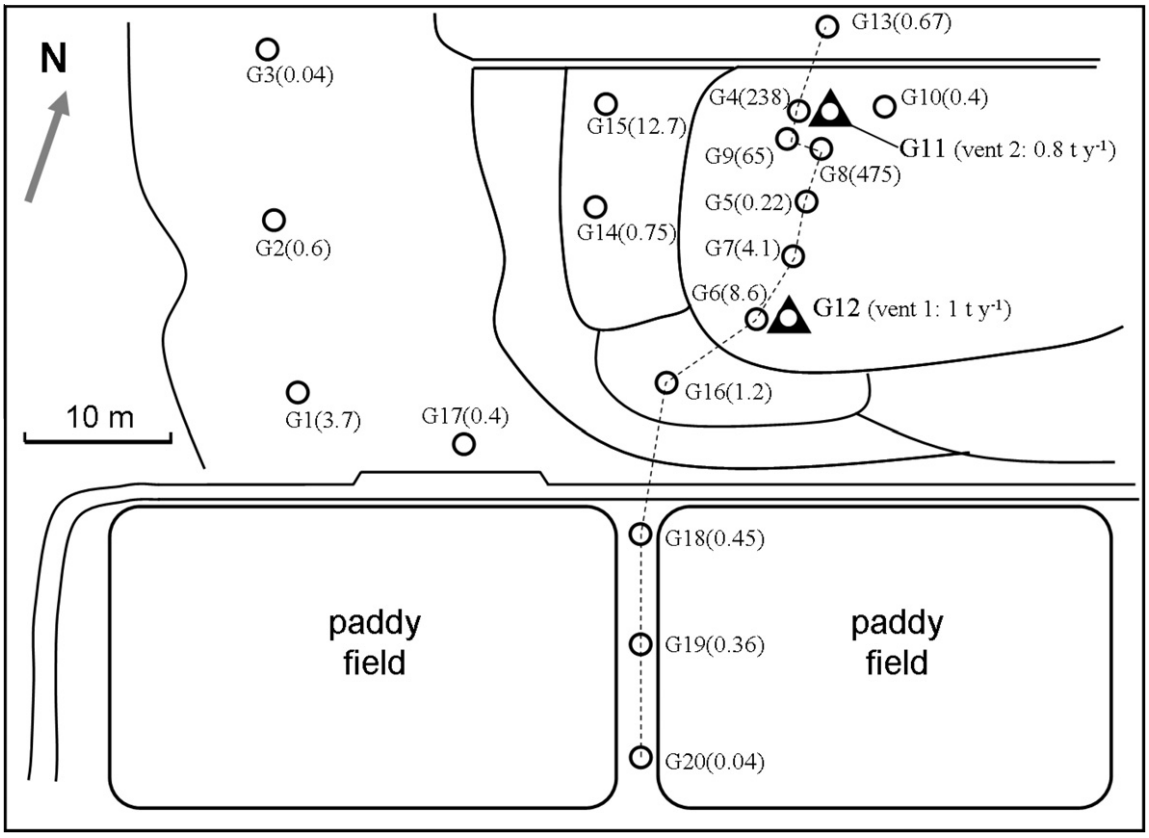

Fig. 5. Map of flux measurement points at Kamou, CH_4 flux values are in brackets (g m^{-2} d^{-1}).

the survey performed in May 2010 (Fig. 3 and 5). Previously, fluid eruptions with a gas pressure up to 1.6 MPa were also observed in a tunnel excavated 150 m underground near Kamou (Matsushita et al., 2000).

Geological surveys, including borehole drilling (Ishihara and Tanaka, 2009), geophysical prospecting such as Controlled-Source Audio-Frequency Magnetotellurics (CSAMT), electrical prospecting (Suzuki et al., 2009) and surface wave inversion (Onishi et al., 2009) allowed defining the position, geometry and fluid charge of the underground chamber: it is filled with highly saline groundwater and mud, and is associated with diatremes composed of mud breccia. Geochemical analyses suggest a deep water origin, likely ascending from depths of 3400 to 4000 m by abnormal fluid pressure, probably related to dehydration of clay minerals (Ishihara and Tanaka, 2009).

3. Methodology

3.1. Gas sampling and analyses

Three gas samples, two from Murono (vent 2 and vent 3; Fig. 2) and one from Kamou (vent 1; Fig. 3), were collected by an inverted funnel connected to a syringe and a silicon tube equipped with a *T*-valve, in order to reduce atmospheric air contamination. Gas samples were stored in 100 mL glass tubes equipped with two vacuum stop-cocks. The samples from Murono vent 2 and Kamou vent 1 were analyzed at Isotech Labs Inc. (Illinois, USA) for C_1–C_6 hydrocarbons, He, H_2S, H_2, Ar, O_2, CO_2, N_2, (Carle AGC 100–400 TCD-FID GC; detection limits of CO_2, N_2, H_2, Ar, O_2: 40 ppmv; H_2S: 150 ppmv; He and HC: 10 ppmv; precision 2%; 10% at the detection limit), and isotopic compositions $\delta^{13}C_1$, $\delta^{13}C_2$, $\delta^{13}C_3$, δD_1, $\delta^{13}CO_2$ (Finnigan Delta Plus XL mass spectrometer, precision ±0.1‰ for ^{13}C and ±2‰ for ^{2}H). The sample from Murono vent 3 was analysed at the Dept. of Environmental Chemistry & Engineering, Tokyo Institute of Technology, for C_1–C_3 hydrocarbons (GC/MS HP5975, detection limit: 5 ppmv; precision 1%; 10% at the detection limit), Ar, O_2, CO_2, N_2, (Shimazu GC-8A TCD, GC; detection limits of CO_2, N_2, Ar, O_2: 50 ppmv; precision 1%; 10% at the detection limit), and $\delta^{13}C_{CH4}$–δD_{CH4} isotopic ratios (Finnigan MAT 252 isotope ratio mass spectrometer, precision ±0.07‰ for ^{13}C and ±1.5‰ for ^{2}H).

3.2. Gas flux measurements

Methane and CO_2 fluxes from macro-seeps and diffuse seepage (miniseepage and microseepage) were measured by a closed-chamber system (Fig. 2; West Systems srl, Italy) equipped with portable CH_4 and CO_2 sensors and wireless data communication to a palm-top computer; the gas fluxes are automatically calculated through a linear regression of the gas concentration build-up in the chamber. The CH_4 sensor includes semiconductor (range 0–2000 ppmv; lower detection limit: 1 ppmv; resolution: 1 ppmv), catalytic (range: 2000 ppmv – 3% v/v), and thermal conductivity (3% – 100% v/v) detectors (precision of 5%). Maximum accumulation time of 15 min allowed detecting fluxes down to 10 mg m^{-2} d^{-1}. The CO_2 detector is a double beam infrared sensor (Licor) with an accuracy of 2%, repeatability ±5 ppmv and full scale range of 2000 ppmv. The chamber was equipped with a Nafion® dryer for humidity removal. Laboratory tests based on known gas fluxes suggested a reproducibility better than 5%.

At Murono, flux measurements were performed at the four main vents (vent 1 and vent 2, corresponding to the two mud volcano craters; vent 3 and vent 4 corresponding to cracks in the asphalt pavement; Fig. 2), and were homogeneously distributed,

Table 1
Gas composition and isotopic data of Murono and Kamou mud volcanoes, and surrounding seeps.

Sample (year.month)	Molecular composition (vol.%)										Isotopic ratios ($\delta^{13}C$: ‰, VPDB; δD: ‰, VSMOW)				
	N_2	CO_2	CH_4	C_2H_6	C_3H_8	*i*-C_4	*n*-C_4	*i*-C_5	*n*-C_5	C_{6+}	$\delta^{13}C_1$	δD_1	$\delta^{13}C_2$	$\delta^{13}C_3$	$\delta^{13}C_{CO2}$
Murono															
MV vent 2 (10.5)	0.00	5.62	93.72	0.43	0.22	0.01	0.00	0.00	0.00	0.002	−36.21	−174.5	−24.44	−13.38	+28.32
MV vent 3 (10.5)	0.06	3.56	95.20	1.19							−32.89	−161.2			
MV (04.8)[1]	0.24	6.01	93.04	0.50	0.20	0.00	0.00	0.00	0.00	0.00	−33.1		−26.5		+30.8
MV (05.5) [2]	0.00	4.59	94.70	0.41	0.28	0.00	0.00	0.00	0.00	0.00	−34.5		−26.0	−11.6	+19.2
MV (06.6) [2]	1.89	5.50	91.84	0.45	0.31	0.01	0.00	0.00	0.00	0.00	−35.1		−25.8	−12.0	+21.2
PF1 (04.4) [1]	1.65	3.73	94.54	0.04	0.03	0.00	0.00	0.00	0.00	0.00	−36.6				+23.9
PF2 (04.4)[1]	3.03	4.39	92.56	0.02	0.00	0.00	0.00	0.00	0.00	0.00	−37.1				+23.5
PF3 (05.6)[2]	2.43	3.90	86.74	3.87	1.85	0.25	0.55	0.14	0.13	0.00	−35.3		−24.7	−22.1	+9.4
Kamou															
MV vent 1 (10.5)	0.28	2.91	95.44	0.78	0.10	0.24	0.05	0.09	0.00	0.11	−33.89	−171.7			+10.93
MV (04.4)[1]	0.01	1.80	96.92	0.75	0.11	0.22	0.04	0.03	0.07	0.04	−33.7		−21.1		+18.0
MV (04.8)[1]	0.79	6.70	91.81	0.64	0.02	0.03	0.00	0.00	0.00	0.01	−34.5		−21.0		+7.8
MV (05.5)[2]	3.13	3.91	91.63	0.79	0.11	0.24	0.05	0.11	0.01	0.01	−32.9		−20.0	−8.9	+4.3
MV (06.6)[2]	2.46	3.45	92.84	0.78	0.10	0.22	0.05	0.09	0.01	0.01	−33.5		−19.9	−8.6	+8.9
PF1 (04.4)[1]	12.56	3.17	83.86	0.40	0.02	0.00	0.00	0.00	0.00	0.00	−33.7		−22.2		−12.1
PF2 (04.4)[2]	3.35	3.17	92.98	0.38	0.05	0.02	0.03	0.02	0.00	0.00	−34.0		−23.9		−2.5

MV: mud volcano; PF: paddy field; H_2, He and H_2S, not included in the table, are below the detection limit (<40 ppmv, <10 ppmv and <150 ppmv, respectively). All data are corrected for air contamination; the raw analyses in 2010 showed O_2 contamination of 0.4 vol.% and 0.1 vol.% (Murono vents 2 and 3), and 0.05 vol.% (Kamou vent 1); Ar concentrations were always below 0.023 vol.%).
[1] Data from Kato et al. (2009).
[2] Data from Mizobe (2007).

where soil exists, throughout the area of the car test track, for a total of 34 measurements (Fig. 4). A further 18 measurements were performed the following day along a 200 m long transect, crossing the vents sites. At Kamou, 11 measurements from soil were performed along a 65 m long transect running close to the two mud volcano vents; other 7 measurements were made at the vents and from soil as shown in Fig. 5. A further five flux measurements were carried out, as a test and for background evaluation, in a grassland soil located about 20 km from the mud volcano zones. Murono flux data were elaborated with commercial kriging interpolation software in order to provide 3D maps and an estimate of the total gas output.

4. Results and discussions

4.1. Gas chemistry

4.1.1. Gas origin

Methane is the dominant gas of both Murono and Kamou mud volcanoes, with concentrations above 93 vol.% (Table 1). Ethane (C_2H_6) and propane (C_3H_8) concentrations are above 0.4 vol.% and 0.1 vol.%, respectively. Helium, H_2 and H_2S are below the analytical detection limit (10, 40 and 150 ppmv, respectively). Compositional data acquired in this work are basically consistent with those reported by Mizobe (2007) and Kato et al. (2009) for the analyses carried out in 2004, 2005 and 2006. The mud volcanoes gas composition is typical of natural gas of sedimentary basins, clearly different from geothermal or hydrothermal CO_2- or N_2-rich gases related to the volcanic arc in central Japan (Fig. 6).

Isotopic data confirm the thermogenic origin of CH_4 in both mud volcanoes (Murono $\delta^{13}C_1$: −36.2‰ and −32.9‰; Kamou $\delta^{13}C_1$: −33.9‰). Kato et al. (2009) also reported data for seeps sampled in rice paddy fields around the mud volcanoes (PF in Table 1): the gas here is also clearly thermogenic and it is not related to biologic production of rice cultivation. Bubbles were observed in the paddy field close to vent 3 area (Fig. 4). The "Bernard $\delta^{13}C_1$ vs. $C_1/(C_2 + C_3)$" and "Schoell $\delta^{13}C_1$ vs. δD_1" diagrams are shown in Fig. 7. All data fall within the field of thermogenic gas with condensate (T_C, Fig. 7a; Hunt, 1996), which indicates the possible association of gas with oil. This is confirmed by the presence of oil slicks at Kamou, observed both during the survey (2010) and in 2004 (Kato et al., 2009). The gas from both mud volcanoes does not show significant molecular fractionation: the ratio $C_1/(C_2 + C_3)$ is relatively low in comparison with that frequently observed in other mud volcanoes worldwide (based on the global data set of Etiope et al., 2009a), represented by the fields confined within the dashed lines in Fig. 7.

4.1.2. Signals of subsurface petroleum biodegradation

The C isotopic ratio of CO_2 is positive in both mud volcanoes, reaching +28.3‰ at Murono, consistently for the analyses performed from 2004 to 2006 (Mizobe, 2007; Kato et al., 2009). ^{13}C-enriched CO_2 is typically indicative of secondary methanogenesis following hydrocarbon biodegradation (e.g., Pallasser, 2000; Etiope et al., 2009b). The positive $\delta^{13}C_{CO2}$ value indicates residual

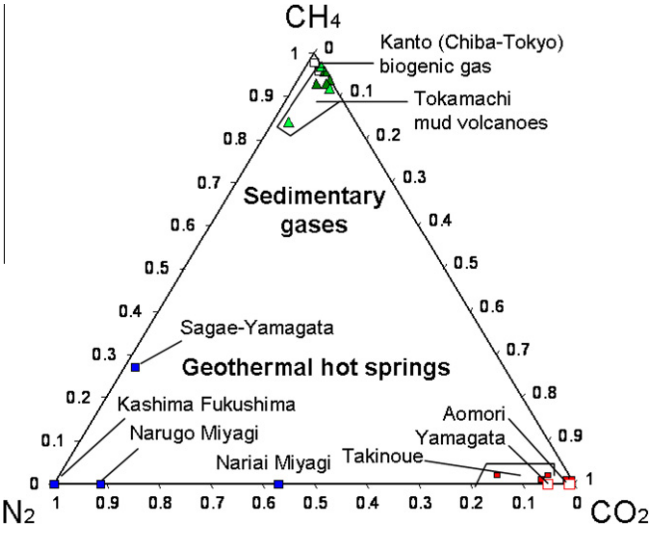

Fig. 6. Ternary plot of CH_4–CO_2–N_2 composition of the Tokamachi mud volcanoes, compared with biogenic gas of the Kanto district (Chiba and Tokyo) and geothermal gas from fumaroles or hot springs in central Japan, closer to the volcanic front (Fig. 1). Kanto, Yamagata, Fukushima, Miyagi and Aomori data are from Urabe et al. (1985); Takinoue data are from Kiyosu and Yoshida (1988).

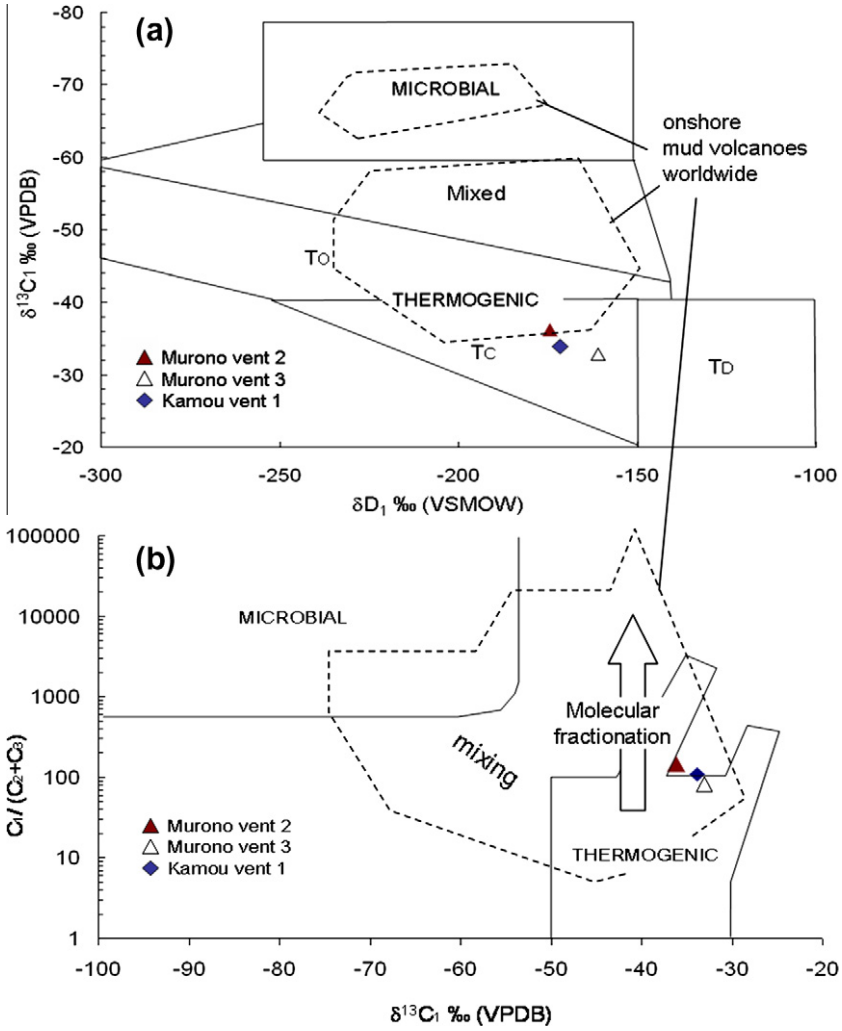

Fig. 7. Genetic zonation of CH_4 released from Murono and Kamou mud volcanoes. (a) Methane C and H isotope diagram (Schoell, 1983; Hunt, 1996). (b) CH_4 carbon isotope vs. methane–ethane–propane molecular composition (Bernard et al., 1978). Dashed lines encompass the fields of mud volcanoes reported in the global data set of Etiope et al. (2009a). T_O = thermogenic with oil; T_C = thermogenic with condensate; T_D = dry thermogenic.

CO_2 from reduction to CH_4 (secondary microbial CH_4) after CO_2 was produced by petroleum anaerobic degradation. This biodegradation preferentially affects C_3H_8 and other *n*-alkanes leading to large isotopic separations between successive *n*-alkanes (Pallasser, 2000; Etiope et al., 2009b). Both Murono and Kamou shows a large isotopic separation between C_2 and C_3 with high $\delta^{13}C_3$ values (Fig. 8), which appear above the maturity curve (vitrinite reflectance/isotope composition) derived from kerogen of the Niigata Basin (Waseda and Iwano, 2008). This is a general behaviour of many mud volcanoes which show ^{13}C-enriched CO_2 (Etiope et al., 2009b).

Subsurface petroleum biodegradation can also induce high C_2/C_3 (ethane/propane) ratios (Pallasser, 2000). Murono and Kamou gases have C_3H_8 concentrations similar to that of many other mud volcanoes with positive $\delta^{13}C_{CO2}$ values; but a statistical evaluation of a large data set of mud volcanoes worldwide does not show any significant correlation between C_3H_8 concentration and $\delta^{13}C_{CO2}$ values (Etiope et al., 2009b). Probably C_{3+} concentrations in mud volcanoes are mainly controlled by molecular fractionation during advective migration (Deville et al., 2003; Waseda and Iwano, 2008; Etiope et al., 2009a). Due to molecular adsorption on solid grains of mud and differential solubility, seeping gas becomes dryer (more CH_4, less heavier alkanes) than reservoir gas. It seems that such a molecular fractionation is inversely proportional to the flux or velocity of gas uprising to the surface, i.e. it is directly proportional to the residence times and gas–water interaction processes, as specifically observed in mud volcanoes in Italy and Taiwan (Etiope et al., 2007b; 2009a; Chao et al., 2010). In this

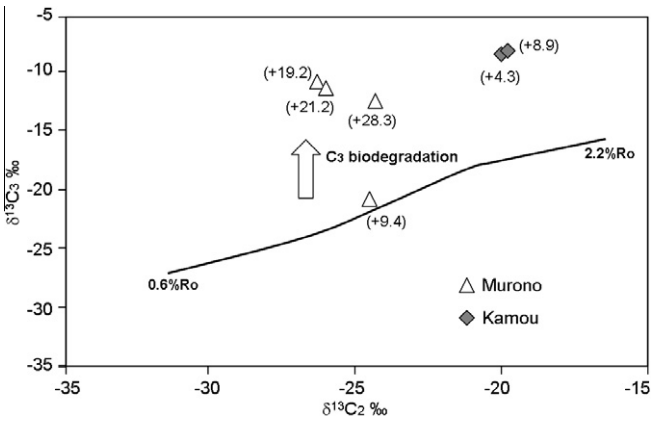

Fig. 8. Relationship between C_2 and C_3 carbon isotopes. The continuous line is the maturity curve (vitrinite reflectance/isotope composition) based on the model by Berner and Faber (1996) and calibrated for reservoirs of the Niigata Basin; Waseda and Iwano, 2008). $\delta^{13}C_{CO2}$ values are in brackets.

respect, the behavior of Murono and Kamou is going to be examined in Section 4.2.4., after the discussion of the gas fluxes.

Secondary microbial CH_4 may have a relatively high $\delta^{13}C$ value, due to the heavy C isotopic signature of the oil substrate, so that it can be indistinguishable from thermogenic CH_4 (Milkov, 2010; Brown, 2011); in the "Bernard plot" (Fig. 7b) secondary CH_4 typically falls within the same sector of molecular fractionation, above the thermogenic field (e.g., Milkov, 2010).

4.2. Gas flux

4.2.1. Background test area

In the five background sites on the grassland soil, located 20 km from the mud volcanoes, CH_4 flux was always below the detection limit (<10 mg m^{-2} d^{-1}, after a chamber accumulation time of 15 min) and CO_2 flux ranged from 15 to 36 g m^{-2} d^{-1}. In normal dry soil conditions CH_4 flux is typically negative or nil, due to consumption by methanotrophic bacteria (Etiope and Klusman, 2010). The measured CO_2 fluxes are coherent with soil respiration in temperate climate soils measured in central Japan (5–33 g m^{-2} d^{-1}; Moriizumi et al., 2007).

4.2.2. Murono mud volcano

Methane and CO_2 flux data are listed in Tables 2a and 2b. Macro-seep CH_4 flux (Table 2a), measured at nine points in correspondence with the visible vents 1–4, ranged from 670 to 41,500 g m^{-2} d^{-1}. Methane output from isolated clusters of bubble trains (in the mud volcano crater or at the cracks in the asphalt pavement) ranged from 0.03 to 1.1 ton a^{-1}. A large gas flux was also measured throughout the wet mud of vent 1 (the larger mud seep). For 1 m^2 of muddy ground, CH_4 output is about 2 ton a^{-1}, which is almost three times higher than the flux from the visible bubble train in the central crater (Table 2a, points M17 and M15).

Methane exhalation from invisible seepage (mini- and microseepage; Table 2b) ranged from zero (actually <10 mg m^{-2} d^{-1}, the lowest detection limit) to 446 g m^{-2} d^{-1}. Fig. 9 shows a 3D reconstruction, through kriging interpolation, of the distribution of gas fluxes. Positive CH_4 fluxes, from tens to thousands of mg m^{-2} d^{-1}, were recorded in the soil patches throughout the investigated area, about 4900 m^2 (Fig. 4), except for the farthest point, MP1, at the easternmost side of the E–W profile, about 90 m from the mud volcano vents (Fig. 10a).

Table 2a
Macroseepage CH_4 and CO_2 fluxes at Murono.

Site N. (Fig. 4)	CH_4	CO_2	CH_4/CO_2	CH_4 output[a]	CO_2 output[a]
	(g m^{-2} d^{-1})		vol.	(ton y^{-1})	
M15 vent 1 (center, bubble 1)	27,200	3910	19.2	0.7	0.1
M16 vent 1 (bubble 2)	1028	212	14.2	0.03 (×3)[b]	0.01 (×3)[b]
M17 vent 1 (1 m^2 mud)	5624	897	17.5	2	0.33
M18 vent 2 (center)	41,500	8094	15.3	1.1	0.21
M21 vent 3 (bubble 1)	6475	1072	16.8	0.17 (×3)[b]	0.03 (×3)[b]
M22 vent 3 (bubble 2)	1232	270	13.2	0.03 (×5)[b]	0.01 (×5)[b]
M28 vent 3 (bubble 3)	5225	1058	13.8	0.13	0.03
M29 vent 3 (bubble 4)	5927	968	17.1	0.15	0.02
M34 vent 4 (no bubbles)	670	165	12.1	0.02	0.004
Total output				~5	~0.9

[a] The gas output from individual vents is calculated from the flux measured by the closed-chamber (columns 2 and 3) multiplied by the chamber area (0.07 m^2), which corresponds to or is slightly smaller than the actual gas vent area (e.g., for M15: CH_4 output is 27,200 g m^{-2} d^{-1} × 0.07 m^2 × 365 day/10^6 = 0.7 ton y^{-1}).

[b] The output of other three bubble trains is assumed equal to that of measured bubble flux at M16, which shows similar activity (bubble size and frequency). The same procedure is applied to other three bubble trains similar to M21 and 5 bubble trains similar to M22.

Carbon dioxide fluxes at the macro-seeps ranged from 165 to 8094 g m^{-2} d^{-1}, and are directly proportional to CH_4 fluxes. Fig. 9 shows that CH_4 and CO_2 have exactly the same spatial pattern, CO_2 being a mud volcano gas component (Table 1). It is interesting to note that the volumetric ratios between CH_4 flux and CO_2 flux in the macro-seeps range from 12 to 19 (mean of 15.5; Table 2a) and are similar to the compositional CH_4/CO_2 volume ratio (16.7 measured in the gas vent 2, 26 in vent 3; Table 1). A high ratio (~17) is also observed in the high flux from wet mud around vent 1 crater (M17). It implies that wet mud is very permeable to gas exhalation and that the gas flow is rapid enough to continuously replace CH_4 in the mud, preventing significant oxidation. This high CH_4/CO_2 flux ratio is not maintained in the diffuse fluxes from soil, where both CH_4 consumption by methanotrophic bacteria and addition of biologic CO_2 from soil respiration occur (Table 2b, fourth column). Methane/CO_2 ratios around 15 appear only in the soil which is very close to macro-seeps (MP8) or corresponding with a manhole cover (M15), below which gas bubbling seems to occur from underground flowing water.

Table 2b
Mini- and microseepage CH_4 and CO_2 fluxes (g m^{-2} d^{-1}) at Murono.

Site N. (Fig. 4)	CH_4	CO_2	CH_4/CO_2 vol.
Murono areal			
M1	0.90	14	0.18
M2	0.41	16	0.07
M3	3.3	30	0.30
M4	446	212	5.80
M5	10	49	0.57
M6	0.04	22	0.01
M7	0.77	32	0.07
M8	0.68	26	0.07
M9	0.09	14	0.02
M10	0.18	14	0.03
M11	3.44	28	0.33
M12	0.06	17	0.01
M13	0.34	21	0.05
M14	1.25	15	0.24
M19	3.80	29	0.36
M20	0.33	19	0.05
M23	4.75	35	0.37
M24	0.67	21	0.09
M25	0.2	28	0.02
M26	0.48	12	0.11
M27	324	125	7.18
M30	0.09	11	0.02
M31	0.33	14	0.06
M32	0.03	7	0.00
M33	0.18	16	0.03
Murono profile			
MP1	0	8	0.00
MP2	0.03	44	0.00
MP3	0.11	45	0.01
MP4	0.01	14	0.00
MP5	0.15	20	0.02
MP6	0.21	23	0.02
MP7	0.45	3	0.43
MP8[a]	40	7	14.60
MP9	0.71	25	0.08
MP10	0.47	20	0.06
MP11[b]	249	535	1.28
MP12	1.36	19	0.20
MP13	0.24	27	0.02
MP14[c]	412	149	7.58
MP15[d]	41	7	15.00
MP16	0.09	54	0.00
MP17	0.22	27	0.02
MP18	0.04	32	0.00

[a] Close to vent 4.
[b] Close to vent 1.
[c] Close to vent 3.
[d] Above manhole cover.

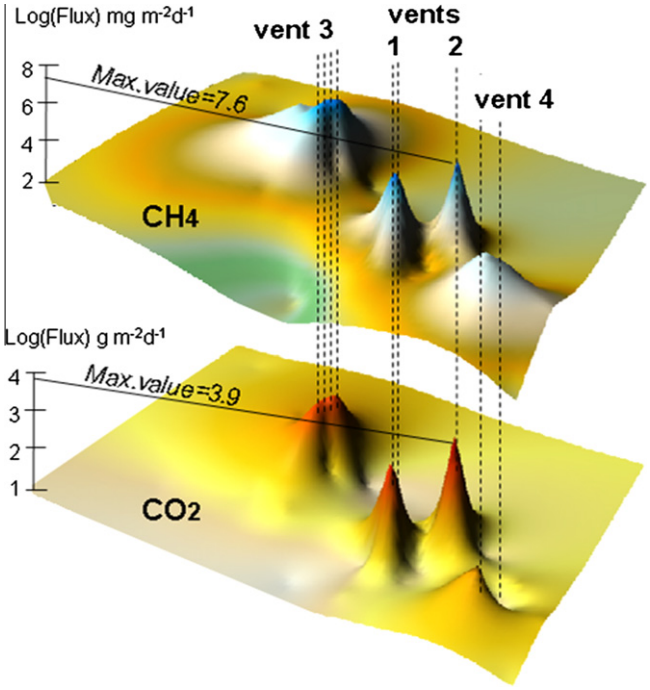

Fig. 9. 3D plots of CH_4 and CO_2 flux distribution at Murono mud volcano (kriging interpolation of logaritmic flux values).

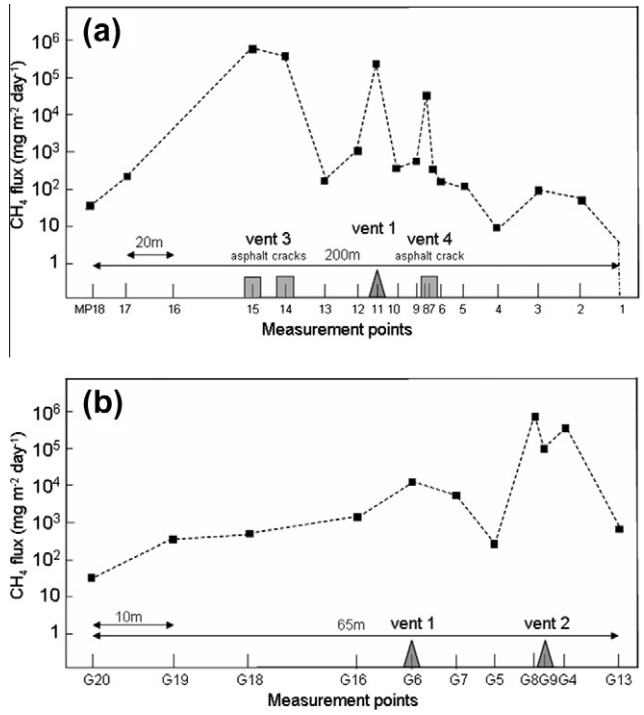

Fig. 10. Methane flux from soil along profiles running close to the Murono (a) and Kamou (b) vents (traces on Figs. 4 and 5). Murono point 11 is 1 m from vent 1; points 7, 14 and 5 are directly over cracks in the asphalt pavement. Kamou points G6, G8, G9 and G4 are 1 m from the vents.

Total CH_4 output from macro-seepage (the sum of emissions measured from all vents; Table 2a) is estimated to be about 5 ton a^{-1}. Total gas output from the diffuse exhalation from soil (mini- and microseepage) was derived by spatial interpolation between the individual gas measurements. Applying "natural neighbor" interpolation separately for microseepage (flux values with lower variance) and miniseepage (flux values with higher variance) yields an output of about 16 ton CH_4 a^{-1}. Total CH_4 emission from the Murono area (4900 m^2) would be therefore >20 ton a^{-1}; thus, more than 75% of this emission is from the diffuse seepage surrounding the visible mud volcano vents.

In the same way, a total CO_2 emission of 0.9 ton a^{-1} is estimated from macro-seeps (Table 1). The diffuse CO_2 flux from soil would include biologic CO_2 from soil respiration, which is quite variable, depending on local soil conditions, and is difficult to distinguish from geologic (thermogenic) CO_2 related to the mud volcano system. The geo-CO_2 fraction in the soil flux can be assessed only by stable C (positive $\delta^{13}C$ for geo-CO_2 as reported in Table 1, and from −10 to −25‰ for bio-CO_2) or radiocarbon analyses (geo-CO_2 is ^{14}C-free).

4.2.3. Kamou mud volcano

The CH_4 flux values measured at Kamou are shown in Fig. 5. The two craters are similar (in terms of both size and bubbling activity) to those of Murono, and release about 1 and 0.8 ton CH_4 a^{-1}. Also in this case CH_4 flux was quite high throughout the investigated area (about 1000 m^2), and decreased below 50 mg m^{-2} d^{-1} at about 50 m from the mud volcano craters (Fig. 10b). Also in this case the CH_4/CO_2 volume ratio in the macro-seep flux (29 for vent 1) was close to the compositional volume ratio (32.8), and it was generally <1 for the diffuse flux from soil, as occurred in the Murono area. Total CH_4 emission from the investigated area is estimated at 3.7 ton a^{-1} (of which 52% was from diffuse seepage).

4.2.4. Gas flux vs. C_{2+} concentration

Fig. 11 shows a diagram of macro-flux vs. $C_1/(C_2 + C_3)$ for Murono and Kamou, compared with mud volcanoes and other gas seeps in Italy (Etiope et al., 2007b), Romania (Etiope et al., 2004a, 2009a), Switzerland (Etiope et al., 2010) and Taiwan (Chao et al., 2010) The macro-flux refers to the gas flow from a single vent from which molecular composition was determined. The plot shows a trend that is consistent with the hypothesis that molecular fractionation may increase as gas migration flux decreases (Etiope et al., 2007b; Chao et al., 2010): the higher the gas flux, the higher the gas velocity, the lower the time available for gas–water–mud interaction, the lower the fractionation. The "Bernard ratio", $C_1/(C_2 + C_3)$, however may also increase due to hydrocarbon biodegradation, which preferentially consumes C_3H_8 and *n*-alkanes (Pallasser, 2000). The Giswil seep (point 9; Etiope et al., 2010), as well as Murono and Kamou (black triangles) are examples of gas related to significant hydrocarbon biodegradation. More data are necessary to verify this preliminary model.

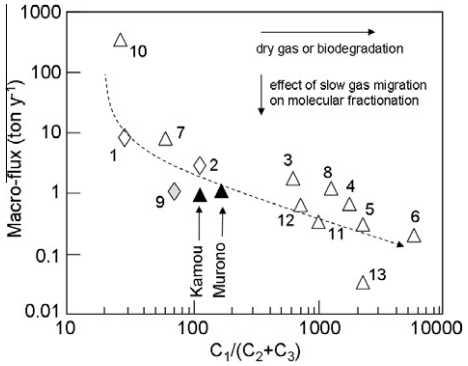

Fig. 11. Diagram of macro-flux vs. $C_1/(C_2 + C_3)$ for Murono and Kamou, compared with mud volcanoes (triangles) and other gas seeps (diamonds) releasing thermogenic gas (with CH_4 > 90 vol.%) in Italy (1: M.Busca, 2: Censo fire, 3: Regnano, 4: Nirano, 5: Ospitaletto, 6: Rivalta; Etiope et al., 2007b), Romania (7: Paclele Mari, 8: Paclele Mici; Etiope et al., 2004a, 2009a), Switzerland (9: Giswil; Etiope et al., 2010) and Taiwan (10: YNH, 11: YSJ, 12: LGH; 13:YSK; Chao et al., 2010).

4.2.5. Emission factor and its importance for global CH_4 emission estimates

Murono and Kamou mud volcanoes show an emission factor (defined in Introduction) of about 4300 ton km^{-2} a^{-1} (i.e., 21 ton a^{-1} divided by 0.0049 km^2) and 3000 ton km^{-2} a^{-1} (i.e., 3 ton a^{-1} divided by 0.001 km^2), respectively. These values are similar to those derived in other mud volcanoes of the same size and activity, as discussed below.

According to the EMEP-EEA (2009) guidelines, for area sources (pervasive and spatially distributed gas fluxes), the regional or global gas emission is calculated by multiplying the emission factor (typically in terms of g m^{-2} d^{-1} or ton km^{-2} a^{-1}) by the region or global area characterised by that gas flux. For point sources (localized gas emissions) the regional or global emission is given by the emission factor (in terms of kg d^{-1} or ton a^{-1}) multiplied by the number of the emission points occurring in the region or globally. These procedures were used to assess the most recent bottom-up estimates of global CH_4 emission from mud volcanoes (6–9 Mt a^{-1}; Etiope and Milkov, 2004), and from other geological sources (e.g., Etiope et al., 2008). The uncertainty of these estimates strongly depends on the representativeness of the emission factor and its possible disaggregation into different levels: in other words, different emission factors could be associated with mud volcanoes with different size and/or activity. Etiope and Milkov (2004) used emission factors disaggregated into three levels: 100–500 ton km^{-2} a^{-1} for small size mud volcanoes (<0.5 km^2), 500–1000 ton km^{-2} a^{-1} for medium size (0.5–9 km^{-2}) and 1000 ton km^{-2} a^{-1} for large mud volcanoes (>9 km^2). These were based on data from Italy, Romania and rough estimates from Azerbaijan. It was assumed that larger mud volcanoes generally are more active (higher emission factor) than small ones. More recent surveys in other mud volcanoes (e.g., Etiope et al., 2007b; Spulber et al., 2010) show that this hypothesis is not completely or always correct. The uncertainty in the final estimate can only be reduced by extending the experimental data set, knowing the actual emission factor for a larger number of mud volcanoes worldwide. In any case, as suggested also in this work, all levels of seepage, macro-, mini- and microseepage, should be considered (i.e., using only gas emission from visible craters would not give a realistic global emission estimate). Today a wider data-set of CH_4 fluxes is available. Emissions including all seepage levels are known for 27 mud volcanoes: 10 in Italy (Etiope et al., 2007b), 8 in Romania (Etiope et al., 2004a; Spulber et al., 2010), 4 in Taiwan (Hong and Yang, 2007), 3 in Azerbaijan (Etiope et al., 2004b) and 2 in Japan (this work). These represent only 3% of all terrestrial mud volcanoes (a total of 926 onshore structures were suggested by Dimitrov (2002); since the standard deviation of the output values from single mud volcanoes is quite high, the mean (or median) output from 27 cases is not sufficiently representative of the world mud volcano population. But the emission factor, which considers the actual measured area (and does not significantly depend on the mud volcano size), can be used for global up-scaling as for EMEP-EEA (2009) procedures. Almost all investigated cases indicate an emission factor ranging in the order of 10^2–10^3 ton km^{-2} a^{-1}. The frequency distribution is shown in the histogram of Fig. 12. The mean value is 3150 ton km^{-2} a^{-1}. The higher values can be considered spurious as they are related to measurements of gas flux only in restricted high-degassing zones (for example, diffuse degassing tens of meters from the main vents was not measured). Conversely, lower values may reflect a wider investigated area including lower fluxes. This new data set (much wider than that considered 7 years ago by Etiope and Milkov, 2004) suggests that emission factors are frequently higher than 1000 ton km^{-2} a^{-1}, which was the upper limit of Etiope and Milkov (2004). Assuming the average emission factor (3155 ton km^{-2} a^{-1}) as representative of the global mud volcano population, multiplied by the global area covered by mud volcanoes (estimated at about 2880 km^2; Etiope and Milkov, 2004) it would yield a global CH_4 emission, related to quiescent degassing, of 9 Mt a^{-1}. This value is twice the previous upper limit for quiescent degassing and it could double assuming emission from eruptions (Dimitrov, 2002; Etiope and Milkov, 2004). The eruptive component is the weakest point of the global emission estimate, because there are no experimental measurements of gas fluxes during eruptions, and the hypothesis of a global value equivalent to quiescent degassing (Dimitrov, 2002) still needs to be verified. However, the previous estimate of Etiope and Milkov (2004) would be underestimated and the actual global CH_4 emission from mud volcanoes has the potential to be between 10 and 20 Mt a^{-1}. More data are essential to improve the statistics and Murono and Kamou can presently be considered representative of the typical emission factor of mud volcanoes.

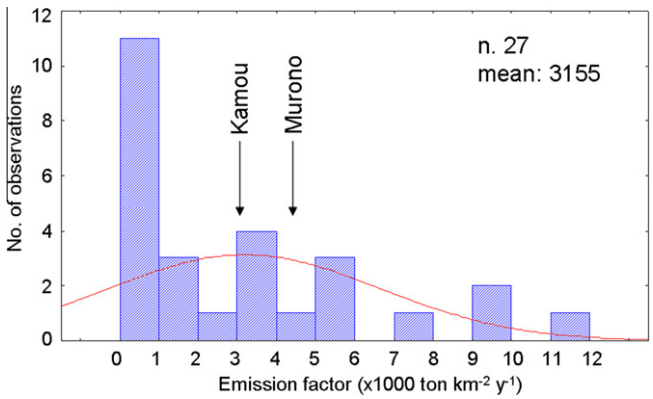

Fig. 12. Histogram of emission factors calculated for 27 mud volcanoes from Azerbaijan (data from Etiope et al., 2004b), Italy (Etiope et al., 2007b), Romania (Etiope et al., 2004a), Taiwan (Hong and Yang, 2007), Japan (Murono and Kamou, this work). Emission factor is derived from the total CH_4 emission (macro-seepage plus diffuse seepage) divided by the area investigated.

5. Summary and conclusions

Gas (CH_4 and CO_2) flux to the atmosphere from the two main active mud volcanoes in central Japan, Murono and Kamou, were measured for the first time. The gas has a deep thermogenic origin, likely associated with oil accumulations and shows isotopic features of CO_2 and C_3H_8 typical of subsurface petroleum biodegradation. A low variability of compositional and isotopic values from 2004 to 2010 was noted. This would imply that the gas source, and post-genetic alteration, did not change, and can be related to the same subsurface gas accumulation. The long-lasting migration from the same source requires a significant and permanent pressure gradient, which may be linked to large and pressurized gas pools. The gas flux activity of a seep, associated with a constant gas geochemistry, could therefore be a proxy of the economic potential of subsurface hydrocarbons.

It is interesting to note, then, that Murono and Kamou offer two cases of "bubbling" in rice paddy fields that are not related to rice cultivation and biologic CH_4 production. This demonstrates that paddy fields located in areas of potential gas seepage (petroliferous or geothermal areas) can host and emit, in part, natural geologic gas. If these fields are subjected to flux measurements, by closed-chambers, micrometeorologic or remote sensing methods, the isotopic determination of CH_4 is recommended in order to avoid misattribution of gas output to the "anthropogenic" rice cultivation.

Gas fluxes from Murono and Kamou are similar to those measured in other active mud volcanoes worldwide of the same size, and have the following main characteristics:

(a) The total output of CH_4 emitted to the atmosphere is estimated to be at least 20 ton a^{-1} for Murono and at least 3.7 ton a^{-1} for Kamou.
(b) CO_2 fluxes at the macro-seeps were directly proportional to CH_4 fluxes: the volumetric ratios between CH_4 flux and CO_2 flux are similar to the compositional CH_4/CO_2 volume ratio only in the macro-seeps, and are much lower in the soil, due to both CH_4 consumption by methanotrophic bacteria and addition of biologic CO_2. Similarly to other traditional (CH_4-rich) mud volcanoes, the total CO_2 output into the atmosphere is, however, extremely low in comparison with geothermal or volcanic emissions, where CO_2 is typically the dominant gas (see tables in Morner and Etiope, 2002, and Etiope et al., 2007b).
(c) Murono and Kamou macro-seep flux data, in addition to those of another 13 mud volcanoes, supported the hypothesis that molecular fractionation (increase of the "Bernard ratio" $C_1/(C_2 + C_3)$) is inversely proportional to macro-seep flux.
(d) More than half of the mud volcano degassing is from invisible diffuse seepage (around the vents and from soil); either wet or dry mud around the craters is not impermeable: it was observed that from 1 m^2 of muddy ground the CH_4 output is almost three times higher than the flux from the visible bubble plume in the central crater; in addition, positive CH_4 fluxes from dry soil were widespread throughout the investigated areas, down to levels of a few tens of mg m^{-2} d^{-1} about 60 m from the macro-seep zone.

These results suggest that in order to assess the actual total gas output from a mud volcano, the flux must be evaluated not only in the visible craters or vents (bubbling pools, gryphons) but also in the surrounding soil, and in particular in the fresh mud close to the active vents.

In this respect, Murono and Kamou fluxes contributed to update a global emission factor data-set, which now includes 27 mud volcanoes from different countries; bottom-up elaboration (following the procedure of Etiope and Milkov, 2004) of the new data-set suggests that global CH_4 emission from mud volcanoes may be twice the previous estimates, in a range between 10 and 20 Mt a^{-1}. This would project the global geological emission of CH_4 (including all other geo-CH_4 sources i.e., onshore seeps and microseepage independent of mud volcanism, submarine seepage, geothermal emissions; Etiope et al., 2008) beyond 60 Mt a^{-1}, i.e. more than 10% of global CH_4 sources and than the emission from other natural or man-made sources, such as termites, wild animals, biomass burning and landfills (Etiope, 2010).

Acknowledgements

The authors are grateful to Waseda University to have allowed access to the Murono car test track. Thanks are due to C.H. Sun and an anonymous reviewer for their helpful comments. The work was partially funded by INGV in the framework of the Specific Objective OS4.5: "Studies on natural degassing and petroleum gases".

References

Aitken, C.M., Jones, D.M., Larter, S.L., 2004. Anaerobic hydrocarbon degradation in deep subsurface reservoirs. Nature 431, 291–294.
Bernard, B.B., Brooks, J.M., Sackett, W.M., 1978. Light hydrocarbons in recent Texas continental shelf and slope sediments. J. Geophys. Res. 83, 4053–4061.
Berner, U., Faber, E., 1996. Empirical carbon isotope/maturity relationships for gases from algal kerogens and terrigenous organic matter, based on dry, open-system pyrolysis. Org. Geochem. 24, 947–955.
Brown, A., in press. Identification of source carbon for microbial methane in unconventional gas reservoirs. Am. Assoc. Petrol. Geol. Bull.
Chang, H.C., Sung, Q.C., Chen, L., 2010. Estimation of the methane flux from mud volcanoes along Chishan Fault, southwestern Taiwan. Environ. Earth Sci. 61, 963–972.
Chao, H.C., You, C.F., Sun, C.H., 2010. Gases in Taiwan mud volcanoes: chemical composition, methane carbon isotopes, and gas fluxes. Appl. Geochem. 25, 428–436.
Deville, E., Battani, A., Griboulard, R., Guerlais, S.H., Herbin, J.P., Houzay, J.P., Muller, C., Prinzhofer, A., 2003. Mud volcanism origin and processes. New insights from Trinidad and the Barbados Prism. In: Van Rensbergen, P., Hillis, R.R., Maltman, A.J., Morley, C. (Eds.), Surface Sediment Mobilization. Geological Society, London. Special Publication 216, pp. 475–490.
Dimitrov, L., 2002. Mud volcanoes – the most important pathway for degassing deeply buried sediments. Earth-Sci. Rev. 59, 49–76.
Dimitrov, L., 2003. Mud volcanoes—a significant source of atmospheric methane. Geo-Mar. Lett. 23, 155–161.
EMEP/EEA, 2009. EMEP/EEA Air Pollutant Emission Inventory Guidebook – 2009. Technical Guidance to Prepare National Emission Inventories. EEA Technical Report No. 6/2009. European Environment Agency, Copenhagen, 10.2800/23924.
Etiope, G., 2009. Natural emissions of methane from geological seepage in Europe. Atmos. Environ. 43, 1430–1443.
Etiope, G., 2010. Geological methane. In: Reay, D., Smith, P., van Amstel, A. (Eds.), Methane and Climate Change. Earthscan, London (Chapter 4).
Etiope, G., Klusman, R.W., 2010. Microseepage in drylands: flux and implications in the global atmospheric source/sink budget of methane. Global Planet. Change 72, 265–274.
Etiope, G., Milkov, A.V., 2004. A new estimate of global methane flux from onshore and shallow submarine mud volcanoes to the atmosphere. Environ. Geol. 46, 997–1002.
Etiope, G., Baciu, C., Caracausi, A., Italiano, F., Cosma, C., 2004a. Gas flux to the atmosphere from mud volcanoes in Eastern Romania. Terra Nova 16, 179–184.
Etiope, G., Caracausi, A., Favara, R., Italiano, F., Baciu, C., 2002. Methane emission from the mud volcanoes of Sicily (Italy). Geophys. Res. Lett. 29, 8. doi:10.1029/2001GL014340.
Etiope, G., Feyzullayev, A., Baciu, C.L., 2009a. Terrestrial methane seeps and mud volcanoes: a global perspective of gas origin. Mar. Petrol. Geol. 26, 333–344.
Etiope, G., Feyzullayev, A., Baciu, C., Milkov, A.V., 2004b. Methane emission from mud volcanoes in eastern Azerbaijan. Geology 32, 465–468.
Etiope, G., Feyzullayev, A., Milkov, A.V., Waseda, A., Mizobe, K., Sun, C.H., 2009b. Evidence of subsurface anaerobic biodegradation of hydrocarbons and potential secondary methanogenesis in terrestrial mud volcanoes. Mar. Petrol. Geol. 26, 1692–1703.
Etiope, G., Fridriksson, T., Italiano, F., Winiwarter, W., Theloke, J., 2007a. Natural emissions of methane from geothermal and volcanic sources in Europe. J. Volcanol. Geotherm. Res. 165, 76–86.
Etiope, G., Lassey, K.R., Klusman, R.W., Boschi, E., 2008. Reappraisal of the fossil methane budget and related emission from geologic sources. Geophys. Res. Lett. 35, L09307. doi:10.1029/2008GL033623.
Etiope, G., Martinelli, G., Caracausi, A., Italiano, F., 2007b. Methane seeps and mud volcanoes in Italy: gas origin, fractionation and emission to the atmosphere. Geophys. Res. Lett. 34. doi:10.1029/2007GL030341.
Etiope, G., Zwahlen, C., Anselmetti, F.S., Kupfer, R., Schubert, C.J., 2010. Origin and flux of a gas seep in the Northern Alps (Giswil, Switzerland). Geofluids 10, 476–485.
Guliyev, I.S., Feizullayev, A.A., 1997. All About Mud Volcanoes. Baku Pub.House, NAFTA-Press.
Hong, W.L., Yang, T.F., 2007. Methane flux from accretionary prism through mud volcano area in Taiwan – from present to the past. In: Proceedings of 9th International Conference on Gas Geochemistry, October 1–8, 2007, National Taiwan University, pp. 80–81.
Hunt, J.M., 1996. Petroleum Geochemistry and Geology. W.H. Freeman and Co., New York.
Ishihara, T., Tanaka, K., 2009. Geological structure and groundwater geochemistry around mud volcanoes in the Kamou area, Tokamachi city, Niigata Prefecture. J. Geogr. 118, 350–372 (in Japanese with English abstract).
Kato, S., Waseda, A., Nishita, H., Iwano, H., 2009. Geochemistry of crude oils and gases from mud volcanoes and their vicinities in the Higashi-Kubiki area, Niigata Prefecture. J. Geogr. 118, 455–471 (in Japanese with English abstract).
Kikvadze, O., Lavrushin, V., Pokrovskii, B., Polyak, B., 2010. Gases from mud volcanoes of western and central Caucasus. Geofluids 10, 486–496.
Kiyosu, Y., Yoshida, Y., 1988. Origin of some natural gases from Takinoue geothermal area in Japan. Geochem. J. 22, 183–193.
Kopf, A., Delisle, G., Faber, E., Panahi, B., Aliyev, C.S., Guliyev, I., 2009. Long-term in situ monitoring at Dashgil mud volcano, Azerbaijan: a link between seismicity, pore-pressure transients and methane emission. Int. J. Earth Sci. 99, 227–240. and Erratum 99, 241.
Matsushita, Y., Mizoguchi, K., Ohira, T., Doi, N., Ohtsuka, M., 2000. The geological characteristics and the construction methods of heavy sqeezing mudrock at the Nabetachiyama tunnel. Proceedings of 8th International Congress Rock Mechanics, Tokyo, Japan, pp. 491–495.
Milkov, A.V., 2005. Global distribution of mud volcanoes and their significance in petroleum exploration, as a source of methane in the atmosphere and hydrosphere, and as geohazard. In: Martinelli, G., Panahi, B. (Eds.), Mud Volcanoes, Geodynamics and Seismicity. IV Earth and Environmental Sciences, 51, 77–87. NATO Science Series, Springer, pp. 29–34.

Milkov, A.V., 2010. Methanogenic biodegradation of petroleum in the West Siberian Basin (Russia): significance for formation of giant Cenomanian gas pools. Am. Assoc. Petrol. Geol. Bull. 94, 1485–1541.

Mizobe, K., 2007. Geochemical Characteristics of Natural Gases from Mud Volcanoes in Tokamachi City, Niigata Prefecture. Master Thesis, Graduate School of Science and Engineering, Yamaguchi University.

Moriizumi, J., Liu, W., Kawai, S., Yamazawa, H., Iida, T., 2007. $^{14}CO_2$ emission from the ground surface in a Japanese forest. In: International Symposium on Radiometric Dating Studies – Frontier of Technical development and Application of CHIME and AMS 14C Dating Methods, 15–17 January 2007, Nagoya University, Japan.

Morner, N.A., Etiope, G., 2002. Carbon degassing from the lithosphere. Global Planet. Change 33, 185–203.

Onishi, K., Sanada, Y., Yokota, T., Tokunaga, T., Mogi, K., Safani, J., O'Neill, A., 2009. Investigation of subsurface S-wave velocity structures beneath a mud volcano in the Matsudai–Murono District by surface wave method. J. Geogr. 118, 390–407 (in Japanese with English abstract).

Pallasser, R.J., 2000. Recognising biodegradation in gas/oil accumulations through the $\delta^{13}C$ compositions of gas components. Org. Geochem. 31, 1363–1373.

Rhakmanov, R.R., 1987. Mud Volcanoes and Their Importance in Forecasting of Subsurface Petroleum Potential. Nedra, Moscow (in Russian).

Schoell, M., 1983. Genetic characterization of natural gases. Am. Assoc. Petrol. Geol. Bull. 67, 2225–2238.

Shinya, T., Tanaka, K., 2005. Mud volcanoes in Matsudai, Tokamachi city, Niigata Prefecture. J. Japan Soc. Natural Disaster Sci. 24, 49–58 (in Japanese with English abstract).

Spulber, L., Etiope, G., Baciu, C., Malos, C., Vlad, S.N., 2010. Methane emission from natural gas seeps and mud volcanoes in Transylvania (Romania). Geofluids 10, 463–475.

Stadnitskaia, A., Ivanov, M.K., Poludetkina, E.N., Kreulen, R., van Weering, T.C.E., 2008. Sources of hydrocarbon gases in mud volcanoes from the Sorokin Trough, NE Black Sea, based on molecular and carbon isotopic compositions. Mar. Petrol. Geol. 25, 1040–1057.

Sun, C.H., Chang, S.C., Kuo, C.L., Wu, J.C., Shao, P.H., Oung, J.N., 2010. Origins of Taiwan's mud volcanoes: evidence from geochemistry. J. Asian Earth Sci. 37, 105–116.

Suzuki, K., Tokuyasu, S., Tanaka, K., 2009. Undergound structure of mud volcanoes in Tokamachi city, Niigata Prefecture determined by electromagnetic exploration, and geographical and geological surveys. J. Geogr. 118, 373–389 (in Japanese with English abstract).

Takeuchi, K., Yoshikawa, T., Kamai, T., 2000. Geology of the Matsunoyama onsen district with geological map at 1:50,000. Geol. Surv. Japan (in Japanese with English abstract).

Tomaru, H., Lu, Z., Fehn, U., Muramatsu, Y., 2009. Origin of hydrocarbons in the Green Tuff region of Japan: ^{129}I results from oil field brines and hot springs in the Akita and Niigata Basins. Chem. Geol. 264, 221–231.

Urabe, A., Tominaga, T., Nakamura, Y., Wakita, H., 1985. Chemical composition of natural gases in Japan. Geochem. J. 19, 11–25.

Waseda, A., Iwano, H., 2008. Characterization of natural gases in Japan based on molecular and carbon isotope compositions. Geofluids 8, 286–292.

Xu, H.L., Shen, J.W., Zhou, X.W., 2006. Geochemistry of geopressured hydrothermal waters in the Niigata sedimentary basin, Japan. Island Arc 15, 199–209.

Yang, T.F., Yeh, G.H., Fu, C.C., Wang, C.C., Lan, T.F., Lee, H.F., Chen, C-H., Walia, V., Sung, Q.C., 2004. Composition and exhalation flux of gases from mud volcanoes in Taiwan. Environ. Geol. 46, 1003–1011.